Daresbury Laboratory

PROCEEDINGS OF THE 4TH EUROPEAN WORKSHOP ON DIAGNOSTICS AND INSTRUMENTATION FOR PARTICLE ACCELERATORS

Queen Hotel, City Road, Chester, UK

16-18 May 1999

Edited by B. G. Martlew
& R. J. Smith

This, the fourth European Workshop on Beam Instrumentation and Diagnostics for Particle Accelerators (DIPAC) was held at the Queen Hotel, Chester in The UK from 16^{th} to 18^{th} of May, 1999. This year the Workshop was sponsored and organised by Daresbury Laboratory, part of the Central Laboratory of the Research Councils. Daresbury is the home of the UK's National Synchrotron Radiation Source (SRS). With guidance from a multi-laboratory programme committee from locations across Europe, the DIPAC workshops are held to encourage and assist the exchange of experience and ideas amongst the European accelerator diagnostics and instrumentation community.
Over 100 Participants from Europe, Eastern Europe and America took participated in the workshop. The format consisted of a mixture of invited, contributed, oral and poster presentations, with discussion groups for popular specialist areas of discussion. An industrial exhibition was also included with the poster sessions, used by many as discussion area to review the latest techniques.
These proceedings include the papers for the invited oral presentations, the contributed presentations, the oral presentations and posters in that order. An accompanying CD, which will follow these proceedings will contain the information within these proceedings and also the overheads used during presentations. It is intended to include some audio reproduction of the presentations also.

At the time of compiling these proceedings, Daresbury Laboratory is under threat due to a pressure for change in the UJ's laboratory system. As you know, the SRS at Daresbury was the world's first machine dedicated to the production and use of synchrotron radiation (first user experiments in 1980/81) for users. It, and the staff here at the laboratory have worked diligently to operate, maintain and upgrade the SRS to remain competitive amongst other newer and better machines, coming on-line throughout the world since it first became operational. The efforts of the staff to provide the best source possible was underlined by the awarding of the Nobel Prize for Chemistry to Dr John Walker of the Medical Research Council's Laboratory of Molecular Biology in Cambridge, and a user of the Protein Crystalograpphy facility at Daresbury.
As professionals, we realised that the SRS needs replacing, so we started to work on designs for replacing the SRS with a source worthy of our users requirements. We listened to what they wanted and duly produced schemes and plans for a new synchrotron, the name of which we now know and love, DIAMOND. Over the last 10 years, the expert staff here at Daresbury have planned and designed DIAMOND to come up with a design that satisfies our users into the next millennium. Importantly, this would be co-locate alongside the SRS to ensure that it was fully dupported during the DIAMOND build to meet requirements for no 'dark' period. Through all this time, we have had the full support of our user communities, our local councils who have already granted planning permission, and the North West regional development agency. Finally after our 10 years of quiet work on the project, we received the announcement that the political will and the funding was there to make our DIAMOND a reality. A once in a lifetime opportunity for most, to make a significant contribution to the nations cultural and scientific wealth, to build a machine and to restate the ability of the Daresbury staff to produce a world class facility like the SRS once was.
At this time, the staff are actively involved in an public campaign to secure DIAMOND at Daresbury, and ensure the future of this world renowned lab. Many DIPAC99 participants have sent letters of support for Daresbury to the UK Government, and on behalf of the staff, I would like to thank you for your support. It means a great deal to us, and the Northwest region of the UK that this laboratory continues to be the UK's synchrotron radiation facility, a site of scientific excellence, a major resource for future scientists and engineers, and an ambassador for the UK.

Rob.Smith. March 2000

DIPAC

bergoz DIPAC'99

4th European Workshop on Diagnostics for Particle Accelerators
16th - 18th, May. The Queen Hotel, Chester, UK.

	Saturday 15 May 1999
	Dear Colleague It is a great pleasure for me to Chair the 4th European Workshop on Beam Diagnostics and Instrumentation for Particle Accelerators, DIPAC'99 and I am pleased to welcome you to Chester. This year the Workshop on Beam Diagnostics and Instrumentation for Particle Accelerators is sponsored and organised by Daresbury Laboratory, part of the Central Laboratory of the Research Councils. Daresbury is the home of the UK's national Synchrotron Radiation Source (SRS), and on Monday 17th there will be a visit and tour of the Laboratory. The Synchrotron Radiation Source (SRS) at Daresbury was the world's first machine dedicated to the production and use of synchrotron radiation (first user experiments in 1980/81). It is a three-stage machine for accelerating electrons, comprising a linear accelerator (an "electron gun"), a booster synchrotron and a storage ring. Here the electrons travel in a vacuum inside a tube around the 96m circumference of the ring and remain stored in orbit producing synchrotron radiation for 10 or 20 hours at a time. Synchrotron radiation is produced at each of the 16 bending magnets and 5 insertion devices in the storage ring. This light is fed to over 30 experimental areas, where researchers select the portion of the spectrum that they need and use it to perform experiments. X-rays will be chosen to investigate the structure of proteins, for example, whilst ultra-violet light will be used for investigations into the fundamental properties of atoms or molecules. The Local Organising Committee has handled the entire organisation, and I am particularly grateful to the Workshop Secretary Sue Waller. Sue and her assistants will be pleased to help with any queries during the workshop. Yours sincerely DM Dykes D.M.Dykes *(Chairman DIPAC'99)*
16:00 19:00	Registration –Conference Desk Reception

	Sunday 16 May 1999
09:00 09:15 09.50 10:00	Registration *Welcome and Opening Presentation* Chairman – D M Dykes *Invited Talk I1 Recent Advances in Synchrotron Radiation and its Applications – D Norman* Conference Photograph *1 invited and 2 contributed talks* Chairman - ***Invited Talk I2 The Role of Diagnostics in the Performance Improvement of SLC – P Raimondi*** Contributed Talks C1. Measurements with a Versatile Test Bench for Commissioning of the New GSI High Current LINAC C2. Determination of Radial ion Beam Profile from The Energy Spectrum of Residual Gas ions accelerated in The Beam Potential
11:15 11:45	Coffee 1 invited and 2 contributed talks Chairman – ***Invited Talk I3 Beam Loss Monitors – G Naylor, ESRF*** Contributed Talks C3. 500 fS Streak Camera for UV-Hard X-Rays in 1kHz Accumulating Mode With Optical -Jitter Free- Synchronisation C4. Bunch Length Measurements in LEP
13.00	Lunch
14:30 15:30 16:00	Posters Posters must be manned from 15:00 to 16:00 More posters this session Coffee **Discussion Groups**
	1. Optical Diagnostics Chairmen- M Ferianis K Scheidt, AN Other 2. Commercial Technology – Chairman - J. Bergoz

	Monday 17 May 1999
09.00	2 invited and 2 contributed talks Chairman – ***Invited Talk I4 Fast Positional Global Feedback – E Plouviez, ESRF*** ***Invited Talk I5 Fast (40 MHz) Comparison of Analogue Signal Processing for BPMs – G Vismara*** Contributed Talks C5. Daresbury SRS Beam Position Feedback Systems C6. Developments and Plans for Diagnostics on the ISIS Synchrotron
10:45	Coffee
11:15	2 invited and 2 contributed talks Chairman – ***Invited Talk I6 Instability Feedback*** ***Invited Talk I7 Fast Bunch Length Measurements – M Geitz, DESY*** Contributed Talks C7. The ELETTRA Streak Camera: System Set-up and First Results C8. Adaptive Optics for The LEP2 Synchrotron Light Monitors
13.00	Lunch
14.00 14.30	Coach to Daresbury Laboratory Visit Daresbury Laboratory The visit will include a tour of the Synchrotron Radiation Source and its facilities. The SRS is a 2 GeV electron storage ring with a 12 MeV Linac and 600 MeV Booster Synchrotron injector system. The visit will also include the new Science Centre which gives examples of some of the science carried out at Daresbury Laboratory.
16.30	Leave Daresbury and return to Hotel
18.30	Coach to Peckforton Castle
19.00	Medieval Banquet
23.00 23.30	Coaches return to Queen Hotel

<table>
<tr><td></td><td colspan="2">Tuesday 18 May 199</td></tr>
<tr><td>09.00

10:45</td><td colspan="2">2 invited and 2 contributed talks
Chairman –

Invited Talk I8 Diagnostics and Controls for Medical Machines –H Eickhoff

Invited Talk I9 Diagnostics in Heavy Ion Machines – P Strehl

Contributed Talks
C9. Luminosity Optimization in DAFNE
C10. Real Time Display of the Vertical Beam Sizes of Beams in LEP, Using the BEXE X-Ray detector and Fast VME Based Computers

Coffee
Posters
(Posters must be manned from 11.00 to 12.00)</td></tr>
<tr><td>12.00</td><td>Discussion groups

1. Precision BPM’s
Chairmen
H Schmickler
K Unger
V Schlott</td><td>

2. Positional Feedback
Chairmen
S.Smith
E Plouviez</td></tr>
<tr><td>13.00</td><td colspan="2">Lunch</td></tr>
<tr><td>14.00

15.15</td><td colspan="2">1 invited talks + 2 Contributed Talks
Chairman –

Invited Talk I10 Diagnostics for Linear Colliders –

Contributed Talks
C11. The OTR Screen Betatron Matching Monitor of the CERN SPS
C12. The Luminescence Monitor of the CERN SPS

Final Presentation and Closing
Chairman – D M Dykes

Invited Talk I11 History of Beam Diagnostics, H Koziol, CERN</td></tr>
</table>

Contents

Invited Talks

Beam loss monitors at the ESRF

B.Joly, U.Weinrich, G.A.Naylor, ESRF, Grenoble, FRANCE

Abstract

The European Synchrotron radiation facility is a third generation x-ray source providing x-rays on a continuous basis. As a facility available to external users, the monitoring of radiation caused by the loss of high-energy stored beam is of great concern. A network of beam loss monitors has been installed inside the storage ring tunnel so as to detect and localize the slow loss of electrons during a beam decay. This diagnostic tool allows optimization of beam parameters and physical aperture limits as well as giving useful information on the machine to allow the lifetime to be optimized and defects localized.

1 INTRODUCTION

Modern synchrotron light sources are being pushed by users to provide higher photon brilliance. This is achieved both by a reduction of the stored beam emittance and by the increase of magnetic fields with short period undulators. The latter requires the close proximity to the beam of the insertion device magnetic poles. At the European Synchrotron Radiation Facility (ESRF), vacuum chambers of internal dimensions as low as 8mm are used with lengths up to 5m. Large amplitude betatron oscillations excited by Touschek, elastic and inelastic collisions in the vertical plane give rise to a loss of particles on the small aperture insertion device vacuum vessels. The push to low emittance increases significantly the contribution to these losses from Touschek collisions. It is important in order to control these losses that they are continuously monitored. Beam loss detectors have been developed at the ESRF which detect the radiation shower produced by the passage of high energy electrons through the vacuum chamber walls. Two types of detector have been developed:

i) Short fast losses during injection pulses and sudden beam losses.

ii) Prolonged beam loss during the decay period of a stored beam.

The former type are required to be very sensitive, whereas the second type should be designed so as to measure linearly very large bursts of radiation.

A good review of the different beam loss detector types is given in [1] and is summarised in table 1.

In all cases care should be taken in the case of a synchrotron light source that the signal detected is not significantly perturbed by the contribution from the background high-energy synchrotron radiation. This may be achieved as in [2] by the coincidence detection on two photodiodes. At the ESRF the higher energy radiation due to the Bremstrahlung of electrons escaping the vacuum chamber is discriminated from the synchrotron radiation by shielding the detector with 10mm thickness of lead and placing the detector on the inside of the storage ring. For the case of the fast detectors, synchrotron radiation is not a problem as they are only sensitive to large bursts from beam losses. A simple detector system is employed using a perspex rod as a scintillator coupled to a high gain photo-multiplier. This method was chosen to allow a large number of detectors to be installed. The average anode current is monitored rather than the count rate of scintillation events. Although in principle scintillation counting should give better linearity over a greater dynamic range, in practice the particle revolution rate and the filling pattern limit the maximum achievable count rate. This maximum rate is different for different filling patterns (eg single bunch and multi-bunch) thus affecting the performance in different filling modes, similarly the maximum count rate during injection is limited to 10Hz by the injection rate. The photo-diode solution although providing a simple solution gave too low a count rate at the locations at which the detectors were to be located. A fast beam loss detector using a 1mm Perspex fibre coupled to a silicon photodiode is also used. Each of the 32 cells of the ESRF storage ring is equipped with one slow beam loss detector and 3 fast beam loss detectors.

Type of Beam loss detector	Advantages	Disadvantages
Long ionisation chamber [7]	Can give position sensitivity	Expensive and complex electronics
Short ionisation chamber [3]	Linear over many decades	Measurement of very low currents is very expensive
Scintillator + Photomultiplier (PM) [6]	Simple and cheap	Long term degradation of scintillator and drift of PM
Pin Photo-diode [5]	Simple and cheap	Limited count rate.

Table 1: Different beam loss detector types.

In practice the slow beam loss detectors have also been useful in detecting injection losses by reducing dramatically the injected current from the linac so as not to saturate the detectors. This latter mode of injection optimisation is particularly important as this operation normally involves injection over very long periods of time and significant accumulated doses around the accelerator structure if the full injection beam current is used.

2 DETECTOR CONSTRUCTION

The construction of the slow detector is shown in figure 1 and the fast beam loss detector in figure 2.

In each case a scintillating Perspex light guide channels part of the scintillations produced by the passage of high energy particles in the medium to a photodetector.

2.1 Slow detector.

A 60cm long, 25mm diameter rod of perspex is used as the scintillator. A high sensitivity visible light sensitive photomultiplier is used to collect the light (Electron tubes device P30CW12 with bialkali photocathode and integrated high voltage supply.). The device is shielded from synchrotron radiation with a 10mm wall thickness lead tube. The anode current from the photomultiplier is amplified in an electronic card outside the tunnel with a gain of 5x. 10^7 V/A. The sensitivity of the device can be adjusted over several decades and set to a calibrated level by introducing a small known light intensity into the top of the device and changing the control voltage to the photomultiplier high voltage supply.

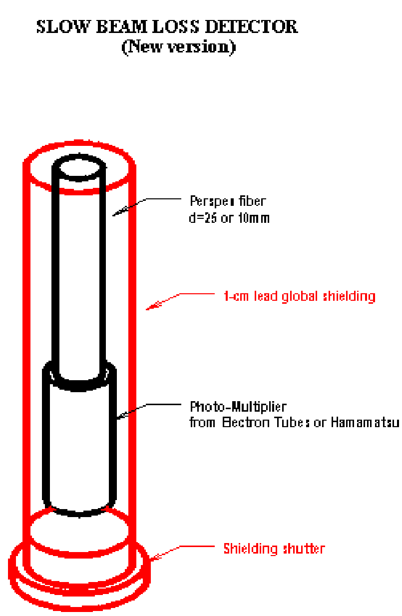

Figure 1: Slow beam loss detector

2.2 Fast Detector

A 1mm diameter Perspex fibre 60cm long is coupled to a photodiode. The fibre is shielded in a 2mm-wall thickness lead tube. The photodiode signal is directly amplified with a gain of 10^8 V/A. This amplifier is connected using a single co-axial cable to the outside of the tunnel. An electronic card outside of the tunnel is used to provide a supply voltage bias to the connecting cable and receive the incoming pulse. This electronic card gives a further gain of about 20 with a rise time of about 50ms and a fall time of about 2 seconds.

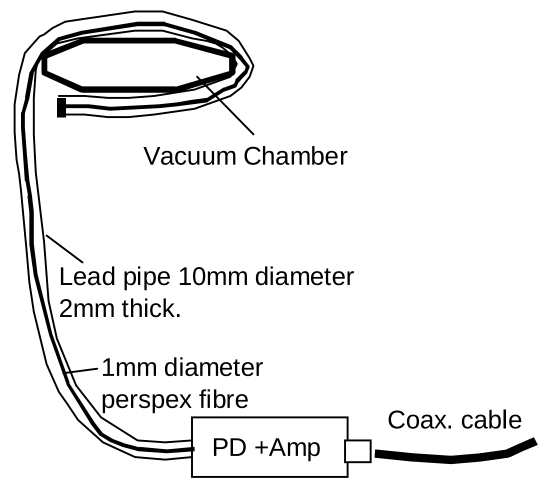

Figure 2: Fast beam loss detector

The signals from the two detector types are available as slowly varying analogue signals, which are read by an analogue to digital converter and processed for display and storage on the control system terminals in the control room. The system is summarised in figure 3.

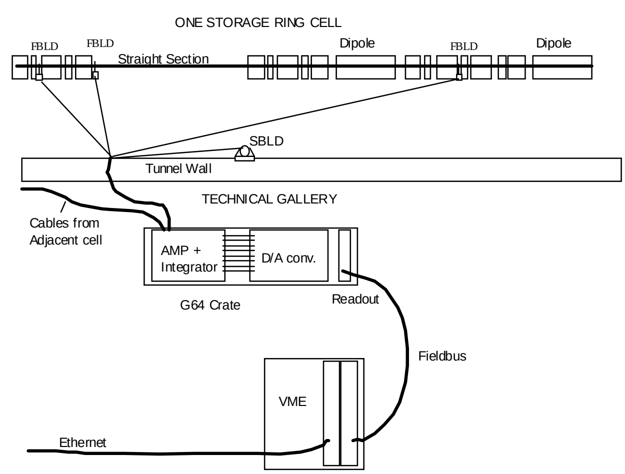

Figure 3: Acquisition system

The signals from all the detectors are summarised in a graphical application, which shows the time variation of all the detectors (figure 4).

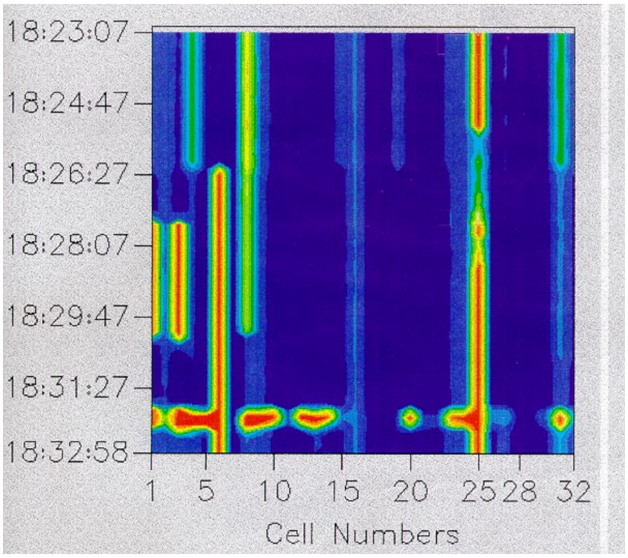

Figure 4: Graphical display of a class of detectors

3 USE OF BEAM LOSS DETECTION AT THE ESRF

Some of the current applications of the beam loss detectors are given below.

3.1 Detection of defective components.

The lifetime may be suddenly reduced by a local reduction in physical aperture due for example to the deformation of an RF finger. This will become immediately apparent on the slow detectors in the following cells or on the fast detectors when trying to re-inject.

3.2 Detection of poor vacuum

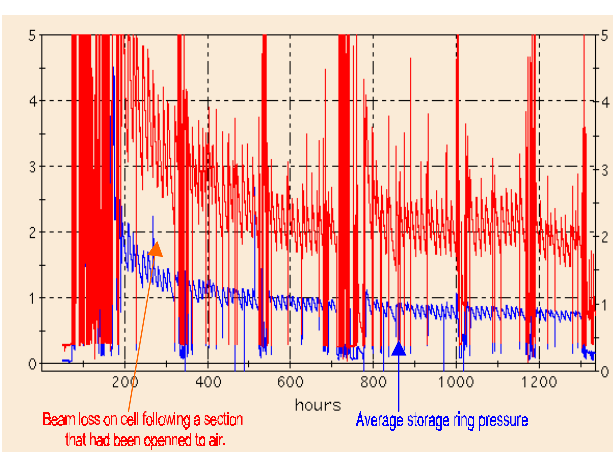

Figure 5: Vacuum conditioning after a shutdown

Following interventions on vacuum on the storage ring, the vacuum improves from a relatively poor value, due to conditioning, over several weeks. This is evident from the lifetime and beam losses on straight section vacuum vessels (figure 5). A growing leak in a cell may be detected by increases in the losses on the insertion device vessel in the following cell (figure 6).

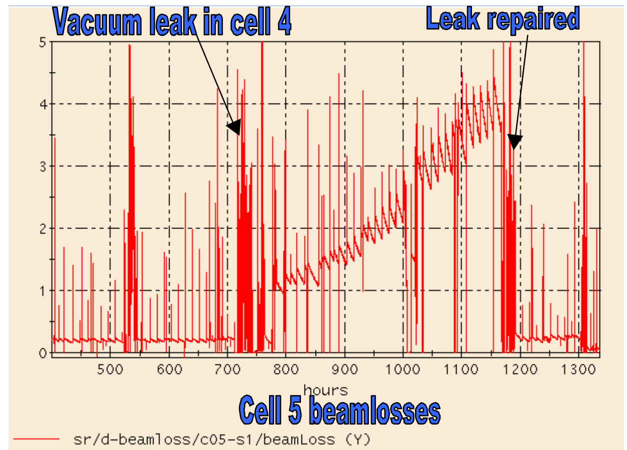

Figure 6: Indication of vacuum problems

3.3 Optimisation of scraper settings

The losses on the small vacuum vessels are a problem due to increased Bremstrahlung on the beam line and due to activation of the vacuum chamber. The losses can be dramatically reduced and concentrated at the position of the scraper by optimising its position (figure 7).

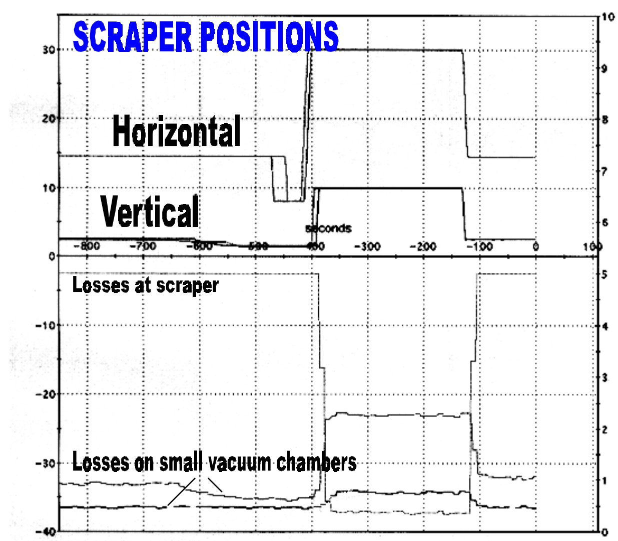

Figure 7: Scraper optimisation

3.4 Detection of tuning problems.

Increased loss of particles may occur due to poorly corrected resonances which may become apparent due to insertion device gap dependent tune changes. This affects the lifetime but is also very visible as increased losses at the small gap vacuum chambers. The fast response of the signal allows rapid optimisation (figure 8).

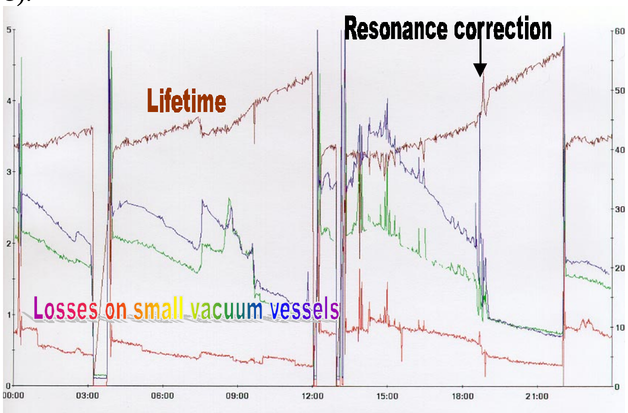

Figure 8: Detection of tuning problems.

3.5 Injection optimisation.

The requirement of minimising the total number of lost electrons in order to satisfy radiation safety limits implies that injection optimisation should be done with very low injected currents. The use of current transformers to measure the efficiency becomes very noisy, whereas the sensitive signals from the slow beam loss detectors around the storage ring allow the losses to be quickly and easily minimised.

4 SUMMARY

Fast and slow beam loss detectors are installed all around the ESRF storage ring. The slow beam loss detectors are very useful as a diagnostic in monitoring various machine defects including losses during injection.

5 ACKNOWLEDGEMENTS

We would like to thank the computer control group and the digital electronics group for their work in setting up the data acquisition system and Paul Berkvens for his advice on radiation screening appropriate for the conditions in the storage ring tunnel.

REFERENCES

[1] "Beam loss detection" K.Wittenburg Proc 1st DIPAC 93 CERN PS/93-35 (DB) pp11-20
[2] W.Bialowans, F.Ridoutt, K.Wittenburg DESY "Electron beam loss monitors for HERA" EPAC 1994
[3] M.Plum, D.Brown, A.Browman, R.Macek "Ion-chamber beam loss monitor system for the Los Alamos Meson Physics facility PAC 1995
[4] O.Kaul, B.Sarau, K.Wittenburg DESY "Fast measurement of lifetime changes and beam losses in DORIS by the use of Bremstrahlung from a collimator"
[5] "Monitoring Beam losses at the Synchrotron Radiation Elettra facility" ST/M-TN-94/4
[6] J.R.Parker et al "A beam spill monitor for LAMPF" IEEE Trans. On Nucl. Science Vol 20 3 (1973) p 596-598
[7] J.Rolfe et al "Long ionisation chamber system for the SLC" SLAC-PUB-4925, (1989)

FAST POSITIONNAL GLOBAL FEEDBACK FOR STORAGE RINGS

E. Plouviez. ESRF, Grenoble, France

Abstract

Stability of the closed orbit of a storage ring is limited by the stability of the components defining this orbit: magnets position and field values. Measurements of the variation of the stored beam orbit with respect to a nominal orbit and application of orbit correction derived from these measurements can reduce these distortions. The subject of this talk is the implementation of such correction at high frequencies (up to about 100Hz) using global correction schemes.

The basic theoretical aspects of the problem will be presented:

-Global versus local scheme

-Feedback loop dynamics.

The technical problems associated with the implementation of such systems will also be addressed:

-BPM and correctors design

- Feedback loop electronic design

1 INTRODUCTION

Most modern lepton machines have emittances of the order of 10nmrad and 1% coupling. In order to offer optimum performance to their users, storage rings must achieve excellent orbit stability, especially at the source points on synchrotron radiation sources or interaction points on colliders. The requirements on this orbit stability are usually specified in terms of tolerated orbit centroid motion with respect to the beam size. Depending on the local value betatron function, the beam sizes and divergences are 10µm and 1µrad or less. So, in order to take advantage of such small beam size, we aim at controlling the orbit with micron accuracy at these specific locations. In the case of light sources the problem is more demanding due to the greater number of source points spread all over the ring compared to the few interaction points of colliders. The reduction of the orbit distortion in the rest of the machine is also mandatory in order to achieve these emittance figures, to obtain a good lifetime and to protect the vacuum chamber against the synchrotron radiation thoug in the latter case the stability requirements are slightly less stringent [1]. Various sources of perturbation of the closed orbit can be found on most machines [2][3]. Below .1Hz we will find ground motion due to seasonal or tidal causes and thermal effects. They will be dealt with by machine realignements (seasonal effects) and beam position measurements followed by closed orbit corrections using correctors dipoles magnets[4]. Between .1Hz and 100Hz, the perturbation will come from the ground vibration transmitted by the magnet girders, the water circulation, the AC power distribution. A typical spectrum of these perturbations is shown on figure 4. These additional fast sources of perturbation should be minimised at their source, but the residual orbit perturbation level can still be above 1 µm, even on well designed machines[2][3]. This level is not high enough to spoil the machine tuning but can increase the apparent emittance for the users. These fast residual perturbations can also be reduced by closed orbit corrections but the repetition rate of these corrections poses specific challenging problems for the orbit control.

2 CLOSED ORBIT DISTORTION AND CORRECTION

2-1 Principle

Variations of the position of quadrupoles or sextupoles, tilts of the dipoles orientation, fields fluctuations, will result in the addition of angular kicks to the nominal dipolar fields of the ring. These kicks are compensated by a change in the closed orbit in order to obtain a new closed orbit, where the perturbation kicks effect is compensated by the kicks produced by the offset of the new perturbed beam closed orbit with respect to the quadrupole center as shown on figure 1. To perform a closed orbit correction an orbit measurement is done, using a set of e^- (or photons) BPMs and a set of correction kicks is applied to the beam using correctors dipole magnets in order to cancel the difference between the reading and the desired value.

2-2 Global correction

With this scheme, an adequate number of M BPMs, spread all over the machine are used to measure the orbit distortion. The vector δd of the M beam position offsets is used to calculate a correction vector $\delta\theta$ containing the values of N correction kicks using a M*N correction matrix R^{-1}. $R^{-1}$is deduced from the N*M response matrix R formed by the response of the M BPMs to individual correctors unit kicks. R can be obtained from a theoretical model or from measurements. The calculation of the correction matrix R^{-1} can be done using various methods; The most common method seems to be the Singular Values Decomposition (SVD)[1]; the SVD method is very flexible and does not require R to be square. The adequate number and location of the BPMs and correctors are function of the lattice design, of the space available on the machine, and of the quality of the correction needed. The number of BPMs and correctors used can be very large (224 BPMs and 96 correctors at ESRF for a 32 cells Chassman-Green lattice). However, due to the quasi periodic pattern of a beam distortion due to random kicks, a significant reduction of a distortion can already be obtained using a much smaller number of BPMs and correctors. A rule of thumb is that using a number of BPMs and correctors equal to the tune number of the plane considered, you can achieve a reduction by a factor of 3 to 5 of most random orbit distortions as shown on figure 1

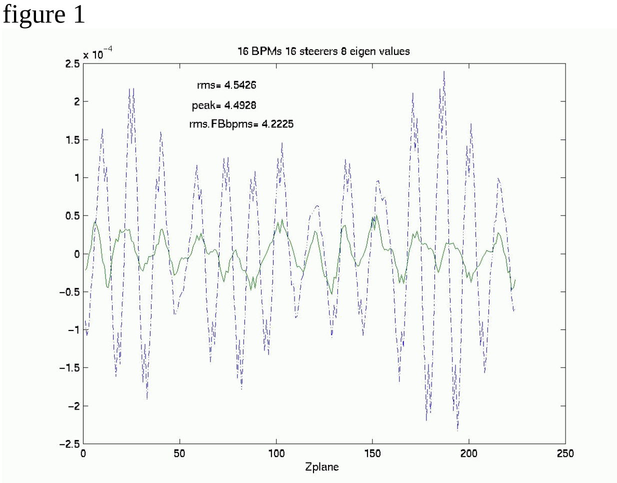

Figure 1: correction of a random vertical orbit distortion on the ESRF lattice with 16 BPMs and 16 correctors.

2-3 Local correction

Since the orbit stability is particularly important at some discrete locations like insertion devices or interaction points, the correction can be aimed at suppressing the orbit distortion only at these location using a closed bump, leaving the rest of the machine uncorrected. Such a scheme requires two BPMs for the orbit distortion measurements in a straight section and four correctors for the local cancellation of both position and angle and the bump closing.

3 FAST CORRECTIONS

3-1 Feedback loop basics

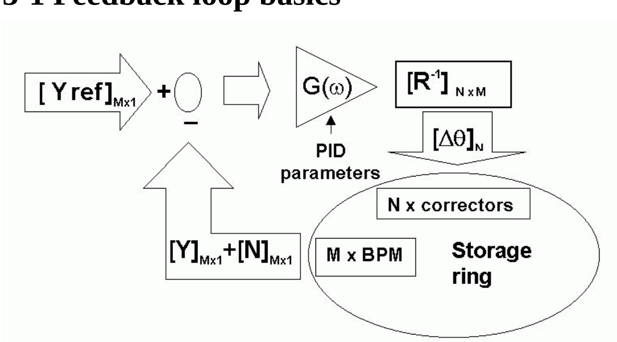

Figure2: Block diagram of a feedback loop orbit

If we control the orbit distortion with the feedback loop of the figure 2, corrected orbit will be given by :

$$\delta c = (\delta d + G.N)/(1+G)$$

with:

Y= measured orbit vector,
Yref = reference orbit vector
δd , δc = (Y-Yref) without and with feedback
G = gain of the corrector, N= noise of the BPMs

A G value as high as possible seems to offer the largest $\delta d/\delta c$ damping potential. But if τ, delay in the loop, is not null, at some frequency the phase due to this delay will revert the sign of the correction and the system will be unstable. The delay τ will come from the sampling and multiplexing process in the BPMs, the correction processing time (in a digital correction system) and from the rise time of the correctors field (eddy currents and power supplies rise time). A very popular way to design a stable and efficient corrector is to use a PID corrector [5]. In a PID corrector, G response is a combination of a proportional response with a gain P, integral response with a gain I and derivative response with a gain D; in this way, an very large gain is achieved at low frequencies, the stability of the loop is improved by the proportional part near the cutoff frequency fc, and the derivative gain can improve the step response if necessary. This corrector can be implemented in an analog design as well as using a DSP. The limiting factors in the choice of the I gain which sets the cutoff frequency will be the noise of the BPMs and the delay of the loop. If the noise spectral density of the BPMs is too high, this contribution to δc, integrated up to the cutoff frequency can be higher than the initial orbit distortion, spoiling the effect of the correction.

3-2 Optimisation of the feedback parameters

Let us roughly estimate acceptable values for fc, N(ω) and τ with the motion spectrum of the figure 4: To be useful, a fast feedback system should be able to damp the orbit distortions up to 50Hz, so fc=150Hz at least to have a damping of 3 at 50Hz and τ must be less than 1/(10.fc) = .6ms to have a stable loop with this fc value; and if we aim at a closed orbit reduction below 1µm, the BPMs noise contribution should stay below .3µm over this 150Hz span which requires a noise spectral density N(ω) below 20nm/√Hz. The damping actually achieved will also be function of the spectrum of the initial orbit distortion. For instance , with the spectrum of the figure 4, observed at ESRF, a damping of 3 over the 0 to 200 Hz span could be expected on the initial 2µm wide band distortion at the BPM location with the parameters fc, τ, N(ω) chosen above, assuming a perfect static correction. No increase of the numbers of BPM and corrector will make up for the limitation of the correction accuracy due to the bandwidth limitation, so this figure will be used , in the case of a global feedback, to set the optimum number of BPM and corrector to be used in the dynamic correction. In our case a static damping of 3 to 5 is adequate.

3-3 Local and global scheme comparison for fast corrections

For a good performance of a machine in term of emittance, lifetime, resonance limitation, a slow orbit correction system based on a large number of BPMs and correctors is needed (see 1). The rate of the corrections possible with such a large number of components will be limited (especially by the correctors bandwidth as explained in 4-3). Additional corrections at a higher rate can be needed in a limited number n of discrete locations, for instance at the emission points of a light source. If n is small, the implementation of N additional local correction systems (using 2 x n BPMs and 4 x n correctors) can be the solution. However if n becomes large a fast global scheme using a limited number of dedicated wide band BPMs and correctors is a better solution for the following reasons:

1- The perfect closure of a local bump at high frequency is difficult to achieve due to the different dynamic responses of the four different correctors; so the operation of too many fast local feedbacks will eventually result in some increase of the orbit distortion outside of the bumps and eventually to unstable loops behaviors due to cross talk.

2- As shown in 2-2 and 3-1, the same damping is achieved by a global feedback on the whole ring, using much less BPMs and correctors than local feedbacks, with the same efficiency.

Conclusion: The adequate solution to extend the orbit corrections in frequency above a few Hz is to implement an additional system using a limited number of wide band BPMs and correctors; depending on the number of locations where the correction is needed, this system will be a local or a global feedback.

4 TECHNICAL ISSUES

4-1 General guideline

The number of component (BPMs, correctors, control interfaces) needed for the fast corrections is only a fraction of the number needed for the slow corrections. If the performance required for the fast corrections components cannot be achieved by the slow corrections components without extra cost or compromise on the performance level (principally speed and BPMs noise spectral density), it will be more efficient to implement specific components for this application. If adopted, this separation will require a de coupling of the two systems; different decoupling schemes are possible[1]. The choice of a frequency separation of the slow and fast system can ease the design of the BPMs and correctors as explained below.

4-2 BPMs

4-2-1 Electron BPMs

I will give below examples of difference in the design optimisation of a DC slow BPM and a wideband AC BPM.

1- For slow correction, the wide band spectral noise density of the BPMs output signal is not a major concern to achieve a good resolution, since it is possible to filter this noise with a low pass filter; for a fast BPM, this filtering cannot be applied and this noise density must be kept as low as possible. On the other hand linearity of the position measurements versus beam current is a major concern for DC position measurements; it requires to operate the analog components of the pick up signals processing electronics far enough from their saturation level, which is not the best way to lower the signal to noise ratio at the BPM output. This linearity concern is less important for AC measurements used in a closed loop feedback. The multiplexing scheme with single heterodyne RF receiver is very popular for the processing of signals of the BPMs electrodes. It has the advantage of an easy and accurate absolute DC calibration, good DC measurements reproducibility in a wide current dynamic range and is cheap to implement. These qualities are very much appreciated for DC orbit measurements. However, compared to non multiplexed schemes, its noise figure is at least 6 dB worse, the level of the signals to process in the RF mixer is higher, and the multiplexing frequency must be very carefully chosen in order to avoid unwanted aliasing of high frequency signals (revolution frequency, synchrotron and betatron oscillation frequencies).

4-2-2 Photon BPMs

Due to the smaller space between their electrodes, and to the high synchrotron radiation power available, the photon BPMs can achieve a lower noise spectral density for wide band position measurements than electron BPMs. Dipole emission can only be used for vertical position mesurements; insertion device emission can be used in both planes; but their use in electron beam orbit local correction systems in straight sections is impaired by the pollution of the photon signal of the insertion device by the adjacent dipoles emission. However, for a global vertical orbit correction system, photon vertical BPMs using the dipoles emission would be very good candidates compared to electron BPMs; the high vertical β value at the dipole source point is an advantage, and the resolution of electron BPMs in the vertical plane can be at the limit of what is required on some recent storage rings.

4-3 Correctors magnets and power supply

Given the low delay and high bandwidth required, the correctors must be air cored magnets installed on high resistivity wall vacuum chamber sectors (thin stainless steel wall for instance). Air cored magnets are bulkier than iron core magnets, so their number should be limited to what is required for the fast corrections. If these magnets are used only for the corrections of vibrations without delivering DC currents, this will also relax the power requirements for their power supply. To drive an inductive load, with a flat frequency response and a low delay is not easy. Two solutions are possible: to damp the inductance with a low value resistor and to use an over dimensioned voltage power supply, or to use a PWM switched current power supply[6], with a current control loop optimised for the magnet load. Values of components used on a system in operation at ESRF are given in 4-2.

4-5 Control system

Even with a moderate number of BPMs and correctors (16 BPMs and 16 correctors on the ESRF described below), the calibration and tuning of a loop implemented with analog controllers would be impossible. So the control of the feedback will be done using a digital signal processing technology. CPU boards and programming tools adequate for this application are widely available due to the extensive use of DSPs in the industry. The signals transmission between the BPMs , the correctors and the controller can be analog or digital; the choice will depend mostly on the size of the machine; a popular device for the digital data transfer for this application is the reflexive memory [7][8] but others approaches are possible [9].

5 AN EXEMPLE OF DESIGN: THE ESRF VERTICAL GLOBAL FEEDBACK

5-1 Orbit correction requirement

The ESRF storage ring is a high brilliance source with low emittance values (ε_x =4.10^{-9}m.rad and ε_z=4.10^{-11} m.rad) and generates Xray from insertion devices installed on 5 m long straight sections. With β_x=36m and β_z=2.5m in the center of the high horizontal beta straight sections, the rms beam sizes at the BPM locations on both ends of the straight sections are σ_x= 380µm and σ_z= 14µm. The parasitic motion of the beam due to slow drifts or high frequency vibrations of the quadrupoles support girders must be kept at low enough values to avoid spoiling this emittance figure. We observe two kinds of motions: very slow drifts and vibrations at 7Hz, 30Hz and 60Hz as shown on the figure 4. The amplitude of these vibrations at the ends of these straight sections is 12µm rms horizontally and 2µm rms vertically. The slow drifts are corrected every 30seconds by a global correction method using the measurements made over the whole machine by the 224 BPMs of the closed orbit measurement system [4]. These vertical vibrations are smaller compared to the horizontal vibrations, but not negligible compared to the incoherent motion due to the vertical emittance. We have added a vertical fast global orbit correction system to damp these vibrations in the vertical. In the design of this system we have used the approach exposed in this talk.

5-2 System configuration

Since the vertical tune value is 14.39 this system uses 16 BPMs and 16 correctors to correct the orbit at a 4.4KHz rate in order to provide an extra damping in the 10^{-2} to 200Hz frequency range. The layout of the system is shown on figure 3.

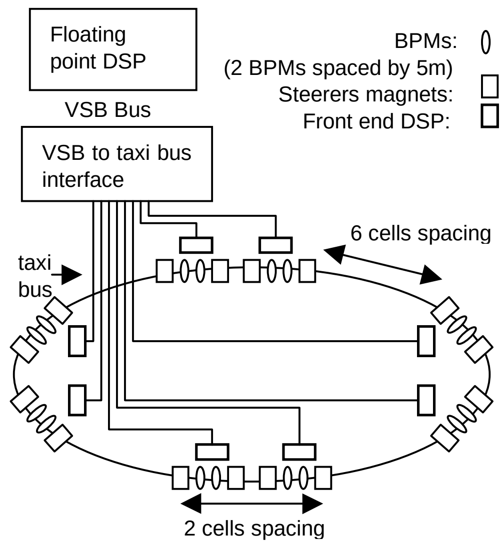

Figure 3: Layout of the ESRF global feedback system.

5-2-1 Beam position measurement

The beam positions are measured using capacitive electrodes installed at both ends of the straight section.. The electrode signals are detected with an RF multiplexing system; as pointed in 4-2-1 it is easy to implement though it does not have the lowest potential noise figure. However special attention has been paid to the noise of the electronics allowing to achieve a resolution of 20nm/√Hz over the full operation intensity range from 5mA (in single bunch) to 200mA . Special features of these BPMs are: impedance matching of the electrodes by resonant RF transformers, 4.4KHz multiplexing synchronized with the beam revolution, low noise amplifiers and gain control [9].

5-2-2 Orbit corrections

The correction kicks are produced by sixteen air coil steerer dipoles. The stainless steel vacuum chamber at the steerers location is 2mm thick giving the beam a flat frequency response to the magnet field up to 1KHz; the steerers inductance is 40mH. The steerers are powered by wide band power amplifiers and are able to produce 4µradian/A kicks in a 1KHz bandwidth. The amplifiers are voltage controlled bipolar PWM current mode switched power supplies developed at ESRF. They can produce a peak voltage of 100V and a peak current of 5A. The total contribution of eddy currents and power supply rise time to the loop delay is .25ms.

5-2-3. Digital signal processing hardware

The digital signal processing is implemented as shown on figure 3. The corrections are computed at a 4.4 KHz rate by a LSI DBV44 VME board housing a TI C40 floating point DSP and a VSB bus. The datas are transmitted on eight optical digital data links to eight front-end VME crates developed at ESRF [11]; these crates carry IP modules format DACs and ADCs, and are controlled by front end fixed point AD2600 DSP for the data preprocessing and transfer control. The data transfer at both ends of the optical fibers is done with "taxi bus" data link drivers implemented on IP modules also developed at ESRF. The data acquisition and transfer to and from the main DSP takes 100 µs leaving 125 µs for the main algorithm execution. The VME bus itself is not used for any fast data transfers.

5-3 Correction calculation

With the 16 positions we calculate a correction vector using the matrix of the response of the feedback BPMs to each steerer, inverted using the SVD method. We use 8 eigen vectors. This correction vector is used to compute the actual correction applied to the beam using the previous correction values and a proportional integral iterative algorithm (PID type). In addition, the correction is cancelled at very low frequency (10^{-2} Hz) to decouple the fast orbit correction from the slow orbit correction. The repetition rate of the BPMs measurements and correction calculation is 4.4 KHz, a convenient sub harmonic of the 355 KHz beam revolution frequency. These dynamic parameters have been chosen as explained in 3-1: We aim at a cut off frequency fc=150Hz; this fc value demands a total delay τ of less than .6ms. The delay in the correctors is .26ms. We perform the position acquisitions, correction calculation and apply the correction inside a 4.4 KHz clock period. The delay due to the multiplexing in the BPMs is τ_{mux}=.175ms and the delay due to the correction computation and data transfer time is τ_{cpu} =.225 ms so the total loop delay is τ = .65 ms .

5–4 Correction effect

The figure 4 shows the spectrum of a dipole emission beam motion due to fast orbit distortions measured 25 m away from the source with feedback off and on. Without feedback, the main perturbation is a 7 Hz line due to the mechanical resonance of the dipole girders as pointed out in 1. With the feedback on, as shown in figures 4, the amplitude of this line is reduced by 10 dB and the wide band motion integrated over 140Hz is reduced by 6 dB.

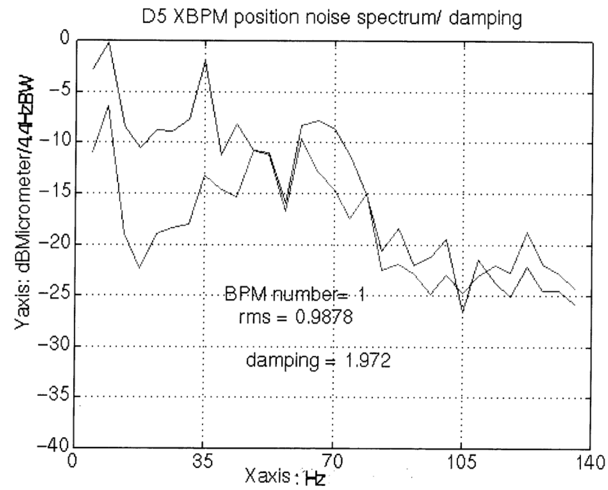

Figure 4: spectrum of the ESRF beam vertical motion with feedback off and on (5dB/div, 140Hz span)

6 CONCLUSION

The principle of the fast orbit corrections is not original but the efficiency of this scheme at high frequency and on very small orbit distortion requires a careful optimisation of the performances of its different components. The key parameters in such a system according to our experience are the noise of the BPMs, the bandwidth of the correctors, the number and location of the BPMs and correctors and the delay in the loop.

REFERENCES

[1] C.J. Bocchetta, Sinchrotrone Trieste, Trieste, Italy, “Review of orbit control”, EPAC,(1998).

[2] G. Decker, ”Fundamental limits on Beam stability at the APS”, Beam Instrumentation Workshop, SLAC, (1998)

[3] L. Zhang, “Vibration at the ESRF” EPAC,(1996)

[4] L. Farvacque, “Beam stability”, CERN accelerator school on synchrotron radiation sources and free electron lasers (1996)

[5] J. Proakis, D. Manolakis, “Digital Signal Processing” New York, Mac Millan Publishing Company (1992).

[6] M. BROWN “Power supply cookbook” Butterwort – Heineman (1994)

[7] J.A. Cawardine and F.R. LenksZus, “Real time orbit feedback at the APS”, Beam Instrumentation Workshop, SLAC, (1998)

[8] C.H. Kuo et al “Digital global orbit feedback system developing in SRRC”, PAC, (1997)

[9] J.M..Koch, E. Plouviez, F. Uberto “A fast global feedback system to correct the beam position deviation in the ESRF storage ring’, EPAC , (1998)

[10] J.M. Koch “Use of DSP Based Systems for the ESRF Storage Ring Diagnostics and Beam Position Feedback”, DIPAC 97, Frascati,1997.

THE COMPARISON OF SIGNAL PROCESSING SYSTEMS FOR BEAM POSITION MONITORS

G. Vismara – CERN - Geneva 23- Switzerland

Abstract

At first sight the problem of determining the beam position from the ratio of the induced charges of the opposite electrodes of a beam monitor seems trivial, but up to now no unique solution has been found that fits the various demands of all particle accelerators.

The purpose of this paper is to help instrumentalist in choosing the best processing system for their particular application.

The paper will present the different families in which the processing systems can be grouped.

A general description of the operating principles with relative advantages and disadvantages for the most employed processing systems is also presented.

INTRODUCTION

Beam position monitors (BPM) can be found in every accelerator.

BPM systems have largely evolved since the early days, from the simple scope visualization of coaxial multiplexed P.U. signals into a very complex system. These systems are now capable of digitizing individual bunches separated by a few tenths of ns, with spatial resolution in the micron range, while the resulting orbit or trajectory collected from several hundred planes can be displayed in a fraction of second.

To obtain such a performance the processing electronics have to be optimized to the machine and beam parameters.

A unique solution capable of covering all the possible combinations with satisfactory results seems almost impossible to realize. This is the reason for the wide spectrum of signal processing in use today.

The BPM applications are not only limited to Orbit & Trajectory measurements, but can perform static and dynamic beam parameter measurements by exploiting the large amount of data collected and stored in their memories[i].

Turn-by-turn measurement can give information on; Betatron oscillation, transfer function, phase advance, optics checks, local chromaticity, etc.

The high resolution allows for energy calibration and machine impedance measurements.

The BPM is also employed in feedback systems to stabilize the beam and even as beam position interlock[ii].

These applications are much more performance demanding than a simple position measurement.

1. PROCESSING SYSTEM FAMILIES

The various signal processing systems can be grouped into different families according to the employed techniques. At least three different criteria can be used to group them.

1.1 Signal recombination

Four main categories are nowadays mainly employed:

- ***Individual signal treatment:*** The maximum signal information is still available, therefore a wide-band processing is the most suitable. Due to a very large Gain-Bandwidth, it offers a limited dynamic range.
- ***Time MPX***: Electrode signals are sequentially time-multiplexed and processed by a single electronic system. It offers an excellent long-term stability but cannot perform turn-by-turn measurements.
- ***Δ/Σ***: The individual signals are immediately converted by the use of hybrids into Δ and Σ. This offers excellent center position stability but requires switchable gain amplifiers.
- ***Passive Normalization***: The signal's amplitude ratio is convert into a phase or time difference. It is amplitude independent but loses the intensity information.

1.2 Normalization processes

The Normalization is an analog process that will produce a signal proportional to the position information that is independent of the input signal level. Three conditions apply to all normalization processes: 1) The intensity information is lost. 2) The digitization requires a smaller number of bits. 3) No gain selection is required.

Two active and two passive techniques are actually employed.

- ***Constant Sum:*** The Normalization is obtained by keeping constant the sum of the two electrode signals using AGC amplifiers. This approach is only valid for the time MPX process where the signals exploit the same amplification chain.
- ***Logarithmic conversion***: Since the ratio of the logarithm of two signals is equal to the difference of the logarithm, the signals can be converted by logarithmic amplifiers to give the normalized signal as the difference of the output. It offers a large dynamic range, but limited linearity.
- ***Amplitude to time:*** This is based on the sum of a direct and a delayed signal coming from the two

electrodes. The zero crossing of the sum signal varies with time proportionally to the signal ratio, and hence to the position. It offers large bandwidth but is limited to bunched beams.

- ***Amplitude to Phase:*** Is a similar process where time is replaced by phase and a single period by multiple oscillations. It is a simple solution but requires accurate phase matching (Filters).

All other processes that require computing software to extract the position information from the recorded data are known as **un-normalized processes.**

1.3 Acquisition time

This is the time required for the BPM to supply a full set of data to the digital processor. Three categories can be created:

- ***Wide-band:*** It groups all processing systems capable of measuring individual bunches separated by >10 ns down to a single bunch. The bandwidth can be as high as 100 MHz. Systems that belong to this group include Sample/Track & Hold, Logarithmic amplifiers, Amplitude to Time normalizers.
- ***Narrow-band:*** It groups all processing systems capable of resolving one machine revolution period and in some cases can measure individual bunches separated by >100 ns. The bandwidth ranges from a few 100 kHz up to a few MHz. The Heterodyne and Amplitude to Phase processors belongs to this group.
- ***Slow acquisition***: A special class is reserved for the Time MPX processing which, while having an equivalent bandwidth relative to other heterodyne systems, is penalized in the acquisition rate by the time multiplexing. (See Fig. 1)

It should be pointed out that unexplored combinations among the present solutions could offer specific advantages. For example a turn-by-turn acquisition can be obtained from a time MPX processor combined with the Δ & Σ system. The Σ signal is first selected to establish the right gain for the AGC action, and then by switching to the Δ input and the use of a Peak & Hold circuit, consecutive position measurements can be obtained.

2. DETAILED PROCESSING DESCRIPTION

2.1 Time Multiplexed processor[iii]

The processor is conceived for closed orbit measurement of stable stored beams. (See Fig. 2)

The input MPX is usually realized with a multiple configuration of GaAs switches; the channel isolation should be >50 dB for frequencies up to 1 GHz.

A band-pass filter is used to select the largest line of the signal spectrum; its selectivity is not critical.

The essential element is the pre-amplifier which should handle a very large signal dynamic (>75 dB) and compress it by >50 dB. Its input admittance should be kept stable as function of the gain to avoid a zero offset drift. The global noise figure is increased by different insertion losses and should be optimized for the largest gain.

Figure 1 gives a schematic representation of the different families and their interconnections.

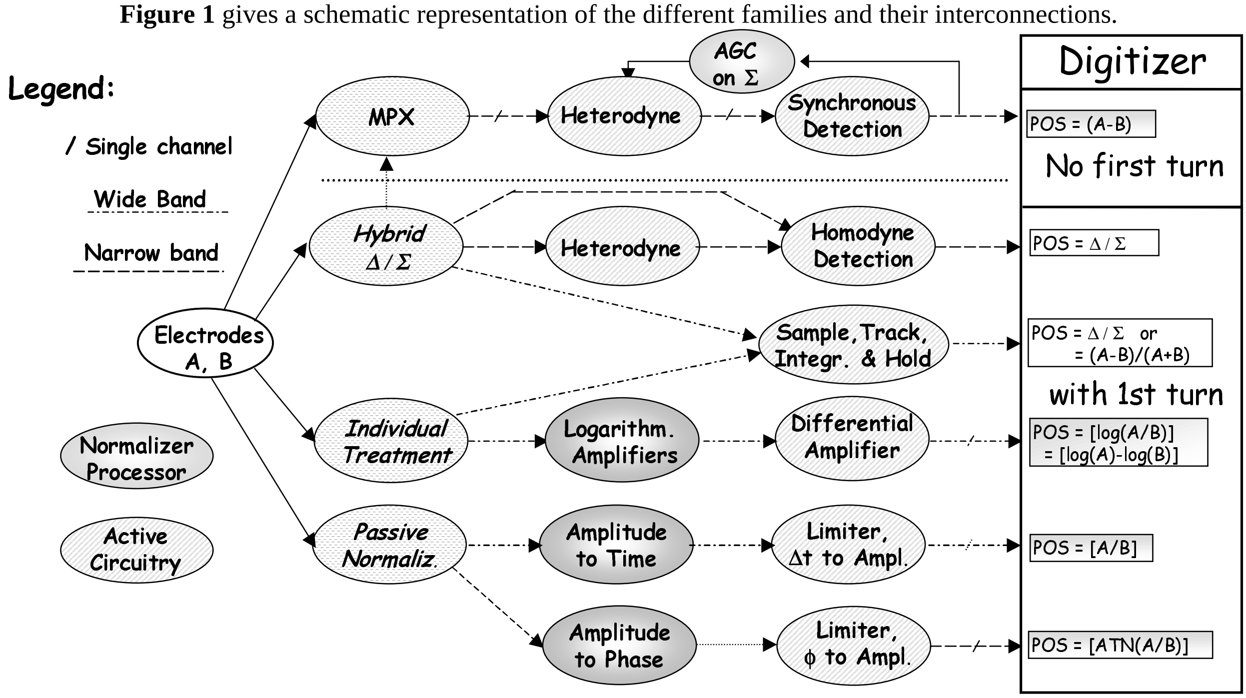

Figure 2

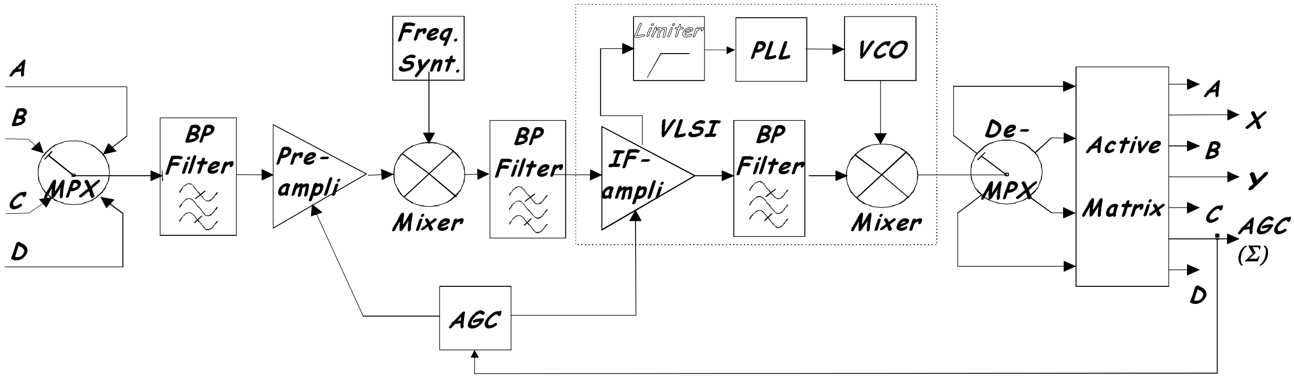

An active mixer, making use of a frequency synthesizer to reduce the noise contribution, is used to down convert the signal to a standard intermediate frequency (IF usually 10.7 MHz or a multiple). The IF amplifier and the demodulator are usually integrated telecom circuits. The IF bandwidth is selective enough to suppress side bands at the revolution frequency (multiple bunches) but sufficiently wide to allow for fast switching among channels (100 kHz > BW < 1MHz). Synchronous detection is obtained by comparing the phase of a sample of the carrier frequency with a reference signal and driving a VCO in a phase locked loop. Synchronous detection offers a clean detected DC signal but it slows down the MPX switching time since the PLL has to relock after each switching (even with accurate phase adjustment).

The last part of the chain is composed of an output de-multiplexer, four track & hold amplifiers and an active matrix of video amplifiers to produce the AGC sum and X,Y positions[iv].

Advantages	Limitations
Normalization process	*Requires a stable beam during the scanning*
Reduced number of channels (x4)	*No turn by turn acquisition*
Identical gain for all the channels	*Slow acquisition rate* (MPX)
Large dynamic range (>80dB)	*Reduced Noise Figure* (gain matching & MPX insertion losses, AGC pre-ampli.)
Excellent position stability	*Reduced linearity, for non-linear PU's since the Σ is not constant*
No temperature dependence and components aging	*Large engineering*

2.2 Δ & Σ Processor

When using this approach it is convenient to convert the input signals into their equivalent difference and sum at the earliest possible stage. This action is realized by a simple and reliable passive element called the **"180°hybrid".** The input signals should be in-phase, which means tight tolerances on the interconnection cables. Since the hybrid is radiation resistant, it can be connected directly to the electrodes.

Figure 3

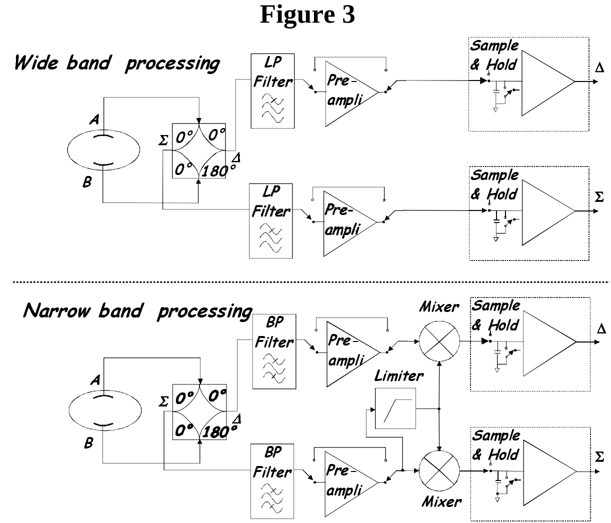

__Narrow Band__: In most of the cases, the hardware is similar to that of the time MPX. In some application, the heterodyne conversion is suppressed. The pre-amplifiers have low NF (< 2dB), programmable gain through pin diodes switches, and will absorb a large input dynamic (> 90 dB). A fraction of the Σ signal is limited and used as a local oscillator in a homodyne detector. The Δ & Σ signals are digitized by a track and hold circuit and externally triggered ADCs. This scheme is also used for single bunch measurement in complex injector machines[v] (SPS), where the bunch excites the BP filter to resonate on its central frequency (see amplitude to phase normalizer). No hardware modifications are necessary but even tighter tolerances on the phase matching are required.

Wide-band: The LP filters will just stretch the pulses. The pre-amplifiers have a large BW and programmable gain but a limited dynamic range. For long bunches, the S & H circuits are suppressed and FADCs (1 GS/s) directly digitize the signal[vi].

Advantages	Limitations
The central position is independent on input intensity	*Programmable gain amplifiers*
Intensity measurement is available	*Multiple calibration coefficients*
Excellent Noise Figure	*The absolute position is f(gain)*
[Wide band allows measurements on multiple bunches (Δt <20 ns)]	*{Tight phase matching (Δ, Σ) at all the gains required by the synchronous detection (±5°) }*
{Large dynamic > 90 dB}	*{ Pedestal error on Σ }*

[W.B.] & {N.B.}

2.3 Logarithmic amplifiers[vii viii]

The demodulating logarithmic amplifiers compress each signal. The outputs are filtered and applied to a differential amplifier. The position response is:

$$\text{Pos.} \equiv [\log(A/B)] = [\log(A) - \log(B)] \equiv (V_{out})$$

Figure 4

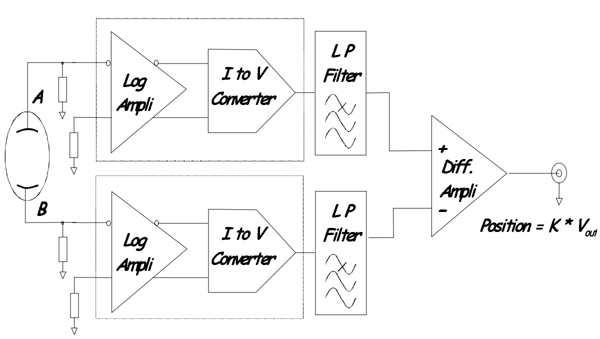

Behind such a simple equation is hidden a very sophisticated electronic circuit which is required to approach the ideal function[ix]. New generation circuits use several cascaded limiting amplifiers, with fixed gain and a wide bandwidth. Full wave rms detectors are applied at each stage and by summing theirs output signals, a good approximation to a logarithmic transfer function is obtained.

States of the art parameters are:

Input dynamic range:	>90	dB
Input noise:	<1.5	nV/√Hz
Non conformance lin.:	<± 0.3	dB
Limiter Bandwidth:	D.C. to >2	GHz
Video Bandwidth:	D.C. to 30	MHz

The demand of the consumer market (primarily telecommunication) for these products has resulted in a wide variety of new circuits, each one optimized for a specific parameter.

Advantages	Limitations
Possible applications in the time and frequency domain (NB & WB)	*State of the art performances are not simultaneously available*
Very large dynamic range (>90 dB)	*Poor position stability vs. input level, for peculiar conditions*
Wide input bandwidth	*Limited linearity (few % of the NA)*
No bunch shape dependency	*Limited long term stability*
Simultaneous digitization of + and - charges	*Temperature dependence*
Simple engineering	

2.4 Amplitude to Time Normalization

This new normalization idea is derived from the “Amplitude to phase” principle where “phase“ is replaced by “time“ and the applied signal has a single oscillation period. It applies to bunched beams and works in the time domain[x xi] (See Fig. 5).

The LP filters produce the correct pulse shape. The signals from both electrodes are split in two and one branch is delayed by a time T_1. The delayed signal of one channel is then added to the direct signal of the other channel, and vice versa. At C, the time of the zero crossing varies according to the signal ratio, up to a maximum of T_1. At the output D, you have the same signal amplitude but the time variation has opposite sign. The maximum time difference is therefore $2T_1$. The delay offset T_2 is required to avoid sign ambiguity and should always be larger than T_1. The zero crossing is independent of amplitude and easy to detect by fast comparator circuits. Their outputs drive an AND gate, which generates a pulse with a width proportional to the beam position.

$$\text{Position} \equiv \Delta t = 2T_1\,[(A - B)/(A + B)] + T_2$$

Figure 5

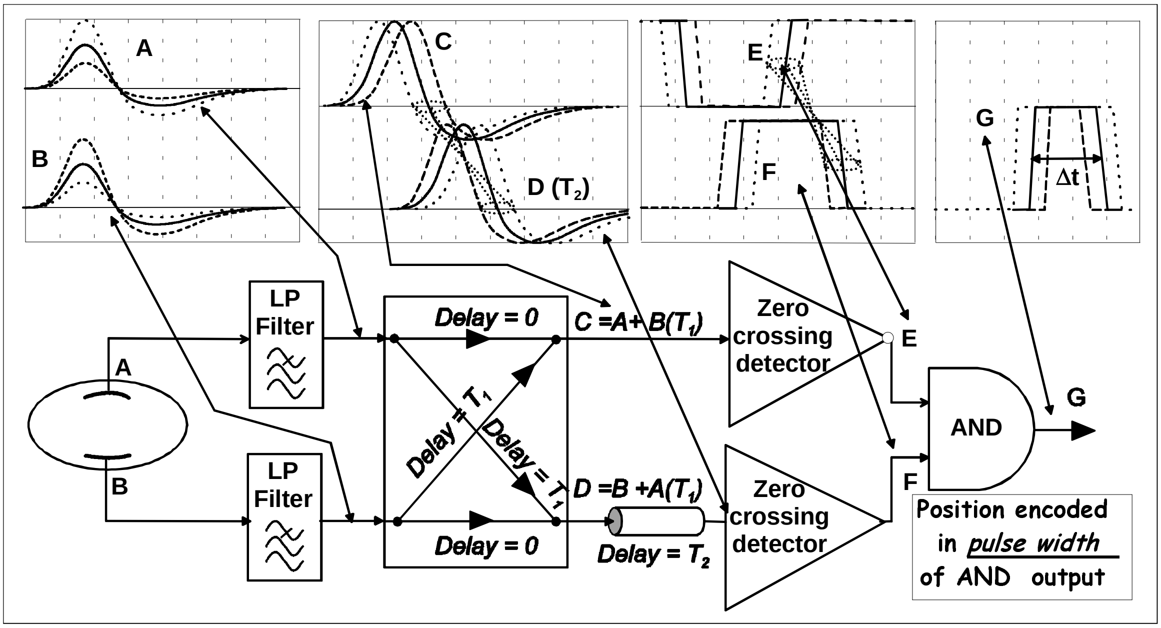

By integrating this pulse, the time variation is transformed into amplitude that can be read by an ADC.

The normalization is obtained by the use of hybrids and cables which can be directly connected to the electrodes.

Advantages	Limitations
Fastest normalization process (> 40 MS/s)	*Can only be employed with bunched beams*
Reduced number of channels (x2)	*No Intensity information*
Input dynamic > 50 dB	
~10 dB reduction on the position dependent dynamic due to signals recombination	*Tight time adjustment*
Dynamic is independent on the number of bunches	*Propagation delay between comparators*
Almost independent on the bunch length	

Remark: A specifically designed monolithic Ga-As chip will allow for a large speed breakthrough.

2.5 Amplitude to Phase Normalization

This technique was first developed for RF signals working in the frequency domain and rapidly adapted to short pulses working in the time domain[xii] (See Fig. 6)

The two electrode signals are converted into a RF burst or a permanent RF signal, according to the beam shape, by the use of a BP filter. These in-phase signals are applied to the inputs of a “90° Hybrid”. Each signal is split into two branches; one of them is shifted by 90° and added to the opposite in-phase signal, and vice versa. The outputs are of equal amplitude and have a phase difference ($\Delta\varphi$) proportional to the position.

$$\text{Position} \equiv \Delta\varphi = 2*\text{Arc-tangent}\,(A / B) - \pi/2$$

This relation is valid for both a continuous wave or for a burst after proper settling time, which depends on the bandwidth. To avoid an ambiguity in sign, one output is delayed by 90 degree.

The two signals are applied to comparators that suppress the amplitude dependence. The phase difference is reconverted into an amplitude variation by the use of XOR logic. The position information has a variable duty cycle at twice the filter frequency, and is digitized by an ADC driven by LP filter and a video buffer.

Two cases should be distinguished:

Current modulated beam: The BP filters are tuned to the largest line in the frequency spectrum. Theirs selectivity (BW) should suppress all spurious frequencies (rejection > 40 dB) but be wide enough to accept the small frequencies changes that may occur during the accelerating cycle. The BP filters are not a critical element and the phase shift need only be matched to within a few percent.

Frequency down conversion[xiii]: For frequencies above 150 MHz, comparators are getting less performant and signal is therefore down converted by using a heterodyne. The acquisition time is increased by the ratio f_{RF}/f_{if}.

Figure 6

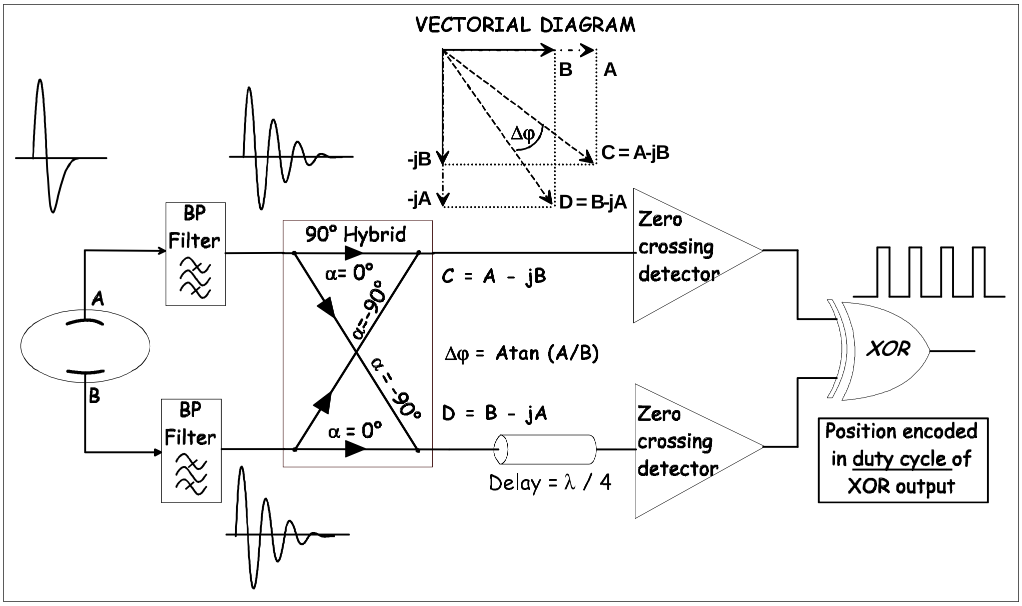

Bunch modulated beams (single or multi bunches) the induced signals charge the BP filter, which in turns will start a free oscillation on its central frequency for a predetermined time. The pulse width should be shorter than the oscillation period ($W_{(fwhm)} < 1/4*f_o$) to obtain the maximum signal. The bunch spacing should be larger than the damping time of the filter to allow for individual measurements. Acquisition rates up to a few MHz can be achieved, so that turn-by-turn and individual bunch acquisition is feasible. Since the BP filter selectivity is not critical, a single resonator can be employed. However, this results in a longer dumping time and therefore requires a longer bunch separation[xiv]. Several BP filter parameters should be accurately matched in order to preserve the correct relative phase over several oscillation periods.

Advantages	Limitations
Normalization process	*Upper frequency limit < 150 MHz*
Reduced number of channels (x2)	*Tight phase adjustment*
Input dynamic > 50 dB	*[Minimum bunch spacing (> 100 ns)]*
~10 dB reduction on the position dependent dynamic due to signals recombination (90° sum)	*[Matched pair BP filters (tight tolerances)]*
[Dynamic is independent of the number of bunches]	*Hardware; limited technological improvements foreseen*
Simultaneous digitization of + and - charges	*{Current modulated beams}*
Simple & Reliable	*[Bunched beams]*

3. APPLICATION EXAMPLE

Lets try to choose the best processing system for a future machine like the Large Hadron Collider (LHC) where a large scale, cost effective processor is required.

The tables present some of the main parameters of the machine and the BPM system.

LHC Machine Parameters		
Circumference	27	Km
Rev. period	89	ms
Bunch length	10/30	cm
Bunch separation	>25	ns
Intensity (pilot)	5E9	p/b
N of bunches	1 to 2835	
Bunch dynamic	>32	dB
Pos. dynamic (.5 NA)	>12	dB

BPM Specifications			
~2000 planes (Button type electrodes)			
Single turn & Orbit measurements			
Simultaneous 16 bunches (among any), turn-by-turn measurements			
Beam	Pilot	Nominal	
Scaling Factor accuracy	2	.5	%
Linearity	2	.5	%
Resolution	1	.1	%
Position stability vs. intensity	.3		%
Offset	1	.3	%
(Single shot)	rms	rms	NA

The first choice will concern the acquisition rate. Specifications impose a wide-band processor to satisfy the first turn and the measurement of any bunch among the 2835, spaced by 25 ns.

An un-normalized processor (wide-band Δ/Σ,

S & H) will require at least a 13 bit ADC running at 40 MS/s, to satisfy the single shot resolution and the scaling factor accuracy. This coupled with the high cost of such a system makes this choice quite problematic.

The logarithmic amplifier offers an excellent dynamic range and an insensitivity to bunch length variation but can not satisfy the bunch separation, the linearity and the position stability.

The Time Normalizer appears to be the unique solution to the required specifications and that's why it has been adopted for the LHC machine.

CONCLUSIONS

Experience has proved that every new machine requires a new approach to the same problem. This provides engineers with a challenge for new ideas.

Several different combinations among the currently available processing systems have still to be explored and may prove to provide solutions for particular cases.

The telecommunications field has similar needs and is extremely dynamic. Full advantage should be taken of their technological progress and of the reduced prices of components on the consumer market.

Technology improvements (speed) will allow some signal processes systems to excel.

My personal feeling toward the ideal solution will pass trough a passive normalization combined with a wide-band signal processing system; this will cover the widest range of possible applications.

REFERENCES

[i] A. Hofmann, "Beam diagnostics and applications", BIW98, pg.3.

[ii] F. Loyer & K. Scheidt / ESRF, "Electron beam position monitor: performances considerations" Proc. of Dipac 93, pg. 21.

[iii] R. Biscardi, J.W. Bitter, "Switched detector for Beam Position Monitor" Proc. IEEE Particle Accelerator Conference, San Francisco CA (1991) Cat N°89CH2669-0, Vol.3, pp.1154 – 1156.

[iv] J.A. Hinkson, K.B. Unser, "Precision analog signal processor for BPM in electron storage ring" Proc. of Dipac 95, Travemunde (D).

[v] R. Bossart et al. "Synchronous receivers for beam position measurement", IEEE trans. Nucl. Sci. 32, 1899 (1985).

[vi] M. Le Gras, D.J. Williams, "Trajectory measurement of bunches ejected from the CERN PSB", Proc. of Dipac97, pg.

[vii] R.E. Shafer, G. Swain et al. "Beam position monitor upgrade for Los Alamos proton storage ring", U.S.PAC Conf. Proc.(1989), page 1562.

[viii] G. Aiello, M.R. Mills,"Log-ratio technique for beam position monitor systems", BIW92, AIP Conf. Proc. xxx, page 301.

[ix] R.E. Shafer, "Log-ratio signal processing technique for beam position monitors", BIW92, AIP Conf. Proc. xxx, page 120.

[x] G. Vismara et al. "From narrow to wide band normalizer for orbit and trajectory measurements" BIW 98, AIP conference proceeding 451, page 246.

[xi] D. Cocq " The wide band normalizer – a new circuit to measure transverse bunch position in accelerator and collider" NIM A 416 (1998) I-8.

[xii] G. Vismara SL/BI Note.

[xiii] F.D. Wells & S.P. Jachim "A technique for improving the accuracy and dynamic range of BPM" Proc. 1989 PAC.

[xiv] J. Borer et al. "The second generation and optimized beam orbit measurement system of LEP. Hardware and performance description" 2nd DIPAC, Travemunde 1995.

BUNCH LENGTH MEASUREMENTS

M. Geitz, Deutsches Elektronen Synchrotron, D-22603 Hamburg, Germany

Abstract

An rf photo-injector in combination with a magnetic bunch compressor is suited to produce high-charged sub-picosecond electron bunches required for electron-drive linacs for VUV and X-ray FELs. This report summarizes time- and frequency domain bunch length measurement techniques with sub-picosecond resolution.

1 INTRODUCTION

Future electron-drive linacs for VUV and X-ray Free Electron Lasers (FEL) require the acceleration of bunches whose length is well in the sub-picosecond regime [1]. A common source for high-charged sub-picosecond electron bunches is an rf gun based on a photo injector using an intense ultraviolet laser beam (typically 20 mJ) to produce up to $5 \cdot 10^{10}$ electrons per bunch from a $CsTe_2$ photo cathode. The electron bunches are accelerated rapidly by the strong electric fields (about 40 MeV/m) of the gun cavity to avoid an emittance blowup due to space charge. The bunch length obtained from an rf gun depends on both the laser pulse length (typically $\sigma_t = 5$ps) and the compression occurring from the rf field within the first centimeters of the gun cavity. By a proper choice of the rf phase a velocity modulation can be impressed on the electron bunch leading to a reduction of its length within the gun cavity. Very short bunches can be obtained at the price of sacrificing a large fraction of the bunch charge. In an electron drive linac only a moderate bunch compression is applied, because of the need of intense electron beams. Further compression can be obtained by combining an off-crest rf acceleration with a magnetic chicane. The off-crest acceleration produces a correlated energy spread with higher energy electrons trailing lower energy electrons. The higher energy electrons then travel on a shorter path through the magnetic chicane than the lower energy electrons and a bunch compression is obtained. In the following an overview of established and future time-domain and frequency-domain bunch length measurement techniques with sub-picosecond resolution will be presented.

2 TIME DOMAIN MEASUREMENTS

Streak Camera: The streak camera is a device for a direct (single-shot) determination of the longitudinal bunch charge distribution. The present resolution limit is 370 fs (FWHM) [2]. The light pulse generated by an

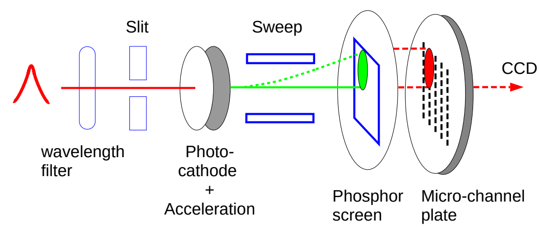

Figure 1: Principle of the streak camera.

electron bunch travels through a dispersion-free optical system, an interference filter and a slit before hitting the photo-cathode of the streak camera. A wavelength filter selects a narrow frequency band and the slit reduces the transverse dimension of the image on the photo cathode. The light pulse is converted to an electron pulse, which is accelerated and swept transversely by a fast rf electric field. The resulting transverse distribution is projected onto a phosphor screen. The image is amplified by a multi-channel plate and then detected by a CCD camera. Space charge effects inside the streak camera tube and the achievable sweeping speed limit the temporal resolution. The energy spread of the electrons generated by the photo-cathode and the dependence of the photo electron energy on the wavelength of the incident light pulse add to the time resolution limit.

A state-of-the-art streak camera measurement performed at the University of Tokyo using a BNL-type rf photo-injector in combination with a magnetic bunch compressor shows a successful compression of a 13 picosecond electron bunch to 440 femtoseconds (FWHM) [3] as shown in Figure 2. The measurement was performed with a bunch charge of 250 pC at an electron energy of 35 MeV.

Rf Kicker Cavity: An interesting proposal to obtain sub-picosecond resolution is the application of the streak camera principle to the electron beam itself [4]. An rf kicker cavity operated in the TM_{110} mode can be used to sweep the electron bunch transversely across a screen located in the vacuum chamber downstream. The transverse

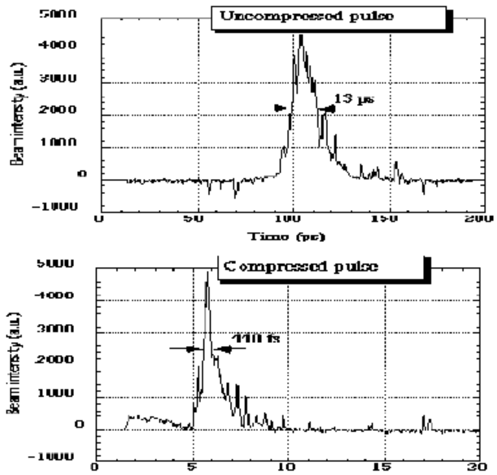

Figure 2: 250 pC electron bunch at 35 MeV beam energy before and after compression with a magnetic chicane compressor at the University of Tokyo [3].

kick k imposed on the bunch with energy E is proportional to

$$k \sim \sqrt{(PQ)} f/E \tag{1}$$

where P denotes the applied power, f the rf frequency and Q the quality factor of the cavity. It is estimated that a resolution of 100 femtosecond can be realized by either using a high-frequency high-power or high-Q superconducting cavity [4].

Energy Spread Measurements: An efficient and inexpensive way to determine the bunch length is the evaluation of the bunch energy distribution. Figure 4 shows a magnetic bunch compressor chicane followed by an rf cavity and a dispersive section to image the energy profile. The longitudinal dynamics of the system can be described

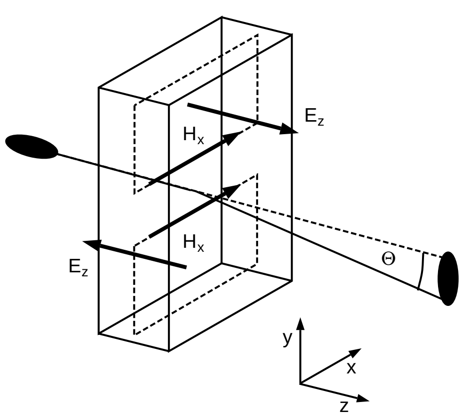

Figure 3: Kicker cavity operated in TM_{110} mode. The bunch is kicked vertically by the magnetic field.

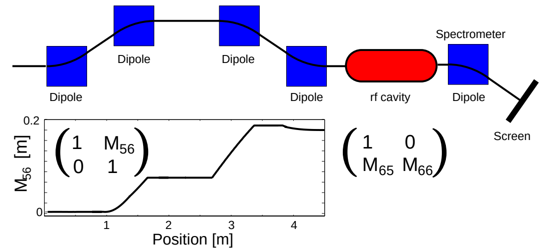

Figure 4: A magnetic bunch compressor chicane followed by an off-crest acceleration can be used to determine the longitudinal bunch charge distribution.

by the transport matrix

$$\left(\begin{array}{c} L \\ \frac{\Delta E}{E} \end{array}\right)\Bigg|_{\mathrm{f}} = \left(\begin{array}{cc} 1 & M_{56} \\ M_{65} & M_{56}M_{65} + M_{66} \end{array}\right) \left(\begin{array}{c} L \\ \frac{\Delta E}{E} \end{array}\right)\Bigg|_{\mathrm{i}} \tag{2}$$

where M_{56}, M_{65} and M_{66} denote transfer matrix elements of the chicane and the rf cavity of Figure 4. If we choose the matrix elements such that $M_{56}M_{65} + M_{66} \to 0$, the energy profile measured behind the spectrometer dipole magnet is a direct image of the longitudinal bunch charge distribution in front of the compression section [5]. Figure 5 shows energy profile measurements performed at the TESLA Test Facility Linac. With different parameter settings it is possible to measure the longitudinal charge distribution at various positions along the magnetic chicane. The lower plots show the reconstructed compression of the electron bunch

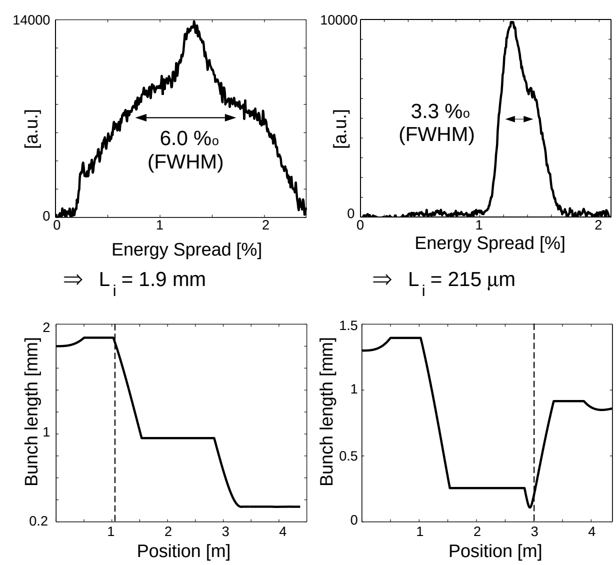

Figure 5: Two energy spread measurements at the end of the TESLA Test Facility Linac. The lower plot shows the reconstructed compression of the bunch length through the chicane compressor. The dashed line shows the longitudinal position where the measured energy profile matches the longitudinal charge distribution. Left: optimum compression. Right: over-compression.

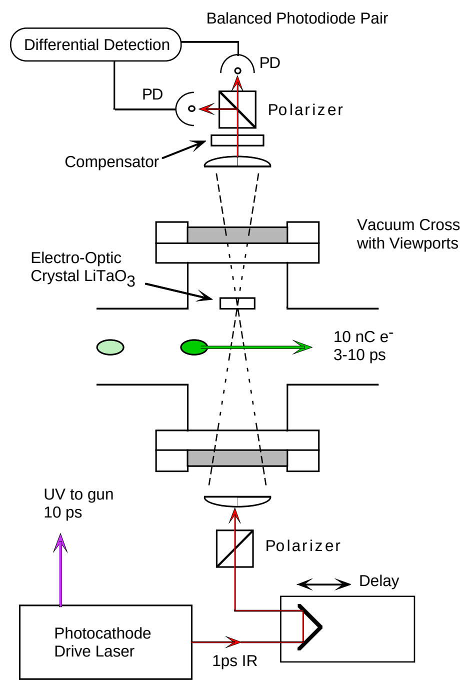

Figure 6: Electro-optic sampling of electric fields carried by the charge distribution by picosecond laser pulses.

within the magnetic chicane. The dashed line indicates the longitudinal position where the energy profile matches the longitudinal charge distribution. This technique is limited by the resolution of the spectrometer and the validity of linear beam transfer. If the bunches become too short, non-linear effects like wake-fields and space charge will have to be taken into account.

Electro-optic Sampling: The principle of electro-optic sampling is to use short laser pulses to probe the change of birefringence in a ZnTe or $LiTaO_3$ crystal introduced by the strong electric fields ($E \approx 3MV/m$) moving with the electron bunch. The laser pulse needed for the photo injector and the electro-optic sampling experiment are produced by the same IR laser to obtain the needed time synchronization. The probe laser beam is delayed by a roof mirror and polarized at 45^o with respect to the axis of ordinary and extra-ordinary refraction of the electro-optic crystal. The imposed elliptical polarization on the probe laser beam is analysed by a polarizing beam splitter and two photo-diodes. By detecting the difference current between the pair of photo-diodes a small modulation depth can be observed. The longitudinal charge distribution is then scanned by delaying the sampling laser pulse with respect to the electron beam [6]. The time resolution is estimated to be in the order of the probe laser pulse length. Electro-optical sampling is a time-domain technique with a large measurement window of about 100 picoseconds (by delaying the sampling laser beam).

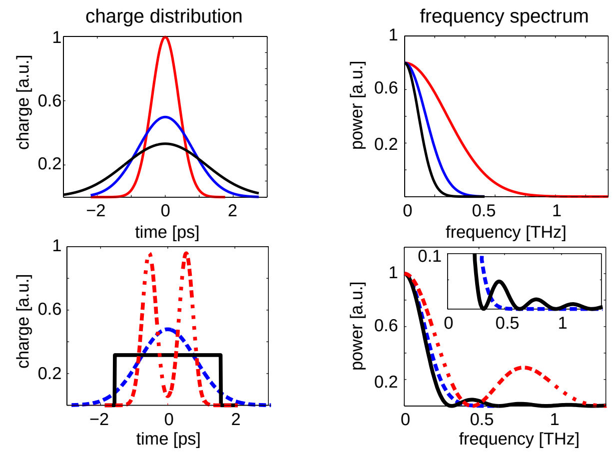

Figure 7: The bunch length and the bunch shape can be distinguished by the obversation of the coherent radiation spectrum. Top: Time- and frequency-domain presentation of three Gaussian bunches of different width. Bottom: Comparison of three bunches of different shape but with equal rms width.

Electro-optic Sampling with Chirped Laser Pulses: The method of electro-optic sampling can be extended to a single-shot measurement by using chirped laser pulses [7] (long wavelengths are leading the short wavelengths). The long laser wavelength samples the beginning, the short laser wavelength the end of the bunch electric fields. The temporal distribution of the electron bunch can be visualized by a diffraction grating viewed by a CCD camera.

3 FREQUENCY DOMAIN MEASUREMENTS

Coherent Transition Radiation (CTR) can be used to determine the longitudinal charge distribution. The radiator is a thin aluminum foil arranged at an angle of 45^o with respect to the beam direction so that the backward lobe of the radiation is emitted at 90^o and is easily extractable from the vacuum chamber. The spectral intensity emitted by a bunch of N particles is

$$I_{\text{tot}}(\omega) = I_1(\omega)\left(N + N(N-1)\,|f(\omega)|^2\right) \qquad (3)$$

where $I_1(\omega)$ is the intensity radiated by a single electron at a given frequency ω and $f(\omega)$ is the longitudinal bunch form-factor [8, 9, 10] defined as the Fourier transform of the normalized charge distribution ρ. For a relativistic bunch whose transverse dimensions are small compared to the length the form factor becomes

$$f(\omega) = \int \rho(z)\exp(i\omega z/c)dz = \int c\rho(ct)\exp(i\omega t)dt\ . \quad (4)$$

For wavelength in the order of the bunch length the form-factor approaches unity. The emitted radiation radiation is then coherent and permits a direct measurement of $|f(\omega)|^2$. Figure 7 shows the expected power spectrum for various bunch length and shapes.

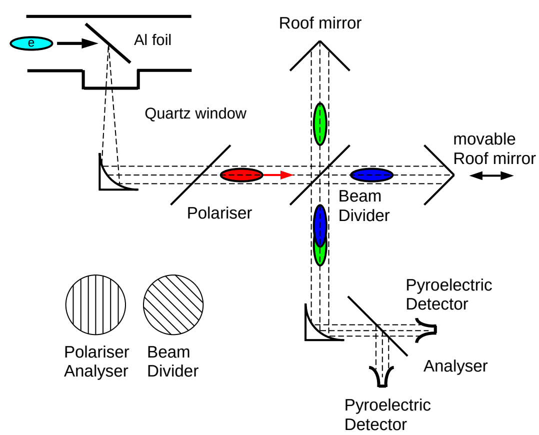

Figure 8: The Martin-Puplett Interferometer.

Fourier Transform Spectroscopy: At the TESLA Test Facility a Martin-Puplett interferometer, shown schematically in Figure 8, has been used to measure the autocorrelation function of the radiation pulse [11]. The diverging transition radiation beam leaving the CTR radiator is transformed into a parallel beam entering the interferometer by a parabolic mirror. The incident radiation pulse is polarized horizontally by the first grid and then splitted by the beam divider into components of different polarization entering the two spectrometer arms. The polarization is flipped by the roof mirrors, hence the component first transmitted at the beam splitter is now reflected and vice versa. The recombined radiation is in general elliptically polarized, depending on the path difference between the two arms. The analyzing grid transmits one polarization component into detector 1 and reflects the orthogonal component into detector 2. Two pyroelectric detectors equipped with horn antennas are used as detection devices for the sub-millimeter wavelength radiation.

A Fourier transformation of the autocorrelation function yields only the absolute magnitude $|f(\omega)|$ of the form factor. A Kramers-Kronig dispersion relation approach can be used to compute the phase of the form factor. The so-called minimal phase ψ is given by [12]

$$\psi(\omega) = \frac{-2\omega}{\pi}\int_0^\infty \frac{\ln[|f(u)|/|f(\omega)|]}{u^2-\omega^2}du\ . \qquad (5)$$

To carry out the Kramers-Kronig integration a polynomial extrapolation of the form factor towards small frequencies has to be applied [12]. The inverse Fourier transformation then yields the desired longitudinal charge distribution

$$\rho(z) = \int_0^\infty |f(\omega)|\cos\left(\psi(\omega)+\omega z/c\right)d\omega\ . \qquad (6)$$

The steps of the analysis are depicted by the graphs in Figure 9. The drop of the form factor towards small frequencies is explained by a low frequency cut-off of the interferometric device and the acceptance of the pyroelectric detectors. Fourier-transform spectroscopy is a technique with enhanced performance as the bunch length reach the subpicosecond scale. The coherent frequency spectrum then extends well into the THz regime and the high-pass filter effects of the device become less important. Also a greater variety of detecting devices (pyroelectric detectors, Golay-cell detectors, bolometers) is available.

Hilbert Transform Spectroscopy: Hilbert-transform spectroscopy of coherent transition radiation using Josephson junctions offers the possibility for high-speed frequency domain measurements [13, 14, 15]. The electric properties of a junction are determined by Cooper-pair tunneling which leads to the I-U characteristics shown as the dashed curve in Figure 10. A dc current I_0 can be passed through the junction without observing a voltage drop as long as the current stays below a critical value I_c (dc Josephson effect). For currents above I_c a voltage drop across the junction is observed accompanied with an alternating current whose frequency is given by the relation $\omega = 2eU/\hbar$ (ac Josephson effect, $f_{Jos} = \omega/2\pi = 483.6$ GHz for $U = 1$ mV). When the Josephson junction is exposed to monochromatic radiation of (angular) frequency ω the current-voltage characteristic acquires a current step ΔI at the voltage $\overline{U} = (\hbar\omega/2e)$, see Figure 10 ($\overline{U}$ is obtained by averaging over the Josephson oscillation). Within the framework of the Resistively Shunted Junction (RSJ) model [16], and in small-signal approximation, the magnitude of this step is proportional to the power of the incident radiation. Hence the junction acts as a quadratic detector and can be used to measure the spectral intensity of a continuous radiation spectrum. For this purpose we define a

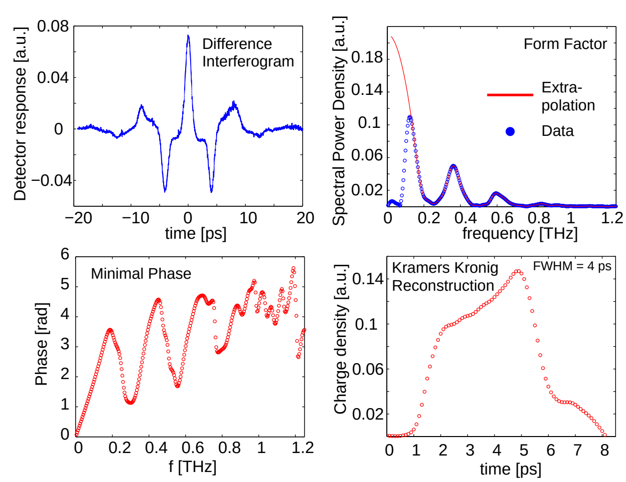

Figure 9: The measured interferogram (upper left) is Fourier-transformed to determine the longitudinal form factor (upper right). The minimal phase is evaluated (lower left) and then used to determine the longitudinal electron charge distribution (lower right) by a Fourier transformation back to time domain.

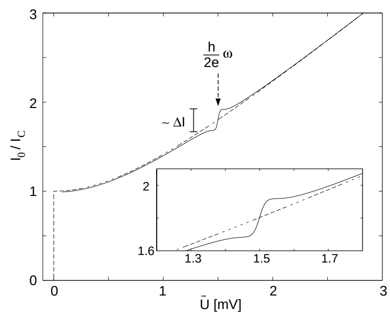

Figure 10: Dashed curve: voltage across the junction as a function of the dc bias current. Solid curve: modification of the dc characteristic curve due to monochromatic incident radiation.

characteristic function

$$g(\overline{U}) = \frac{8}{\pi}\frac{\hbar}{2e} \cdot \frac{\Delta I(\overline{U}) I(\overline{U})\overline{U}}{R^2 I_c^2} \quad (7)$$

where R is the ohmic resistance of the junction. The spectral intensity is derived from g by an inverse Hilbert transform [13]

$$S(\omega) = \frac{1}{\pi}\mathcal{P}\int_{-\infty}^{\infty}\frac{g(\omega_0)\,d\omega_0}{\omega - \omega_0} \quad \text{where} \quad \omega_0 = \frac{2e}{\hbar}\overline{U}\ . \quad (8)$$

Here $\mathcal{P}$ denotes the principal value of the integral.

Figure 11 shows a coherent power spectrum measured at the TTF linac [15] using a $YBa_2Cu_3O_7$ junction. Also here, the measurement is limited at low frequencies because of the spectral acceptance of the detector. The data are not yet precise enough to derive the bunch shape. Applying a Gaussian fit (solid curve in figure 11) yields σ_t = 1.6ps. Hilbert-transform spectroscopy is a high-speed technique because of the purely electronic measurement. Using fast read-out electronics (several MHz bandwidth) to sample the I-U curve permits a quick determination of the bunch form factor. Hilbert-transform spectroscopy is limited by the energy gap of the high T_c superconductor that

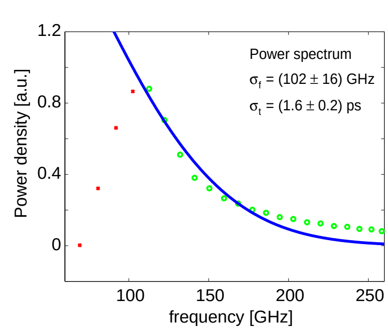

Figure 11: The coherent radiation spectrum as obtained from a discrete Hilbert transform of the characteristic function g. Solid line: Gaussian fit to the power spectrum.

allows for a maximum detectable frequency (generally several THz) before leaving the superconducting state.

4 CONCLUSION AND OUTLOOK

An rf photo-injector in combination with a magnetic bunch compressor has become a successful instrument for the production of high charged sub-picosecond electron bunches. Bunches as short as σ_t = 240 fs, 250 pC charge at an energy of 35 MeV and σ_t = 10 fs, 20 pC charge at an energy of 70 MeV have been produced. Time-domain measurement techniques are usually applied to single bunches and deliver on-line information of the longitudinal charge distribution. Frequency domain measurement techniques are ideally suited for shorter bunches but have the drawback of longer data acquisition times and rather indirect Fourier analysis methods. The resolution is determined either by the positioning accuracy of the interferometer mirrors and beam-splitter or by the maximum detectable frequency of the Josephson junction determined by Cooper-pair breakup.

5 REFERENCES

[1] TESLA - Collaboration, DESY-TESLA 95-01 (1995).

[2] M. Uesaka et al. , Nucl. Instr. Meth. A 406, (1998), 371 - 379.

[3] M. Uesaka et al. , Proc. of 8^{th} AAC workshop, Baltimore, 1998, to be published.

[4] X. J, Wang, Proc. of PAC Conference, New York, 1999, to be published.

[5] K. N. Ricci et al. , Proc. of FEL Conference, Williamsburg, 1998.

[6] M. J. Fitch et al. , Proc. of PAC Conference, New York, 1999, to be published.

[7] I. Wilke et al. , DESY TTF Report, 1999, to be published.

[8] C. J. Hirschmugl et al. , Phys. Rev. A, Vol. 44, No. 2, (1991).

[9] J. S. Nodvick et al. , Phys. Rev. A, Vol. 96, No. 2, (1954).

[10] E. B. Blum et al. , Nucl. Instr. Meth. A 307, (1991).

[11] B. Leissner et. al. , Proc. of PAC Conference, New York, 1999, to be published.

[12] R. Lai et al. , Nucl. Inst. Meth. A 397, (1997), 221 - 231.

[13] Y. Y. Divin et al. , Appl. Phys. Lett. 68 (11), 1996.

[14] M. Geitz et al., DESY TESLA 98-10, 1998.

[15] M. Geitz et al., Proc. of PAC Conference, New York, 1999, to be published.

[16] K. K. Likharev, Dynamics of Josephson Junctions and Circuits, New York, Gordon Breach, 1996.

Controls and Beam Diagnostics for Therapy-Accelerators

H. Eickhoff
GSI, Darmstadt

1) Summary

During the last four years GSI has developed a new procedure for cancer treatment by means of the intensity controlled rasterscan-method. This method includes active variations of beam parameters during the treatment session and the integration of 'on-line' PET monitoring.
Starting in 1997 several patients have been successfully treated within this GSI experimental cancer treatment program; within this program about 350 patients shall be treated in the next 5 years. The developments and experiences of this program accompanied by intensive discussions with the medical community led to a proposal for a hospital based light ion accelerator facility for the clinic in Heidelberg. [1] An essential part for patients treatments is the measurement of the beam properties within acceptance and constancy tests and especially for the rasterscan method during the treatment sessions.
The presented description of the accelerator controls and beam diagnostic devices mainly covers the requests for the active scanning method, which are partly more crucial than for the passive scattering methods.

2) Passive scattering and Rasterscan method

a) Passive scattering
At presently existing therapy-dedicated proton- and light-ion accelerators for cancer treatment the particle beam is delivered to the patient after 'passive' manipulations. A broad and uniform beam profile is generated by wobbling magnets with horizontal and vertical deflection in combination with scatter plates. Whereas the tranverse beam profile is matched to the target dimension by means of a collimator, the requested range dose distribution is achieved with range shifters and adequately formed boli.
In general for this treatment mode the beam properties requested from the accelerator are constant over the treatment time.

b) The Intensity controlled Rasterscan
An alternative to the passive method is the rasterscan method, which allows an accurate confirmation also of a very irregular tumor volume and avoids mechanical insertion devices for beam shaping and thus minimizes the production of fragment or stray particles, that also contribute to the dose distribution.
One of the key aspects of a future particle therapy accelerator is the use of the intensity controlled rasterscan technique (Fig. 1), which is a novel treatment concept, developed at GSI and successfully applied within patient treatments of the GSI pilot therapy program.

This treatment method demands fast, active energy-variations on a pulse to pulse base to achieve different penetration depths and intensity-variation to minimize the treatment time.

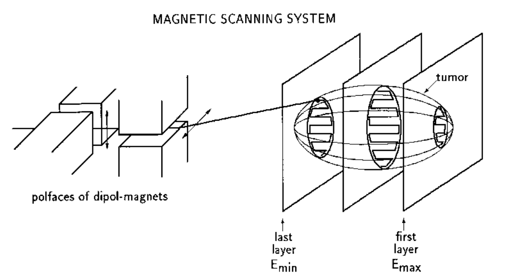

Fig. 1 Rasterscan-Method

The accelerated and slowly extracted beam enters 2 fast scanner magnets, that deflect the beam both in horizontal and vertical direction to cover the lateral dimensions of the tumor. The various ranges in the tumor tissue are realized by different extraction energies of the accelerator.
Fast multiwire proportional counters detect the position and beam width at each scanning point. Ionization chambers in front of the patient measure the number of ions at a specific irradiation point and control the scanner excitation. When a required dose limit has been reached the beam extraction is interrupted very fast (< 0.5 ms).

3) Accelerator requirements

The basis of the accelerator concept has to satisfy the demands of the medical community for the treatment procedures.

Table. 1: Therapy requirements
- 3 treatment areas to treat a large number of patients
- integration of isocentric gantries
- treatment both with low and high LET-ions
- relatively fast change of ion species
- intensity-controlled rasterscan method
- wide range of particle intensities
- ion-species : p, He, C, O
- ion-range (in water) : 20 - 300 mm
- ion-energy : 50 - 430 MeV/u
- extraction-time : 1 - 10 s
- beam-diameter : 4 - 10 mm (hor., vert.)
- intens. (ions/spill) : $1*10^6$ to $4*10^{10}$ (dependent. upon ion species)

The main requirements of the proposed facility for light ion cancer treatment were intensively discussed with radiotherapists and biophysicists and can be summarized in Table 1.

The essential characteristics of this facility are the application of the rasterscan method with active intensity-, energy-, and beamsize- variation in combination with the usage of isocentric light ion gantries. The proposed accelerator is designed to accelerate both low LET ions (p, He) and high LET ions (C, O) to cover the specific medical requirements.

Major aspects of the design are influenced from the experiences of the GSI cancer treatment program; the requirements of this facility, however, exceed in many fields those of this GSI therapy program.

A dedicated accelerator for cancer treatment with the requested parameters described in the previous section demands a quite different accelerator control than facilities used for experimental physics. Whereas high flexibility is requested for the latter ones a hospital based therapy facility demands an easy to use operation with high reliability and extended safety standards to avoid treatment faults.

At the GSI pilot project these requests have been successfully fulfilled by the following means:

- the settings for all accelerator components and all possible parameter variations are stored on device level in nonvolatile memory.
- the settings are approved in dedicated acceptance test procedures and regularly checked within constancy tests.
- during patients treatments the accelerator is locked which permits parameter modifications.
- all beam-destructive elements are automatically removed at the beginning of a treatment session.
- beam delivery takes place only after verification of the requested energy-, intensity- and focusing steps.
- the control of the appropriate beam parameters is performed with a fast, redundant diagnostic system in front of the treatment room.

As all components settings are approved and stored in general no accelerator tuning is necessary; therefore the accelerator sections can be operated (nearly) without operators. The main operator task is to perform predefined constancy tests and to organize maintenance in case of components failures.

4) Beam diagnostics systems

The requested beam diagnosis components have to assure correct beam energy, -intensity ,-position and -beamwidth within the various accelerator sections and especially at the treatment place.

a) Components in the accelerator sections

For measurements of beam intensity

- current transformers in the linac- and low energy beam transport sections and in the synchrotron.
- Ionization chambers and scintillators in the high energy transport system due to the low average current of the slowly extracted beam from the synchrotron.

For measurements of beam- position and beam width

- profile grids and viewing screens in all transport sections at relevant locations.
- beam halo counters (scintillators) during the treatment time
- pick-up probes to determine the beam position in the synchrotron

Schottky pick-ups are suggested for the measurement of the extraction energy from the synchrotron .

The mentioned components are 'standard', approved devices

b) Components at the treatment area

For the intensity controlled rasterscan method fast and accurate intensity measurements are extremely important as they directly determine the dose that is applied to the patients. At GSI two redundant ionization chambers are integrated in a control loop for the operation of the raster scan magnets. In addition one independent recycling capacitor is in operation.

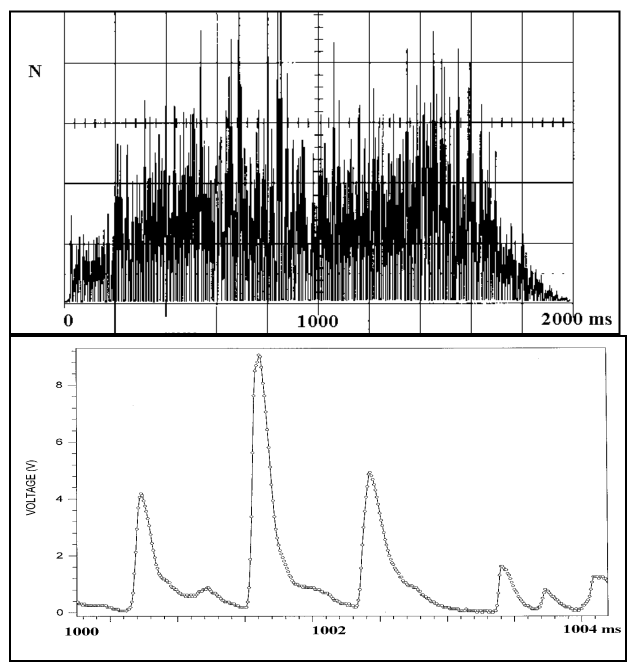

Fig. 2 Measured Spill-structure (total and zoomed) in the lower figure the measurement intervals (12.5 µs) are indicated

In spite of the strongly modulated time structure of the extracted beam (see Fig. 2) the requested dose homogenity of +- 5% can be achieved. due to the fast intensity measurements and the speed of the scanning magnets

Beside the intensity control the beam position control is an important issue. At GSI two redundant multiwire

proportional chambers (MWPC) with an active area of 200 * 200 mm^2 are in operation. The distance of the wires is 1 mm in each plane; the position and beam widths are measured every 150 µs. In addition to monitor the beam parameters a fine adjustment of the beam position was successfully tested by means of a feed forward control of the scanning magnets.
These MWPC-monitors are also essential for the determination of the time dependence of beam position and beam width over the spill duration, which is important for the dose homogenity of the rasterscan technique.
Both the intensity and the beam-position measurements are connected to an interlock unit, which activates redundant spill abort channels when predefined tolerance levels are ecceeded.

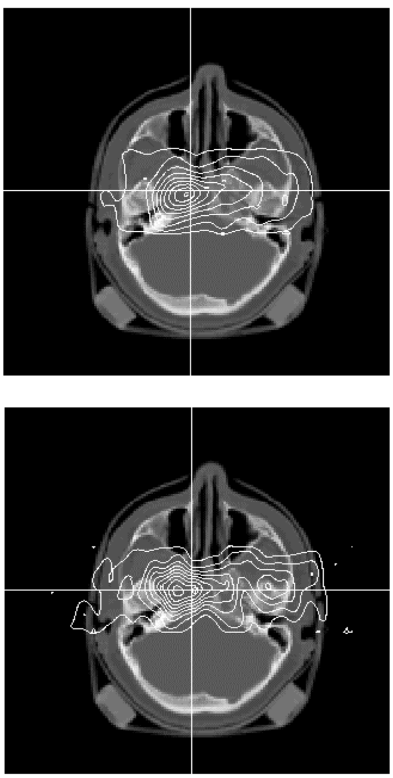

Fig. 3 PET imaging (above: measurement, below: PET-reconstruction)

A third diagnosis system is the 'on-line'-Positron Emission Tomography (PET)-camera. The decay of radioactive isotopes (mainly ^{11}C projectile fragments) is measured during the treatment time. The analysis of these decays gives a three dimensional picture of the dose distribution.
For the acceptance and constancy tests previous to the treatment sessions additional beam diagnostic devices are used.
As the MWPCs and ICs are not located at the isocenter, the beam parameters at the treatment point are measured with separate profile grids or viewing screens and CCD-cameras with digital data processing. The exposure of films is used as well to determine the homogenity of the particle fluence with defined testcycles
For dose verification calibrated thimble ionization chambers are used either in a water tank or located inside predifined phantoms. For fast on line 3D dose verification stack arrays of large area ionization chambers sandwitched between plastic plates are used, which measure the dose simultaniously at different depths of the target volume.[2] Such a device also serves as a verification unit of the particle energy by determination of the bragg peak locations.

5) Controls, Operation

As the environment of a dedicated therapy accelerator is in general a hospital and not a research institute large effort has to be spent on a controls and opertion system, which can be handeled by non accelerator experts.
Within the GSI pilot project predefined procedures have been developed, which both for the accelerator sections and the treatment area allow to confirm the requested beam properties for the large amount of variation possibilities desribed in chapter 3.
For the accelerator predefined test cycles have been prepared to determine the constancy of the requested beam performance. Within these tests a sequence of accelerator cycles for different extraction energies, particle intensities and beamwidths at the treatment place is activated and the beam properties are measured with he appropriate diagnosis components, e.g. ionization chambers, current transformers and profile grids. These data are processed (determination of beam center of gavity and beam-width), stored and displayed to the operator in a graphical representation, which also includes the predefined tolerance levels.

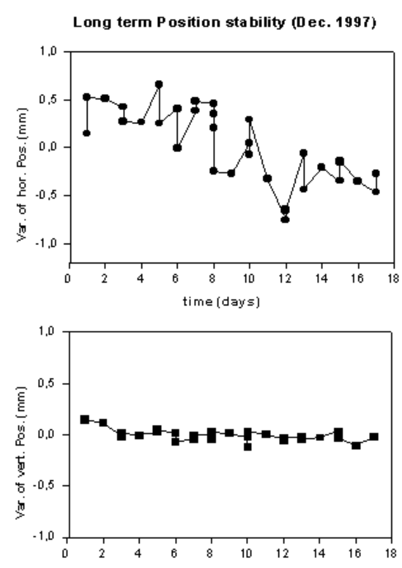

Fig. 4: long term beam position stability

Fig. 4 shows an example of the measured long term position stability of the beam. Each measurement is the meanvalue of position over a complete test cycle with variations of the beam energy and beam widths.
In case of unacceptable deviations from the tolerance levels correction have to be performed. For corrections of the beam position in the high energy transport system to the treatment area an automated beam alignment programm is available, which allows relatively fast position corrections for the whole energy range by means of a correlation of beam position measurements and beam optics calculations [3].

The most crucial demands for the required beam diagnostics occur at the treatment place, as these components have to provide reliable input data for the

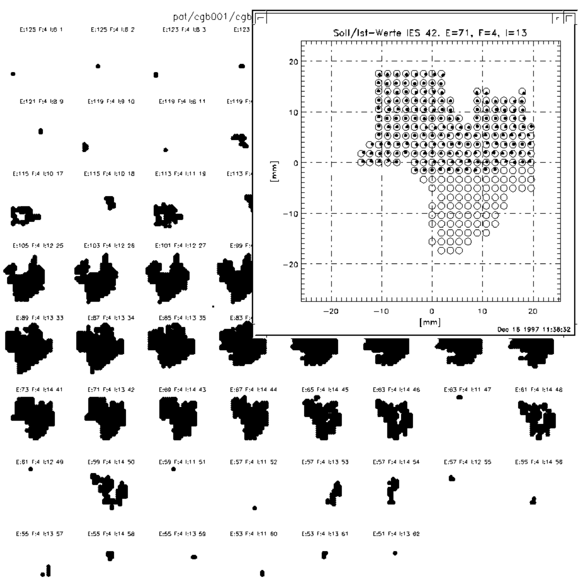

Fig. 5: Observation and control of the irradiation process

control of the scanning magnets and to supervise the requested beam parameters for each treatment point. In addition operating tools have to be available, which despite of the speed and complexity of this treatment modality allow an insight into the actual irradiation progress and a fast, effective response of physicians as non accelerator experts in case of failures.
Figures 5 and 6 give an example of such a measurement and visualization tool. Fig. 5 shows for a specific treatment cycle the individual slices of the tumor volume and the individual treatment locations in each of these slices. The zoomed image indicates, whether the mreasured beam position is inside a predefined tolerance. As all essential data of the treatment are stored a reconstruction and analysis of the beam properties is possible.
Fig. 6 shows the values of the beam position and their deviations from the set value and the intensity variation for a treatment cycle

Appropriate color indications are used in order to give a good overview of the measurements to the physicians. At GSI the commercial IDL graphic package is in use for thze generation of such two- and three-dimensional diagrams.

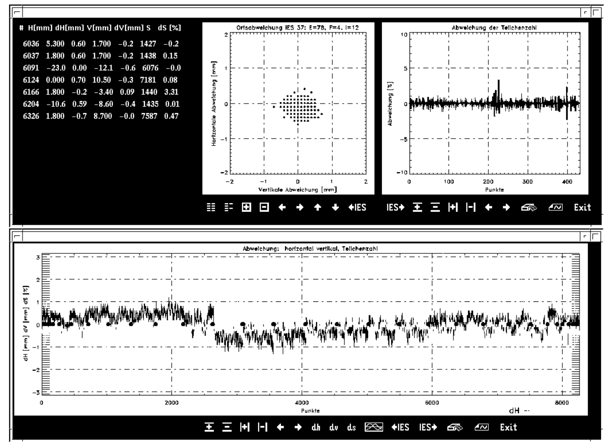

Fig. 6: Observation and Control of beam parameter deviations (position, intensity)

6) Essential future developments

One of the future main goals is to reduce both the treatment time and those periods needed for the acceptance and constancy tests without affecting the patients sefety requests. For the intensity controlled rasterscan technique the amount of patients that can be treated is not primarily defined by the intensity, that can be delivered from the accelerator, but by the required test procedures and the time needed for the measurement and control of the beam properties for each treatment point.
The required test procedures, which even with a horizontal beam line at the GSI facility consume a considerable time, will have to be extended significantly in case of the use of a gantry and additional ion species. These procedures have to be time optimized by means of a larger degree of automatization. In addition automated control and corrections of accelerator settings are essential.
A large effort is necessary to convert the measurement and control tools into an environment that can be handled by non accelerator experts.

[1] J. Debus et al., 'Proposal for a dedicated ion beam facility for cancer therapy', 1998
[2] D. Schardt, 'Beam Delivery Systems and Dose Verification Techniques at Heavy-Ion Therapy Facilities, DIPAC 97, p. 6
[3] B. Franczak. 'Data generation for SIS and the beam lines of the GSI Therapy project', EPAC96

DIAGNOSTICS IN HEAVY ION MACHINES

P. Strehl
Gesellschaft für Schwerionenforschung, Darmstadt, Germany

Abstract

An overview of the measurements of most important beam parameters in heavy ion machines is given. The special characteristics of heavy ions concerning the great variety of parameters with respect to the type of accelerator (linac, circular machine), the species of accelerated ions as well as their energy, beam intensity, beam emittance and time structure are considered. The consequences for the design of beam diagnostic systems are discussed. Typical examples of measuring systems are given. Experimental results taken during the long operating time of the GSI facilities, covering a wide range of parameters, are reported.

1 INTRODUCTION

Due to the large mass, the great variety of isotopes and, especially the large nuclear charge of heavy ions, the lay-out of a beam diagnostic systems may differ considerably from the design for electron or even proton machines. Considering rf-linacs the velocity of accelerated heavy ions will be in general small in comparison to the velocity of light. Therefore, due to the extremely small penetration depth thermal aspects of beam intercepting diagnostic devices become essential. Furthermore, concerning signal calculation for non-destructive pick-ups, the low velocity results in advanced electrical fields, which have to be taken into account designing pick-ups as well as the interpretation of measured signals. In case of circular machines the relativistic mass increase results in an enormous change of revolution frequency and a rather complex relation between rf-frequency and revolution time which may have consequences on the design of diagnostic systems for rings, too. Moreover, depending on the kind of extraction the time structure of the extracted beam can be very different and, considering slow extraction the beam intensity in the external beam lines can be very low. Furthermore, the necessity to separate different charge states and isotopes, generated in the ion sources as well as the need to analyze complex stripper spectra may require special design of diagnostic tools in hard- and software. In the following a short survey on heavy ion beam diagnostics will be presented discussing especially aspects related to the special characteristics of heavy ions. Although contributions are derived mainly from the GSI-facilities, a great variety of heavy ion diagnostics systems has been developed and implemented looking around the laboratories. An review of beam diagnostics in ion linacs is given in [1] and [2].

2 INTENSITY MEASUREMENTS

2.1 Rf-linacs

In most cases heavy ion beams have a time structure with macropulse lengths of some 100 μs up to some ms and a bunch structure, determined by the rather low accelerating rf of some 100 ps up to some ns. Of course, for macropulse currents below some $\mu A's$, Faraday cups are the most frequent used destructive measuring devices. Due to the very small penetration depth of heavy ions in the order of some μm, the heat transfer into cooler regions of the material and, especially to the cooling water may be not fast enough resulting in melting of the cup surface in spite of water-cooling. Some simple formulas for calculation of heat transfer, especially on short time scales are derived in [3].

Above some $\mu A's$ beam transformers offer a non-destructive absolute measurement including monitoring of macropulse shape. The design of beam transformers is discussed in detail for example in [4]. Since sensitivity, resolution, and dynamic range are related to the macropulse length, designing a transformer for heavy ion linacs may require special attention if the macropulse length is in the order of some ms.

2.2 Circular machines

Due to the wide spectrum of ion species and the flexibility of modern machines concerning time structure of the delivered beams, the intensities can be vary from some particles per second (pps) up to about some 10^{12} pps. Figure 1 shows how this wide range of charged particle fluxes can be covered by use of various techniques.

Coming from the very low intensity side, particles can be counted by hitting a scintillation material (plastics, liquids) connected to a photomultiplier. This absolute measurement of particle flux works up to about 10^5 pps using conventional scintillation material in connection with conventional signal processing methods. A very new development is the use of diamond as detector in connection with modern broadband signal processing techniques, extending the range of particle counting more than 2 decades up to some 10^8 pps (see Figure 1). Although the new method of particle counting is described detailed in [5], Figure 2 gives an impression about the capability of the new detector system.

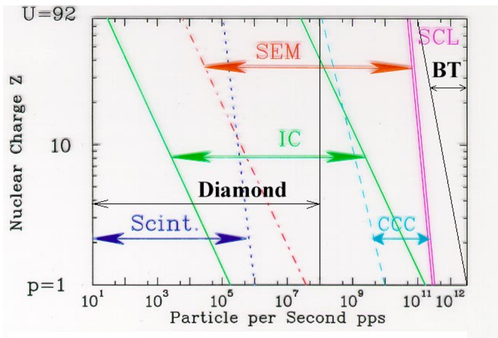

Figure 1: Typical intensity range in the slow extraction mode.

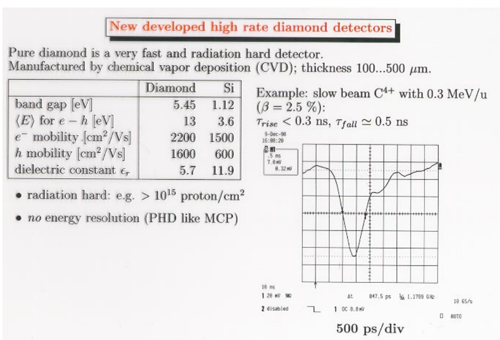

Figure 2: Most important parameters of diamond and silizium detectors and measured output signal.

Since 10^8 pps of for example 50^+ charged heavy ions correspond to a current of only 0.8 nA and conventional beam transformers can be used from some μA upwards it is not possible to cover the whole range shown in Fig. 1 by absolute intensity measurements.The gap is bridged by ionization chambers (IC) and secondary electron monitors (SEM). Calibration of the IC is performed in the overlapping regions with scintillation or diamond counters. Advantageous is a combination of a SEM, an ionization chamber and a scintillation particle counter. Due to saturation of the ionization chambers the SEM, which can be calibrated with the ionization chamber, has to be used at higher intensities. Coming from the high intensity end of Fig. 2 the region of absolute current measurements has been extended downwards by the development of the cryogenic current comparator (CCC) which is described in [6].

2.3 *Identification of isotopes, charge states*

Due to uncontrolled sputtering of materials in an ion source (PIG for example) or an unfavorable selection of the auxiliary gas, strange ions, having nearly the same charge over mass ratio as the required ion may be produced. If an ECR ion source is used to produce metal ions also ions from the material of the oven may be contained in the ion beam. In some cases it may be not possible to separate the isotopes using a magnetic analyzing system. A very typical example is $^{207}Pb^{9+}$ $(A/\zeta = 22.9973)$ and $^{184}W^{8+}$ $(A/\zeta = 22.9939)$ and similar cases are given by the combinations : $^{96}Mo^{4+}$ and $^{144}Sm^{6+}$, ^{40}Ar and ^{40}Ca, $^{76}Ge^{4+}$, $^{38}Ar^{2+}$ and $^{57}Fe^{3+}$. To analyze the composition of the beam, a set-up based on x-ray spectroscopy may be used [7]. The ions are excited by a thin carbon foil and the emitted radiation is analyzed by a semiconductor detector. Fig. 3 shows an X-ray spectrum of a ^{76}Ge beam with mixtures of ^{38}Ar and ^{57}Fe with a schematic view of the arrangement in the insert.

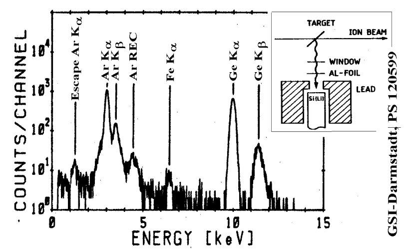

Figure 3: X-ray spectrum of a ^{76}Ge beam with mixtures of ^{38}Ar and ^{57}Fe.

Another typical example is the identification and separation of charge states behind strippers. Figure 4 shows two typical stripper spectra of uranium, demonstrating the efficiency of computer-aided beam diagnostics. In a first step a spline fit is performed to get a mathematical description of all peaks. After that various least squares fits can be applied. Assuming the energy is known, the charge states ζ_i are identified by applying a least squares fit according to:

$$\sum_i \left[B_i - \frac{3.10715 A\beta\gamma}{\rho\zeta_i} \right]^2 = Min$$

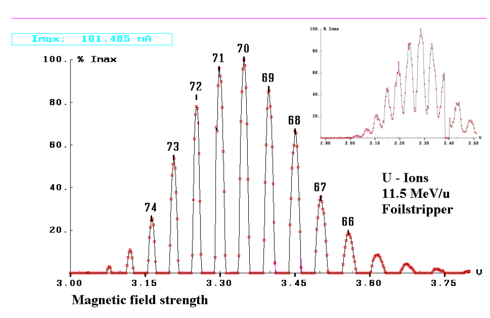

Figure 4: Measured stripper spectra of uranium and charge state identification by least squares fit.

3 BEAM PROFILE MEASUREMENTS

3.1 Rf-linacs

Mostly used devices are profile grids, wire scanners, viewing screens and residual gas ionization monitors. In general viewing screens will stop the particles completely and due to the wide range of intensities, ion species and beam energy, it may become difficult to find the right screen material concerning sensitivity and decay time. Since harps and wire scanners let pass through the main part of the beam they may be more convenient. Using modern signal processing the relation between beam intensity and profile signal will be linear over more than 5 decades. Concerning signal amplification two, in principle different methods have to be considered: Performing current to voltage conversion with a maximum gain in the lowest range of about 2 nA/V or applying the switched integrator principle, where the output voltage is determined by the product of current $times$ integration time. Taking the IC ACF2101 as an example, a charge of Q=10^{-10} As has to be collected to get an output signal of 1 V. Therefore, for a beam pulse length below about 50 ms the I/U-converter principle should be preferred, while in case of long pulses or even DC, the switched integrator gives better performance. Due to the low penetration depth the maximum ratings concerning thermal heating become essential in case of heavy ions. Considering wires made from a tungsten-rhenium alloy the following values have been calculated and confirmed experimentally: The maximum DC, respectively mean beam power should be below 0.25 - 0.5 Watts per mm length of those part of the wire hit by the beam. Considering the pulse power, the energy of one beam pulse should be below the energy needed to melt the so-called range volume, which is given by the penetration depth *times* the area hit by the beam. In case of tungsten this figures out to be 14.5 Ws/mm^3.

The high ionization rate of heavy ions offers the possibility to take advantage of residual gas ionization for beam profile monitoring using the same electronics as for profile grids. Experience at the UNILAC has shown that the expected signal can be calculated within about a factor of 2. Figure 5 shows the calculated maximum signal in the center of the beam in dependence of beam energy for Ne-, Ar-, Xe-, and U-ions taking energy loss data from [8] and [9], assuming 36.5 eV as ionization energy to generate one electron-ion pair in a gas mixture of 80% H_2 and 20% N_2. By designing such a profile monitor, collection of ions should be preferred due to the larger deflection of electrons in the space charge field of moving, non-compensated bunches.

3.2 Circular machines

Non-destructive or even nearly non-destructive methods cannot be applied. Due to the extremely high energy loss of heavy ions even flying wire techniques cannot be used. But taking advantage of the high ionization of heavy ions residual monitors may be an alternative method, [10]. Figure 6 shows the principle of a monitor which is in development at GSI to measure beam profiles in the SIS.

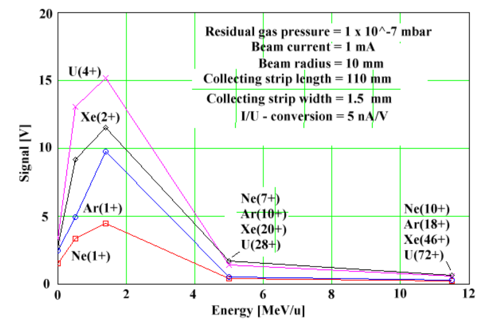

Figure 5: Calculation of signal strengths for detection of H_2-, N_2- ions from residual gas ionization.

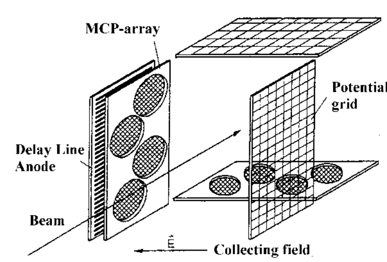

Figure 6: Scheme of a residual gas ionization profile monitor using Multi-Channel-Plates (MCP) for first signal amplification.

Although the residual gas pressure is down to 10^{-11} mbar the MCP's will compensate this by a gain of up to 10^6 and therefore, nearly the same signal strength as given in Fig. 5 can be expected. Of course, beam profile may be measured destructively by use of scrapers.

4 MEASUREMENTS OF PHASE SPACE DISTRIBUTIONS

A review has been given in [11].

4.1 Transverse phase space

The conventional slit-detector method can be modified by using a multi-slit plate in front of a scintillator screen [12], [13], which gives the opportunity to measure the emittance in one transverse phase plane within a single pulse. Taking advantage of modern PC-controlled CCD-cameras a pepper-pot system which gives the intensity distribution even in the 4-dimensional phase space within one pulse has been designed at GSI [14]. Figure 7 shows very first original pictures from the commissioning of the new GSI high current linac. The complex mathematical algorithms to extract emittances from those data are described in [15].

Single shot systems may be the only destructive device to measure emittances in case of high intense heavy ion beams. Furthermore, those systems offer the possibility to study fluctuations of ion sources from pulse to pulse or even within one pulse.

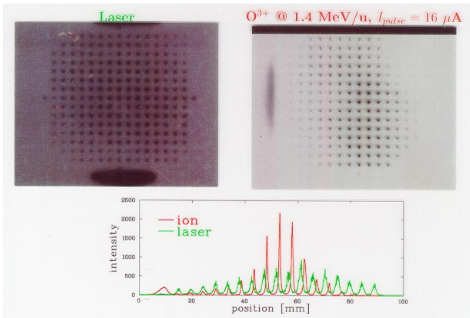

Figure 7: Light spots observed on the viewing screen of a pepper-pot device. Top left: Spots generated for calibration using a laser beam. Top right: Spots from an oxygen beam. Bottom: Intensity distribution along one line.

In case of circular machines transverse emittances can be determined according to the relation between profile width and $\sqrt{\varepsilon\beta}$.

4.2 Longitudinal phase space

There is a great variety of measuring schemes [1], [16]. A set-up using a MCP and diamond counters to measure longitudinal emittances during the commissioning of the new Unilac prestripper is described in [17]. The primary ion beam goes through a thin gold-foil (120 $\mu g/cm^2$). Some particles will be scattered out of the beam by Rutherford scattering which reduces the count rate to a tolerable level. The scattered particles then have to pass two very small apertures. Behind the second aperture a very thin carbon foil is located. The particles passing the carbon foil will generate secondary electrons. The signal is amplified by a MCP and gives a start signal to a TDC (Time to Digital Converter). A second start signal will be generated from the passing particle hitting a diamond counter in some distance behind the carbon foil. Since the stop is always derived from the accelerating rf the method results in a determination of the intensity distribution in the longitudinal phase space.

4.3 Longitudinal bunch shape measurements

The scheme discussed above can be simplified to measure the time structure of bunches with only one diamond counter. Fig. 8 shows the results of a measurement behind the new RFQ of GSI at a final energy of 120 keV/u. Due to the very low velocity of the ions the bunch structure and broadening of the bunch after a drift space observed with the diamond counter cannot be resolved with a capacitive pick-up.

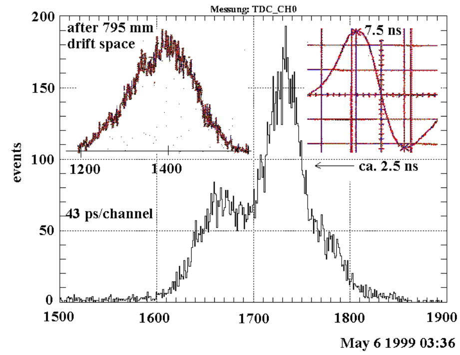

Figure 8: Bunch shape observed with a diamond counter in comparison with the signal of a capacitive pick-up.

Bunch shape monitors based on the analysis of secondary electrons arising from a thin tungsten wire hit by the primary beam have been used successful at various facilities [1]. Considering the maximum ratings with respect to thermal destruction given in section 3.1, this method may fail in case of intense heavy ion beams. Taking over the principle, but detecting electrons from the residual gas ionization a rather complex monitor is in development at GSI [18].

4.4 Measurements of spill micro-structure

Considering heavy ion synchrotrons in slow extraction mode, measurement of spill structure becomes important. Due to the very low ratio between typical revolution times in the μs - region and spill times up to some seconds the intensity of the extracted beam may cover the whole range shown in Fig. 1.Therefore, the measuring system has to be designed very carefully with respect to sensitivity and bandwidth. Figure 9 shows an example [6] from the SIS, measured with the cryogenic current comparator (CCC in Fig. 1). Although the time average over the spill is only

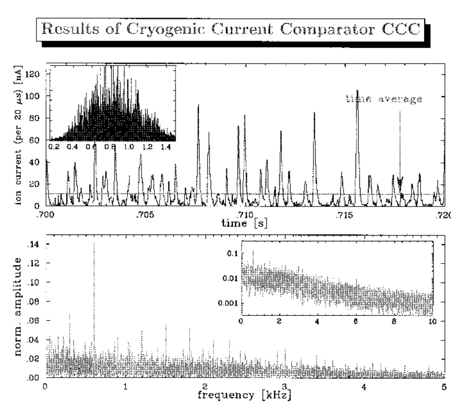

Figure 9: Measurement of spill micro-structure with the CCC.

about 10 nA, peak currents in the order of 100 nA and gaps of some 100 μs have been observed. Of course, the ratio peak to average depends on the integration time (bandwidth) of the measuring system and, in case of SIS, can be improved considerably if the rf-voltage of the accelerating cavity remains on during the flat-top.

5 BPM-SIGNAL PROCESSING

As already mentioned in the introduction, measuring systems in heavy ion synchrotrons differ from e-, p-machines due to the large change of frequency during acceleration. Therefore, considering broadband systems with the possibility to monitor single bunches at a determined time and a selected BPM, the large change of velocity has to be taken into account. At the SIS this has been realized by a so-called timing generator [19], which produces rf-synchronous gate pulses using a fast RAM-table, whereby addressing is performed by an rf-related clock frequency. Of course, this can be realized now by use of modern DSP's. Due to the wide range of different particles resulting in a wide range of intensities and the large change of the geometric bunchlength during acceleration, a broadband signal processing system for heavy ion machines has to cover a larger dynamic range compared to e-, p-machines. In case of the SIS the total dynamic range covers 140 dB (-80 dBm+60 dBm). The advantage of single bunch observation is demonstrated in Fig. 10.

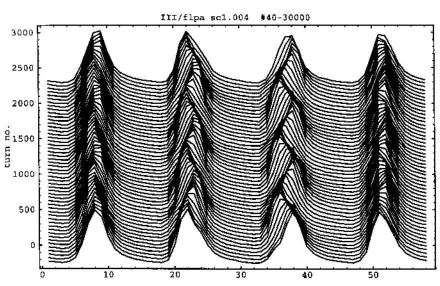

Figure 10: Bunch oscillations observed with a broadband system at flattop of SIS.

Considering narrowband systems, the large change of frequency range can be covered by use of modern phase locked loops and mixing the frequency-swept bunch signal into constant intermediate frequency signals which then can be amplified with a determined bandwidth. Of course, in comparison to the broadband system the sensitivity increases depending on the selected bandwidth. Figure 11 gives the SIS-BPM sensitivity versus resolution bandwidth [20], which holds for all similar BPM systems.

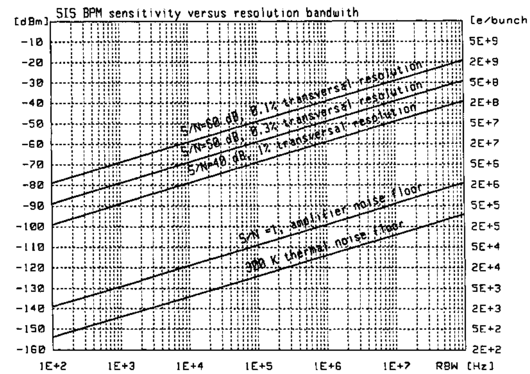

Figure 11: Sensitivity of narrowband systems versus resolution bandwidth.

6 REFERENCES

[1] Ostroumov, P. N., Proc. of LINAC 98, Chicago, (1998), and references therein, in print

[2] Strehl, P., Chapter 5 in the Handbook Ion Sources, CRC Press (1995), and references therein

[3] Müller, R. W., Strehl, P., Nucl. Instr. Meth. A 425 (1998) p. 305-309

[4] Unser, K. B., DIPAC 1993, Montreux, (1993), CERN PS/93-35, p. 105-109

[5] Moritz, P. et al., Beam Instrumentation Workshop, Stanford, CA (1998), p. 514-521.

[6] Peters, A. et al., Recent Improvements of the Cryogenic Current Comparator for Measuring nA Beams with High Dynamics from the SIS, and references therein, this workshop's proceedings.

[7] Krause, U., IEEE Trans. Nucl. Sci., NS 32, 5, (1985), p. 1941-1943.

[8] Lindhard, J., Scharff, M., Phys. Rev., 124, (1961), p. 128.

[9] Ziegler, J. F., Handbook of Stopping Cross-Sections for Energetic Ions in all Elements, Vol. 5, Pergammon Press, 1984.

[10] Meyer, U. et al., EPAC-98, Stockholm, (1998), p. 1562-1564, and references therein.

[11] Riehl, G. et al., DIPAC 1995, Travemünde, (1995), DESY M-9507, p. 6-10

[12] Bovet, C. et al., EPAC-98, Stockholm, (1998), p. 1488-1490

[13] Clark-Gayther, M. et al., EPAC-98, Stockholm, (1998), p. 1491-1493

[14] Domke, M. et al., DIPAC 1997, LNF-INFN Frascati (Rome) Italy (1997), p. 141-143.

[15] Dolinska, M. et al., Emittance Measurements at the new Unilac Pre-Stripper using a Pepper-Pot with a PC-controlled CCD-Camera, this workshop's proceedings.

[16] Strehl, P., Joint Universities Accelerator School 1999, Archamps, (1999), in print.

[17] Forck, P. et al., Aspects of Bunch Shape Measurements for Slow, Intense Ion Beams, this workshop's proceedings.

[18] Forck, P. et al., EPAC-98, Stockholm, (1998), p. 1500-1502

[19] Fradj, M., Moritz, P. Strehl, P., Vilhjalmsson, H., GSI-report 88-1 (1988), p. 375

[20] Moritz, P., Beckert, K., DIPAC 1993, Montreux, (1993), CERN PS/93-35, p. 131-135

BEAM DIAGNOSTICS, OLD AND NEW*

H. Koziol, CERN, Geneva, Switzerland

Abstract

The performance of accelerators and storage rings depends critically on the completeness and quality of their beam diagnostic systems. It is essential to equip them from inception with all the instruments providing the information on the properties and the behaviour of the beams, needed during running-in, in operation, and for development of performance towards the design goal and often well beyond. Most of the instruments have proven their worth since decades, but their power has been increased through the modern means of data acquisition and treatment. A few new instruments have made their appearance in recent years, some still under development and scrutiny for their operational value and precision. The multi-accelerator chains of today's and tomorrow's big colliders have tight tolerances on beam loss and emittance blow-up. For beam diagnostics this means a great challenge for precision and consistency of measurements all along the chain.

1 INTRODUCTORY REMARKS

Despite an all-encompassing title, evidently not all areas of beam diagnostics can be covered. Specialities like instrumentation for linear colliders, feedback-damping, beam-loss monitoring, collider luminosity measurement and ultra-fast bunch length measurement, must be left aside here. Excellent presentations were given on these subjects at recent conferences. Also, repetition of what was offered in similar review talks will be avoided.

On the other hand, some weight will be given to the diagnostics aspect of CERN's accelerator chain for the future Large Hadron Collider (LHC), and rather than giving detailed descriptions of systems and the results obtained with them, trends of evolution, challenges and open needs will be pointed out.

2 SOME EVERGREENS

It is quite amazing to see many tools of beam diagnostics of a venerable age of many decades, and even up to a century, around accelerators built with the most modern technologies. For example, Röntgen saw the first X-ray images in 1895 on luminescent screens, and still today these are one of the most basic and popular beam diagnostic means, although now more correctly called scintillator screens.

Other examples are: the Faraday-cup, to measure current or charge of beams delivered by low energy accelerators, such as RFQs; the "pepper-pot", which was the first crude instrument for measuring emittance, also limited to low energy beams; the ionization chamber, still an appreciated means for sensitive detection of beam loss and radiation levels; secondary emission detectors in a great variety of constellations; and so on.

All these venerable detectors have undergone considerable evolution in many aspects, such as resolution, both temporal and spatial, dynamic range and sensitivity. The most remarkable advance came with the advent of digital data acquisition and treatment: with its help one can draw rather precise quantitative data from instruments which previously offered only qualitative information.

We shall mention two examples of aged instruments rejuvenated in this way: the scintillator screen and the pepper-pot.

Scintillator screens are inserted into the path of the beam by a remotely controlled mechanism. The light which is produced when the beam particles strike the screen is observed with a TV camera. The screen may have a graticule, made visible by external illumination (Fig. 1).

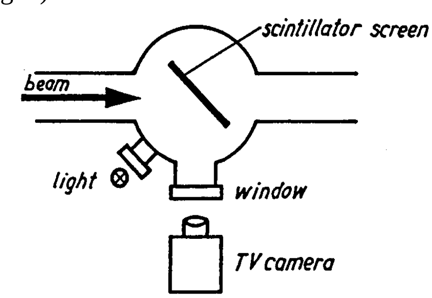

Figure 1: Typical arrangement for observation of beam position and size with a scintillator screen and a TV camera [1].

The light spot observed on a remote monitor permits rather accurate determination of beam position, to 0.5 mm under favourable conditions. One only gets a rough impression of the beam size, because the commonly used systems are driven into saturation, such that on a dark background one only sees a rather uniform white spot, the size of which depends on beam intensity and various equipment settings.

A modern version [2] will use a CCD-camera for good linearity, digital data acquisition (a "frame grabber") and treatment such that a 2-dimensional density distribution can be derived (Fig.2).

* This is essentially a repeat of "Beam Diagnostics Revisited", invited talk given at EPAC, Stockholm, June 1998.

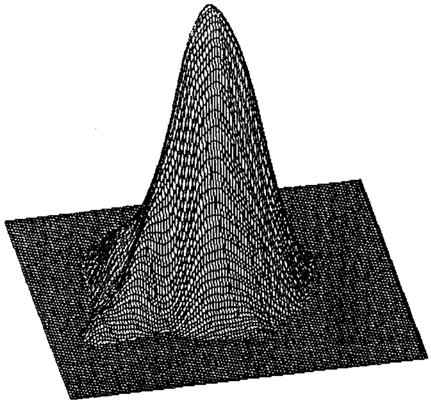

Figure 2: 2-dimensional beam density distribution derived from the light-spot on a scintillator screen [3].

The pepper-pot, as its name suggests, is a metal plate with small holes in it. The plate is thick enough to stop the low-energy beam that one is measuring. The particles that pass through the holes are left to diverge over a drift-space, so that when they strike a scintillator screen they form elongated images (Fig.3). The position of the holes determines the coordinates of the particles and the elongations are a measure for the divergence at those coordinates, so that with the help of a ruler and a slide-rule one quickly obtained a good estimate of the beam's emittance.

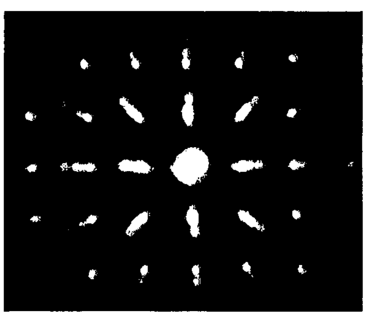

Figure 3: The particles passing through the holes of a pepper-pot and a drift space form elongated images on a scintillator screen [4].

Modern digital techniques have brought about a come-back of this old-fashioned device and turned it into a convenient real-time and fairly accurate instru-ment. It is used, e.g., at the Heavy Ion Linac of the CERN PS Complex, for Pb^{27+} ions at 4.2 MeV/u [5]; at the LASER Ion Source, being developed for the same linac [6]; and a further system has become available at GSI, Darmstadt, for 1.4 MeV/u Uranium ions [7].

3 SOME NOVELTIES

A full and fair account of "novelties" is impossible to give. The criterion for what constitutes a novelty is rather fuzzy, as the basic idea may have been around for many years, until someone, perhaps driven by a particular need, picked it up and brought it to fruition. Rather than attempt to give a complete list, a quite subjective selection of devices and methods shall serve as illustration that beam diagnostics is an innovative and prospering branch of accelerator physics.

Over the last few years a most useful tool for RFQs and linacs was brought to operational perfection, the principle of which was proposed and a first-generation version built some two decades ago [8]: the Bunch-Length Detector (BLD), and several variants of it [9]. The secondary electrons emitted from a thin wire, placed in the beam, are accelerated towards a transverse deflector driven by the linac RF. The density distribution of the secondary electrons in the detector plane is then an image of the longitudinal density distribution of the beam particles in a linac bunch (Fig.4). By scanning the wire through the beam, the complete 3-dimensional bunch density distribution can be determined. This is a great step forward in understanding the effects of the linac's parameters and bringing the linac to high performance.

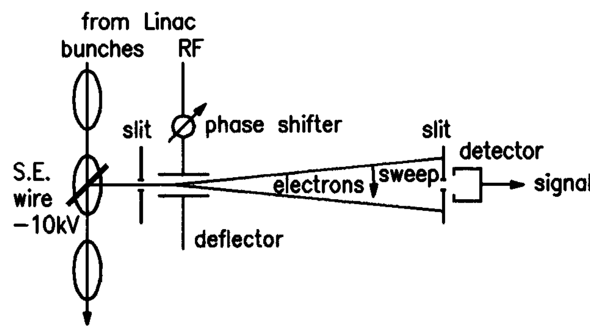

Figure 4: Basic layout of a Bunch Length Detector (BLD, according to [9]).

Optical Transition Radiation (OTR) increasingly replaces scintillation as a means of observing beam position and size in transfer lines [10]. OTR screens can be made very much thinner than scintillator screens, so that the effects on the beam, energy-loss and multiple Coulomb scattering causing emittance blow-up, are much weaker. Moreover, they do not suffer from two limitations of scintillator screens, namely saturation and propagation of light within the screen.

One of the nearly-non-destructive means to measure profiles of circulating beams is the fast wire-scanner, brought to a high degree of perfection in recent years. The increase of speed to 20 m/s, made possible through real-time controlled optimized movement, minimizes the blow-up caused to the beam, together with the use of thin strands of carbon fibres (instead of W-, Ti- or Be-wires), which also greatly improved the lifetime. The fast wire-scanners in the CERN 26 GeV PS [11,12] cause hardly any blow-up in a single sweep at an injection energy of 1 GeV, and have been demonstrated to perform well in the preceding Booster down to its injection energy of 50

MeV, although causing significant blow-up at such a low energy.

Another detector that has a long history before it came to practical fruition recently, is the Cryogenic Current Comparator [13]. Essentially a variant of the dc beam current transformer, using a superconducting transducer and a SQUID, it pushes the sensitivity up by 3 orders of magnitude. Despite a considerably greater technological complication, a typical resolution of 1 nA makes it the ideal tool for measuring the low intensities of slow extracted beams from ion accelerators, including those for medical application.

A particularly powerful means available to accelerator physics is the “Schottky scan”, the paragon of non-invasive diagnostics. It is based on the granu-larity in the density distribution of circulating beams, which produces beam-induced noise in specially built, highly sensitive, pick-ups. This “Schottky noise” consists of the harmonics of the revolution frequency, nf_{rev}, and, when the pick-up is position-sensitive, the “betatron sidebands”, $(m \pm Q)f_{rev}$. Signal analysis with scanning frequency analyzers has led to the term “Schottky scan”. First applied to a particle beam in 1972 at the CERN ISR [14], diagnosis based on Schottky signals has undergone a spectacular evolution, profitting from technological advances in low-noise amplifiers, special pick-up structures and digital signal processing (FFT). It has become one of the most refined means of measuring beam and machine properties, as varied as beam intensity, frequency and momentum spread, Q-values and chromaticity, rms betatron amplitude and emittance. For the measurement of intensity, they are first calibrated against a beam current transformer and can then extend the measurement to very low intensities. The record resolution was achieved at the Initial Cooling Experiment (ICE) at CERN, where a beam was measured to consist of 80 ± 13 antiprotons. Schottky scans take time and are therefore mostly used at storage rings. Since one observes incoherent signals, scans are mostly made on coasting beams, but with the necessary precautions, bunched beams can be observed too [15].

One can often not distinguish between a novel detector and a novel method of using existing detectors. As an example, let us look at the verification of betatron matching upon injection into a circular accelerator. Incorrect matching will lead to coherent quadrupole oscillations, i.e. a beating of the beam width, until decoherence turns them into an emittance increase. One of the devices capable of detecting beam-width-beating is the quadrupole pick-up, which can sense variations of the ellipticity of beam cross section. However, information on ellipticity is easily swamped by the common-mode signal when the beam is not perfectly centred in the pick-up. It took the development of a new way of treating the signals from the four electrodes to permit practical use [16], but very good centring of the beam is still a prerequisite.

A further method for observation of the coherent variation of beam size was proposed [17]. At high energies, one can insert a screen (scintillator or OTR), in the path of the beam and, with digital image acquisition and treatment, derive beam width turn-by-turn. A gradual increase in width, due to multiple Coulomb scattering, will be superimposed. Similarly, a secondary emission grid can be used [18], (Fig. 5).

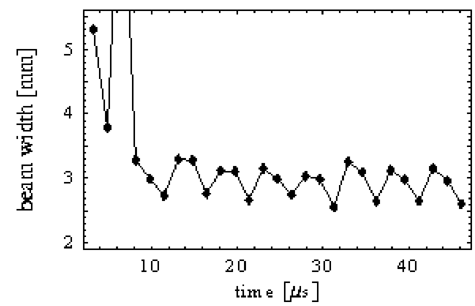

Figure 5: Periodic variation of beam width (σ) following mismatched injection. From multi-traversals of 50 MeV protons through a low-mass secondary emission grid in the CERN PS Booster. The initial transients are an inherent consequence of the multiturn injection process. Betatron tune Q = 4.34 [27].

The development of position pick-ups to unpre-cedented resolution has brought a new impetus to the time-honoured method of variation of quadrupole currents. In fact, the precision alignment of CERN's LEP and of other machines is obtained using "k-modulation" [19]. This, together with modern means of controls and on-line optics calculation, has also returned respectability to its application in transfer lines, where it allows economically, and without doubts about relative alignment, the determination of whether a beam passes through the centre of a quadrupole or how far off it is. In other words, every quadrupole can serve as a position detector.

4 SOME CHALLENGES

Apart from the instrumentation for linear colliders, the greatest challenge is precise and coherent measurement of beam parameters throughout the long chains of accelerators in today's and tomorrow's big circular hadron colliders, in which no synchrotron radiation damping covers up the imperfections of beam-handling at all stages. Foremost amongst these parameters is transverse emittance. Witness to the importance of this subject is the fact that an ICFA Workshop was recently dedicated to it [20].

There are several reasons for this being a challenge. Emittance is measured at the various stages with instruments of quite different nature. Let us take as an example the injector chain of the future LHC. At the RFQ and the 50 MeV linac one uses instruments basically resembling the pepper-pot, and another one is derived from the above-mentioned BLD. Secondary Emission Monitors (SEM-grids) measure the profiles on the way to and into the 1 GeV Booster. When the beam circulates there, it is measured with a fast wire-scanner, which measures projected density distribution, and, in a destructive way, with the BEAMSCOPE [21], which really measures amplitude distribution. On the way to the 26 GeV PS, there are again SEM-grids, and on the beam circulating in it again a fast wire-scanner and partially destructive measurement targets, indicating amplitude distribution. SEM-grids provide quality checks after ejection from the PS and upon injection into the SPS. At that machine, it is foreseen to add OTR screens with quantitive evaluation for profile measurements at injection and at ejection towards the LHC, where again a panoply of different instruments will measure profiles.

Measuring profiles is one thing, obtaining emittance is another. In a circular machine one must know accurately the value of the beta-function. In transfer lines, where emittance is calculated from several profiles, one must know equally accurately the transfer matrices between the usual 3 SEM-grids or screens. And all of this is only valid when there is no coupling.

The density profiles obtained from such basically different instruments, and the emittances derived from them, must be treated mathematically such that a valid comparison can be made. This is no mean task when one aims at an absolute precision of typically 5% in emittance, i.e. 2.5 % in beam "size". The definition of size is a further difficulty in obtaining coherence of data. A beam never has a Gaussian distribution and the way this fact is dealt with mathematically is often a matter of ideology. Suffice it to say that definition and treatment should be representative for the bulk of the beam when the final concern is collider luminosity [21, 22, 23].

One challenge that stands out is the development of a detector which, in machines like PS, SPS and LHC, measures the profile of the beam during acceleration in a non-destructive and continuous way, with a precision of the order of 0.1 mm in the PS, demanded for beams destined for the LHC.

Synchrotron light and Compton scattering, so successfully used on electrons and positrons, are not accessible. The one instrument that comes close is the residual gas monitor, in which electrons and/or ions, created in the residual gas through the ionizing action of the beam, are extracted with electric fields and used for imaging the beam density profile. However, to obtain a sufficient spatial resolution, one would need to use very high electric fields and a strong focussing magnetic field in the same direction. These perturb the beam and must be compensated, so that it becomes an altogether very voluminous and clumsy apparatus.

Two lines may be pursued. The one is using the light emitted from the residual gas produced by the excitation of its atoms through the beam particles. Attempts at using this method have been made in the past [24, 25], and showed a number of perturbing effects. Still, a new look at it is worth the effort. The other is based on the deflection suffered by a thin ion-beam, swept transversely across the circulating beam, in the latter's electric and magnetic field. Promising experiments were made [27].

5 CONCLUDING SERMON

When setting about conceiving diagnostic systems for an accelerator, one should first thoroughly acquaint oneself with the machine and all possible modes of operation and with the properties and behaviour of the beams under various conditions. That is, not only the nominal beam, but also as it may be at an early stage of running-in and under abnormal conditions, when one particularly depends on diagnostics. One will aim for easily perceived information for routine operation, and will provide for the special needs of accelerator physics experiments.

When making the detailed design of an accelerator, diagnostics is to be included at an early stage: for the trivial reason that space must be foreseen for the detectors, but also because the capabilities of the diagnostic systems, and the information they deliver, can have repercussions on the design of the accelerator (e.g. through the possibilities offered by feedback systems).

Accelerators ought to be equipped with a complete set of diagnostics from the day of first beam, as it is during the running-in that it is dearly needed. However, one must be aware of the fact that also the diagnostic systems need their own running-in, with beam.

For each diagnostic system there should be an expert who sees it as a whole, from the detector in the tunnel, through the electronics, data acquisition and treatment, to the display in the control room. Otherwise, efficiency of use suffers and unnecessary complication is added.

Finally, on-line calibration, on user-request or automatic, during routine operation, is needed for always correct results and to instill the users with confidence.

REFERENCES

[1] H. Koziol, "Beam Diagnostics for Accelerators", CAS, Jyväskylä, Finland, September 1992; CERN 94-01, 1994.
[2] R. Jung, "Image Acquisition and Processing for Beam Observation", 1st DIPAC'93, Montreux, May 1993; CERN PS/93-35 (BD), SL/93-35(BI), 1993.
[3] F. Marti, R.A. Blue, J. Johnson, J. Kuchar, J.A. Nolen, R. Putt, B. Sherill, J. Yurkon, "Beam Diagnostic

Developments at NSCL", 12th International Conference on Cyclotrons, Berlin, 1989.
[4] R. Scrivens, private communication (PS LASER Ion-Source).
[5] M. Crescenti, U. Raich, "A Single-Pulse Beam Emittance Measurement for the CERN Heavy Ion Linac", 2nd DIPAC'95, Travemünde, May 1995; DESY M-9507, 1995.
[6] R. Scrivens, A. Shumshurov, J. Tambini, "Further Emittance Measurements on the CERN Laser Ion Source", PS/HI Note 96-13.
[7] M. Domke, Ch. Dorn, P. Forck, H. Kraus, A. Peters, P. Strehl, "A Single-Shot Emittance Measuring System for Intense Heavy Ion Beams", 3rd DIPAC'97, Frascati, October 1997; LNF-97/048 (IR), 1997.
[8] R.L. Wittkover, "A Non-Destructive Bunch Length Monitor for a Proton Linear Accelerator", Nucl. Instrum. Meth.137 (1976).
[9] A.V. Feschenko, P.N. Ostroumov, "Bunch Shape Measuring Technique and its Application for Ion Linac Tuning", Linear Accelerator Conference, SLAC, Stanford, June 1986, SLAC-303, CONF-860629, UC-28.
[10] D. Giove, C. De Martinis, G. D'Auria, M. Ferianis, C. Rossi, X. Artru, L. Wartski, R. Chehab, K. Honkavaara, M. Taurigna-Quere, A. Variola, M. Castellano, L. Catani, P. Patteri, R.J. Colchester, G. Ferioli, R. Jung, "Optical Transition Radiation Diagnostics", 3rd DIPAC'97, Frascati, October 1997; LNF-97/048 (IR), 1997.
[11] Ch. Steinbach, "Emittance Measurements with the CERN PS Wire Scanner", International Workshop on Particle Dynamics in Accelerators, Tsukuba, Japan, 1994; CERN/PS 95-04(OP), 1995.
[12] P. Elmfors, A. Fassò, M. Huhtinen, M. Lindroos, J. Olsfors, U. Raich, "Wire Scanners in Low Energy Accelerators", Nucl. Instrum. Meth. A 396 (1997).
[13] A. Peters, H. Reeg, C.H. Schroeder, W. Vodel, H. Koch, R. Neubert, "Absolute Measurements and Analysis of nA-Ion Beams", 3rd DIPAC'97, Frascati, October 1997; LNF-97/048 (IR), 1997.
[14] J. Borer, P. Bramham, H.G. Hereward, K. Hübner, W. Schnell, L. Thorndahl, "Non-Destructive Diagnostics of Coasting Beams with Schottky Noise", IX Intern. Conf. High Energy Accel., SLAC, May 1974; CERN/ISR-DI/RF74-23.
[15] S. van der Meer, "Diagnostics with Schottky Noise", Joint US-CERN School on Part. Accel., Capri, October 1998; CERN/PS/88-60 (AR).
[16] V. Chohan, F. Pedersen, S. van der Meer, D.J. Williams, "Measurement of Coherent Quadrupole Oscillations at Injection into the Antiproton Accumulator", EPAC'90, Nice, June 1990; CERN PS/AR/90-31.
[17] C. Bovet, R. Jung, "A New Diagnostic for Betatron Phase Space Matching at Injection into a Circular Accelerator", LHC Project Report 3, Rev., 1996.
[18] C. Bovet, R. Colchester, C. Dutriat, G. Ferioli, J.J. Gras, R. Jung, P. Knaus, U. Raich, J.M. Vouillot, "First Results from Betatron Matching Monitors Installed in the CERN PSB and SPS", EPAC'98, Stockholm, June 1998; CERN SL-98-037 BI, 1998.
[19] I. Barnett, A. Beuret, B. Dehning, K. Henrichsen, M. Jonker, M.G. Morpurgo, M. Placidi, R. Schmidt, L. Vos, J. Wenninger, I. Reichel, F. Tecker, "Dynamic Beam Based Calibration of Orbit Monitors at LEP", 2nd DIPAC'95, Travemünde, May 1995; DESY M-9507, 1995; CERN SL/95-55 (BI).
[20] 4th ICFA Beam Dynamics Mini-Workshop on Transverse Emittance Preservation and Measurement, CERN, November 1997; CERN PS/DI/Note 98-03, ed. R. Cappi.
[21] M. Martini, H. Schönauer, "Emittance Measurements in the CERN PS Complex", LHC'96, Montreux, October 1996; CERN PS/97-18 (CA), 1997.
[22] M. Arruat, C. Carli, H. Koziol, M. Lindroos, M. Martini, J. Olsfors, U. Raich, H. Schönauer, "A Comparative Study of Fast Wire Scanners, BeamScope and SEM-Grids for Emittance Measurement at the PS Booster", 3rd DIPAC'97, Frascati, October 1997; LNF-97/048 (IR), 1997.
[23] C. Bovet, C. Fischer, R. Jung, "Comparison of Different Methods for Transverse Emittance Measurement", 3rd DIPAC'97, Frascati, October 1997; LNF-97/048 (IR), 1997.
[24] D. Bloess, H. Riege, "Instrumentation for Beam Profile Measurement in the PS", PS/EI Note 79-3, 1979.
[25] T. Kawakubo, E. Kadokura, T. Kubo, T. Ishida, H. Yamaguchi, "Non-Destructive Beam Profile Measuring System Observing Fluorescence Generated by Circulating Beam", PAC'95, Dallas, May 1995; KEK Preprint 95-13, 1995.
[26] J. Bosser, A. Feschenko, R. Maccaferri, "Ion Profilometer for the SPS and LHC Accelerators", PS/BD/Note 99-07, 1999.
[27] P. Knaus, U. Raich, private communication.

USE OF SUPERIMPOSED ALTERNATING CURRENTS IN QUADRUPOLES TO MEASURE BEAM POSITION WITH RESPECT TO THEIR MAGNETIC CENTRE

S.A.Griffiths, D.J.Holder, N. Marks, CLRC Daresbury Laboratory, Warrington, WA4 4AD, UK.

Abstract

The positional stability of the electron beam in a modern state-of-the-art synchrotron radiation source is critical, as the many experimental users require consistency in the position and dimensions of the incoming photon beams which are incident on their experimental samples. At the Daresbury Synchrotron Radiation Source (SRS), inaccuracies in the measurements of the positions of both beam position monitors and the lattice quadrupoles can be overcome by measuring the position of the electron beam with respect to the magnetic centres of the quadrupoles. This was achieved by superimposing an alternating ('ripple') current on the direct current excitation of a single lattice quadrupole and examining the resulting beam oscillations at remote positions in the storage ring. If the electron beam is then subjected to a local distortion at the position of this quadrupole, the amplitude of the beam oscillation induced by the superimposed current is minimised (nominally zero) when the beam is at the quadrupole's magnetic centre. This paper presents details of the electrical circuit developed to inject an alternating current into the coils of individual quadrupoles and gives details of the results achieved to date.

1 BEAM POSITION IN THE DARESBURY SRS

The Daresbury Synchrotron Radiation Source (SRS) is an electron storage ring which generates intense beams of electromagnetic radiation to support a wide range of experimental techniques. The facility parameters are given in Table 1.

Table 1: Basic parameters of the Daresbury SRS.

Electron beam energy	2 GeV
Circumference	96 m
Number of experimental stations	~ 40
Magnet lattice	FODO
Number of cells	16
Number of 'F' quadrupoles	16
Number of 'D' quadrupoles	16

The position of the electron beam in the storage ring and the emerging radiation beams are critical because:

- radiation must be supplied simultaneously to the many beam lines and users;
- users require very high beam positional stability throughout the period that they are accumulating experimental data;
- the lifetime of the stored beam should be maximised, which requires the electron beam to be accurately positioned in the centre of the narrow gap and other ring vacuum vessels.

The storage ring therefore contains vertical and horizontal electron beam position monitors (B.P.M.s) in each straight section and the beam lines have tungsten vane monitors (T.V.M.s) at their front ends for measuring the X-ray beam position. However, these all have alignment survey errors and consequentially their true positions are not known, a situation which also applies to the lattice magnets. Furthermore, it is known that all the storage ring elements move with time and hence, some time after a survey has been performed, there are even greater uncertainties concerning the positions of the B.P.M.s and the magnets. It is clear that an electron beam positioned centrally with respect to the B.P.M.s will not be central in the magnets. An off-centre beam in a dipole will not result in any first-order errors in the electron trajectories, but in the quadrupole, if the beam passes through the magnet at a vertical or horizontal position which is not coincident with the quadrupole's magnetic centre, unwanted deflections will occur. Hence the true positions of the electron beam with respect to the magnetic centres of each quadrupole is very relevant to the efficient and stable operation of the storage ring and is required information. In the measurement method described below, a deliberately induced beam deflection is used to locate the centre of the magnet with respect to the beam.

2 EXPERIMENTAL METHOD

A circulating beam in the storage ring is corrected to a central orbit, as indicated by the B.P.M.s. A small, low frequency alternating current is then superimposed on the direct excitation current in the windings of the quadrupole under investigation. If the electron beam is not central in the quadrupole, the non-zero field at the beam position will induce a small closed orbit deflection of the beam around the complete storage ring lattice; this will have a d.c. component and an oscillating component at the frequency of the alternating ripple induced in the quadrupole. The signals from one or more B.P.M.s or T.V.M.s, at remote positions in the ring, are then examined and Fourier analysis of the signals used to extract the amplitude of this oscillation at the positions of the monitors. The beam position at the perturbed quadrupole is then adjusted by a static, local beam deflection (a ‘beam-bump') and as the amplitude and polarity of this displacement is varied, the amplitude of the oscillation detected at the remote monitor will also change. The beam position is perturbed on either side of the magnet centre and the magnitude of the beam oscillation and the apparent beam position, as measured at the B.P.M. next to the quadrupole, is recorded.

When the beam is centred in the quadrupole, no deflection will occur and the induced positional oscillation will be at a minimum and ideally zero. Data obtained using this technique will indicate the displacement of the beam away from the magnetic centre of the quadrupole at the commencement of the measurement and the value of the bump needed to centre the beam in the quadrupole.

3 GENERATING THE SUPERIMPOSED OSCILLATING CURRENT

The circuit used to generate an alternating component, which is superimposed on the direct current in the quadrupole windings, is shown in Fig. 1.

The technique uses an active current shunt in parallel with the magnet, with a feedback circuit to control the bypass current. This design requires no additional power source, as it utilises the resistive voltage drop across the quadrupoles. It is therefore cheaper and simpler than circuits which inject an alternating current on top of the main direct current excitation.

The uni-directional bypass current is controlled by the mosfet shown in the centre of the circuit. This is driven from a high gain isolating operational amplifier, which takes an error signal from the difference of a sinusoidal, variable frequency, variable amplitude reference and a direct current transformer, which samples the bypass current. The design uses four shunts per sixteen series connected quadrupoles, with one shunt switched between four quadrupoles by means of the relays shown in the diagram.

The parameters of the system are given below; Table 2 gives the basic parameters of the F and D quadrupole magnets. Table 3 provides information on the ripple system.

Table 2: Storage Ring Quadrupole Parameters at 2 GeV.

	‘F’ Quads	‘D’ Quads
Operating direct current (A)	1021	423
Operating direct voltage (V)	378	115
Direct volts per quad (V)	23.6	7.2
Max volts to earth (V)	189	115
Inductance per quad (mH)	23.6	20.8

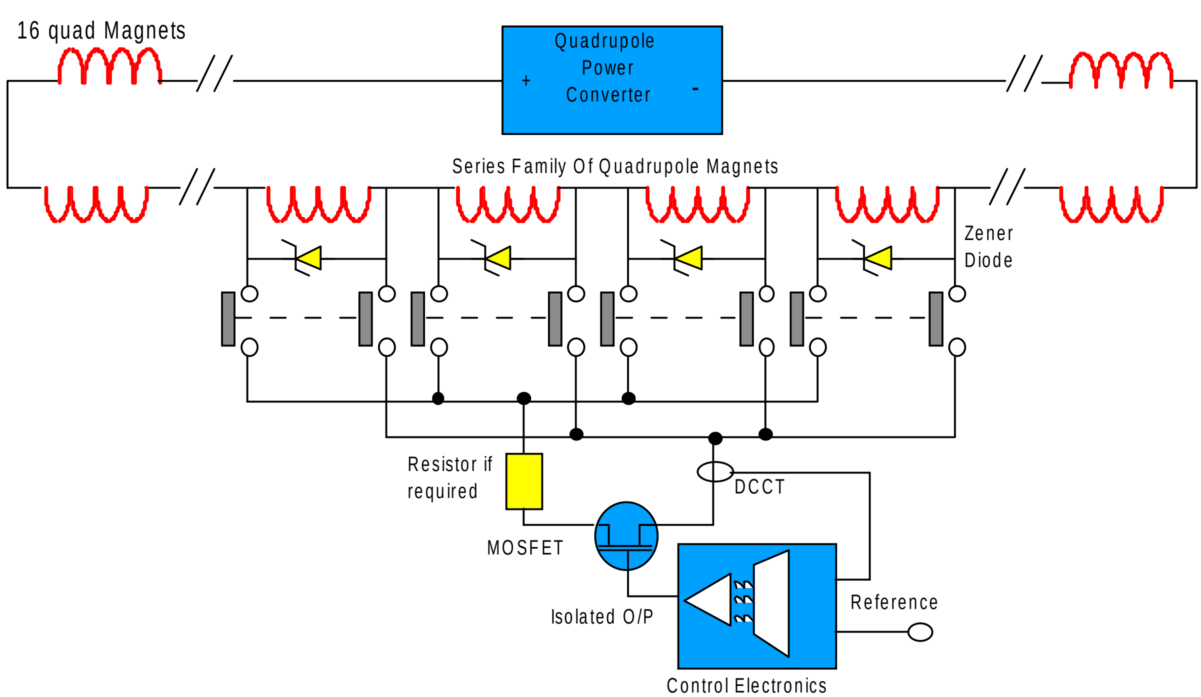

Figure 1: Circuit used to generate an alternating current in the quadrupole windings

Table 3: Ripple system parameters.

Peak to peak ripple current (A)	Variable, 0 -10
Ripple frequency (Hz)	Variable, 1 - 5
Peak to peak reactive volts demand, F-Quad (V)	7.4
Peak to peak reactive volts demand, D-Quad (V)	6.5
Hold-off voltage (isolating amplifier) (kV)	1.0

In the circuit utilised, the resistive direct voltage drop in the magnet coils drives the reduction in current in the inductive magnet during the descending part of the ripple sinusoid. This negative gradient is limited to the value of di/dt which is equal to the resistive voltage divided by the magnet inductance. At this value, the mosfet voltage drops to zero and no faster decrease can be obtained. During the positive gradient in the sinusoid, the mosfet will have a positive voltage which is in excess of the magnet's resistive direct voltage. It is necessary for the main quadrupole power supply, which is the source of direct current in the series connected magnets, to modulate its output voltage to withstand the raised voltage in the circuit without changing the direct current in the other series connected quadrupoles; i.e. the main power supply must remain a current source at the frequency of quadrupole ripple.

3 EXPERIMENTAL RESULTS

The ripple system has been used to measure the beam position in each of the 32 quadrupole magnets in the SRS storage ring, measuring horizontal positions in the 'F' quads (horizontal beam position indicators and beam-bumps) and vertical positions in the 'D' quads (vertical beam position indicators and beam-bumps). Settings used for the measurements were:

- Beam energy: 2 GeV;
- Ripple current amplitude: 10 A (p-p);
- Ripple frequency: 5 Hz.

For the measurement of the vertical alignment in the 'D' quadrupoles, the beam oscillations were observed on two tungsten vane monitors (T.V.M.s) at the up-stream end of a number of beam ports, whilst for the 'F' quadrupoles a horizontal pickup was used. With ripple current excited in a single quadrupole, the variations in the 5 Hz signals from the monitors were recorded as the local beam position at the quadrupole was varied using a beam-bump. The magnitude of the 5 Hz signal was then plotted against the beam position indicated on the B.P.M. located at the quadrupole under investigation.

The method was found to be sensitive and reproducible. In most cases, a linear regression of the excitation amplitude against beam position in the quadrupole gave a consistent and clear minimum. This is shown in Fig. 2.

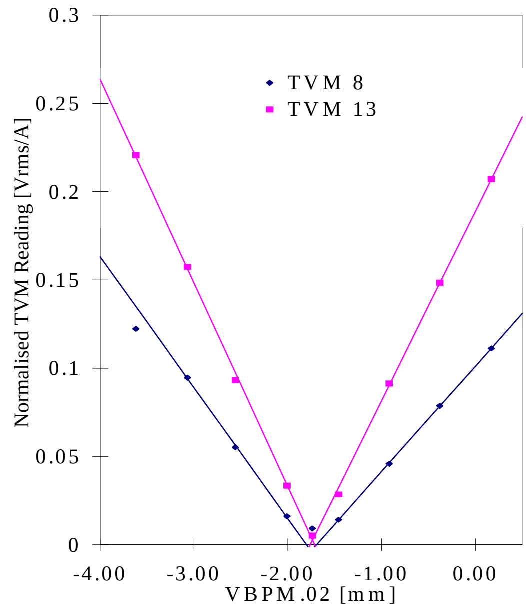

Figure 2: Variation of two TVM signals against beam position at D quadrupole 2.

If the linear regression on the two independent T.V.M. data sets indicated any inconsistency in the minimum position, or the quality of the fit was poor, quadratic fits to the square of the oscillation amplitudes gave more consistent results. The results obtained from the investigation of the vertical beam position in 'D' quadrupole 15 are shown in Fig. 3.

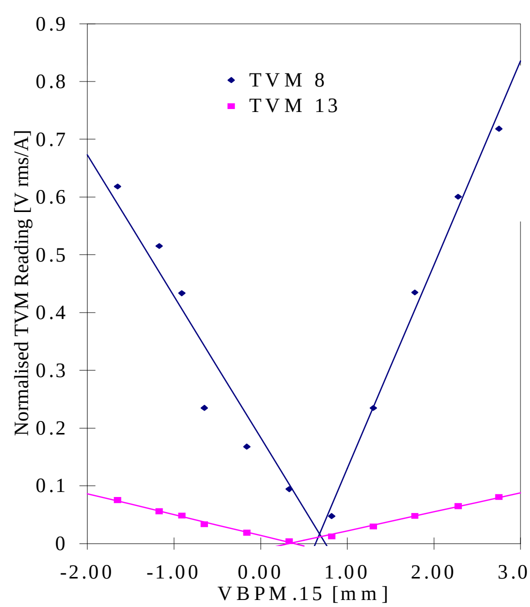

Figure 3: Variation of two TVM signals against beam position at D quadrupole 15.

For this measurement, data from T.V.M.s 8 and 13 were used. It can be seen that the linear fits to the data series from the two different monitors give a discrepancy of the order of 0.4 mm.

However, the analysis of the same data using a quadratic fit to the square of the 5 Hz oscillation amplitude, shown in Fig. 4, is far more consistent. Agreement between the

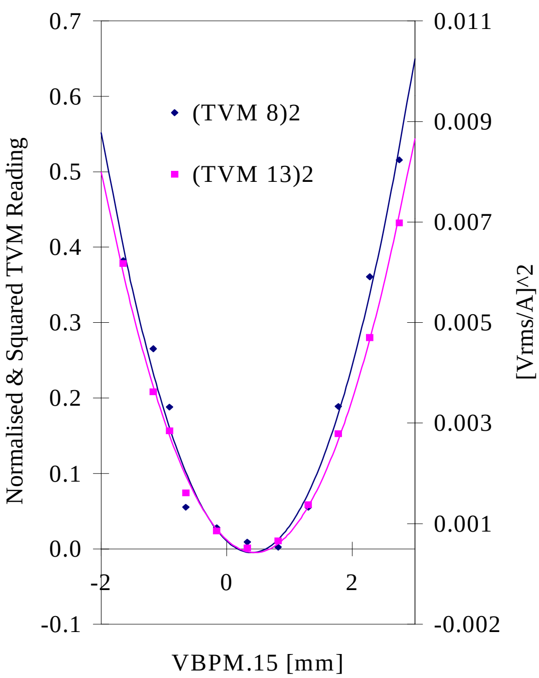

two data series is of the order of 0.1 mm or better.

Figure 4: Variation of the square of two TVM signals against beam position at D quadrupole 15 (quadratic regression).

The differences measured between the nominal (B.P.M. determined) central orbit and the centre of the D quadrupoles determined using this technique are shown in Fig 5.

4 CONCLUSION

The quadrupole ripple system now provides accurate and informative data on the positioning of the B.P.M.s relative to quadrupole magnetic centres. The measurement can be done very quickly; all sixteen quadrupoles can be measured in one plane in one eight hour period. The technique has been shown to provide high sensitivity, of the order of 0.1 mm and it is expected that it will be used as a standard diagnostic tool during beam alignment exercises in the future. The technique also presents opportunities for the measurement of other lattice parameters. The dynamic shunt is also able to conduct a steady direct current away from a quadrupole.

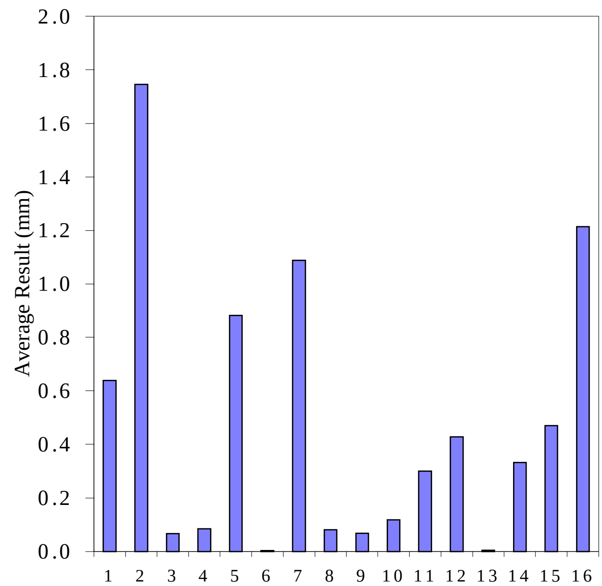

This should

Figure 5: Differences between the nominal (B.P.M. determined) central orbit and the centre of the D quadrupoles.

enable the lattice amplitude functions (βx and βy) to be measured at each quadrupole by observing the small change in machine tunes as the individual quadrupole currents are perturbed.

Contributed Talks

MEASUREMENTS WITH A VERSATILE TEST BENCH FOR THE COMMISSIONING OF THE NEW GSI HIGH CURRENT LINAC

P. Forck, P. Strehl
Gesellschaft für Schwerionenforschung, Darmstadt, Germany

Abstract

For the commissioning of the new GSI pre-stripper a conventional slit-detector system and a single shot pepper-pot system has been installed on a mobile test bench to measure intensity distributions in the two transverse phase spaces. To determine intensity distributions in the longitudinal phase space, including beam energy capacitive pick-ups and newly developed diamond counters have been installed on the test bench. The set-up of the test bench provides also redundant information for beam current, beam profile and beam position. The most important features of all measuring systems including signal processing and data evaluation are reported. First results from the commissioning of the upgraded pre-stripper of the UNILAC at GSI are reported.

1 INTRODUCTION

The Wideröe pre-stripper part of the UNILAC has been removed at the beginning of 1999. The new pre-stripper [1] consists of an RFQ [2] with a final energy of 120 keV/u followed by two IH structures [3] with the final energies of 743 keV/u (IH1) and 1.4 MeV/u (IH2). The commissioning of the new accelerator structures including the injector has been started in March 1999 and will be performed step by step up to October 1999 using a transportable test bench.

2 GENERAL DESCRIPTION OF THE TEST BENCH

The type of beam diagnostic elements as well as their arrangement on the test bench depends on the expected relevant beam parameters and, therefore on the section under commissioning. The following systems have been provided for installation on the bench:

- An emittance measuring system consisting of a horizontal and a vertical slit - detector, using independently movable harps as detectors. Taking advantage of this feature the resolution in divergence can be improved by intermediate steps of the harp. Additionally, measurable maximum divergences can be extended by so-called off-set positions of the harp with respect to the slit position to cover misaligned beams, too. The system is controlled by a PC including appropriate evaluation of emittance data.
- A newly designed pepper-pot system provided especially for single shot emittance measurements at higher beam energies. The system has been described more detailed in [4] and the mathematical algorithms to extract emittance data are discussed in [5].
- One beam transformer for beam current measurement and monitoring of macro pulse shape.
- One residual gas ionization monitor for nondestructive beam profile measurements.
- One profile grid to compare profiles measured with the residual gas ionization monitor.
- Two segmented capacitive pick ups to determine beam energy and energy jitter by time-of-flight (TOF) measurements as well as nondestructive beam position determination.
- A large vacuum chamber equipped with a thin scattering foil and various detectors to measure parameters in the longitudinal phase space [6].
- To stop the high intense beam, a beam stopper provided for 1.5 MW pulse power can be mounted at the end of the test bench.
- To perform destructive beam profile measurements at full beam power, a movable slit designed also for high pulse power can be mounted in front of the beam stopper.

The test bench has an overall length of nearly 3 meters and is equipped with its own vacuum pump.

3 COMMISSIONING OF THE NEW INJECTOR

Due to the low energy of 2.2 keV/u the maximum pulse power in this section is always below 2.5 kW and therefore all destructive beam diagnostic elements can be used without restrictions. Since there are no prebunchers foreseen monitors provided for measurements in the longitudinal phase space are not needed. The test bench has been equipped as shown schematically in Fig. 1.

Since matching to the RFQ requires a double waist at the RFQ-input, which will be forced by a collimator in front of the RFQ (see Fig. 1) the movable horizontal and vertical slits have been installed just at the position of this waist.

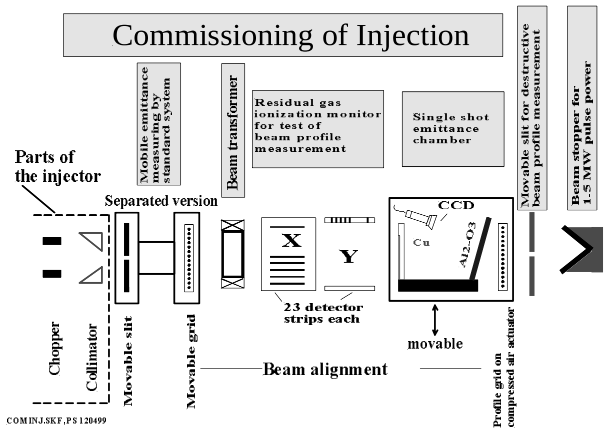

Figure 1: Scheme of the test bench for commissioning of the new injector section

To ensure focusing by the last quadruplet in front of the RFQ (not shown in Fig. 1) without restrictions, the collimator has been left out during commissioning. Figures 2 and 3 demonstrate the capability of the emittance measuring system. The theoretical settings of the beam transport elements in the injector section were confirmed. To

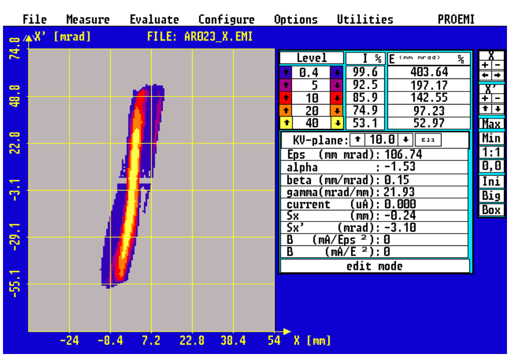

Figure 2: Measured emittance at the position of the RFQ-input. Horizontal phase plane, 10 mA Ar^{1+} with an energy of 2.2 kev/u

study the dependencies more than 30 emittance measurements have been performed in dependence of various settings of the ion source parameters, various settings of the beam transport elements and different ion beam intensities. Additionally, delay and width of the gate pulse have been varied for emittance measurements along the macropulse.

To test the pepper-pot system and especially the algorithms implemented to extract emittances in the two transversal phase planes from the measured intensity distribution in the 4-dimensional phase space, a Ni - beam from a MEVVA ion source has been analyzed with both systems. Figure 4 shows the measured horizontal emittance at the movable slit and Fig. 5 shows the picture observed on the screen of the pepper-pot system. Since the final version of software for the evaluation of emittances is yet under devel-

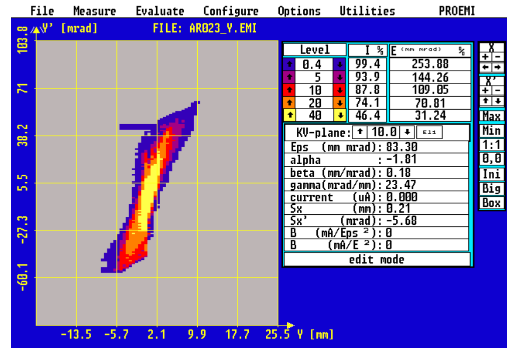

Figure 3: Measured emittance at the position of the RFQ-input. Vertical phase plane, 10 mA Ar^{1+} with an energy of 2.2 kev/u

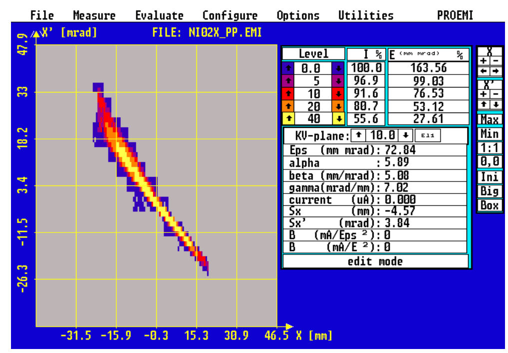

Figure 4: Convergent beam at the slit of the first emittance measuring system to test the pepper-pot-system. Ni^{1+} -ions, ca. 4 mA, MEVVA ion source.

opment, a practical, semi-manual algorithm which will be described detailed in [4], has been applied. Figure 6 shows the result. Taking into account the drift of about 1.5 m from the slit of the first emittance measurement to the pepper-pot we find good agreement concerning size and orientation. The measurement also confirms the theoretical set-

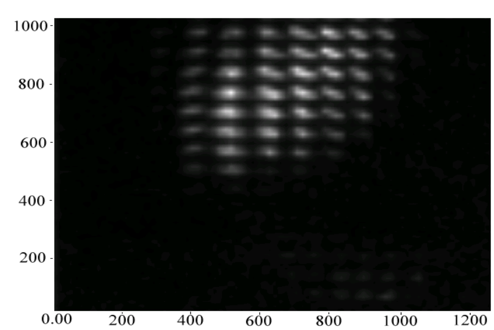

Figure 5: Observed spots on the viewing screen behind the pepper-pot plate. Ni^{1+} - ions, ca. 4 mA, MEVVA ion source. Values at the abscissa and ordinate give the pixel number of the CCD-camera.

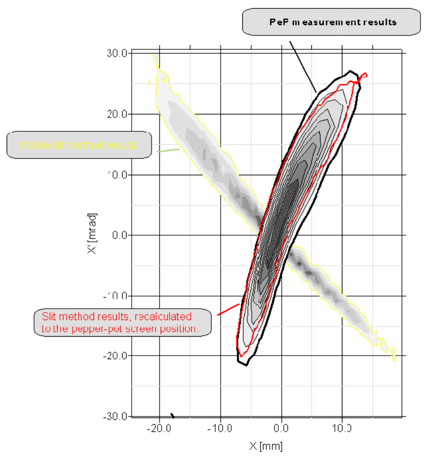

Figure 6: Evaluation of the spot pattern of Fig. 5. The Figure shows also the data of Fig. 4 and their transformation to the pepper-pot location.

ting of the quadruplet which has been adjusted to result in a waist in between both measuring systems. Furthermore, the transfer matrix of the quadruplet in front of the RFQ has been tested by measuring the profile width at the profile grid on the test bench in dependence of the quadrupole gradient. The calculated emittance has been transformed theoretically to the profile grid taking a set-value for this quadrupole corresponding to the observed waist at the profile grid. Figure 7 demonstrates the good agreement.

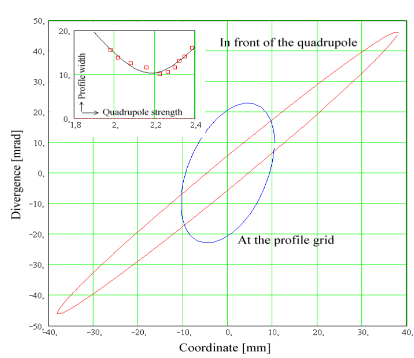

Figure 7: Emittance measurement by variation of the quadrupole gradient in front of the profile grid at the test bench.

Due to the higher beam power (217 kW pulse power behind RFQ, 730 kW behind IH1 and 1.37 kW behind IH2) profile grids cannot be used without restrictions concerning beam power and/or beam pulse length. Therefore, tests of the residual gas ionization monitor provided for non-destructive profile measurements at high intensities become essential. There are two important questions: which accuracy can be achieved in the calculation of the expected signal strength from known energy loss data taking into account different kinds of ions at various energies and has the space charge of non-compensated moving bunches an influence on the measured profiles. Due to missing bunches and the reasonable assumption of a nearly compensated beam in the injection section the second question is not relevant here and will be discussed later. To compare measured profiles with the calculated ones some measurements have been performed with the residual gas ionization monitor of the test bench. Figure 8 compares the measured profile with the calculated signal taking energy loss data from [7] and assuming a mean energy of 36 eV to produce an electron - ion pair. Furthermore, a mixture of 80% H_2 and 20% N_2 has been considered for the calculation of energy losses. Since the profile has been measured in the 50nA/V - range, the calculated data have been scaled to the same range. Considering all the uncertainties concerning pressure, gas-mixture, energy loss data, the agreement is excellent.

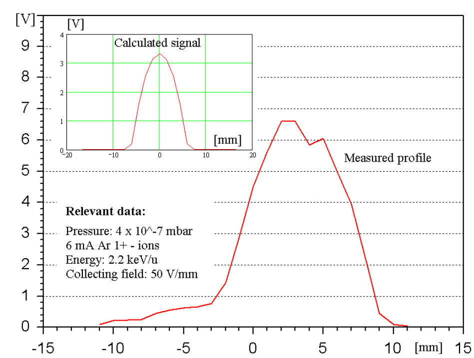

Figure 8: Comparison of measured and calculated signal strength for the residual gas ionization monitor.

4 COMMISSIONING OF THE RFQ

Commissioning of the RFQ is foreseen in two steps. First step is without the so-called superlens provided for matching the beam in all 3 phase planes for the input into the IH1-structure, while in the second step the superlens has to be included for the planned test measurements. At present only the first step has been started and, therefore it will be reported here about the measurements in the configuration shown in Fig. 9. Fig. 10 is a photo of the whole set-up. Of course, most interesting parameters commissioning a new type of accelerator are the output energy and bunch shape. The output energy of the RFQ has been measured in dependence of the rf-voltage by measuring the time of flight (TOF) between the two capacitive pick-ups. Due to the rather low output energy of 120 keV/u (design value) which corresponds to $\beta = v/c = 0.016$, the spacing between the bunches is only about 133 mm corresponding to an accelerating frequency of 36.136 MHz. Since the drift space between the two pick-ups is 3249 mm this corresponds to $N = 24$ bunches between the pick-ups which results at one hand in a very precise flight time determination but a rather

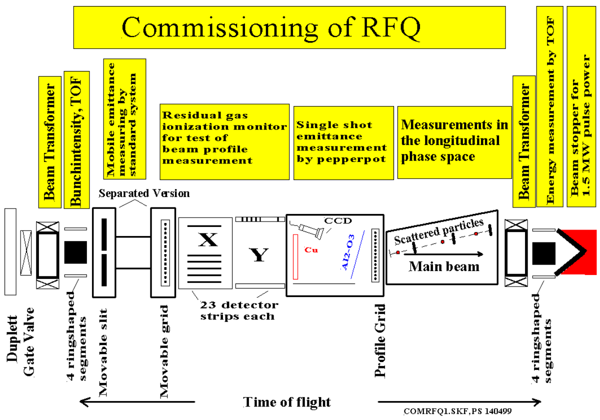

Figure 9: Scheme of the test bench for commssioning of the RFQ.

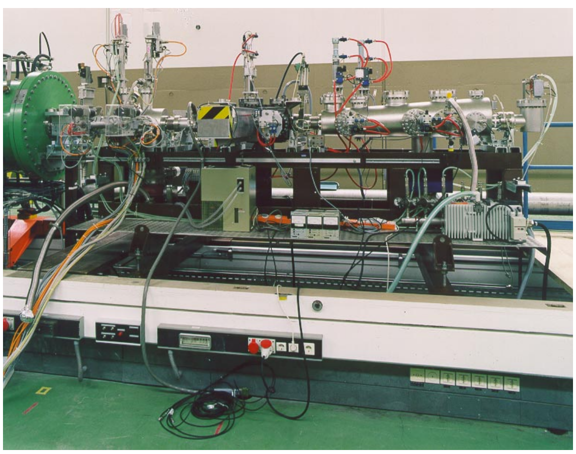

Figure 10: Picture of the test bench provided for commssioning of the new RFQ.

small separation of energies, belonging to $N \pm 1$. Figure 11 shows the result of the first energy determination. The

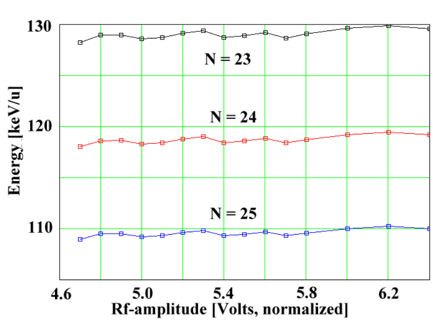

Figure 11: Energy determination by TOF-technique.

value of $N = 24$ has been confirmed using a third pick-up mounted directly behind the RFQ. To give an impression on the accuracy: an error in time of 100 ps leads to a change of 0.036 keV/u, while an error of 1mm in distance results in a change of 0.075 keV/u.

Due to the very low velocity of the ions the time structure of the bunches cannot be measured with capacitive pick-ups. But, assuming a width of 60 degrees of the rf-period, which results in a width (FWHM) of 2.5 ns the measured capacitive pick-up signal has been compared with the calculated signal. The result is shown in Figure 12. In the calculation losses in the cables (-2 dB for 20 m RG 214 and -6.2 dB for 160 m Flexwell) and losses in the electronics (-2.5 dB for pick-up selection by a multiplexer and - 1.9 dB for summing up the signals of two segments) as well as a gain of 32 dB has been taken into consideration.

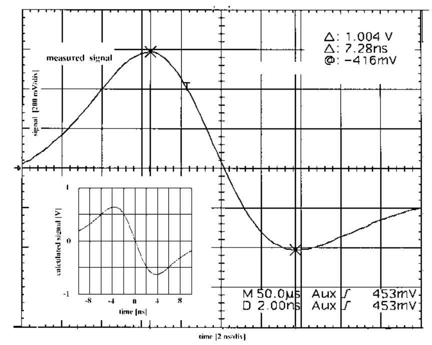

Figure 12: Comparison of measured signal from the first capacitive pick-up on the test bench with the calculated signal.

To measure the time structure of the bunches and longitudinal emittance a complex measuring system has been designed and installed into the large chamber at the end of the test bench. A very small number of particles is scattered out by Rutherford scattering on a very thin gold foil (120 $\mu g/cm^2$), passes a second thin carbon foil (5 $\mu g/cm^2$) and is analyzed by counting the particles rf-synchronously at the position of the carbon foil using a MCP. After a drift space of about 800 mm the particles are counted again, using a newly developed diamond counter [8], [6]. Figure 13 shows a bunch shape (rf-settings not optimized) from a first measurement with only one diamond counter. More results, their evaluation as well as the parameters of the system are discussed in [6].

After acceleration has been proved by the measurements in the longitudinal phase plane emittances have been measured again using the slit-detector system in comparison with the pepper-pot. Figure 14 shows a 3-dimensional display of the measured data. In this first measurement the beam current has been reduced to about 1 mA Ar^{1+} - ions for later comparison with a highly space charge dominated beam. The data obtained with the pepper-pot, shown in Fig. 15 compare very well.

During the commissioning of the RFQ profile measurements with the residual gas ionization monitor have been compared with the conventional profile grids, too. Figure 16 shows the measured profiles in both transverse direc-

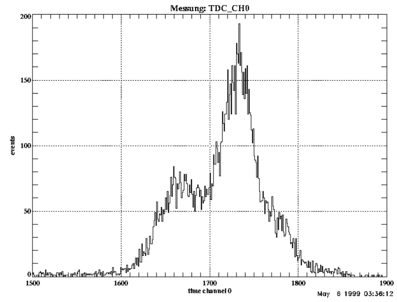

Figure 13: First time spectrum of bunches, measured with a diamond counter. Resolution 48 ps/channel, halfwidth of the main peak about 2.5 ns.

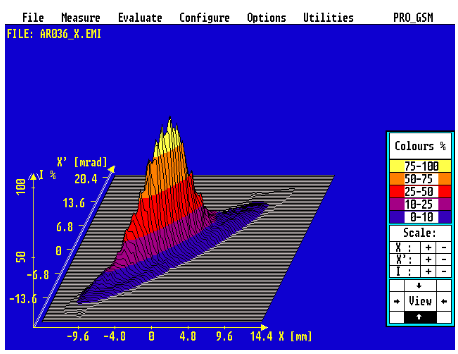

Figure 14: Measured emittance in the horizontal plane using the slit-detector system.

tions. The signal calculation taking energy loss data from [9] results in a maximum signal of about 1 Volt, again in a reasonable agreement with the measurement.

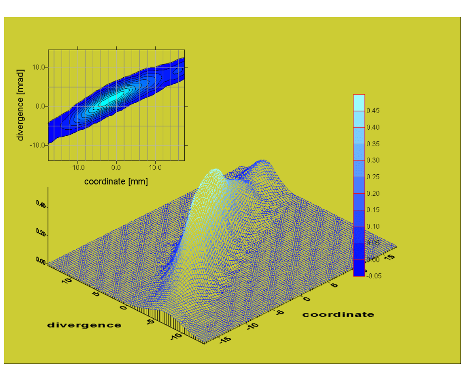

Figure 15: Emittance data in the horizontal phase plane from the pepper-pot.

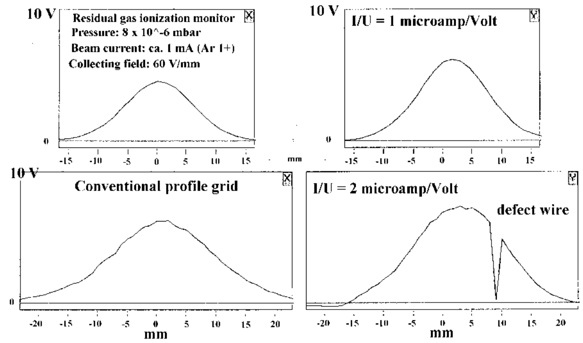

Figure 16: Comparison of transverse beam profiles.

5 ACKNOWLEDGMENTS

The whole set-up of the test bench including assembling, alignment, vacuum tests, electronics, cabling and signal processing results from a team effort of our beam diagnostics group at GSI; many thanks to all of them. The authors also wish to thank H. Kraus and J. Störmer for the mechanical design of all components. Furthermore, the technical support of the accelerator- and experimental service group of GSI as well as the help of the operations group and the Linac group performing the extensive measurements are gratefully acknowledged. The authors wish also to thank D. Liakin and M. Dolinska for implementation of mathematical procedures concerning evaluation of pepper-pot data and P. Kainberger for implementing all software for TOF-measurements.

6 REFERENCES

[1] GSI Report, GSI-99-05, 1995.

[2] Schempp, A., Proc.

[3] Ratzinger, U., Proc. XVIII Intern. Lin. Acc. Conf., Aug. 1996, Geneva, Switzerland, p. 288.

[4] Domke, M. et al., Proc. 3^{RD} European Workshop on Beam Diagnostics and Instrumentation for Particle Accelerators, LNF-INFN Frascati (Rome) Italy Oct. 1997, P 141-143.

[5] Dolinska, M. et al., Emittance Measurements at the new Unilac Pre-Stripper using a Pepper-Pot with a PC-controlled CCD-Camera, this workshop's proceedings.

[6] Forck, P. et al., Aspects of Bunch Shape Measurements for Slow, Intense Ion Beams, this workshop's proceedings.

[7] Lindhard, J., Scharff, M., Phys. Rev., 124, (1961), p. 128.

[8] Moritz, P. et al., Beam Instrumentation Workshop, Stanford, CA (1998), p. 514-521.

[9] Ziegler, J. F., Handbook of Stopping Cross-Sections for Energetic Ions in all Elements, Vol. 5, Pergammon Press, 1984.

Determination of Radial Ion Beam Profile from the Energy Spectrum of Residual Gas Ions Accelerated in the Beam Potential

R. Dölling, Institut für Angewandte Physik der Universität Frankfurt, D-60054 Frankfurt, Germany
(now at Paul Scherrer Institut, CH-5232 Villigen-PSI, Switzerland)

Abstract

Residual gas ions (RGI) created from collisions of positive beam ions (BI) with residual gas atoms are accelerated out of the ion beam by its space charge potential. It is demonstrated that with one-dimensional radial symmetry the radial distributions of BI density and space charge potential can be determined from the energy distribution of RGI radially leaving the beam tube. RGI energy spectra were taken with an electrostatic analyser of Hughes-Rojansky type on a 10 keV 1.5 mA He^+ beam. For comparison the radial BI density distribution was determined with a radial wire probe, an electron beam probe and a beam transport calculation based on an emittance measurement located downstream.

1 INFORMATION INCLUDED IN RGI ENERGY SPECTRA

1.1 Dependencies of BI number density, current and space potential

Cylindrical symmetry is assumed throughout. We start from a positive ion beam with radial distribution of number density $n_{\mathrm{BI}}(r)$ inside a tube of radius r_{wall}. The space potential is defined to be zero at r_{wall}. The beam current inside radius r is given by

$$I_{\mathrm{BI}}(r) = \frac{k\, q_{\mathrm{BI}}}{\varepsilon_0} \int_{r'=0}^{r} n_{\mathrm{BI}}(r')\, r'\, dr' \tag{1a}$$

with $k \equiv 2\pi\varepsilon_0 v_{\mathrm{BI}}$ and q_{BI}, v_{BI} charge and velocity of BI. The total beam current is defined as $I_{\mathrm{BItot}} \equiv I_{\mathrm{BI}}(r_{\mathrm{wall}})$.

The space potential follows from the Maxwell-Eq. as

$$\Phi(r) = \frac{1}{k} \int_{r'=r}^{r_{\mathrm{wall}}} \frac{I_{\mathrm{BI}}(r')}{r'}\, dr' . \tag{2a}$$

(It is assumed that the contribution of other particle species to the space potential is negligible. This is true for RGI if the residual gas density is low. For electrons this is valid as long as space-charge compensation does not occur or is suppressed.)

Differentiation of Eq. (2a) and looking at Φ instead of r as the independent variable yields the current from that part of the beam where the potential is higher than Φ:

$$I_{\mathrm{BI}}(\Phi) = -k \frac{r(\Phi)}{\frac{dr(\Phi)}{d\Phi}} . \tag{3a}$$

In practice Eqs. (1a), (2a) and correlation of the results are sufficient to calculate $I_{\mathrm{BI}}(\Phi)$ from $n_{\mathrm{BI}}(r)$.

To perform the calculation in the opposite direction Eqs. (1a), (2a) are rewritten by differentiation as

$$n_{\mathrm{BI}}(r) = \frac{\varepsilon_0}{q_{\mathrm{BI}}\, k} \frac{1}{r} \frac{dI_{\mathrm{BI}}(r)}{dr} \tag{1b}$$

$$I_{\mathrm{BI}}(r) = -k\, r\, \frac{d\Phi(r)}{dr} \tag{2b}$$

and Eq. (3a) is rewritten by integration

$$-k \int_{\Phi'=0}^{\Phi} \frac{1}{I_{\mathrm{BI}}(\Phi')}\, d\Phi' = \int_{\Phi'=0}^{\Phi} \frac{\frac{dr(\Phi')}{d\Phi'}}{r(\Phi')}\, d\Phi' = \ln \frac{r(\Phi)}{r_{\mathrm{wall}}}$$

and expressing as the exponent

$$r(\Phi) = r_{\mathrm{wall}}\, \mathrm{e}^{-k \int_{\Phi'=0}^{\Phi} \frac{1}{I_{\mathrm{BI}}(\Phi')} d\Phi'} . \tag{3b}$$

In practice Eq. (3b) and correlation of its results to $I_{\mathrm{BI}}(\Phi)$ together with Eq. (1b) are sufficient to calculate $n_{\mathrm{BI}}(r)$ from $I_{\mathrm{BI}}(\Phi)$.

1.2 Energy spectrum of RGI at the beam tube wall

A residual gas present in the beam tube undergoes ionisation and charge exchange by the BI. RGI are produced at a local source strength

$$\dot{n}_{\mathrm{RGI}}(r) = n_{\mathrm{BI}}(r)\, n_{\mathrm{RGA}}\, \sigma_{\mathrm{RGI}}\, v_{\mathrm{BI}} \tag{4}$$

with σ_{RGI} production cross section of RGI. (The number density of gas atoms n_{RGA} is assumed to be homogeneous. This holds as long as thinning of the background gas by the ionisation can be neglected. This is the case if

$$\frac{2\, I_{\mathrm{BItot}}\, \sigma_{\mathrm{RGI}}}{\pi\, r_{\mathrm{beam}}\, q_{\mathrm{BI}} \left\langle \left| v_{\mathrm{RGA}} \right| \right\rangle} << 1 \tag{5}$$

with r_{beam} radius of the ion beam and v_{RGA} thermal velocities of gas atoms.)

From Eqs. (4), (1a) follows the line current (along the beam) of RGI produced inside radius r (or at potentials higher than $\Phi(r)$) as

$$I'_{\mathrm{RGI}}(r) = I_{\mathrm{BI}}(r)\,\frac{q_{\mathrm{RGI}}}{q_{\mathrm{BI}}}\,n_{\mathrm{RGA}}\,\sigma_{\mathrm{RGI}} \tag{6}$$

with q_{RGI} charge of RGI. The total line current is defined as $I'_{\mathrm{RGItot}} \equiv I'_{\mathrm{RGI}}(r_{\mathrm{wall}})$. Moreover is valid

$$I'_{\mathrm{RGI}}(r)/I'_{\mathrm{RGItot}} = I_{\mathrm{BI}}(r)/I_{\mathrm{BItot}}\,. \tag{7}$$

The RGI created by the beam are accelerated radially outwards by space-charge forces. The acceleration voltage Φ_{acc} a RGI has experienced when reaching the beam tube wall is determined by the space potential at the location of its creation:

$$\Phi_{\mathrm{acc}}(r) = \Phi(r) \tag{8}$$

It is assumed now that the kinetic energy of the RGI at the point of creation can be neglected. (For the case that the space-potential height is above 1 V this is true at least for monoatomic gases where the initial energy stems predominantly from the thermal movement of the gas atoms.) Therefore an "energy"-analyser (EA) located at the beam tube wall or outside the beam tube will just measure the acceleration voltage $\Phi_{\mathrm{acc}}(r)$ experienced by a RGI *due to the space potential*. ("energy" is set in quotation marks when acceleration voltage is meant.)

The integral "energy"-spectrum of the RGI at the beam tube wall $I'_{\mathrm{RGI}}(\Phi_{\mathrm{acc}})$ (i. e. the line current of RGI with acceleration voltages greater than $\Phi_{\mathrm{acc}}(r)$) is given by Eqs. (1a), (2a), (6), (8).

1.3 The opposite way: deduction of BI density distribution from RGI "energy"-spectrum

The combination of Eqs. (1b), (3b) with Eq. (7) yields

$$n_{\mathrm{BI}}(r) = \frac{\varepsilon_0\,I_{\mathrm{BItot}}}{q_{\mathrm{BI}}\,k}\,\frac{1}{r}\,\frac{d\left(I'_{\mathrm{RGI}}(r)/I'_{\mathrm{RGItot}}\right)}{dr} \tag{1c}$$

$$r(\Phi) = r_{\mathrm{wall}}\,\mathrm{e}^{-\frac{k}{I_{\mathrm{BItot}}}\int_{\Phi'=0}^{\Phi}\frac{1}{I'_{\mathrm{RGI}}(\Phi')/I'_{\mathrm{RGItot}}}\,d\Phi'}\,. \tag{3c}$$

By the use of Eqs. (8), (3c), (1c) the radial distributions of number density $n_{\mathrm{BI}}(r)$ and space potential $\Phi(r)$ can be deduced from an integral "energy"-spectrum $I'_{\mathrm{RGI}}(\Phi_{\mathrm{acc}})$ and the total beam current I_{BItot} (and of course q_{BI}, v_{BI}, r_{wall}). (It is possible to replace I_{BItot} via Eq. (6) by I'_{RGItot}, q_{RGI}, n_{RGA}, σ_{RGI}. Nevertheless this is not recommendable since n_{RGA} often cannot be measured with good accuracy at the position of the EA and the analyser efficiency sometimes is lower than theoretically expected for reasons partly not understood.)

1.4 Differential energy analyser

RGI leaving the beam tube by a window fell on the entrance slit of an electrostatic EA of Hughes-Rojansky type (corrected 127° segment of cylinder condensator) [1]. The amplitude of the differential "energy"-spectrum is given by (9)

$$-\frac{dI'_{\mathrm{RGI}}(\Phi_{\mathrm{acc}})}{d\Phi_{\mathrm{acc}}} = \frac{I_{\mathrm{det}}(\Phi_{\mathrm{acc}})}{\Phi_{\mathrm{acc}}\,\eta(\Phi_{\mathrm{acc}})}\,\frac{r_{\mathrm{ref}}}{d_{\mathrm{slit}}\,z_{\mathrm{EA}}\,\varphi_{\mathrm{EA}}/2\pi}$$

and the detected "energy" itself is given by

$$\Phi_{\mathrm{acc}} = \frac{U_{\mathrm{EA}}/2}{\ln\left(r_2/r_1\right)} \quad \text{with} \tag{10}$$

I_{det}	RGI current passing both slits of the EA
$r_{\mathrm{ref}} = \sqrt{r_2\,r_1}$	radius of reference path through EA
r_1, r_1	radii of inner and outer electrode of EA
d_{slit}	width of entrance and exit slits
z_{EA}, φ_{EA}	dimension of entrance aperture in axial and azimuthal direction (ref. to beam)
$\pm U_{\mathrm{EA}}/2$	voltages applied to outer and inner electrode.

The decrease of the detected RGI current due to the combined effect of the limited acceptance angle $\pm\alpha_{\max}$ of the EA (in one coordinate) together with the small angles of the incident RGI trajectories introduced by the initial thermal velocities of the newly born RGI (with mean kinetic energy W_{th}) is reflected by the factor

$$\eta(\Phi_{\mathrm{acc}}) = \mathrm{erf}\left(\sqrt{\frac{\Phi_{\mathrm{acc}}}{W_{\mathrm{th}}/q_{\mathrm{RGI}}}}\right)\sin\alpha_{\max}\,. \tag{11}$$

The differential "energy" spectrum is derived from the measured dependency $I_{\mathrm{det}}(U_{\mathrm{EA}})$. The integral "energy" spectrum follows as

$$I'_{\mathrm{RGI}}(\Phi_{\mathrm{acc}}) = \int_{\Phi'_{\mathrm{acc}}=\Phi_{\mathrm{acc}}}^{\Phi_a}\frac{-\,dI'_{\mathrm{RGI}}(\Phi'_{\mathrm{acc}})}{d\Phi'_{\mathrm{acc}}}\,d\Phi'_{\mathrm{acc}}\,. \tag{12}$$

1.5 Combination with other information

In the problem under discussion from one of the functions $n_{\mathrm{BI}}(r)$, $\Phi(r)$, $I'_{\mathrm{RGI}}(\Phi_{\mathrm{acc}})$ the two others can be derived. (This holds even if a non-neglectable fraction of the space charge is provided by RGI because under the above assumptions the radial density distribution of RGI is fully determined.) In the presence of compensating electrons two of the dependencies $n_{\mathrm{CE}}(r)$, $n_{\mathrm{BI}}(r)$, $\Phi(r)$, $I'_{\mathrm{RGI}}(\Phi_{\mathrm{acc}})$ are needed to derive the others. It has been attempted to derive the radial density distribution $n_{\mathrm{CE}}(r)$ of compensating electrons or the total charge density (equivalent to $\Phi(r)$) in a partly space-charge compensated beam via the three 2-out-of-3 combinations of $n_{\mathrm{BI}}(r)$, $\Phi(r)$, $I'_{\mathrm{RGI}}(\Phi_{\mathrm{acc}})$ [2]. The success of this kind of combination was limited due to the accumulation of errors.

2 APPARATUS

Measurements were performed at a drifting rotational symmetric 10 keV 1.5 mA He^+ ion beam passing a cylindrical test chamber of 30 cm length and 10 cm diameter. In the central plane of the chamber the radial distribution of space potential was measured with an electron beam probe [3, 4], the RGI "energy" spectrum was taken with the EA and a radial wire probe (Ø 0.7 mm) could be moved radially through the beam. (The probe current was measured while the probe was biased to +200V in order to prevent secondary electron emission.) 30 cm downstream it was possible to measure beam emittance and profile. The beam current was measured with a Faraday-cup at the chamber entrance. An electrostatic einzel lens was used to focus the beam behind the ion source. Its strong aberrations resulted in a characteristic beam profile including a central peak and a thin halo. The halo was partly cut off by the entrance aperture of the test chamber and therefore had a sharp boundary inside the chamber. Space-charge compensation was prevented by a positively biased circular electrode following the entrance aperture. Negatively biased electrodes at both ends of the chamber prevented secondary electrons from entering. The background gas was helium with a pressure of $6.9 \cdot 10^{-5}$ hPa in the test chamber. A detailed description of the apparatus and the diagnostics is given in Refs. [2, 5].

3 EXPERIMENTAL RESULTS

The derivation of the radial density profile of the beam from a measured RGI "energy"-spectrum is depicted in Fig. 1. An indication of the good quality of the spectrum is its sharp edge at the high energy end. (a vertical drop is predicted from theory.) The sharp edge of the halo and details in the radial density profile are clearly visible. The height of the central peak depends on the sharpness of the edge of the spectrum and should not be taken too seriously at radii below 1 mm. The overall height and width of the density distribution is dependent on the value of the total beam current used in the derivation as demonstrated in Fig. 2.

For comparison the results of three independent diagnostics are shown in Fig. 3. The radial density distribution derived from the electron beam probe measurement is cut off due to the limited range of the impact parameter between electron and ion beam. The on-axis density is not shown due to the divergence of the inverse Abel-transformation at $r = 0$.

The beam profile derived from the downstream emittance measurement (Fig. 4 a) by a beam transport calculation (taking into account space-charge forces and boundary conditions) is cut off due to the limited area covered by the emittance scanner.

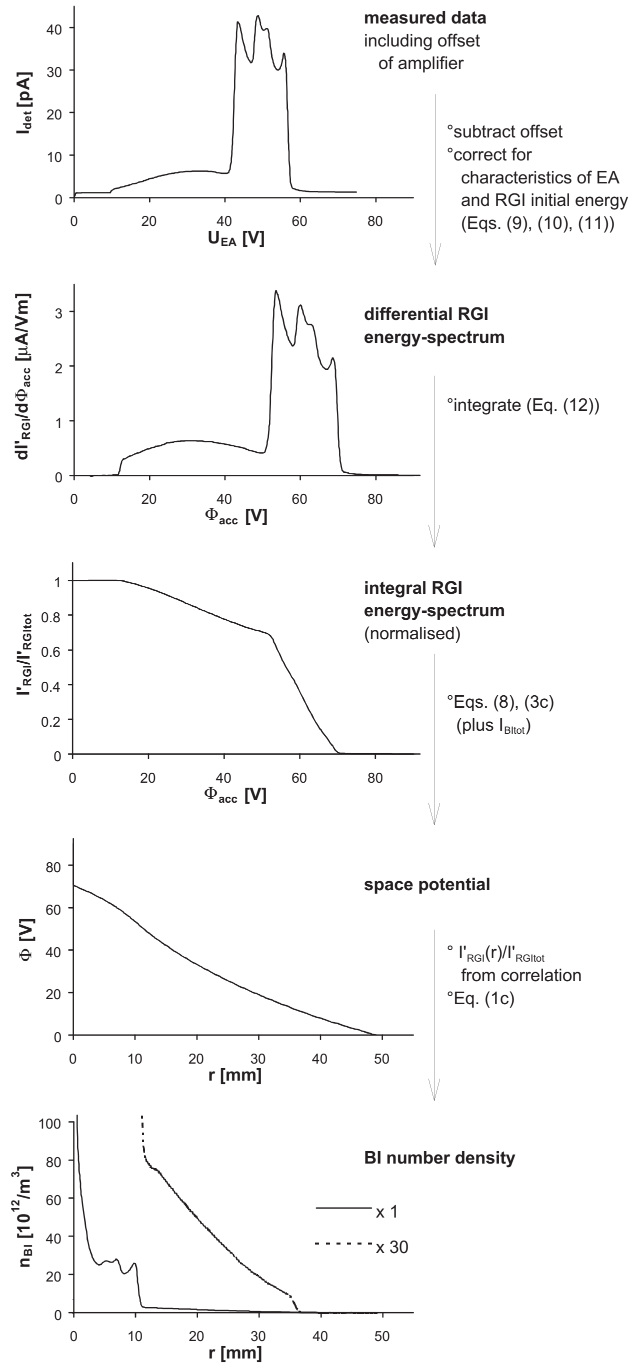

Figure 1: Derivation of radial beam profile.

Differentiation of the current to the radial wire probe with respect to the probe tip position again yields the beam profile. The edge of the halo is visible at the right end. Its position was reproducible although the measured data were very noisy and had to be smoothed. (Beam and probe position were adjusted within ± 1 mm.)

The two-dimensional beam profile measured downstream is shown in Fig. 4 b, c for the beam decompensated (as in Figs. 1 to 3) and space-charge compensated in the test chamber. (Edge of halo outside scanned region in both cases.) The lower space-charge forces resulted in a higher central peak. In the center of the test chamber where the (difference of) space-charge forces have had an effect on the beam only along a short distance, the profile resembles Fig. 4 c for all degrees of compensation.

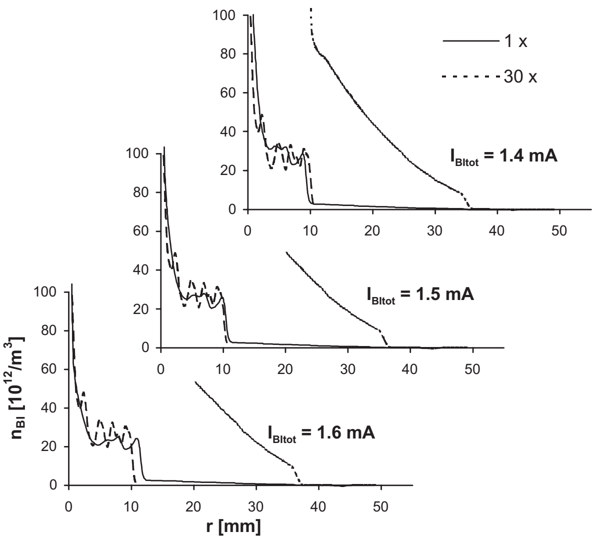

Figure 2: Dependency of derived beam profile on the assumed value of total beam current. (Measured current: 1.5 mA. For comparison, dashed line: beam profile derived from emittance measurement.)

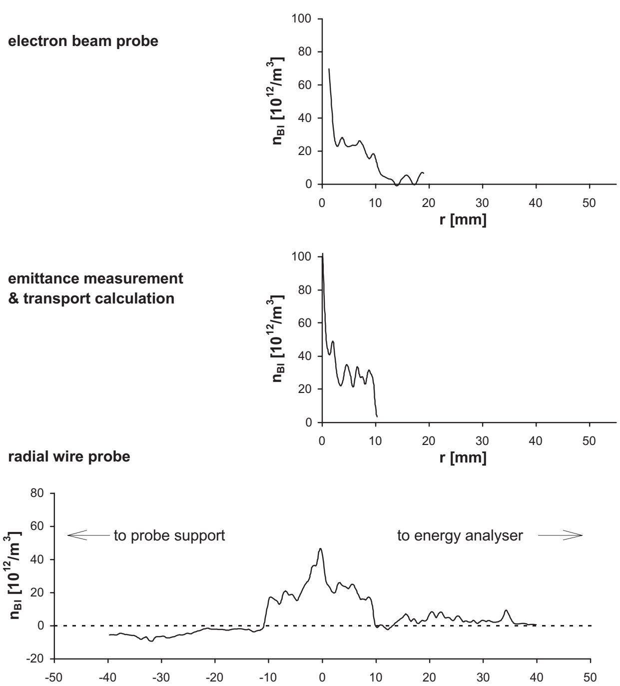

Figure 3: Results of three independent diagnostics at the same beam.

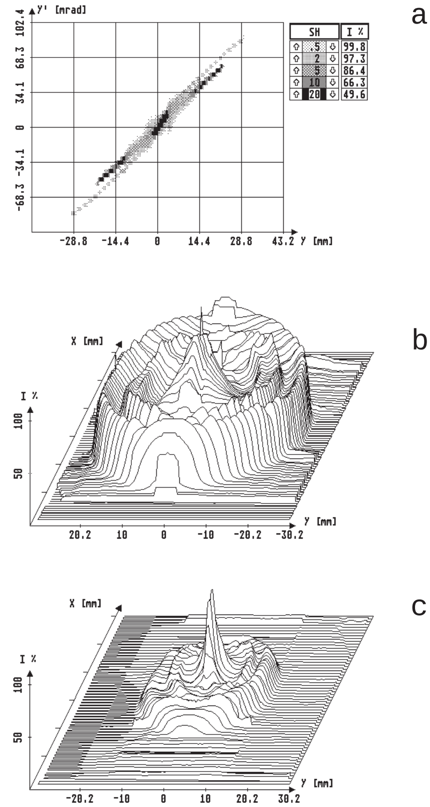

Figure 4: a, b: Emittance and beam profile of the decompensated beam measured downstream; c: beam profile of compensated beam.

Under the present well defined experimental conditions (cylindrical symmetry, low beam noise, no space-charge compensation, low electric and magnetic stray fields, no charging of isolated or dielectric surfaces) the derivation of the beam profile from the RGI "energy"-spectrum provides good spatial resolution without disturbing the beam.

REFERENCES

[1] A. L. Hughes and V. Rojansky, Phys. Rev. 34 (1929) 284.

[2] R. Dölling, dissertation, Johann Wolfgang Goethe-University, Frankfurt am Main, Germany, 1994.

[3] C. H. Stallings, J. Appl. Phys. 42 (1971) 2831.

[4] P. Gross, diploma thesis, Johann Wolfgang Goethe-University, Frankfurt am Main, Germany, 1989.

[5] R. Dölling, J. Pozimski, P. Gross, Rev. Sci. Instrum. 69 (1998) 1094. (rf resonance probe not mounted in present experimental setup.)

500 FS STREAK CAMERA FOR UV-HARD X RAYS IN 1KHZ ACCUMULATING MODE WITH OPTICAL -JITTER FREE- SYNCHRONISATION

K.Scheidt and G.Naylor, ESRF, Grenoble France

Abstract

The development at the ESRF of a jitter-free, laser triggered Streak Camera has now yielded time resolution results as short as 460fs while operating in accumulating mode. The so-called jitter-free synchronisation between the laser light and the Streak Camera is performed through a GaAs photo-switch in a simple HV circuit that connects directly to the Streak tube's deflection plates.

The novelty of this technique permits to obtain excellent dynamic range measurements in a shot-to-shot accumulation of ultra fast (laser stimulated) events at up to 1Khz without degrading the time resolution.

Important insight was obtained on the quality of this optical synchronisation and its dependence on the laser characteristics, the switch circuit, and the structure of the GaAs switch itself. This permitted to suppress the jitter causes and today the 500fs limitation is imposed by the streak tube's intrinsic time resolution. This work was done by measuring (with Au or Pd photo-cathodes) the 3rd harmonic (i.e. 267nm) of a 100fs Ti:Saph laser.

Also important progress was made with the reliability of the photo-switch and problems of HV break-down and structural degradation have been completely resolved.

Since the principal use of this system at the ESRF is in ultra-fast X-ray diffraction experiments the exchangeable photo-cathode structure of this tube covers the entire UV-to-X-rays spectrum. The QE of various photo-cathode materials was measured in the 8-30KeV range.

1 MOTIVATION & INTRODUCTION

1.1 Ultra fast Pump-Probe X-ray *experiments*

A number of ultra-fast time-resolved X-ray scattering experiments can now benefit from both the ESRF unrivalled high brilliance X-ray source and state-of-the-art ultra-fast laser and detector technology. [1] In such an experiment a broad X-ray pulse (typ. 100picosec) probes the structure of the sample under study (e.g. a crystal) while an ultra-short (typ. 100femtosec) laser pulse (λ=200-1000nm by an OPA) triggers an ultra-fast reaction in it (see fig.1). The latter becomes apparent by a modification of the diffracted X-ray beam. An X-ray Streak Camera having this beam centered on its photo-cathode will measure the broad probe pulse while the ultra-fast modulation contained in it will be detectable

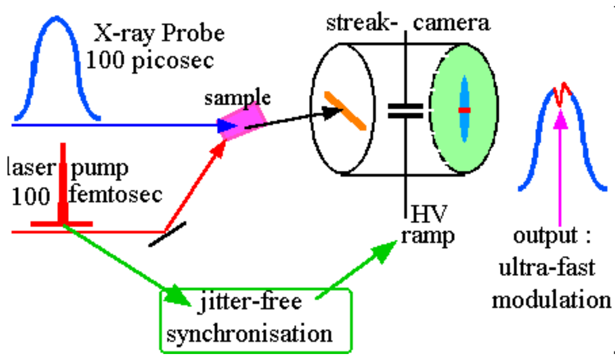

Fig.1 Pump-Probe experiment with Streak Camera optically synchronised

within the time resolution limits of the Streak Camera.

This intrinsic time resolution for X-rays has been measured independantly at the INRS with an ultra-fast 3KeV source and is estimated at below 700femtosec. [2]

1.2 Accumulation for High Dynamic range

However, in single-shot operation the dynamic range of the obtained data will be extremely limited as the intra-tube space charge effects only allow small input photon flux per shot to avoid the loss of the tube's intrinsic time resolution. This is a general problem with all ultra-fast streak cameras.

The requirement for the above experiments of high quality data to discern relatively weak signals within it make operation in repetitive, accumulation mode imperative. However, the effective time resolution of the system in accumulation mode would be impaired unless the un-precision of the trigger synchronisation, or the so-called jitter, would be negilible compared to the tube's time resolution.

2 JITTER-FREE SYNCHRONISATION THROUGH PHOTOSWITCH

The innovation in this system is to obtain this synchronisation optically between the Streak Tube and laser pump pulse by the use of a photo-conductive switch and to attain a truly jitter-free performance.

The generation of the High Voltage Sweep Ramp on the Streak Camera's deflection plates is directly triggered by the laser light on the photo-switch. Its transition to a conductive state is essentially instantaneous and for a perfectly stable ultra short laser pulse the triggering should be intrinsically free of jitter and drift.

Semi-insulating Gallium Arsenide is the preferred material because of the combination of high resistivity (>106ohm.cm) and high break-down field in the dark (>100KV/cm), together with high carrier mobility (>5000cm2/V.s).

The recently developed version is greatly improved in performance and reliability from the original design [3] through the optimisation of the electrode geometry, process and material properties. In particular, because of the short optical absorption depth (of order 1µm), it is necessary to process the GaAs surface in order to lower surface recombination velocities to values yielding photo-conduction decay times significantly longer than the sweep ramp duration. In conductive state the switch resistance of a few ohm is obtained with laser pulse energy of the order of 10µJ.

The GaAs switch is a chip of 10x15mm2 with interdigitated electrodes. The gap between the electrodes is 1.7mm and the voltage applied in the dark corresponds to a typical electric field of 20KV/cm.

3 CONFIGURATION FOR JITTER-FREE TESTS WITH UV LIGHT

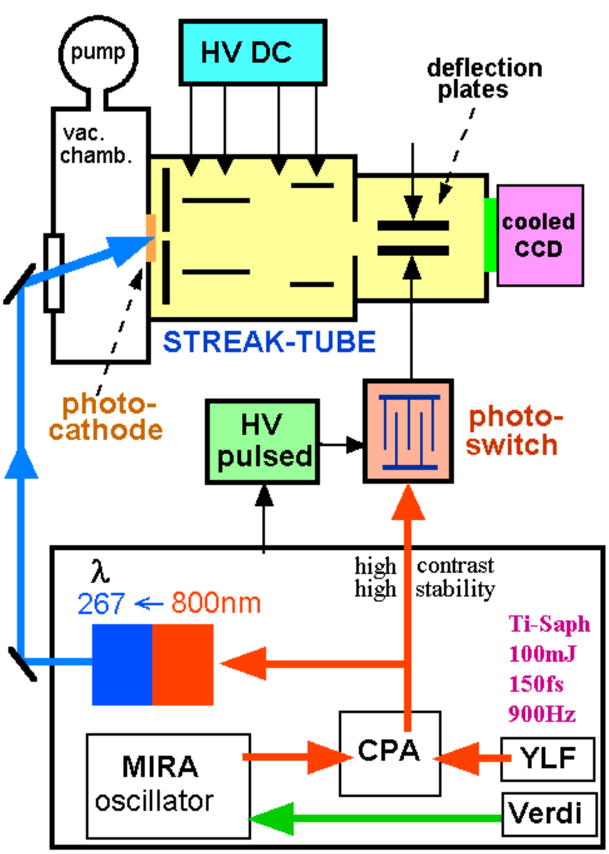

Fig2. Jitter-Free tests with 150fs UV light

The tests and measurements of the quality of the optical synchronisation can be done in an easy and straitforward manner by simply measuring the 100femtosec pulse from our laser with the streak camera system. The 3rd harmonic (i.e. 267nm) is generated in a crystal set-up and is directed to the Gold or Palladium photo-cathodes used.

A laser beam at the fundamental wavelength is used to trigger the photo-switch. The adjustment of the timing between the UV (input light) and the IR (trigger light) is achieved by simple optical delay lines.

The characteristics of the IR trigger beam can be varied in a controlled and independent way. This permits to analyse the sensitivity of the optical synchronisation to these laser characteristics. In particular the effects of total pulse energy, pulse stability, pulse cleanliness or contrast, pulse duration, size and uniformity of laser spot on the photo-switch have been examined.

In this way the jitter-causes can be tracked down and an optimum working point for the system can be determined. The same configuration also permits to easily fine-tune the High Voltages on the streak tube for optimum focussing for different sweep speeds, and to verify the correct functioning of the subsystems like the HV supplies and the CCD camera.

The latter is a commercial device with 1242 X 1152 pixels of 22.5µm. It is in direct fiber-plate contact with the Phosphor screen and can be cooled to below –30C.

4 STREAK TUBE IMPROVEMENTS

4.1 Streak Tube Characteristics

The Streak tube used in the first stage of the project development is the Philips P860X/D1. With its so-called bilamellar electron optics, good spatial and temporal resolution are preserved with minimum space charge effects and electron transit time spread. The tube has a spatial resolution at the Phosphor screen of 40µm (fwhm).

The photo-cathode has a width of 10mm so one spatial domain of the detector is preserved and useable in experiments. The tube operates with 5 independent High Voltages : 15KV for the accelerating field of the photo-cathode, two focussing electrodes (around 6KV) and two quadrupole electrodes (around 500V).

4.2 Improvements and New Tube

The tube is open at the light input side which permits an easy exchange of the photo-cathode. This photo-cathode itself is a small 30x3mm circular pellet with a slit in its centre on which a foil is attached. This photo-cathode exchangeability makes it possible to use the material best suited to the photon energy of the experiment. The selection of the material can be governed by requirements on absolute sensitivity (QE) or time resolution (photo-electron energy spread).

The open input structure also allows to modify the distance between the photo-cathode and the accelerator slit and thus the acceleration field for the photo-electrons. This nominal distance is at 3mm but values as small as 2mm (i.e. 7.5KV/mm) have been tried with success after a complete re-design of the photo-cathode and its holder to assure a smooth and uniform field in order to minimise the risk of HV break-down. Also the Vacuum system was improved, a pressure of <3.10^{-7}Torr reduces the risk of HV breakdown or spurious emissions.

Increasing the strength of this acceleration field is of great importance as it limits time dispersion effects due to the energy spread of the emitted photo-electrons [4]

The deflection sensitivity of the above tube's deflection plates being about 18µm/V meant that the photo-switch had to be strained with voltages as high as 4KV to attain a sweep speed of 200fs per pixel on the CCD camera. A new tube with modified deflection plates was designed, realised and successfully operated since. The sensitivity is increased to above 27µm/V.

5 SINGLE SWITCH CIRCUIT

An electric circuitry is needed to interconnect, the photo-switch, the HV supplies, and the sweep plates. An approach using 2 switches (1 per plate) was initially used but was unsatisfactory in terms of performance, reliability and practical use.

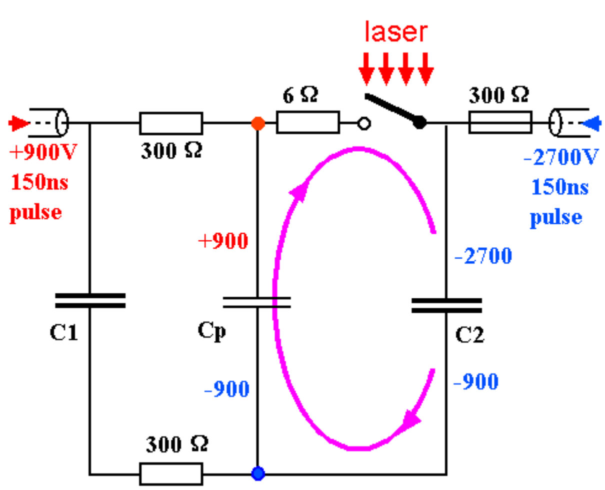

Fig.3 Single photo-switch circuit to 2 plates' deflection yielding 125femtosec/pix (5.5ps/mm) sweep speed

A complete new design was realised that uses only one single switch to obtain a symmetric HV ramp on both plates (see Fig.3). The two capacitors C1 & C2 (100pF each) are arranged so that the deflection plates (represented by Cp=10pF) are symmetrically pre-charged (+U and –U) by a two HV pulses (amplitudes +U and –3U) of 150ns that are applied by commercial HV Pulsers through two 50Ω coaxial cables.

The trigger pulse for the HV Pulsers comes from the laser timing and is arranged so that the IR laser arrives about 0.5µsec later on the switch. Upon this laser triggering the switch will form a short circuit between Cp, C2 and the 6Ω resistor (the 300Ω resistors de-couple the this fast loop from the surrounding part). Because C2 is a factor 10 bigger in capacity the charge transition between these two will result in an inversion of the polarity on the plates (Cp). This rapid inversion constitutes the HV ramp for the sweep plates, at the voltages indicated it is about 6V/ps, it is mainly determined by inevitable parasitic inductances in the circuitry (notably the intra-tube connections) and not by the series resistor of 6Ω which merely limits the post-sweep HV-ringing in the circuit.

The circuit is positioned very close to the tube and interconnected with a few cm long cables. It offers the advantages of excellent reliability and practical use (only one laser beam to be conditioned and aligned) while using only 2 HV pulsers (and no HV bias supplies). Moreover, their HV amplitude variations do not affect the streak image position on the Phosphor screen (when centred), this is of importance for our system operating in accumulation mode.

6 ANALYSIS & SUPPRESSION OF JITTER CAUSES

The 15KV supply to the photo-cathode has a stability of 50ppm, its contribution to timing jitter in the system is below 100femtosec. For the other static HV the stability is far less critical, and as said above, for the HV Pulsers in the switch circuit a stability of 10^{-3} is sufficient.

Several characteristics of the IR laser pulse were examined to precisely assess their influence on the quality of the optical synchronisation. The laser contrast, the laser amplitude stability, and the laser spot (size and uniformity) on the switch were found to be essential factors.

The 100fs laser pulse is preceded by laser energy that has two different origins : ASE built-up in the regenerative amplifier (CPA), and pre-pulses from leakage through the pockels cell. Although both can be minimised by careful alignment and timing arrangements their level remains prohibitively high since it causes a pre-triggering that is detrimental to both the reliability and jitter-free performance of the switch.

The needed contrast improvement was obtained through a saturable absorber that is formed by a RG850 filter in an adapted optics and cooling arrangement. The purity is now such that the energy in the 2ns preceding the laser pulse is less than 10^{-4} of the energy within the 100fs laser pulse. Any small fluctuations of this pre-pulse energy have only negligible effect on the optical synchronisation.

The effect of the laser amplitude stability was assessed by varying this amplitude in a controlled, independent, and calibrated way and measuring the corresponding time shift of the streak image. It was found that even when applying high energy levels to the photo-switch (>50µJ, i.e. driving the switch well into saturation level) the system would remain sensitive to small variations of the laser energy. This problem was tackled successfully by the optimisation of the GaAs switch geometry and structure, the adaptation of the circuit, and the improvement of the laser amplitude stability.

The latter was achieved by eliminating heat sources on the optical table and the application of beam path covers in the optical cavity, the compressor and the pump laser of the laser system in order to suppress the heat turbulence effects on beam pointing stability.

The single switch circuit as described above has only half the sensitivity to energy variations as the circuit that applies two photo-switches and bias voltages.

Various versions of GaAs switches have been tested to determine the most suitable based on the criteria of reliability, laser energy requirements, and in-sensitivity to laser amplitude variations.

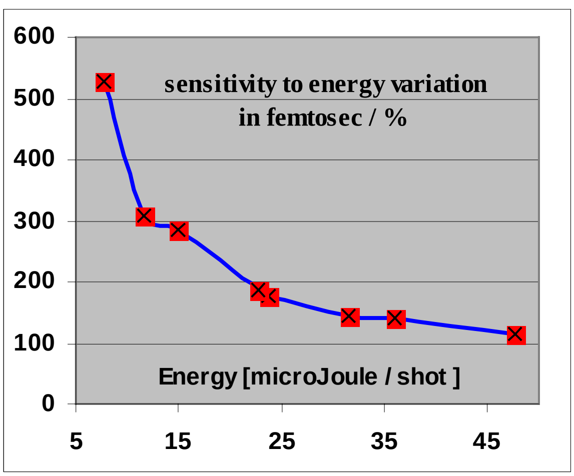

As is shown in the above graph this sensitivity is dependant on the laser energy and is below 150fs per percent energy variation at laser energy above 25µJ.

With the laser improvements a short-term stability of 0.25% is now achieved which means that its jitter contribution to the total effective time resolution of the system is below 100fs (fwhm).

For the correct and reliable operation two separate diffusers make that the projected IR spot on the switch surface covers the full active area and has a high degree of uniformity to avoid local stress.

7 RESULTS

In the picture of the streak image shown here above the time axis is horizontally while the vertically the spatial width of the photo-cathode is represented. The curvature in the image is the explained by the relative time delay of the photo-electrons from the edges of the photo-cathode with respect to those emitted from the centre. Note the high quality of the image and the absence of noise. The time profile in the 2 graphs here above is taken over one single pixel of such a picture.

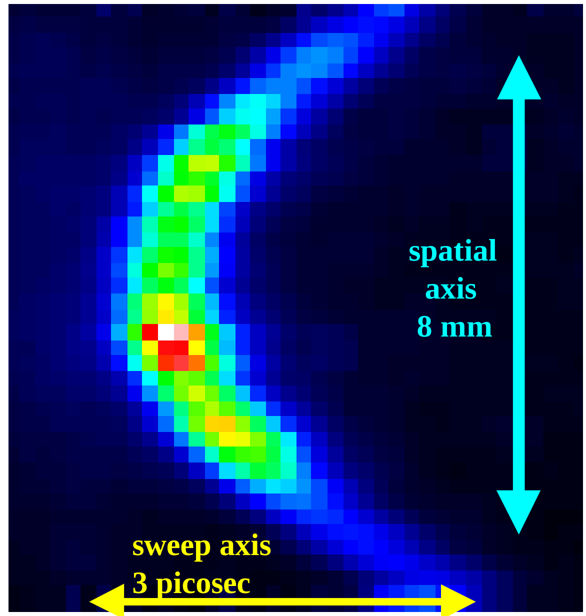

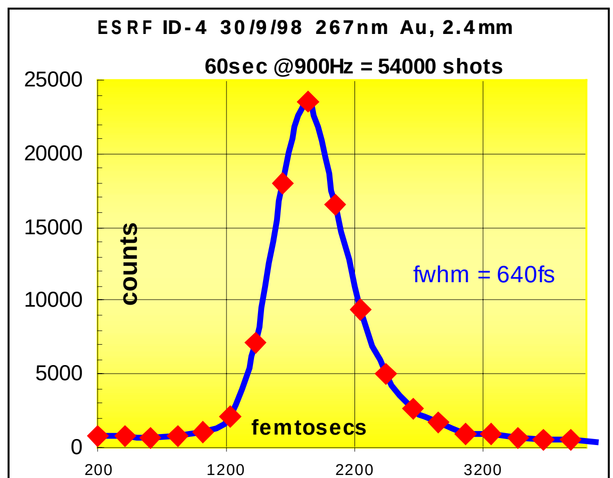

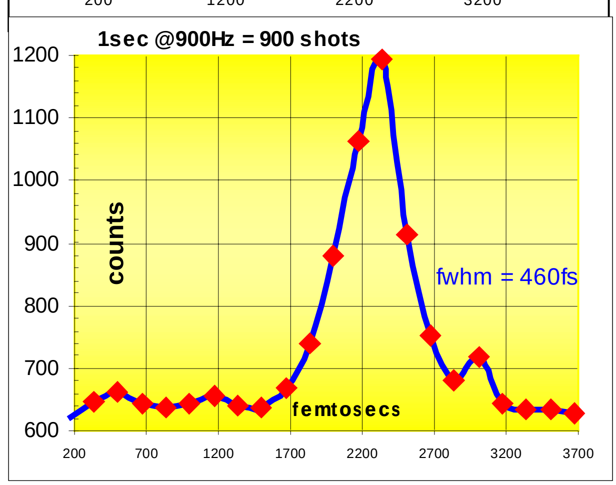

The performance of the system, i.e. the total effective time resolution, is shown for accumulation times of 1second and 1minute (i.e. integrating respectively 900 and 54000 shots). This was with the first version of the streak tube, with UV on Au photo-cathode and a 15KV/2.4mm acceleration field.

With an optical synchronisation of this quality it is the intrinsic time resolution of the streak tube that now dominates the effective time resolution of the system. Identical results were obtained with the new streak tube but no improvements were obtained so far by increasing the acceleration field further or other modifications of the accelerator slit.

8 X-RAY QE MEASUREMENTS

A total of 10 photo-cathodes have been measured for their QE in the system for X-ray energies in the 8-30KeV range. The streak camera is in static mode (not sweeping) and the QE value of the whole system (i.e. photo-cathode, tube, CCD camera) is determined by measuring the total number of counts (on the CCD) and to divide it by the number of photons that hit the active area of the photo-cathode. The latter is determined independently by a calibrated slit, foil pin-diode and picoAmp meter.

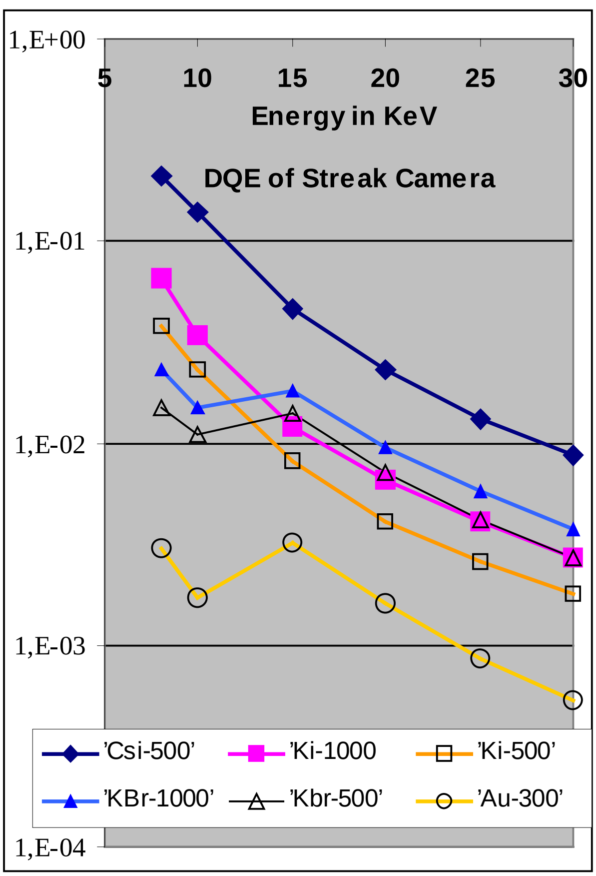

The results show a clear decrease of QE with increasing energy. The CsI has by far the highest QE, a factor >3 more than the KI and KBr, materials which are believed to be give better time resolution thanks to smaller energy spread of emitted photo-electrons.

The thickness of 100nm in comparison to 50nm yields a gain of about 40%. However, a decrease of QE during a time period of only a few hours was observed on the KI photo-cathodes together with a change of colour. The long term behaviour of these materials is to be assessed more precisely in another measurement campaign.

9 CONCLUSION , FUTURE TESTS

Our streak camera system has now attained time-resolution of the order of 500fs in accumulation mode thanks to the successful application of the optical synchronisation by means of GaAs photo-switches to a femtosec laser. The system works reliably and the optimum performance can be reproduced for easy routine operation. This was demonstrated for UV light and Gold photo-cathode.

The next test foreseen in July 1999 is to measure this time-resolution for hard X-rays by a so-called surface disordering experiment that produces the ultra-fast modulation in the broad X-ray pulse from the ESRF source.

10 ACKNOWLEDGEMENTS

The present state of performance of the system has been made possible through the collaboration with D.Kaplan of Fastlite for the design and provision of the photoswitches, and the careful adaption of them to our system.

For the Streak Tube developments we are much indebted to JC.Rebuffie of Photonis who designed and manufactured both versions.

We also would like to thank M.Wulff and A.Souvorov for the support in design and carry-out of tests and experiments with X-rays on the ID-9 and D5 beam lines.

REFERENCES

[1] K.Scheidt, "Development of jitter-free, laser-triggered X-ray Streak Camera with femtosec time resolution", DIPAC Frascati Oct. 1998

[2] J-C.Kieffer, "characterisation of P860X/D1 tube with pulsed X-ray source", final report INRS to ESRF, Feb. 1999

[3] G.Mourou et al ,"signal averaging X-ray streak camera with picosec. jitter", Rev.Sci. Instr. 67 (3), March 1996

[4] Z.Chang et al, "demonstration of a 0.54pS X-ray streak camera", SPIE Vol.2869/971

BUNCH LENGTH MEASUREMENTS IN LEP

A. J. Burns, H. Schmickler, CERN, Geneva, Switzerland

Abstract

For many years a streak camera has been used for observing the longitudinal distribution of the particles in any LEP e^+ or e^- bunch (5-50 ps r.m.s. length) on a turn by turn basis, using synchrotron light. In 1996, a comparison made with the longitudinal vertex distributions of 3 LEP experiments allowed the identification and elimination of certain systematic errors in the streak camera measurements. In 1997, a new bunch length measurement technique was commissioned that uses the high frequency slope of the bunch power spectrum from a button pickup. In 1998, this new method was confronted with measurements from the streak camera and the LEP experiments. The measurements made in 1996 and 1998 are presented, with emphasis on the calibration of the two instrumental methods and their respective precision and limitations.

1. STREAK CAMERA SET-UP

Synchrotron light pulses are produced when e^+ and e^- bunches pass through small wiggler magnets on either side of intersection point 1 of LEP [1]. The visible light is extracted by two thin beryllium mirrors and focused on a double sweep streak camera [2] in an underground optical laboratory [3]. The optical set-up allows the simultaneous observation of the *top* and *side* views of any photon bunch from both LEP beams within the same fast sweep [4]. The photon bunch length and longitudinal density distribution corresponds to that of the particle bunch that emitted it. The slow sweep allows up to 100 fast sweeps to be recorded on one image, which can be used to follow successive bunch passages. Although originally requiring local manipulation, the camera can now be fully operated via the control system network [5]. Bunch dimension averages are transferred every 10 s to the LEP measurement database, and a high bandwidth video transmission allows the streak camera images and processed results to be viewed in real time (at 25 Hz) in the LEP control room (Figure 1).

2. STREAK CAMERA BUNCH LENGTH MEASUREMENTS (1995-96)

During an experiment to investigate the LEP machine impedance in August 1995, the lengths of very low current (3μA ≡ 2 10^9 e^+) bunches were measured. This was the first reliable indication of the existence of a 10 mm^2 offset in the square of the bunch length measured by the streak camera (Figure 2).

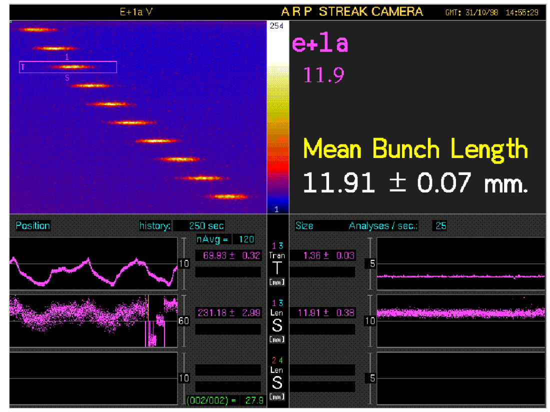

Figure 1: Control room video display updated at 25Hz.

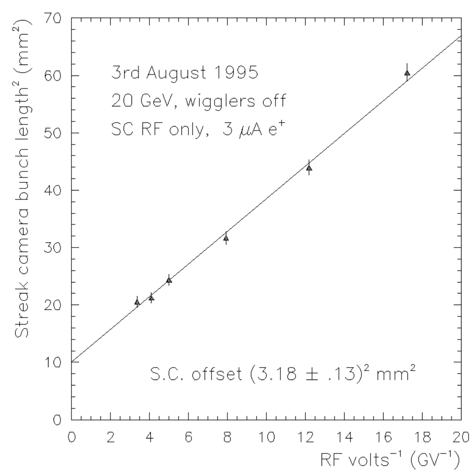

Figure 2: Streak camera bunch length^2 as a function of inverse RF total voltage at 20 GeV (August 1995), showing clearly the 10 mm^2 offset present at that time.

As the bunch current was well below the turbulent threshold at which bunch length starts to rise with current, the r.m.s. bunch length in metres, σ_s , is given by:

$$\sigma_s = \frac{\alpha_C R}{Q_S}\frac{\sigma_E}{E} \qquad (1)$$

where α_C is the momentum compaction, R the radius of LEP, Q_S the synchrotron tune, and σ_E / E the relative r.m.s. beam energy spread.

Using the relation $Q_S^2 \propto V_{RF}$ where V_{RF} is the total RF voltage per turn (which has been experimentally verified to apply up to 45 GeV) one obtains:

$$\sigma_s^2 \propto \frac{1}{V_{RF}} \qquad (2)$$

The good agreement of the data in Figure 2 with a linear fit implies that the measured bunch lengths need to be corrected according to:

$$\sigma_s^2 = \sigma_{meas}^2 - \sigma_{corr}^2 \qquad (3)$$

This is equivalent to the deconvolution of the observed longitudinal bunch profile with a Gaussian of width σ_{corr}. However, the value of σ_{corr} is much too large to be due to the finite instrumental resolution.

Bunch length measurements made in December 1994 had also indicated a substantial correction term (of at least 50 mm^2) [6]. However, in the analysis presented, an error had been made in the computation of the transverse spot size correction.[1] Once this error was rectified, the measurements of bunches below 12 mm were consistent with a correction term in the range 0-20 mm^2.

2.1 *Comparison with LEP experiments' data*

The measured bunch length is defined as the observed r.m.s. longitudinal deviation of the particles about the bunch centre of charge. Making the reasonable assumption that both beams have the same bunch length and shape, the bunch length defined in this way is a factor of √2 greater than the r.m.s longitudinal deviation of e^+e^- interactions about the average position in each experiment. This is true for any bunch shape, and so is insensitive to departures of the actual bunch shape from a pure Gaussian distribution.

A comparison made in 1993 between the streak camera measurements and the longitudinal vertex distributions of the LEP experiments had demonstrated agreement within 5-10% between the two sets of measurements, for bunch lengths of 9-13 mm [8]. As a 10 mm^2 correction alters a 10 mm bunch length by only 5%, in 1996 the additional RF capacity installed for running LEP above 80 GeV was used to produce bunches with σ_s below 5 mm at 45 GeV.

To ensure that the vertex distribution widths accurately reflected the corresponding bunch lengths, various cuts and checks were made on the raw data from the LEP experiments (event reconstruction quality, numbers of tracks, distribution symmetry, hour-glass effect,…) [9].

The first comparison made in August 1996 (Figure 3) confirmed a 10-12 mm^2 quadratic offset, similar to the August 1995 data. A second comparison made in October-November 1996 (Figure 4) produced a much smaller offset of 1.6 ± 0.6 mm^2, by using an interference orange-red filter (FWHM 9 nm) in front of the streak camera.

These comparisons also confirmed the correctness of the streak camera "scale factor" to a few % (slope of streak camera versus experiments correlation consistent with unity), which also corresponds to the accuracy of the calibrations using an optical delay line [9].

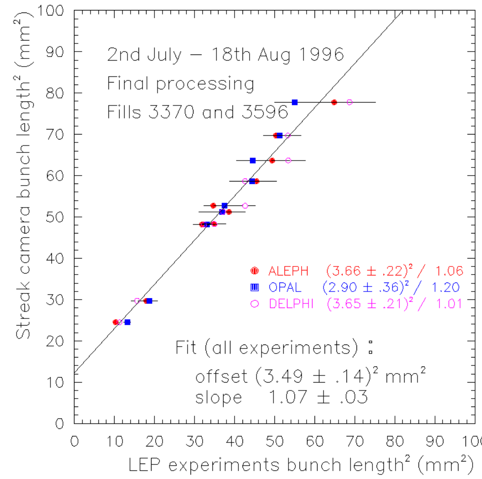

Figure 3: Streak camera bunch length^2 as a function of LEP experiments' bunch length^2 (August 1996).

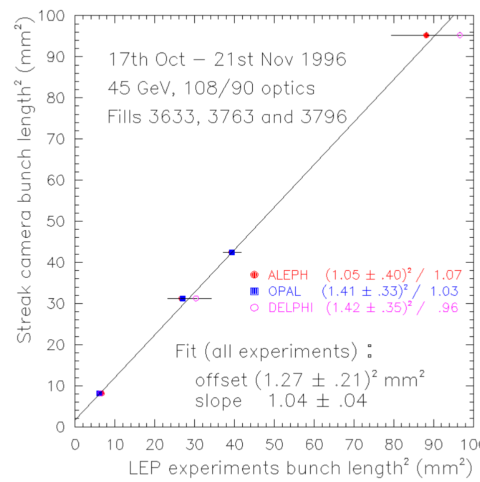

Figure 4: Streak camera bunch length^2 measured with orange-red monochromatic filter as a function of LEP experiments' bunch length^2 (Oct.-Nov. 1996).

A similar offset of 0.9 ± 0.1 mm^2 was also obtained when short bunches (1-2 mm) were measured at different RF voltages at 22 GeV with orange/red light.

2.2 *White light effects*

Group velocity dispersion (GVD) is a physical phenomenon that is well known in the domain of laser pulse transmission in optical fibres. The variation of the group velocity with wavelength separates in time the different wavelength components of the synchrotron radiation pulses. The white light pulses measured by the streak camera are therefore lengthened compared to the pulses generated in LEP.

The group velocity, that characterises the rate of the transmission of energy, can be derived from elementary wave packet theory as:

[1] The transverse spot size in the direction of the fast sweep, σ_T, adds quadratically to the bunch length, σ_s, to produce the observed streak length, σ_L [7]: $\sigma_L^2 = \sigma_s^2 + \sigma_T^2$

$$g(\lambda) = v(\lambda) - \frac{dv}{d\lambda} \tag{4}$$

where $v(\lambda)$ is the phase velocity of the individual simple harmonic wave components and is related to the refractive index of the medium, $n(\lambda)$, by $v(\lambda) = \dfrac{c}{n(\lambda)}$.

Measurements of the chromatic separation produced by the dispersive material in the original e^+ *side* path (~25 cm of glass and quartz) are shown in Figure 5, with respect to the arrival of the 620 nm component of the pulse.

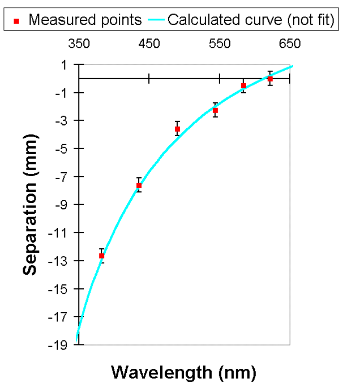

Figure 5: Measured separation of different wavelength components of synchrotron light pulses at entrance to streak camera.

The calculated curve was obtained from the thickness of quartz and BK-7 glass in the optical path and the group velocities g (λ) calculated from the known refractive indices of the two materials.

In order to estimate the amount of pulse lengthening produced on the measured "white" light pulses, the proportion of different wavelengths contributing to the final steak image had to be measured. This produced slightly different spectra for each light path, but on average the spectra were centred at 500 nm with a FWHM of ~150 nm.

Numerically convoluting these spectra with the expected GVD produced the result that the r.m.s. length of the original white light pulses were increased quadratically by the square of 0.10-0.11 mm per cm of quartz (or 0.8 cm of BK-7 glass) in the optical path. As an example, the 28 cm of quartz-equivalent (quartz + 1.25*glass) in the e^+ *side* path should produce a lengthening term of ~ 8 mm^2 (2.8^2).

There is in addition a small reduction in measured bunch length as the wavelength of the light used is increased. Measurements with different wavelength filters showed decreases in bunch length of 0.4-0.5 mm in going from blue to red light (Figure 6).

The different slopes indicate that this effect does not produce a constant mm^2 offset for a given wavelength shift. Nevertheless, the magnitude of the difference between measuring at the average wavelength of the white light spectrum (~500 nm ≡ 2.5 eV) and with a 600 nm filter (≡ 2.0 eV) can be seen to be 1-2 mm^2.

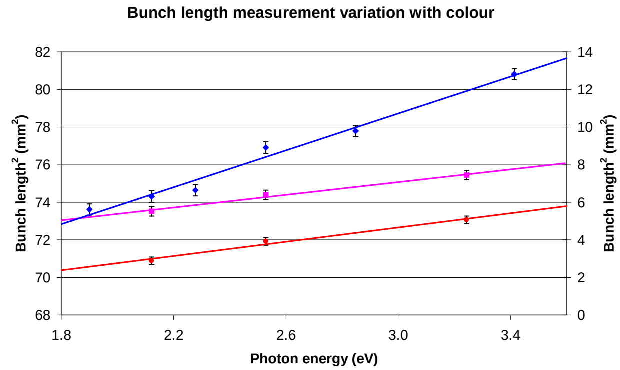

Figure 6: Measured bunch length^2 as a function of photon energy for 8.5 mm (top data), 2.2 mm (middle data) and 1.6 mm (bottom data) bunches.

Thus the total difference in quadratic offset between measuring with white light and with a orange-red filter is expected to be 9-10 mm^2, in reasonable agreement with the comparison with the LEP experiments.

3. BUTTON MONITOR BUNCH LENGTH INSTRUMENT

A new technique for measuring bunch lengths in LEP was tested in 1996 and commissioned in [10]. It is based on the spectral analysis of signals from a small (7 mm diameter) button pickup. Assuming Gaussian bunches and after correction for the calculated system transfer function, the slope of log (amplitude) versus frequency^2 gives the bunch length^2.

In practice 2 or 3 frequency zones (around 6.2, 7.6 and 8.9 GHz) are used, in which there are no dominant resonances from the BPM, cable, or feedthroughs. The highest frequency zone is excluded from the analysis when it is too close to the noise level. In 1997, bunch length measurements in the range 3-12 mm were made as a function of bunch current at different energies and led to an estimate of the longitudinal inductive impedance, Im (Z/n) ≅ 0.2 Ω [10,11]. No cross-check was made with the streak camera.

4. STREAK CAMERA-BUTTON MONITOR CROSS-CALIBRATION (1998)

4.1 Changes to streak camera set-up

The streak camera set-up used in 1998 was optimised taking into account the results of 1996. Although special measurements at 45 GeV and below could still be done with the mini-wigglers, routine monitoring at all beam energies up to 94.5 GeV used a "parasitic" light source in a quadrupole. This was done to avoid the risk of damage to other instrumentation from the very hard X-rays emitted by the mini-wigglers from high energy beams. The loss of light intensity was compensated by eliminating the *top/side* split (gaining a factor of 4) and a 50% split to a test bench. The light was focused to the smallest possible spot to minimise the importance of the spot size correction needed with "wider" streak images. Finally, the chromatic effects described in section 2.2 were made negligible by using a cut-off filter transmitting only the orange-red end of the spectrum and removing the Dove prisms used to rotate the transverse axes of the beam images. The total amount of dispersive material in the optical path was thus reduced by a factor of 2 compared to 1996. The image in figure 1 was taken in these conditions at 94.5 GeV.

4.2 Bunch length comparisons

Differences of ~1.5 mm between the button measurements using all 3 frequency bands or only the lower 2 bands led first of all to the elimination of the 8.9 GHz band from the analysis. There was then reasonable agreement between the streak camera and button measurements in the bunch length range 9-12 mm.

However, a dedicated machine experiment with short bunches (2-5 mm) at 22 and 45 GeV showed that there remained considerable disagreement in the lower range of bunch length [12]. Figure 7 shows measurements from both instruments at 45 GeV as a function of inverse Q_S, as well as the 100 µA current prediction (dashed line) from the longitudinal inductive impedance measurements of 1997 [11] and the zero current prediction (dotted line). An offset of 2 mm^2, obtained from plotting bunch length^2 against inverse square of Q_S, was removed from the streak camera data.

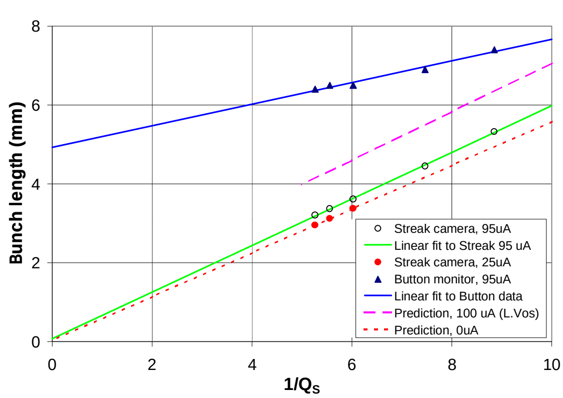

Figure 7: Streak camera and button monitor measured and predicted bunch lengths as a function of inverse Q_S at 45 GeV (July 1998).

As well as a substantial difference between the two instrumental methods, the 25-95 µA bunch length difference measured by the streak camera was much less than the prediction.

The absolute calibration of the streak camera made in 1996 required that both this prediction and the button measurements must be wrong. Advantage was therefore taken of a 45 GeV calibration period in October 1998 to repeat the comparison with the experiments' vertex distributions. As before, reducing the current in the wigglers and increasing the total RF voltage during Z^0 physics coasts enabled measurements to be made at a few distinct bunch lengths in the range 2.5–6.5 mm.

The LEP experiments confirmed the calibration of the streak camera measurements to within 5% and indicated the presence of an average offset in the square of the bunch length of 3.9 ± 0.5 mm^2. On the other hand, the button pickup measurements suffered from a very large offset of around 40 mm^2.

During the entire Z^0 runs, constant monitoring of the bunch length measurements from the streak camera and button pickup allowed numerous additional comparisons to be made between the 2 instruments over the bunch length range up to 10 mm. Measurements from subsequent 94.5 GeV fills extended this to 11.5 mm. This data is shown in Figure 8, together with data from a number of 94.5 GeV fills in July.

The measured average quadratic offset of 4 mm^2 has been subtracted from the streak camera values, whereas no correction has been applied to the button pickup data.

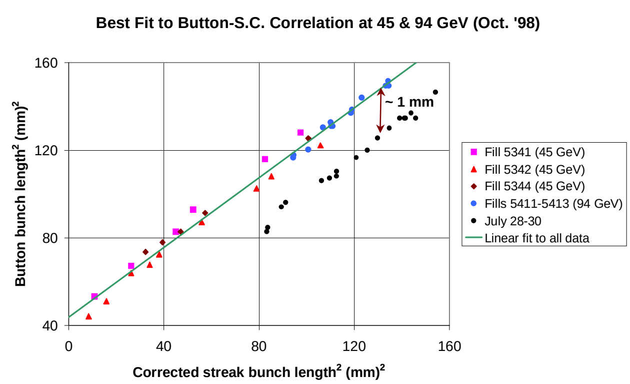

Figure 8: Correlation between streak camera and button monitor bunch length^2 at 45 and 94 GeV (October 1998).

The line represents a linear fit to the data from the Z^0 runs and subsequent high energy runs of October 1998 and corresponds to the formula:

$$\sigma_s^2 = 1.25\left(\text{Button}\,\sigma_s^2 - 44\right)\ \text{mm}^2 \qquad (5)$$

Using this as a correction formula, the button pickup values then agree with the corrected streak camera values to ± 0.5 mm over the range 5-11.5 mm. Shorter bunch lengths are not well corrected by this means; but given the large measurement offset of (6.5 mm)^2 and its poor stability (e.g. a systematic shift of 7 mm^2 between data from fills 5341 and 5342), it is not reasonable to try and measure such short bunches with the button pickup anyway.

Finally, although the July 1998 data have the same slope as the October data, they are offset by about -20 mm^2. Indeed applying the correction formula (5) produces an error of 1-2 mm with respect to the corrected streak camera values. Such an unexplained shift would imply that, without continual cross-calibration, even the "corrected" button pickup values could be wrong by typically ± 1.5 mm.

4.3 Bunch current dependence

The bunch current from which measurements are possible with the streak camera depends on the synchrotron light source used (mini-wiggler or parasitic), the bunch length, the optical attenuation (especially chromatic filtering), the camera sweep speed and image intensifier gain. In the normal operating conditions described in section 4.1 using parasitic light from 10 mm bunches, adequate measurements are possible from 30-50 µA per bunch and good quality measurements from 50-100 µA. The use of the dedicated mini-wiggler source and less chromatic filtering allows the measurement of bunches down to a few µA of current (few 10^9 particles).

The power measured by the button pickup is integrated over all bunches in LEP and therefore depends on the total beam current. During filling, the bunch length generated by the spectrum analysis algorithm was observed to rise from low values and slowly approach a stable value. In the case of 15 mm bunches, less than 4 mm was "measured" with 1 mA and a total beam current of 2.3 mA was needed before 90% of the final bunch length was reached. During the same period, the bunch length measured by the streak camera changed by less than 5%. Shorter bunches, that produce more relative power in the higher frequency band, can be measured at lower current, e.g. 1.1 mA for 10 mm and 0.8 mA for 3.5 mm bunches

These observations differ from the previously published conclusion that *"for a 10 mm long bunch at least 200 µA total beam current is required to make a proper measurement"* [11]. In addition, even using 2 beams of 8 bunches each ("bunch-train" mode), it would seem impossible to make meaningful measurements of the dependence of bunch length on current below bunch currents of around 50-70 µA, without first calibrating the instrumental beam current dependence.

5. CONCLUSIONS

Two different methods for measuring bunch lengths have been used in LEP. After correction of a large offset in the results from the spectral analysis of button monitor signals, it is found that bunch lengths in the range 5-12 mm can be measured with an absolute precision of ± 1.5 mm for sufficiently high total beam currents (typically above 1 mA, i.e. 6 10^{11} particles). The large measurement offset (that can be assimilated to an error in the transfer function) indicates that the transfer impedance is difficult to calculate in the presence of other effects in the spectra.

The image analysis of synchrotron light pulses incident on a streak camera remains the most accurate bunch length measurement technique in LEP. For precise measurements on "short" bunches (< 8 mm), the path length in dispersive media must be minimised and the spectral acceptance limited (preferably in the longest wavelength part of the spectrum). Comparisons with LEP experiments in 1996 and 1998 confirmed the correct calibration to 3-5% and indicated a small quadratic offset in the range 2-4 mm^2.

ACKNOWLEDGEMENTS

The collaboration of P. Bright-Thomas (ALEPH, 1996), B. Pietrzyk (ALEPH, 1998), R. Hawkings (OPAL) and W. Murray (DELPHI), who provided longitudinal vertex position data from their respective experiments, is gratefully acknowledged.

REFERENCES

[1] C. Bovet, M. Placidi, "A dedicated synchrotron radiation source for LEP diagnostics", LEP note 532, April 1985.

[2] Manufactured by A.R.P. (now Photonetics, Honsellstrasse 8, 77694 Kehl, Germany).

[3] E. Rossa et al., "Double sweep streak camera for LEP", Proceedings of the 2nd European Particle Accelerator Conference, Nice, June 1990, pp. 783-785.

[4] E. Rossa et al., "Real time measurement of bunch instabilities in LEP in three dimensions using a streak camera", Proceedings of the 3rd European Particle Accelerator Conference, Berlin, June 1992, pp. 144-146.

[5] A. J. Burns, J. J. Savioz, J. C. de Vries, "Remote Control of a Streak Camera for Real Time Bunch Size Measurements in LEP", Proceedings of the 1995 International Conference on Accelerator and Large Experimental Physics Control Systems, Chicago, October 1995. http://adwww.fnal.gov/www/icalepcs/abstracts/PDF/wpo13.pdf.

[6] B. Zotter, "News on Impedance and Intensity Limits", Proceedings of the 5th LEP Performance Workshop, Chamonix, January 1995. http://www.cern.ch/CERN/Divisions/SL/publications/proc95/bz2_15.pdf.

[7] F. Tecker, "Evaluation of the performance of a streak camera in beam diagnostics at LEP", CERN SL/Note 95-66 (BI), June 1995 & diploma work PITHA 93/7, Physichalische Institute RWTH Aachen, Germany, November 1993.

[8] K. Hanke, "Measurement of the bunch length of LEP with a streak camera and comparison with results from LEP-experiments", CERN SL/Note 95-65 (BI), June 1995 & diploma work, Physichalische Institute RWTH Aachen, Germany, May 1994.

[9] A.J. Burns, "Measurement of picosecond bunch lengths in the LEP collider using a streak camera and a low capacitance button pick-up", to be submitted to Nuclear Instruments and Methods in Physics Research A.

[10] L.Vos, "Impedance from Bunch Length Measurement in LEP", SL-MD Note 249, November 1997. http://nicewww.cern.ch/sl/Publications/md97-249.pdf.

[11] L. Vos, "Electro-Magnetic Bunch Length Measurement in LEP", Proceedings of the 6th European Particle Accelerator Conference, Stockholm, June 1998, pp. 1626-1628. http://www.cern.ch/accelconf/e98/PAPERS/WEP19H.PDF.

[12] A.J. Burns et al., "Comparison and calibration of LEP bunch length measurements", SL-Note-98-060 MD, September 1998. http://nicewww.cern.ch/sl/Publications/md98-060.pdf.

DARESBURY SRS POSITIONAL FEEDBACK SYSTEMS

S. L. Smith and S. F. Hill , CLRC Daresbury Laboratory, Warrington, WA4 4AD UK.

Abstract

The Daresbury SRS is a second generation synchrotron radiation source which ramps from its injection energy of 600 MeV to 2.0 GeV. Beam orbit feedback systems have been in routine operation on the SRS since 1994 and are now an essential element in delivering stable photon beams to experimental stations. The most recent enhancements to these systems have included the introduction of a ramp servo system to provide the orbit control demanded by the installation of two new narrow gap insertion device and development of the vertical orbit feedback system to cope with an increasing number of photon beamlines. This paper summaries the current status of these systems and briefly discusses proposed developments.

1 INTRODUCTION

Orbit position control has been employed at Daresbury to stabilise the photon beam position routinely since 1994. The global horizontal feedback system [1] has been in routine operation for many years and uses a simple inversion of the 16 x 16 response matrix to apply a correction every 30 sec. A global vertical orbit feedback [2] has now replaced the individual local servo systems [3] that pioneered vertical orbit correction for beamlines on the SRS. This global vertical system provides orbit control using tungsten vane monitors (TVMs) at all commissioned ports and will allow expansion of correction to new beamlines including two new multipole wiggler (MPW) sources. A consequence of the introduction of these MPWs and their associated small aperture vessels was an increased requirement for orbit control during the energy ramp. This has been provided by a flexible, automatic orbit control program [4], which runs a dual plane global feedback system using the electron beam position monitors (BPMs).

2 HORIZONTAL GLOBAL FEEDBACK

The global horizontal feedback system reads the horizontal electron orbit at 16 BPMs and applies a global correction at the 16 steering magnets (HSTRs), the strength of the correction is determined by a straight inversion of the steering magnet response matrix. The orbit is read and a correction is applied every 30 sec. This system has been in used on the SRS for many years and considerable experience has been gained. The system has been highly successful in suppressing the orbit shape distortions, although the average radius change is not corrected. This is because the machine orbit is relatively insensitive to changes in the average position of quadrupole magnets and as a result correction of this orbit component is vulnerable to systematic movements in the BPMs. The global horizontal feedback system corrects all the BPMs to the average of the 16 BPMs, within a precision of the order of the BPM resolution (better than 5 μm). The latest work on this system has concentrated on dealing with the malfunction of an individual BPM. Clearly with only 15 monitors and 16 correctors a simple matrix inversion is no longer applicable, however it has been shown that an SVD algorithm provides a good solution to the missing BPM problem and work is currently underway to integrate this algorithm and the detection of BPM problems into the global feedback system.

3 VERTICAL GLOBAL FEEDBACK

Currently the global servo system includes TVMs on dipoles 1,2,3,4,6,7,8 and 13, super-conducting wigglers in straights 9 and 16 and an undulator in straight 5. Each port has one TVM except super-conducting wiggler, W16, which has two TVMs at different distances from the source however, the beam is only steered to one of these two monitors. TVMs were fitted as close as possible to the typical experiment distance but this can be anything from 3 - 15 m. So the vertical global feedback in the SRS could potentially use 11 photon monitors and 16 vertical BPMs, with correction supplied by up to 2 x 16 vertical correctors.

An EXCEL program was used as a flexible development environment. This program was designed to provide on-line correction and servo feedback of the orbit together with off-line simulation.. A singular value decomposition, SVD, routine was used to “invert” the appropriate measured orbit response matrix of the corrector magnets at the chosen monitors.

The photon monitors were used for feedback because of problems with the position stability of the vertical BPMs due to thermally induced movements of the vessels. Simulations and beam tests were carried out using 32 and 16 vertical correctors. It was determined that the use of only one family of 16 correctors was adequate to correct the orbit at one TVM on each of the 11 ports.

A simplified version of the correction program has been used for operations. The system has been designed to deal with the slow drift in orbit due to thermal effects in the machine that can be several 100 microns over a stored beam of up to 23 hours duration. Although it would be possible to run at around 2 second update, a correction every 30 sec has been chosen, as this matched the performance achieved at only few ports using the previous local correction system. At this update rate, even at the start of a fill when the drift is fastest, the applied correctors are only a few LSBs.

Figure 1 shows the results achieved using this global feedback system during a user beam. The data illustrates that the system operates with a correction accuracy of around a few µm on all the corrected TVMs. This is probably the limit of achievable accuracy as the expected RMS error due to setting errors on the 16 magnets is 1.5 µm and the resolution of the TVMs is around 1 µm. For comparison, Figure 2 shows a prediction of the drifts that would have occurred during the same period without the feedback on.

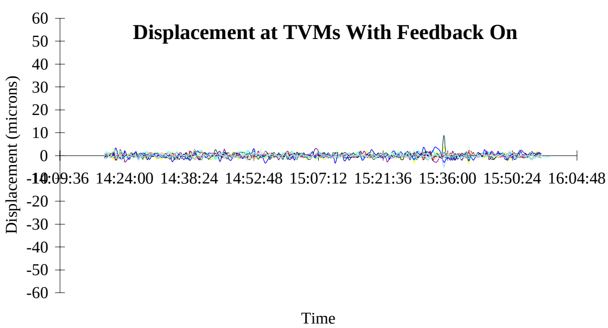

Figure 1: Operation of global vertical.

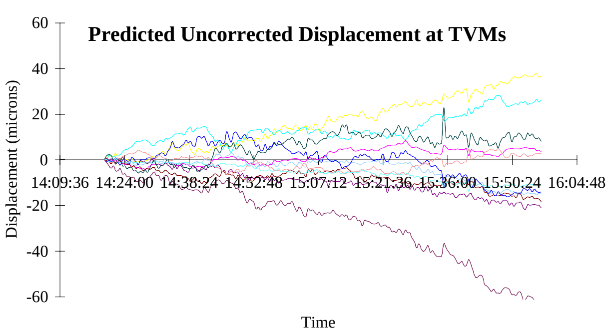

Figure 2: Predicted drift at TVMs without feedback

The system had to be designed to load a new response matrix if a port was shut and the associated photon monitor no longer available or a monitor failed in some manner.

The SRS is still expanding the number of operational beam ports, the most recent addition was a new port on dipole 5. This is in a particularly densely populated region of the ring as there is an undulator in straight 5 and dipole sources on adjacent dipoles.

The response matrix was extended to include the measured response at the new TVM and the off-line simulator was used to assess the predicted correction with the additional TVM present. The decomposition immediately highlighted that the present operational arrangement for correction using only the 16 VSTM magnets would have problems. However, the addition of just one corrector (VSTR.05) in this region gave a far more "stable" system. The simulation predicted much more effective correctors for full orbit correction. These solutions were investigated using the simulator. The corrector strengths required to correct 100 different random orbits that were recorded with and without correction at the new TVM. The results are shown in Figure 3. These show clearly that the 16 magnet solution would require the use of very strong correctors. This would be impractical, as the increased sensitivity to realistic errors in response would produce unacceptable errors.

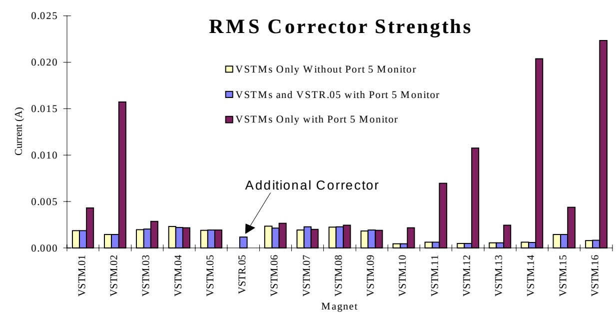

Figure 3: RMS corrector strengths required to correct the orbit at the TVMs with and without dipole 5 TVM.

Testing with beam of combined VSTM and VSTR correction will take place shortly when the port is fully commissioned and available during beam studies. Further expansion of the system is planned later in 1999 with the addition of two new multipole wigglers in straights 6 and 14.

4 RAMP ORBIT FEEDBACK

Survey errors and "magnet walks" in the SRS mean that without orbit control deviations of over 10 mm can develop in some areas during the energy ramp from 0.6 to 2.0 GeV. The orbit feedback system that operates in both planes has been designed to control these orbit excursions and meet the stringent demands due to the installation of relatively small gap MPW vessels.

The SRS has is a 16 cell FODO lattice with one vertical and one horizontal BPM per cell. The corrector and monitor layout is shown in Figure 4.

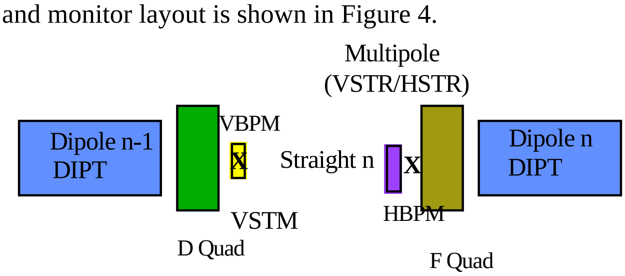

Figure 4: Correctors and monitors in an SRS lattice cell

The vertical steering magnets, VSTMs, are dedicated vertical corrector magnets, The multipole magnet has 12 windings which can be individually programmed for horizontal deflection (HSTR), vertical deflection (VSTR) and octupole field. Each dipole has a trim coil (DIPT) for horizontal correction.

The energy ramp feedback system is based on an extension of the simple matrix inversion technique, used for horizontal global feedback, to both planes. Vertical orbit correction is made using the 16 dedicated vertical steering magnets (VSTMs) and the 16 vertical BPMs. The horizontal correction involves the use of both sets of horizontal correctors. At low energy the multipole is required to provide a strong stabilising octupole field and the horizontal correction is applied using the relatively weak dipole trim coils. At higher energy, the feedback program dynamically swaps to provide correction using the HSTR configuration of the programmed multipole and tailors the octupole component on the multipole to avoid winding saturation.

Injection is achieved in the SRS with a large, ~ 11 mm bump. This bump takes the ideal closed orbit beyond the linear region of the BPM response. A non-linear fit to measured BPM response data is used by the feedback program to ensure accurate correction in this region.

This feedback system is required to maintain control during the relatively fast energy ramp of ~ 70 sec, the maximum correction frequency is limited to 1.4 sec due to the various delays involved in the acquisition of through a hybrid of several computer systems.

Figures 5 and 6 show the typical performance of the ramp servo during beam stacking, energy ramping and wiggler ramping phases.

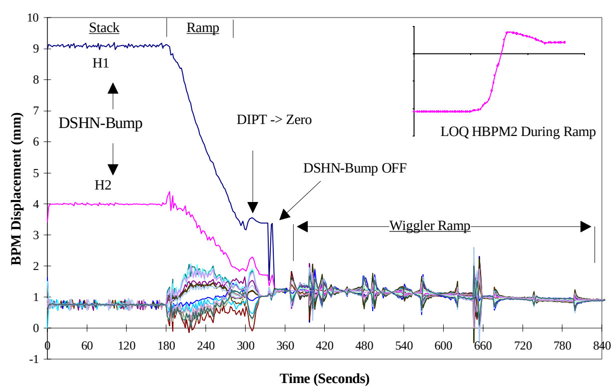

Figure 5: Horizontal Orbit Control During Stacking and Ramping.

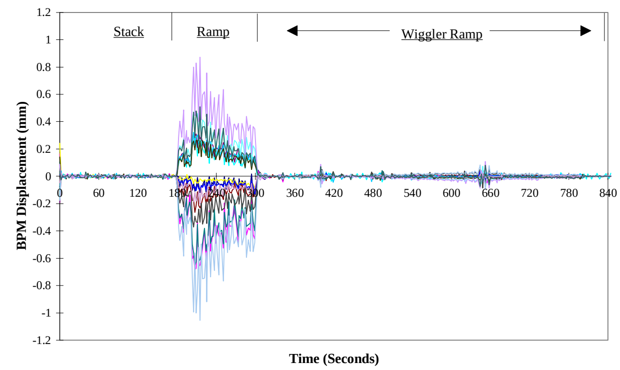

Figure 6: Vertical Orbit Control During Stacking and Ramping.

5 SUMMARY AND OUTLOOK

The horizontal global feedback system has operated very successfully to reduce the closed orbit ripple for many years. Developments are now centred on the introduction of a new SVD system to allow continued operation in the presence of a monitor or magnet failure.

The global vertical orbit feedback system has been developed to meet the demands of an increased number of beamlines in the SRS. It has been demonstrated to be highly effective at providing stable photon beam. This system provides beams, stable to the micron level, at a monitor in a beamline on each port in the SRS. The facility will be extended to cope with the proposed new beamlines.

The extension of global feedback on the electron beam monitors to both planes for operation during the energy ramp has provided the necessary orbit control to cope with reduced aperture vessels due to the installation of the new MPWs.

REFERENCES

[1] J.B. Fitzgerald et al., "The Daresbury Global Horizontal Servo Feedback System: Status and Outlook", European Particle Accelerator Conference, Sitges, Spain, June 1996 p1848.

[2] S.L.Smith "Recent Improvements in Vertical Orbit Feedback at the Daresbury SRS", European Particle Accelerator Conference, Stockholm, June 1998, p1741

[3] J B Fitzgerald et al., "Operational Performance of the Local Vertical Servo System on the Daresbury SRS", European Particle Accelerator Conference, Sitges, Spain, June 1996 p1854.

[4] S.F. Hill "An Improved Closed Orbit Servo for Energy Ramps on the SRS at Daresbury", European Particle Accelerator Conference, Stockholm, June 1998, p1711.

DEVELOPMENTS AND PLANS FOR DIAGNOSTICS ON THE ISIS SYNCHROTRON.

C M Warsop, D J Adams, K Tilley, Rutherford Appleton Laboratory, Oxfordshire, UK.

Abstract

Developments of diagnostics on the 800 MeV High Intensity Proton Synchrotron of ISIS, the Spallation Neutron Source at the Rutherford Appleton Laboratory in the UK, are described. Recent upgrades to instrumentation and control computers have made much more information readily available, which is valuable for control of a loss limited, high intensity machine. Measurements on high intensity beams have fundamental limitations in terms of accuracy, detail and interpretation. However, it is found that use of specially configured low intensity *diagnostic beams* can provide much detailed information not otherwise available, which is extremely valuable after careful interpretation. The methods and systems being developed to help trouble shooting, to find optimal conditions rapidly and systematically, and to improve understanding of high intensity performance are described.

1. INTRODUCTION

Previous papers [1,2,3] have detailed diagnostics developments and progress on the ISIS Synchrotron. Here, overall progress and plans are reviewed. In particular, specialist methods developed in the context of optimising a high intensity machine are highlighted.

The ISIS Synchrotron cycles at 50 Hz, accelerating 2.5×10^{13} protons per pulse from 70 to 800 MeV. Mean beam current and power are 200 μA and 160 kW respectively. The 22 mA H^- injector beam is stripped to H^+ with an aluminium oxide foil as it enters the ring acceptance; ~2.8×10^{13} protons accumulate over the 200 μs, 120 turn injection process. 2D transverse phase space painting minimises the space charge effects. The initially unbunched beam is trapped and accelerated to 800 MeV in 10 ms by the h=2 RF system. There are six ferrite-tuned RF cavities, which provide up to 140 kV/turn and sweep over 1.3-3.1 MHz. Beam is extracted in a single turn with a fast kicker and transported to the target.

Running intensity is limited by the maximum tolerable losses, which are carefully controlled to keep activation levels low enough for hands on maintenance. Dominant losses of 10 % occur in the first 2 ms of acceleration and are a result of non-adiabatic trapping and space charge. These loss levels depend critically on many parameters, which require careful optimisation. Methods for measuring, optimising and understanding these parameters are the aim of this work.

2. DIAGNOSTICS AT HIGH INTENSITY

2.1 Type and Use of Diagnostics

The ISIS Synchrotron was built with a comprehensive suite of diagnostic devices [4], including 15 capacitative position monitors per plane, residual gas profile monitors, intensity toroids and 40 beam loss monitors spread around the circumference. These give much beam information, including detailed measurement of losses, which ultimately determine running intensity. The beam is set up so that loss levels, times and locations are within strict limits; most is localised on the collector system. Standard use of these devices at high intensity has been very effective over the years, and allowed ISIS to run beyond its design intensity.

Two developments, using the same diagnostic devices, are now making much more information available: improved data acquisition and use of low intensity beams. It is expected that the more detailed knowledge of the machine this gives will allow more consistent running at the highest intensities.

2.2 High and Low Intensity Diagnostics

Though diagnostics on high intensity beams provide much essential information, they do not give all that is available and important. A high intensity beam often fills a large fraction of the available acceptances. This means that any measurement of the, necessarily small amplitude, coherent motion, is of limited accuracy. Generally, much detailed motion is masked from external observation by incoherent motion of particles. Equally importantly, observed motion is also difficult to interpret because of high intensity effects. As a result, the ability to measure many beam parameters in detail, most of which affect high intensity running, is severely limited.

Many of these problems can be overcome with a specially configured, low intensity *diagnostic beam*, which occupies a small fraction of the ring acceptances. Large coherent oscillations can be accurately measured, with negligible high intensity effects, providing detailed information not otherwise available.

Parameters measured at high and low intensity are not generally comparable, but they are complementary; with correct treatment differences illuminate high intensity effects. Comparison of measurements at varying levels of intensity is also valuable. Low intensity diagnostics are valuable probes of ‘zero intensity’ beam dynamics, and allow study of initial conditions before high intensity effects become significant. These measurements can also be valuable in identifying precise machine set-up, when parameters have been empirically optimised at high intensity.

2.3 Hardware Changes

The diagnostic devices used are essentially the same for low and high intensity. Most important are capacitative monitors for transverse centroid position and longitudinal pulse shape measurements. Some electronics modifications have been required to allow for smaller, low intensity signals.

The most important upgrades [2] have been: addition of many fast digitiser channels, introduction of powerful computers with ability to control accelerator and acquisition hardware, and improved high level processing and display software. The principle applications of digitisers are acquiring data from many position monitors and detailed longitudinal pulse shapes. Automatic signal switching into the digitisers is included, which allows linking in with other diagnostics in the future. The system is designed for automated measurement. The aim is for quick, convenient access to more beam information, with appropriate analysis and correction software to exploit it.

2.4 Practicalities of Diagnostic Beams

On the ISIS ring a diagnostic beam is conveniently produced with an electrostatic chopper in the injection line. This reduces the normal 200 μs (120 turn) injected pulse down to a well-defined 'chopped beam' pulse of ≥100 ns, (≥1/15 of a turn). This beam occupies small fractions of all acceptances, as required, and may be injected at any time during the normal injection pulse length.

Most chopped beam measurements so far have been at injection, when the beam is ideally configured, with undiluted small emittances and convenient mechanisms available for excitation. In principle, chopped beams can be accelerated and used at any time in the machine cycle, as long as mismatches are controlled and small emittances conserved. Work is underway to achieve this, and measurements throughout the cycle are planned.

Beam can be chopped on 1 in every 128 of the 50 Hz pulses, leaving interleaved pulses unaffected. Many machine parameters can also be pulsed to experimental values at this rate. This means experimentation is possible during operational running, with a very small loss of operational current (<1%). The low power associated with chopped beams is also an advantage, making them an ideal non-destructive probe.

3. INJECTION

3.1 Importance of Injection Set up

Most beam loss occurs early in the cycle, at low energy, when space charge forces are most important and occupancy of acceptances peaks. Transversely, the painting process aims to approximate a uniform real space distribution, to minimise losses associated with incoherent Q shifts. Longitudinally, the non-adiabatic capture is a major cause of loss, and its minimisation requires precise control of injected momentum spread. As a result, beam loss levels are highly dependent on injection parameters. Chopped beams are particularly valuable for checking the variation of all key parameters through injection.

3.2 Transverse Painting and Matching

On ISIS, painting of the ~ 20 π mm mr injected emittance over the ~ 400 π mm mr acceptances is anti-correlated in the transverse planes. Vertically, the injection point is moved with a steering magnet in the injection beam line; horizontally, the closed orbit is swept by the falling main magnet field. A schematic of injection is shown in Figure 1. Optimal set up depends on many parameters in the ring and injector and is thus easily perturbed. Standard measurements on the accumulating high intensity beam, e.g. positions and profiles, give useful information, but chopped beams provide a direct measurement of the painting process.

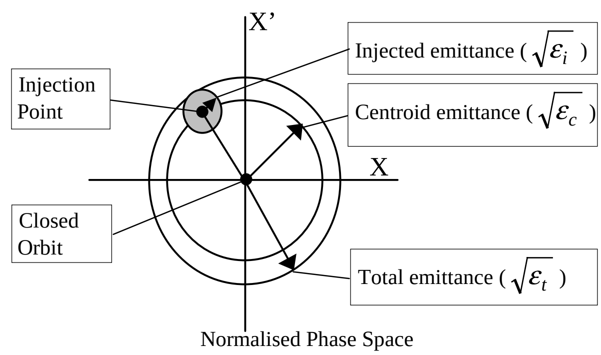

Figure 1: Injection Painting.

A chopped beam occupying a fraction of a turn is injected, and the centroid transverse positions at a monitor measured over the first ~ 40 turns. These are then least squares fitted to a function of the form (1) giving the position y_n on the n^{th} turn. This describes the sampled betatron oscillation and includes decoherence damping due to an assumed Gaussian Q spread [3]. Good measurements of betatron amplitude (A), Q, phase (ϕ), Q spread (δQ) and closed orbit (y_{co}) can all then be extracted. Note that this allows betatron amplitude *before* damping to be calculated. Chopped beams can be injected at any point during the normal injection process, thus variation of betatron amplitude and closed orbit through injection can be determined. This is a direct measurement of the injection painting of the beam centroid, Figure 2. Knowledge of lattice functions and apertures allows this to be related to machine acceptance.

$$y_n = A \cdot \exp\left[-\frac{(\pi \cdot n \cdot \delta Q)^2}{2}\right] \cdot \cos[2\pi \cdot n \cdot Q + \phi] + y_{co} \quad (1)$$

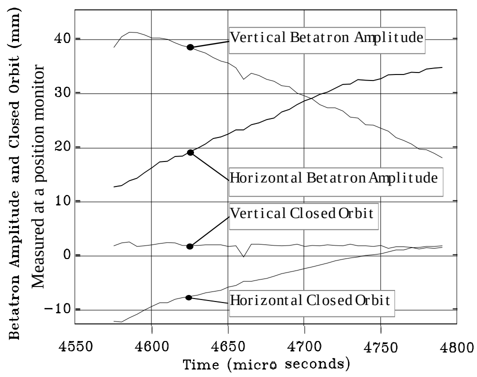

Figure 2: Measurement of Centroid Painting

Severe transverse mismatch can also prevent optimal painting. Again, a chopped beam occupying less than a turn is injected, its centroid motion is monitored as above, and its width measured simultaneously at a profile monitor. Time response of profile monitors on ISIS means measured widths are averaged over about 10 turns. Figure 1 shows the essentials; the total emittance of a painted beam ε_t, is related to the centroid emittance ε_c and effective injected emittance ε_i by

$$\sqrt{\varepsilon_t} = \sqrt{\varepsilon_c} + \sqrt{\varepsilon_i} \quad (2)$$

Assuming beta functions are known, ε_c is deduced from betatron amplitude $A=\sqrt{(\beta\varepsilon_c)}$ in equation (1), and ε_t deduced similarly from full width, many turn measurements at the profile monitor. From this ε_i can be estimated. Measurements on ISIS by this method indicate emittance dilution by up to a factor of ~ 3, but this is not yet a well developed diagnostic.

3.3 Longitudinal Set up

During the normal injection process, a continuous 'DC' beam is accumulated, which occupies the whole ring circumference. Later, the ring RF provides focusing for formation of two bunches. A very important property of the injected beam is its momentum spread, which directly affects trapping efficiency. Chopped beams allow direct measurement of the momentum distribution.

A short (100 ns) 'square' pulse, occupying a small fraction of a turn (T_{rev}=1.48 µs), is injected. Its debunching is then observed on a pick-up over ~100 turns with the Ring RF off. The 200 MHz microstructure from the linac disappears over the first few turns in the ring and has little effect. However, this structure means that, to a good approximation, the distribution of momentum along the length of the 100 ns diagnostic bunch is uniform. Debunching in the ring is emittance dominated, and this means the profile on the n^{th} turn (D[t,n]) is a convolution of the momentum distribution (f[dP/P]) with line density on the first turn g[t]:

$$D[t,n] = \int g[t_e] \cdot f\left[\frac{(t-t_e)}{n \cdot \eta \cdot T_0}\right] \cdot dt_e \quad (3)$$

Here $\eta=(\Delta f/f)/(\Delta P/P)$ and T_o the revolution time [3]. The momentum distribution may therefore be extracted from the debunching data D[t,n]. Repeating measurements at different times gives the momentum distribution through injection. This is a direct check on longitudinal injection conditions. Problematic conditions of the linac are quickly picked up and corrected using a debuncher cavity in the injection line. An example of measured momentum spread against debuncher setting is shown in Figure 3.

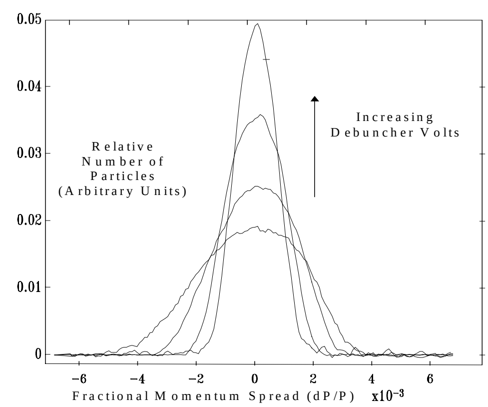

Figure 3: Measured Debuncher Action

4. BETATRON Q VALUES

4.1 Introduction

Optimisation of Q is critical for high intensity running, and essentially it involves minimising particle resonance crossing. Many mechanisms shift and spread Q values by varying amounts through the machine cycle; this demands time dependent correction. Nominal Q values are Q_h=4.31, Q_v=3.83; dominant resonances are the nearest half and whole integers.

The main lattice magnet fields scale together sinusoidally and determine the basic Q values. There are also two independently programmable trim quadrupoles in each of the 10 superperiods, which allow independent control of horizontal and vertical Q through the machine cycle. It is convenient to discuss low and high intensity effects separately.

4.2 Low Intensity Effects and Correction

The low intensity factors determining Q are main lattice magnets, trim quadrupoles and momentum via chromaticity. The fast cycling magnets are susceptible to eddy current and saturation effects, which must be corrected. Similarly, the 20 programmable trim quads must all operate to within tight limits to give desired corrections. To allow for Q spread and offsets caused by momentum spread, momentum offset, or main magnet scaling errors, chromaticity (ξ=(dQ/Q)/(dP/P)), must be known. Chopped beams allow detailed measurement and control of all these optical effects.

Chopped beam Q measurements, based on fitting function (1) to turn by turn positions, are accurate (~ ±0.004) and unambiguous, effectively at zero intensity. Such measurements have been effective at injection and are planned throughout acceleration. This allows all systems determining Q to be checked and corrected: the Q of the main lattice magnets (trim quadrupoles off); the expected change of Q due to trim quadrupoles; and the final resulting Q. Chopped beams are also ideal for chromaticity measurement. Basic procedures measuring Q as a function of energy, or main magnet scaling provide accurate values. Measurements on ISIS give values, in both planes, of about ξ=-1.4±0.1. Collectively, these measurements give all the information required to optimise low intensity Q.

4.3 High Intensity Effects

As intensity increases Q values shift and spread from the single zero intensity value and occupy a larger area in the Q plane. In a high intensity beam the coherent Q, the oscillation of the whole beam, and incoherent Q, the oscillation of particles within the beam, differ and must be allowed for. To optimise Q, both coherent and incoherent Q must be kept away from resonances. Shifts and spreads in Q are caused by direct space charge forces and image effects in the beam surroundings. Q shifts are functions of many parameters [5], e.g. intensity, energy, beam distributions and geometry, many of which vary through the machine cycle.

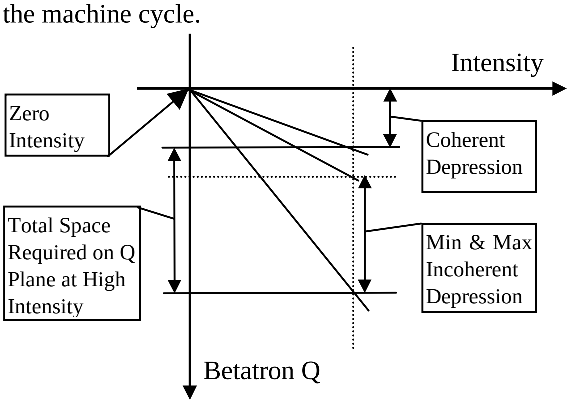

Figure 4: Schematic Change of Q with Intensity

Q set up is most important at low energy, when direct space charge tune shifts are largest, and the total Q spread peaks. Spreads increase with intensity, and this gives rise to a high intensity limit, when all regions in the Q plane free of dominant resonances are occupied. Optimisation consists of (i) moving the spread of Q's optimally between resonances and (ii) minimising all factors contributing to Q spread.

On ISIS, maximum incoherent tune shifts in both planes peak at -0.4 early in the machine cycle [6], and force particles to reach the dominant resonances. At these times the coherent Q depressions are about -0.1, and so lie above the minimum incoherent shift. The Q changes are shown schematically in Figure 4. The basic aim is to place the coherent Q value as high as possible *below* the nearest resonance in the working diagram, allowing maximum space below for tune depression.

4.4 Practical High Intensity Q Optimisation

The basic principles of high intensity Q optimisation described are well established, and have been crucial in achieving high ISIS currents. However, much more detailed routine measurement and optimisation is planned, exploiting improved diagnostics. Two sets of measurements are required: (i) coherent Q as a function of intensity, and (ii) loss as a function of Q, as it is swept between resonances with trim quadrupoles. These are required at regular intervals through the machine cycle.

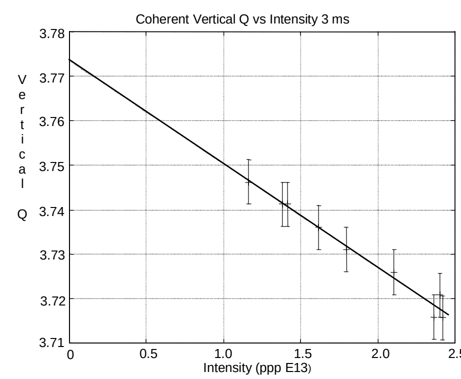

Figure 5: Measured Coherent Q vs Intensity

An example of a coherent Q-intensity measurement is given in Figure 5, and shows the expected linear form. These measurements are complemented by 'zero' intensity Q values provided by chopped beams. Once the Q-intensity relations are known they form a basis for optimisation. To be consistent, low intensity effects, e.g. chromaticity and magnet variation must be allowed for. Generally, early in the cycle coherent Q will be placed as high as possible, and adjusted with the intensity.

Measurement of loss as a function of Q gives an empirical optimisation of Q, and an estimate of total Q spread. Increase of loss as Q changes indicates more particles crossing known resonances; differences between these and coherent Q give the total Q spread. Factors affecting Q distribution are beam transverse and longitudinal distributions, which are functions of injection and RF set-up. Tuning these parameters and remeasurement of Q spread allow it to be minimised. Repetition of the total Q spread measurement as a function of intensity can also be useful, indicating when the high intensity limit is reached. It is hoped some consistent tie up with theory will be possible, relating measured longitudinal and transverse distributions to measured Q spread. Full Q optimisation must include all effects, high and low intensity, as they vary through the cycle; the above measurements give most of the relevant information.

5. TRANSVERSE DYNAMICS

5.1 Introduction

Good instrumentation is making large amounts of detailed information available, with low and high intensity beams. Appropriate systems allow these measurements to be taken quickly, automatically, and with minimal impact on operations. Below, an outline of the measurements presently being implemented [1] is given.

5.2 Low Intensity Measurements

Use of many digitisers linked to position monitors enables simultaneous acquisition of turn by turn positions at many points around the ring. If a chopped beam is introduced and excited, its betatron motion can be fitted to a function of the form in equation (1) at all monitors, and the parameters A, ϕ, y_{co}, are now given around the ring. From these values, relative beta functions at monitors, local phase advance, and detailed beam trajectories can be deduced. Use of chopped beams again provides accurate values, effectively at zero intensity.

The measurement of beam position at all monitors as a function of current in all steering magnets allows steering coefficients to be measured. These give data on lattice functions and valuable checks on correct operation of steering magnets and position monitors. The measurement of Q as a function of current in each trim quad provides beta at 20 lattice locations. This measurement also serves as a useful check on trim quadrupole operation. Collectively, these measurements should form the basis of an excellent zero intensity lattice model, which is valuable for error correction.

5.3 High Intensity Measurements; Correction

Most of the measurements described can also be taken at high intensity, which is valuable for two essential parts of machine optimisation; closed orbit and gradient error correction. The systems for correcting closed orbits are already much improved [1]. Detailed studies at various intensities, optimising orbit corrections which show some interesting high intensity properties [6], are planned.

6. LONGITUDINAL DYNAMICS

6.1 Introduction

Work studying longitudinal dynamics in more detail is now underway, and is particularly important in view of the proposed dual harmonic RF upgrade [7]. Set-up of the RF system is essential for high intensity running, as it affects all main loss mechanisms.

These measurements are based on digitising longitudinal bunch shapes from a capacitative pick-up over thousands of turns. The RF waveform is simultaneously digitised, which allows the instantaneous intensity verses RF phase to be reconstructed on every turn through the cycle. From this data most features of longitudinal dynamics can be probed, e.g. analysis of first and second moments yields dipole and quadrupole synchrotron oscillations.

6.2 Low and High Intensity Measurement

Many features of longitudinal motion can be directly observed with a low intensity beam filling a fraction of an RF bucket. A chopped beam can be placed at any RF phase during injection. Observation of its motion gives zero intensity synchrotron frequency, synchronous phase, and limits of stability. In principle, development of the RF bucket structure can be probed.

Measurements on a high intensity beam give detailed information on the size of stable regions, and the size of dipole and quadrupole oscillations. A more detailed optimisation of the RF should result, providing optimal longitudinal distributions and thus lowest losses. This work is still in progress [1].

7. CONCLUSIONS

Coupled with appropriate hardware, low intensity diagnostic beams are a powerful tool for optimising and understanding a high intensity machine.

REFERENCES

[1] D J Adams et al, “The ISIS Synchrotron Beam Control and Study Programme”, Proc. of PAC 99.

[2] D J Adams et al, “Development of the ISIS Synchrotron Diagnostics”, Proc. of EPAC 98.

[3] C M Warsop, “Low Intensity and Injection Studies on the ISIS Synchrotron”, Proc. of EPAC 94.

[4] B Boardman, “Spallation Neutron Source, Description of Accelerator and Target”, RAL Report RL-82-006

[5] B. Zotter, “Betatron Frequency Shifts Due to Image and Direct Fields”, CERN 85-19

[6] G H Rees, “High Intensity Performance of The ISIS Synchrotron”, Workshop on Beam Instabilities in Storage Rings, Hefei, China 1994.

[7] M R Harold et al, “A Possible Upgrade for ISIS”, Proc. of PAC 97.

THE ELETTRA STREAK CAMERA: SYSTEM SET-UP AND FIRST RESULTS

M. Ferianis, Sincrotrone Trieste, Trieste, Italy

Abstract

At ELETTRA, a Streak Camera system has been installed and tested. The bunch length is a significant machine parameter to measure, as it allows a direct derivation of fundamental machine characteristics, like its broadband impedance. At ELETTRA the Light from a Storage Ring Dipole is delivered through an optical system to an Optical Laboratory where it can be observed and analysed.

The Streak Camera is equipped with different time-bases, allowing both single sweep and dual sweep operation modes, including the Synchroscan mode. The Synchroscan frequency equal to 250 MHz, which is half of the ELETTRA RF frequency, allows the acquisition of consecutive bunches, 2ns apart. To fully exploit the performances of the Streak Camera, an optical path has been arranged which includes a fast opto-electronic shutter. By doing so, the optical power deposited on the photo-cathode is reduced in the different ELETTRA fillings.

1 INTRODUCTION

The bunch length measurement on Storage Rings has to be non-destructive; therefore a classical approach to the problem is to measure the length of the Synchrotron Light Pulses generated by the transversely deflected electrons, as it happens in the Bending magnets (Dipoles).

This is correct as the light pulses propagating from the source point to the measurement point preserve, in their longitudinal profile, the electron longitudinal distribution, that is the Bunch Length (σ_B).

In third generation light sources, this measurement is critical due both to the very short duration of the synchrotron light pulses, which lies in the range of Pico-seconds, and to the low energy per pulse available.

Streak Cameras are routinely used as powerful diagnostics tools in both linear (usually observing Transition Radiation rather than Synchrotron Radiation) and circular accelerators.

The main features of a Streak Camera are:

- Pico-second resolution, even in Single Shot
- very high (100s of MHz) repetition rate of the fast sweeps with dual-sweep “Synchroscan” mode
- high sensitivity, thanks to built-in photo multiplier

2 SYSTEM SET-UP

At ELETTRA the Light from a Storage Ring Dipole [1] is delivered through an optical system to an Optical Laboratory: the first vacuum mirror allows only the Visible and near-UV part of the Synchrotron Light Spectrum to be used. Beside a Transverse Profile Monitor system [1], other instruments [2, 3 and 4] have been installed and tested. Bunch Length measurements have been already performed [5], both with a Streak Camera and an Ultra-Fast Photodiode.

At ELETTRA, a Streak Camera (SC), specifically manufactured by Photonetics [6], has been recently installed and successfully tested [7,8].

The basic operating principle of a SC is a time-to-space conversion of ultra-fast optical events. The incoming photons are converted into electrons by a photo cathode. The emitted electrons are accelerated and deflected by a high-voltage fast ramp applied to deflection electrodes.

As a result, electrons are streaked out on the back-end phosphor screen creating a strip, whose length is proportional to the duration of the photon bunch. The image formed on the phosphor screen is amplified with a Micro Channel Plate (MCP) image intensifier and acquired by a CCD camera.

The ELETTRA SC is equipped with different sweep Units [9], which allow the following operation modes:

- single sweep, providing <2ps $_{FWHM}$ resolution
- dual sweep, with Synchroscan Unit at 250MHz

Synchroscan is a deflection technique, widely used in streak cameras, where the high-voltage deflection is driven by a sinusoid rather than a saw-tooth ramp. Thanks to the narrow-band deflection signal, the linearity of the high-voltage deflection amplifier is more easily achieved than in a wide-band amplifier, which is needed for a saw-tooth linear deflection.

The Single sweep unit (FTSU-1) provides the following full-screen deflections: 176ps, 441ps, 882ps, 1.7ns, 4.4ns, 8.8ns and 17.6ns, with <2ps$_{FWHM}$ resolution.

The Synchroscan unit (FSSU-1) operates at a frequency of 250MHz (res.=3.2ps$_{FWHM}$). The Secondary sweep units (FTSU-2 and STSU-2), used for vertically displacing successive Synchroscan traces, can cover the range from 9.15ns to 69.35ms.

3 THE OPTICAL PATH

The optical path (partial view shown in fig.1) performs the following operations on the synchrotron light:

1. deflection and focusing onto the SC input pin-hole (with 50, 100 or 200μm diameter)
2. band-pass (λ=500nm) filtering and attenuation
3. shutter for interlock purposes
4. optical power reduction

The reduction of the optical power on the time scales typical of a SC is not a straightforward task.

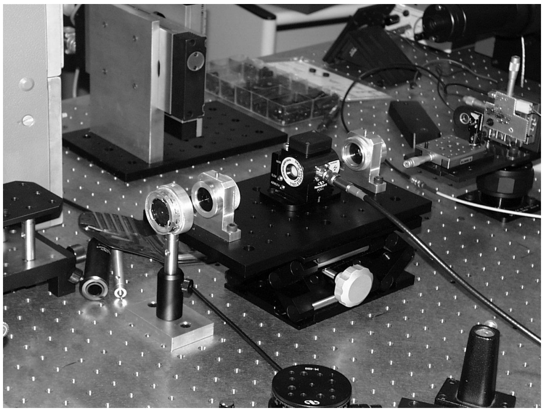

Fig. 1: A partial view of the Optical Path to the SC showing the Pockels Cell system.

The timings needed to achieve an effective reduction are reported in Table 1. Furthermore, the shutter operation has to be synchronous with the light pulses.

ON/OFF ratio	>100	a. u.
T_{ON} ; T_{OFF}	<5	ns
$GATE_{MIN}$	100	ns
$GATE_{MAX}$	50	ms
$f_{REP\ MIN}$	1	Hz
$f_{REP\ MAX}$	1	kHz

Table 1: fast shutter parameter list.

To meet the requirements, a Pockels Cell opto-electronic shutter [10] has been adopted.

3.1 Pockels Cell operation

A Pockels Cell [11] introduces a rotation (typically by 90^o) on the polarisation axis of the incident wave, upon the application of an external electric field E_T. By placing two polarisers, rotated by 90^o, respectively up-stream and down-stream the Pockels Cell, such a system acts as a fast shutter, driven by E_T.

To operate the system, a careful alignment of its elements is required. Furthermore, two pinholes are necessary to remove unwanted spots, which generate inside the system due to spurious reflections.

By carefully aligning all these elements, the ON/OFF ratio of the light can be maximised, while keeping a good transmission through the shutter.

The low-frequency trigger pulses, synchronous to the synchrotron light pulses, for the Pockels Cell high voltage (V_p=2.5kV) driver [12] are generated by the SC timing system. The duration of the trigger pulse (GATE) can be varied according to the SC operation mode and to the synchrotron light time structure.

3.2 Pockels Cell characterisation

The correct operation of the Pockels Cell shutter has been checked at low repetition rates (1 Hz), with long opening times (5ms) for direct eye-observation, while at higher repetition rates, up to 2kHz with the nominal opening time (100ns to 10µs) a wide-band (1GHz) photodiode has been used.

At the highest repetition rates (>2KHz), the closing of the Cell begins to show a ringing (fig.2), which is believed to be due to an opto-acoustic phenomenon induced by the piezoelectric effect. A similar effect has been observed by other authors [13].

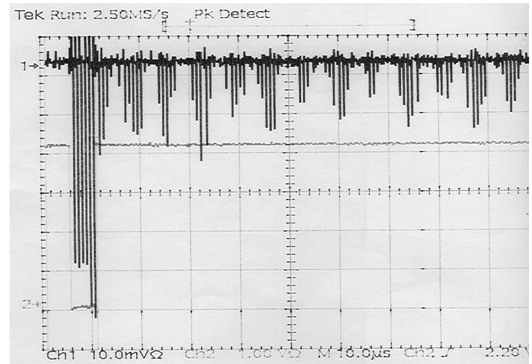

Fig. 2: Pockels Cell ringing, hor. scale = 10 µs/div.

With long Gates (>50 µs), an amplitude modulation effect of the transmitted light (observed with a laser on the photodiode and with the synchrotron light on the Streak Camera) shows up. It has to be taken into account for accurate beam stability observations.

The final check on the shutter operation has been performed "live" with the SC sweeping: in fig.3 the Pockels Cell effect is shown on a Synchroscan acquisition.

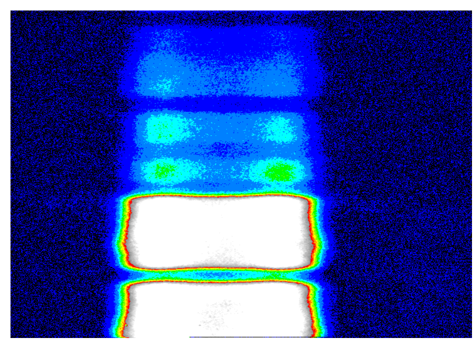

Fig.3: Pockels Cell effect on a Synchroscan acquisition. HOR.=441ps, VERT.=3.46•s. (full screen).

The Pockels Cell shutter is now currently used to improve the photo cathode lifetime; typical operating conditions are: f_{REP} < 20Hz, 200ns < GATE < 20µs. For stability studies, on long time scales, it may be removed.

4 THE SYNCHROSCAN OPERATION

The main advantage of Synchroscan deflection, associated to a dual-sweep streak tube, is to provide picosecond resolution at a very high repetition rate, typically less than 150MHz. To fully exploit this technique, both positive and negative slopes of the sinusoid are used. For ELETTRA, a dedicated streak tube has been developed by Photek [14]: this unit provides stable Synchroscan operation at 250MHz, with $3.2ps_{FWHM}$ resolution.

For the f_{RF} for ELETTRA is 499.654MHz and this feature has led to the unique possibility of observing consecutive bunches of a multi-bunch beam. Another outstanding feature of the ELETTRA SC is that the fastest sweep on the orthogonal slow axis is equal to 9.14ns. This feature allows the observation of a small number of consecutive bunches; five are shown in fig. 4 (acquisition in average mode). Filling MB, 80%, I=220mA, E=1GeV.

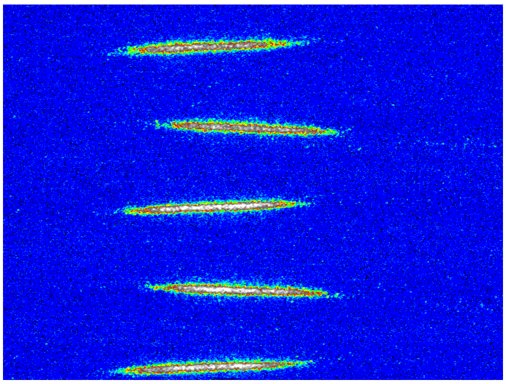

Fig. 4: Synchroscan acquisition at 250 MHz. Scales (full screen): HOR.=441ps, VERT.=9.14ns.

Due to the longitudinal coupled-bunch instabilities, present at the time of measurement, and also because of the average acquisition mode, each bunch image is much longer than its natural value. The operation of Synchroscan sweeping is made evident by the slope of the even and odd bunches.

5 THE STREAK CAMERA LOCAL CONTROL SYSTEM

The ELETTRA SC has been delivered with a user-friendly interface (Optoscope [9]) running on a desktop Personal Computer (PC) under Win95®. Through this graphical interface it is possible to control:

- The sweep units and MCP intensifier gain
- The status of the shutter
- The image acquisition and analysis processes
- The storage and export of the images

The SC and the PC are linked via a standard Serial line. The image acquisition and analysis functions are implemented on a powerful Image Analysis board [15], with a TMS 320C40 DSP chip on-board. A push-button keypad is also provided for direct control of the SC.

5.1 The Local Control system

It is based on two Personal Computers:

1. the desktop PC, delivered with the Streak Camera
2. a VXI-PC, developed in-house

The following functions are integrated:

- control over SC sweep units, MCP and shutter
- acquisition and analysis of the SC output images
- control on the timing system used to generate the appropriate trigger pulses and Synchroscan signal
- control on the safety and interlock functions
- generation of the video signal for the Control Room

The main reason for using two PCs is the cutting of development times, which has been achieved thanks to the full integration of the desktop PC in the Local Control System, leaving the only internal developments to be the timing and interlock boards.

5.2 The timing/interlock control computer

The timing and interlock functions have been implemented on VME/VXI custom boards, on a VXI crate with an Intel-based VME CPU. This solution provides the typical VXI hardware environment (EMI/EMC, ease of integrating custom boards, power supplies) with the Win95® OS software environment. The safety-critical interlock functions are hardware implemented on a custom board and use the software only for signalling its internal status.

5.2.1 The CPU of the VXI PC

Different CPU boards and operating systems have been tested. A PCVXI-745 (486 µP @ 66MHz) board, from National Instruments running LabView® under Win95®, has been tested first [16]. A Eurocom-128 (Pentium®100) from Eltec, running Linux has been used due to the temporary unavailability of the PCVXI-745. The final solution will adopt a VME-7591-941 board (Pentium®233$_{MMX}$) from VMIC, running either Win95® or Linux. This was the only board with the PMC [17] connector used for the PMC frame grabber (Control Room video signal generation).

The Control Room monitor will provide the operator with a “live” image of the SC output together with the relevant data (time axis, computed σ_B, peak-to-peak amplitude of longitudinal oscillations etc.).

5.2.2 The timing system

The timing system generates the:

- Trigger signal for FTSU-1, FTSU-2 and STSU-2
- Synchroscan signal for FSSU-1
- Pockels Cell GATE

These signals have to be synchronous to the light pulses, with a minimum jitter (< 3ps). To have the light pulse exactly in the middle of a fast sweep, the trigger to FTSU-1 has to be adjustable in 2ns steps, for one revolution period (864ns at ELETTRA), with a fine adjustment in 10ps steps. The repetition frequency ranges from 2.5kHz (FTSU-1 average acquisition) down to 1Hz (slowest sweep of STSU-2).

The Synchroscan signal is a pure sinusoid (0dBm), derived directly from the RF accelerating voltage. Thanks to a loan from E. Rossa at CERN, we are presently using the CERN Pico timing [18] VME board to obtain the divide-by-2 ($f_{RF/2}$) version of the RF and the Turn Clock signal (f_{RF} divided-by-(432x20)=57.83kHz).

At the time of writing, a new RF programmable-divider board has been developed, using the same

ECLinPS® Motorola family [19]. Measured jitter is <2ps: it could replace, in the future, the Picotiming module.

A second auxiliary board [20] is presently under development and will perform:

- further programmable divisions and level conditioning on the TCK to obtain the required low-frequency Trigger signal
- filtering and amplification are applied to the $f_{RF/2}$ to obtain the sinusoid for the Synchroscan signal
- Pockels Cell GATE generation
- intensity loop control (on-board 16-bit μP [21])
- interlock function

5.2.3 The interlock system

The interlock system checks the following conditions:

- light intensity level trespass (detected by means of a photodiode with hardware threshold and comparator)
- absence of the f_{RF} and Trigger signals

These alarm conditions are OR-ed together so that, as soon as any of these become true, the shutter to the SC is closed and a message sent to the Local Control Panel.

5.3 The Local Control Panel

At present no remote control will be delivered to the Control Room. The reasons for this are:

- precautions in using the photo cathode and MCP
- the Storage Ring FEL [22] control will be close to the SC Optical Laboratory
- development cost and time: to safely remotise the SC control, a non-negligible effort is required

A Control Panel will be developed on the desktop PC using the CVI® (National Instruments) development environment [23]. This panel will integrate the functions available on both PCs, using links both to the Optodll.dll (image analysis library provided by Photonetics) and to the VXI-PC by using CVI built-in TCP client-server library functions. This Control panel will also enable the non-expert user to safely use the SC.

6 MEASUREMENT RESULTS

The SC was delivered to Sincrotrone at the end of November, last year. Since then, in a two-month period, full performance has been achieved.

The goals for these commissioning tests were:

- to acquire single shot images, both with single-bunch (SB) and multi-bunch (MB) beams
- to operate the Synchroscan at 250 MHz
- to test the fast opto-electronic shutter with the SC

The SC has been also operated without the Pockels Cell, mainly on slow sweeps (10-50 ms) where the effect of optical power reduction, introduced by the fast shutter, is minimum.

Since February, during dedicated shifts, the first measurements of the ELETTRA beam were taken under different machine conditions, multi-bunch and single-bunch.

6.1 Preliminary tests of the SC system

The operation of the peripheral devices and the SC compliance to the specifications has been verified.

The jitter of the Trigger pulse to the SC has been measured to be less than 3ps, with the repetition frequency varying from 2Hz up to 2kHz.

The spectral purity and the level (0dBm) of the 250 MHz Synchroscan signal have been checked.

The synchronous opening of the Pockels Cell has been checked by directly cutting the light of the beam, with a (T_{OFF}-T_{ON}) time down to few nanoseconds.

Synchroscan has been operated at 250 MHz, although ELETTRA σ_B (>10ps) doesn't allow a direct verification of the Streak Camera time resolution (<3.2ps_{FWHM}).

6.1.2 Single Shot measurements

In a single shot measurement the light pulse is acquired with a single trigger event, without any possible averaging effect. In a Synchrotron light source, the worse case for single shot acquisition is with MB beams. The bunch charge may be some 10-100 time less than SB beam. Single Shot acquisitions were compared to averaged acquisitions and the negligible differences confirmed the jitter-free operation of the whole Streak Camera system.

6.2 Multi-bunch (MB) measurements

At ELETTRA, MB mode is the standard User Mode: 345 buckets filled, out of a total of 432 (80%). The injection current is 300mA, @2GeV. The coupled-bunch longitudinal instabilities are cured by tuning the RF cavity temperatures and by checking the beam spectrum.

A direct observation of these longitudinal oscillations is now possible, as shown inf fig.5. At 2.4GeV a more stable beam is observed compared to 2GeV.

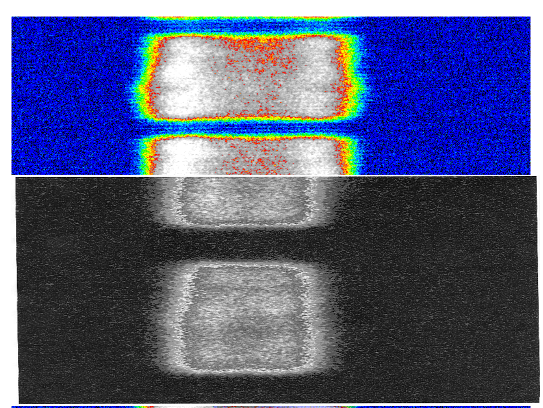

Fig.5: comparison of beams at 2.0GeV (upper half) and 2.4GeV(lower half) with two Synchroscan acquisitions.

6.3 Single-bunch (SB) measurements

In SB mode, two different fillings were measured:

- a single bunch (T_{REV} = 846ns)

- 4 bunches, evenly spaced, T_{BUNCH}=216ns

New long time scale information was obtained on beam stability. These studies are an important factor in understanding operation of the Storage Ring (SR) Free Electron Laser (FEL) [22].

The σ_B vs. current was measured (0 to 30mA in single bunch; 0 to 100mA in 4-bunch filling). In fig.6, single bunch profiles, at different currents, are shown. These profiles show that the electron distribution is close to a Gaussian distribution, as predicted by the theory.

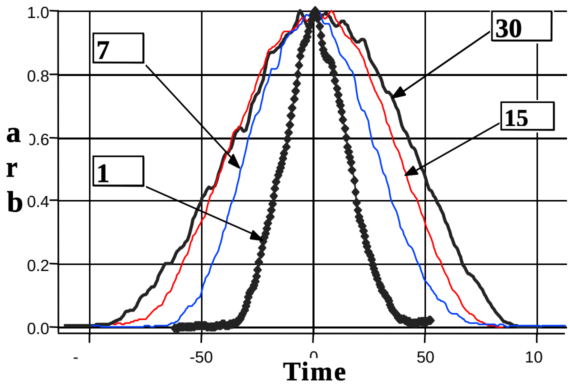

Fig.6: single bunch profiles at 1, 7, 15 and 30mA.

The charge/bunch being equal for both fillings, a direct comparison of the acquired data has been possible. The data show a very good agreement, except at higher currents where a small difference of 2 to 3ps is visible. This small increase in the four-bunch mode is not at present understood. It is not thought to be due to bunch oscillations since other streak camera images, as well as other measurements, indicated an absence of bunch motion.

6.3.1 Stability investigations

For these measurements the SC has been used in Syncroscan mode, with the fast axis set to 441ps and the slow axis ranging from 1µs to 35ms. For FEL operation the SC confirmed the instability free settings, see fig.7.

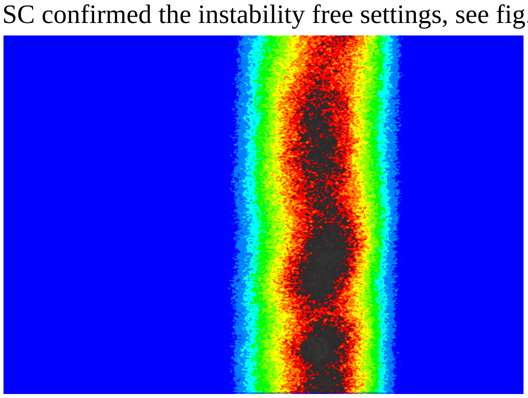

Fig.7: synchroscan image of four-bunch mode beam. Scales: HOR.=441ps, VERT.=34µs.

7 CONCLUSIONS

The Streak Camera system recently installed at ELETTRA has been presented in this paper. A description of the system has been given together with the first measurements. Future work will provide a Local Control Panel which will enable non-expert Users to safely perform measurements with this powerful diagnostic tool.

8 ACKNOWLEDGEMENTS

The author thanks the colleagues and students of the ELETTRA Instrumentation Group, who have helped him in setting up the Streak Camera system, C. J. Bocchetta and R. P. Walker for their support, R. Roux for the active participation in measurements and for data post-processing.

9 REFERENCES

[1] M. Ferianis et al. “The Optics of the ELETTRA Transverse Profile Monitor”, EPAC’94, London
[2] M. Ferianis et al. “An Optical System for the observation of Transverse Beam Motion” EPAC’96, Barcelona
[3] M. Ferianis, M. Pros “A New Frequency-domain method for Bunch Length measurement”, PAC’97, Chicago
[4] M. Ferianis et al. “Operation and Control of the Slow Beam Motion Monitor at ELETTRA”, DIPAC’97, Frascati
[5] M. Ferianis et al. “Bunch Length measurements at ELETTRA”, DIPAC’97, Frascati
[6] PHOTONETICS Gmbh, D-77694 KEHL.
[7] Elettra News, issue n.29, http://www.elettra.trieste.it/
[8] Elettra News, issue n.33, http://www.elettra.trieste.it/
[9] Optoscope user’s manual, Photonetics
[10] S. Parker “Optics Source Book”, McGraw-Hill 1987
[11] Optics Guide, CASIX inc. www.casix.com
[12] HVP-5LP User’s Manual, Quantum Technology, FL 32746-6212 USA
[13] E. Fulkerson et al. “Driving Pockels Cell Using Avalanche Transistor Pulsers”, 11th IEEE Int. Pulse Power Conf., Baltimore 1997
[14] Photek UK
[15] Oculus F-64 Frame Grabber; CORECO inc., Canada
[16] S. Bassanese “Studio e realizzazione del sistema di misura della Streak Camera ad ELETTRA”, degree thesis Dec.1998, Univ. di Trieste
[17] PCI Mezzanine Connector
[18] P. Joudrier, E. Rossa “Picosecond Bunch Train Module” CERN SL/BI internal Note, 1995
[19] ECLinPS IC family, www.motorola.com
[20] P. Buoncompagno “Progetto e realizzazione della scheda Ausiliaria per il sistema di controllo della Streak Camera”, degree thesis under preparation, Univ. di Trieste
[21] SIEMENS C166 µ-Controller, www.siemens.com
[22] R. P. Walker “European Project to develop a UV/VUV Free Electron Laser Facility on the ELETTRA Storage Ring”, NIM A to be published
[23] LabWindows/CVI User Manual, National Instruments

ADAPTIVE OPTICS FOR THE LEP 2 SYNCHROTRON LIGHT MONITORS

G. Burtin, R.J. Colchester, G. Ferioli, J.J. Gras, R. Jung, J.M. Vouillot
CERN, Geneva, Switzerland

Abstract

The image obtained with the LEP synchrotron radiation telescopes deteriorates, giving multiple and deformed images, when the beam energy goes beyond 80 GeV at beam currents above 2 mA. This problem is due to the deformation of the light extracting beryllium mirror, by as little as 1 µm, and had been predicted at the design stage. To overcome this problem, several changes together with an adaptive optics set-up have been introduced. These essentially consist of a cylindrically deformable mirror to compensate the cylindrical deformation of the beryllium mirror and a movable detector to compensate the spherical deformation. Both components are continuously adjusted as a function of beam current and energy.

1. INTRODUCTION

Four Synchrotron Radiation (SR) telescopes are installed in LEP around IP8 [1]. For each particle type there are two telescopes, one of them looks at the light emitted in the first normal dipole at the exit of the experimental straight section, where the Dispersion is very small, and one is located in the arc where the Dispersion is large: Fig. 1. With the data from the two telescopes it is possible to calculate the emittances and the energy spread of the beam for both horizontal and vertical directions.

The long distance between the telescopes and the accessible area in IP8 means that the telescopes have to be self-contained units incorporating all tuning facilities by remote control.

The optical set-up, the detector and the image signal processing have been optimised during the LEP 1 running period to provide the profile measurements with best precision [2]. The achieved accuracy has been established during cross-calibration runs by comparison with the wire scanners and the luminosity detectors of the experiments. The agreement of the vertical emittances determined by the different instruments has been demonstrated to be within 0 ± 0.1nm [3].

2. THE LEP 1 SR TELESCOPES

Each telescope is mounted on a standard 3.2 m optical bench housed inside a 3.5 m stainless steel tube for stability and protection. The telescope uses a spherical mirror, with a focal length of 4 m, as imaging device. A Magnification G = 0.2 is achieved with the help of folding mirrors. Chromatic filters, polarisation selection filters and linear density filters are incorporated in the set-up to control the wavelength, the polarisation components and to match the light intensity to the detector sensitivity to give the highest dynamic range.

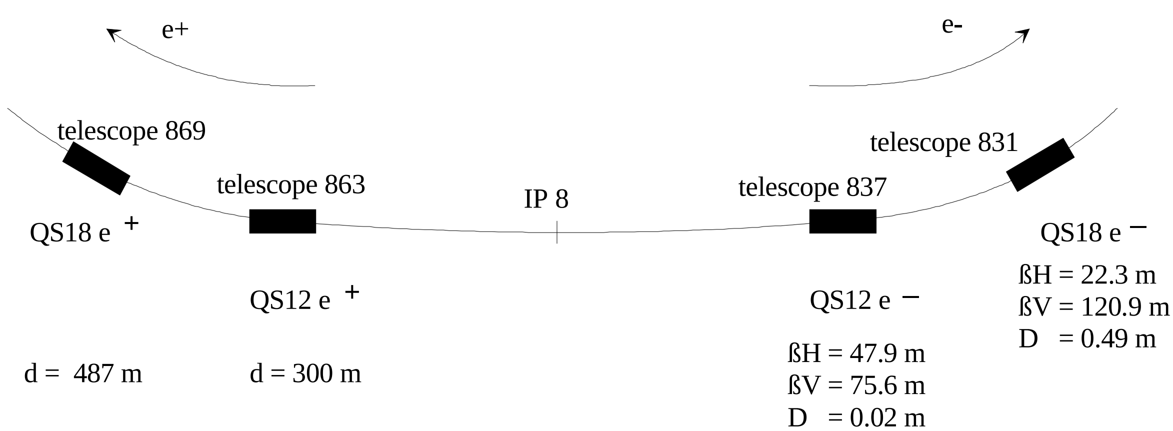

Figure 1: Layout of the Synchrotron Radiation Telescopes in LEP.

The light is extracted from the vacuum chamber by a Beryllium mirror 10 mm thick with a reflecting surface of 23 x 23 mm^2. In order to be outside the nominal LEP acceptance, this extraction mirror has to be located at 21.7 m from the SR source being measured. This mirror has been placed at an angle of 30° with respect to the vertical, mainly to reduce the material thickness presented to the energetic part of the SR, as it had been clear from the beginning that the reflecting surface would deform because of the heating due to power deposition of the SR. This effect had been estimated to deform the mirror mostly cylindrically with a curvature radius of the order of 1000 m during the LEP 1 period.

A major difficulty, due to the large bending radius of LEP of nearly 3100 m, is the precise selection of the centre of the light source and of the longitudinal acceptance along the beam path. A special set-up had to be made to solve this problem as the mechanical alignment of the telescope would not have been sufficiently precise. The principle is illustrated in Fig.2 using the horizontal phase-space defined in [4]. The origin of the phase-space is at the ideal source point of the light and the axes are the horizontal machine axis x and the trajectory angle θ with respect to this origin. In this phase-space, the beam trajectory is a parabola, the extraction mirror is defined by a skewed acceptance band, and a vertical slit located at the focal point of the spherical imaging mirror is represented by a horizontal acceptance band. As can be seen in this diagram, such a slit defines precisely the centre of the light source and the longitudinal acceptance. By moving the slit, the whole acceptance defined by the extraction mirror can be explored. It can be seen that the telescope acceptance doesn't change when the position of the beam orbit changes by as much as ± 5 mm. A slit and not an iris was chosen as the limiting horizontal aperture so as not to introduce additional diffraction in the vertical plane.

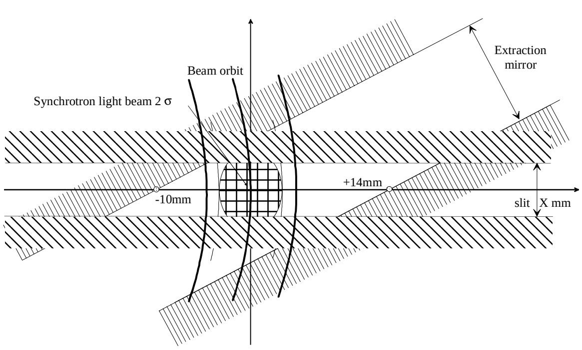

Figure 2: Telescope horizontal phase space, with beam trajectories (δx = -5, 0, +5 mm), extraction mirror and slit at the focal point of the imaging mirror.

It was assumed that a gaussian approximation of the various perturbing contributions was acceptable for the on-line deconvolution of the beam size measurement.

If w is the slit width, it has been shown that the longitudinal acceptance introduces an image broadening at the detector of the type:

$$\sigma_{LA} = k_{LA}\, w \qquad (1)$$

The major optical limitation of the instrument in LEP 1 was however the diffraction. In the vertical direction, the diffraction pattern at the detector can be approximated by a gaussian with a standard deviation

$$\sigma_{DV} = k_{DV}\ \lambda^{2/3} \qquad (2)$$

At the light extraction location of the telescope, the SR is a horizontal band which is limited by the light extraction mirror and afterwards by the slit having a width w. With a uniform window, it will generate a diffraction pattern, the width of which at the detector was approximated by a gaussian of standard deviation.

$$\sigma_{DH} = k_{DH}\, \lambda / w \qquad (3)$$

The design aim was to minimise these effects and to be able to measure precisely and independently the remaining contributions. For both directions, the diffraction broadening of the light spot will decrease when decreasing λ, hence the smallest possible wavelength is used in routine operation, i.e. 450 nm with a normal CCD.

Using the remote control facilities, the slit position is adjusted to centre precisely the SR source at 2 m from the bending magnet entrance, then the slit width and the chromatic filters are changed to estimate the coefficients from equations (1) to (3). To be able to measure without ambiguity the various contributions, a perfectly achromatic set-up using only mirrors has been chosen for the telescope, despite its higher complexity.

The LEP 1 campaign gave the following values:

$$k_{DV} = 3.9 \pm 0.1$$
$$k_{DH} = 1.6 \pm 0.2$$
$$k_{LA} = 40 \pm 10$$

if the σ's are expressed in μm, λ in nm and w in mm.

With these corrections it was possible to measure vertical emittances smaller than 1nm to ± 0.1nm. The major contribution to the uncertainty on the emittances was however coming from the knowledge of the LEP beam optics [3].

An additional limitation comes from the vertically polarised component of the synchrotron light. The horizontal component is a single lobe containing all the information about the beam and can be imaged in the usual way onto a detector. The vertical component unfortunately has four lobes [5] which are critical for the precision of the measurement because they generate additional diffraction and define a very limited longitudinal acceptance before deforming the beam image on the detector where they generate two horizontal light spots when slightly out of focus. Even though the horizontal polarisation component contains 3/4 of the total energy, it is still beneficial to filter out the vertical polarisation component. This was however not a serious problem at LEP 1.

Two additional devices were installed for special studies: a “corona” filter attenuating the dense core to study the beam tails with a 10^5 dynamic range, and a CCD with a pulsed intensifier to investigate the behaviour of individual bunches on selected turns [6].

3. THE LEP 2 SR TELESCOPES

When the LEP energy was raised above 80 GeV, the slit position scans clearly showed that the beam image was no longer focused in the same location in H and V, pointing to the cylindrical deformation expected. At that time, a mobile camera was introduced to optimise the telescope either for the vertical or for the horizontal measurement and to confirm the validity of the slit scans. When the power was raised above 90 GeV, the effect became even more dramatic. At this level of SR power, the deterioration was visible on the beam image which became difficult to use by the control room crew: see Fig.3.

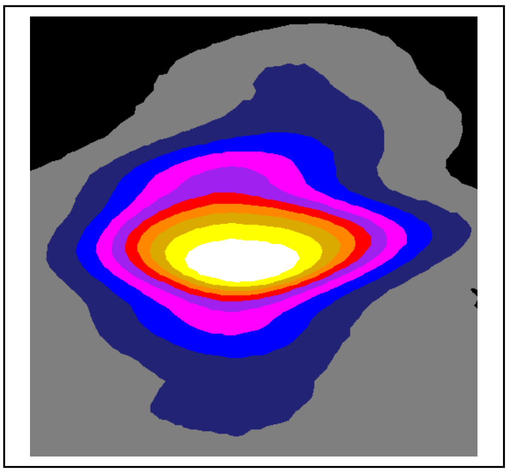

Figure 3: Beam image for a 2 mA beam at 91.5 GeV

It was clear that the performance of the telescopes was seriously compromised and needed drastic changes to the telescope set-up. As a side-effect of the energy increase, the radiation level at the telescope location increased beyond 10^3 Gray/year which even though attenuated at the CCD level, could not be reduced enough for the detector to survive a whole year of operation.

Because of this high radiation level, it was decided to suppress a number of facilities of the LEP 1 telescopes and to aim at maximum reliability rather than maximum possibilities. For that reason, the pulsed MCP detector and the corona filter were suppressed and a unique mobile CCD detector protected by heavy lead shielding was used.

The SR power generates several problems due to the deformation of the Beryllium extraction mirror.

The first effect is a small angular deformation which shifts the light source towards the entry of the bending magnet. For the QS12 telescopes, it can extend the longitudinal acceptance to the whole straight section up to the opposite QS12 telescope which results in multiple images originating from the various quadrupoles where the beam is not exactly centred. This can be corrected by decreasing the slit width from 2 mm in LEP 1 to 1 mm in LEP 2, and by adjusting the slit position.

As can be seen in Fig. 3, side lobes appear on the beam image. These lobes can be explained by the combination of the remaining vertical polarisation component of the SR and the cylindrical deformation of the Be mirror. The lobes being of smaller angular aperture than the main horizontal component, they contain enough energy to become clearly visible. The original metallic polarisation filtering [1] has been supplemented by an additional dichroic sheet polariser having an extinction ratio of 1/4000 to attenuate further these lobes. The polariser is mounted in a rotating housing to provide both maximum attenuation for normal operation and maximum transmission which is useful for optimising the tuning of the telescope. This strongly attenuates the vertical polarisation lobes and is sufficient for a good measurement of the beam sizes using a gaussian fit applied above a software defined threshold. But as the video signal is used for a TV display in the control room and because of the characteristics of the TV monitor and of the human eye, the lobes were still apparent and these “ghosts” were disturbing for the operations crew. For that reason an electronic “ghost buster” was implemented on the video signal for the comfort of the crew. It is linked to the data processing program and suppresses the video signal below the threshold defined for the fitting routine applied on the image data.

With this set-up, it was possible to measure with good precision the beam dimensions by using the two telescopes of each beam, one tuned for vertical and the other for horizontal measurements, and also having good TV observation conditions. This was acceptable for a limited time, and was useful to precisely measure the deformation of the Be mirror as a function of beam energy and intensity. It was however felt that a better correction scheme was needed in anticipation of the LEP beam energy increase towards 100 GeV with currents above 3 mA per beam when a SR power of more than 1.5 kW is expected to hit the mirror.

4. THE DEFORMABLE MIRRORS

The possibility to correct for the deformation of the Be mirror has been investigated during the LEP 1 period. As it is not possible to decrease further its deformation, the easiest scheme was to replace the first flat bending mirror by a cylindrically deformable mirror whose deformation compensates the main deformation of the Be mirror, with the possibility to introduce an additional spherical correction with the mobile camera.

A series of measurements were made at 94.5 GeV which show the evolution of the deformation of the Be mirror as a function of beam current: see Fig.4. Using deformation measurements taken at different energies, a scaling was defined to estimate the curvature radius needed at higher energies. It is estimated that the curvature radius will follow a law of the type:

$$R \sim 3600\, I_b^{-2}\, (E_b/90)^{-6} \qquad (4)$$

with the radius R in [m], the beam intensity I_b in [mA], and the beam energy E_b in [GeV].

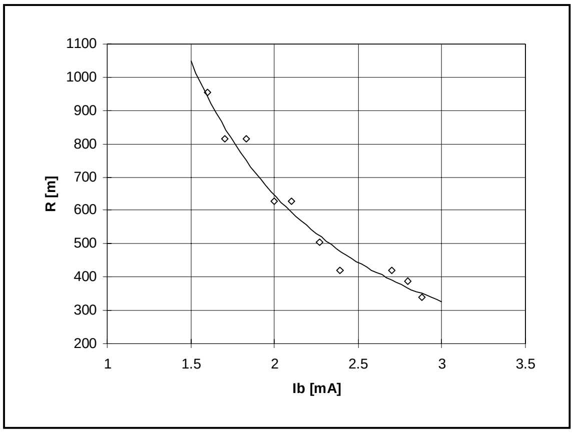

Figure 4: Curvature radius of the Be mirror as a function of beam current measured at 94.5 GeV.

As a result of a call for tenders, the most economical solution proposed was that of a U-shaped mirror deformed by a force generated by a spring compressed by a stepping motor. The motor is of the type standardised in the telescopes and can be driven by the existing multiplexed system in use in the telescopes.

The mirrors have a reflecting surface of 50x90 mm^2. One of these mirrors is shown in Fig. 5. They have been measured at the manufacturer's premises and found to have a cylindrical deformation from flat to a radius of curvature of 350 m. The deviation from a perfect cylinder is less than $\lambda/10$ over the full range. In order to have an optimum mirror lifetime, the manufacturer recommends to limit the deformation of the mirror to a curvature radius of 400 m. This limits the beam current which can be corrected to slightly less than 3 mA per beam at 94.5 GeV.

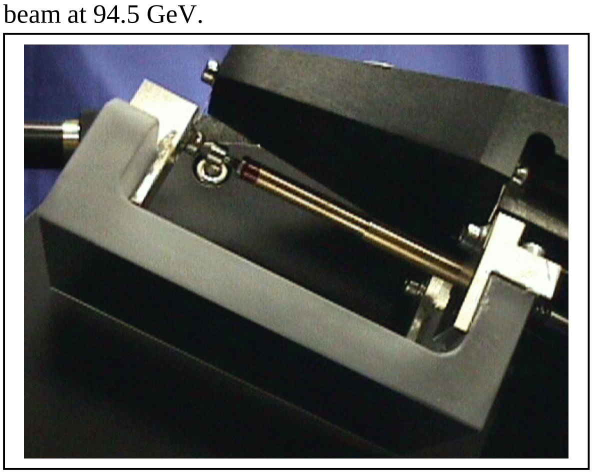

Figure 5: Detail of the U-shaped deformable mirror: the reflecting surface is towards the bottom, the force is applied at the top, on the left arm of the U by the spring-loaded piston.

The mobile camera has to be used for currents beyond 3 mA per beam. This was verified during the 1998 run and gives a correction capability of an additional 1 mA beam current, which will bring the telescopes close to the LEP limit.

For economical reasons, only the QS12 telescopes, which are the main ones, have been equipped with such mirrors. It is nevertheless important to keep the QS18 telescopes available as a back-up for the main QS12 ones and for studies on the telescope performance.

A second type of deformable mirror was designed using the original flat mirrors of 40 x 60 mm^2: see Fig. 6. In this set-up, an invar bar is cemented to the central part of the mirror the edges of which are blocked against the mirror support. The central part is pulled by a variable force generated by two springs put in tension via a cam driven by a stepping motor. A mirror of this type has been measured together with a U-shaped mirror and gave a bending radius from 1.4 km to 270 m in the bend plane with a radius varying from 1.3 km to 82 km in the perpendicular direction, which is excellent. The origin of the slight spherical shape at minimum stress is not clear, but it is easily corrected by the mobile camera. It should be possible with this mirror to reach a 2.7 mA beam current at 100 GeV before having to move the camera.

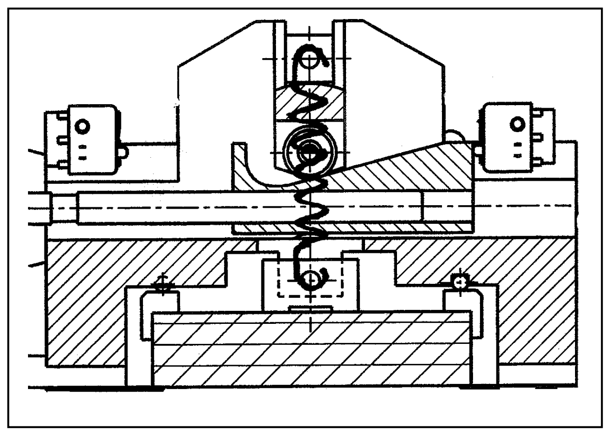

Figure 6: Drawing of the 2nd type of deformable mirror: the reflecting surface is towards the bottom, the central part of the mirror is pulled upwards by the spring which is put in tension by a piston displaced by the cam.

5. RESULTS WITH BEAM

The layout in Fig. 7 was chosen for the LEP 2 situation and implemented in the electron telescopes 837 and 831 for the 1998 run. The previously determined deformation law for the Be mirror and its compensation were refined. The telescope control software was modified so as to monitor every minute the beam energy and current and to deform accordingly the folding mirror. The dichroic polariser was fine tuned by maximising the vertical polarisation lobes and then rotated by 90° for maximum vertical polarisation attenuation. The slit position has been adjusted to centre the SR origin 2 m inside the corresponding bending magnet at top energy and the slit width adjusted to 1 mm for a longitudinal acceptance of ± 40 cm.

It was verified that under these conditions, both telescopes gave the same emittance, within the errors on the beta values.

The importance of the deformable mirrors is very well demonstrated in Fig. 8, where the same beam is imaged with and without deforming the mirror and filtering the vertical polarisation.

For the 1999 run, all telescopes have been put in the LEP 2 configuration and a campaign to re-measure the correction coefficients will be undertaken.

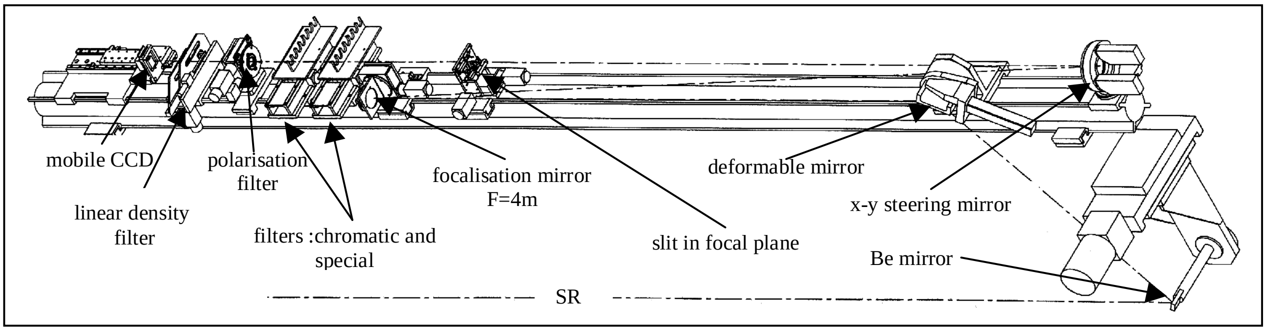

Figure 7: Layout of the SR telescope in the LEP 2 version

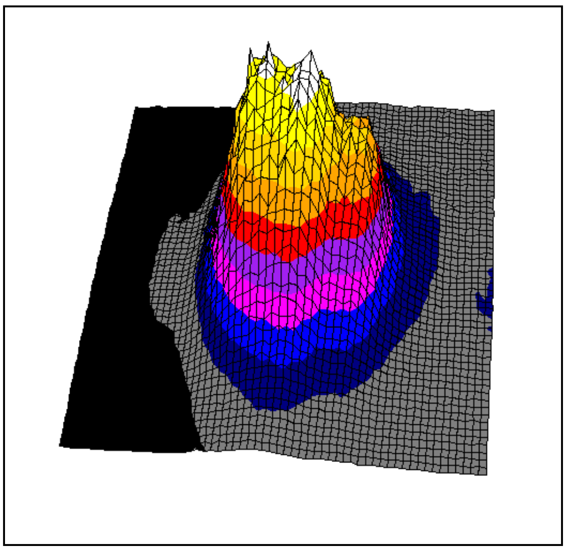

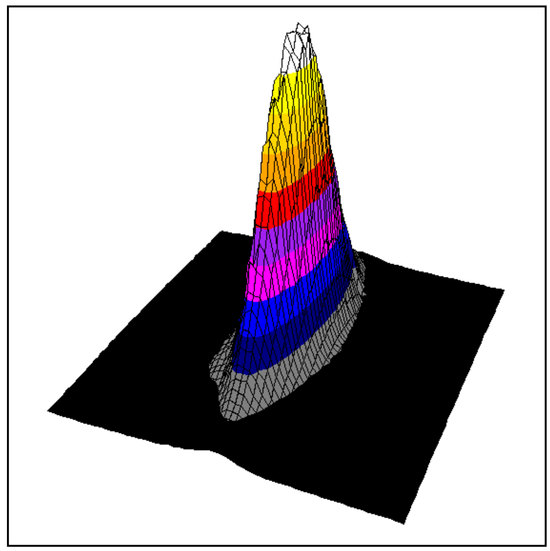

Figure 8: Left: beam imaged with the flat folding mirror and no polarisation filtering, for 2.2 mA at 94.5 GeV. Right: same beam with folding mirror set to calculated curvature and vertical polarisation attenuated.

ACKNOWLEDGEMENTS

R. Perret designed the second type of deformable mirror and provided us with the technical illustrations. His help is always much appreciated.

REFERENCES

[1] C. Bovet et al: “The LEP synchrotron light monitors” CERN SL/91-25 (BI), 1991, and Proc. of the 1991 IEEE PAC, San Francisco, 1991.

[2] R. Jung: “Precision emittance measurements in LEP with imaging telescopes, comparison with wire scanner and X-ray detector measurements”, CERN SL/95-63 (BI), and KEK Proc. 95-7, Sept 1995, A.

[3] P. Castro et al.: “Cross-calibration of emittance measuring instruments in LEP”, SL MD Note 202, February 1996.

[4] A.P. Saberski: “The geometry and optics of synchrotron radiation”, Particle Accelerators, Vol.5, pp 199-206, 1973.

[5] A.A. Sokolov and I.M. Ternov: “Synchrotron Radiation”, Pergamon Press, 1966.

[6] R. Jung: “Image sensor technology for beam instrumentation”, CERN SL-98-061 BI, 1998, and BIW 98 Proc, AIP Conf. Proc. 451,1998.

LUMINOSITY OPTIMIZATION IN DAΦNE

F. Sannibale for the DAΦNE Commissioning Team[1], INFN LNF, Frascati, Italy

Abstract

DAΦNE the Frascati Φ-factory, started the two beams commissioning on March 1998. Since then a relevant amount of experience concerning the techniques and procedures for optimizing the luminosity has been acquired. All the schemes used are strongly based on the use of various diagnostic systems including a dedicated luminosity monitor, orbit measurement, tune monitor, synchrotron light monitor and others. A summary of the used techniques, with accent on the diagnostic aspects, is presented.

1 INTRODUCTION

DAΦNE is an electron-positron collider with separated vacuum chamber rings and two interaction regions (IR) with horizontal crossing angle [1]. The main design parameters are listed in Tab. 1, while a general lay-out is shown in Fig. 1.

Table 1: DAΦNE Design Parameters

Energy	510 MeV/beam
Single Bunch Luminosity	4.4 10^{30} cm^{-2} s^{-1}
Multibunch Lum. (30/120 bunches)	1.3/5.3 10^{32} cm^{-2} s^{-1}
Beam-beam Tune Shift (H/V)	0.04/0.04
Ring Length	97.69 m
Dipole Bending Radius	1.4 m
Natural Emittance	10^{-6} m rad
Coupling	0.01
Natural Relative Energy Spread	4 10^{-4}
r.m.s. Bunch Length	3 10^{-2} m
Damping Times (L/T)	17.8/36.0 ms
Beta Functions @ IP (V/H)	4.5/450 cm
Horizontal Crossing Angle	10-15 mrad
Particles/Bunch	8.9 10^{10}
Number of Bunches	30÷120
RF Frequency	368.26 MHz

The center of mass energy of the beams is tuned on the mass of the Φ meson in order to study the rare phenomenon of the CP violation that can appear when the Φ's decay in neutral kaons. In order to collect sufficient statistics a very high integrated luminosity is required.

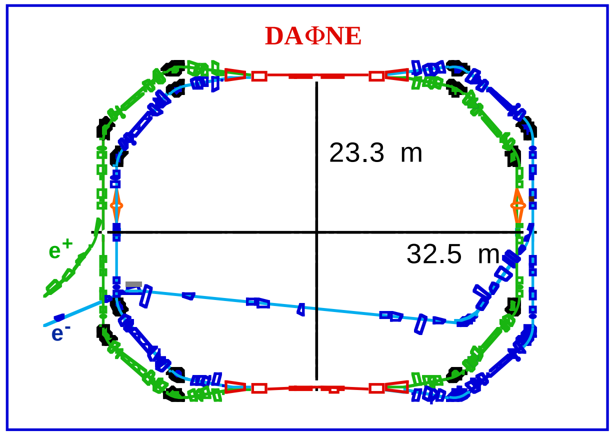

Figure 1: DAΦNE Main Rings Lay-out.

The luminosity commissioning of DAΦNE was organized in two different phases. During the first period, that started on March 1998 and ended on November 1998, the main goal was to obtain a single bunch luminosity of 10^{30} cm^{-2} s^{-1} as a test of the machine capabilities. In order to gain enough comprehension and operational experience, the IR was equipped with a provisional insertion in which all the quadrupoles in the low-beta triplets were normal conducting, instead of permanent magnet type, the vacuum chamber was instrumented with a beam position monitor (BPM) just at the IP and with additional BPM's of electrostatic (button) and directional (strip-line) types. No experiment detector was present at that time. A four months shutdown period followed, during which the CP violation experiment KLOE [2] was installed with its. detector totally immersed in the magnetic field of a ~6 m diameter superconducting solenoid. The second phase of the two beams commissioning started few weeks ago, on April 1999, with the solenoidal magnetic field (2.4 Tm) of the detector on. At the low energy of DAΦNE, this field creates a strong perturbation that must be carefully compensated. The compensation operation was successfully performed in few days and since April 14, the KLOE detector is collecting Φ events, making of DAΦNE the first factory running physics. Table 2 shows the main results so far obtained.

Table 2: DAΦNE Achieved Results

Single Bunch Luminosity	1.4 10^{30} cm^{-2} s^{-1}
Multibunch Luminosity (13 bunches)	1.5 10^{31} cm^{-2} s^{-1}
Particles/Bunch	2.3 10^{11}
30 bunches Stored Current (e^+/e^-) (design: 1.1 A)	0.56/0.54 A
Integrated Luminosity to KLOE Experiment (May 12, 1999)	30 nb^{-1}

[1] DAΦNE Commissioning Team: M.E. Biagini, C. Biscari, R. Boni, M. Boscolo, V. Chimenti, A. Clozza, G. Delle Monache, S. De Simone, G. Di Pirro, A. Drago, A. Gallo, A. Ghigo, S. Guiducci, F. Marcellini, C. Marchetti, G. Mazzitelli, C. Milardi, L. Pellegrino, M.A. Preger, R. Ricci, C. Sanelli, F. Sannibale, M. Serio, F. Sgamma, A. Stecchi, A. Stella, C. Vaccarezza, M. Vescovi, G. Vignola, M. Zobov.

Table 3: Luminosity Parameters and Diagnostic Systems Matrix.

	Tune Measurement System	Orbit Acquisition System	Synchrotron Light Monitor	Oscilloscope Monitor	Longitudinal Feedback	Stored Current Monitor	Luminosity Monitor
IR Orbit		**o**					
Longitudinal Position@IP				**o**			**o**
IP Vertical Position		**o**					**o**
IP Vertical Angle		**o**					**o**
IP Horizontal Position		**o**					**o**
IP Horizontal Angle		**o**					**o**
IP Transverse Tilt			**x**				**o**
IR Optical Functions	**o**	**x**					**o**
Coupling &Emittance	**x**		**o**			**x**	
Working Point	**o**						
Beam-Beam Effects	**o**	**o**	**x**			**x**	**o**
Instabilities	**o**		**x**	**x**	**o**		
Dynamic Aperture						**o**	

The luminosity tuning up passes through the optimization of several machine parameters. This operation is performed by means of the continuous and intensive use of most of the different diagnostic systems present in DAΦNE. Table 3 indicates these machine parameters and the diagnostic systems that are used for their optimization. In the table the dots indicate the primary importance regulations while the crosses the secondary ones.

The machine parameters, relevant in the luminosity optimization, can be separated in two main categories. The first one concerns the optimization of the interaction point (IP) 'geometry', or in other words, of the mutual position of the two beams at IP. The second category includes those parameters that allow to increase the maximum beam-beam tune shift and then to maximize the number of particles able to stay in collision steadily. The quantities in the upper half of Tab. 3 belong to the first category, while the remaining parameters belong to the second one.

The typical luminosity optimization process in DAΦNE consists in a number of steps. First of all, the single beam parameters are tuned. That includes, for example, the optimization of the coupling and of the transverse tilt by the synchrotron light monitor, of the working point and of the betatron functions at IP by the tune measurement system, of the IP geometry by the orbit acquisition system. Once one of the beams has been properly tuned, the whole operation must be repeated for the other one. At this point, if everything has been done correctly, the beams are ready for the last phase of the luminosity optimization. Few mA of each beam are stored and brought into collision. By using the luminosity monitor it is now possible to fine tune the geometry at the IP. Vertical position and angle, longitudinal position, horizontal position and angle and transverse tilt can be now adjusted in order to maximize the luminosity. Actually these adjustments affect each other and some iterations are necessary to achieve the best result. It is worth to remark the importance of this optimization phase performed with the luminosity monitor. To be efficient this monitor must be independent from the experiment detectors and completely available to the machine personnel. Additionally, it must be fast enough to permit real time adjustment of the machine parameters. The next paragraph will include a brief description of the diagnostic systems together with some examples of the measurements used for luminosity optimization.

2 DIAGNOSTIC SYSTEMS FOR LUMINOSITY OPTIMIZATION

2.1 Tune Measurement System

Figure 2 shows the two different systems used in DAΦNE for measuring the fractional part of the horizontal and vertical betatron tunes.

The first one uses a 'classic' scheme where the RF output of a network analyzer (HP 4195A 10 Hz - 500 MHz), amplified up to 100 W by class A amplifiers, generates the sweeping excitation for a transverse kicker. The beam response is then picked-up by BPM's whose signals, properly combined, are sent back to the network analyzer, where a simultaneous analysis of the tunes in both the planes is performed. The single measurement takes the time necessary for a complete sweeping cycle, making this system not suitable for real time monitoring of the tunes. Fast measurements are instead possible by means of the second system, where the excitation is now provided by a white noise generator. The beam response signal is sent to a spectrum analyzer (HP 70000 system) operating as a detector in zero span mode. The spectrum analyzer IF is then down-converted by a HP 89411A module and finally processed by a FFT signal analyzer, HP 3587S, with 23 bits resolution and 10 MHz sampling rate. The two systems can be used for both the beams indifferently.

The tune measurement system plays a primary role in the luminosity optimization process. Measurements such as tune plane working point, tune shifts induced by quadrupole strength variations for evaluating the beta functions at IR, coupling measurements by the closest tune approach, coherent beam-beam tune shift are some of the fundamental measurements that are heavily used during the luminosity optimization. Moreover the spectrum analyzer combined with the real time signal analyzer is very powerful and useful in identifying and in the observation of instabilities.

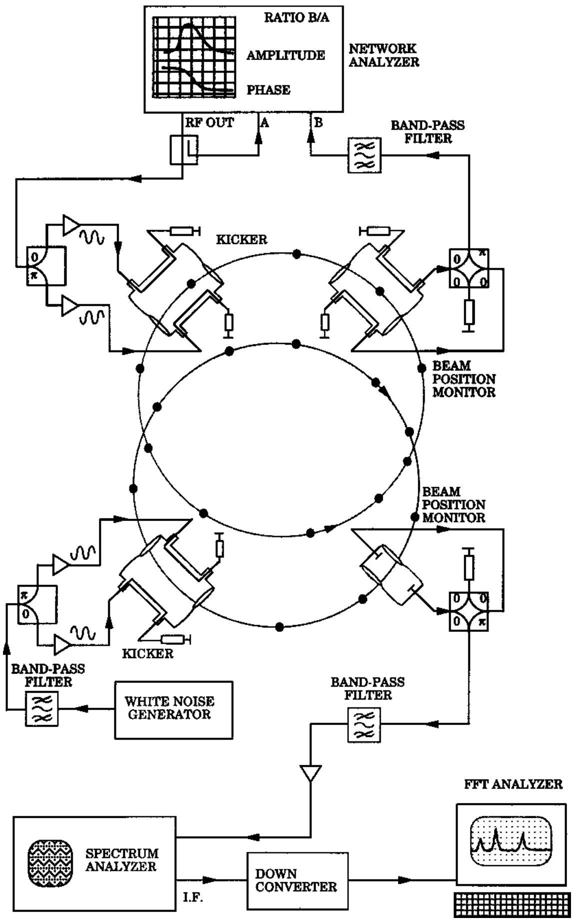

Figure 2: Tune Measurement System Schematic

Figure 3 shows an example of a coherent beam-beam tune shift measurement performed on the positron beam with the real time system.

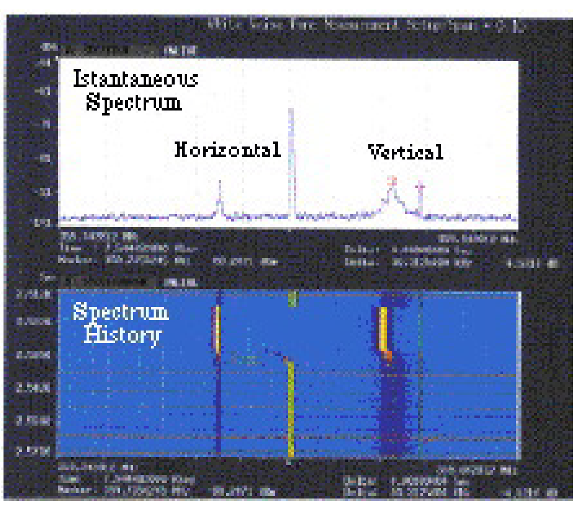

Figure 3: Coherent Beam-beam Tune Shift

2.2 *Orbit Acquisition System*

The 45 beam position monitors (BPM), of the button type, distributed along each of the Main Rings allow efficient closed orbit measurements in DAΦNE [3]. The electronic detector, one per each BPM, is a commercial board by BERGOZ built according to DAΦNE specifications. The scheme is based on a super heterodyne receiver, which converts the beam spectrum selected harmonic into an intermediate frequency before the amplitude detection. The board analog outputs are then sent to four VME acquisition systems, one per machine quarter. Each of these systems is composed by a bank of HP1352 FET Multiplexers connected to a HP1326B Digital Multimeter. The hardware control and the data acquisition are performed by the DAΦNE Control System processor board [4], based on a Motorola 68030 CPU, which runs a purpose built LabView application. The whole orbit acquisition rate is 5 Hz, the rms resolution is about 20 μm and stable measurements can be performed down to 1 mA of stored current.

The orbit acquisition system is a very important tool during luminosity optimization. In fact the geometry of the interaction region, in all its degrees of freedom, must be first tuned by this system. Moreover, as Fig. 4 shows, global orbit measurements when the beams are in collision can evidence beam-beam deflection effects. By minimizing this collision induced orbit, by local bumps at the IR, it is possible to optimize the overlap at the IP.

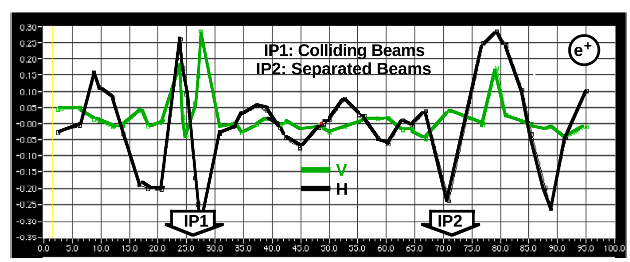

Figure 4: Beam-Beam Deflection Orbit. Horizontal scale 5 m/div, vertical scale 50 μm/div.

2.3 *Synchrotron Light Monitor*

Two synchrotron light monitors (SLM) are present in DAΦNE, one in each of the rings. In order to be able to perform beam emittance measurements, the source points have been chosen in dipoles with very small horizontal dispersion. Because of the large emittance, the transverse beam dimensions in DAΦNE remain relatively large even down to a coupling factor smaller than 0.01. This situation allows the use of the visible portion of the synchrotron radiation maintaining, at the same time, the monitor resolution sufficiently small. In the present configuration a water cooled 45° aluminum mirror, placed inside the vacuum chamber, deflects the light through a vacuum window and a slit into a CCD camera. In the final configuration [5] the light will be transported to a dedicated laboratory outside the controlled area by an achromatic optical channel, aberration free up to the second order, to extend the measurement capabilities of the monitor and provide the maximum flexibility of use.

From the point of view of the luminosity, the most relevant measurements that can be performed by the SLM include emittance, coupling and transverse tilt.

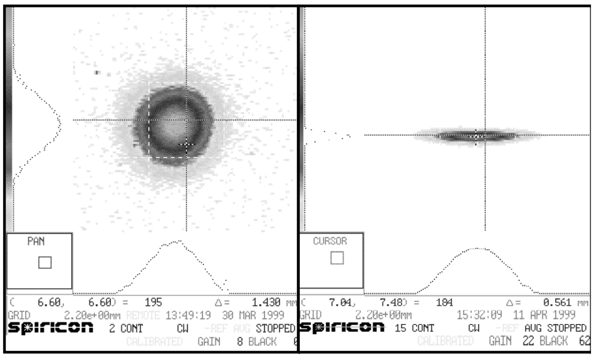

Figure 5: Coupling Measurements by the DAΦNE SLM

Additionally, from the simple observation of the beam spot, some useful indications can be derived concerning beam-beam effects such as tails, distribution variations, induced instabilities and so on. The example in Fig. 5 shows coupling measurements performed on April 99 when, left side, for the first time the positron beam was stored with the KLOE field on (45% of coupling) and, right side, when after few days the field effects were properly compensated and the coupling was reduced to 1.1%.

2.4 Oscilloscope System

This system is based on a 4 channel 2.5 Gsamples/s 500 MHz oscilloscope and on a hierarchical (1.3 GHz) RF MUX tree housed on VME crates and controlled by a CPU running under the DAΦNE Control System which provides also a friendly user interface able to select each of the signals connected to the lower level of the multiplexer tree and, additionally, the proper timing system signal for triggering the oscilloscope. Several beam pickups, including wall current monitors, together with a variety of other useful signals, such as the ones from the injection kickers, can be monitored by this system.

As already mentioned, DAΦNE is a collider with separated vacuum chambers. Each of the beams runs through a different magnetic structure and has its own RF cavity driven by the same master RF generator. This situation requires a very fine tuning of the times of arrival at the IP. This delicate operation is performed by selecting the couple of BPM's placed just at the ends of the IR, equally spaced from the IP, and by measuring the difference in time between the passage of the 2 beams in each of the 2 BPM's. By varying the RF phase of one of the cavities it is possible to make these time differences equal, which imply that the beams cross each other exactly at the IP. The resolution offered by this scope based adjustment is about 100 ps. The system is also used during the multibunch luminosity optimization. In fact, if the signal coming from a pickup is observed on the scope on a long time base, it is then possible to verify the multibunch filling pattern. Even filling patterns are important because they make the longitudinal feedback operation more efficient allowing to increase the stored current.

2.5 Longitudinal Feedback

The DAΦNE bunch-by-bunch longitudinal feedback has been developed in collaboration with SLAC and LBL [6]. The system, see Fig. 6, is composed by a front end that extracts, from a pick-up signal, the phase of the bunch center of mass by a phase detector working at 6 times the DAΦNE RF (368 MHz).

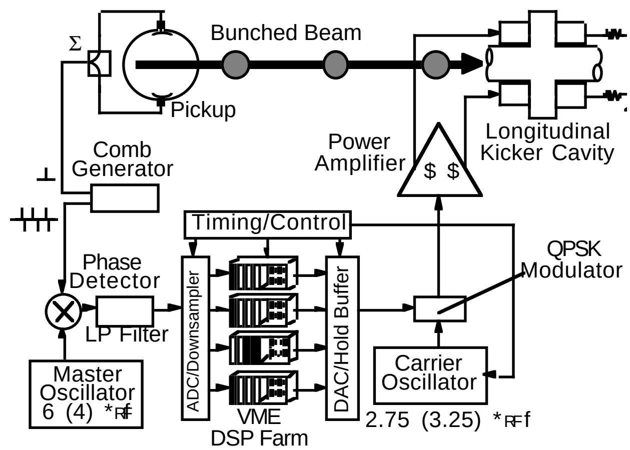

Figure 6: Longitudinal Feedback Schematic

The phase error signal is then sent to an ADC, with clock at 368 MHz, that converts the signal for the feedback digital part, where a FIR filter is implemented by the real time software. The digital part is based on a fast VME Digital Signal Processor farm of 60+60 ATT DSP1610 processors. The FIR filter type, gain and phase are run time programmable. The chain is then completed by a DAC that sends the correction signal to RF class A power amplifiers and to a 'cavity-type' longitudinal kicker that finally performs the phase correction on the bunch.

The main task of this system is, of course, to maximize the luminosity with more than one bunch in the rings, by damping the instabilities that can limit the total beam current, decrease the beam lifetime, and make the currents between different bunches strongly unequal. Additionally the feedback front end can be used as a powerful diagnostic tool. In fact a purpose built software application allows to perform instability mode analysis and bunch by bunch current measurements.

2.6 Stored Current Monitor

The beam current monitor system is based on a toroidal DCCT sensor by BERGOZ, a signal conditioning apparatus, a VME digital voltmeter (DVM) and a VME processor. The DCCT connected to the signal conditioning electronics provides a voltage output proportional to the average value of the stored beam current. The DVM, triggered at 50 Hz, performs the conversion of the analog voltage over an integration time of 2.5 ms and stores the value into an internal register accessible through the VME bus. The VME processor is again the DAΦNE Control System processor board, based on a Motorola 68030, running an application written in LabView. The processor performs the on-line acquisition of the 2 DCCT's (one for each of the rings) and after an immediate conversion stores the floating point values into two circular buffers on VME RAM, each one holding the last 2000 acquisitions. The processor calculates and updates also the average current for the last 10 s of run for both the rings. Lifetime calculation is also performed.

In the single bunch mode, luminosity is proportional to the product of the currents of the colliding beams. By means of current and luminosity measurements it is possible to evaluate this very important proportionality constant, that gives a clear and direct measurement of the degree of optimization of most of the quantities related to luminosity: the higher the constant value, the better the optimization. Moreover beam lifetime measurements during collision give useful information about beam-beam effects and dynamic aperture of the machine. DAΦNE is a collider with flat beams with lifetime dominated by the Touschek effect. This situation implies that the lifetime value is with a good approximation proportional to the square root of the coupling factor. By the 'lifetime method' it is possible to measure coupling values smaller than the ones allowed by the synchrotron light monitor which is resolution limited to ~ 0.005.

2.7 *Luminosity Monitor*

DAΦNE is equipped with 2 independent luminosity monitors [7], one for each of the interaction regions. The electromagnetic reaction at IP used for measuring the luminosity is the single bremsstrahlung (SB) where an electron and a positron scatter with the emission of a gamma photon. Luminosity is proportional to the gamma photon counting rate. The monitor detector consists of a high resolution "spaghetti calorimeter" proportional counter, where thin layers of lead and scintillating fibers are alternately packed together in order to obtain a very efficient configuration for photon detection in the gamma range. The calorimeter is equipped with a photomultiplier read-out whose output signal is sent to the electronic chain visible in Fig. 7. During collisions the very high rate and sharp angular distribution of the SB process allow an on-line luminosity measurement within an overall accuracy of 10÷15%. The system and electronic chain are calibrated by measuring the energy spectra of the well-known gas bremsstrahlung process (GB), scattering between beam particles and residual gas molecules with the emission of a gamma photon.

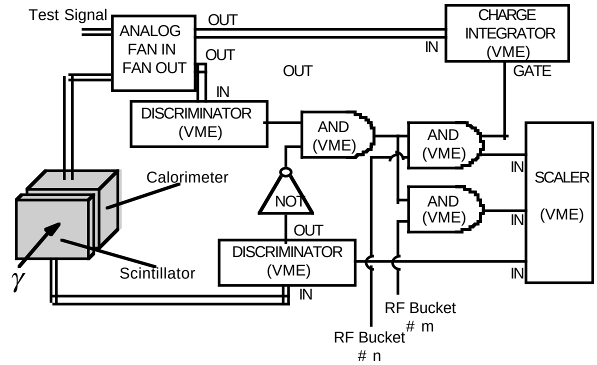

Figure 7: Luminosity Monitor Block Diagram

The system, as previously pointed out, has shown its fundamental role in the fine tuning of the IP geometry during the luminosity optimization. Figure 8 shows, as example, the luminosity monitor read-out window, during a luminosity relative measurement dedicated to the optimization of the vertical overlap of the beams at IP. Vertical position bumps at IR were performed looking for the SB counting rate relative maxima (peaks in the clear trace of the figure).

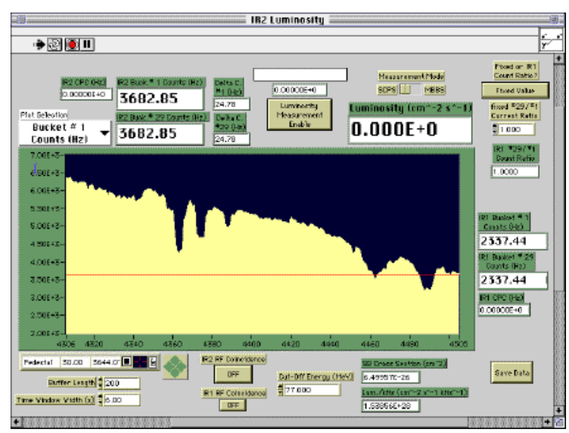

Figure 8: Luminosity Monitor Read-out Window

REFERENCES

[1] "DAΦNE operating Experience", S. Guiducci, DAΦNE Commissioning Team, PAC 99, New York, March-April 1999.

[2] "KLOE a general purpose detector for DAΦNE", The KLOE Collaboration, LNF-92/019(IR), April 1992.

[3] "Beam Position Monitor System of DAΦNE ", A.Stella et al., BIW 98, Stanford, May 1998.

[4] "Integration of Diagnostics in the DAΦNE Control System", G. Di Pirro et al., DIPAC97, Frascati, October 1997.

[5] "Synchrotron radiation monitor for DAΦNE", A. Ghigo, F. Sannibale, M. Serio, BIW 94, Vancouver, October 1994.

[6] "Multibunch longitudinal dynamics and diagnostics via a digital feedback system at PEP-II, DAΦNE, ALS and SPEAR", J.D. Fox et al., EPAC 98, Stockholm, June 1998.

[7] "The DAΦNE luminosity monitor", G. Di Pirro et al., BIW 98, Stanford, May 1998.

REAL TIME DISPLAY OF THE VERTICAL BEAM SIZES IN LEP USING THE BEXE X-RAY DETECTOR AND FAST VME BASED COMPUTERS

Jones, R.; Manarin, A.; Pignard, G.; Rossa, E.; Schmickler, H.; Sillanoli, M.; Surback, C.
SL Division- European Laboratory for Particle Physics (CERN) - Geneva - Switzerland

Abstract

Fast X-ray detectors based on CdTe photoconductors have been installed in LEP since the beginning of its operation in 1989. The angular divergence of the high energy photons from the synchrotron radiation (x-rays) and the narrow spacing of the 64 photoconductors of the detector allow a good measurement of vertical beam profiles down to an rms beam size of 300 µm.

This paper presents some specific parameters and experimental results of an upgrade program in which the local processing power of the front-end electronics has been increased by a factor 50. Such a powerful tool has allowed a real time display of the time evolution of the vertical beam sizes. An online correlation plot between the electron and positron beam sizes (turn by turn) is also displayed.

These online video images are available in the LEP control room and are used in daily operation for luminosity optimisation.

1. PRINCIPLE OF THE DETECTOR

The vertical beam sizes in LEP are measured, in single shot, by a photoconductive device known as the BEXE detector. A detailed description of this detector can be found in references [1] to [6]. Figure 1 gives an overview of the whole system. The synchrotron X-rays emitted by the bunches give an image of the vertical beam profile via the 64 channels of the detector [3]. All these signals are digitised by 8 bits Flash ADCs. The digitised raw data are used in two ways. One set is sent to the old master crate working with a 68k-CPU. This produces a PAL video image, which was used by the main control-room for daily operation during the commissioning of the slave crate. A copy of the data is also sent to the new slave crate, which uses a Power-PC running under LYNX-OS for the data analysis. This increases the processing power by a factor 50. The raw-data are analysed very quickly and sent through a dedicated video channel to the main-control room, thus providing a real time display of the results.

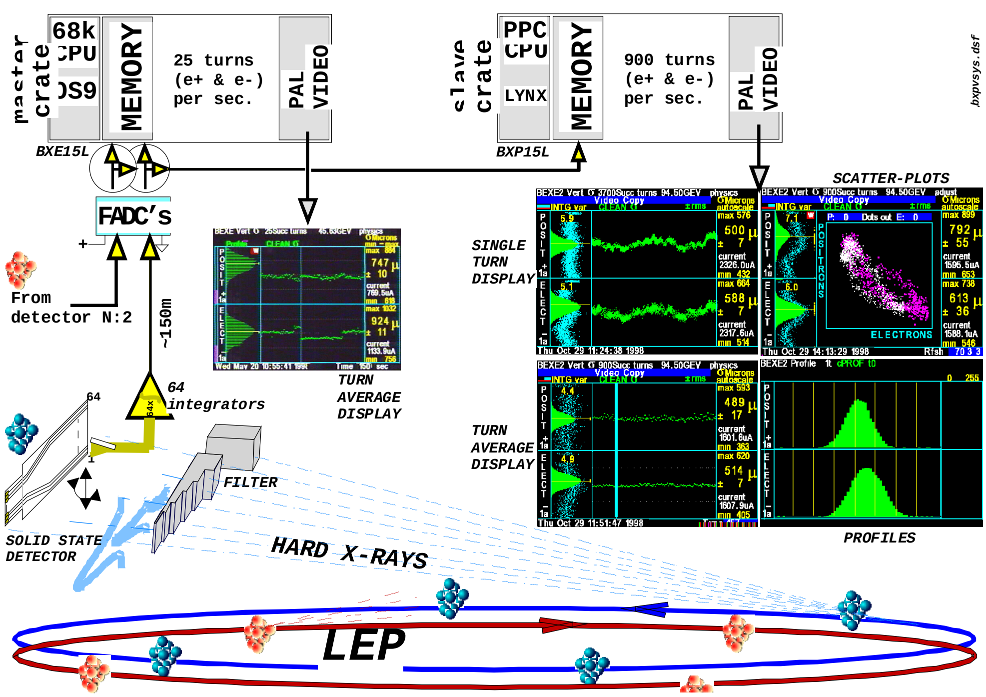

Figure 1: Synoptic of the whole.

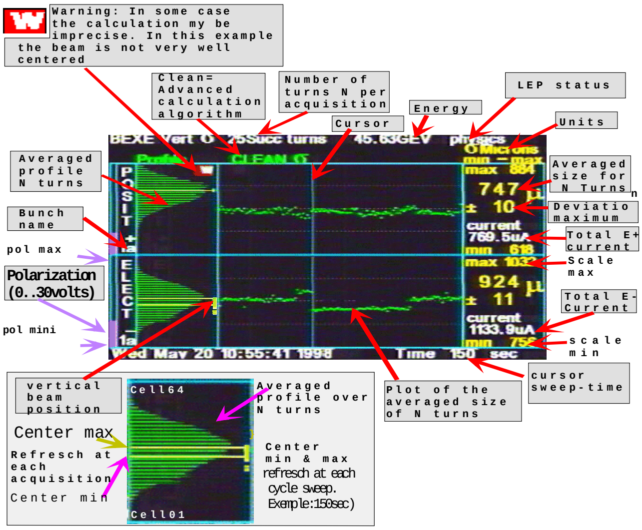

Figure 2: Explanation of the video signal displayed in the main-control room.

2. REAL TIME DISPLAYS

Several different real time displays are possible. The operator makes the selection from the main control room via an easy to used graphical interface, which is described in more detail later on.

2.1. History of the bunch size

The size of electrons and positions bunches are displayed on the same screen simultaneously. Figure 2 is a copy of the video image available for the operator. The image is updated in real time with the cursor moving from the left to right, to create a history of the beam size.

2.2. The BEXE Graphical Interface

The BEXE detector is controlled via a graphical user interface running under the UNIX operating system.

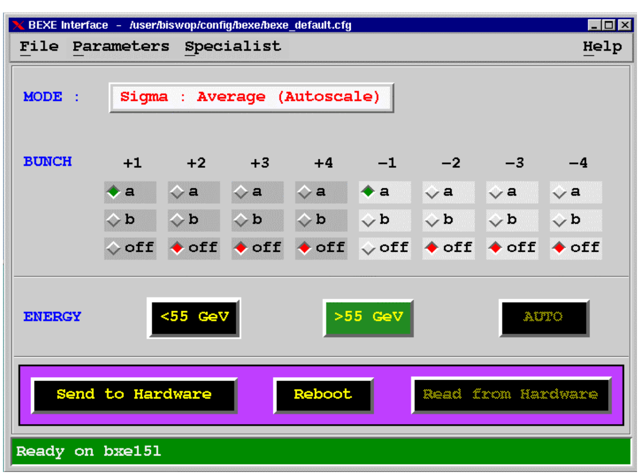

Figure 3: The main BEXE graphical interface.

The main display, shown in Figure 3, provides the operator with a simple way of changing the BEXE settings for different machine conditions. The display mode determines the type of analysis that is displayed in real-time on the operation console. Available display modes include:

Bunch History - shown in figure 2. This mode is used during physics runs to optimise the luminosity by minimising the vertical beam size of both the electron and positron beams. The main interface also allows the operator to select the bunch or bunches for which the analysis is to be carried out and hardware settings.

Scatter Plot - This plots the electron beam size history against the positron beam size history, and has been used to study the effect of beam-beam interactions. Such a plot is shown in Figure 1, where the interaction is seen as a correlation between electron and positron bunch sizes, which results in the elliptical scatter plots.

Bunch Profiles - Here the actual beam profile measured by the BEXE detector is displayed. This mode is used for the calibration described in section 3.

3. CALIBRATION OF THE DETECTOR

In order to obtain an accurate representation of the vertical beam profile, a calibration of each pixel is required. The two procedures developed for the calibration of the 64 channels and their associated chain of front-end electronics are described in the following sections.

3.1. Gain calibration using a Gain Scan

This calibration procedure involves scanning the detector vertically across the beam and recording the beam profile at several positions. Typically 64 acquisitions are made by moving the detector in steps of 100 µm, which corresponds to the distance between each channel. An off-line calibration extracts the relative gain for the 64 channels by comparing the peak amplitude for each channel. Since such a calibration scan requires some minutes for completion, it is sensitive to the beam instability. The procedure is therefore always carried out during a stable physics run, with the intensity of the beam logged for each acquisition. After a calibration, these gains are cross-checked by applying them in the real-time analysis, and verifying that the beam is the same for all vertical positions of the detector.

3.2. Gain calibration by Gaussian Fits

Historically this method was the first tested with the beam. Only few acquisitions were made, with the beam profile centred at the top, middle and bottom of the detector. Then the program performs a gaussian fit on each profile, from which it extracts the relative gains for each channel. The disadvantage of this method is the difficulty in normalising the gains between the different profile positions and also its inability to give a good fit at the edge of the detector.

3.3. Comparison of the two methods

Figure 4 shows the relative gains for each of the 64channels of the detector calculated using both calibration methods. A good agreement is seen in the central region, while large differences exist at both ends of the detector, where the gaussian fit becomes less valid.

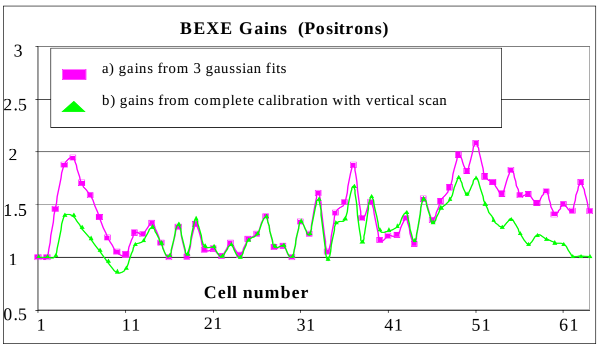

Figure 4: Comparison of the results obtained by the two methods of calibration.

The calibration of the LEP BEXE detectors will therefore be carried out two to three times a year.

4. ONLINE BEAM SIZE CALCULATION

In addition to applying the gain coefficient to each channel, the algorithm used in the calculation of the beam size also has to take into account noise sources. Stepping motor low frequency noise was found to introduce a pedestal on the data, the slope of which could change from turn to turn. The algorithm used in the original 68K CPU therefore had to strike a balance between speed and precision to allow a fast calculation of the bunch size. A straightforward fit of a gaussian curve proved to take too long for on-line calculation and therefore the analysis was performed in the following way:

1) Apply the calibration gain-coefficients to each channel.
2) Calculate the RMS value, mean value, and centre of gravity of the profile.
3) Filter the data with a filter that becomes stronger the further the cells are from the centre of the profile.
4) Calculate the pedestal (slope and offset) for each profile.
5) Calculate the final RMS value after the subtraction of the pedestal.

These calculations were tested with simulated data using random noise and a random pedestal. A precision around one per cent in the RMS compared to the sigma value was found for noise levels of the same order of magnitude as those found in LEP.

Figures 5 and 6 show the results of the turn-by-turn calculation of the rms and centre of gravity of the beam profile respectively. The vertical beam size have a standard deviation of less than 3 microns for the most stable beam measured in LEP. The same is also true for the vertical position (centre of gravity of the beam), where the fluctuations are again in the order of a few microns in single-shot measurement.

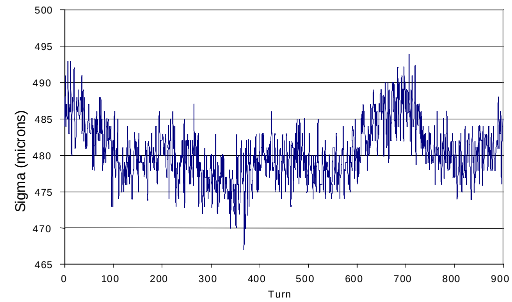

Figure 5: The turn by turn calculation of the beam size.

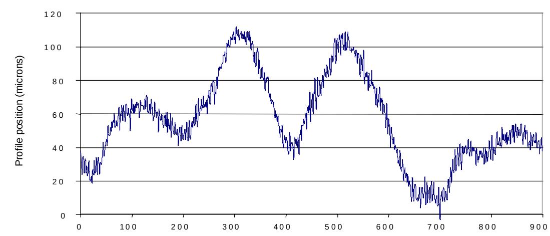

Figure 6: The turn by turn calculation of the centre of gravity of the beam profile.

5. CONCLUSION

The BEXE X-ray detectors have proved to be an invaluable tool for luminosity optimisation in LEP. The detectors are capable of withstanding extremely high radiation doses (>10^{14} Gray). The addition of power PC based analysis software has allowed the detectors to be exploited for real-time applications such as:

- Luminosity optimisation using the real-time display of the evolution of the vertical beam sizes.
- The study of beam-beam interactions using the scatter plot correlation display of electron and positron beam sizes.

REFERENCES

[1] E. Rossa et al., CERN/SL/90-23 (BI), Second European Particle Accelerator Conference (EPAC), Nice, 12-16 June, 1990.

[2] E. Rossa "*Picosecond Diagnostic*", Optical Eng., Vol 34, No.8, pp. 2353-2359, August, 1995.

[3] D. Cocq et al., N.I.M A.380 (1996) pp. 366-370; also CERN SL/ 95-82 (BI).

[4] C. Bovet and E. Rossa, in Workshop on Advanced Beam Instrumentation, KEK, Tsukuba (Japan), 1991, pp. 201-208.

[5] C. Bovet, "*Vertical emittance measurement in LEP with X-ray imaging*", CERN / SL-Note 97-14 (BI).

[6] C. Bovet, D. Cocq, A. Manarin, G. Morpurgo and E. Rossa, "*Turn by turn observation of vertical size of LEP bunches with an X-ray detector*", DIPAC'95, Travemünde, 28-31 May, 1995, pp. 102-5, also available from CERN SL/95-46 (BI).

THE OTR SCREEN BETATRON MATCHING MONITOR OF THE CERN SPS

C. Bovet, R.J. Colchester, G. Ferioli, J.J. Gras, R. Jung, J.M. Vouillot
CERN, Geneva, Switzerland

Abstract

In order to satisfy the stringent emittance requirements of LHC, betatron matching monitors, based on multiturn beam profile measurements, have been proposed for the SPS and LHC. A test monitor has been installed for evaluation in the CERN SPS first in 1996 and improved in 1997. It is based on an OTR screen and a fast beam profile acquisition system. It has been used with proton beams to assess the quality of the betatron matching from the PS to the SPS in 1998. Experience and results are presented.

1. INTRODUCTION

During the many transfers needed in the injector chain for the LHC it is vital to preserve the highest possible phase space density by avoiding emittance blow-up due to mismatch of beam optics. With bunch to bucket transfer from one circular machine to the next, the loss of phase space density results from filamentation of bunches which are not well placed and shaped in the 6-dimensional phase space.

Filamentation which is responsible for the emittance blow-up, does not occur in transfer lines where the chromaticity is too small to give significant phase shifts in a single passage. If the transfer line aperture is large enough, no blow-up or beam loss should happen and therefore matching becomes a real issue only when the beam reaches the next circular machine.

Twelve parameters are needed to adjust the centre and the shape of beam ellipses in the three phase planes. Adjusting to theoretical values is a good first approximation and is, of course, implemented at the beginning to get a circulating beam. But a final transfer optimisation can best be achieved by the fine tuning of some elements in the transfer line, as a function of observations made on the beam circulating after injection:

i) the injection trajectory in 6-dimensions (x, x', y, y', z, Dp/p) is optimised by minimisation of coherent oscillations measured with beam position monitors;

ii) in longitudinal phase plane, ellipse matching is obtained by minimising quadrupolar oscillations that can be observed with a wide-band pick-up;

iii) transverse phase plane matching is traditionally done by observing the beam size with three detectors in the transfer line, separated by known optical conditions and relying on the optical matching of the transfer line to the downstream circular machine. But values obtained from MAD for the Courant & Snyder invariants cannot be trusted, since those invariants are, in reality, sensitive to all magnet imperfections which are not known to the optics modelling program. LEP has shown beta beating of up to 40% !

The diagnostic method proposed for performing the third step mentioned above, does not rely on a precise knowledge of machine optics. The idea is to observe the beam for many turns, after its injection in the considered circular machine, with the help of a single detector.

A detailed simulation of the process is described in Ref. [1] where the cases of SPS and LHC are exemplified with realistic machine optics, beam properties and existing detector characteristics, and the effect of multiple scattering in the detector is rigorously taken into account. Thin screens observed with a CCD camera working in a fast acquisition mode, are proposed as a practical solution for the detector. It is an inexpensive and extremely powerful solution. After the number of turns necessary for data taking, the beam is dumped to protect the detector from overheating and to reduce the flux of secondaries produced in nuclear interactions. The beam energy loss due to dE/dx is less than one per mil even after 80 turns and can be taken into account in the data analysis.

2. DIAGNOSTIC PRINCIPLE

Betatron matching at injection is traditionally done using the knowledge of the beam emittance measured either in the previous machine or in the transfer line and the knowledge of the optics of the machine where the injection takes place. Regardless of the care put into the process, this methodology has a weak point with large accelerators where beta-beating can alter completely the invariants of motion obtained from a computation of the machine optics with ideal quadrupoles. The resulting emittance blow-up cannot be avoided and will, in most cases, be measured only after filamentation, with beam profile monitors like wire scanners or synchrotron radiation telescopes.

In order to detect any potential blow-up due to betatron mismatch, all one needs is to measure the beam size during a certain number of turns, after injection. This is a very sensitive means since 10% modulation of the r.m.s. beam size would result, after filamentation, in an emittance blow-up of only 1 % because this effect adds in quadrature to the r.m.s. betatron amplitude distribution. When there is no beam size modulation, the matching is perfect. Of course, with hadrons, present non-intercepting detectors have not been capable of doing this measurement turn by turn, but thin detectors like SEM grids and screens can be used with the only prerequisite of dumping the beam soon after the measurement, in order to protect the detector. One difficulty is due to multiple scattering induced on the beam at each passage through the detector but this effect can be taken into account and does not prevent a precise optimisation of betatron matching as shown in Ref. [1].

The real power of this method comes from the fact that it requires the knowledge of only one machine optics parameter, i.e. the betatron phase advance per turn, q_x or q_y (fractional part of Qx or Qy) which can be adjusted and measured with great accuracy. The perfect matching is achieved when the r.m.s. beam sizes measured on successive turns are constant (corrected for multiple scattering) which does not even require that the monitor be calibrated, nor that machine physicists agree on a definition of emittance !

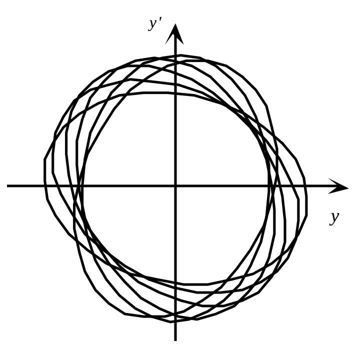

Figure 1: Phase plane ellipse seen at 6 successive turns with a fractional tune q = 0.06.

As seen in Fig. 1, the beam size will show a modulation at twice the betatron frequency: 2q or 2(1–q). Therefore with q = 0 or q = 0.5 this method will not work.

Another more subtle trap is when q = 0.25 or q = 0.75 which would also hide the size modulation for a mismatched beam injected with a phase of 45^o, see Fig. 2. For a clear observation of betatron mismatch any q value will be adequate, provided it is different from q = 0, 0.25, 0.5 or 0.75, by more than 1/2n, where n is the number of turns for which the beam size is measured.

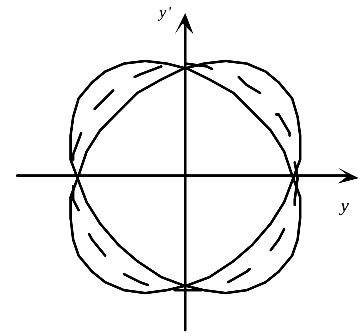

Figure 2: Phase plane ellipses traced at successive turns with a fractional tune q = ±0.25.

In principle these techniques can be applied to any machine, but of course will be more easy to use with large machines where the injection energy is high (small multiple scattering) and the revolution frequency is low (which eases the readout). In Ref. [1] the cases of SPS and LHC have been studied in detail. The effect of multiple scattering in the detector is calculated and simulations are shown of the amplitude modulation that can be expected for a mismatch of 20%. Turn by turn beam size measurements can be achieved with an accuracy of 1% with the help of only about 20 channels (lines or columns).

Therefore one can expect to detect mismatches of the order of 0.1%, using these techniques and since the phase of the mismatch can be determined, systematic corrections can be applied to optimise the matching. It should also be noted that the injection steering (in the 6-dimensional phase space) which should have been done prior to betatron matching, will also be checked during the analysis described above.

3. THE OTR SCREEN MATCHING MONITOR IN THE SPS

A 12 µm thin Titanium screen was installed in 1996 in a Luminescent Screen tank in the SPS for preliminary tests, which were encouraging. The foil was placed at 45° with respect to the beam trajectory and used as an Optical Transition Radiation (OTR) generator in the reflective mode. It was noted that the beam could be left circulating with the foil in place for at least 300 turns without damaging the Titanium foil.

For the 1997 run, a dedicated monitor was installed with optimised OTR light collection at the low injection energy, i.e. low γ. It provides the visualisation of the proton beam injected into the SPS at 26 GeV for about 100 turns, after which the beam starts to show appreciable blow-up.

It also uses the OTR from a thin 12 µm Titanium screen located in LSS4 of the SPS, through which the injected beam passes for 130 revolutions before being dumped. The set-up is represented schematically in Fig. 3.

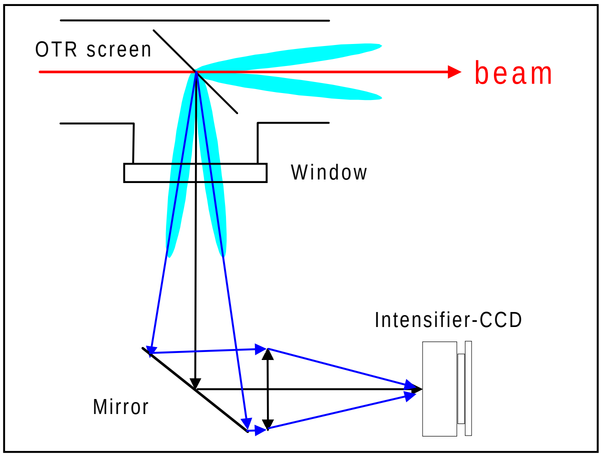

Figure 3: Matching monitor set-up in the SPS

The beam light is sampled by a pulsed intensifier and acquired on a CCD used as a fast buffer memory to acquire successive turns of the beam as described in Ref. [2]. A measurement result is given in Fig. 4. It shows a very clean signal, with only a few noise peaks on the whole CCD surface and a slope of thermal origin which can be subtracted during the processing. Due to the large emittance of the beams delivered by the PS at the time of the test, only one out of two images was acquired to have well separated projections. So only four instead of the normal nine profiles per injection have been acquired.

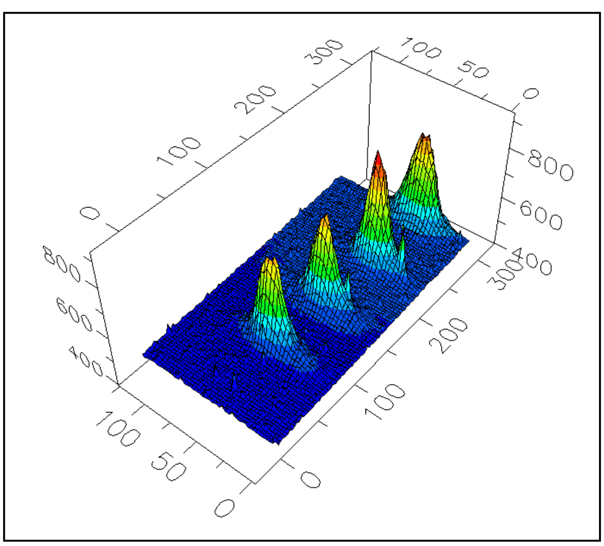

Figure 4: Result of the digitisation of four beam profiles from different SPS turns memorised on the CCD. The beam dimensions are given in pixels [500µm/px] and the amplitudes in counts of the 12 bit ADC.

At the beginning of the measurement sequence, a reference image is taken before the first injection. This reference image will be subtracted from the following measurements, suppressing the thermal slope as well as dark current noise inhomogeneities.

The Horizontal and Vertical projections are obtained from the individual beam images, from which the beam sizes are calculated with a gaussian fit using a χ^2 minimisation routine, see Fig.5.

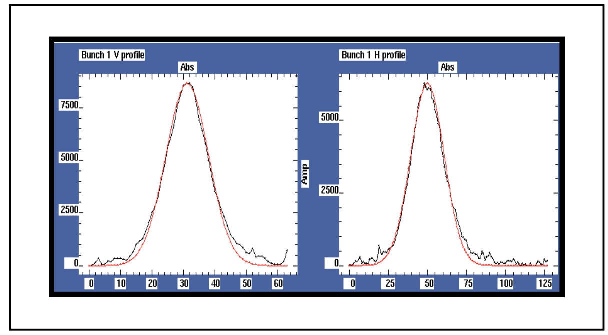

Figure 5: Horizontal and vertical projections of a selected revolution together with their gaussian fits.

The main limitation in the image acquisition rate was found to be the acceptable repetition rate of the intensifier. The rate, and hence the image acquisition, could be increased to 10 kHz only by using a high strip current MCP intensifier [3]. To have some safety margin, the acquisition rate was decreased in 1998 to one every eight SPS turns, i.e. 5.62 kHz, still much higher than the usual 25 Hz rate of normal frame grabbers.

To fill in the data of the missing turns, a timing sequencer was developed to automatically scan the missing turns by displacing the first acquired turn for subsequent injections. A typical measurement result is given in Fig. 6. A full profile history over 32 revolutions reconstructed with 8 successive injected pulses takes less than three minutes. It has to be verified that during this duration, the whole process from PS to SPS is stable. It was found during a Machine Development (MD) run in 1998 that this assumption is valid in the vertical plane, but may be questioned in the horizontal plane for various reasons, one of them being a radial displacement of the first bunch of the batch at the time of the MD [4].

The tune values measured with the Q-meter were $q_h = 0.6294$ and $q_v = 0.5825$. The 8 turn sampling was a compromise between the MCP frequency limit and the vertical tune. It is clear that it was not favourable for the horizontal plane for a given single measurement sequence since the eight turn phase advance is so close to integer ! The curves in figures 6 and 8 have been obtained with a fit of an amplitude oscillation with the known tune value. The phase, the amplitude and the slope representing the emittance blow-up have been obtained by a Monte-Carlo selection of parameters. The beam has suffered multiple scattering due to many foil traversals and the average vertical beam size increase is clearly visible and amounts to about 9% for

32 turns which is perfectly acceptable and does not affect the mismatch observation.

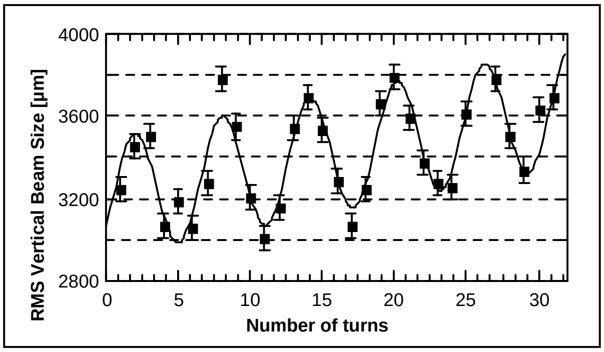

Figure 6: R.m.s. vertical beam size modulation measured over 32 turns in the SPS for a mismatched beam.

During the same MD, the vertical matching optics were changed [5] and the resulting beam size oscillations measured by the monitor, see Fig. 7.

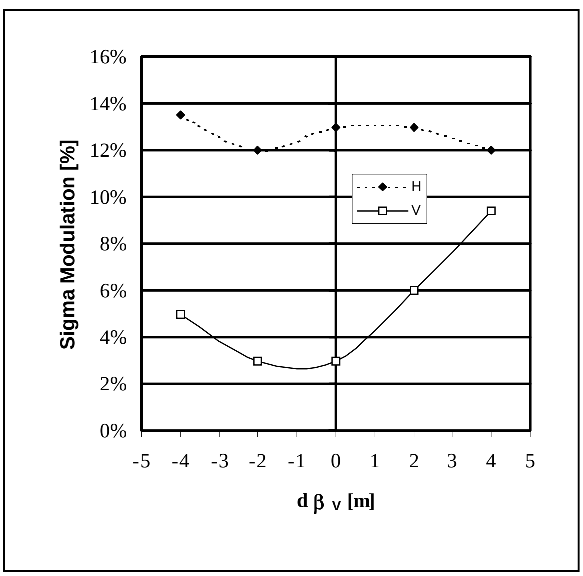

Figure 7: Evolution of the Vertical (Full line) and Horizontal (dashed line) beam size oscillations measured when changing the vertical matching optics.

In Fig. 7 it is quite clear that the vertical matching goes through a minimum, reaching a modulation of only 3 % which is a remarkably small value (see Fig. 8) leading to a filamentation blow-up of about 0.1 %. On the other hand the horizontal mismatch was virtually unaffected by changing the vertical optics.

From these results it seems possible to close a control loop for achieving in a semi-automatic way an optimum matching by searching for a minimum beam size oscillation. It is planned to test this facility during 1999 MDs.

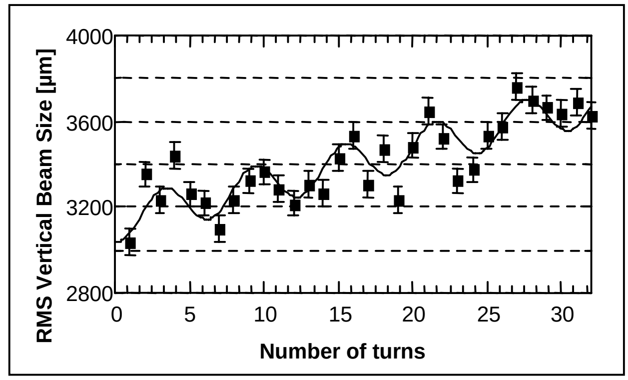

Figure 8: R.m.s. vertical beam size modulation measured over 32 turns in the SPS for a matched beam.

On the other hand it will be important to check that the matching does not change during the filling of LHC. This check can obviously not be performed by the described monitor. Non-intercepting monitors will be needed such as the Ion Profile Monitor [6] or a Luminescence Monitor [7], both working in the single turn mode described previously. They will probably not achieve the same precision, but must be able to detect turn-by-turn beam size changes at nominal intensity.

4. CONCLUSION

The SPS matching monitor is able to detect beam size oscillations over at least 30 revolutions with an OTR screen observed with a CCD read in a fast mode. Beam size oscillations of a few percent have been measured, which give confidence to limit the resulting beam blow-up through filamentation to less than 1%.

The screen has survived 300 consecutive traversals, which is far more than needed. The beam blow-up due to the present screen is acceptable. In the future it is envisaged to reduce the screen thickness to 5 µm of Titanium or to 2 µm of aluminised mylar which will reduce the beam blow-up even further.

The complete measurement is presently made with a number of injections (8) because of the limitation in acquisition rate of present MCPs. This number can probably be decreased by a factor of two. This situation will be difficult to improve, but is not felt to be a serious limitation. Since LHC has a revolution period of 89 µs, turn-by-turn measurements will be possible in LHC with the OTR detector.

It is hoped to test in 1999 a closed loop matching control to go towards an automated matching procedure.

With some software improvement, the monitor will be ready for use by non-specialists in SPS to fulfil the required check on emittance preservation. The same system will be available for use in the LHC and special efforts will be devoted to develop non-intercepting beam size monitors to check on-line the conservation of the betatron matching during the filling of LHC.

ACKNOWLEDGEMENTS

G. Burtin, J. Camas, R. Perret and M. Sillanoli took care of the mechanical set-up of the monitor. E. Carlier modified the beam dumping to protect the screen. M. Giovannozzi in PS and G. Arduini in SPS provided the test beams and K. Hanke the “tuning knob” to modify the beam matching during the quoted MD session.

It is a pleasure to acknowledge their contributions to the success of the monitor.

REFERENCES

1. C. Bovet, R. Jung: “A New Diagnostic for Betatron Phase Space Matching at Injection into a Circular Accelerator”, LHC Project Report 3, Rev., May 1996, extended version of the paper in the Proc. of EPAC’96, Sitgès, Spain, 1996.
2. R.J. Colchester et al.: “Towards the limits of frame Transfer CCDs in Beam Observation”, BIW96, Argonne, May 1996, AIP Conf. Proc.390, 1996 and CERN-SL-96-10 (BI), 1996.
3. R. Jung: “Image sensor technology for beam instrumentation”, BIW98, SLAC May 1998, AIP Conf. Proc. 451, 1998, and CERN-SL 98-061 BI, 1998.
4. G. Ferioli, J.J. Gras: “Beam Profile measurements at 40MHz in the PS to SPS transfer channels”, these Proceedings.
5. G. Arduini, K. Hanke: “Tuning knobs for the PS-SPS transfer line”, Proc. of the 1999 PAC, New-York, March 1999.
6. C. Fischer, J. Koopman: “Ionization Profile Monitor tests in SPS”, these Proceedings.
7. R.J. Colchester et al.: “Preliminary test of a Luminescence profile monitor in the CERN SPS”, these Proceedings.

PRELIMINARY TEST OF A LUMINESCENCE PROFILE MONITOR IN THE CERN SPS

J. Camas, R. J. Colchester, G. Ferioli, R. Jung, J. Koopman
CERN, Geneva, Switzerland

Abstract

In order to satisfy the tight emittance requirements of LHC, a non-intercepting beam profile monitor is needed in the SPS to follow the beam emittance evolution during the acceleration cycle from 26 to 450 GeV. Beyond 300 GeV, the synchrotron light monitor can be used. To cover the energy range from injection at 26 GeV to 300 GeV, a monitor based on the luminescence of gas injected in the vacuum chamber has been tested and has given interesting results. This monitor could also be used in LHC, where the same problem arises. Design and results are presented for the SPS monitor.

1. INTRODUCTION

For the LHC project, there is a severe constraint on the transverse emittance preservation from PS ejection to LHC. The allowable beam blow-up will be from 3μm to 3.4 μm for the normalised one sigma emittances in both transverse directions. As presented in other papers [1,2], the emittances will be measured in the transfer channel TT10 and the matching from PS to SPS checked on dedicated injections by means of an OTR screen in the SPS ring where the injected beam will be dumped after 100 revolutions. A specific beam monitor is then needed to check the emittance preservation in the SPS up to the extraction towards the LHC.

Wire Scanners are available for precision reference measurements, but they are beam perturbing and of low repetition rate, allowing a maximum rate of only two measurements per SPS cycle.

A non-intercepting beam profile monitor with a high sampling rate of at least 25 Hz is essential to identify beam blow-ups and their causes.

From 300 GeV to the extraction at 450 GeV, a Synchrotron Radiation (SR) monitor is available, but from injection at 26 GeV up to 300 GeV, no monitor is yet available. If this monitor is fast and sensitive enough, it could also be used to check on-line the matching preservation which has been established with the OTR screen monitor.

Two types of monitors are being considered for this task: the Ionisation Profile Monitor (IPM) of which a monitor from DESY has been installed in the SPS and is being tested [3] and a Luminescence monitor which will be discussed in this paper. In the Luminescence monitor, the information is transported by photons and will not be influenced by the beam space charge as is the case for the IPM. This is very interesting and makes the effort to test the usefulness of such a device as a beam profile monitor worthwhile.

2. THE LUMINESCENCE MONITOR

This type of monitor has been used at Los Alamos in the late seventies where it gave interesting results with low energy and high intensity proton beams passing in Nitrogen [4]. It seems that this type of monitor has never been used in high energy accelerators. This is probably because it was felt that the light production is too low at higher energies, above several tens of MeV [5], despite a study made for HERA [6].

The luminescence monitor makes use of the excitation of gas molecules by the particle beam to generate light. This light production is proportional to the particle density and to the gas pressure [7]. Several types of gas can be considered. Nitrogen has been studied for many years in the context of the aurorae borealis. It is a good candidate, because it emits light close to the lower limit of the visible spectrum, within the sensitivity region of normal intensifiers. The light production cross section of nitrogen is high and is well known at low energies [7]. An additional advantage of Nitrogen is that it is easily pumped by the vacuum system.

As the available data is given for energies below 1 MeV, the light production at SPS energies was estimated by using the Bethe-Bloch equation: Fig. 1.

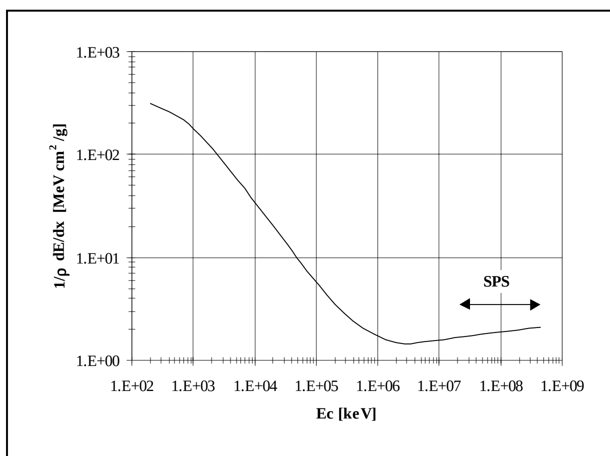

Figure 1: Energy dependence of the normalised proton energy loss to Nitrogen molecules as a function of proton energy as given by the Bethe-Bloch equation.

If the light production is only proportional to the energy loss of the charged particle, then there is a reduction factor of nearly 200 at the SPS energies with respect to the available 200 keV data. Nevertheless, it appeared that enough photons should be available from a reasonable Nitrogen pressure bump to make beam profile measurements possible with the usual intensified detectors: see Appendix.

3. BEAM TESTS WITH PROTONS

To assess rapidly the possibilities of such a monitor, preliminary tests were performed in early 1998 [8] by making use of a standard “quatro” vacuum vessel installed in the SPS for another purpose. One of the free horizontal ports was fitted with a window and a leak valve was installed to introduce the gas under study in a controlled way in this vacuum tank. In this set-up, the vertical size of the beam is observed along the visible part of the trajectory. The light emission was observed with a standard SPS intensified CCD camera, using a lens-coupled single stage MCP intensifier. The images were acquired by the usual VME 8 bit frame grabber and the data processed by the standard software, producing 2-dimensional images (Fig.2), projections (Fig.3), and 3-dimensional images, where the third dimension represents the pixel light level, which visualises clearly light inhomogeneities.

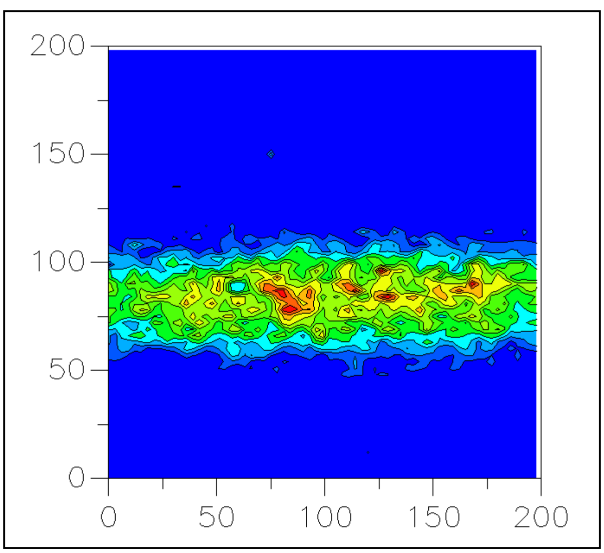

Figure 2: Side view of the beam (vertical dimension) as seen by the camera: the units are in pixels [156 µm/px]. The beam length seen in the 200 pixels window is 31 mm.

The tests were performed with Nitrogen pressures of between 10^{-5} and 10^{-6} T, which were felt to be close to the highest acceptable limit. Even so, no detrimental effect on the beam was observed by the Control Room team.

From these tests it was confirmed that the light was scarce and that the efforts had to be directed in priority towards an improvement in the light collection set-up. It was also clear that the light had to be taken over the longest trajectory length possible and used to perform the projection of the detector data along this direction thus decreasing the effect of the statistical photon fluctuations. There is no hope, nor reason, to consider single beam cross-sections.

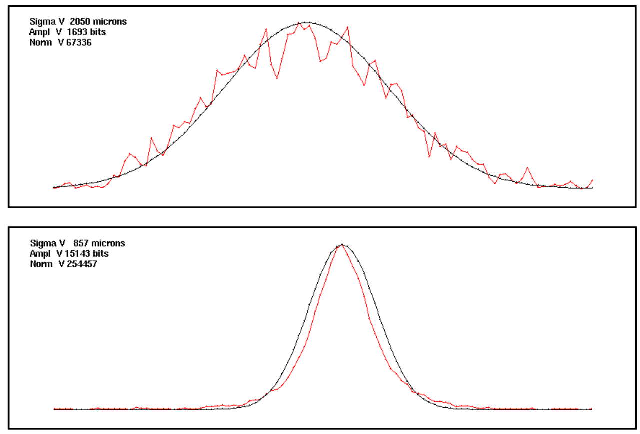

Figure 3: Vertical Beam Profiles (summed over the observation window) measured at 14 GeV (top) and 450 GeV (bottom) together with their gaussian fits.

A crosscheck of the measured beam sizes, to assess the precision of the device, was made with a Wire Scanner, which was located at 1.5 m from this monitor. Both instruments agreed within 6%, at a beam sigma of 860 µm at 450 GeV.

A complete vertical beam size history over a full SPS cycle was also taken: Fig. 4.

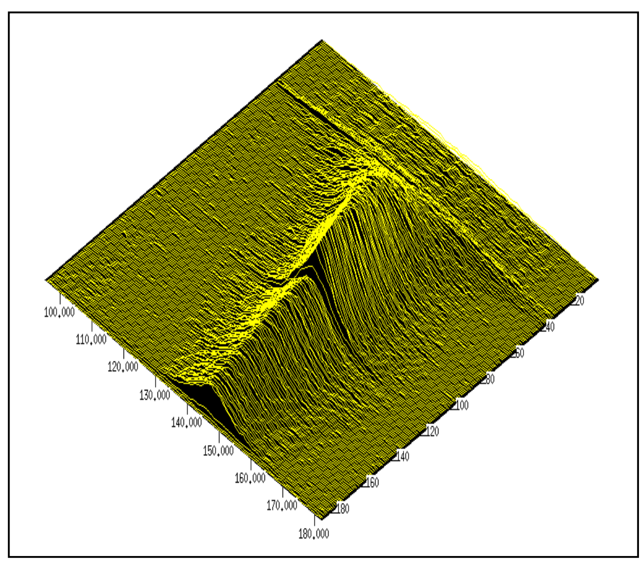

Figure 4: Mountain range view of 182 profiles of the vertical beam dimension [156 µm/px] for a full SPS cycle: from right to left: Injection at 14 GeV, Ramp to 450 GeV, and Extractions: 1st Fast, Slow and 2nd Fast extractions.

The movement of the nitrogen molecules between the time they have been excited and the time they emit the photons can be a source of beam size broadening. To evaluate this possibility, the intensified camera was replaced by a photomultiplier in single photon counting mode with a 200 ns gate length. The light pulse length of a single batch circulating in the SPS together with the length of the batch measured with a SEM foil in the transfer line is given in Fig. 5.

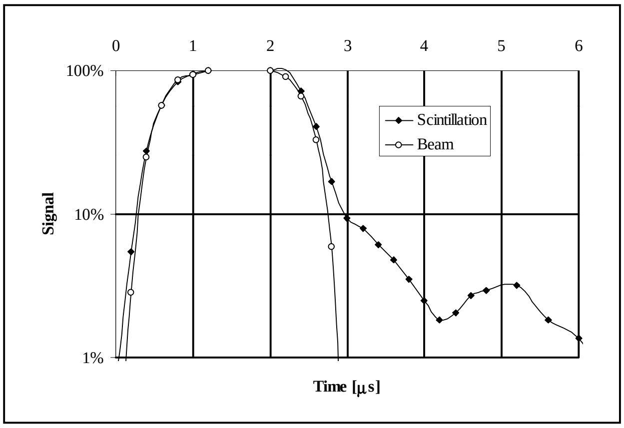

Figure 5: Comparison of beam and scintillation signal lengths. There is a long afterglow tail below the 10% level with respect to the maximum light signal.

At the 10% level, the light signal is trailing behind the beam signal by approximately 200 ns, compatible with a lifetime of N_2^{+}* around 60 ns. As the beam size is calculated with a gaussian fit above the 30% limit of the maximum signal, the time to be considered is of the order of 50 ns. It seems that in the luminescence signal there are at least two other components with longer time constants, which are most probably due to different spectral lines, from different molecules in the rest gas, having longer afterglow characteristics. This low intensity structure was also present in tests made with Argon, which indicates that it is not exclusively related to Nitrogen. If the excited molecule is ionised, which is most likely the case, the ion will move during this time under the influence of the electric field generated by the beam, which will then result in a broadening of the light envelope. The molecules close to the core of the beam will see the smallest integral field and move very little, whereas the ones at the periphery will see the largest field and move more. Hence the beam tails rather than the beam core will be enlarged. Even these peripheral molecules will move only a few tens of micrometers. This has been confirmed by comparison with the beam size measured by the wire scanner which gives a beam broadening of only 50 μm.

4. BEAM TESTS WITH LEAD IONS

Between the proton and the Lead ion run of the SPS, the set-up was modified to improve its sensitivity, i.e. decrease the pressure for a given Signal-to-Noise ratio. The major modifications were the use of a two lens optical system for increasing the light collection efficiency and the use of a two-stage MCP, fibre-optically coupled to a Peltier-cooled CCD in order to increase the light “amplification” and decrease the thermal noise generated in the CCD. The corresponding mechanical set-up is depicted in Fig. 6. The light collecting lens is a F = 500 mm achromat of 80 mm diameter placed at 350 mm from the beam centre, the objective has a 50 mm focal length and an aperture of 71 mm.

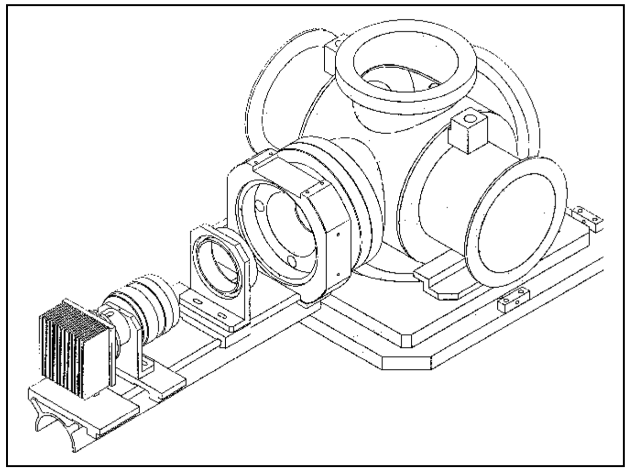

Figure 6: The test monitor set-up: Right: the “quatro” tank with the left horizontal port fitted with a glass window. Left: the optics set-up with a 500 mm achromat followed by a 50 mm lens, a double stage MCP and the Peltier-cooled CCD with radiator.

As there is ample resolution, the magnification was decreased to 177μm/px, which increases the number of photons collected per pixel by 30%.

Tests were performed with Lead ions at pressures of $5\ 10^{-6}$ to $1\ 10^{-7}$ T with beams of $8\ 10^{8}$ Pb^{82} ions. It could be verified that the light signal is proportional to the Nitrogen pressure, see Fig. 7, and increases about as predicted by the Bethe-Bloch equation, i.e. an increase by Z^2 =6724 of the sensitivity. The lack of precision is due to the change of set-up between the proton and the Lead run.

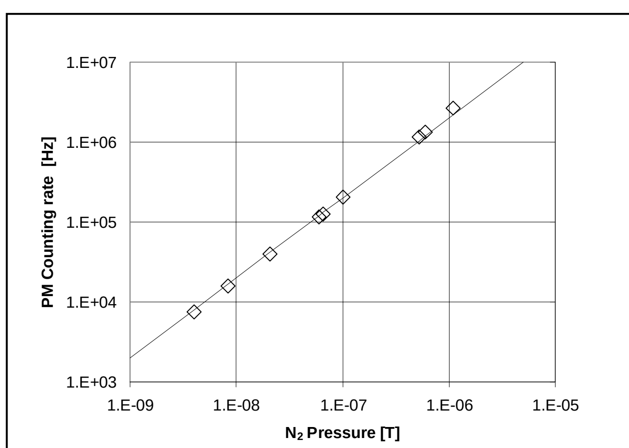

Figure 7: Light signal as a function of the N_2 pressure measured with a photomultiplier in counting mode.

A typical set of measurements is given in Fig.8, where the beam image (vertical side view) which is the same as that seen on a TV monitor, the 3-dimensional view and the projection on the vertical axis of the 200 x 200 pixels window are given.

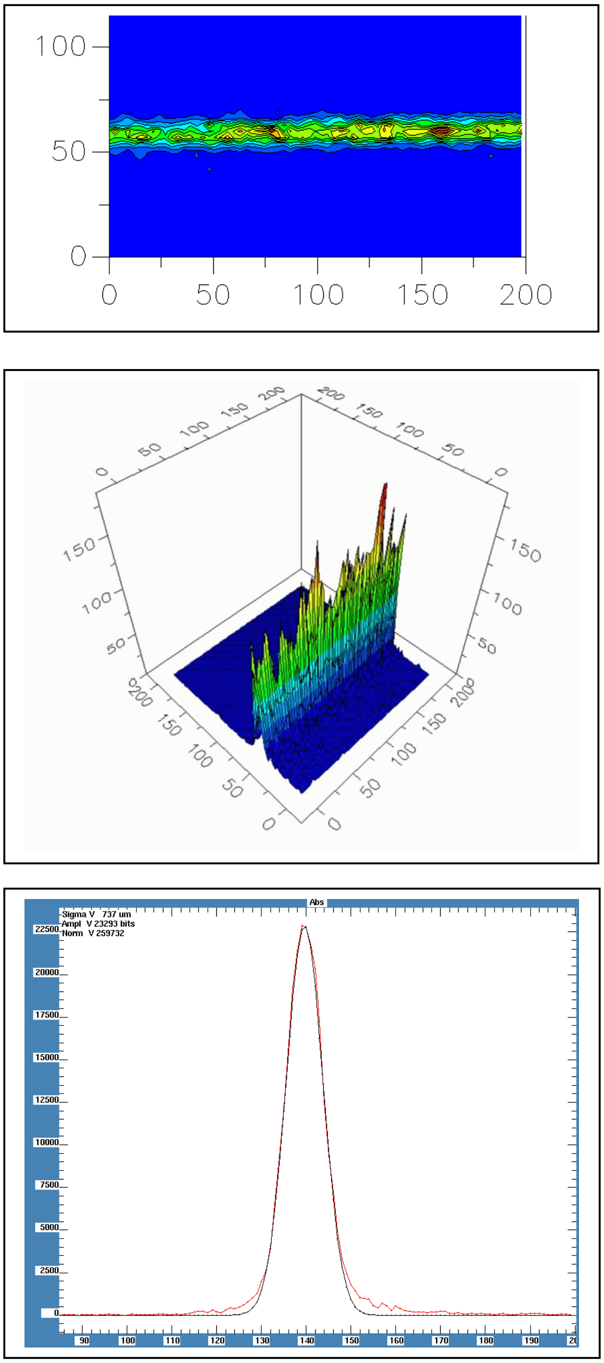

Figure 8: From top to bottom: Side view (vertical), 3-D view and Projection (vertical) with gaussian fit, of a 8 10^8 Lead ion beam at 150 GeV/nucleon with an N_2 pressure of 5 10^{-6} T. The dimensions are in pixels, with 177µm/px.

The 3-dimensional view demonstrates most clearly the statistical nature of the luminescence signal, with wild variations of the individual pixel signals; they smooth out remarkably well when summed for producing the vertical projection. In this case, the signal is integrated over 35 mm along the beam trajectory.

The beam projection is given together with the gaussian fit calculated with the data above 30% of the signal maximum. The excess beam tails are clearly visible. It seems that they are less pronounced on the Wire Scanner measurements, i.e. they may be due to an instrumental effect produced by the afterglow considered earlier. This will have to be checked more precisely.

The lowest useable signal was obtained at a pressure of 1 10^{-7} T: Fig. 9. The same signal should be obtained at a pressure of 3 x 10^{-8} T for a proton beam of 2 10^{13} particles. This would result in an average pressure increase in the SPS of 1%, which is negligible. The profile is noisy, but should still be suitable for beam size comparisons.

The monitor could not profit from the maximum MCP gain available. Only gains up to 10^3 could be used. Above this gain, the 3-D picture showed many random high level spikes which gave even more noisy profiles than the one in Fig. 9. One of the reasons could be that the detector set-up was located in the machine plane, and that stray particles were hitting the detector.

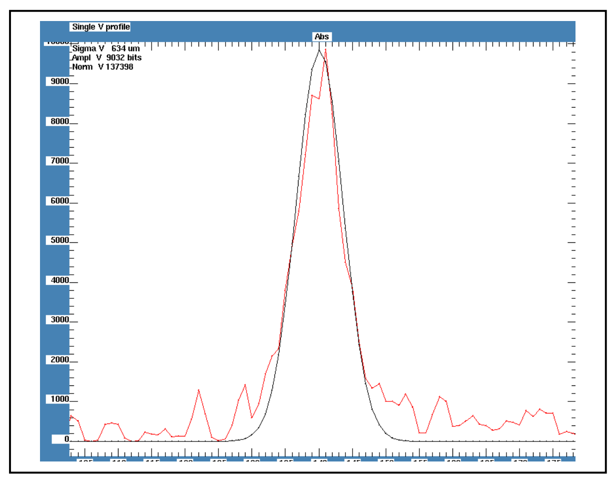

Figure 9: Beam projection obtained at 1 10^{-7} T with 8 10^8 Lead ions.

5. PLANS FOR THE FUTURE

For the 1999 run, a dedicated monitor has been installed on the SPS ring. It comprises of a dedicated "quatro" tank and has two ports equipped with quartz windows, for best transmission down to the UV and little risk of browning due to radiation.

For the start-up, only the vertical port, giving the horizontal profile this time, has been instrumented. The detector is at 750 mm below the medium plane of the SPS, protected from stray particles by its distance to the beam level and by the addition of iron shielding blocks. This should enable the MCP gain to be increased and to compensate any loss in light collection.

The magnification has been reduced to a value giving a scaling factor of 565µm/px to favour the measurements at injection energy where the beams are largest.

The CCD will be digitised over 12 bits and the whole CCD height of 288 pixels will be acquired. If necessary, the CCD can be rotated by 90° to increase the length to 384 pixels. The integration will either be done numerically or directly on the CCD by the "fast projection" mode [9]. The integration time will be adjustable from 1 revolution to 100 ms, depending on the desired time resolution and the acceptable local pressure bump. The MCP voltage will be adjustable during the SPS cycle to compensate for the change in beam size, i.e. light density, see Fig. 3 for instance.

Measurements on the beam tails and light production by the rest gas will have to be remade with better precision.

A collaboration with the Vacuum group has been initiated to improve the vacuum part of the monitor design. If the length of the pressure bump can be reduced, bearing in mind that only 15 cm beam trajectory are used for light collection, then the pressure can be increased while still staying within a 5% limit of the average SPS pressure increase.

Other issues on hand are the test of different gases and gas mixtures, which may be more efficient in light production [10], but have to be checked for decay times and compatibility with the vacuum system.

ACKNOWLEDGEMENTS

Thanks are due to J. Bosser and R. Maccaferri for allowing us to use a port of the "quatro" tank which we had installed for them in the SPS for testing their Ion Beam Scanner under development for LHC, as well as for their interest for the preliminary tests.

The collaboration and help of the LHC Vacuum Group was important and is appreciated.

REFERENCES

1. G. Ferioli et al.: "Beam Profile measurements at 40MHz in the PS to SPS transfer channels", these Proceedings.
2. C. Bovet et al.: "The OTR screen betatron matching monitor of the CERN SPS", these Proceedings.
3. C. Fischer, J. Koopman: "Ionization Profile Monitor tests in SPS", these Proceedings.
4. D.D. Chamberlin et al.: "Noninterceptive transverse beam diagnostics", IEEE Trans. on Nucl. Sc., Vol. NS-28, no. 3, June 1981.
5. J.S. Fraser: "Development in non-destructive beam diagnostics", IEEE Trans. on Nucl. Sc., Vol. NS-28, no. 3, June 1981.
6. F. Hornstra: "A beam induced gas scintillation (BIGS) profile monitor for HERA", DESY HERA 89-04, January 1989.
7. R.H. Hugues, J.L. Philpot: "Spectra induced by 200 keV proton impact on Nitrogen", Phys. Rev., Vol. 123, Nb 6, September 15, 1961, p. 2084-2086.
8. J. Camas et al.: "First test in the SPS of a gas scintillation beam profile monitor", SL-Note-98-037 MD SPS, June 1998.
9. R.J. Colchester et al.: "Towards the limits of frame Transfer CCDs in Beam Observation", BIW96, Argonne, May 1996, AIP Conf. Proc.390, 1996 and CERN-SL-96-10 (BI), 1996.
10. F. Sauli: private communication.

APPENDIX

Given below is an evaluation of the CCD signal at injection in the SPS for the major spectral line of N_2 [7]. This calculation has to be made for each spectral line and the results have to be summed for estimating the total signal level at the detector.

	Spectral Line	
Major line: λ	391.4	nm
Cross section [7]	$3.3\ 10^{-7}$	cm^2 at 200 keV
N_2 pressure	$5\ 10^{-7}$	T
	SPS beam	
Np	$2\ 10^{13}$	Protons
Frev	$44\ 10^{3}$	Hz
Energy	26	GeV
σv	3000	µm
	Optics & Detector	
Magnification	0.04	
Transmission	41	%
MCP gain	4000	
Acceptance	0.33	%
CCD pixel	23	µm H & V
CCD saturation	0.18	$\mu J/cm^2$
	Signal	
Bethe-Bloch	1/185	attenuation
photons	$4\ 10^{10}$	s^{-1}
CCD signal	40	% of Vsat

Posters Sunday

CHROMATICITY MEASUREMENTS AT HERA-P USING THE HEAD-TAIL TECHNIQUE WITH CHIRP EXCITATION

A. Boudsko, TRIUMF, Vancouver, Canada
O. R. Jones, H. Schmickler, CERN, Geneva, Switzerland
M. Wendt, F. Willeke, DESY, Hamburg, Germany

Abstract

Experiments have been performed in the HERA proton ring (HERA-p) to test a quasi non-destructive method of chromaticity measurements for protons. The method is based on the detection of the head-tail phase shift of coherend betatron oscillations using a broadband beam position pickup and a commercial "fast-frame" oscilloscope. Previous experiments have relied on a single kick for transverse excitation, whereas the results presented here were carried out using swept frequency "chirp" excitation. The tests proved to be successful, and the method seems to be a good candidate for chromaticity measurement in new large hadron accelerators, such as LHC.

1 INTRODUCTION

In any superconducting accelerator the control of *chromaticity* during machine transitions like energy ramping or beta squeezing is of paramount importance. The classical method of chromaticity determination, i.e. measurements of the betatron tunes for different settings of the beam momentum, is in this case only of limited use. In this paper we describe the results of applying the so-called *head-tail* chromaticity measurement [1] to the beams in HERA-p. This method relies on the fact that for non-zero chromaticity a dephasing/rephasing of the betatron oscillations occurs between the head and the tail of a bunch during synchrotron oscillations. After transverse excitation, the measurement of the turn-by-turn position of two longitudinal positions in a bunch allows the relative phases to be extracted and the chromaticity to be calculated.

In contrast to the results reported in previous publications [1, 2] which used a single kick for beam excitation, the data in this report is obtained by *resonant chirp beam excitation*. Altough the primary motivation for using this technique in HERA-p is the lack of a sufficiently strong deflection kicker in the vertical plane, the results are of general interest.

2 THE HEAD-TAIL PRINCIPLE

Assuming longitudinal stability, a single particle will rotate in longitudinal phase-space at a frequency equal to the synchrotron frequency. During this longitudinal motion the particle also undergoes transverse motion, which can be described by the change in the betatron phase, $\Theta(t)$, along the synchrotron orbit. If the whole bunch is kicked transversely, then the resulting transverse oscillations for a given longitudinal position within the bunch can be shown [1] to be given by

$$y(n) = A\cos\left[2\pi n Q_0 + \omega_\xi\,\hat{\tau}\left(\cos\left(2\pi n Q_s\right) - 1\right)\right] \quad (1)$$

where n is the number of turns since the kick, Q_0 is the betatron tune, Q_s is the synchrotron tune, $\hat{\tau}$ is the longitudinal position with respect to the centre of the bunch, and ω_ξ is the chromatic frequency and is given by

$$\omega_\xi = Q'\,\omega_0 \frac{1}{\eta} \quad (2)$$

Here Q' is the chromaticity, ω_0 is the revolution frequency and $\eta = 1/\gamma^2 - 1/\gamma_{tr}^2$. If we now consider the evolution of two longitudinal positions within a single bunch separated in time by $\Delta\tau$, then from (1) it follows that the phase difference in the transverse oscillation of these two positions is given by

$$\Delta\Psi(n) = -\omega_\xi\,\Delta\tau\left(\cos\left(2\pi n Q_s\right) - 1\right) \quad (3)$$

This phase difference is a maximum when $nQ_s \approx 1/2$, i.e. after half a synchrotron period, giving

$$\Delta\Psi_{\text{max}} = -2\,\omega_\xi\,\Delta\tau \quad (4)$$

The chromaticity can therefore be written as

$$\begin{aligned} Q' &= \frac{-\eta\,\Delta\Psi(n)}{\omega_0\,\Delta\tau\left(\cos\left(2\pi n Q_s\right) - 1\right)} \\ Q' &= \frac{\eta\,\Delta\Psi_{\text{max}}}{2\,\omega_0\,\Delta\tau} \end{aligned} \quad (5)$$

3 EXPERIMENTAL PROCEDURE

3.1 Hardware Setup

Fig. 1 shows the hardware setup. The transverse displacement signal of the proton beam was detected with the two horizontal 40 cm long stripline-like electrodes of a broadband beam position pickup ($\beta \approx 33$ m) [1]. Their signals were adjusted in time with a variable delay-line and combined in a Δ/Σ-hybrid (*M/A COM*, model H-9). Additional fixed and variable attenuators were used to minimize the common mode signal due to the static beam displacement, i.e. the transverse beam orbit. Both output signals of the hybrid, Δ (displacement) and Σ (intensity), were acquired using a *Tektronix* 784C digital oscilloscope (1 GHz analogue

[1] slotted coaxial electrodes, usable bandwidth $\approx$ 4 GHz

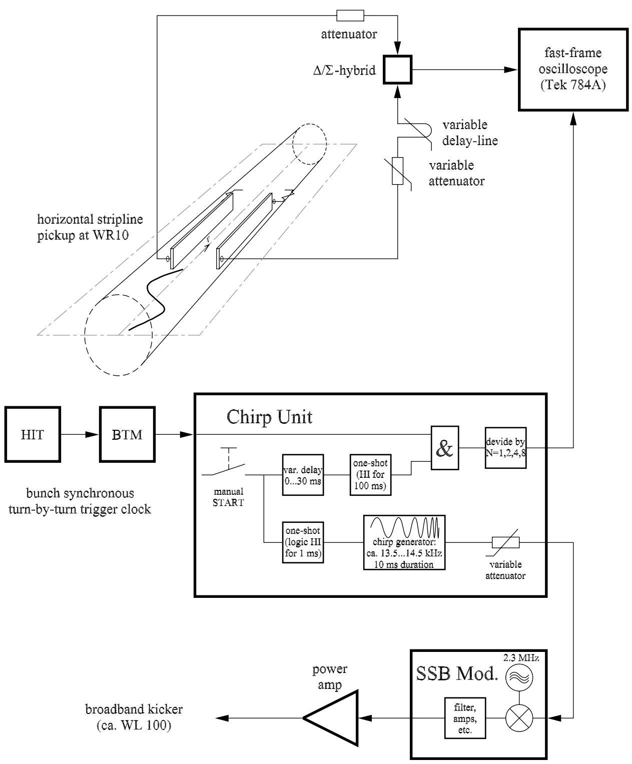

Figure 1: Hardware setup for the chromaticity measurements with chirp excitation.

bandwidth, 4 GS/s single channel sampling rate). The Σ signal was used in the off-line analysis to reduce the effect of jitter in the trigger signals. The necessity of this second signal channel limited the sampling rate to 2 GS/s. The oscilloscope was set to "fast-frame" mode, which allowed the capture of signals for up to 372 consecutive turns [2]. Each "frame" covered 25ns, with 50 sample points spaced by 500 ps, giving the displacement vs. time of a single bunch.

The chirp excitation was started manually. This opened a 100 ms gate that passed bunch-synchronous turn-by-turn triggers to the oscilloscope. This signal was provided by the *HERA Intergrated Timing* (HIT) system. The chirp duration and its lower and upper frequencies were programmed by varying R-C combinations. The output signal was added to the SSB modulator of the resonant excitation kicker of the betatron tune measurement system.

The oscilloscope was PC-controlled via GPIB. A HP-VEE program dumped the data of all 372 frames automatically into an Excel spreadsheet and stored it with a time-stamp. The PC was also used for a brief off-line analysis of the data.

3.2 Measurements

The experiments were carried out during 5 shifts on the weekend 12/13 December, 1998 [3].

After establishing a sufficient chirp excitation *amplitude*, *frequency range* (13.5. . .14.5 kHz ≡ 0.285. . .0.31 tune) and *duration* (10 ms ≡ 500 turns) the method was tested by staying at the 40 GeV proton injection energy of HERA-p. Starting with 10 freshly injected bunches (≈ 5 mA beam current) 3 chirp measurements per sextupole setting were carried out and compared with the classical rf-variation/tune-detection method. The sextupoles were varied to give 7 different chromaticity settings in the range of -10. . .+10 units. No beam breakup or losses were observed at this energy, but a reduced proton lifetime was noticed during the chirp excitation.

Further measurements, again using 10 bunches, were carried out at the start of each ramp file (at 70, 150 and 300 GeV), as well as during the ramp. A chirp measurement above 300 GeV proved to be difficult to achieved, due to the weak excitation level at this energy, and the tendency of the beam to get unstable for negative chromaticities.

[2]or the 2nd, 4th or 8th multiple by trigger division

4 DATA ANALYSIS

Since the sampling clock of the digital oscilloscope used in these experiments could not be synchronised to the turn-by-turn bunch trigger, it was necessary to sample both, the Σ and Δ signals from the hybrid coupler. The Σ signal was then used to re-align each frame and hence correct for this jitter. This frame-by-frame correction factor was then applied to the Δ signal before starting the analysis. The head and tail analysis times were chosen so as to be symmetrical about the bunch centre. The transverse positions at these times in the bunch were estimated by linear interpolation of the two nearest sampling points. Having obtained a set of head and tail data, phase demodulation using Hilbert transformation was carried out to obtain the turn-by-turn head and tail phase relative to a reference frequency. This reference frequency was chosen to be the average betatron frequency calculated from the Fourier power spectrum of both the head and tail data. The choice of reference frequency is however not critical, since we are ultimately only interested in the phase difference between the head and tail oscillations. The chromaticity was calculated by applying Equation (5) directly to the phase difference between the head and tail.

5 RESULTS

Figure 2 shows the typical response of the head and tail of a bunch to chirp excitation. This is characterised by a growing oscillation amplitude followed by an amplitude "beating" for which the depth of the trough is a function of the width of the betatron tune peak and the rate at which the chirp is swept across the betatron resonance. The quoted head and tail timing is always relative to the centre of the bunch. The dependence of the phase evolution on different longitudinal positions in the head and tail of the bunch is shown in Figure 3. Here the swept "chirp" frequency crosses the betatron frequency at around turn 50, from which time the head and tail phases start to diverge from each other. What is also visible is that the response

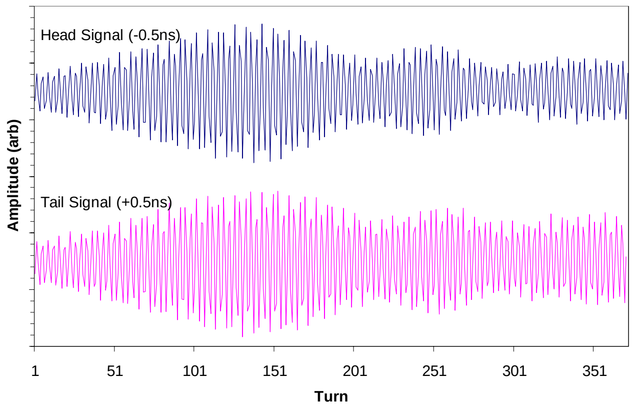

Figure 2: Transverse signals from the head and tail of a bunch after chirp excitation (70 GeV, horizontal chromaticity = +4).

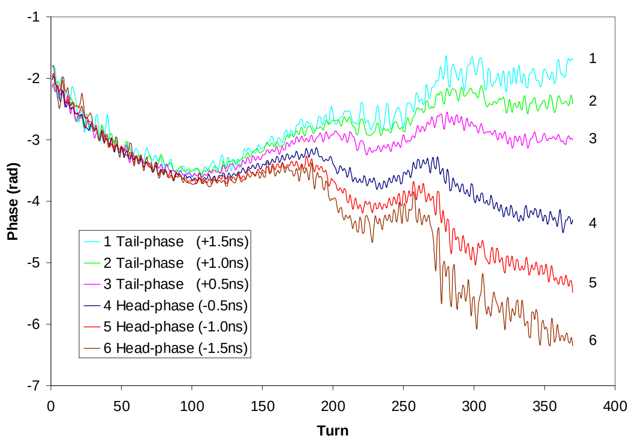

Figure 3: Phase evolution of several longitudinal positions within the same bunch relative to the centre of the bunch (70 GeV, horizontal chromaticity = +4).

of the bunch to the chirp itself produces a perturbation in the phase evolution. This proved to be a problem for certain chromaticities, where the troughs seen in Figure 2 went down to virtually zero, leading to large phase pertubations.

Figure 4 is the result of applying Equation (5) to the phase differences of the head and tail phases shown in Figure 3. By averaging the perturbations caused by the chirp, the resulting chromaticity is seen to lie between +3 and +5 units, which compares quite well with the +3 units measured using the classical method in the control room.

Figure 5 shows the result of two measurements performed at 300 GeV for positive and negative chromaticity. Again we see that the calculated chromaticities agree very well with the values measured classically.

6 CONCLUSIONS

The results presented demonstrate the possibility of mesuring chromaticity using chirp excitation in less than 1000 turns, at energies up to 300 GeV. The main advantage of this technique over the current chromaticity measurement in HERA-p is that it can be performed during the energy

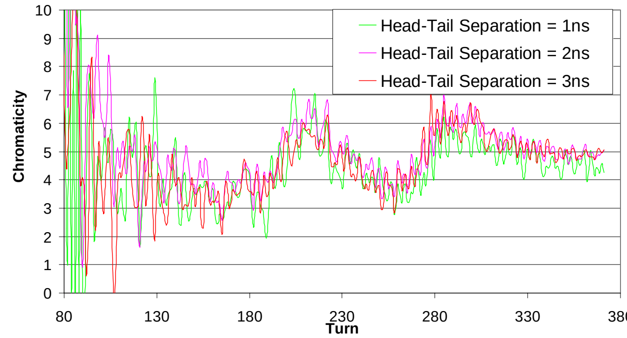

Figure 4: Turn-by-turn chromaticity for three different head-tail separations (70 GeV, hor. chromaticity = +4).

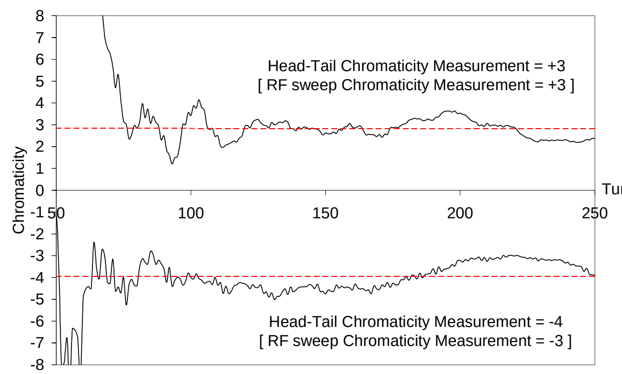

Figure 5: Turn-by-turn chromaticity for positive and negative chromaticity at 300 GeV ($\pm$1 ns head-tail separation).

ramp. Since only 15 % of the total available kick strength was used in obtaining these results, measurements at higher energies could be made possible simply by increasing the strength of the chirp signal. A beam break-up tendency during chirp excitation was observed at higher energies ($>$300 GeV), but only for negative chromaticity.

Errors in the measured chromaticity were mainly due to the phase perturbations introduced by the chirp itself, and the fact that the chirp was not synchronized to the data acquisition. The latter meant that the turn at which the chirp crossed the betatron frequency had to be estimated by eye from the phase evolution plots, which could lead to errors of up to $\pm$2 units in the calculation of chromaticity. Synchronising the chirp to the acquisition would allow the resonant tune to be calculated from the measured betatron tune and a knowledge of the chirp parameters.

7 REFERENCES

[1] D. Cocq, O. R. Jones, H. Schmickler, "The Measurement of Chromaticity via a Head-Tail Phase Shift", 8th Beam Instrumentation Workshop BIW '98, Stanford, CA, USA; 4 - 7 May 1998.

[2] O. R. Jones, H. Schmickler, M. Wendt, F. Willeke, "HEAD-TAIL Chromaticity Measurements at HERA-P (9/7/1998)", CERN Internal Note, SL Division, 29/7/98.

[3] logbook HERA-"E"u."P"-XXXIV, pp. 129-132.

INFLUENCE OF TRANSVERSE BEAM DIMENSIONS ON BEAM POSITION MONITOR SIGNALS

A. Jankowiak, T. Weis, DELTA, Institute for Accelerator Physics and Synchrotron Radiation, University of Dortmund, Germany

Abstract

In this paper we will evaluate the influence of transverse beam dimensions on the signal functions of a beam position monitor (BPM) with capacitive pick-up electrodes. The error which occurs in the determination of the beam position when disregarding these effects is calculated as an example for the DELTA[1] BPM.

The possibility to use this effect for the measurement of the beam size / emittance is discussed.

1 CALCULATION OF THE SIGNAL FUNCTIONS

Fig.1 shows a typical BPM with 4 capacitive pick-up electrodes. When the beam passes through the BPM, the electric field, accompanying the beam, induces a charge pulse on the pick-up electrode, which depends on the beam charge and the position of the beam in the cross section of the BPM. To determine the beam position it is necessary to know the signal function S_i for each pick-up i. These $S_i(x,y)$ represents the response of the pick-ups for a normalised point charge (q=1) at the position (x,y).

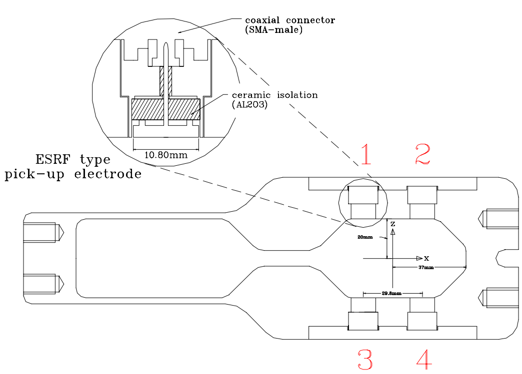

Fig.1 Sketch of the DELTA BPM.

In the case of relativistic beams ($\gamma >> 1$) the electric and magnetic fields are nearly transversal and therefore the determination of the signal functions can be treated as a 2-d problem.

[1] **D**ortmund **EL**ectron **T**est **A**ccelerator (1.5 GeV Synchrotron Radiation Source)

1.1 Signal Function of a Point Charge

The obvious solution to calculate the S_i is to solve for the electric field E of a point charge (pencil beam) at position (x,y) and to integrate E over the surface of pick-up i to get the induced charge which is proportional to the signal function. Because these calculations must be repeated for each position (x,y) a more clever way is to make use of the reciprocity theorem [1].

The potential $\phi_{\text{pick-up}}$ is allocated to pick-up i and the Laplace equation $\Delta\phi_i\,(x,y)=0$ with the vacuum chamber on zero potential is solved. The solution ϕ_i is proportional to the signal function. These calculation can easily done by using programs like MAFIA or Poisson (see. Fig. 3).

1.2 Signal Function of a Gaussian Charge Distribution

In most cases a good representation for the transverse charge distribution $\rho(x',y')$ of a particle beam at position (x,y) is a 2-d Gaussian distribution.

$$\rho(x',y') = \frac{1}{2\pi \cdot \sigma_x \cdot \sigma_y} \cdot \exp\left[-\frac{1}{2}\left(\left(\frac{x-x'}{\sigma_x}\right)^2 + \left(\frac{y-y'}{\sigma_y}\right)^2 \right) \right]$$

The signal function $\tilde{S}_i(x,y)$ of a beam with beam size σ_x and σ_y can be described in the following way:

$$\tilde{S}(x,y) = \iint \rho(x',y') \cdot S(x',y')\,dxdy \quad (1)$$

To study the effect on the determination of the beam position usually the calculation will be done numerically. To get a better understanding of the influence of the beam size we will give a analytical solution.

In the following we expand, at a fixed position, the signal function S_i in a Taylor series and use a Cartesian co-ordinate system with the origin at the centre of the beam. This gives (after evaluating the double integral and using identities concerning integration of Gaussian distributions [2]) for a fixed beam centre

$$\tilde{S} = \sum_{i=0}^{\infty} \sum_{j=0}^{\infty} a_{2i,2j} \cdot m_{2i,2j} \cdot \sigma_x^{2i} \cdot \sigma_y^{2j} \quad (2)$$

where the $a_{2i,2j}$ are coefficients of the taylor series and the $m_{2i,2j}$ can be written as

$$m_{2i,2j} = \prod_{m=0}^{i} |2m-1| \cdot \prod_{n=0}^{j} |2n-1| \quad (3)$$

Because the signal function S is a solution of the Laplace equation

$$\frac{\partial^2}{\partial x^2} S(x,y) + \frac{\partial^2}{\partial y^2} S(x,y) = 0 \ ,$$

we find the following relation for the coefficient $a_{i,j}$

$$a_{i,j} = -a_{i-2,j+2} \cdot \frac{(j+1)(j+2)}{(i-1)i} \quad (4)$$

Using equations (3) and (4) and rearranging equation (2) leads to the following exact representation of the signal function of a beam with Gaussian charge distribution:

$$\tilde{S}(\sigma_x, \sigma_y) = \sum_{i=0}^{\infty} c_i \cdot (\sigma_x^2 - \sigma_y^2)^i \quad (5)$$
$$c_i = a_{2i,0} \cdot m_{2i,0}$$

This result shows that the variation of the signal function with the beam size depends only on the difference between the squares of the transverse sigmas. A round beam especially leaves the signal function unchanged. A polynomial fit with MAFIA calculated values for the signal functions for different beam sizes to σ_x^2-σ_y^2 shows, that the summands with i>1 in eq. (5) are nearly vanishing (see. Fig. 4). It should also be mentioned that the constant summand $a_{0,0}$ in (5) is the value of the signal function for a pencil beam.

2 POSITION ERRORS DUE TO TRANSVERSE GAUSSIAN CHARGE DISTRIBUTION OF THE PARTICLE BEAM

In most accelerator control systems the signal functions (calculated numerically or measured on a test bench) of a pencil beam are used to calculate the beam position from the measured signals of the BPMs. In Fig.2 we have calculated the position error due to disregarding the transverse beam size in the case of DELTA, a 3rd generation light source, as a worst case estimation for the BPM with the biggest beam size.

To simplify the representation we have calculated the distance between the given centre of the beam and the calculated beam position.

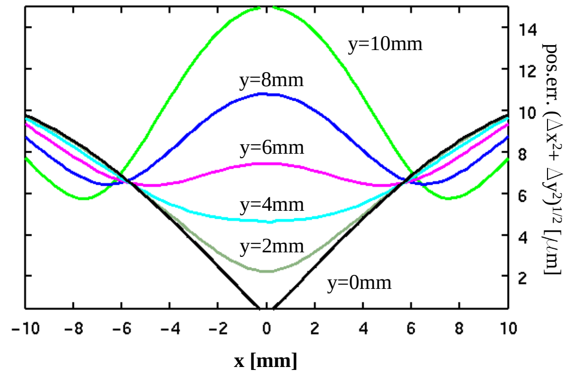

Fig.2 Absolute position error for a beam with σ_x=500µm and σ_y=50µm.

A 3rd generation light source has an emittance in the order of some nmrad and operates often with a emittance coupling in the order of some %. Therefore the horizontal beam size is in the order of 100 µm and the vertical of 10 µm. In the case of DELTA at 1.5GeV we have maximum values of 500 µm horizontal and 50-100 µm vertical. The resulting error is for most cases smaller than 10 µm. Therefore no influence on routine operation is expected.

On the other hand we should keep in mind that modern closed-orbit measuring and orbit-feedback systems have a resolution in the order of some µm. All coherent movements of the beam, maybe induced by instabilities, power supply ripple or the tune measuring system, with time constants smaller than the integration time of the measuring system, can also be seen as a beam with changing size, resulting in an virtual orbit drift. At facilities with much greater beam sizes, a significant influence can be expected because eq. 5 shows a quadratic dependency of the σ.

3 ELECTROSTATIC EMITTANCE MONITOR

In chapter 1 we have shown, that the signal functions of a beam with transverse Gaussian charge distribution depends on σ_x^2-σ_y^2. Therefore it should be possible to extract information on the beam sizes by measuring normalized pick-up signals for know positions of the particle beam in comparison with the signals for pencil beams. These reference signals must be calculated or measured in the laboratory.

Fig.3. shows a sketch of a pick-up monitor which can be used to determine the beam size.

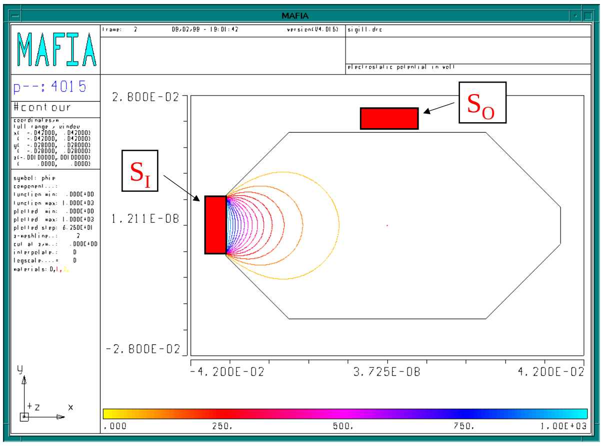

Fig.3 Simplified monitor design for an "electrostatic" emittance monitor.

The procedure is the following: The beam must be centred at a fixed position (how this can be done will be described later on). Then the signals S_I and S_O are measured and the current independent value

$$S_I^{norm} = \frac{S_I}{S_I + S_O}$$

is calculated. The deviation ΔS_I^{norm} from the calibrated one for the pencil beam at this position is a function of σ_x^2-σ_y^2.

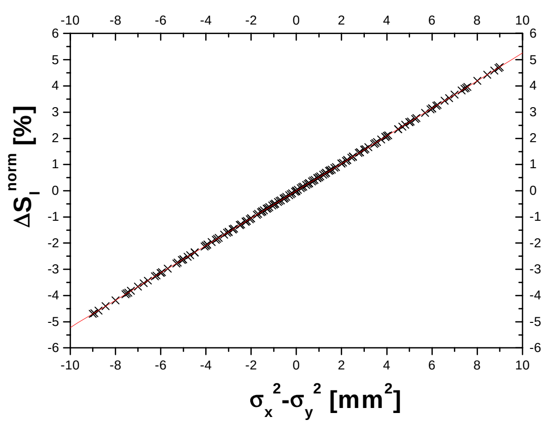

Fig.4 Relative variation of the normalised signal ΔS_I^{norm} as a function of σ_x^2-σ_y^2 at a fixed beam position (x=0mm and y=0mm)

Fig.4 shows this relative variation ΔS_I^{norm} as a function of σ_x^2-σ_y^2, which can also be written as

$$\sigma_x^2 - \sigma_y^2 = \varepsilon_x \cdot \beta_x - \varepsilon_y \cdot \beta_y \qquad (6)$$

$$= \sigma_x^2 \cdot \left(1 - k\frac{\beta_y}{\beta_x}\right) \qquad (7)$$

$$(\ \sigma_{x,y} = \sqrt{\beta_{x,y} \cdot \varepsilon_{x,y}} \quad , \quad \varepsilon_y = k \cdot \varepsilon_x\ )$$

Eq. 7 shows, that the horizontal beam size can be calculated from one measurement if k << 1 and β_x << β_y.

If it is possible to perform this measurement at 2 different monitors with well selected beta functions eq. 6 gives the possibility to calculate the horizontal and vertical emittance independently.

As mentioned earlier it is absolutely necessary to place the beam at a well known position during the data taking. This can be done on 2 different ways:

1. Especially the positioning of the beam in the centre of the BPM is possible by adding the 2 pick-ups from Fig.3 to a monitor as shown in Fig.1 (without the pumping channel). The determination of a centred beam with the 4 pick-ups, which are placed symmetrically around the centre, is possible independent of the beam size (if the bpm is calibrated and all transfer functions well adjusted). Even for a beam with small offsets (<0.25mm) the position error is smaller than 10 µm for a wide variation of beam sizes, which turns out to be sufficient. This method needs a very carefully calibrated BPM, with well adjusted electronics for position and emittance measurements.
2. By combining the 2 pick-up BPM with a dedicated, well aligned quadrupole magnet. Because the response of the beam to the quadrupole field is linear, it is possible to use methods based on beam based calibration techniques [3][4] to centre the beam independent of the beam sizes. This arrangement has also the great advantage that it allow for the measurement of the beta-functions at the same position where the beam size is measured and gives therefore directly the emittance. This solution needs a pick-up monitor which is well centred on the magnetic axis of the quadrupole and needs a absolute accuracy concerning the positioning of the beam at the axis of better than 10µm. At DELTA we have realised values of < 70 µm [5] and we expect to reach smaller values in the future.

REFERENCES

[1] R. Heisterhagen, "Entwicklung eines neuartigen Emittanzmonitors mit elektrostatischen Elektroden", Ph. D. Thesis, 1993, University of Dortmund
[2] I.N. Bronstein, K.A. Semendjajew, "Handbook of Mathematics", 3rd edition, Springer B, 1988
[3] P. Röjsel, "Experience of the QSBPM System on MAX II", Beam Instrumentation Workshop, SLAC-SSRL, 1998
[4] B. Dehning et al., "Dynamic Beam Based Calibration of Beam Position Monitors", EPAC, Stockholm, 1998
[5] A. Jankowiak et al., "The DELTA Beam Based Calibration System", Beam Instrumentation Workshop, SLAC-SSRL, 1998

RECENT IMPROVEMENTS OF A CRYOGENIC CURRENT COMPARATOR FOR nA ION BEAMS WITH HIGH INTENSITY DYNAMICS

A. Peters, H. Reeg, P. Forck, GSI, Darmstadt, Germany
W. Vodel, R. Neubert, Institut für Festkörperphysik,
Friedrich Schiller Universität, Jena, Germany
e-mail: A.Peters@gsi.de

Abstract

Former measurements of exctracted ion beams from the GSI heavy ion synchroton SIS showed large current fluctuations in the microsecond region with a high peak-to-average ratio. To adapt our Cryogenic Current Comparator (CCC) to this time structure the detector's electronics have been carefully modified.

The most important improvement of the new DC SQUID system affects the enlargement of the bandwidth and the slew rate of the measuring system. In addition the existing data acquisition system for e.g. SEMs (Secondary Emission Monitors) was extended to digitize the CCC signals simultaneously. Measurements of Argon beams will be shown to demonstrate the improved capabilities of the upgraded Cryogenic Current Comparator.

1 MODIFICATION OF THE SQUID ELECTRONICS

The CCC has demonstrated its excellent capabilities to measure nA beams with absolute calibration [1]. The most important component of the CCC is the new DC SQUID system developed and manufactured at the Friedrich Schiller University Jena, Germany. This device is able to detect extremely low magnetic fields, for instance, caused by the extracted ion beam of the SIS. For this reason the SQUID input coil is connected with the pick-up coil for the ion beam. This pick-up coil consists of a superconducting niobium toroid containing a special VITROVAC 6025-F core (VAC GmbH, Hanau, Germany) providing a high permeability, even at the low working temperature of 4.2 K. The large diameter of the pick-up coil of 200 mm provides a "warm" hole for the ion beam passing the dewar (see Fig. 1). Both the SQUID input coil and the pick-up coil form a closed superconducting loop so that the CCC is also able to detect DC currents.

As already known from earlier measurements the spill structure of the extracted ion beam pulses shows a strong modulation with current peaks up to 130 nA while the average current is only about 15 nA [2]. The beam consists of individual bursts with a steep rise and a slower fall. As a consequence, the current rise time of this spill structure sometimes exceeds the slew rate limit of the SQUID system, if the value goes beyond 5000 Φ_0/s or about 1 nA/μs. In those cases the feedback loop of the CCC electronics becomes unstable and negative spikes or other unpredictable effects could be observed [3]. For this reason a further development of the CCC was necessary and, above all, a new DC-SQUID system with a higher slew rate was designed and realized within the last year. The simplified block diagram of the DC SQUID Control is shown in Fig. 1.

The main improvement affects the enlargement of the bandwidth. For this reason a wide band transformer at room temperature is used instead of a cooled high quality factor resonant circuit for the readout electronics of the SQUID signal. The corresponding increase of the intrinsic noise of the SQUID system is much lower than the noise level of the CCC. It is caused, mainly, by the VITROVAC core of the antenna and can be neglected. Furthermore, the modulation frequency of the PLL-loop was essentially increased from 125 kHz in the former SQUID system up to 500 kHz using faster operational amplifiers in the SQUID controller. As a result of these design features the system bandwidth of the SQUID system was increased up to 50 kHz per 1 flux quantum (full range signal). This corresponds to an increase of the slew rate of the CCC up to 1.6×10^5 Φ_0/s or 28×10^6 nA/s. But with the detector system connected and a calibration signal as the input a reduced value of 6×10^4 Φ_0/s was measured. For this phenomena we have no electronic model up to now and further investigations are necessary to understand this.

Another important feature is the realization of a distance of 25 m between the preamplifier on top of the cryostat and the SQUID controller in order to allow the operation of the SQUID system also when the beam line is activated. To meet this requirement without decreasing the current resolution of the CCC several special buffers for most of the leads and a special double-screened cable between preamplifier and SQUID controller were used to avoid rf interferences.

A point of special interest is the coupling of the SQUID output with an A/D converter and the data aquisition unit (see Fig. 2). According to our experience this is only possible by using an optical coupler between the analog and digital circuits. Otherwise the whole SQUID system is not working at all because of the disturbances generated by the digital circuits. In addition, the analog output of the SQUID electronics is equipped with an isolating amplifier.

As the result of all improvements the CCC is now working at a sufficiently high slew rate so that we can mea-

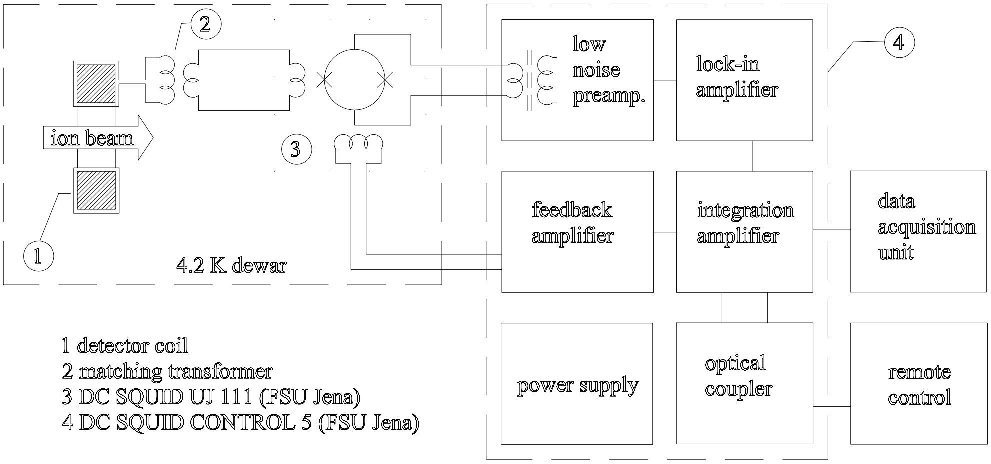

Figure 1: Block diagram of the modified DC SQUID electronics

sure also short current peaks at a level of several hundred nA with an extreme high current resolution of about 250 pA/$\sqrt{Hz}$.

2 DATA ACQUISITION SYSTEM

For the data acquisition of other beam diagnostic detectors like scintillators, ionization chambers and secondary emission monitors (SEM) a GSI product called **M**ulti **B**ranch **S**ystem [4] is used.

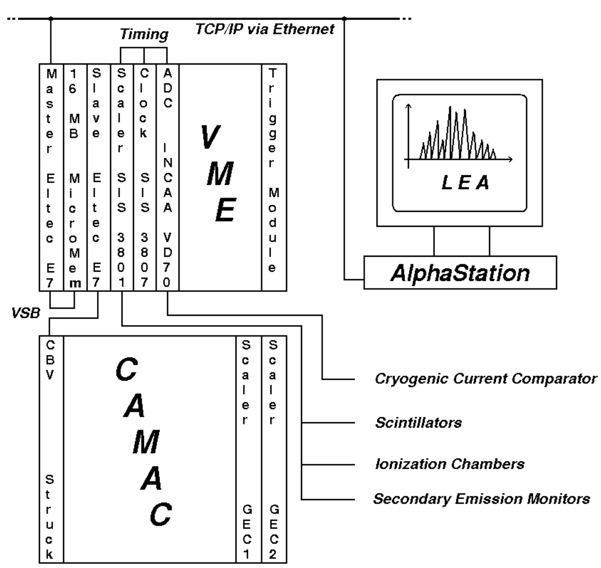

Figure 2: Schematic drawing of the data acquisition system

To digitize the output signal of the CCC the existing VME system was extended by a 12-bit ADC with 2 MSamples memory [5]. A clock module in the VME crate provides the timing for the simultaneous acquisition of the scaler inputs as well as the ADC data up to 10^5 datasets per second. The whole acquisition process is controlled by two ELTEC E7 VME processors running under Lynx-OS, which share a 16 MByte VME/VSB memory (see Fig. 2). The slave processor collects the data from all VME and CAMAC modules and writes them to the shared memory via VME. The master processor reads the shared memory via VSB, formats the data and handles all kind of transport, e.g. via network or to a tape drive.

For the on-line control of the measurements a special software package called LEA [6] is used. The data are received over the network via TCP/IP and can be displayed on a VMS or UNIX workstation. For an off-line analysis the data are stored in ASCII format on disk.

3 SPILL MEASUREMENTS WITH HIGH DYNAMICS

With the upgraded SQUID electronics and the extended data acqusition system enhanced measurements of the ion beam extracted from the SIS are possible. Fig. 3 shows such a measurement of a 300 MeV/u $^{40}Ar^{11+}$-beam, where 7×10^9 ions are extracted in about 1.2 seconds effectively. The mean current is only 11.2 nA but the peak-to-average ratio is in the order of 26 (!). Thus the single beam bursts have an enormous current slew rate, up to 290 nA in 40 μs were observed. This measured value is equivalent to a slew rate of about 4×10^4 Φ_0/s, which is in good correspondence to the measured performance of the enhanced CCC detector electronics.

This allows to make further studies of the spill structure with high resolution. These measurements will start again in winter 1999 when the new high current injector at GSI will deliver beams for the synchroton reaching the incoherent space charge limit [7].

4 CALIBRATION OF SEM DETECTORS AT HIGH INTENSITIES

A SEM made of three Al foils [8] is mounted closely behind the CCC to provide a comparable measurement device. Again for a $^{40}Ar^{11+}$-beam at 300 MeV/u the particles per spill were determined with the SEM and the CCC. A plot of these data is shown in Fig. 4. The output current of the CCC is converted to particles by numerical integra-

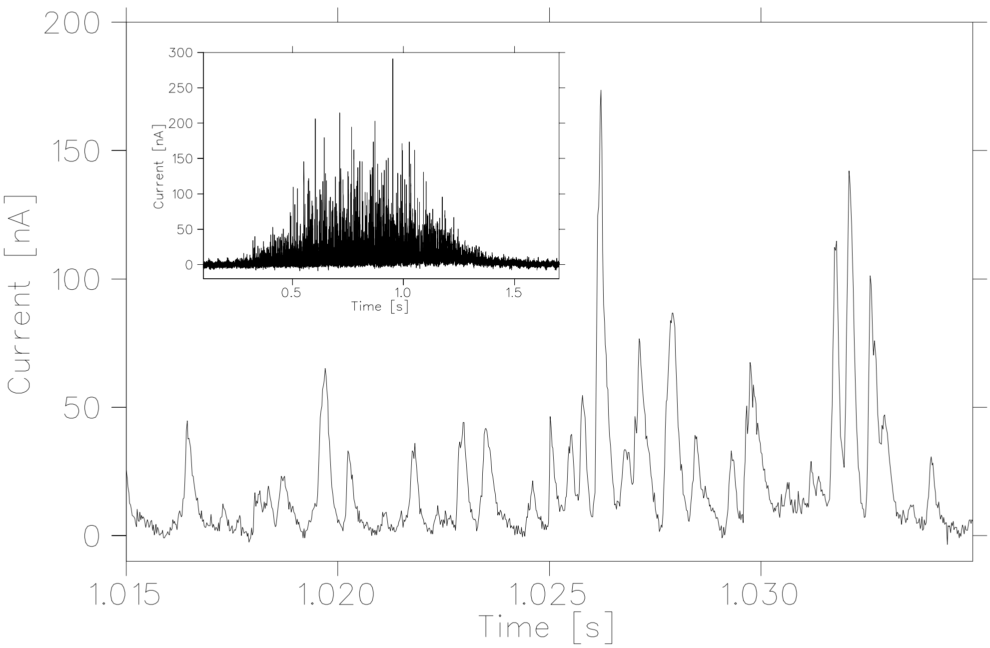

Figure 3: Spill structure of a 300 MeV/u $^{40}Ar^{11+}$-beam. An enlarged view (20 ms) of the spill with the typical burst-structure is displayed. The inset shows the whole spill of 7×10^9 ions extracted in about 1.2 seconds. The data were taken with a sampling frequency of 50 kHz.

tion of each measured spill and plotted against the SEM output. The data show a good linear correlation over one order of magnitude. This overlap is sufficient to calibrate the SEM detectors at high intensities. Further comparative measurements with various ion species will be carried out whenever the beam time schedule will permit this.

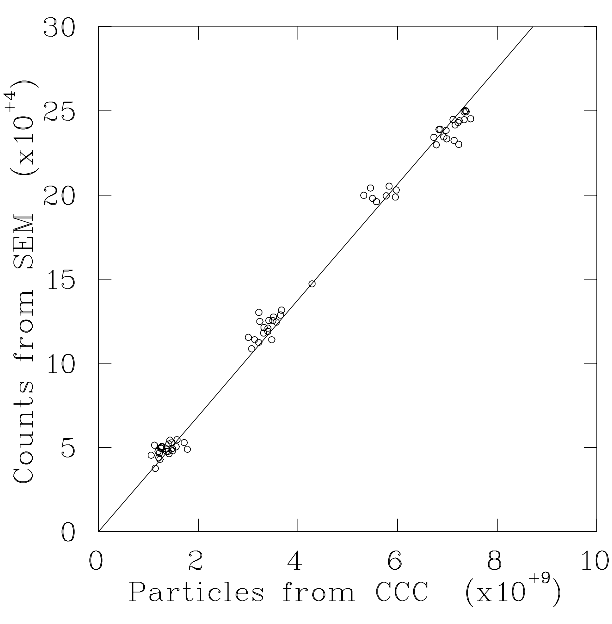

Figure 4: Comparison of CCC and SEM data. Each point represents one spill measured simultaneously. The CCC output is converted into particle numbers by numerical integration of the spill current.

5 ACKNOWLEDGEMENT

The authors would like to thank T. Hoffmann and U. Meyer for the setup of the data acqusition system. We also would like to express our thank to C.H. Schroeder for his help in any questions concerning cryogenics.

6 REFERENCES

[1] A. Peters, W. Vodel, H. Koch, R. Neubert, H. Reeg, C.H. Schroeder, "A Cryogenic Current Comparator for the absolute measurement of nA beams", Proceedings of the Eighth Beam Instrumentation Workshop, Stanford, CA 1998, AIP Conference Proceedings 451, pp. 163-180

[2] A. Peters, H. Reeg, C.H. Schroeder, W. Vodel, H. Koch, R. Neubert, "Absolute Measurements and Analysis of nA-Ion Beams", Proceedings of the Third European Workshop on Beam Diagnostics and Instrumentation for Particle Accelerators, Frascati, 1997, pp. 180-182

[3] A. Peters, H. Reeg, C.H. Schroeder, W. Vodel, H. Koch, R. Neubert, H. Mühlig, "Review of the Experimental Results with a Cryogenic Current Comparator", Proceedings of the 5^{th} EPAC , June 1996, Sitges, Spain, pp. 1627-1629

[4] H.G. Essel, N. Kurz, W. Ott, "Upgrades to the GSI Data Acquistion System MBS", GSI Scientific Report 1997, 98-1, pp. 205-206

[5] B.J. Sijbrandij (INCAA Computers), "User's Guide of the VME-VD70-5790", Apeldoorn-Holland, 1997

[6] H.G. Essel, "GSI Lean Easy Analysis", GSI, 1997, see: http://www-gsi-vms.gsi.de/anal/lea.html

[7] U. Ratzinger. "The New GSI Prestripper LINAC for High Current Heavy Ion Beams", Proceedings of the 1196 LINAC Conference, Geneva, p. 288

[8] P. Forck, P. Heeg, A. Peters, "Intensity measurement of high energy heavy ions at the GSI facility", Proceedings of the 7^{th} Beam Instrumentation Workshop, Argonne, 1996, AIP Conference Proceedings 390, pp. 422-429

TURN-BY-TURN PHASE SPACE DIAGRAM CONSTRUCTION FOR NON-LINEAR BETATRON OSCILLATION

A. Kalinin, V.Smaluk, Budker Institute of Nuclear Physics, Novosibirsk, Russia

Abstract

The problem of phase space diagram construction for non-linear betatron oscillation measured by pickup, is considered. The conventional two-pickup method [1] of phase trajectory construction was improved. Discrete Fourier filter applied to data measured yields a large dividend in accuracy. The result of our investigations is the method of turn-by-turn phase trajectory construction using data measured by single pickup. The single-pickup method developed was tested by computer simulation of non-linear betatron oscillation in several models of magnet lattice. Practicality of the method and its accuracy limitation were studied. The method applying for experimental study of beam dynamic is discussed.

1 INTRODUCTION

Phase space diagram of non-linear betatron oscillation gives a lot of information about the non-linearity type, non-linear resonances, dynamic aperture, etc. It is useful to compare phase trajectories of the beam motion measured with results of analytical estimations and numerical simulations.

A problem of phase trajectory construction is obtaining $x'(x)$ dependence, where $x(t)$ is transverse coordinate, and $x'(t)$ is transverse momentum of a beam centre of charge, t is a time variable. The problem is troublesome because of impossibility to measure directly the momentum $x'(t)$.

Diagnostic systems give an information about beam motion as series of turn-by-turn samples x_k of the coordinate measured by pickup. Due to the discreteness, calculation of the momentum samples x'_k, by numerical differentiation of the x_k, is impossible in general.

Let's consider a problem of construction of turn-by-turn phase trajectory $x'_k(x_k)$ of non-linear betatron oscillation using the coordinate samples x_k.

It is convenient to analyse phase trajectories in the $(x, \bar{x}')$ coordinates defined by the variables conversion:

$$\bar{x}' = \alpha x + \beta x'. \tag{1}$$

A shape of phase trajectory in these coordinates is independent of the value of alpha-function $\alpha = -\beta'/2$, but this shape is determined by pure non-linear effect.

2 TWO-PICKUP METHOD

There are conventional two-pickup method [1] of turn-by-turn phase trajectory construction. Let's consider particle motion in a linear section of magnet lattice with two pickups, first of them placed at the input of the section and second at the output of it.

If a particle passes through the section, its coordinate x_2 measured by the second pickup is:

$$x_2 = (\beta_2/\beta_1)^{1/2}\cdot(x_1 \cos\Delta\psi_{21} + \bar{x}'_1\cdot\sin\Delta\psi_{21}), \tag{2}$$

here x_1 is the coordinate and $\bar{x}'_1$ is the normalized momentum at the first pickup, $\beta_{1,2}$ are the values of beta-function at the pickups, $\Delta\psi_{21}$ is the betatron phase advance between the pickups. From this expression an equation of turn-by-turn phase trajectory is derived:

$$\bar{x}'_{1k} = [(\beta_2/\beta_1)^{1/2}\cdot x_{2k} - x_{1k}\cos\Delta\psi_{21}]/\sin\Delta\psi_{21}\ . \tag{3}$$

If $\beta_1 = \beta_2$ and $\Delta\psi_{21} = \pi/2+\pi n$, then $\bar{x}'_{1k} = x_{2k}$.

An accuracy of the method is determined by pickup resolution in the frequency band with upper bound equal to the revolution frequency. The noise error leads to poor quality of phase trajectories constructed by this method.

For decrease the noise error, a method of discrete Fourier filtering was developed. Let's expand the arrays x_{1k} and x_{2k} of N turn-by-turn coordinate samples in terms of harmonics $\Phi_{1,2j}=A_{1,2j}+iB_{1,2j}$ of betatron frequency Q:

$$A_{1,2j} = 2/N\cdot\sum_{k=0}^{N-1} x_{1,2k}\cdot\cos(2\pi k\cdot jQ) \tag{4}$$
$$B_{1,2j} = 2/N\cdot\sum_{k=0}^{N-1} x_{1,2k}\cdot\sin(2\pi k\cdot jQ)$$

Amplitude of harmonics $|\Phi_{1,2j}| = (A_{1,2j}^2+B_{1,2j}^2)^{1/2}$ in (4) decreases rapidly with the harmonic number j.

Procedure of turn-by-turn phase trajectory construction is just the synthesis of the arrays X_{1k}, X_{2k}:

$$X_{1,2k} = \sum_{j=1}^{n} (A_{1,2j}\cdot\cos 2\pi kjQ + B_{1,2j}\cdot\sin 2\pi kjQ) \tag{5}$$

The $X_{2k}(X_{1k})$ dependence describes the phase trajectory.

Noise component of the j–th harmonic in (5) is $N^{1/2}$ times lower than broad-band noise component of the x_{1k}, x_{2k} arrays. If the number of harmonics in (5) $n << N$, then noise reduction is $(N/n)^{1/2}$. So, combination of the expansion (4) with the synthesis (5) is a discrete filter. Usually $N = 1024$, $n = 4\div8$, so typical noise reduction by the filter is 10÷15 times.

An example of the filter applying to the two-pickup method is given in Fig. 1. There are phase trajectories of radial betatron oscillation in the VEPP-4M near the sextupole resonance $3Q_x = 26$. The trajectory $x_{2k}(x_{1k})$, constructed by the two-pickup method without filtering, is plotted by circles, the trajectory $X_{2k}(X_{1k})$ constructed using the filter is plotted by triangles.

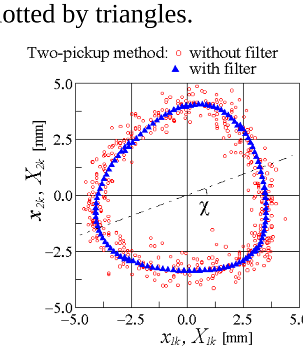

Figure 1: Applying of the discrete Fourier filter.

Broad-band noise resolution of the turn-by-turn pickup is about 100 μm, the filter decreases noise error down to ~10 μm.

3 SINGLE-PICKUP METHOD

There is a limitation of practicality of the two-pickup method, imposed by non-linear field components of the elements placed between the pickups. In presence of the components, coordinate transform is not described by (2).

Thus, if a magnet lattice has no linear section with betatron phase advance of the order of π/2, the two-pickup method had failed. In this case the problem of phase trajectory construction using coordinate samples measured by single pickup, is of a special interest.

Let's analyse a particle motion in the two utmost models of non-linear lattice: the lattice with a uniform distribution of non-linearity and the lattice with a single non-linear element.

3.1 Uniformly Distributed Non-linearity

Equation of particle motion in a magnet lattice with a uniform distribution of non-linearity is:

$$x'' + \Omega^2 x = f_n \cdot x^n, \qquad (6)$$

here $\Omega^2 = K_x$ is focusing, f_n is n-th order multipole coefficient of non-linear force.

For $\Omega^2 = \mathrm{const}$ (azimuthal symmetric field), this equation can be solved analytically, solution has a form of $x'(x)$ and describes a phase trajectory of the motion. For sextupole non-linearity ($n = 2$) turn-by-turn relation between momentum x'_k and coordinate x_k is:

$$x'_k = \pm\Omega^{-1} \cdot (C - x_k^2 \pm 2/3 \cdot \Omega^{-2} \cdot f_n \cdot x_k^3)^{1/2}. \ (7)$$

The coefficients f_n and C can be obtained by analysis of the array x_k of turn-by-turn coordinate samples.

Thus, for a magnet lattice with a uniform distribution of non-linearity, there are turn-by-turn relations between x'_k and x_k independent of non-linearity magnitude and oscillation amplitude.

3.2 Single Non-linear Element

Equation of particle motion in a magnet lattice with a single non-linear element is:

$$x'' + \Omega^2 x = \Sigma_{k=0}^{\infty} f(x) \cdot \delta(\theta - \Delta\theta + 2\pi k), \qquad (8)$$

here $\Omega^2 = K_x$ is focusing, non-linear element placed at the $\Delta\theta$ azimuth is modeled by the product of non-linear function $f(x)$ by delta-function $\delta(\theta-\Delta\theta+2\pi k)$ "switching on" non-linear force at each turn.

This equation can be solved analytically at each turn using Laplace transform. Turn-by-turn samples of coordinate x_k and momentum x'_k are:

$$x_k = x_0 \cos 2\pi kQ + \beta x'_0 \cdot \sin 2\pi kQ - \\ - \beta \cdot \Sigma_{m=0}^{k-1} f_m \cdot \sin[2\pi Q(k-m) - \Delta\psi], \qquad (9)$$

$$x'_k = -1/\beta \cdot x_0 \sin 2\pi kQ + x'_0 \cdot \cos 2\pi kQ - \\ - \Sigma_{m=0}^{k-1} f_m \cdot \cos[2\pi Q(k-m) - \Delta\psi], \qquad (10)$$

here Q is betatron frequency, $\Delta\psi = Q\Delta\theta$ is betatron phase advance between non-linear element and pickup.

From the expressions (9), (10) for k-th and (k+1)-st turns, a recurrent formula to calculate the momentum x'_{k+1} is derived:

$$x'_{k+1} = [x_{k+1} \cdot \cos(2\pi Q - \Delta\psi) - x_k \cdot \cos\Delta\psi - \\ - \beta \cdot x'_k \cdot \sin\Delta\psi]/\beta\sin(2\pi Q - \Delta\psi), \qquad (11)$$

It is remarkable that the non-linear force f_k at each turn can be calculated by the formula:

$$f_k = (x_k \cos 2\pi Q - x_{k+1} + \beta x'_k \cdot \sin 2\pi Q)/\beta\sin(2\pi Q - \Delta\psi), \qquad (12)$$

Sorting $f_k(x_k)$ by increase of x_k, one can approximate the function $f(x)$ and determine type of the non-linearity.

Note, that the phase trajectory constructed for $\Delta\psi \neq 0$ is transformed by rotation on the $-\Delta\psi$ angle to the phase trajectory constructed for $\Delta\psi = 0$:

$$x'_{k+1} = (x_{k+1} \cdot \cos 2\pi Q - x_k)/\beta \sin 2\pi Q, \ (13)$$

Thus, for a magnet lattice with a single non-linear element, there is a recurrent formula (11) to calculate the turn-by-turn momentum x'_k from the coordinate x_k.

Analysis of these two utmost cases gives promise that for some distributions of non-linear lattice elements there are relations between x'_k and x_k independent of non-linearity magnitude and oscillation amplitude.

3.3 Amplitude-independent relations between coordinate and momentum spectra

As it was clarified, turn-by-turn samples of coordinate x_k and momentum x'_k are related to each other. This suggests that relations independent of non-linearity magnitude and oscillation amplitude are valid between coordinate Φ_j and momentum Φ'_j spectra.

An expansion of x_k array of N samples in terms of harmonics $\Phi_j = A_j + iB_j$ of betatron frequency Q is:

$$A_j = 2/N \cdot \Sigma_{k=0}^{N-1} x_k \cdot \cos(2\pi k \cdot jQ)\ , \qquad (14) \\ B_j = 2/N \cdot \Sigma_{k=0}^{N-1} x_k \cdot \sin(2\pi k \cdot jQ).$$

For the model lattice with a single non-linear element, frequency depended expressions for the relations between momentum harmonics $\Phi'_j = A'_j + iB'_j$ and coordinate ones $\Phi_j = A_j + iB_j$ are derived from the recurrent formula (11) using the harmonic expansion (14), with neglect of the terms of the order $1/N$.

$$A'_j = [A_j (\cos 2\pi Q - \cos 2\pi jQ) - B_j \cdot \sin 2\pi jQ]/\beta\sin 2\pi Q, \quad (15) \\ B'_j = [A_j \cdot \sin 2\pi jQ - B_j (\cos 2\pi Q - \cos 2\pi jQ)]/\beta\sin 2\pi Q, \\ j = 1, 2, \ldots, N \qquad Q \neq 0, 0.5, 1, \ldots$$

For the lattice with uniformly distributed non-linearity, there are simple expressions for the relations between normalized amplitudes a'_j/a'_1 and phases φ'_j of momentum harmonics and a_j/a_1, φ_j of coordinate ones:

$$a'_j/a'_1 = j \cdot a_j/a_1, \qquad \varphi_j - \varphi'_j = \pi/2, \qquad (16)$$

Note, that the amplitude-phase relations (16) are independent of betatron frequency Q unlike the (15).

Non-linear oscillation in several types of magnet lattice was studied by computer simulation. One more example of such the relations using is presented in [2]. The amplitude-phase relations empirically obtained were used for phase trajectory construction at LEP:

$$a'_j/a'_1 = a_j/a_1, \qquad \varphi_j - \varphi'_j = \pi/2, \qquad (17)$$

Thus, if non-linear oscillation can be described by equation of motion, the amplitude-phase relations can be tabulated by analytical or numerical solution of the equation.

In general, amplitude-phase relations between coordinate and momentum spectra can be obtained in one way or another. These relations are independent of non-linearity magnitude and oscillation amplitude and can be use for turn-by-turn phase trajectory construction.

4 PRACTICAL USE OF THE METHOD

The formulas (11), (15) obtained by analysis of the simple model lattice with a single non-linear element can be used for study of non-linear betatron oscillation in real accelerators. This model approximately describes a motion in accelerator with low-order symmetry, lattice of which has final focus. In this case sextupole chromaticity correctors are placed close to final focus quadrupoles where beta functions is large (at VEPP-4M — more than 10 times greater than the mean value), and these sextupole correctors are dominated in the non-linearity.

Practicality of the single-pickup method was tested using computer simulation. Phase trajectories constructed by the method were compared with results of particle tracking in the VEPP-4M lattice with sextupoles.

As an accuracy criterion of the method, the correlation coefficient between the phase trajectory constructed and the phase trajectory calculated by computer tracking, was used. A value of the coefficient close to 1 attests that the phase trajectories are close to one another, and the method accuracy is rather good. It was discovered that in the practically interesting range 8.62÷8.75 of the VEPP-4M radial betatron frequency, the correlation coefficient is more than 0.9.

The single-pickup method was tested also by comparison with the conventional two-pickup method. Example of the phase trajectory constructed by these methods is shown in Fig. 2. The trajectory plotted by circles was constructed by the two-pickup method with Fourier filtering, the trajectory plotted by triangles was constructed by the single-pickup method.

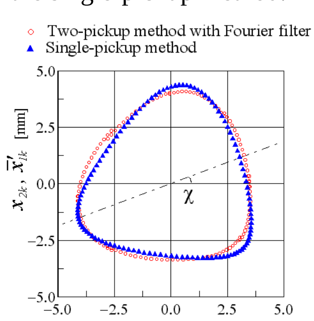

Figure 2: Two-pickup and single-pickup methods.

The single-pickup method was used for experimental study of non-linear beam dynamics at the VEPP-4M [3]. In Fig. 3 examples of the phase trajectories constructed by the single-pickup method are presented. Fig. 3*a* illustrates betatron oscillation of varied amplitude near the $3Q_x$=26 resonance, Fig. 3*b* and Fig. 3*c* demonstrates non-linear resonances $4Q_x$=35 and $5Q_x$=43 respectively.

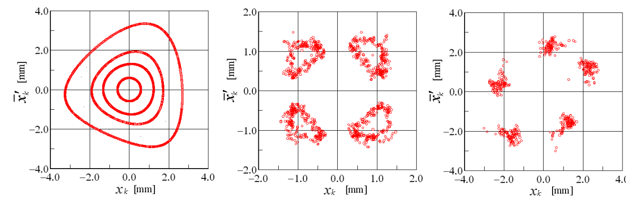

Figure 3: Examples of phase trajectories measured.

The single-pickup method can also be used for construction of phase trajectory of synchrotron oscillations. Synchrotron oscillation produces oscillation of radial coordinate, turn-by-turn samples of which are:

$$x_k(\theta) = R\cdot\psi(\theta)\cdot(\Delta E/E)_k\cdot\exp[i(2\pi k\Omega/\omega_0+\chi)], \quad (18)$$

here $\psi(\theta)$ is dispersion function, $\Delta E/E$ is an energy deviation, proportional to time derivation of the synchrotron phase ϕ:

$$\Delta E/E = 1/q\omega_0 K_s\cdot d\phi/dt. \quad (19)$$

Phase trajectory of synchrotron oscillation can be constructed using the amplitude-phase relations:

$$a_{\phi j}/a_{\phi 1} = (a_{Ej}/a_{E1})\cdot j^{-1}, \qquad \varphi_{\phi j} - \varphi_{Ej} = -\pi/2. \quad (20)$$

Fig. 4 shows the phase trajectory of synchrotron oscillation constructed from data measured in comparison with the result of computer simulation.

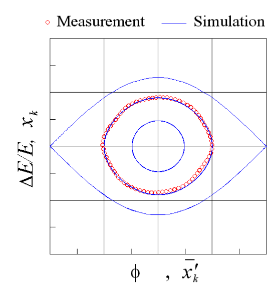

Figure 4: Phase trajectory of synchrotron oscillation.

REFERENCES

[1] P.L.Morton, et. al. “ A Diagnostic for Dynamic Aperture ”, Proc. of 1985 PAC, Vancouver.

[2] G.Morpurgo, “The BOM 1000 turns display: A tool to visualize the transverse phase-space topology at LEP”, Proc. of EPAC'98, Stockholm.

[3] V.Kiselev, E.Levichev, V.Sajaev, V.Smaluk, “Experimental Study of Nonlinear Beam Dynamics at VEPP-4M ”, NIM, A 406 (1998) 356-370.

TRAJECTORY MEASUREMENTS IN THE DAΦNE TRANSFER LINES

A. Stella, C. Milardi, M. Serio, INFN-LNF, Frascati (Rome), Italy

Abstract

An improved beam position monitor system has been installed in the Transfer Lines (TL) connecting the DAΦNE Linac to the collider Main Rings through the Damping Ring, to monitor the beam trajectory and optimize the transmission efficiency.

Signals from stripline type beam position monitors are stretched, sampled through Track & Hold circuits and digitized to 12 bits. The sampling stage is triggered, according to the timing of the desired beam, to measure the amplitude of the signals induced on a BPM.

Hardware control, data collection and reconstruction of the beam position along the Transfer Lines are performed by the DAΦNE Control System on a VME standard local processor.

Design issues, implementation and performance of the system are presented.

1 INTRODUCTION

The injector chain of DAΦNE consists of a e+/e- Linac injecting into an intermediate storage ring (Accumulator), employed to accumulate the required single bunch current and to damp the longitudinal and transverse emittances before the injection in the DAΦNE main rings.

Linac, Accumulator and Main Rings are interconnected by ~140 m of Transfer Lines altogether.

Due to the requirement of using the pre-existing buildings, the TL are designed in such a way that different beams (electrons or positrons from the Linac into the Damping Ring and from the Damping Ring into either one of the Main Rings) traverse the same portion of the TL in opposite directions with different timing.

2 SYSTEM OVERVIEW

2.1 Pick-up Electrodes and Signal Processing

The low repetition rate (50 Hz from the Linac to the Damping Ring and 1 Hz for the injection in the Main Rings) requires a single shot detection system to measure the beam position.

To acquire the whole trajectory of the beam, 23 beam position monitors (BPMs) are installed along the lines.

The BPMs consist of 50Ω strip-line electrodes, with 0.15 m length and 30 degrees angular width, short circuited at one end inside the vacuum chamber of 37 mm radius.

The signal induced by the beam consists of two pulses of opposite polarities, according to the shape of the bunch. The different characteristics of the beam injected and extracted from the Damping Ring (Tab. 1) give a wide range of amplitudes and widths of the pulses (Fig. 1).

Table 1: DAΦNE Injector Beam Parameters

Parameter	Typical
LINAC bunch charge	1 nC
LINAC bunch length	10 ns FWHM
LINAC repetition rate	25-50 Hz
ACC bunch charge	3÷12 nC
ACC bunch length	300 ps FWHM
ACC repetition rate	1-2 Hz

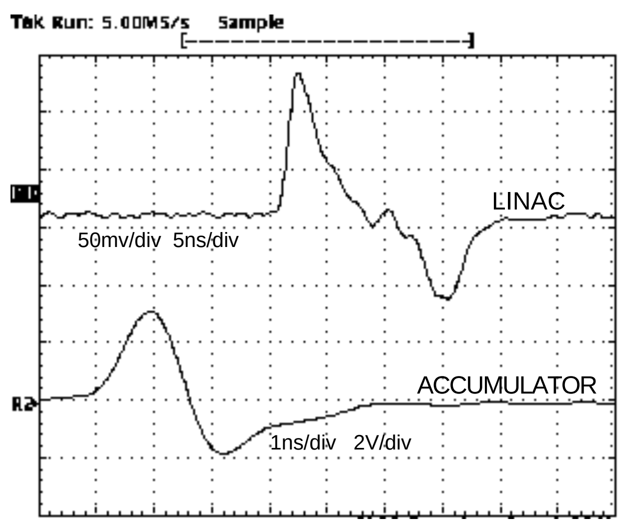

Figure 1: Typical pickup signals at the input of the BPM detection electronics, induced by the Linac beam and the Accumulator, measured at the end of ~50 m long coaxial cables.

In our case the Linac delivers bunches with a 10 ns FWHM length, while the damped beam extracted from the Accumulator has a 300 ps FWHM bunch length.

Each pickup signal is sent (through coaxial cables of typical length between 40m and 100m) to a wide band multiplexer system equipped with HP-E1366A boards and then to the detection electronics.

The beam position is determined by measuring the peak amplitude of the signals induced on each electrode, then calculated from a linear combination of the measured voltages through a non linear fitting function, in order to correct the non linear response of the BPMs.

The fitting function has been derived through a bench calibration with the wire method.

2.2 Detection Electronics

The block schematic of the detection electronic is reported in Fig. 2.

The peak amplitude of each pickup signal is sampled with different Track & Hold (T/H) Amplifiers (ANALOG DEVICES AD9101), which are triggered to hold the peak values for 5 µs.

Before arriving to the sampling stage each pulse is stretched through low pass filters in order to get a flat crest for accurate hold of the subsequent T/H stage.

Bessel-Thomson low pass filters (Mini-Circuits BBLP-117), which provide a flat time delay design to preserve the pulse shape and avoid overshoot and ringing, have been employed.

The 3 dB frequency of the filters has been chosen as a compromise between the conflicting requirements of slowing down the fast risetime of the pulses from the accumulator beam and the requirement of performing measurements also at low currents.

The expected peak signal induced by a gaussian bunch with a σ rms length in a strip line through a gaussian filter can be deduced from (for σ_{eff}>(l/c)):

$$V_p = Q\left(\frac{\varphi}{2\pi}\right)Z_0 \frac{l}{c\sqrt{2\pi e}\sigma_{eff}^2} \qquad (1)$$

where Q is the bunch charge, $\sigma_{eff}^2 = \sigma^2 + \sigma_F^2$ with σ_F the width of the filter finite impulse response, φ is the opening angle of the electrode, Z_0=50 Ω the characteristic impedance of the transmission line, l the stripline length, and c the speed of light.

The analog to digital conversion is performed by a VME ADC Board (Green Spring IP-HiADC) based on Analog Devices AD684JQ sample and hold amplifiers and Analog Devices AD1671 analog to digital converter.

The ADC board, programmed through a VME CPU and externally triggered, allows the simultaneous acquisition of the four channels through its sampling input stage and the final A/D conversion within 800 ns for each channel.

The timing for the trigger of T/H amplifiers and the ADC board is provided by delaying of a proper amount of time, different for each BPM, the DAΦNE injection and extraction trigger provided by the timing system, with a Stanford DG535 Pulse Generator controlled through a GPIB interface, in order to hold the signal peak for the following ADC stage.

Since the pickup signals induced by the beam extracted from the Accumulator can exceed the T/H input range, voltage controlled attenuators (MiniCircuits ZAS-1) are placed before the T/H stage and controlled with a VME DAC board (Green Spring IP-DAC).

A calibration signal with a programmable amplitude has been introduced into the electronic system to measure the gain of each channel and subtract the corresponding offset from the measured beam position.

A VME local processor based on a Motorola 68000 CPU, which is an integral part of the DAΦNE Control System, controls the hardware, collects and reconstructs the beam position along the TL through a dedicated software developed in LabView. The VME processor also makes the measured trajectory available to the control system.

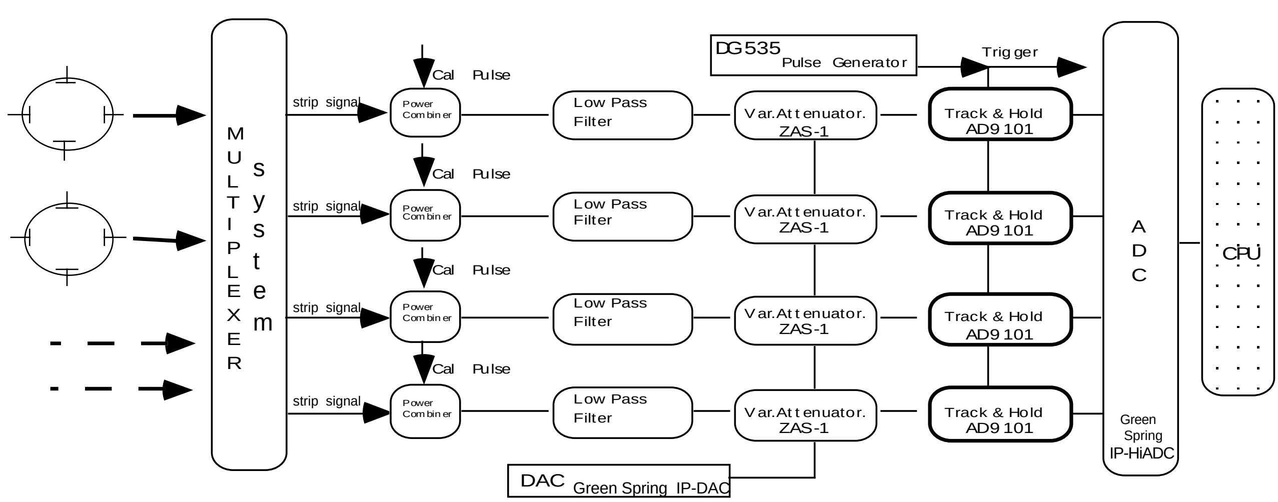

Figure 2: Block schematic of the detection electronics

3 MEASUREMENT RESULTS

3.1 Bench Tests

From bench calibration we can calculate the ratio between the peak amplitudes of the pickup signals as a function of the beam offset, and compare it to the dynamic range of the detection electronics. The input dynamic range of the T/H sampling amplifiers is compatible with a maximum beam offset of 20 mm from the center of the vacuum chamber.

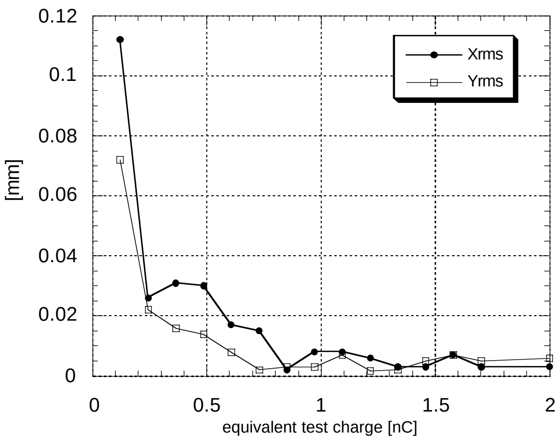

Figure 3: rms values of the measured beam position over 50 readings as a function of a test charge.

The resolution of the detection system has been measured by reading the position data as a function of the level of a test pulse. A typical diagram of the rms measured position is reported in Fig. 3, the pulse height of the calibration pulse, which spans the whole input range, has been converted into an equivalent test charge by using the eq. (1) to correlate the measurements directly to the beam intensity. The nonlinearity of the BPM detector produces a position offset which depends from the input level. The gain of each channel has been measured and is reported in Fig. 4 as a function of the equivalent test charge.

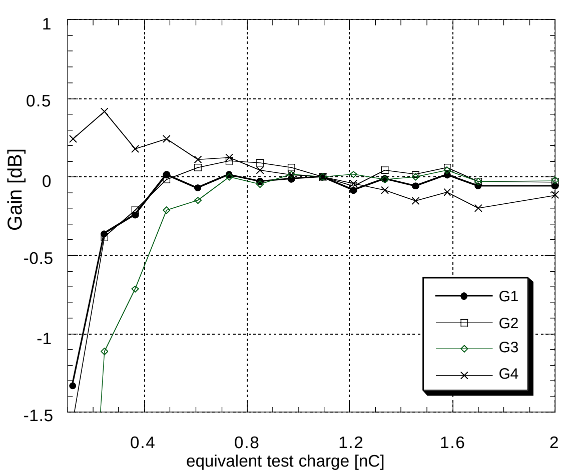

Figure 4: Normalized gain of the four channels as a function of a test charge.

A large difference between the four channels gain occurs in the low input level region. One source of this nonlinearity may be due to the droop rate of the T/H amplifiers.

3.2 Beam Tests

The BPM system has been installed, tested and will be fully integrated in the DAΦNE control system soon.

Examples of measured beam positions at different BPMs for several consecutive bunch passages are shown in Fig. 5a-b. Data refer to the beam extracted from the damping ring with a bunch charge of ~2 nC, they have been acquired using a temporary interface.

The actual resolution appears worse than expected, a possible reason may be a jitter of the trigger signal used to detect the bunch passage, which results in an inaccurate holding of the peak pulses.

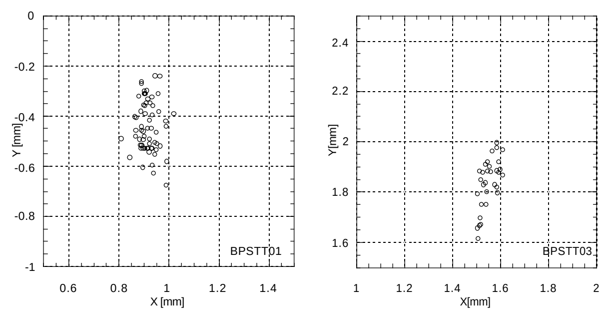

Figure 5a-b: measured beam positions over several bunch passages at different BPMs.

In the past the transfer line trajectory acquisition system relied on an oscilloscope and has been operated through a user interface available within the DAΦNE control system [1]. The interface allows to select the devices involved in the measurement and provides data access to the control system general database for saving and recovering purpose. The peak amplitude over the pickup signals is summed up for each BPM and presented as an histogram providing a rough measurement of the beam current, that gives an immediate and useful feeling of the beam transport efficiency along the TL.

The integration of the new BPM system in the existing user interface is straightforward. It will provide a fast and versatile tool for trajectory measurements. Automatic tasks to optimize the transport along the DAΦNE injection system are under study.

ACKNOWLEDGMENTS

Authors wish to thank A. Drago, A. Ghigo for useful discussions, O. Giacinti for the realization of the electronic boards and O. Coiro for technical support.

REFERENCES

[1] G. Di Pirro et al.: "Integration of Diagnostic in the DAΦNE Control System", Proc. DIPAC97, pp. 67 (Frascati 1997).

BEAM STEERING WITH IMAGE PROCESSING IN THE CRYRING INJECTION BEAMLINE

A. Källberg, A. Simonsson, Manne Siegbahn Laboratory,
Frescativägen 24, SE-104 05 Stockholm, Sweden

Abstract

By varying six quadrupoles and observing how the beam spot moves on three fluorescent screens the beam is aligned in the injection beamline. The method is now automated and upgraded by using image processing of the picture to get the position of the beam.

1 CRYRING

CRYRING is a 52-m circumference storage ring for atomic and molecular ions [1]. In the injection line an RFQ pre-accelerates ions with q/m>0.22. Thus, in the injection line right before injection, where the system below is used, the beam can be of two types: "Fast", 290 keV/u and q/m>0.22, or "slow" with 40q keV total energy. Examples of ions are Pb^{54+}, HCN^{+}, and Sr^{+}. The beam current varies from 20 µA down to below 50 nA. For the fast beam the pulse length is 0.1 ms and the repetition rate is 3 Hz.

2 THE OLD SYSTEM

For several years a Pascal program running on the PDP-11 computer has been used which aligns the beam horizontally in three focusing quadrupoles and vertically in three defocusing quadrupoles. The magnets are varied approximately 15% up and down while the operator looks at a monitor showing the beam spot on a fluorescent screen.

Changing the focusing naturally changes the shape of the beam, but when the centre of the beam moves the beam doesn't go through the centre of the quadrupole and the preceding steering element should be adjusted.

Figure 1. Grey-scale picture of the beam spot.

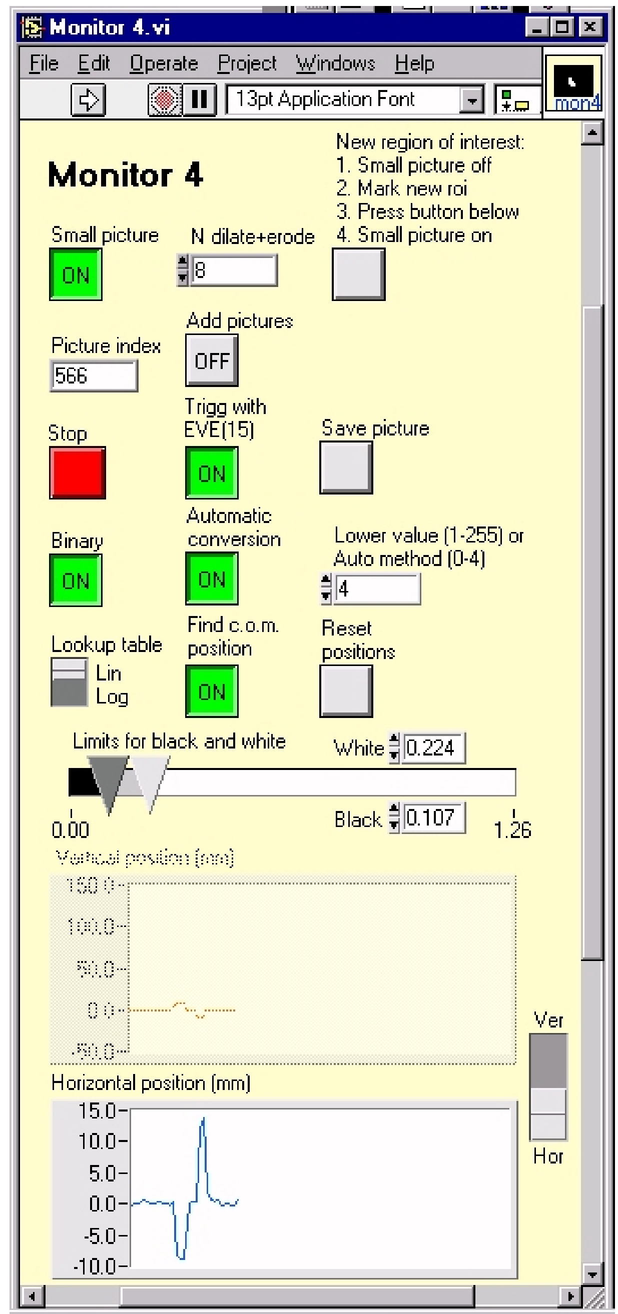

Figure 2. The front panel of the LabVIEW program shows the image processing options. The diagram at the bottom shows large movements of the horizontal beam position when a focusing quadrupole is varied.

Next a new setting of the steering element is calculated from the change of the beam position.

This method is also much used in electron machines where one can view the synchrotron radiation and measure changes of the beam position with high precision.

In order to cope with varying beam intensities the pulse length can be varied, from one μs up to several ms.

The method works rather well, although it is a bit cumbersome to use and it takes approximately half an hour to align the beam.

When the beam is very weak the beam spot is difficult to see, and since there is a large interest from the users in clusters and molecular ions that only can be produced in tiny quantities, an increased sensitivity is desired.

3 THE IMPROVED METHOD

With the help of a frame grabber board a PC calculates the position of the beam spot. At present the value is entered manually into the old program, but the goal is to get a more or less automatic system.

Firstly the grey-scale picture (fig 1) is transformed to a binary picture, and afterwards the centre of gravity of the beam spot in the binary picture is calculated.

One clear advantage is that one now uses a triggered picture with constant light conditions, while the running video used earlier have bright flashes every 0.35 s and then a fading after-glow.

4 HARDWARE AND SOFTWARE

The cameras are standard video cameras, i.e. Hamamatsu and Kappa. The PC program is written in LabVIEW with an IMAQ PCI-1408 frame grabber board and IMAQ Vision software for image processing.

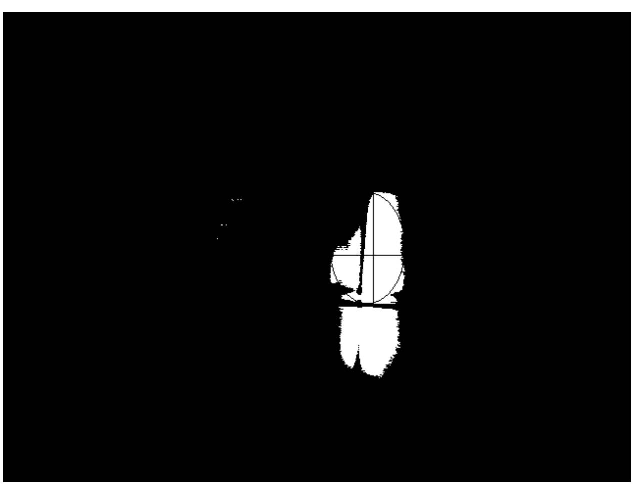

Figure 3. Binary picture where the beam spot is divided in two parts by a cross on the screen. The program chooses the upper half of the beam spot since it is the largest one. The thin cross shows the calculated centre of gravity.

5 SOME PROBLEMS AND IMAGE PROCESSING SOLUTIONS

5.1 Crosses on the screens disturb the measurements

To be able to get the absolute beam position there are crosses on the fluorescent screens, but these often divide the beam spot into two or four spots, and the program then selects the largest one as the beam spot (fig 3). When the beam moves, frequently another one becomes larger, and the change of position cannot be read. This problem is solved by dilation followed by erosion, 5-10 pixels dilation is needed (fig 4).

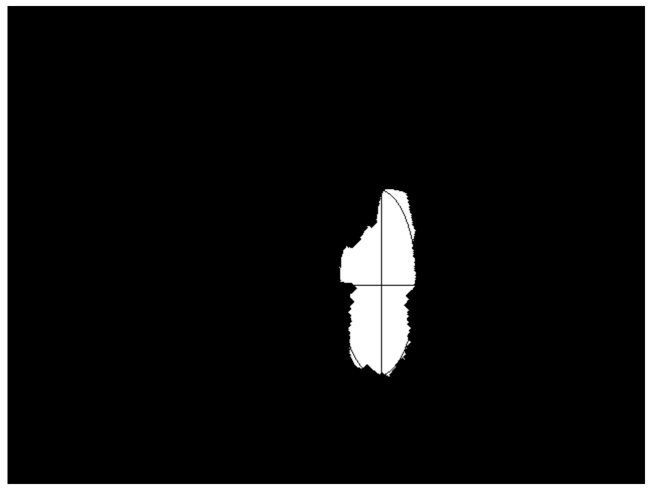

Figure 4. Beam spot after dilation and erosion. The cross in figure 3 is removed.

5.2 Weak beam

Three different methods are used to enhance weak pictures. Firstly stretching of the grey-scale, i.e. adjusting the thresholds for black and white. Secondly a logarithmic look-up table works better than a linear one for weak signals, and finally several consecutive pictures can be added.

5.3 Aperture limitations give false movements of the beam spot

When the shape of the beam is changed a part might fall either outside the aperture in the beam line or outside the fluorescent screen. Since such a cut is asymmetrical the apparent centre of gravity will change erronesly. This problem has not been addressed but one can e.g. decrease the quadrupole jumps or in some way check for this behaviour in the software.

REFERENCE

[1] G. Andler et al., “Progress Report for the CRYRING Facility”, EPAC’98, Stockholm, June 1998

IONISATION LOSSES AND WIRE SCANNER HEATING: EVALUATION, POSSIBLE SOLUTIONS, APPLICATION TO THE LHC.

C. Fischer
CERN - CH-1211 Geneva 23, Switzerland

Abstract

Harmful heating mechanisms, resulting in wire breakage, limit the utilisation of wire scanner monitors to below a given beam intensity. This threshold depends on the accelerator design parameters. In lepton colliders, the short beam bunches generate strong wake-fields inside the vacuum pipe which are sensed by the wire and are the predominant current limit. These effects can be minimised by a smooth design of the monitor cross section and by choosing a wire made of an insulating material [1].

A second source of energy deposition inside the wire, also present in hadron machines, and even when the wire material is insulating, results from collision and ionisation of the wire material atoms by the incident beam particles. Calculations are presented to evaluate the efficiency of this process and a possible solution is suggested which may reduce this limitation. An example is given for the case of the LHC.

1. INTRODUCTION

In wire scanner monitors, excessive heating may result in wire breakage. The main heating mechanism in proton accelerators results from energy deposition inside the wire due to ionisation of the wire material atoms by the incident beam. Calculations will first be developed in a view to evaluate the efficiency of this process. The two cases of 55 GeV leptons and 450 GeV protons are considered. The resulting limitations in the use of wire scanner monitors in LEP and in the future for the LHC [2] are discussed. A solution is suggested which, by using a special mechanical design of the monitor, permits to increase the beam current limit. An application is then made in the case of the LHC beam parameters.

2. HEATING FROM COLLISION LOSSES

2.1 Collision losses

For a high energy particle, ionisation losses are [3]:

$$\frac{1}{\rho}\frac{dE}{dx}=\frac{0.1535}{\beta^2}\frac{Z}{A}\left(F(\beta)-2\ln I-\delta(X)\right)[\mathrm{MeV\ \ cm^2\ \ g^{-1}}] \quad \textbf{(1)}$$

Z and A are the atomic and the mass numbers of the material atoms and ρ is the material density. The expression of *F(β)* depends on the incident particle rest mass and energy [3], [4]. *F (β)* =19.032 and 10.920 respectively for 55 GeV electrons and 450 GeV protons. The binding atomic electron energy into Carbon is I = 78 eV and δ(X), describing the density effect of the medium, is given by:

$$\delta(X) = 4.605\,X + C, \text{ with } X = \log(\beta\gamma).$$

For high energy particles, C = 2.868. Hence, density effects decrease the ionisation losses by respectively 39 % and 22 % for either type of particle mentioned above such that 1/ρ. dE/dx is equal to 2.41 MeV cm^2 g^{-1} for an electron at 55 GeV and 2.56 MeV cm^2 g^{-1} for a proton at 450 GeV.

2.2. Energy transferred to knock-on electrons

By collision with an incident particle of charge z, some atomic electrons are ejected from the wire material lattice. The number of these knock-on electrons with energy E is [4]:

$$\frac{d^2N}{dEdx}=0.153\frac{Z}{A}\frac{z^2}{\beta^2}\rho\frac{F}{E^2}$$

for I<< E ≤ T_{max}., with T_{max}, the maximum energy transfer. For leptons, T_{max} is one half of the incident particle energy, and for 450 GeV protons T_{max} is given by [4]:

$$T_{max} \cong 2m_0 c^2\beta^2\gamma^2 / (1+2\gamma\, m_0/M)$$
$$= 154.4 \text{ GeV}$$

with m_0 and M the electron and proton rest mass. F is a spin dependent factor nearly equal to 1 in our case and ρ = 2.2 g/cm^3 for Carbon. The energy transferred between E and E + dE at a depth x by a particle is:

$$dW = \frac{d^2N}{dEdx}ExdE$$
$$= 0.153\,(Z/A)\,\rho\, x\, dE/E$$

and between I, the binding electron energy, and T_{max}, each particle will deposit*:*

$$W = \int_I^{T\max} dW$$

$$W = 0.153\, x \ln(T_{max} / I), \text{ with x in cm.} \quad \textbf{(2)}$$

For a complete scan, x is the average wire thickness seen by each particle of the beam, and is given by:

$$<x> = \frac{\pi D^2}{4D}\frac{D}{vT}$$
$$= \frac{\pi D^2}{4vT}$$

where D is the wire diameter, v the wire speed and T the beam revolution period, 88.9 µs for LEP or the LHC and 22 µs in the SPS.

The energy transmitted to knock-on electrons by a beam of N particles during a scan is:

$$\Delta W_{scan} = N <x> W$$

whereas the energy actually lost by the incident beam through the wire is:

$$\Delta E_{scan} = \frac{1}{\rho}\frac{dE}{dx}\rho < x > N \qquad \textbf{(3)}$$

Hence the fraction η_1 of energy transmitted to knock-on electrons can be determined:

$$\eta_1 = \Delta W_{scan} / \Delta E_{scan}$$

However, all knock-on electrons will not contribute to the wire heating. Some of them escape the wire with a given momentum. The fraction η_2 of electrons leaving the wire must now be evaluated.

2.3 Escaping knock-on electrons

The practical range of an electron with energy E is [5],

$$r_{[g/cm^2]} = 0.71\ E^{1.72}_{[MeV]}$$

hence, the corresponding electron energy is:

$$E_{[MeV]} = (\rho \quad r_{[cm]} / 0.71)^{0.581}$$

At a depth x, the energy threshold allowing an electron to leave the wire is:

$$E_{thresh.} = (\rho \quad (t-x) / 0.71)^{0.581}$$

with t, the material thickness, which is in average $<t>=\pi D/4$ for particles traversing the wire. The energy threshold averaged through the wire thickness is therefore:

$$< E_{ion} >= \frac{1}{< t >}\int_0^{<t>} E_{thresh}\, dx$$

$$= \frac{1}{<t>}\left(\frac{\rho}{0.71}\right)^{0.581}\left[\frac{(x-<t>)^{1.581}}{1.581}\right]_0^{<t>}$$

or, $\quad <E_{ion}>_{[MeV]} = 0.772\ (\rho \ <t>_{[cm]})^{0.581}$

$$= 0.038 \text{ MeV}.$$

Out of all the generated knock-on electrons, the fraction getting enough energy to escape the wire is then, referring to Equation. (2):

$$\eta_2 = \frac{\ln(T_{max} / < E_{ion.} >)}{\ln(T_{max} / I)}$$

Results for electrons and protons are summarised in Table 1

2.4 Overall heating efficiency

Finally, the energy actually deposited inside the wire is:

$$E_d = \Delta E_{scan}\ \eta$$

with η, the overall wire heating efficiency given by:

$$\eta = (1-\eta_1) + (1-\eta_2)\ \eta_1 \qquad \textbf{(4)}$$

The first term of Equation 4 represents the fraction of energy lost by incident particles by other processes than knock-on electrons, and which is supposed to remain within the wire. The second one is the contribution of non escaping knock-on electrons. Applying the previous calculations to the LEP and SPS wire scanners, using 36 µm diameter Carbon wires, one get the results of Table 1. Values of η between 30 % and 35% have been quoted in the past [6].

Particles	Energy (GeV)	σ_{orth} (mm)	Wire speed (m/s)	η_1	η_2	η
$3.2.10^{12}$ $e^{\pm}$	55	0.4	0.4	62%	68%	**58%**
$2\ 10^{13}$ p	450	1	5	64%	71%	**55%**

Table 1

Other calculations performed in the case of LEP [1], with quartz and Carbon wires of various diameters lead to about the same results, showing a tendency of η_2 to increase to around 75% for wire diameters of 10 µm.

These data can be checked, considering the restricted energy loss rate, i.e. collisions with energy transfer smaller than a given threshold T_{thresh}. This restricted energy loss can be expressed as [4]:

$$\frac{dE}{dx} = 0.1534\left[\ln\left(\frac{2m_0c^2\beta^2\gamma^2T_{thresh.}}{I^2}\right)^{0.5} - \frac{\beta^2}{2} - \frac{\delta}{2}\right][\text{MeVcm}^2\ \text{g}^{-1}]$$

with $T_{thresh.} << T_{max.}$, all parameters having their previous definition. Taking $T_{thresh} = <E_{ion}>$, restricted energy loss rates dE/dx of 1.35 MeV cm^2 g^{-1} and 1.36 MeV cm^2 g^{-1} are obtained respectively for 55 GeV electrons in LEP and 450 GeV protons in the SPS. Comparing these numbers with the global energy losses calculated in section 1 in presence of the density effects, provides an efficiency η within the wire of 56 % for an electron and 53 % for a proton. The agreement with the data of Table 1 is quite good.

2.5 Wire heating

The energy actually deposited inside the wire during a complete scan is given by Equ. (3) weighed by the heating efficiency η. The wire volume heated in the dense part of the beam , ($\pm\ \sigma_{orth.}$), is:

$$V = (\pi\ D^2 /4)\ 2\ \sigma_{orth}$$

with $\sigma_{orth.}$, the rms beam dimension perpendicular to the scan direction. The temperature increase when scanning this wire region is then:

$$\Delta T = 0.683\ \eta\ \Delta E_{scan} / (V \ \rho \ \ c_p).$$

The Carbon specific heat c_p, averaged from 300 K to 1300 K, is 1.65 J $g^{-1}K^{-1}$ and with the other parameters taken from Table 1, then ΔT = 1000 K and 820 K after a scan performed respectively in LEP and in the SPS.

These results do not consider effects like thermal conduction within the wire, they could account for a few per cent of beneficial cooling, nor eventual small contribution from radiation inside the wire. It must also be remembered that in LEP, the main contribution to heating Carbon wires comes from electromagnetic fields [1].

However when Quartz wires used in LEP are considered, these results lead to temperature increases between

1600 K to 1700 K [1], for beam currents of 7mA. This is very close to the Quartz melting point. An experimental verification was possible. When inspecting a 30 µm wire, it was found thinned down to a few microns in the part interacting with the beam. At the bottom a pearl of melted material was observed, as shown in Figure 1. Hence this effect sets a current limit for the utilisation of wire scanners in LEP.

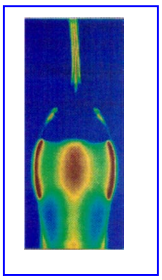

Figure 1: A 30 µm Quartz wire, used in a LEP wire-scanner monitor, after scans through 7mA beams. The thickness of the top part, traversed by the beam, is a few microns.

2.6 The case of the LHC:

In the LHC, the nominal beam intensity will be larger than in LEP by nearly two orders of magnitude. For an adequate measurement precision, the wire speed cannot be increased by more than a factor of 5 and at top energy, (7 TeV), the highest possible rms beam dimensions are smaller than one millimetre. At nominal current, the safest threshold to avoid destroying a Carbon wire by temperature increase is exceeded by more than one order of magnitude. This problem has been investigated in [2].

From the computation of the temperature rise, (section 5), it is obvious that the effect is proportionally reduced if the wire volume heated is increased. One solution is to act on the wire length interacting with the beam. In practice, this means that the wire must move not only in the direction of the scan but also in the orthogonal transverse direction. This is possible by combining the movement of a tilted sustaining mechanism, with the same tilt of the wire on its support such as to maintain it perpendicular to the transverse direction to be scanned. This is represented in Figure 2.

For a speed v_m of the mechanism, the angle θ determines the speed of the wire v_t in the scan direction, hence the distance $\Delta x = v_t T$ between consecutive measurements, with T the revolution period. The value of v_m gives the speed v_l in the direction of the wire and therefore its longitudinal displacement $\Delta l = v_l.T$ between two acquisitions; Δl can be chosen to be of the same order as the dense part of the beam distribution hitting the wire, i.e. $\Delta l = 2\sigma_{orth}$. Considering a round beam with rms dimensions of 0.5 mm, Δl = 1mm is achieved with v_l = 11 m/s. With a tilt θ of 10 degrees, v_t = 2 m/s, which provides a suitable spacing of 178 µm between consecutive points. This sets v_m = 11,2 m/s for the mechanism.

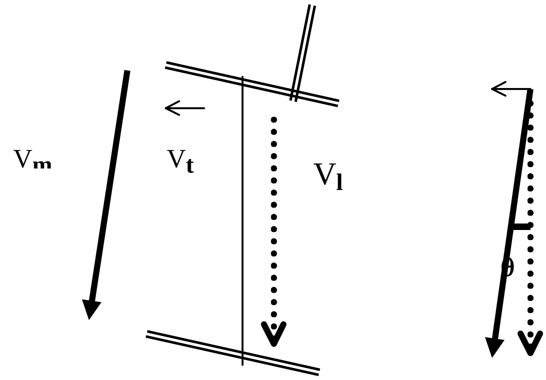

Figure 2: Proposed principle of a wire displacement in both transverse directions and for an horizontal scan.

The portion of wire interacting with the beam is different at each acquisition, and, over the dense part $\pm\sigma$, it is increased by a factor $f = 2\sigma/v_t T$, i.e. f = 6 in this case. The total wire longitudinal displacement over a complete scan, (5 mm), is 30 mm in this case.

This discussion only sets principles. A refined mechanical study is needed before implementation, the acceleration and deceleration phases of the mechanism must in particular be carefully investigated. In this scheme, the wire diameter variation over its active length during a scan must be limited in order to minimise the error made on the signal amplitude.

3. CONCLUSION

These calculations show that in wire scanner monitors, an efficiency of about 55% is to be considered for the heating of the wire by energy deposition from collision losses. The observation of a Quartz wire used in LEP seems to corroborate these figures. For the LHC the limiting current could be increased considerably using the technique described, provided that a proper mechanical movement can be designed.

ACKNOWLEDGMENTS

Wire scanners in LEP were developed thanks to the work of several colleagues. In particular, it is a pleasure to acknowledge R. Jung for numerous discussions and permanent support, J. Koopman for his infallible technical presence, the skill of J. Camas and M Sillanoli to handle mounting and installation and J.J. Gras who made the control software available.

REFERENCES

[1] C. Fischer, R. Jung, J. Koopman, Beam Instrumentation Workshop, Argonne, IL, 1996, page 290.

[2 J. Bosser, C. Bovet, Wire Scanners for the LHC, LHC Project Note 108, september. 97.

[3] R.M. Sternheimer, M.J. Berger, S.M. Seltzer, Atomic Data and Nuclear Data Tables 30, 261-271, 1984.

[4] Review of Particle Physics, Volume 3, Number 1-4, 1998

[5] F. Sauli, Principles of Operation of Multiwire Proportional and Drift Chambers, CERN 77-09, May 1977.

[6] J. Bosser et Al. The Micron Wire Scanner at the SPS, CERN SPS/86-26, December 1986.

IONISATION PROFILE MONITOR TESTS IN THE SPS

C. Fischer, J. Koopman
European Organisation for Nuclear Research (CERN)
CH-1211 Geneva 23, Switzerland

Abstract

A beam profile monitor, from DESY, based on the ionisation of the rest gas, was installed in the SPS in 1997. Horizontal beam profiles obtained from the extracted positive ions are presented. It is known that in this case some broadening affects the signal, which limits the monitor resolution. This broadening results from the transverse momentum that the ions gain within the space charge field of the circulating beam.

In order to improve the resolution for LHC applications, the monitor was modified during the 1998/99 winter stop. A magnetic focusing was incorporated. The aim is to analyse the signal provided by collecting the electrons, rather than the ions, of the ionised rest gas. The details of this new set-up and the expectations for the resolution limit will be compared to the measurement results.

1. INTRODUCTION

Rest gas monitors are used in many high energy accelerators in order to reconstruct transverse beam distributions [1], [2], [3]. The signal which is used results from the collection of either the ions or the electrons produced by the ionisation of the rest gas due to the circulating beam passage. This type of device is used so far to analyse beam RMS dimensions larger than one millimetre. Ions or electrons are produced with a given transverse velocity. During part of their drift to the analysing device, they also experience space charge effects from the circulating beam, and their transverse momentum is enhanced. With their much larger rigidity, ions are less sensitive to these counteracting phenomena although their drift time through the beam space charge forces is longer. But a resolution better than 1 mm is difficult to achieve.

Such a device, obtained from DESY [1], was installed in the SPS in 1997. Tests were performed on proton beams. Figure 1 recapitulates the fundamentals of this monitor suited to work in the horizontal transverse plane. Two grids symmetrically positioned at 50 mm above and underneath the beam orbit, are set at inverse voltages, with a possible amplitude up to 5 kV. Ions and electrons are extracted in opposite directions, depending on the grid voltage polarity. In the basic configuration, positive ions are extracted towards the detection chain. They are then accelerated to a Multi-Channel Plate, which acts as a signal amplifier. The MCP gain can be adjusted by varying the voltage difference between input and output up to 1 kV. Electrons extracted from the MCP are accelerated, by potential differences up to 12 kV, to a high voltage plate supporting a phosphorescent screen. The transmitted light is reflected on a mirror to a CCD camera.

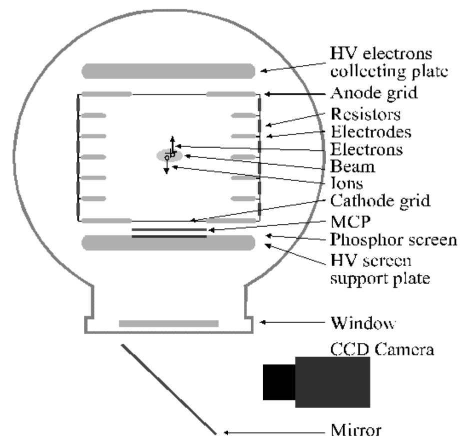

2. RESULTS WITH IONS

Profiles of 10^{13} proton beams were recorded during entire SPS super-cycles, from 26 GeV to 450 GeV, by looking at the signal provided by ions. Results are in Figures 2 and 3.

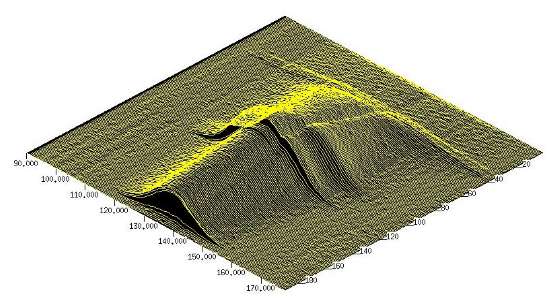

Figure 2: Proton beam horizontal profiles, measured from 26 GeV to 450 GeV using the signal from ions.

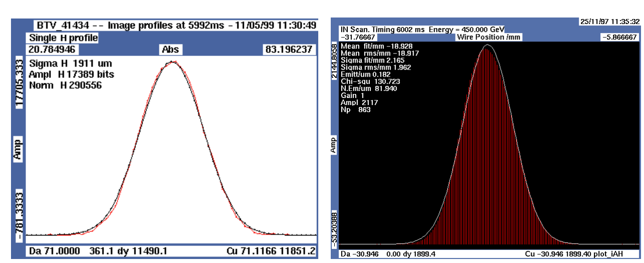

Figure 3: Horizontal proton beam profiles, with gaussian fit, at 450 GeV, taken with the IPM (left) and the wire scanner (right).

Figure 3 shows that both the IPM and the wire scanner monitor, which is our reference, provide a similar proton beam RMS value, respectively 1.9 mm and 2.1 mm. However, considering the ratio of the amplitude function values at the two monitor locations, the IPM should measure a narrower beam by a factor of 1.9, i.e. around 1mm. In this case, an enlargement of the signal of 100 % is observed when using the ion signal. This is not satisfactory to evaluate RMS dimensions below 2 mm.

3. THE IPM IN ELECTRON MODE

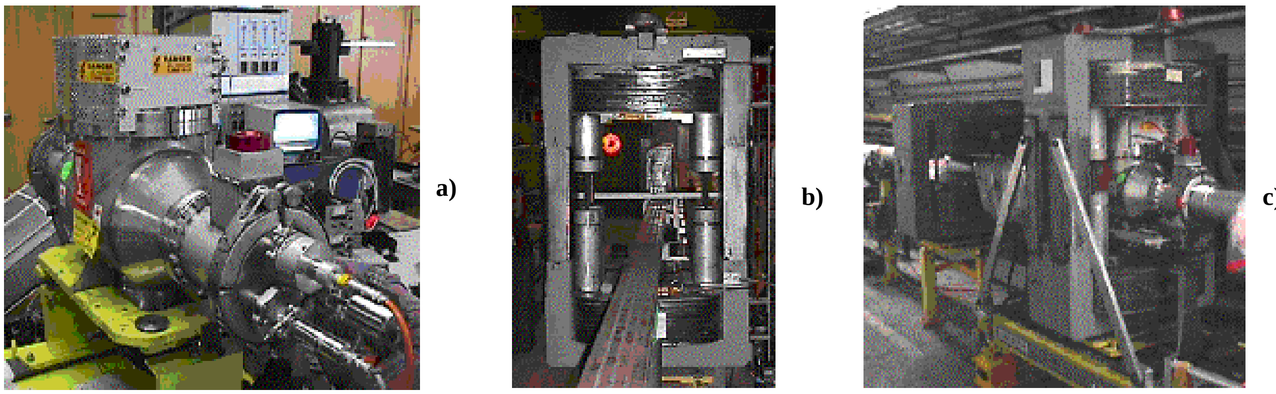

Figure 4: a) the monitor before insertion within the magnet b) the modified magnet on the measuring bench with the two wedges increasing its gap, c) the assembly installed, with, in the back, the orbit distortion correction magnet.

Resolutions far below 1mm are requested for the LHC era, both in the SPS and in the LHC; RMS beam dimensions of this order are expected at 450 GeV. At 450 GeV, the possibility to exploit synchrotron radiation is not established in the LHC yet. An IPM monitor is one of the candidates to measure transverse beam distributions. Looking at the signal of electrons instead of ions should permit to improve the resolution. With their much smaller mass, electrons also experience the parasitic transverse kicks mentioned for the ions, but they are also much easier to channel along a magnetic field with very short precession radius. As mentioned in previous estimations [2], only a few per cent of the electrons are generated with transverse momentum larger than 500 eV. This corresponds to a Larmor radius of 0.375 mm in a magnetic field of 0.2 T.

During the 1998/99 winter stop, the IPM was adapted to make possible the exploitation of the signal from electrons. The adequate polarities were set to the plates providing the accelerating voltages. After a few investigations, the solution retained to generate the magnetic field was to incorporate the monitor within the gap of an available dipole. The monitor height was first reduced, (Figure 4a)), by modifying at the top the different high voltage connections, and at the bottom, by a new design of the extraction system of the light transmitted from the phosphorescent screen. An overall height of 700 mm was achieved. The magnet gap was increased accordingly by a factor of 3 from its initial value of 224mm. This was performed by the insertion, between the two magnet halves, of two steel wedges, as shown in Figure 4b). From the nominal field of 0.24 T, 0.077 T was expected by linear scaling. Magnetic measurements performed on the modified magnet revealed that in the central active part of the monitor a field of 0.060 T was actually produced: stray field effects are slightly enhanced with the larger magnet gap. However, the electron transverse momentum distribution is such that this field should permit the evaluation of beam RMS values of 1 mm with less than 10% of aberration effects. The field variation across the active monitor region is around 5%. Within the SPS supercycle, the magnet is pulsed only during the proton cycle, without acting on leptons.

The integrated field was measured to evaluate the perturbation generated on the beam closed orbit. Results were in accordance with expectations. To compensate for the kick introduced by the magnet, a similar magnet, with standard gap, was installed immediately upstream of it, (Figure 4c)). The resulting local calculated closed orbit distorsion is 2 mm at 14 GeV and becomes negligible throughout the acceleration to 450 GeV. This has been confirmed by measurements.

4. RESULTS WITH ELECTRONS

Preliminary tests of the modified monitor could be performed on proton beams this year during the first two weeks of the SPS setting-up. Starting without the magnetic field, observations were made of a beam of 10^{13} protons injected at 14 GeV and accelerated to 450 GeV. Results are presented in Figures 5, 6 and 7. Corresponding profiles acquired with the wire scanner monitor are also displayed.

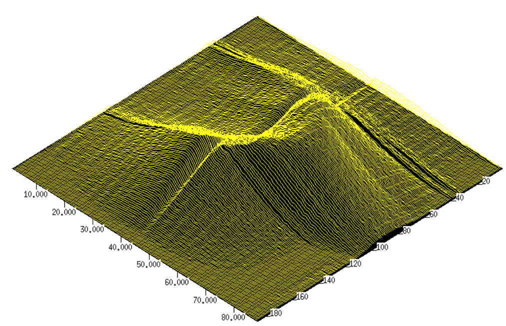

Figure 5: Horizontal profiles recorded using the signal from electrons, without magnetic field, of 10^{13} protons, accelerated from 14 GeV to 450 GeV.

At 14 GeV, a RMS value of 2.815 mm is obtained, (Figure 6), from the IPM. By comparison, the horizontal RMS value provided by the wire scanner is 6.225 mm; by scaling according to the machine optics parameters, one should get 3.28 mm at the IPM. The measured fitted value is 14 % smaller.

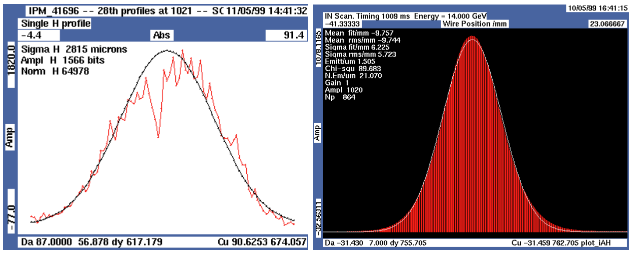

Figure 6: Horizontal profile taken on 10^{13} protons at 14 GeV, with the IPM in e^- mode (left), and the wire scanner (right). B = 0 T

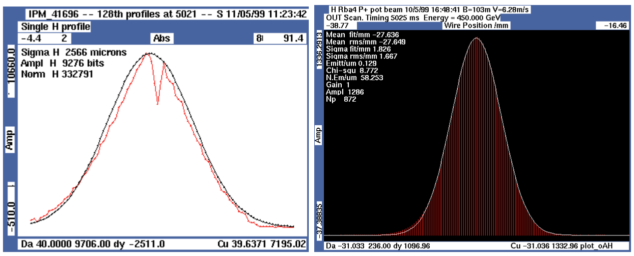

Figure 7: Corresponding profiles measured at 450 GeV during the same acceleration cycle.

The same data taken at 450 GeV are displayed in Figure 7. The beam has shrunk and RMS values of respectively 2.566 mm (IPM), and 1.826 mm (wire scanner), are measured. Again, by scaling with the wire scanner data, a value of 0.960 mm should be observed at the IPM: hence a quadratic enlargement exceeding 200% affects the expected results.

Finally, the magnetic field was switched ON in the monitor, and beams of around 1.6 10^{13} protons were investigated from 14 GeV to 450 GeV. Two magnetic field levels were considered, 0.018 T and 0.036 T. Data measured with the latter value are presented in Figure 8 and Figure 9.

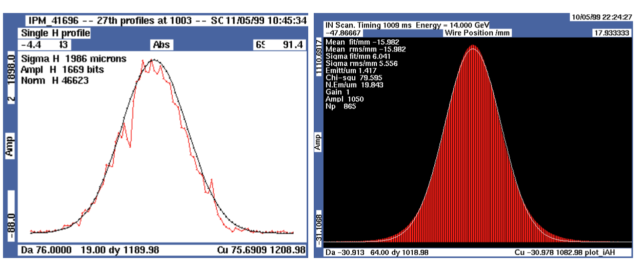

Figure 8: Horizontal profile of 1.6 10^{13} protons at 14 GeV, with the electron signal (left), and the wire scanner (right). B = 0.036 T

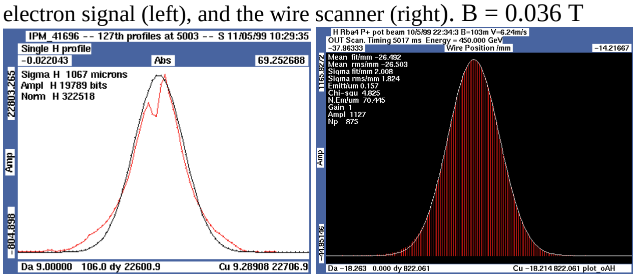

Figure 9: Corresponding profiles measured at 450 GeV.

At 14 GeV, a fitted RMS value of 1.986 mm is obtained from the IPM profile, (Figure 8). With the wire scanner, the corresponding fitted beam width is 6.041 mm, and the resulting RMS width at the IPM should be 3.180 mm. A relative shrinking of 35% is again observed at the IPM. This discrepancy will be investigated later. So far, not enough time was available to clarify it. The same observation was made at the lower field level.

However, looking at the 450 GeV data, an RMS beam width of 1.067 mm is provided from the IPM profile. This fits very well the RMS wire scanner value of 2.008 mm when scaling with the optics. The same conclusion is relevant for the data recorded with a magnetic field of 0.018 T. Thus, RMS dimensions of 1 mm can apparently be measured within a few per cent even with a modest magnetic field. The small fraction of electrons with large transverse momentum, and hence large precession radius, probably appear in the tails which are ignored by the fit, (Figure 9).

5. CONCLUSION

The IPM monitor installed in the SPS has been adapted to analyse the signal provided by the electrons. With the nominal vacuum, the signal to noise ratio is entirely satisfactory. More study remains to be done to fully understand the observations. However, the preliminary observations made recently are very promising. Without magnetic focusing, a signal enlargement of around 2 mm is observed on RMS values of 1 mm. This is slightly worse than what is observed with ions. Obviously, the behaviour difference between ions and electrons depends on space charge forces which, during our tests, were limited by moderate beam intensity.

With the addition of a magnetic field, even set at rather low values, RMS dimensions of 1 mm have been measured with an accuracy of a few per cent. An improved knowledge of the instrument, will hopefully allow us to refine, in the near future, the determination of this resolution limit.

ACKNOWLEDGMENTS

The transformation of the monitor was achieved in a short time thanks to the collaboration of many colleagues. In particular, G. de Rijk helped us to find how to generate the magnetic field, G. Kouba and his team supplied and modified the POD magnet, D. Cornuet and J.M. Dutour organised the magnetic measurements. J. Ramillon handled the mechanical design study of the new monitor, J. Camas and M. Sillanoli took care of assembling and installation. G. Arduini performed simulations, measurements and implementation of the orbit correction, Finally, we thank R. Jung who proposed us this challenging study, H. Schmickler and K. Wittenburg who supplied the monitor and G. Ferioli for private discussions.

REFERENCES

[1] K. Wittenburg, Emittance Measurement in the Proton Accelerator in DESY, Emittance in Circ. Accel., KEK 95-7, Sept. 95.

[2] R. Connolly et Al., A Prototype Ionisation Profile Monitor for RHIC, Proceedings of PAC 1997, Vancouver, p 2152.

[3] J.R. Zagel et Al., FERMILAB Main Ring Ion Profile Monitor System, Proc. of PAC 1997, Vancouver, p 2166.

PERFORMANCE OF THE NEW SPS BEAM POSITION ORBIT SYSTEM (MOPOS)

C. Boccard, T. Bogey, J. Brazier Ltd, J. de Vries, S. Jackson, R. Jones,
J.P. Papis, W. Rawnsley (TRIUMF), K. Rybaltchenko, H. Schmickler.
SL Division- European Laboratory for Particle Physics (CERN) - Geneva - Switzerland

Abstract

The orbit and trajectory measurement system COPOS of the CERN SPS accelerator has been in operation since the construction of the machine in 1976. Over the years the system has been slightly modified in order to follow the evolving demands of the machine, in particular for its operation as a p-pbar collider and, since 1991, for the acceleration of heavy ions.

In 1995 the performance of the system was reviewed and the following shortcomings were identified:
- lack of turn-by-turn position measurements due to the 1ms integration time of the voltage to frequency converters used for the analogue to digital conversion (to be compared with a revolution time of 23 µs),
- ageing effects on the 200 MHz resonating input filters, which had over the years drifted out of tolerance. As a consequence the signal to noise ratio, the linearity and the absolute precision were affected,
- the calibration system based on electromechanical relays had become very unreliable, such that frequent calibrations were no longer possible,
- a remote diagnostic for the observation of timing signals relative to the beam signals was missing.

For the above reasons a large-scale upgrade program was launched, the results of which are described in the following sections.

1. DESCRIPTION OF THE NEW SYSTEM

1.1 Analogue processing chain

The new Multi Orbit Position System (MOPOS) is based on 200 MHz homodyne receivers, which follow a pair of matched 4.4 MHz bandpass filters. In order to enable the system to measure both high intensity proton beams and low intensity heavy ion beams, the dynamic range has been increased to 90 dB with the help of front-end low noise amplifiers. The resulting signal is then sampled or peak-detected, depending on the type of beam, and sent to the acquisition boards as a serial stream after conversion in 14 bit ADCS (see Figure 1).

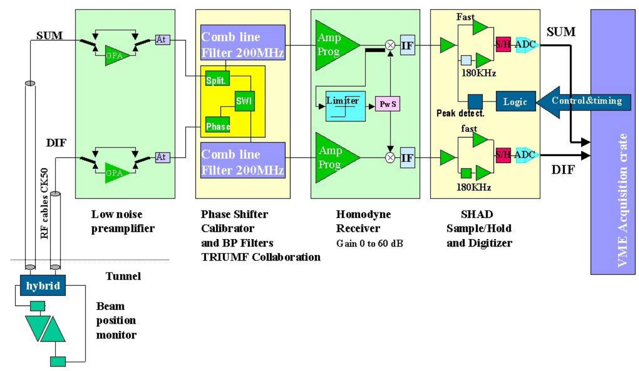

Figure 1: Synoptic of a MOPOS chain.

1.2 Acquisition architecture

The acquisition system is based around the CERN-SL standardised PowerPC (RIO2 8062) and makes full use of its memory, interfaces and processing power.
Using 3 VME slots, the CPU and 2 PCI extension boards can accept up to 6 PCI mezzanine cards (PMC). Each PMC can process data from 20 ADC channels (10 pick-ups). After treatment in a dedicated FPGA, a FIFO collects the acquired data in synchronism with the SPS revolution frequency. Sampling every 23 µs gives a data stream of 8Mbytes/s.
The local PCI DMA controller transfers the data from each FIFO to the main memory at a rate of 70Mbytes/s. A total of 224 Mbytes of memory enables turn by turn data for up to 40 BPMs of a complete SPS super-cycle of up to 28s to be stored.

1.3 Software architecture

The 240 channel SPS Orbit acquisition system is implemented on 6 PowerPCs. These run under the LynxOS operating system, making use of its multi threaded real-time capabilities. Orbit acquisitions process the raw data on request. Calibration and initialisation data tables are stored externally in an Oracle database and locally in a non-volatile RAM board to enable a fast restart.

2. NEW FUNCTIONALITIES

2.1 Multi-turn capability

The previous acquisition system, based on voltage to frequency converters, was not able to give position data on a turn-by-turn basis. By using 14 bit ADCs to sample each SPS turn, the MOPOS system can store multi-turn data, which can then be used in the computation of any relevant machine parameter. The idea is to store each turn of each elementary cycle of the SPS machine, such that the system has a multi-cycle, multi-user capability.
Some examples of the types of simultaneous acquisitions that can occur are listed below:

- Transfer line steering requiring data from the first machine pick-ups.
- Injection optimisation requiring a first turn reading.
- Observations of kicks or bumps requiring a thousand turn reading from several pick-ups.
- Orbit readings (i.e. the 1ms to 20 ms average of beam position data) occurring at any time in the cycle.
- Extraction optimisation using the phase advance measurement that is calculated by the harmonic analysis of transverse excitation signals from the last horizontal BPM before each extraction line.
- Miscellaneous studies - e.g. in 1997, the in-depth analysis of noise on the MOPOS prototype was used to find a noisy extraction power supply [1].

2.2 New calibration hardware and RF filters

Due to the differences between the beams in each elementary SPS cycle (protons, electrons, positrons or heavy ions), the system must be calibrated for each of these machine cycles, and for each receiver gain. Single bunches induce a ringing excitation in the pair of 200MHz filters whereas a train of bunches permits the tracking of a quasi-continuous signal. The new MOPOS filters for the sum and difference channels provide a minimum of 60dB isolation and a 55° phase shift capability to compensate for cable delays.

As part of the LHC SPS upgrade collaboration with the TRIUMF laboratory in Canada a new solid state calibrator was developed which allows frequent calibrations to be performed. The 200 MHz combline filters mentioned in the PAC 97 paper [2] had their cases constructed from 1.5 mm brass sheets, which were folded and soldered to form a box. This technique was not consistent enough to ensure that all pairs were matched to within 3 degrees over the central 1 MHz region. For the production run of 300 pairs a more robust design from Lorch Microwave was used. The new filter cases are machined from aluminum blocks, which gives a much better reproducibility. A minimum wall thickness of 4.8 mm was also introduced for improved rigidity.

Tuning, testing and recording of the calibration parameters for each module was automated with test sequences written to run on a HP 8753D network analyzer. The analyzer was programmed to set the calibrator mode and the phase shifter voltage for each of 62 tests, and prompted the Aimtronics technician to change cable connections and perform tuning procedures when necessary. An example of the results of such a test can be seen in Figure 2.

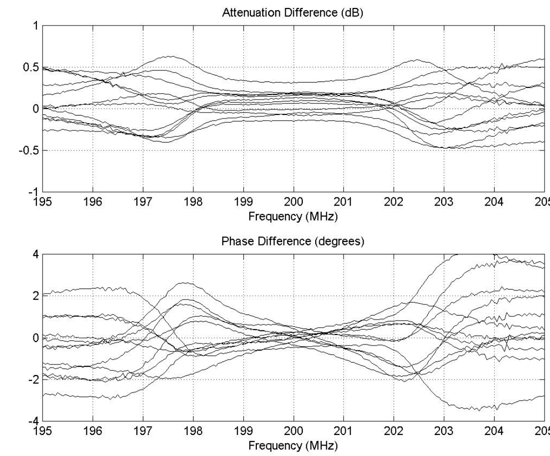

Figure 2: The attenuation and phase matching of 12 pairs of filters. The phase matching easily satisfies the required < 3 degrees over the central 1 MHz region.

2.3 Graphical User Interface

System configuration aspects were implemented in a Broker architecture, where individual threads communicate with an Oracle database and with the acquisition systems.

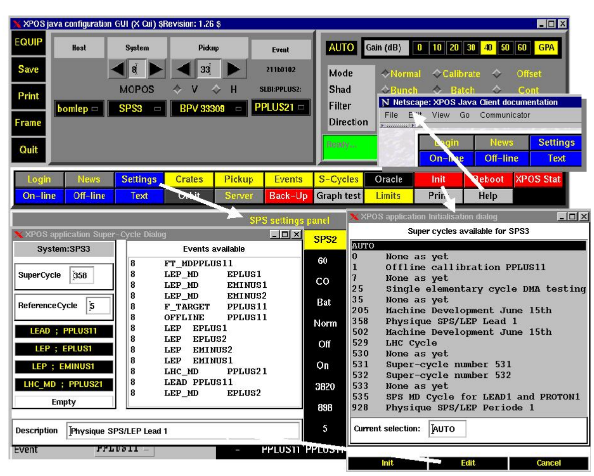

Figure 3: Xpos Java configuration graphical user interface.

This Broker hides the implementation details of the front-end systems. A versatile configuration client is provided in Java, which allows for local graphical user interfaces from any platform and remote WWW access using a dedicated gateway to the SL equipment layer.

2.4 Expert tools

2.4.1 Remote Scope

For diagnostic and timing adjustment purposes, each building is equipped with a GPIB controlled oscilloscope. A signal multiplexer allows the selection of either the sum, difference or timing signal for each channel. Settings are archived and retrieved from the Oracle database.

This diagnostic is integrated in a LabView application, which provides the graphical user interface and allows for data retrieval via the SL-EQUIP package (see Figure 4).

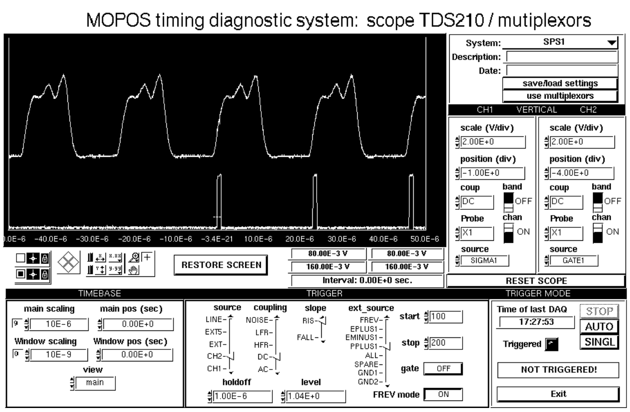

Figure 4: Scope and multiplexer - LabView interface.

2.4.2 Multi-turn trajectories display

A graphical interface is also provided to display up to 1000 turns of the sum signal and either the difference or the position versus time for up to ten selected pick-ups.

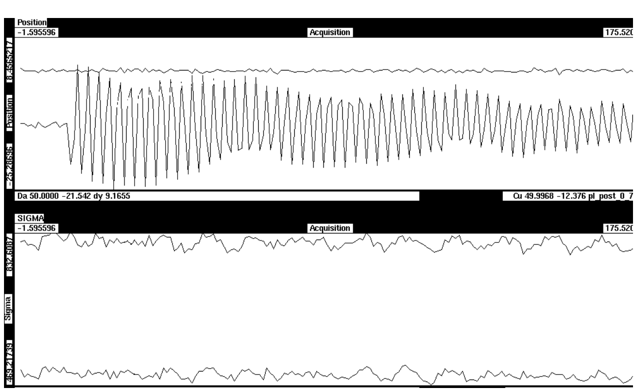

Figure 5: A trajectory on the multi-turn display after a transverse kick (measured on a heavy ion beam)

2.5 Performance

With a proton beam and a gain of 10 dB, the resolution of a 42mm aperture horizontal pick-up is 0.03 mm peak-to-peak, equivalent to a 5 micron rms on the orbit position (Figure 6).

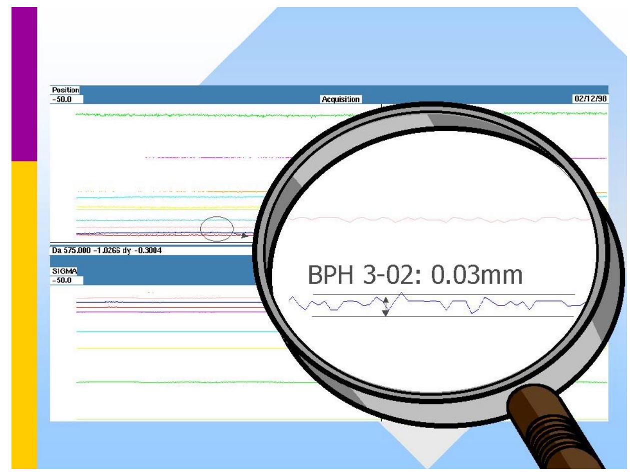

Figure 6: Noise on proton trajectories.

With an ion beam, a gain of 70 dB is necessary [3], and a resolution of 0.51 mm peak-to-peak is obtained (Figure 7).

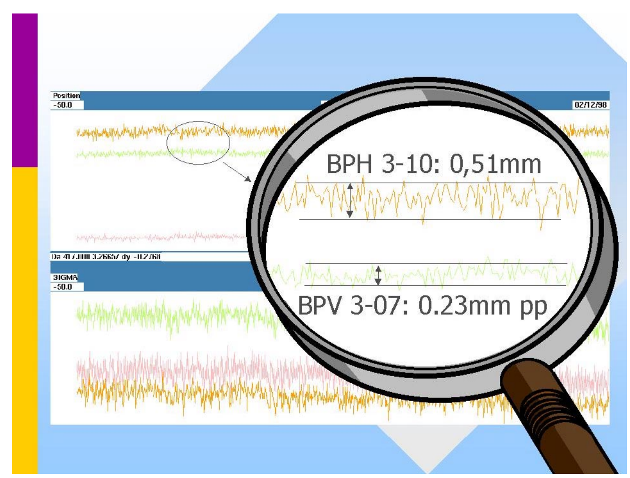

Figure 7: Noise on ion trajectories.

REFERENCES

[1] O. Berrig, “Noise in BA6”, SL-BI,. 1997.

[2] W. Rawnsley, "An RF Signal Processing Module for the SPS Orbit Observation System Upgrade", Proceedings of PAC’97, Vancouver, June 1997.

[3] : C. Boccard, “Performances de Mopos”, Journee de l'instrumentation, SL-BI, Dec. 1998., SL-Note-98-078(BI)

Analysis of the Proton Beam in the DESY Transport Lines by Video Readout

F. Solodovnik, IHEP and T. Limberg, K. Wittenburg; DESY

Abstract

Injection efficiency, beam optic matching and emittance preservation are very important parameters in achieving a high luminosity in large proton accelerators. We improved the analysing system of the phosphor screen readout of the proton transport lines in the accelerator chain of HERA with respect to the parameters above. The screens are read out by simple CCD video cameras. The signals are stored in local frame grabbers. An analogue output of the stored image is multiplexed and read-out by a fast PCI frame grabber card in a PC. The beam orbit and the beam emittance can be measured from each screen. A Visual Basic program is used to displays the trajectory and the envelope of the beam from a single transfer. The same program helps to drive bumps to achieve a proper steering through the line. The beam width can be measured from selected screens to calculate the emittance and other beam parameters including their errors. The read out and analysing system will be described and measurements will be shown.

1 INTRODUCTION

The Position and shape of the proton beam is observed in all transfer lines by thin luminescence screens read-out by TV video cameras (12 screens in the transport line from DESY III to PETRA (P-line) and 20 screens in the line between PETRA and HERA (PR-line)). Some cameras of the PR line were connected to a in-house developed local frame grabber, triggered by the transfer of protons to display a visible spot of a selected screen on a TV screen in the control room. The centre of gravity was determined in this system using all the light detected by the camera, including reflections. This led to large errors in the position measurement due to background problems. A measurement of the beam size was not foreseen.

This old system has been upgraded with new hardware and software (see Fig. 1): 12 new local frame grabbers (Model MBS, Compulog) were installed in the P-line, observing the adjacent 12 screens. They store the two TV-frames following a transfer-trigger. Both grabber types provides an analogue TV output of the stored frames. The analogue signals are connected to two video multiplexers, one for each transport line. A dedicated PC containing a fast PCI frame grabber card (Type: DT3155, Data Translation) is used to control the multiplexers and to collect and analyse all frames from

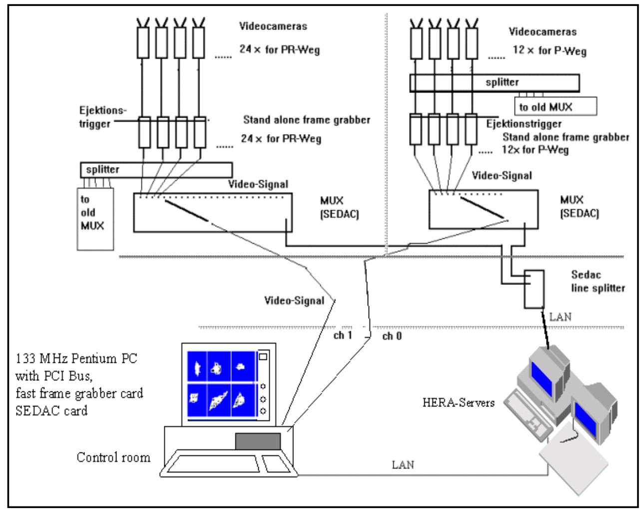

Figure 1: Layout of the readout scheme

one transfer. This provides a fast analysis of the TV signals without the traffic on the local area network (LAN) of the control system which would otherwise be needed to transfer all the frames though the LAN.

2 POSITION MEASUREMENT AND ORBIT CORRECTION

Fig. 2 shows a typical TV image of a screen stored after a beam transfer. The measured positions of the beam are displayed graphically in a Visual Basic program which provides full control of the screens, camera readout and correction magnets. Fig. 3 shows a

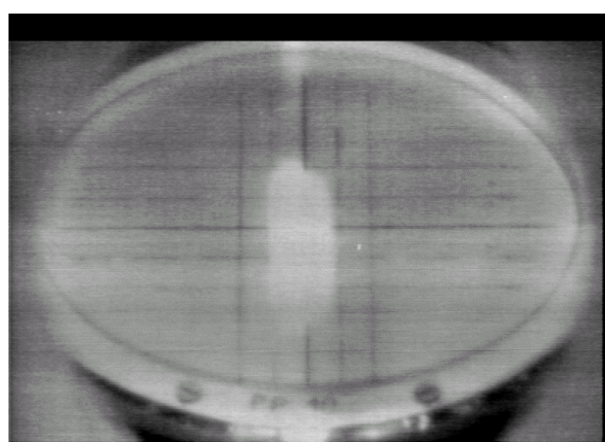

Fig. 2: Beam spot on a screen. The screen is illuminated by an external light source

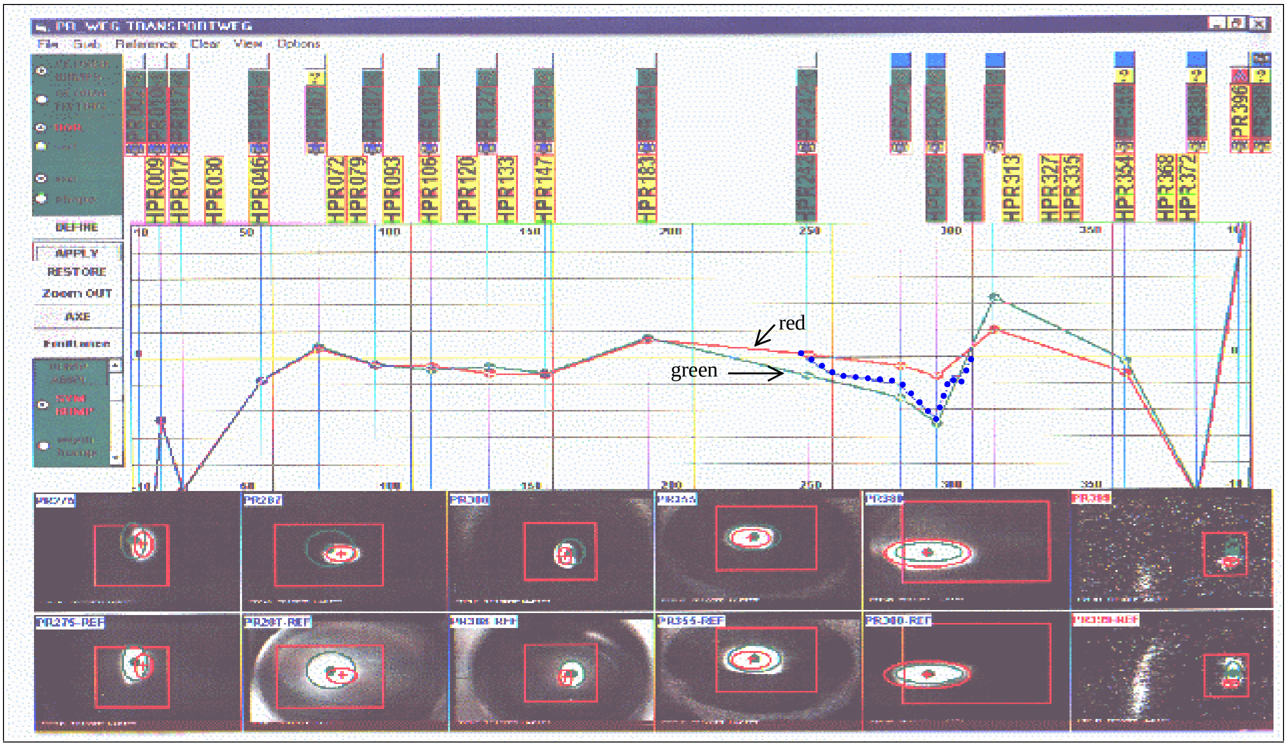

Fig.3: Display of the PR-line Visual Basic Program

display of the program. The two rows on top indicate the screens and the correction coils (the horizontal plane is shown). Each screen and coil can be activated for orbit measurements and corrections. In this example, a local bump is used to correct an orbit deviation. The green trace shows a big excursion (-5 mm) of the beam in this region before applying the bump. Three coils have been activated (dark) to apply a closed bump. The blue (dotted) line indicates the bump needed to correct the excursion. Note that it has to be on top of the deviated orbit to correct the orbit. The red line shows the measured orbit after applying the bump. A fairly good correction was achieved. [1]
The activated screens are shown beneath the orbit window (first row) together with saved reference pictures (second row). The operator can specify a region of interest (red box) for each picture. This feature allows to calculate the position of the beam inside the selected region only, which is helpful for the analysis of noisy pictures: A pixel for pixel subtraction of a stored background reference (made without beam) is done first for each individual image. The position of the beam is determined by the centre of a gaussian fit to the beam profile which was found to be more precise than the centre of gravity method. The centre of the beam (+ and • for reference) and a FWHM line from the gaussian fit is displayed.

[1] The operator can select a single coil, a closed bump or a desired orbit excursion. In the last case the program calculates a superposition of closed bumps which fits best to the desired excursion.

The reproducibility of the position measurement from shot to shot is better than 0.5 mm. The absolute beam position relies on reference marks on the screen and on the positions of the screens in the vacuum chamber and is probably not better than 1-2 mm. However, after optimising a transport line for maximum efficiency, a good reference orbit can be saves in a reference database and used to compare with actual orbits. This provides a simple and fast way to setup and maintain the transport lines for maximum efficiency.

3 PROFILE MEASUREMENTS

The beam image on the screen can also be used to determine the beam size and its emittance. Projections of the region of interest of the video signal result in the (vertical and horizontal) profiles of the spot. Profiles are shown in Fig. 3 together with gaussian fits. Unfortunately many of the screens suffer from saturation of the TV camera signal at full beam intensity which results in large errors in the beam size measurements. Therefore a remotely controllable diaphragm has been installed in front of a few CCD cameras to reduce the amount of light. Reliable profiles could then be measured with emittances consistent with those measured in the circular accelerators. But the diaphragm is typically smaller than 1 mm. Therefore diffraction may broaden the measured profile. Neutral density filters, which may be a better solution, are foreseen in the future. At the moment, the emittance determination relies on the theoretical optical parameters of the transport lines. For the future it is planed to use more than 4 screens in the line to measure all optical parameters together with their errors within one transfer [1].

The program displays the measured width of all screens together with the theoretical beam envelope. Fig. 4. shows such a measurement for the p-line. This view gives immediately a hint to the operator at which location a better orbit steering may increase the efficiency of the transport line by reducing the overlap of the aperture and the beam envelope. Again, the two rows on top indicate the screens and correction coils. The activated screens are shown beneath the orbit window. The beam envelope and the measured size (FWHM) are shown in the middle, together with the aperture limits of the transport line. A line at the positions of the screens indicates the measured beam size. This time, all signals were saturated and show a much bigger size than the theoretical envelope except for screen at 186 m, which is in agreement with the expectation.

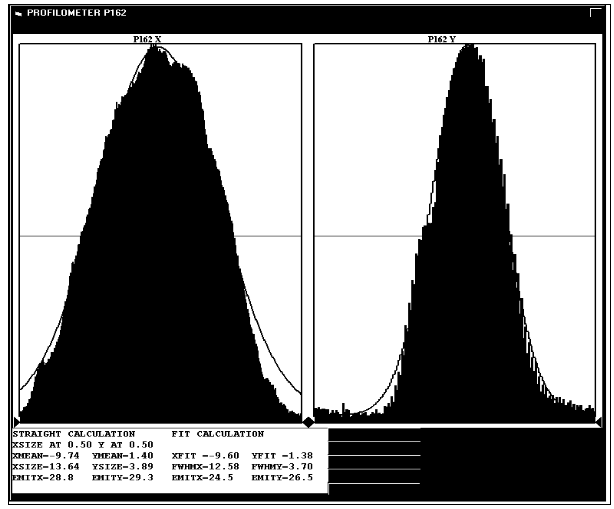

Fig. 3: Horizontal and vertical Profile of the screen 162 in the P-line (after installation of a diaphragm)

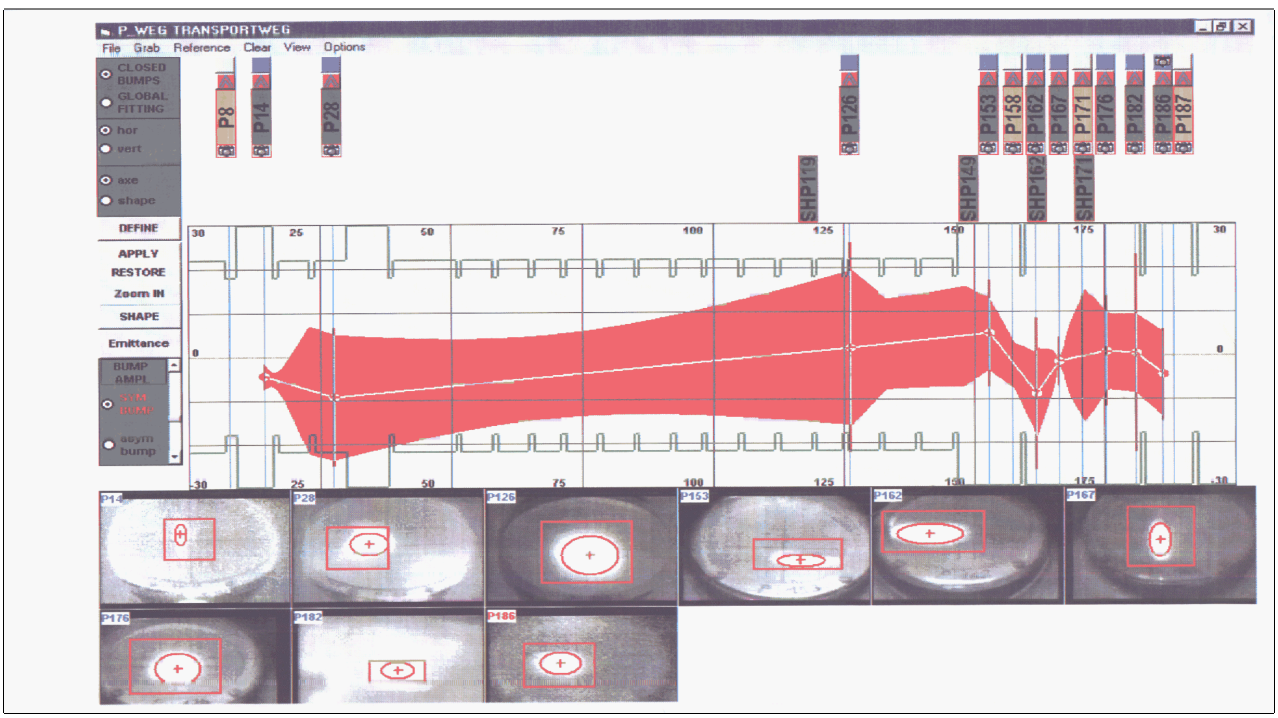

Fig. 4: Display of the beam envelope and the aperture in the p-line.

4 SUMMARY

The diagnostic for the proton transfer lines have been improved by using a simultaneous video grabbing scheme of the phosphor screens. A better analysis of the TV images is most helpful to achieve an optimal efficiency of the lines. To measure the emittance of the beam independent of the theoretical beam parameters by e.g. the 3 gradient method [2] or the position method, the quality of the TV signal needs an improvement, mainly saturation of the cameras has to be avoided.

ACKNOWLEDGEMENT

We would like to thank Mr. Bernd Sarau for preparing the screens and their video readout.

REFERENCES

[1] G. Riehl et al., "Measurements of phase space distributions", DIPAC'95, Travemünde, May 1995.
[2] M.C. Ross et al., "Automated Emittance Measurements in the SLC", Slac-Pub-427

COMPARATIVE TEST RESULTS OF VARIOUS BEAM LOSS MONITORS IN PREPARATION FOR LHC

J. Bosser, G. Ferioli
CERN, Geneva, Switzerland

Abstract

Beam loss detectors will play an important role in the protection of the superconducting LHC magnets.
Different types of detectors have been tested in the SPS ring and secondary beam lines with a view to their possible use for this application.
This paper describes the measurements made with: microcalorimeters at cryogenic temperatures, PIN diodes, ionisation chambers, scintillators, and ACEMs.
Measurements made using proton beams showing their relative sensitivities, linearities in counting or analog mode and minimum detection level will be presented.

1. INTRODUCTION

Beam loss monitors, BLM's, are commonly used on most of the CERN accelerators and transfer lines. They usually provide a relative diagnostic aimed to help the operators in their optimisation but also to protect the machine components against loss damages. For cryogening machines where excessive losses will induce magnet quenches their use is becoming mandatory.
For the LHC the "natural" losses level is such that the storage ring cannot be operated without transverse and longitudinal cleaning using collimators.
In the overall LHC project framework we have tested a few candidates [1] having in mind:
1.1 Criteria: First of all it is essential to have an estimate of the loss level, rate and distribution at the detector level. Then it is essential to question the requested time response and on the remnant dose at the monitor location.
1.2 Signal treatment: Two types are considered, the analog and the counting mode. In analog mode the BLM's signal is generally integrated or passed through filters. In counting mode the BLM's signal consists of pulses feeding a counter. Of course both the detector and its electronic must not saturate.

The LHC will be operated with 2835 bunches of 10^{11} protons each, separated by 25ns and distributed in 12 batches, with a revolution frequency of about 11KHz (10KHz for numerical applications).
With energies from 0.45 to 7 TeV, a magnet quench would occur for the following proton loss rates [2]:

Fast losses: $6{\cdot}10^9$p/(m.10ms), and $6{\cdot}10^7$p/(m.10ms) at 0.45 TeV and 7 TeV respectively.
Slow (or continuous) losses: 10^9p/(m.s) and $8{\cdot}10^6$p/(m.s) at 0.45 TeV and 7 TeV respectively.

Our comparative measurements were partially performed on the SPS machine but mostly on a SPS transfer line where a beam (with about 3cm diameter) of 10^4-10^7 protons at 120GeV/c, was extracted during 2.4s. This well monitored extraction line allows us to calibrate our measurements in view of LHC.

After a short description of the tested monitors we will give some guidelines for a preliminary choice of the monitors which could be retained. Data treatment or monitor controls as such will not be tackled in this paper.

2. DETECTORS

Our tests concerned: Scintillators with their PMT's, PIN Diodes, Ionisation monitors, ACEM's and Cryogenic microcalorimeters.

2.1 Scintillators

As is known, these devices emit light in which intensity is proportional to the energy lost by the particle passing through. The scintillator can be shaped in the most appropriate way (plates, cubes, rods,..). In the present case we make use of rectangular and rod shaped one's. Coupled to a Photo-Multiplier Tube (PMT), and associated with an appropriate electronics system, they allow large dynamic ranges in analog mode and in counting mode (up to 10^6 - 10^7). This BLM is very fast and bunch to bunch measurements can be achieved in both cases. Nowadays PMT sockets integrate high voltage power supply thus avoiding high voltage cables and the overall detector can be housed in a small volume (for our set-up l: 270mm, diam: 35 mm). The main drawback comes from the scintillator darkening when used in a high dose level environment. The gain of PMTs varies within a factor 10, a careful intercalibration of their sensitivities is necessary. Lastly this detector is expensive.

2.2 PIN-Diodes

Our experience is based on PIN Diode Beam Loss Monitor developed at DESY [3]. The system consists of two 10*10 = 100mm^2 area PIN diodes mounted face to face. The coincidence read out can measure a maximum count of 10 MHz with an intrinsic noise rate of less 1 Hz, which gives a dynamic range of more than 10^7.

This BLM is sensitive to MIPs with an efficiency >30%, is very fast, not very expensive, and the radiation resistance is rather modest. Experience made at PS, where relative high dose levels are of concern showed that the detector lifetime did exceed one year.

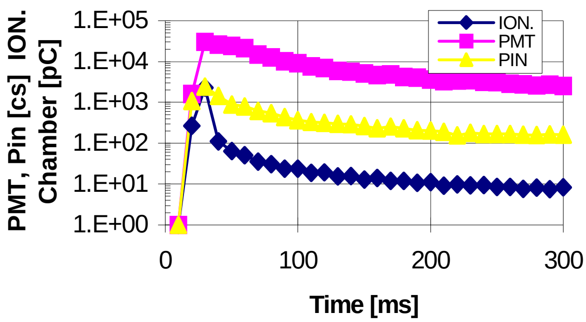

Figure 1: Losses on: PMT, Pin [counts], and Ion chamber [pC], during the first proton injection in the SPS ring.
It appears that the PMT and PIN are saturated.

We are now also considering smaller active area (0.5 – 10 mm^2) devices to get a higher bandwidth (more than 40MHz) and for other reasons, which will appear later. The diodes are commonly used in pulsed mode but analog mode has also been considered.

Pulse mode. Some estimates made for LHC [4] show that a 1cm^2 diode, placed a few meters from the proton impact, will deliver 1 pulse at 0.45 TeV for 1547 lost protons and 1 pulse at 7 TeV for 172 lost protons. These numbers are probabilistic since the shower simulation supposes that MIP passing through the active area follows a Poisson distribution.

As an example let us suppose that the 1cm^2 diode and its electronic can operate above 40 MHz (which is not the case), and that each bunch loses the same number of protons. For fast losses, inducing a quench at 0.45 TeV, the "theoretical" number of lost protons by one bunch every turn will be: $6{\cdot}10^9/(2835{\cdot}100) = 2.12{\cdot}10^4$ which is much larger than $1.54{\cdot}10^3$. The diode will saturate since it will deliver 1 pulse when 1547 or more protons are lost. In this range the detector will not be linear. A more detailed statistical analysis show that saturation occurs at a level which is about a factor 10 less (i.e. when more than $1.54{\cdot}10^2$ protons are lost per bunch and per turn at 0.45 TeV). Saturation effects are even more pronounced, at quench levels, when only part of the bunches (or batches) are of concern. For slow losses saturation should not be feared but care must be taken as accuracy is concerned.

A way to have less probability for such a drawback is to reduce the diode area. Anyway, saturation occurrences cannot be easily diagnosed by the operator. Of course such an effect exists for scintillators. An example is given by Fig. 1 comparing the pulse rate of a PIN-diode assembly and large area Scintillator for which saturation becomes evident (since then more than 1 particle is passing through the detector during its time response).

2.3 Ionization Based Monitors

We used two types of monitors:

a) The New SPS ionisation chamber with a multi-electrode layout (distance between the electrodes is about 5mm) to reduce the drift path and the recombination probability of the ions and electrons, and hence to improve the linearity. Two chambers are housed in the same body with equal volume about 300 cm^3 each.

Linked to two analog type electronics with different gains a very large dynamic range of 10^7 can easily obtained which allows simultaneously measurements with fast and slow losses.

These chambers, filled with air, are fast: the pulse rise time is about 1 µs, and the sensitivity is about $5{*}10^{-6}$ C/Gy [1Gray = 1Joule/kg].

This BLM is very sturdy, the radiation resistance is very good, and it is not expensive. The leakage current of BLM is less than 1 pA, with short cables between the chamber and the electronic $5{*}10^3$ particles can be detected (Fig. 2).

b) The ISR ion chamber made from a modified low attenuation air cored coaxial cable (l: 1m vol.: 200 cm^3) [5]. This BLM has about the same characteristics as the New SPS ionisation chamber. These two types of BLM are mainly used in analog mode and linked to very low bias current (<100 fA) amplifier or integrator can give high sensitivity, which allows very good measurements.

In the LHC the deposited energy per lost proton [4] is $6.2{\cdot}10^{-13}$Gy at 0.45 TeV and $3.8{\cdot}10^{-12}$Gy at 7 TeV. In the worst case, with slow losses at 7 TeV, the ionisation chamber will give about 150 pC/s large enough to make a good detection.

Comparative measurements made on SPS (Fig.1) clearly indicates the PIN-Diode and PMT saturation effect could not be traced without the use of ionisation chambers.

2.4 ACEM

The Aluminium Cathode Electron Multiplier is a photomultiplier where the photo-cathode is replaced by an aluminium foil. This foil works as a secondary electron emitter when irradiated. This detector has been intentionally developed at PS for the purpose of beam monitoring. The dimensions of the tube are 4 cm in diameter and 10 cm length. This BLM is very fast: rise time of signal <10ns, and by adjusting the HV the dynamic is more than 10^3, at high gain has sensitivity for MPI's, and acquisition in counting mode may be done. With medium gain the Anode Dark Current is less than 100pA, low enough to make good measurements in analog mode. Bunch to bunch measurements can be achieved in analog and counting mode.

This commercial tube, although expensive, can operate in a radioactive environment.

Comparative measurements made with an ACEM and an ionisation chamber in analog mode show a very good linearity and a relative gain of 700 (Fig. 2).

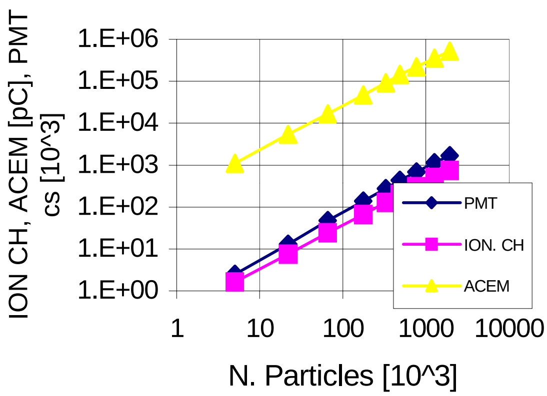

Figure 2: PMT output counts or, ACEM and Ion chamber [pC], versus number of particles crossing the detectors.

2.5 Cryogenic Microcalorimeter

This type of monitor, placed on the cryostat, has already been reported [6]. It uses the properties of carbon resistors which exhibit large values at low temperatures (R (T = 300°K) =100Ω, R (T = 1.8°K) =10^5Ω).

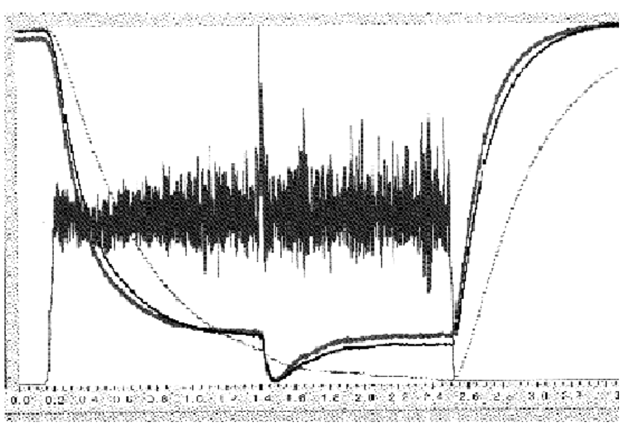

Figure 3: Cryogenic µ-cal. Voltage variation of different resistors as a result of particles crossing the monitor during slow extraction which spill is represented by the "rectangular" plot. Ordinate: arbitrary Units, Abscissa: Time [s].

The carbon resistor is encapsulated in a copper block through a small thermal resistance. The ensemble "block + resistor." is coupled through a larger thermal resistance to the cryostat. The deposited energy [4], 3m away from the proton impact point on the vacuum chamber, is $53 \cdot 10^{-4}$ GeV/ $2cm^3$ at 0.45 TeV and $4 \cdot 10^{-2}$ GeV/$2cm^3$ at 7 TeV.

A reasonable temperature resolution is ΔT = 1m°K such that the corresponding lost proton resolution is equal to Np (0.45TeV)=10^6 and Np (7TeV)=10^5 which is acceptable for the upper LHC loss range.
The time response to losses is about 150ms, Fig. 3 shows a typical measurement made on the SPS transfer line. The "exponential" curves represent the time response of 3 different resistors. At about 1.4s an instantaneous extra-loss is induced which is detected by two of the fastest resistor. A higher sensitivity and faster response time could be obtained with sapphire replacing copper.
A variant is the use of liquid helium ionisation chambers.

3. CONCLUSIONS

According to our measurements a preliminary use of BLM's could be as follows:

a) In the transfer lines, where the beam passes only once: ionisation chambers, used in analog mode,

b) In the cleaning zones (where magnets are hot) the relative high remnant dose level must be taken into account. One could therefore consider ACEM's if individual bunch behaviour need to be analysed and ionisation chamber for slower processes,

c) For the ring cryogenic part, if individual bunch or batch losses must be analysed, PIN-Diodes of different sizes should be used. For slower processes (i.e. integration over 5-100 LHC turns) and more linearity the ion chamber should be also used, as well a long cable of length up to 15m would give valuable measurements for eventual helium leaks.

For special monitors where sensitivity, linearity and high speed are required the PMT will be the best detector.
The Cryogenic Microcalorimeter is probably too slow and has not enough sensitivity for all these applications.

Our monitor comparative tests were based on estimates for LHC obtained from simulations. Even if the actual losses would differ from simulations by one decade, the proposed choice will still remain valid. As shown the choice depends on the type of losses, the data treatment and the dose level at the locations where detectors are placed.

REFERENCES

[1] J. Bosser, G. Ferioli, Part I in PS/BD/Note 97-01 or SL/BI/Note 97-08; Part II in PS/BD/Note 98-03 or SL/BI/Note 98-027; + Private communications.
[2] J.B. Jeanneret, LHC Project Report 44.
[3] K. Wittenburg, NIM A 345 (1994) 226-229.
[4] T. Spickerman and K. Wittenburg LHC Project Note 124 + Private communication.
[5] Tech. Note ISR-OP/BH/cc/TN 76, ISR Performance report Run 1116, 26GeV.
[6] J. Bosser et al, LHC Project Note 71 (1996).

BEAM PROFILE MEASUREMENTS AT 40 MHz IN THE PS TO SPS TRANSFER CHANNEL

G. Ferioli, J.J. Gras, *H. Hiller, R. Jung
CERN, Geneva, Switzerland - *Bruun & Sørensen (France)

Abstract

Bunch to bunch beam profile measurements provide a valuable tool to control the injection lines to the SPS.

A fast profile monitor based on a 2.5µm Mylar coated with Aluminium Optical Transition Radiation (OTR) radiator, has been developed, installed and tested in the transfer line between the PS and SPS.

The OTR beam image is focused onto a fast Linear Multianode Photo Multiplier Tube and the associated electronics sample and store profiles every 25ns.

The paper describes the detector design, the electronic processing, and presents the results of different measurements made with bunches of 10^9-10^{11} protons at 26 GeV, and bunches of 10^6 Pb^{82} ions at 5.11 GeV/u.

1. INTRODUCTION

In the transfer line between PS and SPS different types of beams have to be monitored for a good injection in the SPS. For the Fixed Target operation 2 injections of $2*10^{13}$p at 14 GeV and 10.5 µs long are extracted horizontally in 5 PS turns. With the ions, 4 injections of 16 bunches of $1.5*10^6$ Pb^{82} ions each at 5.11 GeV/u and spaced by 140 ns are used.

In view of the use of the SPS as LHC injector one injection of 16 bunches of 10^9 protons each at 26 GeV and spaced by 140 ns, is presently used for preliminary tests and, from this year one injection of 83 bunches spaced by 25 ns will be tested. For all beams the rms vertical and horizontal sizes are measured by Secondary Emission Grids (SEG) and OTR Beam Television Profiles (BTP).

The SEG electronics integrates all the signals coming from the grids for each injection at intervals defined by the master timing and gives only a single H/V profile. The CCD camera, used in the BTP monitor, integrates the signals during a TV frame (20ms), and the associated processing system computes a single H/V projection and a 2-Dimensional representation [1]. In both cases the evolution of the position, relative intensity, and profiles of the different bunches or structures is lost.

A new fast system able to acquire H/V profiles of bunches spaced by 25ns has been developed, installed in the transfer line and tested with different beams.

2. THE EXPERIMENTAL SET UP

Many OTR radiators made of 12 µm Titanium or 25 µm Mylar coated with 2 µm of Aluminium are currently used in the transfer lines to the SPS. These screens generate light, which reproduces the time structure of the beam and bunches spaced by 25ns can be analyzed [2].

The intensity of the OTR radiation, generated by ion or proton bunches injected in the SPS, is high enough to provide good diagnostics with a CCD camera or a Photomultiplier.

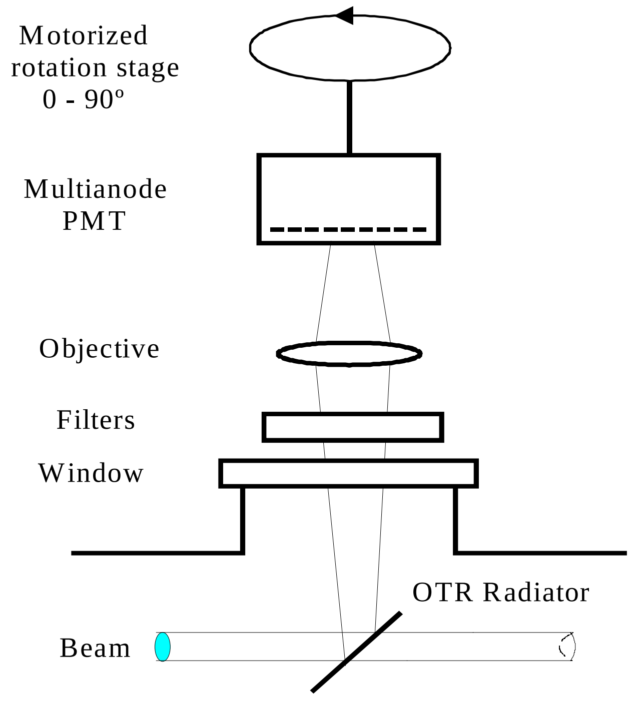

Figure 1: Schematic view of the monitor set-up

The measurement station (Fig. 1) uses a standard BTV SPS tank, where an OTR radiator is placed at 45º with respect to the beam. The radiation, through a window on the vacuum chamber and a set of neutral density filters, is focused by a 75 mm objective onto a Multianode Photo Multiplier Tube (MPMT).

This MPMT (type: Hamamatsu R5900U) with the proximity focusing dynode structure preserves the spatial distribution of intensity between photocathode and anode. This tube is a linear structured version with 16 anodes measuring 0.8*16 mm with a 1mm pitch, and an anode pulse rise time of about 0.6 ns.

A motorized rotation stage can rotate the MPTM from 0º to 90º, so with the same monitor, this allows to take alternatively horizontal or vertical profiles. The set of filters, the gain of MPMT and the rotation stage are remotely controlled.

Fig. 2 shows the detector with the acquisition electronics system mounted on the same support.

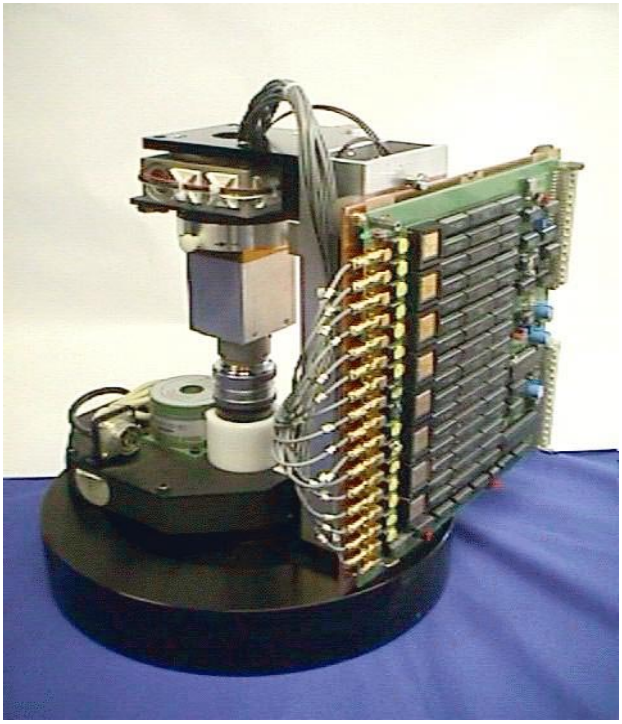

Figure 2: Fast Beam Profile Monitor

3. READOUT ELECTRONICS

A new wide band readout electronics has been developed, in order to digitize and store simultaneously 16 signals at a frequency up 50 MHz (Fig. 3).

Very short cables connect the output of each anode of the MT to an amplifier (used to limit the anode current). his analog signal is digitized by an 8 bits flash ADC and the sampled values are stored in an internal memory of 32 Kbytes.

Two modes of operation have been foreseen: internal clock and bunch auto trigger to work correctly with the different beam structures. In the internal clock mode, used with the continuous transfer of 5 PS turns, an external gate synchronous to the injection resets the counter memory and starts the acquisition process and an internal clock at 40 MHz stores the profiles in the memory.

The bunch auto trigger mode is used to analyse bunched beams; in this case the external gate is used to reset the counter memory and to generate an “enable” for the acquisition process.

A very fast low-level discriminator detects the presence of an analog signal on the anodes, generated by one bunch, and starts one conversion for all channels. The bunches have to be separated by at least 25ns.

In both cases at the end of the injection, on request of the CPU installed in a surface building, the data are transferred to a VME interface over a serial RS 422 line.

4. SOFTWARE DESCRIPTION

The software system is based on a client-server architecture. The server is located in the front-end CPU, a PowerPC VME card (type: CES RIO-8062) running the LynxOS real time system. It has been developed in C and consists in two threads. The first one acquiring continuously the profiles at predefined events (first proton injection, second proton injection...), the second handling the communications with the outside world. On the client side, a graphical user interface has been developed for our HPUX workstations. It allows the user to configure the observed events, to monitor the system settings (PM voltage, acquisition plane...) and of course to retrieve, display (Fig. 4, 6) and store the acquisitions via the server communication thread.

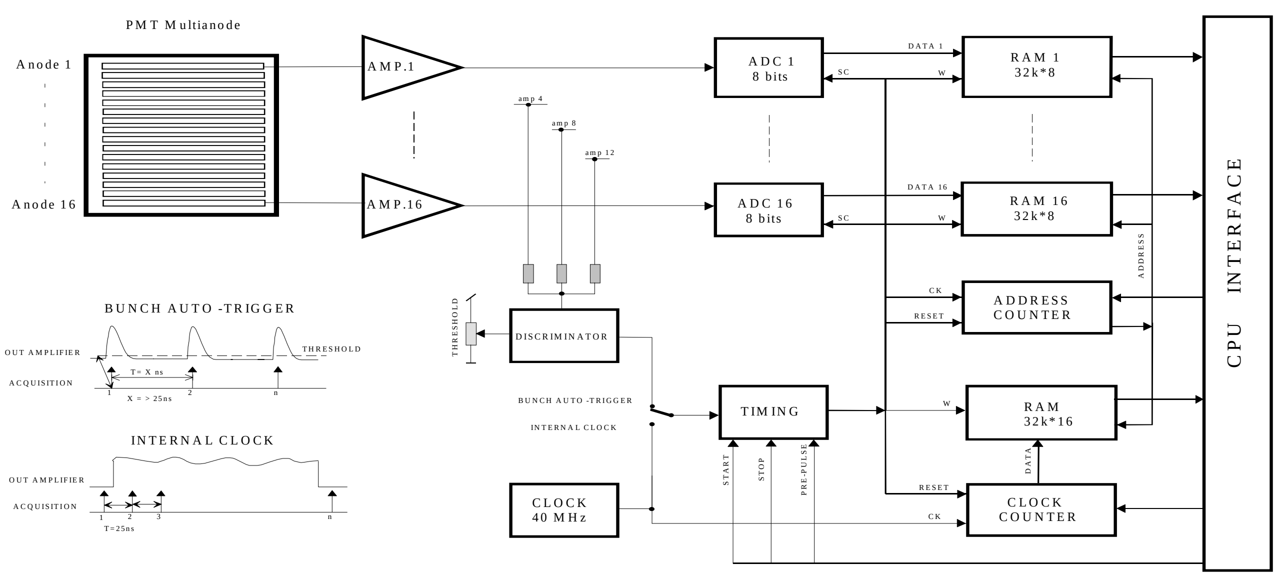

Figure 3: Bloc diagram of MPMT readout electronics.

5. EXPERIMENTAL RESULTS

Profile measurements have been done with ions: Fig. 4 shows the horizontal profiles of the four batches, of 16 bunches each, used in the injection of one SPS cycle.

The system has shown the peculiar behaviour of the first bunch of each batch, a phenomenon impossible to see with the others profile monitors installed in the transfer line.

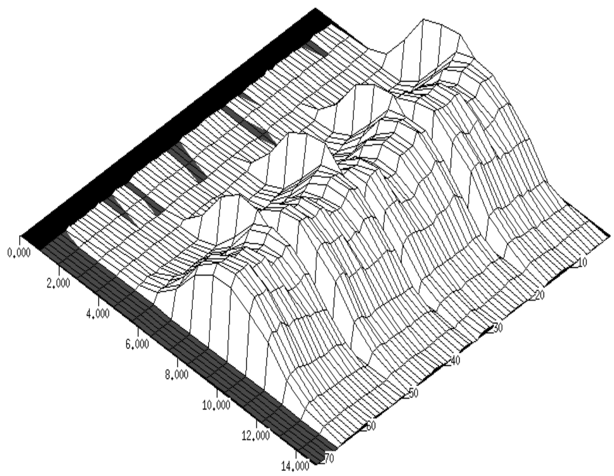

Figure 4: Horizontal profiles of 4 batches of Pb ions of 16 bunches each (from right to left).

In order to correct this problem the timing of the CPS extraction kicker was changed; Fig. 5 shows that the monitor was able to follow the evolution of the position of the bunches. This test has revealed that the length of the kicker pulse was not long enough to perform a good ejection.

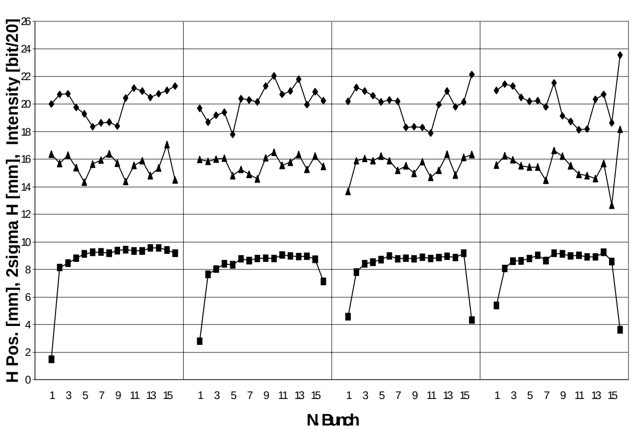

Figure 5: Evolution of first ions batch during the timing tuning of the CPS extraction kicker.

The relative intensity, the position and the beam sizes along the spill of the beam delivered by 5 CPS turns in Continuous Transfer mode have been measured by means of the processing of about 600 profiles acquired during the injection (Fig. 6).

The observation and the improvement of the transverse characteristics of this proton beam are simplified.

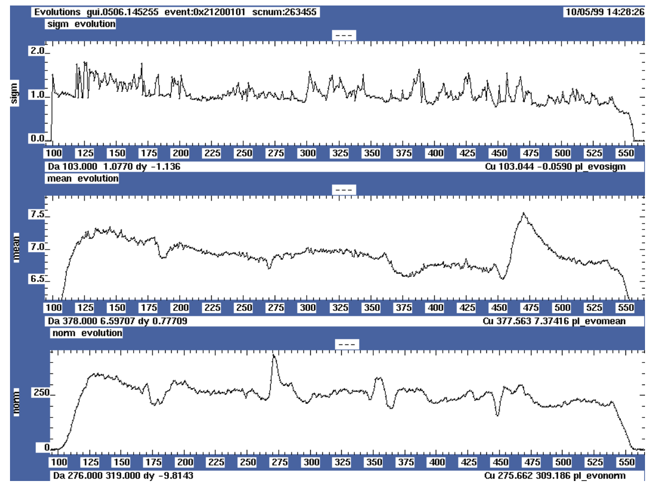

Figure 6: Evolution of: rms size, position and intensity of 5 CPS turns injected in the SPS.

6. CONCLUSION

Single bunch to bunch measurements, by the Fast Beam Profile Monitor, have proven to be feasible. Some phenomena, which would pass undetected by SEM Grid or BTP monitor profile, have been highlighted.

The OTR screen does not significantly blow-up the beams injected into the SPS, and can be used as a permanent monitoring tool.

This diagnostic tool has been extremely useful in the optimisation of different parameters of the injection line.

The small number of channels of the MPMT can be a disadvantage. A limitation appears when resolutions less than 1 mm are needed; a more sophisticated optical setup would be required to overcome this limitation.

ACKNOWLEDGEMENTS

We would like to thank J. Camas and M. Sillanoli who performed the mechanical and installation works, and J. Koopman who provided the Step Control for the rotation stage and filters.

REFERENCES

[1] J. Camas et al: Screen versus Sem grids for single pass measurements. Pro. of DIPAC 95 Travemunde, Germany 28-31 May 95.

[2] J. Bosser et al: Optical Transition Radiation proton beam profile monitor. NIM A238 (1985) 45-22.

THE FAST HEAD-TAIL INSTABILITY SUPPRESSION IN MULTIBUNCH MODE AT VEPP-4M

G.Karpov, V.Kiselev, V.Smaluk, N.Zinevich,
Budker Institute of Nuclear Physics, Novosibirsk, Russia

Abstract

In this paper the bunch-by-bunch transverse feedback system for suppression fast head-tail as well as coupled bunch instabilities is described. The experimental results of the feedback affecting on the current threshold are presented. The effects of reactive and resistive feedback on the current threshold are discussed. Two times as large the bunch current than the threshold current was obtained.

1 INTRODUCTION

The mode of operation of the VEPP-4M facility as a synchrotron light source intends 4 equally spaced along the ring bunches with each bunch average current of about 20 mA. The most fundamental limit for the bunch current at the VEPP-4M presently is vertical fast head-tail instability. The beam losses is usually observed in some tens of milliseconds after injection (this corresponds approximately to the time of radiation damping), Fig.1. The threshold current was 10÷11 mA.

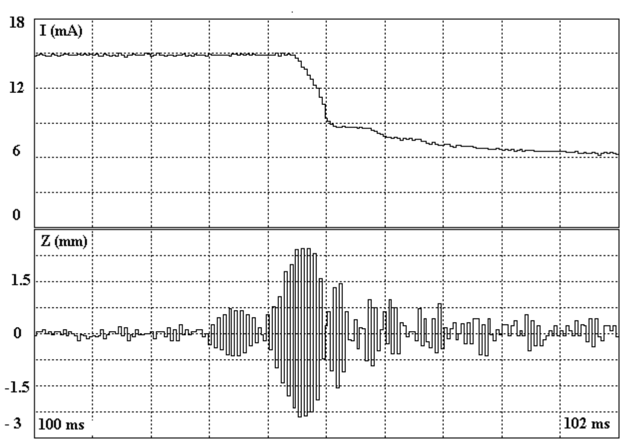

Figure 1: The bunch head-tail instability after injection.

The fast head-tail instability occurs when frequency of the head-tail mode “0” is shifted sufficiently to couple to the “–1” mode. In order to increase an instability threshold it is usually suggested to introduce the reactive feedback to compensate frequency shift of the mode “0”. However, as it follows from experiments [1] it is turned out that the introducing of the pure resistive feedback increases the threshold current up to substantially higher values.

This effect can be explained within the framework of the simple two particle model. In the papers [2,3] it was found the eigenmodes and eigenvalues of the particles oscillations in the bunch. It was shown that in the vicinity of instability threshold eigenmodes are approximately the same, they have close eigenvalues and each mode has the approximately equal amplitudes of the dipole and quadrupole components.

When the resistive feedback is turned on an energy extraction occurs from the eigenmodes of oscillations excited by the head-tail interaction in a bunch through the dipole degree of freedom, thereby preventing the instability growth. This interpretation is additionally supported by the experimental data obtained at VEPP-4M [4].

In this paper the new bunch-by-bunch feedback system for suppression of vertical fast head-tail as well as coupled bunch instabilities is described.

The VEPP-4M related parameters are listed below.

Table 1: The VEPP-4M parameters

Energy	1.8÷5.5 GeV
Rev. frequency, f_{rev}	0.819 MHz
RF frequency	181 MHz
Number of bunches	4
Radiation dumping time at injection (long.,trans.)	30÷60 ms
Bunch length (injection)	20 cm
Tune, vertical	7.59
Tune, longitudinal	0.018
Bunch current threshold	10÷11 mA

2 DESCRIPTION OF THE SYSTEM

The block diagram of the feedback system over the vertical dipole oscillations of a beam is given in Fig.2. The 50 Ohm striplines are used as the pickup of transverse oscillations. The signals from the opposite striplines are applied to the subtracting transformer having the input impedance equal to the wave impedance of striplines. The length of striplines was chosen in such a way that their sensitivity has maximum values in the frequency range 150÷250 MHz.

To provide both the maximum dynamic range and the maximum signal-to-noise ratio we have chosen an analog scheme to process signal from bunches because little bunches number. The signals from four electron bunches are switched to four corresponding channels by front end GaAs FET switches. The gate duration is chosen to be 50 ns to provide bunch to bunch signals isolation.

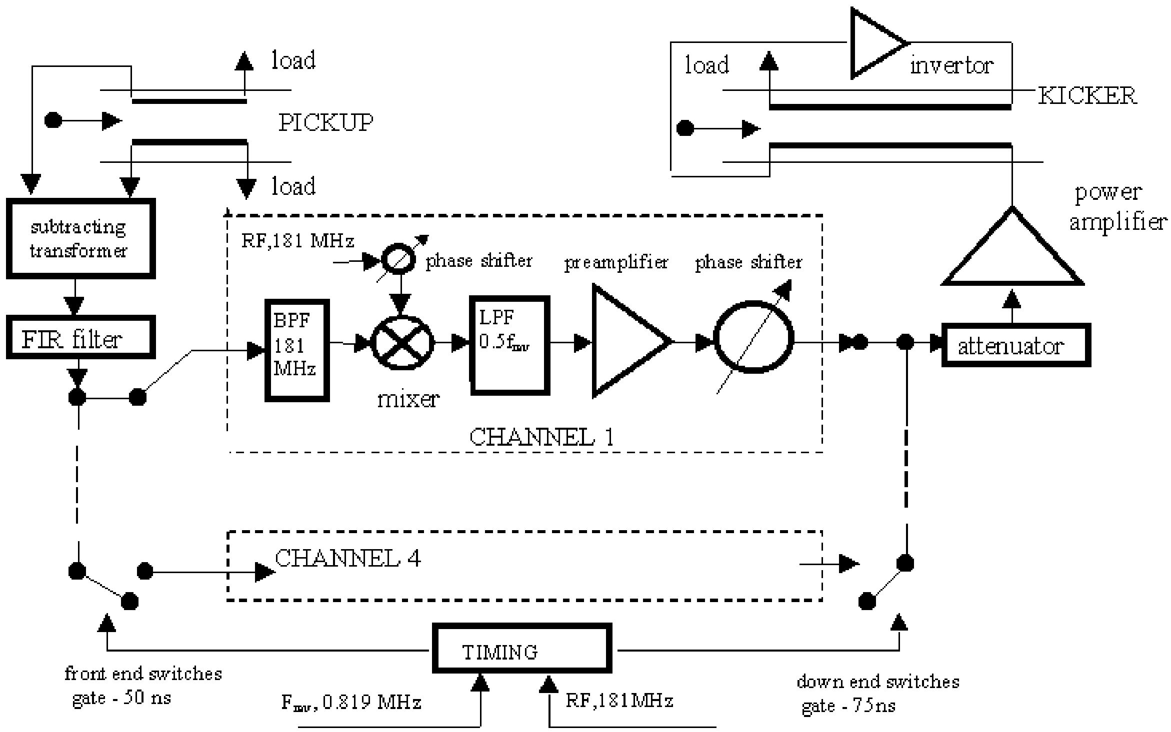

Figure 2: The feedback system block diagram.

The Finite Impulse Response (FIR) filter converts alternative impulse from the transformer output to 7 cycle sine-like burst at the RF frequency. This provides better conformity of the transformer output signals to the dynamic range of the following switches. The FIR filter is performed with coupled microstrip transmission lines.

Each channel consist of selective filter tuned at the RF frequency 181 MHz, frequency converter where the bunch signal is mixed with RF signal from accelerating system, Low Pass Filter with cutoff frequency of $0.5{\cdot}f_{rev}$, preamplifier and phase shifter. The phase is regulated within the range $0{\div}2\pi$ thus enabling both the resistive and reactive feedback. The down end switches provide the delivery the channels feedback signals through the attenuator, power amplifier and kicker to “own” bunches only. The gate duration is 75 ns. The channels isolation defined by front end switches is more than 40 dB.

The pair of the 50 Ohm diametrically opposite matched striplines of 1 m length is used as a kicker. The power applying to the striplines is in series with the use of the inverter transformer. The inter-lines maximum voltage is limited by the power of an output amplifier to the value of 600 V.

3 EXPERIMENTAL RESULTS

The finite dynamic range of the feedback system imposes the limit to the decrement at injection where the bunch oscillation amplitude is quite large because of errors in the injection systems. In our case, at the bunch current of ~10 mA this value was approximately $0.03{\cdot}f_{rev}$ and for lower amplitudes of oscillations it could be increased up to $0.1{\cdot}f_{rev}$. The coherent tune shift, produced by the feedback, corresponding to these two modes of operation was 2π times lower. The ring coherent tune shift caused by the bunch interaction with the storage ring components was 0.012 at the same current value. The summarized feedback parameters at the bunch current of ~ 10 mA are presented below.

Table 2: The feedback parameters

Number of channels	4
Channels isolation	40 dB
Kicker length	1 m
Max. kicker voltage	600 V
Decrement at injection	$0.03{\cdot}f_{rev}$
Max. Decrement	$0.1{\cdot}f_{rev}$
Max. Coherent tune shift	0.016
Ring coherent tune shift	0.012

The experiments with the feedback system were performed at VEPP-4M facility at March – April, 1998. Unfortunately, the VEPP-4M could operate only with two bunches in the ring because longitudinal coupled bunch instability. The best results obtained were under the resistive – reactive feedback. The reactive part of the feedback provided decreasing the ring coherent tune shift. The optimum phase was, approximately, the mean phase between 0 (resistive feedback) and $\pi/2$ (reactive feedback). It was reached that maximum captured and accelerated current in two bunches were 40 mA and 36 mA, accordingly. So, the threshold current was exceeded approximately by two. One should note that maximum captured current in our case is limited not by feedback capabilities but the maximum current of the injected bunch (there is one injection in one bucket).

The results give evidence of an efficiency of the resistive - reactive feedback in suppression of the fast head-tail instability and can be used at other accelerators for the development of similar systems.

REFERENCES

[1] S.Myers, " Stabilization of fast head-tail instability by feedback ", Proc. of IEEE Particle Accelerators, 1987.

[2] A.Chao, SLAC-PUB-2946, June 1982.

[3] M.M. Karliner, private communication, 1994.

[4] M.M. Karliner et. al, "The feedback system for elimination the fast head-tail instability at storage ring VEPP-4M", EPAC 96, Barcelona, 1996.

BEAM PROFILE DETECTORS AT THE NEW FERMILAB INJECTOR AND ASSOCIATED BEAMLINES

Gianni Tassotto, Jim Zagel*

Abstract

During the commissioning of the Main Injector some of the detectors used to optimize the tune of the proton beam were: Flying Wires, Ionization Profile Monitors, and Multiwires.

1 INTRODUCTION

An 8 GeV proton beam is extracted from the Booster and channeled toward the Main Injector (MI) via the MI-8 beamline. From the MI the proton beam can be injected into the Tevatron (TeV) ring for collider and/or fixed target operation via P1 beamline or, to the Antiproton Source, via P1 and P2 beamlines.

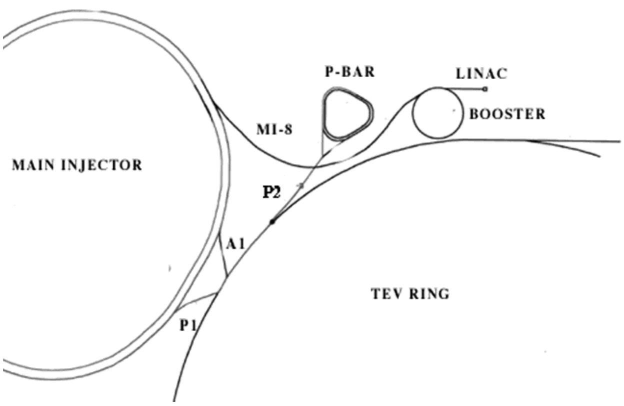

Figure 1: MI and Associated Beamlines Layout

A total of 27 Multiwires are distributed between MI-8, MI, P1, and P2 in order to optimize the beam tune. Just downstream of MI-8 injection is a horizontal (at Quad 102), and vertical (at quad 103), instrumentation section each comprising a multiwire (left) a flying wire (center) and an IPM (right).

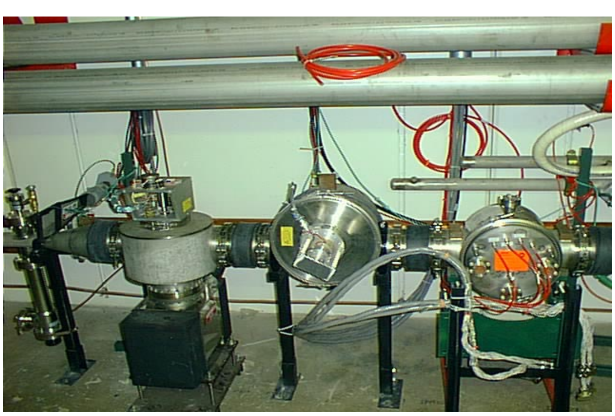

Fig. 2: MI Beam Instrumentation Station

2 MULTIWIRES

These particle detectors are typically used to tune the proton beam and are then removed since they are intercepting devices and degrade the beam. They operate in beamline vacuum, which is of the order of 10^{-8} Torr.

2.1 Types of assemblies

In the 8 GeV transfer line the grids are assembled to display a single profile at the time. In the MI ring, P1, and P2 beamlines the grids are made by first winding a 0.003 inch diameter wire at 80 g of tension on a transfer frame, then, transferring the wind over the wire planes and then soldering the wires on the pads. Each paddle contains both a horizontal and a vertical set of wires. No clearing field plane has been included in the design of this detector. The charge on the wires is measured with a scanner designed by the Controls Group [1].

Fig. 3: New MI Multiwire paddle

* Work supported by the U.S. Department of Energy under Contract No. DEAC02-76CH303000

2.2 Signal strength

The charge collected on a wire due to the secondary emission phenomenon depends on the beam intensity, the beam spot size and the surface area of the wire, and it can be written as:

$Q=\varepsilon N e Q e$ Where: ε=Secondary emission efficiency $\cong$ 3%
Ne = No of protons on a wire
$Q_e = 1.6\mathrm{x}10^{-19}$ Coulomb

Assuming a gaussian distribution: $\dfrac{1}{\sigma\sqrt{2\pi}}e^{-(x-\mu)^2/2\sigma^2}$

Fig 4 shows profiles in the transfer lines P1 and P2. During MI tune-up a 100 micro Farad capacitor and the gain was set to 10. The beam spot size was about 0.5 cm. With these parameters the profile was 90% of full scale. The estimated charge on the center wire was 24 pCoulomb.

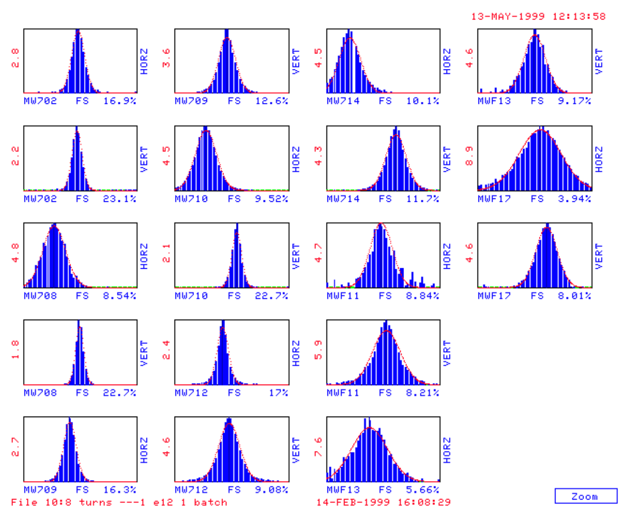

Fig. 4: Multiwire Beam profiles

2.3 Electronics

Charge is accumulated from the multiwire detectors by the individual integrators for a selectable time period.

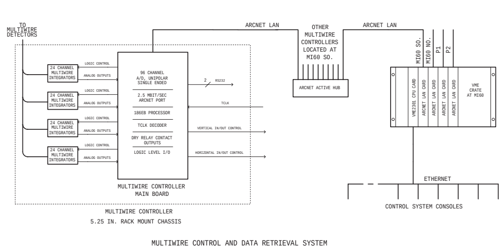

Fig. 5: Multiwire Controls

Both the time aperture and the integrator capacitance are chosen for the charge level anticipated. For the low-level signals, the A/D converters have preamplifier selectable gains of 1, 10, and 100. Simple conversions are held in the controller's memory buffer for retrieval by the VME front end.

5 FLYING WIRES

This system is used to measure the transverse size of the proton beam and also to calculate emittance.

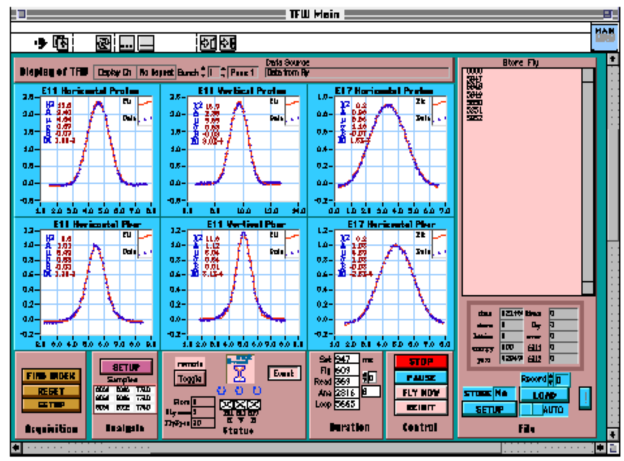

Fig. 6: Flying Wire Beam Profiles

While many old Main Ring systems were transferred to MI [2] this system was cloned from the Tevatron flying wire which had been previously upgraded. The Tevatron systems were discussed in detail in reference [3]. This upgrade included a LabView based system and the use of a resolver instead of an optical encoder for motion control. It also allowed changes to the motion profile that allow a 540 degree fly which results in accelerating to constant speed prior to making two passes through the beam and then decelerating to a final parking position.

By making two passes through the beam, offsets can be normalized and a comparison of sigma's calculated. There is a noticeable difference in the profiles generated by the two passes that are thought to arise from the proximity of the loss monitor detector to the near and far pass. Work is being accomplished to help characterize this phenomenon.

The Flying Wires require multiple turns to complete a profile and are also intercepting detectors that will degrade beam over time.

5 IONIZATION PROFILE MONITORS

These systems have been installed in Booster, MI and Recycler ring. Both the horizontal and vertical Main Injector IPM's [4] have been operational since the first circulating beam. The system captures a complete profile on each turn, takes up to 65K profiles, and causes no beam degradation. The nonlinear gaussian fit routine can easily handle sloping baselines that result from losses at injection any very wide beams that survive the first few revolutions.

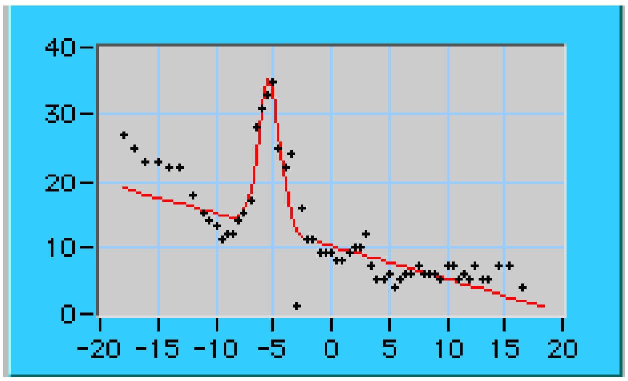

Figure 7: First circulating MI Beam Profile

The system functionality has been continuously upgraded including the latest addition of a tune calculation from the turn by turn samples captured. This feature was used during pinger studies to aid in commissioning the machine.

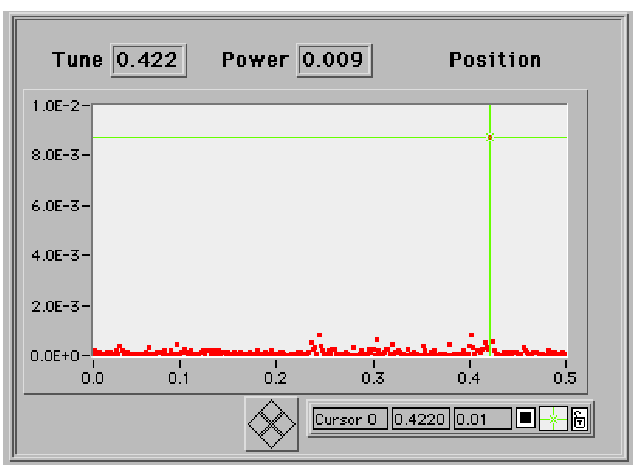

Figure 8: Horizontal Tune Measurement from IPM

The tune calculation is accomplished using the LabView power spectrum function applied to the mean of each sampled profile calculated from turn by turn data. Through the use of various clock delays this measurement can be made any time during the cycle and on any injected bunch.

6 CONCLUSION

The commissioning of the MI has been successfully completed. The Lab is now in the process of accelerating beam in the TeV ring for fixed target operation. During the MI start up phase it was found that some improvements could be made to the Multiwires: The rotary feed thoughs that enable the paddles to be moved in/out of the beam had much more than the manufacturer's specified 0.5 degrees of backlash. Also, to minimize outgassing the plan is to redesign the FR-4 boards that hold the x, y wire planes with ceramic substrates. Finally, to minimize the potential for wiring errors the individual wires that are soldered at one end to the inside of the vacuum feedthrough and at the other to the individual board pads will be replaced with Kapton ribbon cable.

One advantage to collocating the three different profile-monitoring systems is to be able to correlate the data from three different measurements. This work will begin once all of the accelerators are in stable mode of operation.

REFERENCES

[1] Kissel, W., Lublinsky, B., Franck A., "New SWIC Scanner/Control System", presented at ICALEPCS 95, Chicago, IL, Oct.. 1995.

[2] Barsotti, E., Blockland, W., Crisp,J., Fellenz, B., Tassotto, G., Vogel, G., Zagel, J., "Fermilab Main Injector Instrumentation" paper WEA149 at PAC 99, New York City, April 1999

[3] Blokland, W., Vogel, G., Dey, J., "Tevatron Flying wires", IEEE PAC 97CH36167, May 1997

[4] Zagel, J.R., Hahn, A.A., Crisp, J.L., Jensen, C. "Improvements to the Fermilab Ionization Profile Monitor Systems" paper WEA127 at PAC99, New York City, April 1999.

PHOTON COUNTING DETECTORS FOR FILL STRUCTURE MEASUREMENTS AT VISIBLE WAVELENGTHS

H. L. Owen, CLRC Daresbury Laboratory, Warrington WA4 4AD, United Kingdom

Abstract

When making accurate measurements of the relative populations of electron bunches in a storage ring, notably in light sources operating with only a single bunch filled, the method of time-correlated single photon counting gives the greatest dynamic range. The timing resolution and background noise level of the photon detector employed is critically important in determining the overall performance of the system; hitherto the best performance has been obtained detecting X-ray photons using avalanche photodiodes. On the SRS at Daresbury a visible light diagnostic station offers greater ease of access to instrumentation and operational advantages. A review is given of the detector types which have been employed, and the performances which can be obtained using visible light.

1 MEASURING ELECTRON POPULATIONS

A measurement is often needed of the relative populations of the different bunches in a storage ring electron beam. For instance, when a light source storage ring is operated in a user mode which requires only a single bunch to be filled, it is important to be able to distinguish the (unwanted) small populations in the other bunches. The total dynamic range for detection of a small bunch relative to a larger bunch is determined by 2 factors - the time resolution of the detection system and the background noise. The accepted technique which provides the best trade-off between these two requirements for electron storage ring measurements is Time-Correlated Single Photon Counting (TCSPC).

In the TCSPC method individual photons emitted from a source are timed against a reference signal synchronous with the source repetition rate [1]. A histogram of the number of events versus time will give a statistical picture of the time-structure of the source over many events. The reference signal can conveniently be taken from the storage ring RF timing signal, but may also be derived directly from a single bunch beam by using a stripline pickup.

Photon detection, which provides the other channel of the TCSPC system, may be accomplished using a variety of detectors sensitive to different photon wavelengths; generally X-ray or visible photons are detected directly, or X-rays indirectly using scintillators. Photomultipliers (PMTs), microchannel plates (MCPs) or avalanche photodiodes (APDs) have been used. The best dynamic range yet obtained is around 10^8, using an APD directly detecting X-ray photons around 10 keV [3].

2 VISIBLE LIGHT DETECTION

One factor determining the choice of photon counting system is the effort and equipment required to implement it – the ideal is a cheap, turnkey system which can be installed onto an existing beamline. Visible light diagnostic beamlines are an attractive option as most light sources possess one for other diagnostic purposes. With the correct design of beamline - such as at the Synchrotron Radiation Source (SRS) at Daresbury - continuous access to and operation of the diagnostic equipment can be maintained even during storage ring injection – this can greatly increase the flexibility and efficiency of making measurements.

To provide the photon channel for the system, three options for visible photon detection are presented here: these are systems based on PMTs, MCPs or APDs.

2.1 PMT-Based System

This is the type of system presently in use on the SRS at Daresbury Laboratory. A timing base must clearly be used, together with a tube with exceptional timing and noise characteristics. At present, one of the fastest low-noise tubes commercially available is the Photonis (Philips) XP2020 tube [4] which has a transit-time spread of 250ps (similar tubes have been manufactured in the past with slightly better characteristics but are no longer available). Coupled with the appropriate base [5] a dynamic range of greater than 10^5 for most neighbouring bunches can be obtained; this is partly dependent upon the tube temperature (which determines the noise rate of the photocathode), so tubes are generally cooled thermoelectrically [5]. However, artefact peaks arising from the first few dynodes are generally present, and are well correlated in time and magnitude with each real peak; artefacts associated with the largest bunches overlap certain time regions in the beam fill structure, reducing the dynamic range there, although this can be partly overcome using software analysis [5]. The transit-time spread, together with the resolution of the timing electronics (see Figure 1) means that the overall response time is such that very close bunches (within a few ns from the main bunch) have a reduced dynamic range. Whilst this is a restriction for storage rings with bunch spacings of 2 ns it is less so for lower RF frequencies than

500 MHz. The important response width parameter is not the usually quoted FWHM but the peak width at lower levels – these may not scale in a simple way from the FWHM, and must be measured (for instance see Table 2).

2.2 MCP-Based System

The MCP-based system electronics are similar to those for the PMT: a Hamamatsu R3809U integrated photocathode/MCP unit has been used at Daresbury [6]. Additional amplification and different discrimination are necessary to cope with the small, narrow output signal produced by the unit. Although the timing response of the unit is excellent (FWHM of 40 ps), it has similar dark noise characteristics to the PMT. In addition, it is relatively expensive and fragile compared to the PMT system. Overall, this makes it less attractive as an option than a PMT-based system.

2.3 APD-Based System

APDs have an advantage over PMTs in that artefacts are not present in the single photon response of the detector. Although APDs have been used with great success at X-ray wavelengths for timing measurements [2,3] the lower energy of visible photons means that the required amplification to detect them is much greater, generally increasing the dark noise to unacceptable levels. Recently, though, there have been developments in commercially available APD detectors, and both Hamamatsu (model C5331) [6] and EG&G Ortec (models SPCM-AQ) [7] now provide integrated detectors incorporating the APD, temperature compensated bias control and amplifier into a single unit. The EG&G models are particularly interesting as they also include discriminator circuitry to give a convenient TTL timing output, as well as their utilisation of very small area diodes (250 μm). Tests have been carried out at Daresbury using such a detector (model SPCM-AQR-13), which compares favourably in cost with the PMT, thermoelectric cooler and discriminator it replaces.

3 COMPARISON OF PMT AND APD-BASED SYSTEMS

The SPCM-AQR-13 is a mid-range detector which has similar quoted properties to the PMT system in use at Daresbury; these are summarised in Table 1.

Table 1:FWHM single photon response widths and dark noise levels for the APD and PMT detector. APD units with lower noise levels are available.

Detector	APD *(SPCM-AQR-13)*	PMT *(XP2020Q)*
Width [ps]	250	250
Noise [Hz]	140	40 (-2.3kV, -10°C)

The electronic layout used for the PMT and APD systems is shown in Figures 1 and 2. Using a single bunch beam with deliberately added small amounts of charge in the other bunches, a measure of the dynamic range, single photon response width and dark noise was made for the two systems; a comparison of two typical spectra is shown in Figure 3.

As expected, artefacts are not present in the APD spectrum and the dark noise is higher. For most of the bunches the dynamic range of the APD system is 10^4, though this could be improved with a lower-noise detector. However, the measured response widths for the APD system were not as expected (see Table 2), with much larger FWHM values than the quoted 250ps. This

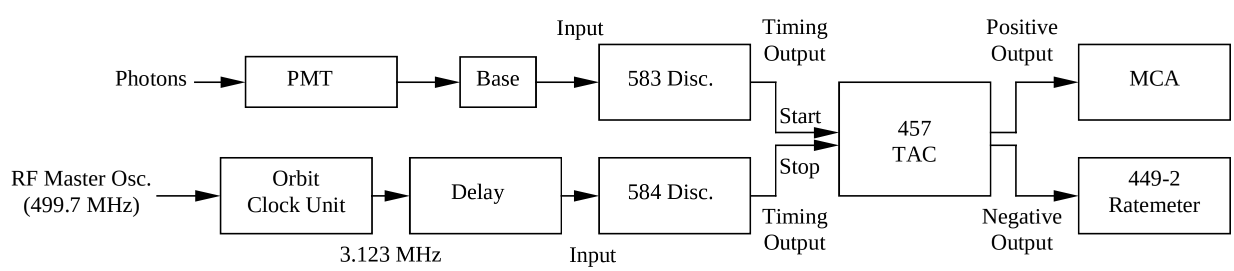

Figure 1. Layout of Photon Counting System based upon the XP2020 PMT. The orbit clock unit is a Daresbury-built unit; other NIM components are Ortec units [7].

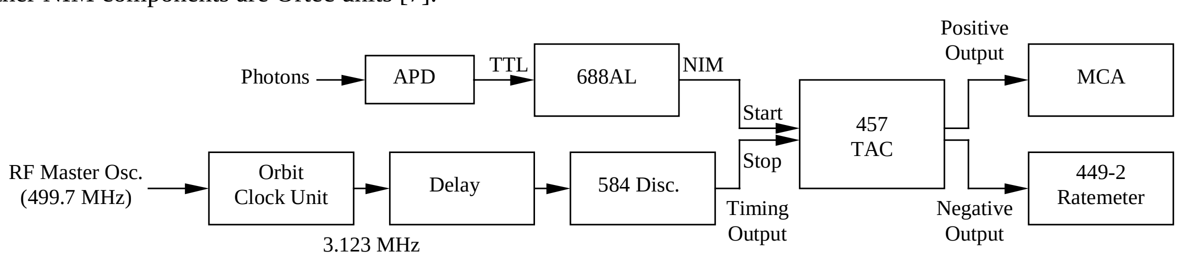

Figure 2. Layout of Photon Counting System based upon the SPCM-AQR-13. TTL to NIM conversion is performed using a LeCroy 688AL converter [8].

restricts the dynamic range within the first few ns from the main bunch.

Table 2: Single photon overall response widths for the APD and PMT-based systems.

Width	APD [ns]	PMT [ns]
FWHM	1.35	0.87
10^{-2}	7.43	2.30
10^{-3}	11.8	3.91

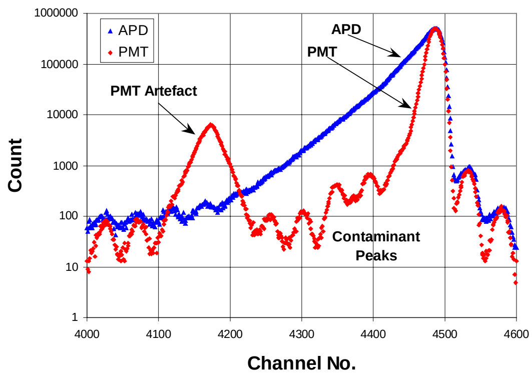

(a)

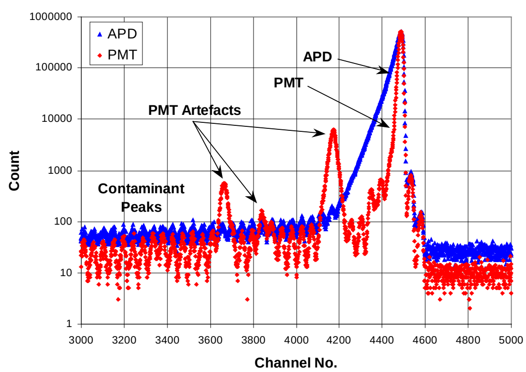

(b)

Figure 3. Comparison of spectrums measured using APD and PMT-based systems with the same stored beam. (a) is a close-up of (b). 23 channels corresponds to 1 ns.

4 DISCUSSION

The APD system as tested does not yield the expected timing resolution; this may have been due to a fault with the diode, and tests with alternative detectors will be carried out in the near future. However, for storage rings whose RF frequency is 50 MHz or lower, a system based on an APD is worth considering for a visible light beamline. If the time resolution issue can be resolved, these devices would be the best choice for any normal RF frequency, due to their relatively low cost, simplicity of use and probably greater ruggedness.

ACKNOWLEDGEMENTS

The author would like to thank Pacer Components Plc [9] for the loan of the SPCM-AQR-13 used in this work.

REFERENCES

[1] See e.g. 'An Introduction to Time Correlated Single Photon Counting for Fluorescence Decay Time Studies' (Application Note), Canberra Industries Inc., 800 Research Parkway, Meriden, Connecticut 06450, USA.

[2] K.Scheidt (ESRF), personal communication. X-ray APD techniques are used both in ESRF and in Japan.

[3] S.Kishimoto, "Recent developments in the avalanche photodiode x-ray detector for timing and fast counting measurements", *Rev.Sci.Inst.* **66(2)**, 2314-2316 (1995).

[4] Photonis SAS (previously Philips Photonique), Avenue Roger Roncier, BP 520, Brive La Gaillarde, France.

[5] H.L.Owen, 'Characteristics, Uses and Developments of the Photon Counting System at the SRS', *Proc. of 3rd European DIPAC Workshop*, Frascati, Italy (1997)

[6] Hamamatsu Corporation, 325-6, Sunayama-cho, Hananatsu City, Shizuoka Pref., 430-0193,Japan

[7] EG&G Ortec, 100 Midland Road, Oak Ridge, TN 37831-0895, USA.

[8] LeCroy Europe, 2 rue du Pre-de-la-Fontaine, PO Box 3341, CH-1217 Meyrin 1 Geneva, Switzerland

[9] Pacer Components Plc, Unit 4 Horseshoe Park, Pangbourne, Reading, Bekshire RG8 7JW.

A CURRENT DIGITIZER FOR IONISATION CHAMBERS/SEMS WITH HIGH RESOLUTION AND FAST RESPONSE

H. Reeg, GSI, Darmstadt, Germany

Abstract

A current-to-frequency converter (CFC), recently developed, exhibits a response time up to the µs region. The frequency limit is raised beyond 1 MHz, extending the linear range by a factor of 100. The conversion factor reaches 10E-13 C/pulse. The converter is employed, combined with ionization chambers (IC) and secondary electron emission monitors (SEM), to measure the intensity of the extracted beam in the transfer lines adjoining GSI´s heavy ion synchrotron (SIS). Fast intensity fluctuations during the particle spill can be observed.

Reduced hum and noise pickup, better handling and mounting flexibility as well as reduced costs are achieved building up the spill monitoring system with distributed components.

1 INTRODUCTION

Scintillation detectors, read out by photo multiplier tubes (PMT), commonly are limited to counting rates in the MHz range. If one has to cope with larger particle currents, other detectors must be used.

Because of an inherently large dynamic range, and easy data transmission and processing capability, a CFC is commonly employed for the measurement of the detector signals mentioned above. The acquisition and display of a spill´s particle count, the intensity envelope, and accompanying short-time fluctuations are facilitated by periodic readout of a digital counter connected to the CFC´s output.

In a SEM, ion spills extracted from the SIS at produce converter input currents with a dynamic range of ~10^{-12} A up to 10^{-7} A; the IC´s secondary current can reach 10^{-5} A. Spill durations from 10 ms to 10 s occur, and the extracted current does not show a perfect DC structure at all, but contains bursts with fast rise times, owing e. g. to magnet power supply ripple etc.

2 DESIGN CONSIDERATIONS

The existing converters comprised a response time constant of 350 ms, a 10 kHz frequency limit, no remote control and had to be mounted into NIM crates. These characteristics mainly prevented realistic interpretation and correct adjustment of the particle spill’s duration, shape and micro-structure.

2.1 Converter Working Principle

A fast response time combined with a frequency limit as high as possible were the most important design aims. These demands require an electronic circuit [1,2] with shortest internal propagation delays. A scheme, well known as “pulsed current-balance” or “recycling integration”, was chosen [Fig.1].

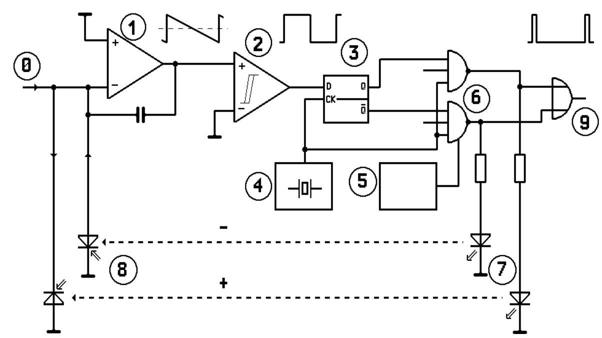

Fig. 1: Pulsed Charge-Balance CFC

Driven by a positive input current (0), the integrator (1) ramps negative. The Schmitt-Trigger (2) switches when the ramp crosses zero. The D-Flip-Flop (3) now passes “High” level to the selected gate (6), which opens for at least one crystal controlled clock (4) pulse of fixed duration, thus powering the opto-electronic “current source” (7,8) in the positive branch. A temperature controlled power supply (5) compensates it´s thermal current gain drift. The integrator is reset by a well defined charge pulse; Schmitt-Trigger and Flip-Flop switch back immediately, and the gate closes for the next clock pulse. Now the cycle starts again and oscillation commences. Every output pulse (9) indicates a fixed charge amount flowing to the input, while the output frequency is proportional to the input current. If the circuit is carefully designed, a linear relation is valid between current and frequency over many decades.

The performance of the circuit is mainly based on speed and precision of the pulsed “current sources” (7,8). Considering an operating frequency of 1 MHz at an input current of 100 nA, the device has to deliver a pulsed charge of 100 fC, e. g. (400 nA * 250 ns). Neither bipolar junction or field effect transistors (JFET) nor diode bridges worked fast enough at this current level. A Silicon PIN-Photodiode (PIN-Pd) with a small active area turned out to be a suitable current source, if it´s load resistance is kept close to zero. The summation point of the integrator (1, Fig.1) has the required characteristics.

Current transfer ratio (CTR)	0.1-0.2 %
CTR temperature coefficient	- 0.14 %/K
Dark resistance at zero voltage	1 GΩ
Shunt capacitance at zero voltage	11pF [3]
Current rise time / 50 Ω load	~ 70 ns

Tab. 1: Electrical characteristics of opto-electronic current source

A Si-PIN-Pd and a GaAlAs-LED, inexpensive devices originally intended for plastic fiber applications, were linked with a short piece of 2mm PMMA light wave guide and confined in a thermo-shrink tube, forming the opto-electronic current source.

3 CONVERTER PERFORMANCE

3.1 Offset current

To preserve the dynamic range also at low current level, the converter input has to be designed with great care for current leakages. Using the best state-of-the-art operational amplifier (OP) and a selected integration capacitor, and by routing all connections to the summation point (0) off the printed circuit board via a PTFE standoff insulator, the only leakage current remaining is the shunt or "dark" resistance of each PIN-Pd. Their effect can be trimmed out by the OP´s offset voltage control.

The bias current of the OP´s JFET input stage is clearly below 1 pA at 293 K. When temperature rises, this error current doubles about every 5 K (Fig. 2).

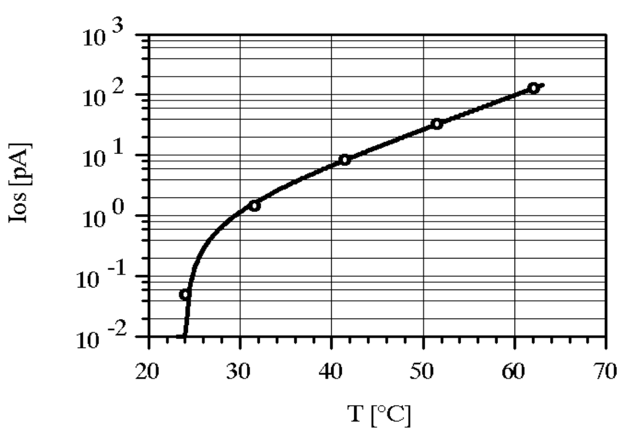

Fig. 2: Offset current of CFC vs. Temperature

3.2 Gain Linearity and Accuracy

Conversion factor calibration and linearity measurements (Fig. 3, 4) were performed using a Keithley 261 current calibrator, which was believed to add less than 3% error, and a HP digital counter.

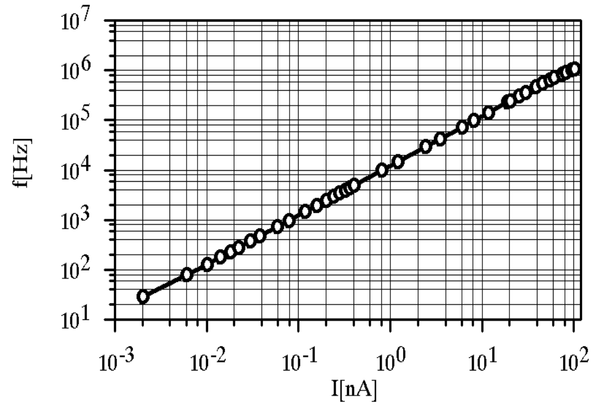

Fig. 3: Output frequency of CFC vs. Input current

At low currents, linearity is affected by the isolation resistance of the integration capacitor (>10 GΩ) and the open loop gain limit of the OP, as well as it´s bias current (see above) and voltage, and finally the resistance of the calibrator, or the detector respectively. The linearity error at high currents depends on the OP´s unity gain frequency of ~ 8 MHz[4], introducing about 40 ns propagation time into the charge-balancing loop, and the limited current rise time of the reset current source (Fig.4).

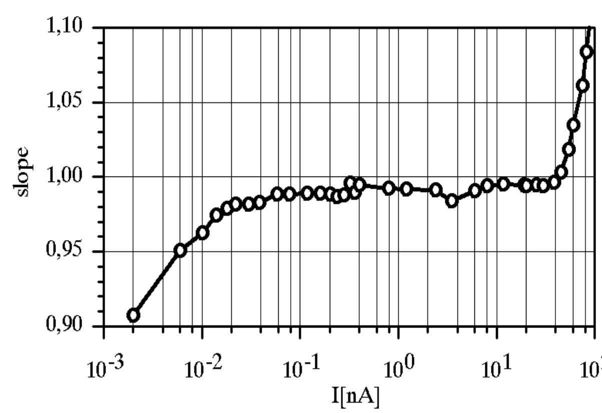

Fig. 4: Linearity error of CFC (slope of Fig. 3)

3.4 Frequency Stability

The output pulse rate stability of the CFC is shown in Fig. 5. It was measured at 10 nA input current (1 % full scale excitation) and displays the pulse event counts in 1000 intervals of 1ms length; a typical distribution due to random sampling is evident.

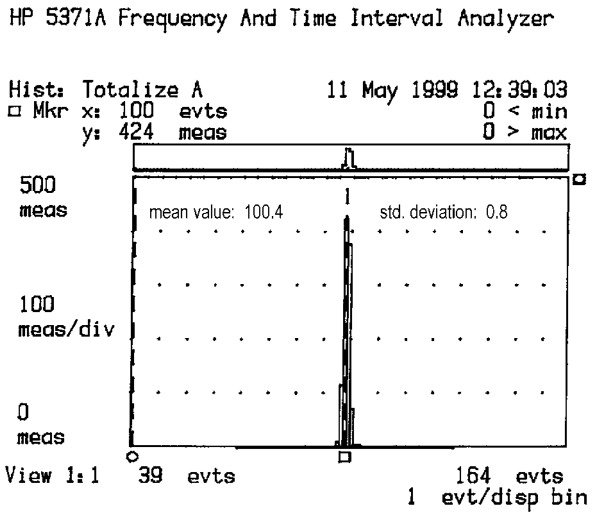

Fig. 5: Pulse count distribution of CFC, 10 nA input current, 1ms counting intervall

3.5 Time Response

The CFC´s response time depends on the propagation delay times inside the charge-balance loop, totally about 70 ns, and half of oscillator´s clock period - 250 ns - , but mostly on the momentary working frequency. After an input current step, the new frequency normally settles within 3 reset cycles, exhibiting no creep or overshoot. The response to fast fluctuations in an ion spill, detected with an IC and a scintillator at the same time, is shown in Fig. 6. The first peak of the displayed interval and the entire middle part of the spill have driven the CFC into overload; this condition obviously causes no latch-up effect.

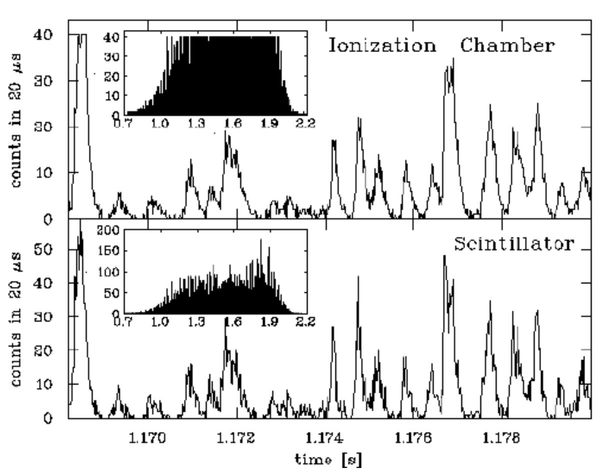

Fig. 6: Fluctuations in a Bi-spill, detected with an IC-CFC set and a SZ simultaneously

4 CONCLUSION

This new CFC is suitable for current measurements between 1 pA and 10 µA, e. g. from ionization chambers or secondary electron monitors as well as photo multiplier tubes or vacuum gauges. It has a linear range of nearly 6 decades and a fast time response – an improvement of several orders of magnitude, if compared to the converter type used in the past.

Two switchable current ranges (100 nA, 10 µA) , polarity selection, overload detection, a test current, an additional NIM output and a remote control are a matter of course.

Each converter has it´s own plug-in power line adaptor. Output pulse transmission is performed by differential RS-485 line drivers via fast optocouplers, allowing for floating operation and a transmission line length of up to 200 m. Specially designed counter stations and interfaces provide data processing and device control.

It has to be mentioned, that gain and offset stability of the new converter, if compared to the earlier type, could not be fully preserved.

The CFC described above is filed under patent no. DE 195 20 315.

6 ACKNOWLEDGEMENTS

The author wishes to thank O. Keller for his help while assembling and testing the prototype, P. Forck for providing the graphics of the ion beam spill, and P. Strehl for encouragement at the start of the project.

[1] Williams, J. (Ed.), Analog Circuit Design, pp 215 - 230, Butterworth-Heinemann, 1991

[2] Shapiro, E. G., Linear Seven Decade Current-To-Frequency Converter, IEEE Trans. Nuclear Science NS-17, 1970, pp 335 - 344

[3] Optoelectronics Databook, SIEMENS AG, 1990

[4] IC Databook Vol. 33c, BURR-BROWN Corp., 1992

Posters Tuesday

CLOSED-ORBIT CORRECTION USING THE NEW BEAM POSITION MONITOR ELECTRONICS OF ELSA BONN

J. Dietrich and I. Mohos, Forschungszentrum Jülich GmbH, Germany
J. Keil, Physikalisches Institut, Universität Bonn, Germany

Abstract

RF and digital electronics, developed at the Forschungszentrum Jülich/IKP were integrated to form the new beam position monitor (BPM) system at the Electron Stretcher Accelerator (ELSA) of the University of Bonn. With this system the preservation of the polarization level during acceleration was currently improved by a good correction of the closed-orbit. All BPM offsets relative to the magnetic quadrupole centers were determined by the method of beam-based alignment. The optics functions measured by the BPM system are in good agreement with theoretical predictions.

1 INTRODUCTION

The 3.5 GeV Electron Stretcher Accelerator at Bonn University was recently upgraded for the acceleration of polarized electrons [1]. During the beam acceleration several strong depolarizing resonances have to be crossed. Steering the beam through the magnetic quadrupole centers of ELSA can reduce the strengths of one type of resonances connected with the vertical closed orbit distortions. A common technique to determine the magnetic axis of a quadrupole relative to the axis of the beam position monitor is the method of beam-based alignment [2]. To make use of this method a BPM system with a good resolution and long term stability is required which can also be used at low currents of some mA typically for the operation of ELSA with polarized electrons. The new BPM electronics forming a 28 BPM orbit measurement equipment are integrated in the control system of ELSA.

2 FRONT-END ELECTRONICS

The BPM front–end electronics [3] were developed at the Forschungszentrum Jülich/IKP and produced by KFKI in Hungary. Each station consists of an RF narrowband signal processing unit and a data acquisition and control unit with capabilities for data preprocessing. Both units are enclosed in an RF-shielded crate with power supply and placed close to the four-button monitor chambers in order to reduce RF interference on the button signals. Altogether 28 monitor stations are connected via four optically coupled serial fieldbuses to the VME host computer.

2.1 RF Signal Processing Unit

A narrowband superhet RF electronics (Fig.1) detects the amplitudes of the four button signals at the fundamental frequency of f_{RF} = 500 MHz. At the input adjustable attenuators equalize the attenuation of the four channels and lowpass filters remove the higher harmonics of f_{RF} from the signal spectrum. An RF multiplexer with programmable button sequence scans the four buttons. The succeeding low noise narrowband preamplifier (B = 5 MHz, G = 20 dB) rejects the image range. For high signal levels a switchable 30 dB attenuator can be inserted. A balanced mixer transposes the desired frequency range to the intermediate frequency, where narrowband filters reduce the bandwidth to ≈200kHz and an amplifier with controlled gain enhances the signal level appropriate for demodulation.

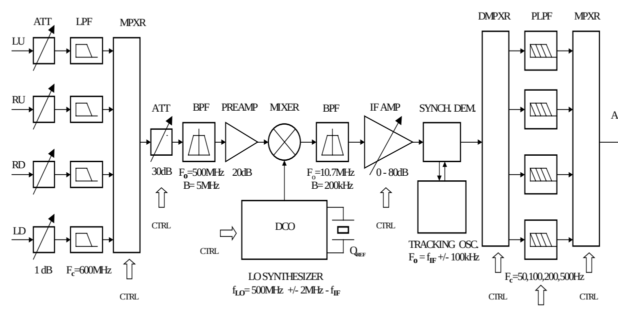

Figure 1: Block diagram of the RF signal processing module

On-board remote-controlled synthesizer generates the LO signal applied to the mixer, determining the band-center frequency of the signal processing.

The band-center frequency is adjustable in the range of 500 MHz ± 2 MHz with steps of 50 kHz. Frequency changes within the IF bandwidth will be automatically tracked in real time. The output signal of the synchronous demodulator with a linearity of ≈0.5 % is proportional to the rms value and carries level changes with frequencies up to 500 Hz. The gain control range of the processing chain is about 100 dB.

Signal level dynamic range of the electronics is between –80 dBm and +10 dBm. The typical equivalent beam position noise is x_{rms} < 0.5 µm at P_{in} = -46 dBm and B = 10 Hz assuming that the BPM sensitivity is K_{BPM} = 14.5 mm (Fig. 2).

Figure 2: Equivalent rms position noise

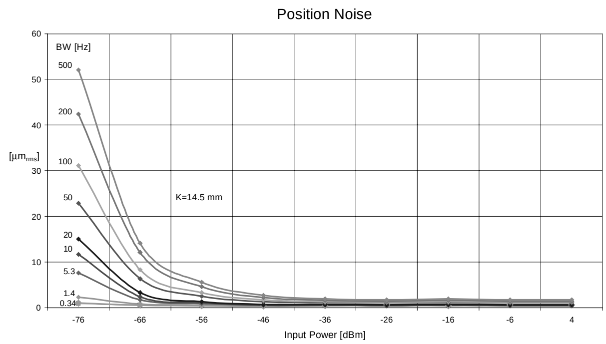

2.2 Data Acquisition Unit

The data acquisition (DAQ) unit consists of an 8 bit microcontroller with 64 kbyte EPROM, 32 kbyte RAM, a built-in timer and a 1 Mbit/s asynchronous serial interface with galvanic isolated twisted-pair transceiver (Fig. 3). A 12 bit ADC digitizes the demodulated electrode signals and 12 bit DAC controls the gain. Several bits are used for timing and bandwidth control and a 3-wire interface for the synthesizer.

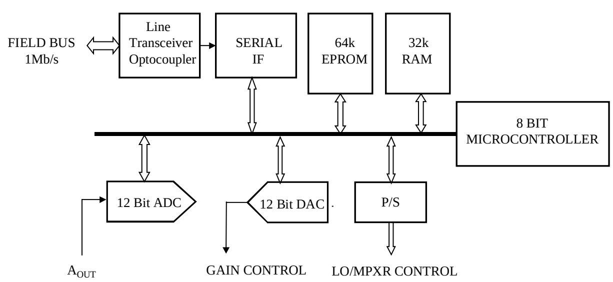

Figure 3: Block diagram of the data acquisition and control module

The built in firmware of the DAQ-unit controls the data acquisition and timing functions and performs some basic preprocessing tasks. The host controls the firmware and the timers by means of R/W registers containing numeric and mode parameters.

3 DATA PROCESSING

3.1 Low Level Data Preprocessing

After sequential digitizing of the four button signals the horizontal and vertical positions are computed. In automatic gain control mode a gain correction value will be prepared for the next cycle. Subsequently a digital lowpass filter algorithm reduces the signal bandwidth. Its cutoff frequency is programmable in 13 steps. The overall bandwidth can be reduced from 500 Hz down to 0.1 Hz. The sampling interval is selectable between 1-256 ms. The number of the samples is programmable for limited (1-4095) or continuous sample stream. On request of the host the acquired and preprocessed data will be transferred in real time, or can be buffered in the 4 kS RAM for slower read or later use.

An optional plug-in can be added to the front-end electronics containing a 4 MB flash memory and an arithmetic processor. Using a downloaded dataset and the raw data delivered by the DAQ-unit, the unit performs scaling, offset and nonlinearity correction according to the BPM chamber geometry.

3.2 BPM Host Computer

The BPM system was integrated in the architecture of the control system of ELSA, which is organized hierarchically in three layers with distributed intelligence. The presentation level is based on HP9000/700 workstations running HP-UX as the operating system. Its purpose is to display the status of the machine and to hold the distributed database. The GUI is based on the X-Window system and OSF/Motif. The process level is connected via Ethernet with the presentation level and is used for data preprocessing from devices using VMEbus boards running the VxWorks real-time operating system on Motorola 68K CPUs. The lowest level is the fieldbus level for the direct communication with the devices.

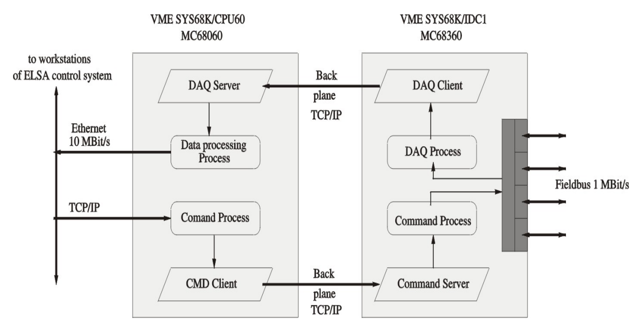

Figure 4: Architecture of the high level data acquisition system

In the case of the BPM system the front-end electronics are connected with four fieldbus lines to a VMEbus communication controller board based on the MC68360 (QUICC) processor. His purpose is to trigger the data acquisition and to read back the measured positions from the BPM stations. Due to the limited floating point capabilities of the QUICC a dedicated MC68060 CPU is used for the high level data processing. The communication between the two VME boards is done over the backplane using TCP sockets (Fig. 4).

3.3 High Level Data Processing

In the free run mode the data acquisition of all BPM stations is triggered in regular intervals by the fieldbus host computer and their data is read by the host. The data of all BPMs is immediately passed over for to the BPM controller CPU. A low priority process read periodically the actual BPM status values. Commands for changing of BPM settings are passed over to the server process using a second TCP connection.

The BPM controller CPU corrects first for unequal electrode attenuations [4] and linearizes the response of the electrode configuration using a combination of a look-up table and a two-dimensional local polynomial approximation of second degree. Closed orbit data is transferred to the workstations and can be displayed and further analysed. Several different orbit correction algorithms like harmonic correction, least square correction using singular value decomposition (SVD), MICADO, and local bumps are available.

4 RESULTS

4.1 BPM Offsets

The technique of beam-based alignment [2] was used to determine the magnetic centers of the quadrupoles, which define the zero position of the nearby BPMs. This is very important for ELSA, because the resonance strengths of the imperfection resonances depend on the correction of the vertical closed orbit during resonance crossing. Offsets of several millimeters where found by this method. The reproducibility of the zero positions is approximately 100 µm.

4.2 Dispersion Function

The horizontal dispersion function $D_x(s)$ was determined by changing the RF frequency and measuring the shift of the closed orbit (Fig. 5). The measurement for standard tunes of ELSA and is in good agreement with the theoretical predictions. The measured rms-value of $D_z(s)$

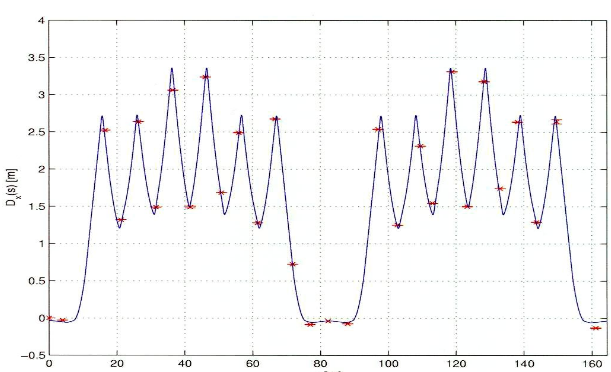

is about 6 cm.

Figure 5: Theoretical (solid line) and measured (data points) dispersion function $D_x(s)$

4.3 Orbit Correction

Before orbit correction the orbit distortion was reduced by a good alignment of the quadrupole and dipole magnets. For the closed orbit 20 horizontal and 18 vertical steerer magnets were used. The uncorrected orbit with x_{rms} = 2.46 mm and z_{rms} = 0.93 mm was reduced after five iterations to values of x_{rms} = 0.126 mm and z_{rms} = 0.141 mm using the SVD orbit correction algorithm. As an example the uncorrected and corrected orbit is shown in Fig. 6.

Figure 6: Uncorrected (solid) and corrected (dashed) horizontal closed orbit

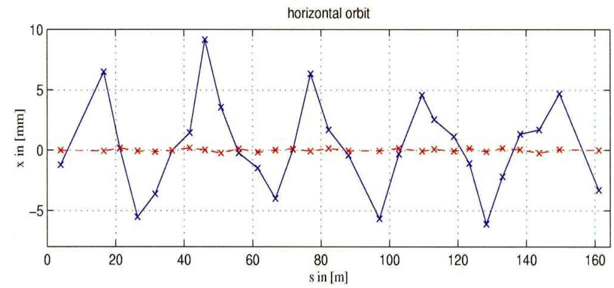

5 CONCLUSIONS

The close placing of the RF and data acquisition electronics to the pick-up reduces effectively the RF interference and allows utilizing the remarkable noise performance of the front-end unit. The galvanically decoupled fieldbus eliminates the disturbances caused by the potential difference between the monitor chambers and the host and enhances the reliability of the data transfer. Software development on the user's side is not necessary for the low-level acquisition, control and preprocessing. The distributed and time-overlapped data processing improves the overall system performance. It is possible with the new BPM system to correct the closed orbit of ELSA up to rms values of 130 µm in the horizontal and 140 µm in the vertical plane.

REFERENCES

[1] Steier, C. et al.: "Acceleration of Polarized Electrons in ELSA", EPAC 98

[2] Röjsel, P.: "A beam position measurement system using quadrupole magnets magnetic centra as the position reference", NIMA 343 (1994) 374

[3] Mohos, I. et al: "500 MHz Narrowband Beam Position Electronics for Electron Synchrotrons", AIP Conf. Proc., No. 451, 1998

[4] Chung, Y. et al: "Offset Calibration of the Beam Position Monitor Using External Means", AIP Conf. Proc., No. 252, 1991

REAL -TIME BETATRON TUNE MEASUREMENT IN THE ACCELERATION RAMP AT COSY – JÜLICH

J. Dietrich and I. Mohos, Forschungszentrum Jülich GmbH, Germany

Abstract

A new real-time method for betatron tune measurements at COSY was developed and tested from the early 1997. A bandlimited broadband noise source was used for beam excitation, the transversal beam position oscillation was bunch-synchronous sampled and digitized with a high resolution ADC. The Fourier transform of the acquired data represents immediately the betatron tune. After the first promising experiments an automatic tunemeter was constructed. The tunemeter is used as routine diagnostic tool since end of 1998.

1 INTRODUCTION

The cooler synchrotron and storage ring COSY, with a circumference of 184 m and single bunch, delivers medium energy protons. The corresponding revolution frequencies in the acceleration ramp are between 0.45 MHz (flat bottom) and 1.6 MHz (flat top). For beam diagnostic measurements magnetic impulse kicker [1] and broadband stripline exciter [2] can be used. The mode of excitation and the strength can be automatically set. A basic task for beam diagnostic is the measurement of the tune in the acceleration ramp.

The betatron tune (Q) is the quotient of the frequency of the betatron oscillation and the particle revolution frequency. The betatron frequency ($f_\beta = Q * f_0$) is usually higher than the revolution frequency, but only the fractional part (q) of the betatron tune can be measured:

$$f_\beta^n = n * f_0 \pm Q * f_0 = (n \pm q) * f_0 .$$

For tune measurements the betatron oscillation of the particles is resonantly enhanced by RF-excitation via the stripline unit. Beam position monitors (BPM) [3] with low noise broadband amplifiers deliver signals proportional to the beam response on the excitation. The sampled and digitized difference signal is processed for monitoring the betatron tune. A bunch-synchronous pulse train, necessary for the sampling, is derived from the sumsignal of the same BPM.

2 SYNCHRONOUS SAMPLING AND FFT

Performing the discrete Fourier transformation of N subsequently acquired samples follows:

$$S\left(\frac{m}{NT}\right) = \sum_{n=0}^{N-1} s(nT) * e^{-j(2\pi nm)/N}$$

with T time interval of the samples,

$s(nT)$ the n-th sample of an array of N samples

$S\left(\frac{m}{NT}\right)$ the m-th Fourier component at $f_m = \frac{m}{NT}$

The frequency of a Fourier component relates to the sampling frequency ($f_s = 1/T$). Due to the bunch-synchronous sampling the frequencies in the FFT array are normalized to the revolution frequency.

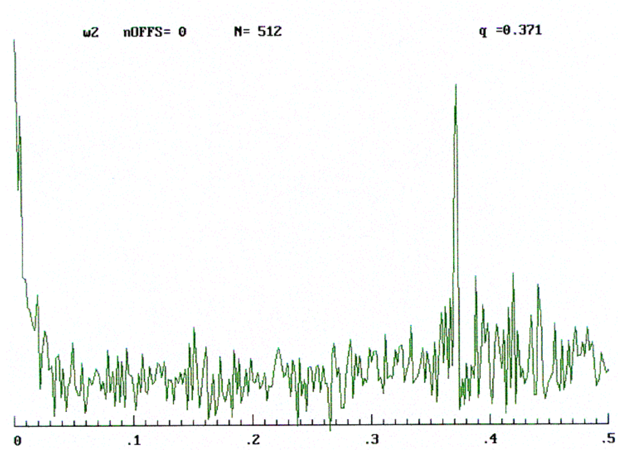

Figure 1: Betatron line in the normalized frequency domain

A sideband caused by the betatron oscillation appears as a peak in the normalized frequency domain. Fig. 1. shows a sideband line in the spectrum [4]. Because of using the revolution frequency as sampling frequency, it follows:

$$q * f_0 = f_q \Leftrightarrow f_{m'} = \frac{m'}{N} * f_0 \qquad \text{therefore}$$

$$q = \frac{m'}{N} \qquad 0 < q \text{ or } (q\text{-}1) < 0.5$$

In the normalized frequency domain the tune value is directly shown. The frequency f_m of the m-th datapoint ($m = 1,.., N / 2$) is $f_m = m / NT$ with $1 / T = f_S = f_0$. If f_m' is the frequency of the sideband it follows $f_m' = m' / N * f_0$ and due to $f_m' = q * f_0$ then: $q = m' / N$. Using $f_s = 1$ the normalized frequency corresponds immediately to the fractional tune.

3 TUNEMETER CONFIGURATION

Via the stripline unit coherent betatron oscillations in horizontal and vertical direction can be raised by means of broadband transversal excitation [5]. The cumulating effect of the subsequent excitations on the circulating beam results in a coherent oscillation at resonance frequencies only, other components of the excitation are neutralized and therefore have virtually no effect on the beam.

A white noise source generates the exciting signal. Bandpass filter with fixed cutoff frequencies (BW= 100 kHz – 2 MHz) limits the excitation bandwidth. The frequency range of the noise covers always at least one betatron sideband at the fundamental harmonics in the whole ramp without frequency feedback. The excitation can be enabled/disabled by means of a fast GaAs switch controlled by either remote commands or a timer unit. The programmable excitation level changes in real-time.

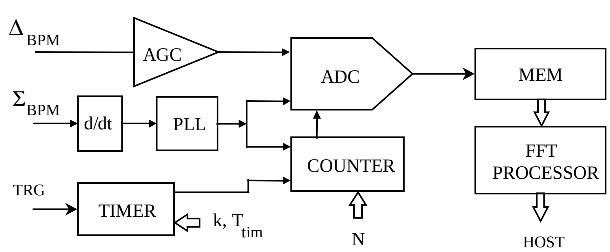

Figure 2: Block diagram of the FFT tunemeter.

A beam position monitor picks up the beam response on the excitation. Low noise gain controlled amplifiers control the level of the sum and difference signals. The bunch-synchronous pulse, necessary for the sampling, is derived from the sum signal of the same BPM. Phase locked loop with narrowband loop filter generates clock pulse with low tracking jitter in the whole range between injection and flat top. With proper signal processing the clock generator tracks also the synchrotron oscillation. For investigation of the synchrotron oscillation a signal proportional to the synchrotron oscillation can be also derived from the tracking circuitry of the clock generator.

A high resolution ADC digitizes the difference signal.. The timers of the measurement trigger and of the excitation gate are synchronized. Fig.2 shows the block diagram of the FFT tunemeter.

4 SIGNAL AND DATA PROCESSING

The betatron oscillation appears as an amplitude modulation on the beam position signal evoking double sidebands around each harmonics of the revolution frequency and also around DC in the spectrum of the position signal of the bunched beam. The peak value of the BPM difference signal, proportional to the beam position, will be sampled by means of a fast sample and hold circuitry and digitized with a high resolution ADC. The positive edges of the bunch-synchronous clock start the sampling at the bunch peaks i.e. at the highest betatron amplitude. The gain controlled amplifiers grant an optimal utilisation of the 14 bit ADC. The peak value of subsequent bunches carrying the betatron oscillation will be recorded. The Fourier transform of this array invokes the fractional betatron tune.

This method combines the functions of a synchronous demodulator and a frequency normalizer. Due to the bunch-synchronous sampling the frequency components of the synchrotron oscillation are suppressed. The sampled data therefore contain mainly the betatron sidebands transposed into the range between DC and f_0 /2. The lowest normalized frequency is zero (DC component), the usable highest is f_0/2, the corresponding range of q or (1-q) is between 0 and 0.5. Subsequently acquired spectra with the same time intervals are displayed as a waterfall diagram showing the tune as a function of the time (Fig.3.) On the left edge of the screen the values of the detected tune peaks are also numerically displayed.

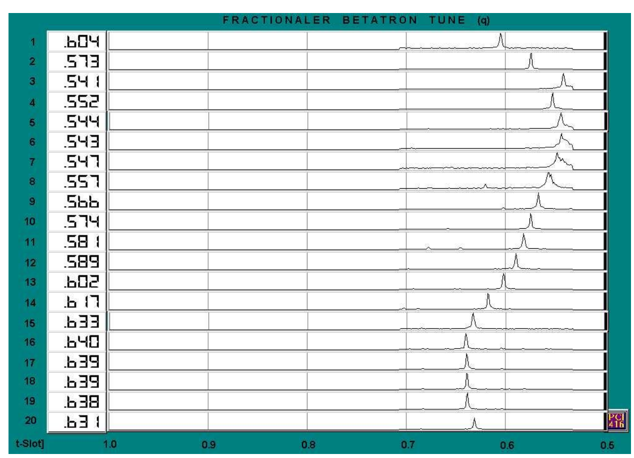

Figure 3: Display of a tune measurement in the ramp consisting of averaged FFT spectra

The beam rigidity is low in the lower energy range, therefore very weak excitation is adequate for a distinct betatron response. In the ramp the excitation strength has to be increased. The time function of the excitation level is programmable. It is held as low as possible for an optimum of signal to noise ratio and as small as possible particle loss. For this reason the excitation is switched on only for the duration of the data acquisition by means of a fast GaAs switch. The data are taken in blocks of N datawords each and are stored sequentially in memory. For start the COSY timing system triggers an internal timing logic, which in turn generates k timing pulses with constant time interval for k tune values. The number k of timing pulses and their interval must be properly chosen, in order to obtain the tune measurement time overlapping the total acceleration ramp time as desired. In a data acquisition cycle $k*N$ samples corresponding k tune value are sequentially acquired.

The acquired datablocks are transformed by FFT resulting in frequency spectra with $N / 2$ datapoints. As the duration of the acquisition depends on N, its value must be properly chosen, because it determines the frequency resolution of the FFT-spectra (equal to $1 / NT$ with $1 / T = f_s$, here $1 / T = f_0$). Although the duration changes in the acceleration ramp, the resolution of the tune ($1 / N$) is constant. As shown above, the bigger the quantity of the samples in the array used for evaluation the higher the frequency resolution and consequently the accuracy of the tune measurement.

The average acquisition time ($N * T_0$) for a tune resolution of $5 * 10^{-3}$ is less then 2 ms. The transformation of a record needs 35 ms in the used configuration, thus the frequency of the real-time tune measurements reaches up to 25 Hz. With fast FFT processor or with stored records and off-line processing equivalent rate above 500 Hz can be achieved. To improve the noise floor the spectra can be averaged. Programmable window selects the region of interest around the tune peak. Graphic and numeric display shows the tune as a function of time.

5 IMPLEMENTATION FOR MULTIBUNCH RING

In multibunch electron synchrotrons containing k bunches the fundamental frequency is $k * f_{REV}$. The betatron sidebands appear around its harmonics ($j * k * f_{REV} \pm q * f_{REV}$, $j = 0, 1, ..$). In case of unevenly filled bunches further lines with double betatron sidebands appear in frequency intervals of f_{REV}.

For the tune measurement signal preprocessing electronics convert the spectrum into a lower frequency range corresponding with the single bunch spectrum. The main RF transposes the difference signal of a BPM. On the output of the mixer the betatron sideband of the fundamental bunch frequency appears between DC and $f_{REV} / 2$. Bandpass and lowpass filters exclude all higher frequency components to avoid aliasing. A divide by k counter generates the sampling frequency ($f_s = f_{REV}$). As the revolution frequency at electron accelerators is usually constant in the ramp, clock recovery from the sum signal is not necessary by all means.

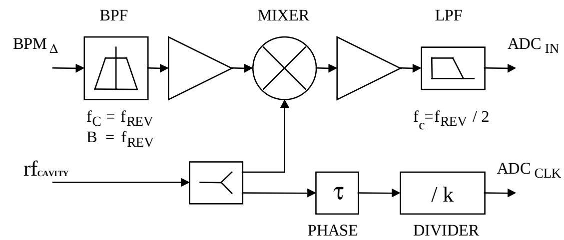

Figure 4: Blockdiagram of the preprocessing unit

Adjustable delay optimizes the sampling phase for the highest sensitivity. However the longitudinal oscillation is not separated without tracking clock. Fig. 4 shows the blockdiagram of the preprocessing unit.

6 CONCLUSIONS

Remarkable advantages: (1) Spurious peaks with constant frequency can easily be recognized and separated. (2) No frequency feedback on the excitation is necessary. (3) The acquisition time is short, nonlinear changes of the tune have less influence on the accuracy. (4) Because of the bunch-synchronous sampling, the FFT-spectra contain only the frequency range up to $0.5 * f_0$. (5) Due to the tracking clock the longitudinal and transversal spectra are separated. (6) The gated low level excitation causes no noticeable particle loss. (7) The method with some additional signal conditioning can easily be implemented at multiple bunch machines.

REFERENCES

[1] Dietrich, J. et al., “Transverse Measurements with Kicker Excitation at COSY-Jülich”, EPAC’96, Barcelona, 1996

[2] Bojowald, J. et al., “Stripline Unit,” Jül-2590, 1992 and Bojowald, J. et al.,”Longitudinal and Transverse Beam Excitations and Tune Measurements,” Jül -2879, 1993

[3] Biri J. et al., ”Beam Position Monitor Electronics at the Cooler Synchrotron COSY-Jülich,” IEEE Trans. Nucl. Sci.,1994

[4] Bojowald, J. et al., “Dynamical Tune Measure-ments at COSY-Julich”, DIPAC97, Frascati, 1997

[5] Dietrich, J. et al., “Broadband FFT method for Tune Measurements in the Acceleration Ramp at COSY Jülich”, BIW’98, Stanford, 1998

Measuring Beam Intensity and Lifetime in BESSY II [1]

R. Bakker, R. Goergen, P. Kuske, J. Kuszynski[2]
Berliner Speicherring-Gesellschaft fuer Synchrotronstahlung mbH
(BESSY) Rudower Chaussee 5 D-12489 Berlin Germany

Abstract

The measurement of the intensity of the beam in the transfer lines and the storage ring are based on current transformers. The pulsed current in the transfer lines is measured with passive Integrating Beam Current Transformers (ICT). The bunch charge is transferred to a DC-voltage and sampled with a multifunction I/O-board of a PC. The beam current of the storage ring is measured with a high precision Parametric Current Transformer (PCT) and sampled by a high quality digital volt meter (DVM). A stand alone PC is used for synchronisation, real-time data acquisition and signal processing.
Current and lifetime data are updated every second and send via CAN- bus to the BESSY II control system. All PC programs are written in LabVIEW.

1 INTRODUCTION

BESSY II started operation as a third generation synchrotron radiation light source at the beginning of this year. The facility consists of the 1.7 GeV electron storage ring and the full energy injection system comprised of the synchrotron cycled at 10 Hz and a 50 MeV microtron as a pre-injector [1]. Along the chain of accelerators and transfer-lines different types of current monitoring devices are employed and have to fulfil the following requirements: measurement of the intensity of the pulsed beams in the two transfer lines, the accurate determination of the intensity of the accelerated beam in the synchrotron, and the high precision current measurement of the stored beam in the ring. All measurements had to be performed in real-time and have to be updated every second in order to allow for the fast and accurate extraction of the injection efficiency and the lifetime of the beam. In addition to these measurements and the determination of related parameters, the system had to supply trigger and timing signals for the beam position monitor (BPM) system running in the single turn mode [2]. In this system 4 shots and the corresponding injected beam intensities are required to determine the position of the beam as accurately as possible. This is achieved by current normalising the 4 data sets. As a solution a stand-alone hardware triggered solution based on a PC running under LabVIEW was chosen and the system has been realised with commercially available components.

2 HARDWARE

The current transformers were manufactured by BERGOZ [3, 4]. In the transfer lines the sensors are mounted over a short insulated piece of vacuum pipe and shielded by an aluminium cover. In the storage ring and in the synchrotron the installation of the DC current transformer (DCCT) has been realised with more care in order to prevent RF fields of the electron beam leaking to the sensor's head and heating it up. In addition onion-like thin soft iron sheets shield the sensor from magnetic stray fields created by nearby magnets. The vacuum chamber for the DCCT is based on the SLAC B-Factory design[5].

The layout of the beam current monitor system is shown in Fig. 1. The stand alone industry PC has been equipped with three additional boards. The first is a multifunction input/output-board AT MIO-16X from National Instruments. This board in combination with additional external trigger electronics creates all the required timing signals for the DVM, the synchronisation of the pulsed beam intensity measurements, and synchronises the single turn beam position measurements with the intensity measurements. The multiplexed 16 bit ADC on the multifunction board is used for the acquisition of the signals delivered by the ICTs. The digital outputs of the board are used to switch the external electronics to the desired modes of operation. The second board is the GPIB interface required for the communication to the high precision DVM HP3458A from Hewlett Packard which measures the current of the stored beam.

Signal processing is performed in the following way: The microtron delivers pulses of approximately 1 µs duration and the bunch train extracted from the synchrotron has a length of 360 ns. Every 100 ms the charge passing through the transfer lines is detected by the ICT. Over a certain amount of time the beam charge monitor integrates the signal and produces a constant output voltage which is finally sampled by the multifunction I/O-board. With the sampling rate of 100kS/s of the ADC a 15 time over-sampling of each channel is obtained.

The beam current of the storage ring is measured with a high precision (PCT) and sampled by the DVM. The intensity of the beam accelerated in the synchrotron can

[1] This work is funded by the Bundesministerium für Bildung, Wissenschaft, Forschung und Technologie and by the Land Berlin.

[2] Email: kuszynski@bii.bessy.de

be digitised through one of the additional ADC channels of the multifunction board. Currently the DC-signal is displayed on a scope in the control room only.
The correct timing of the measurements is realized through the trigger generator which is connected to the accelerator timing system. Inputs are the injection times into the synchrotron and into the storage ring and the revolution frequency of the storage ring for the BPM system.

The communication between the intensity monitor and the central BESSY II control system is realized with a third interface card and through the CAN bus. The PC together with the electronics is mounted in a 19'' rack in the storage ring hall close to the current transformers.

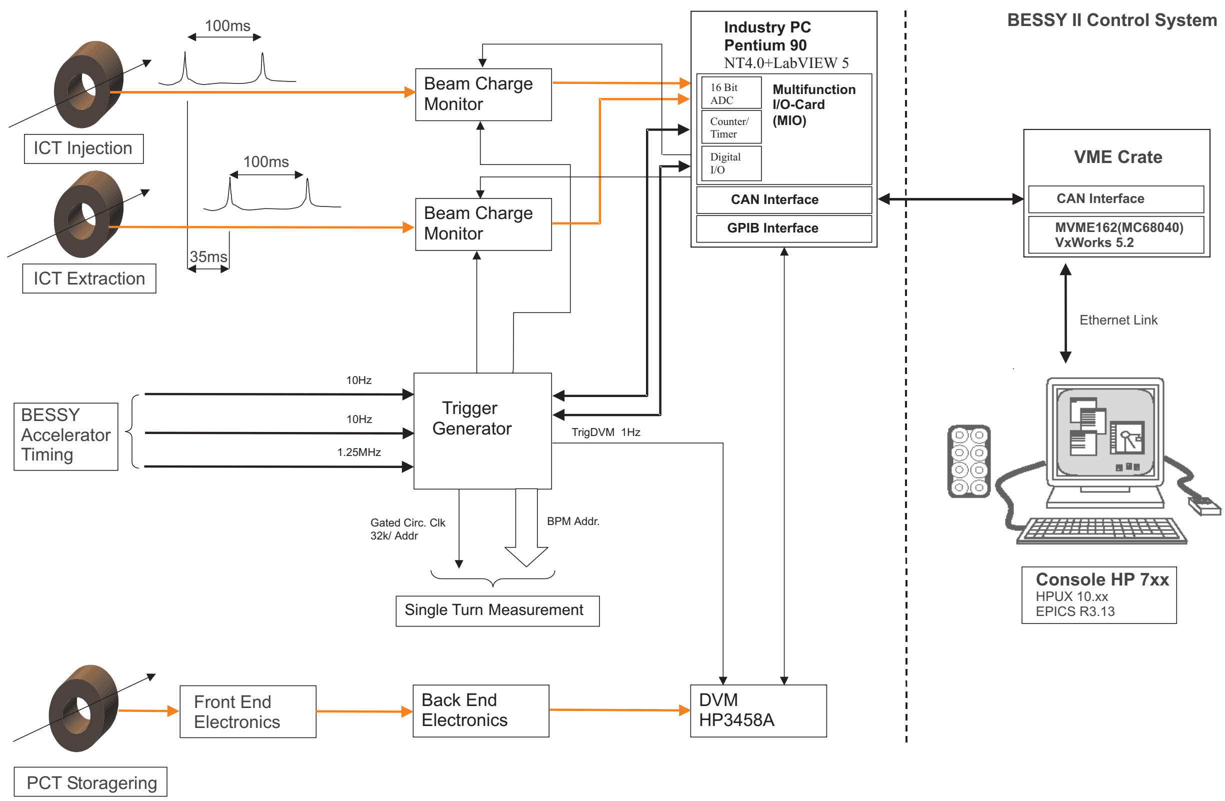

Figure 1: Hardware of the BESSY II beam current measurement system

3 SOFTWARE

The software has to fulfil these requirements:

- Continuous acquisition of the intensities in the transfer lines.
- Measurement of the storage ring current with high precision every second and the calculation of the lifetime from the decay of the intensity over the last 10, 50 and 100 seconds.
- Determination of the injection efficiency.
- Preparation of the results and communication through the CAN bus to the control system with an update rate of 1 per second.
- Synchronization of the BPMs in the single turn mode.

The required real-time operation of the system with all the feature mentioned above was difficult to realize within the BESSY II control system concept which is based on Epics, VxWorks, and the non-deterministic Ethernet. A stand-alone Pentium PC has been chosen as a solution which is running under Windows NT4 and Labview5. LabVIEW is a multitasking system that can run multiple programs in multiple threats. So we could realize the required real-time data acquisition system under the operation system Windows NT4. The program structure is shown in Fig. 2.
The whole system had to be designed in such a way that no special start-up procedure is required. After a power fail the operating system of the PC, the measuring process, the data analysis and the communication to the central control system start automatically.

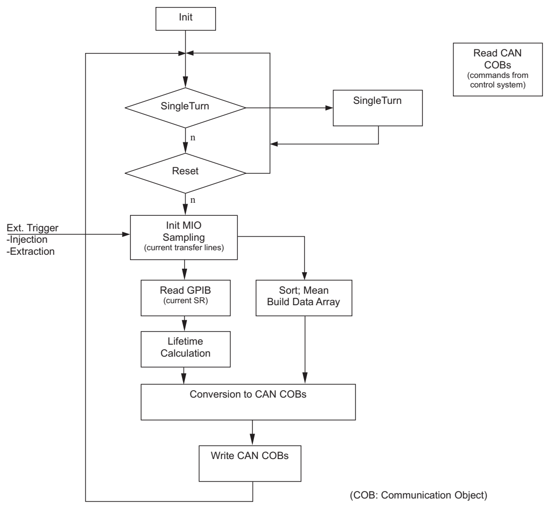

Figure 2: Program structure of data acquisition system

4 MEASUREMENT RESULTS

This beam current measurement system is in operation continuously and without any failure since the beginning of the commissioning in April 1998.

The measurements in the transfer channels are disturbed by high noise levels predominantly created by the pulsed kicker and septa magnets and the pulse forming networks of the microtron. Better signals have been obtained by signal amplification with a 24 dB low noise pre-amplifier very close to the sensor heads and low pass filters in the signal chain. Typical signals are shown in Fig. 3 and 4. Even though the signal-to-noise ratio was not large, these signals and the actual current accelerated in the synchrotron are very helpful in the daily optimization process. In order to achieve an accuracy for the intensities in the injector of better than 1 percent further improvements are required.

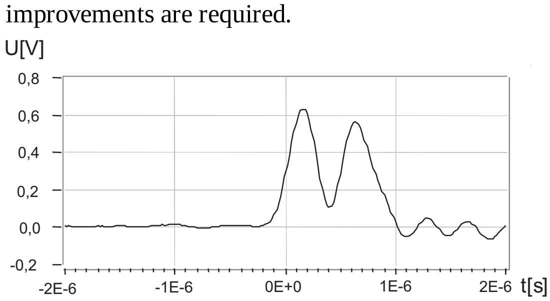

Figure 3: Typical current pulse delivered by the microtron (first pulse 6.5mA/ 550ns)

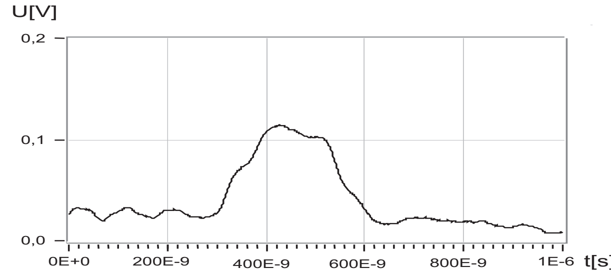

Figure 4: Typical signal of the beam extracted from the synchrotron (1mA/ 300ns)

In the storage ring the beam lifetime is still dominated by the vacuum pressure because the vacuum system had to be opened on several occasions for completing machine elements and user front-ends. Consequently, photon desorption is still the dominant process in reducing the vacuum pressure and the lifetime [6]. Fig. 5 displays the lifetime at 20 and 100 mA. Each time the vacuum system was broken the integrated dose curve was reset. The graph displays logged lifetime data [1].

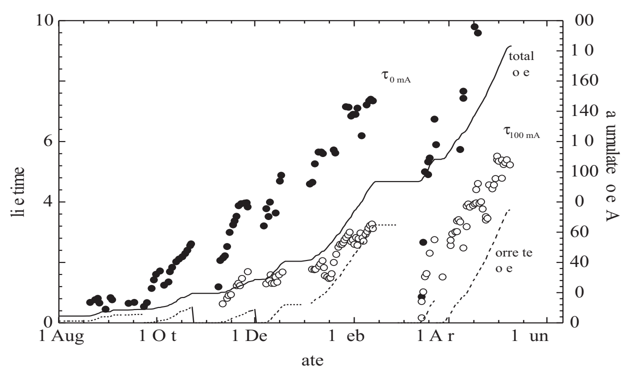

Figure 5: Lifetime at 20mA (solid dots) and 100mA (open dots) and accumulated dose (curve) versus time

REFERENCES

[1] R.Bakker for the BESSY II Project Team: ”Status and Commissioning Results of BESSY II” , EPAC, NewYork (1999)

[2] P. Kuske, et al. ”Experience with the BPM system of the BESSY II Storage Ring”, PAC, NewYork (1999)

[3] BERGOZ: ”Beam Charge Monitor User´s Manual”

[4] BERGOZ: ”Parametric Current Transformer Instruction Manual”

[5] J. Hinkson, private communication

[6] S.Kahn: ”Study of BESSY II Beam Lifetime”, PAC, NewYork (1999)

Radiation Protection System installation for the Accelerator Production of Tritium / Low Energy Demonstration Accelerator Project (APT/LEDA).

J. E. Wilmarth, M. T. Smith, T. L. Tomei
Los Alamos National Laboratory, Los Alamos, NM

Abstract

The APT/LEDA personnel radiation protection system installation was accomplished using a flexible, modular proven system which satisfied regulatory orders, project design criteria, operational modes, and facility requirements. The goal of providing exclusion and safe access of personnel to areas where prompt radiation in the LEDA facility is produced was achieved with the installation of a DOE-approved Personnel Access Control System (PACS). To satisfy the facility configuration design, the PACS, a major component of the overall radiation safety system, conveniently provided five independent areas of personnel access control. Because of its flexibility and adaptability the Los-Alamos Neutron-Science-Center-(LANSCE)-designed Radiation Security System (RSS) was efficiently configured to provide the desired operational modes and satisfy the APT/LEDA project design criteria. The Backbone Beam Enable (BBE) system based on the LANSCE RSS provided the accelerator beam control functions with redundant, hardwired, tamper-resistant hardware. The installation was accomplished using modular components.

RADIATION PROTECTION SYSTEM

Los Alamos National Laboratory's MPF-365 at TA-53 is a four-story building attached to a 470-foot-long underground tunnel. See Figure 1. In 1997 the Accelerator Production Of Tritium (APT) Low Energy Demonstration Accelerator (LEDA) project started installation work in MPF-365. The LEDA project accelerator consists of five major components:

1. The Injector Support Platform, which is movable with a detachable Ion Source Injector (LEBT).
2. The Radio Frequency Quadrapole (RFQ) section.
3. High Energy Beam transport (HEBT).
4. Water Shielded Beam Stop Vessel.
5. Detachable/Movable pump cart which supplies high pressure water to the beam stop.

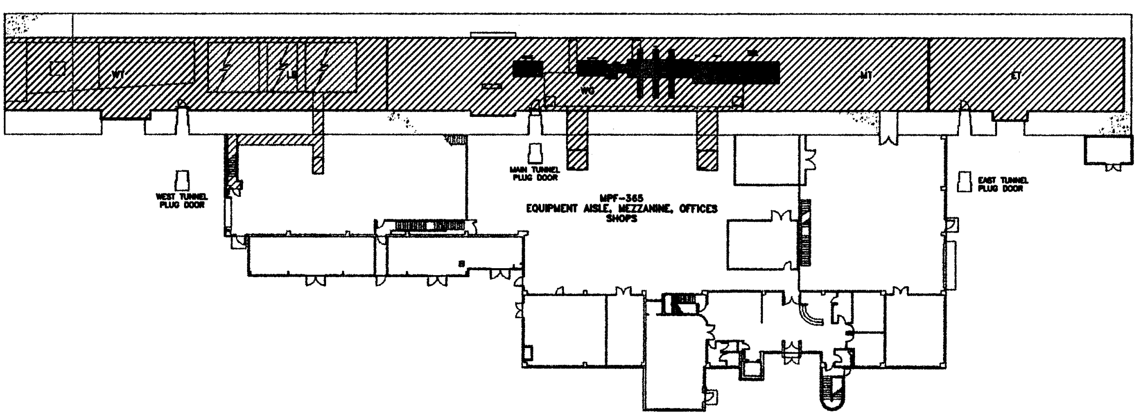

Figure 1 Layout of MPF-365 building

The LEDA accelerator is located over RF tunnels through which the waveguides travel to the RFQ. The foot print of the LEDA accelerator uses only about one-fourth of the accelerator tunnel's available floor area. The accelerator tunnel was divided into three major areas for Personnel Access Control Systems (PACS) protection. The East Tunnel (ET) is separated from the main tunnel (MT) section, where the accelerator is located by a sliding gate and chain link fence. The West Tunnel (WT) is separated from the Main Tunnel (MT) section by a second gate and chain link fence. The Wave Guide Basement (W/G), the fourth PACS area, has two shafts and tunnels from the equipment aisle to a room below the main tunnel. There are two hatches located between the main tunnel and waveguide lower room. The fifth PACS area is an old laser basement (LB) which is accessed from the equipment aisle with stairs and tunnels. It is located below the west tunnel section. There is a shield door in the LB access tunnel hallway. The east and west tunnel areas have roll-up door, and plug-shield-door access to the outside of the facility. The main tunnel has two shield doors and a plug-shield door for access to the equipment aisle.

There are three run permit modes of beam transport operation.

1. Injector Stand roll-back Transport. (ISRB)
2. Low Energy Beam Transport. (LEBT)
3. High Energy Beam Transport. (HEBT)

Run Permit mode	Beam Operations	Prompt Radiation Hazard[1]	Minimum Requirements	
			With HPRF to RFQ	Without HPRF to RFQ
Injector Rolled Back	The injector is physically disconnected from the RFQ. The 75 keV beam may be delivered up through the end of the injector transport.	No	Main Tunnel and Waveguide Basement PACS secured for HPRF operation. No access to accelerator. BBE is made up through Injector Rolled back limit switches.	Beam tunnel may be open. BBE is made up through Injector Rolled back limit switches.
Low Energy Beam Transport (LEBT)	The injector and RFQ are physically connected. The 75 keV beam can only be delivered to the plunging beam stop (PBS) located in the injector transport.	No	Main Tunnel and Waveguide Basement PACS secured. No access to accelerator. BBE made up through PBS in-limit switches.	Beam tunnel may be open. BBE made up through PBS in-limit switches.
High Energy Beam Transport (HEBT)	The injector and RFQ are physically connected. The RFQ is in operation and produces nominal 6.7 MeV beam for delivery to the high power beam stop located at the end of the HEBT. In this mode, the PBS may be inserted during beam operation.	Yes	All PACS are secured, door limit switches indicate closed and SRI water level indicates okay which collectively makes up BBE. No access to accelerator.	Not applicable *because HPRF required for this mode of operation.*

TABLE 1. Description of various LEDA Run Permit Modes.

Two hardware devices were selected by LEDA to ensure protection of personnel from prompt radiation. The two devices are the Injector Plunging Beam Stop (PBS) located at the output of the injector stand and High Voltage Interlock controls for the generation of High Power Radio Frequency (HPRF) energy.

The five areas of PACS system installations were reviewed for entry and exit requirements. Conduit plants were designed and drawn by LEDA personnel with collaboration and guidance from Protective System Team members. Sweep patterns and PACS warning sign placement was a collaborative effort with standards for distance and height supplied by Protection System and the LEDA Safety Team.

Installation of the five areas of Personnel access Control Systems (PACS) began in the summer of 1998. During this installation phase, the operational requirements for a Back Bone Enable System (BBE) were generated and the design of the logic configuration was started. The control for the Injector Plunging Beam Stop (PBS) was assigned to the “B” Backbone of the system. The High Power Radio Frequency (HPFQ) control was assigned to the “A” Backbone of the Backbone Enable system. Fabrication of the BBE equipment started in the fall of 1998.

The different types of access doors and hatches and their locations within the five PACS areas required several solutions. Roll-up doors were implemented with dual door-switch assemblies feeding a single door-monitor assembly. The specially designed door-switch assemblies are located at the bottom on the track for the door curtain. The hatches located between the Main Tunnel (MT) and Wave Guide Tunnel (WG) required dual standard switches mounted on a Wire-way duct located within the Wave Guide (WG) Basement area. Two switches from this switch assembly feed a door monitor for the Main Tunnel (MT) and two switches feed a door monitor for the Wave Guide Tunnel (WG).

A fence and gate were fabricated to control access to the Main Tunnel (MT). The Main Tunnel requirement of fork lift access during open periods required two gates with closed indication for each gate. The right gate was made the primary PACS gate with exit bypass during sweep procedures. The left gate is to be used only during open use periods and is bolted to the floor during beam delivery operations.

The Backbone Enable (BBE) system was designed using criteria from LEDA Operations Team. See Table 1 showing operation modes of LEDA. The off-the-shelf concept with customized logic allowed installation within a 3-month period. There were several hardware adaptations which allowed unusual requirements to be met.

1. Injector stand dual-switch assemblies for the roll-back position using armored cable plant.
2. The PBS became a dual use beam plug, with operational beam controls as well as personnel safety with BBE inputs from dual switches.
3. A mini-dual Protective System Backbone for HPRF control, which uses relay-to-fiber-optic transition for klystrons interlock inputs.
4. The adapting of the water shield design for beam stop water levels indications to dual BBE inputs. Two different levels were used.
5. Adapting double shield doors at the main tunnel entrance and the three radiation shield plug doors to dual BBE inputs.

The goal of initial operation and testing of the APT/LEDA accelerator under a proven safety envelope was achieved in part with the successful installation of the PACS and BBE Systems. Timely installation of five PACS areas and two BBE systems allowed LEDA operations to rapidly achieve readiness and the efforts resulted to four milliamps of beam on Tuesday the 16th of March 1999 at 6:00 PM.

REFERENCES

[1} J. E. Wilmarth, "Radiation Safety System (RSS) Backbone," submitted as a LANSCE-6-98-58-TR Technical Report. LA-UR-98-855,

[2] J. E. Wilmarth, F. R. Gallegos, and J. C. Sturrock, "Radiation Safety System (RSS) Backbones: Design, Engineering, Fabrication and Installation," presented at the 1998 Beam Instrumentation Workshop, Stanford, CA, May 4-7, 1998. LA-UR-98-1935,

[3] J. C. Sturrock, F. R. Gallegos, and M. J. Hall, "LANSCE Personnel Access Control System (PACS)," presented at the Health Physics Society 1997 Midyear Topical meeting, San Jose, CA., January 5-8, 1997. LA-UR-97-3552.

[4] J. E. Wilmarth, "Low Energy Demonstration Accelerator (LEDA) Radiation Safety Systems (RSS) and Personnel Access Control Systems (PACS) System Overview for Installation," submitted as a . LANSCE-6-98-63-TR Technical Report. LA-UR-99-354.

FIRST RESULTS ON CLOSED-LOOP TUNE CONTROL IN THE CERN-SPS

L. Jensen, O. R. Jones, H. Schmickler
CERN SL/BI, Geneva, Switzerland

Abstract

This paper presents the first measurements performed with the SPS Qloop. The emphasis will be laid on the model used for designing the regulation loop and how well it fits reality.

1. MOTIVATION

The SPS Qloop project was started as a follow-up to the 'LHC Dynamic Effects Working Group' workshop [1]. One of the results from this workshop was the expressed need for real-time feedback on the betatron tunes in the LHC, since the extensive use of super-conducting magnets mean that feed-forward tables will not suffice.

2. FEEDBACK PRINCIPLE

The use of feedback is well known in everyday life. An example is the use in air-conditioners. Designing a regulation loop involves knowledge of the time-constants and delays in the system one is trying to control. In the following paragraph we explain how a model was derived for the SPS Qloop.

3. MEASUREMENT OF QD TRANSFER FUNCTION

In the SPS Qloop, we use the main SPS quadrupole strings QD and QF for the correction of the betatron tunes. Measurements done by A. Beuret et al in 1995 showed that the transfer function of the power converter to the magnet has a –3 [dB] cut-off frequency of approx. 40 [Hz]. The measurement did not however take into account the possible time delay between the powering the magnets and their action on the beam. This delay is caused by the time it takes for the magnet flux to pass through the vacuum chamber and plays an important role for the limited bandwidth of the LEP Qloop. The measurement of the transfer function H(s) = Qv(s)/Iqd(s) was done during two SPS MD's, where sine-wave signals of varying amplitude and frequency were super-imposed on the quadrupole DC reference current. By doing harmonic analysis, the transfer function could be calculated [2]. In figures 1A and 1B, the resulting transfer function of the main SPS QD magnet string can be seen. A 2nd order Butterworth low-pass filter has been fitted to the results and a good agreement can be found up to the –3 [dB] frequency of around 28 [Hz].

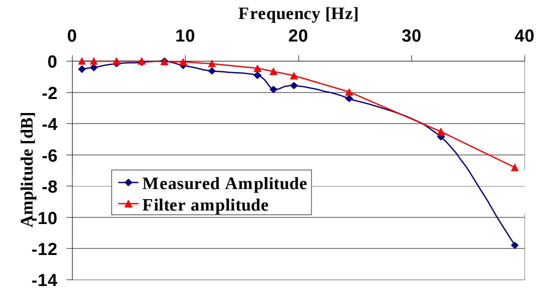

Figure 1A: Amplitude response for transfer function

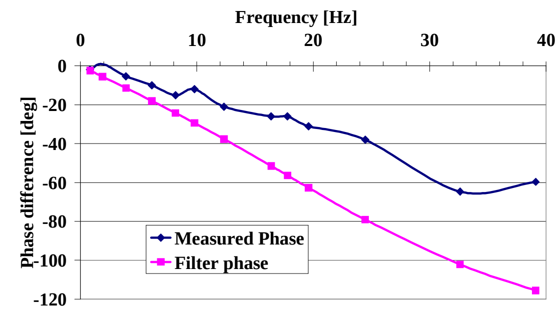

Figure 1B: Phase response for transfer function

4. MATLAB SIMULATIONS

From the above measurements, we learnt that we could approximate the transfer function by a 2nd order low-pass filter with a cut-off frequency of around 28 [Hz]. A widely used computer program called 'Matlab', with the 'Controls' toolbox and the 'Simulink' package, was used to design the regulation loop for the SPS Qloop. One of the most important parameters is the time between corrections, which in our specific case is given by the interval between individual tune measurements. Computation and transmission latencies for the corrections can be neglected in our case. For the tune measurements we are using 10 ms long chirp excitations and FFT transforms of the beam motion with automatic peak finding in the amplitude spectrum. In order to avoid possible problems due to coupling, only one plane is excited at a time. The tunes can therefore not be measured at an interval shorter than 20 ms.

The regulation loop should reduce the error as fast as possible without creating an excessive overshoot (thus requiring a certain phase and gain margin). Several books describe the design criteria for regulation loops (see e.g. [3]).

Figures 2 and 3 show the closed-loop response of the simulated system. The sampling frequency was chosen to be 50 [Hz]. The step response is shown in figure 2, while the error reduction as a function of frequency is shown in figure 3.

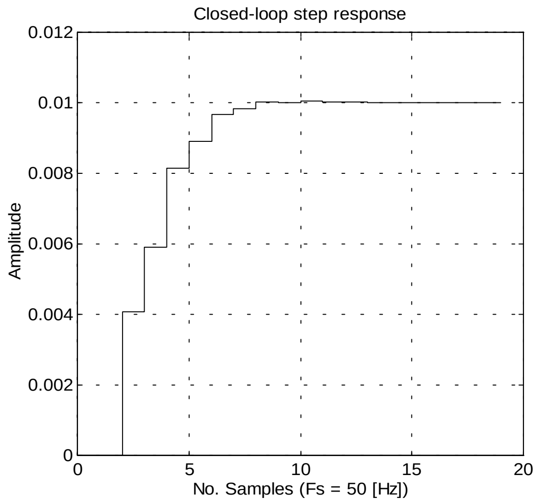

Figure 2: closed-loop step response

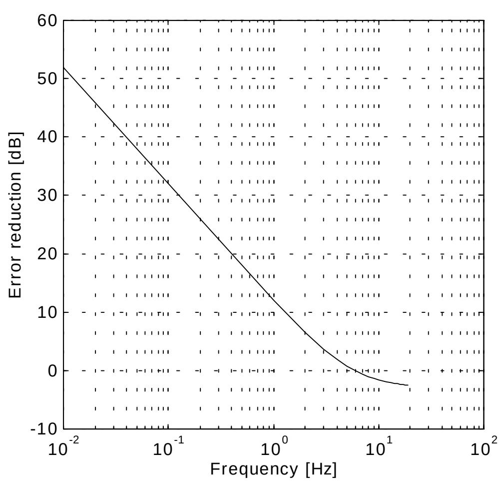

Figure 3: Closed-loop error reduction.

The zero dB roll-off point for the error reduction is found to be at around 5 [Hz], which is 1/10th of the sampling frequency. This is a general feature for sampled regulation loops. As the gain-bandwidth product is constant for a PI type regulation loop, tune excursions occurring at 0.5 Hz would be attenuated by the loop by 20 dB (a factor 10). This is a reasonable performance to correct the main tune excursions during the SPS acceleration period.

5. HARDWARE DESCRIPTION INCLUDING ATM

The SPS Qloop resides in a VME crate. The main CPU is a PowerPC running LynxOS. The real-time handling, which is done on a turn-by-turn basis, is performed using two DSP boards on the VME bus. A two-channel 16-bit input/output module is connected to each of the DSP boards and is used to sample the beam position and send the kicks used to excite the beam. An ATM PMC module is used to transmit the tune trim values to the power converters for QF and QD. This happens via an optical fibre of more than 1 [km] in length. In the power converter system, the trims are multiplied to the present current reference, thus making the knowledge of the present beam energy (quadrupole current) unnecessary. The ATM protocol, which was chosen as a communication prototype for LHC fast control, assures a known latency between sending a trim and receiving it at the other end. We are presently using a 120 Mbit/second connection with ATM AAL5 as interface level [4][5]. Measurements using a GPS module showed an average transfer time of the order of 200 [μsec]. This delay is short compared to the bandwidth of the system and plays no important role.

6. OPEN AND CLOSED-LOOP MEASUREMENTS

To check the performance of the SPS Qloop, several different tune distortions were programmed on the nominal quadrupole reference. We then measured the tune along the cycle with the feedback loop opened and closed. As can be seen from figure 4, the Qloop system managed to take out a triangular shaped distortion. An RMS error improvement of around 20 [dB] was calculated with respect to the nominal tune value of 0.64.

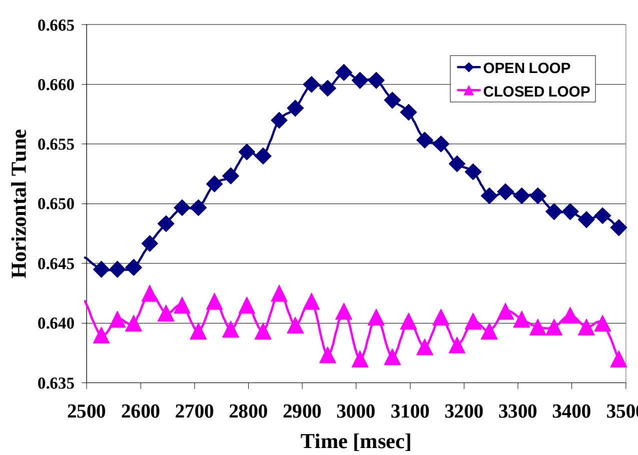

Figure 4: open and closed-loop response for a triangular tune distortion

7. THE FUTURE OF SPS QLOOP USING PLL TUNE MEASUREMENTS.

As discussed in chapter 4, (MATLAB simulations in figures 2 and 3) it will be difficult to achieve a tune regulation loop for the SPS with a gain-bandwidth product larger than 5 [Hz]. This limitation is due to the low bandwidth of the quadrupoles that are available to trim the tunes in the present configuration. Figure 5 shows the measured horizontal tune during the injection and ramp of the SPS. The larger excursions of the tune occur at transition energy. The two straight lines at the tune values 0.61 and 0.64 represent the boundaries, which seem acceptable for the acceleration of the LHC beams in the SPS. Most of the excursions at transition can be regulated out by the present SPS Qloop. Operational experience will show whether a higher bandwidth is required.

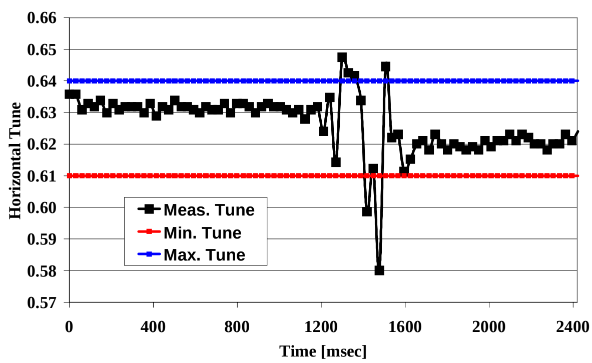

Figure 5: Measured horizontal tune during injection and acceleration

In case a higher bandwidth is required, additional faster quadrupoles will have to be installed in the machine. Such a project has already been studied for the so-called low-gamma transition lattice, which would require 24 additional quadrupoles [6]. If this becomes available, we would have to have to speed up the tune measurements in order to profit from the increased bandwidth of the quadrupoles. Such a faster tune measurement would be based on a Phase Locked Loop (PLL) [7], which could give tune readings at a rate of up to 500 [Hz] (i.e. 1% of the revolution frequency). Simulations, shown in figure 6 performed using the FastMap beam simulator [8] show that it is feasible to measure the tune using a PLL. The dotted line shows the reference tune value. The PLL is started with a tune value of 0.61, and after 400 turns the nominal tune of 0.62 has been reached. At 1000 turns, the reference tune is changed to 0.616, a change which the PLL tracks and locks on to after 200 turns.

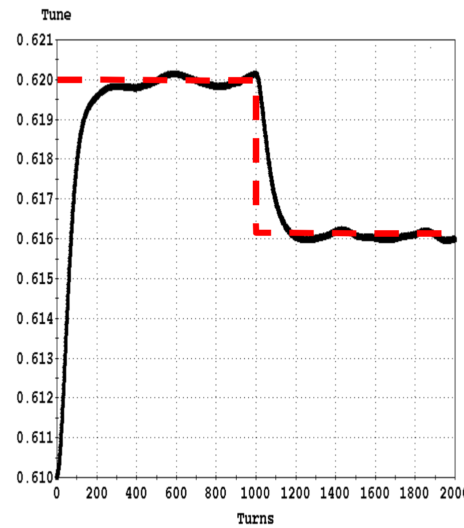

Figure 6: Simulation of lock-in and tracking process of PLL tune measurement

8. CONCLUSION

In this paper we have shown that the SPS Qloop in its present implementation (feedback on main quadrupole string, chirp tune measurements) can correct tune variations with a gain of 10 up to a bandwidth of 0.5 Hz. This speed is sufficient to correct slow tune distortions, which are typically encountered during the setting-up of a new cycle. In order to increase the bandwidth, additional quadrupoles with faster response times would have to be installed and in that case the tune measurements would be implemented using PLL techniques.

9. REFERENCES

[1]: 'LHC DEWG Workshop 1997 Summary'.

[2]: 'Measurement of the transfer function of the main SPS Quadrupoles' (SL-Note-98-047 MD).

[3]: 'Feedback control theory.' by Doyle, John C et al.

[4]: 'The Q-loop Project for the SPS' (SL-Note-98-014-DI).

[5]: 'Real Time Communications Prototyping for LHC Controls' (LHC-PROJECT-NOTE-174).

[6]: 'Additional quadrupoles, what can they be used for ?' (Proceedings of the 9th SPS-LEP performance workshop Chamonix, January 1999).

[7]: 'Phase-locked loops.' 3rd edition by Roland Best.

[8]: 'SPS and LHC Tune Control Studies using the "FastMap" tool (EPAC'98).

New Digital BPM System for the Swiss Light Source

M. Dehler, A. Jaggi, P. Pollet, T. Schilcher, V. Schlott, R. Ursic, PSI, Villigen, Switzerland
R. DeMonte, ELETTRA, Trieste, Italy

Abstract

This paper presents a new digital beam position monitor (DBPM) system which is currently under development for the Swiss Light Source (SLS). It is designed to provide sub-micron position data in normal closed orbit, and feedback mode as well as turn by turn information for machine studies and real time tune measurements. The self calibrating four channel system consists of a RF front end, a digital receiver and a DSP module. The same electronics will be used in all sections of the SLS accelerator complex. The system can be reconfigured in real time to perform different kind of measurements like: pulsed for linac and transfer lines, first turn, turn-by-turn, closed orbit, feedback and even tune mode for booster and storage ring. These reconfigurations only involve downloading of new signal processing software and will be performed via EPICS control system. An independent system for monitoring mechanical drifts of the BPM stations will be installed as well. The measured data will be permanently updated in a database and taken into account, when processing the final electron beam positions.

1 INTRODUCTION

The SLS is a high brilliance synchrotron radiation source presently under construction at the Paul Scherrer Institut (PSI) in Villigen / Switzerland. It is designed to supply highest brightness in the photon energy range from vacuum ultraviolet to soft X-rays and to provide flexibility to accommodate a variety of operation modes. Therefore, the SLS beam position monitor system has to ensure the adequate beam quality throughout the accelerator complex, consisting of a 100 MeV linac, two transfer lines, a full energy booster synchrotron and a 2.4 GeV storage ring.

In order to guarantee simplicity and uniformity of the system it was aspired to implement only one kind of BPM electronics for all SLS machine sections and operation modes. The most challenging requirements in terms of resolution and stability result from the necessity to reduce beam jitter to less than σ/10 of the vertical beam size in the ID sections of the storage ring. This corresponds to sub-micron beam position measurements, which have to be provided at a few kHz bandwidth, in order to successfully operate a fast (global) orbit feedback [1]. Concurrently, machine studies request snap shots of the beam orbit in turn-by-turn mode (TBT). Therefore, the BPM electronics has to deliver position data with more than 0.5 MHz bandwidth. A summary and description of the supported operation modes is given below. The technical specifications are listed in table 1.

- Pulsed Mode
  Intended for injector and transfer line BPM measurements. Assuming 3 Hz injection, one sample will be taken every 333 ms.
- Booster Mode
  Each BPM will provide position measurements throughout the acceleration cycle. Two orthogonal modes are envisioned. First, a single BPM measurement or a group of them is displayed in time domain. This allows tracking of positions as the beam is accelerated. Second, booster closed orbit is displayed at selectable time intervals.
- Turn-by-Turn
  User can select N (1024,…,8192) successive measurements to be taken per each sync. cycle. Time as well as frequency domain data formats are selectable.
- Closed Orbit
  Position measurements are taken continuously. Data is used for closed orbit (CO) display in control room.
- Feedback Mode
  Measurements are taken in the same way as in closed orbit mode and processed continuously to provide position information to global feedback.
- Tune Mode
  Data are taken in the same way as in turn-by-turn mode. However, software algorithm on DSP will calculate FFT and extract tunes.

Table 1: DBPM Specifications

Parameter	CO and Feedback	Pulsed and TBT
Dynamic Range	1-500 mA	1-20 mA
Beam Current Dependence		
full range	< 100 µm	-
relative 1 to 5 range	< 5 µm	-
Position Measuring Radius	5 mm	10 mm
Resolution	< 1 µm	20 µm
Bandwidth	> 2 kHz	0.5 MHz
RF and IF Frequencies		
Carrier RF	500 MHz	500 MHz
Carrier IF	36 MHz	36 MHz
Pilot RF	498.5 MHz	498.5 MHz
Pilot IF	34.5 MHz	34.5 MHz

2 DBPM ELECTRONICS

The newly developed DBPM electronics for SLS is a four channel system, which delivers high speed, medium precision and low to medium speed, high precision measurements. It consists of three major components: a RF front end, a digital receiver and a digital signal processor (DSP) module.

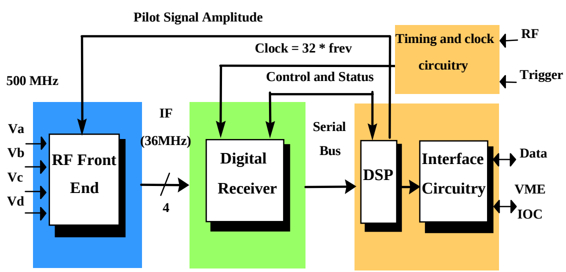

Figure 1: Block diagram of DBPM system for SLS.

2.1 RF Front End

The four RF front end channels tune to 500 MHz, the first harmonic of the machine. They get mixed to an intermediate frequency of 36 MHz and pass through a 5 MHz wide surface acoustic wave (SAW) filter. In order to equalise the gain of the four channels, a separate pilot signal is injected. It's frequency is 1.5 MHz below the frequency of the carrier signal but still within the SAW filter bandwidth. It's level is approximately 10 dB lower than the level of the signals from the four button pick-ups and used to set the total gain of each channel.

2.2 Digital Receiver

At the input of the digital receiver, the band limited IF signals are directly digitised by 12 bit analog-to-digital converters (ADC). Direct sampling at the IF frequency prevents the need of a second down-conversion stage in the RF front end and therefore reduces the problem of non-linearity associated with demodulation. The AD9042 from Analog Devices was selected for analog-to-digital conversion. It has a maximum sampling rate of 41 MHz, 100 MHz analog bandwidth and offers excellent linearity and stability, since the differential and integral non-linearities are ± 0.3 LSB or $\pm 7.3 \cdot 10^{-5}$ FS and ± 0.75 LSB or $\pm 1.8 \cdot 10^{-4}$ FS respectively. A/D conversion is performed at 31.25 MHz for the storage ring BPMs and 27.78 MHz for the booster BPMs. This means that under-sampling technique [2] is applied, which aliases the 36 MHz, band limited IF signals from the third Niquist zone down to 4.75 MHz for the storage ring BPMs 8.22 MHz for the booster BPMs respectively.

The remaining data processing, which include translation of the signals to baseband as well as filtering and decimation of the data streams, can now be done in a digital way. Both, filtering and decimation are important issues. They define the final system bandwidth, which in turn affects the measurement fluctuation and reduce the output data rate with respect to the input. The latter process reduces the requirements for the downstream digital signal processing. We have selected the HSP50214 DDC integrated circuit, which is a very flexible and fully programmable down converter.

2.3 Digital Signal Processor

The decimated data streams from the digital receiver are formatted, serialised and sent to the DSP module. We selected SHARC DSPs from Analog Devices, which are incorporated on the Wiese WS2126 DSP board. The DSP applies correction factors and calculates final beam positions. Moreover, incoming data are filtered and formatted for the desired operation mode, the pilot signal amplitude is adjusted and fast Fourier transformation is executed. In feedback mode, the DSP module calculates the orbit corrections and performs the communication to the adjacent sectors of the SLS storage ring. The sectors are connected via fast SHARC link ports (up to 40 Mb/s) in order to achieve a global correction scheme according to the SVD algorithm [1]. The complete DBPM system is fully integrated in the EPICS control system. This allows to select operation modes, displays beam positions in the control room, archives orbit data in an ORACLE database and constantly updates mechanical drifts of BPM stations, measured with the BPM position monitoring system (POMS), which is described in more detail below.

3 MECHANICAL ALIGNMENT

While the SLS DBPM electronics is designed to provide sub-micron resolution with high long term stability and low beam current dependence (see table 1), alignment and mechanical stability aspects of the BPM stations also become relevant for obtaining reliable and reproducible beam position readings and operating conditions for the users.

In the case of SLS, the vacuum chamber is supported by six BPM stations along a sector of the storage ring. The BPMs are rigidly mounted to the girders, following the SLS alignment concept for the magnets [3], which predefines the BPM centre within ± 25 µm with respect to the adjacent quadrupole axis. Final calibration to less than 10 µm will be obtained with the stored electron beam, applying the method of beam based alignment [4]. A complete BBA-cycle takes about 15 minutes and could be performed after every new start-up of the machine. During operation, any change in ambient temperature or any thermal load on the vacuum system leads to strong forces on the BPM supports, resulting in relative position changes of the BPM stations. This effect has been simulated for the SLS vacuum system and turns out to be in the order of 2 µm/°K. The resulting monitor movements override the alignment and initial calibration of the BPMs, which leads to false readings and corrections of the electron beam positions. It is obvious that this effect can be extremely critical when running a transverse feedback, where beam positions are automatically stabilised in a bandwidth from DC to around 100 Hz. Therefore, the supervision of mechanical drifts will be accomplished by a set of absolute linear encoders, which are firmly clamped to the quadrupole magnets. These sensors serve as dial gauges, which monitor the relative movement of the BPM stations in respect to the adjacent quadrupole magnets. The system's resolution is less than 1 µm over a measuring range of ± 2.5 mm. The raw data from all 12 monitors per sector (6 vertical and 6 horizontal) will be locally interpolated, serialised and finally sent to a single VME card, which is providing the link to the EPICS control system. This way any mechanical drifts are continuously recorded and updated into a database. The information will be used for the final determination of the electron beam position.

A prototype version of such a mechanical position monitoring system (POMS) has been successfully tested at a BPM station at ELETTRA over a period of one week. The results are given in figure 2 and show substantial drifts of the BPM station at start-up of the machine, when closing the tunnel, after each beam dump and new injection cycle.

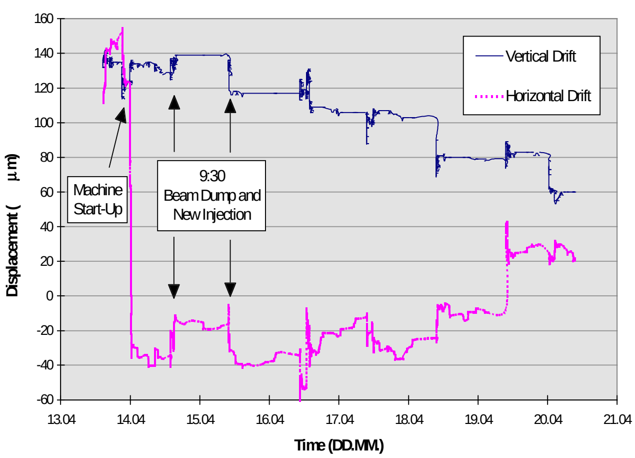

Figure 2: Horizontal and vertical drifts of a BPM station, measured at ELETTRA using a POMS prototype system.

4 PRESENT STATUS

Two prototypes of the RF front end module are being presently tested in laboratory environment with special emphasis on impedance match of all four RF inputs and determination of gain discrepancy between channels over the input dynamic range. So far the gain discrepancy of the four channels has been measured in the laboratory to be below ± 0.1 dB over the whole dynamic range, which meets the original design specification.

After having demonstrated the under-sampling performance of the AD9042 [2], four one-channel digital receiver modules have been designed and successfully operated in the lab at PSI. A block diagram of the DR board is shown in figure 3.

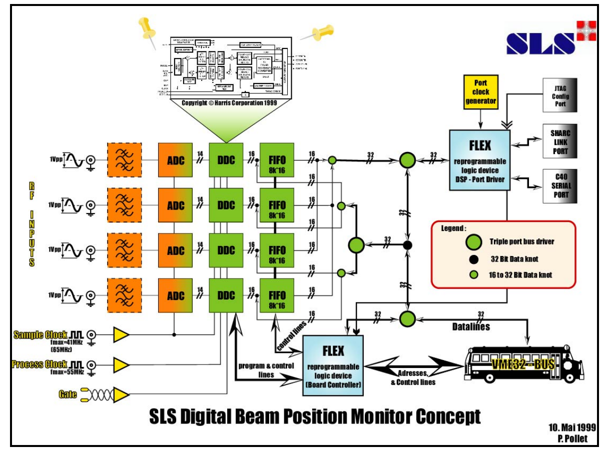

Figure 3: Block diagram of digital receiver module.

System integration tests with beam in feedback and turn-by-turn modes are scheduled for mid June at the synchrotron light facility ELETTRA in Trieste/Italy, already incorporating digital signal processing and EPICS interface via an IOC module.

Data formatting electronics for the linear encoders used in the POMS system, including interpolation and serialisation has been designed and successfully tested. A VME card, providing an EPICS interface via memory mapping is presently under design and will be tested at PSI early June.

ACKNOLEDGEMENTS

The SLS beam diagnostics group would like to thank their colleagues at the synchrotron radiation facility ELETTRA in Trieste/Italy for establishing outstanding and productive collaborations on the DBPM and multibunch feedback systems. Special thanks to Daniele Bulone, Mario Ferianis and Marco Lonza.

REFERENCES

[1] M. Böge, M. Dehler, T. Schilcher, V. Schlott, R. Ursic, "Fast Closed Orbit Control in the SLS Storage Ring", PAC'99, New York, April 1999.

[2] R. Ursic, "Digital Receivers Offer New Solutions for Beam Instrumentation", PAC'99, New York, April 1999.

[3] M. Böge et al., "Lattice Finalisation and Magnet Girder Design", EPAC'98, Stockholm, June 1998.

[4] P. Röjsel, "A Beam Position Measurement System Using Quadrupole Magnets Centra as the Position Reference", NIM A290 (1990) 374.

EMITTANCE MEASUREMENTS AT THE NEW UNILAC PRE-STRIPPER USING A PEPPER-POT WITH A PC-CONTROLLED CCD-CAMERA

M. Dolinska[1], M. Domke, P. Forck, T. Hoffmann, D. Liakin[2], A. Peters, P. Strehl
GSI, Darmstadt, Germany.

Abstract:

The complex mathematical algorithms and procedures to extract emittance data from intensity distributions measured with a single shot pepper-pot device are described. First results of mathematical evaluation from the commissioning of the new GSI pre-stripper linac structures are presented.

1 INTRODUCTION

At present commissioning of the new UNILAC pre-stripper is performed. To assess the performance of new types of ion sources, fluctuations of beam emittances from pulse to pulse and, even within one pulse, a single shot pepper-pot system has been developed. The design criteria have been already reported in [1].

2 STRUCTURE OF SOFTWARE

The software was designed to provide the interconnection between all parts of the installed measuring hardware, a user friendly interface for hardware control and a detailed graphical output for the obtained results. Figure 1 shows the general structure of the software. To control the CCD camera the manufacturer developed system drivers and DLL's have been used. This offers the operator the possibility to change the operation mode of the camera, the exposure time, the resolution and some other parameters related to the actual parameters of the ion beam or the calibration signal. Furthermore, in case of low intensity of the observed light spots it is possible to integrate a series of single shots to improve the quality of the images.

The objective of the CCD-camera is controlled by means of the Tiger-BASIC based microprocessor system, which has been connected to the PC through a conventional RS485 interface. Therefore, no additional system driver had to be installed.

The collected data may be processed immediately via the "Calculation routines DLL" for evaluation of emittances or may be stored on the hard disk in binary or ASCII format for later calculations. Additionally, data may be saved and reloaded in Windows bitmap format.

Information about a current measurement, including commentary and preview pictures, are stored in the local database to provide easiest and systematic access to all results. Information about the kind of accelerated ions, their charges, energy etc., is obtained from the global GSI database.

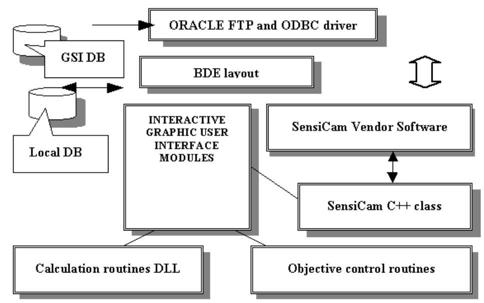

Figure 1: General structure of the pepper-pot system software

3 DATA PROCESSING

3.1 Calibration procedure

In the calibration process a parallel light beam from a laser (see [1] for details) is used to determine the correspondence between the pixels of the camera image and the real physical dimensions. It is assumed that the coordinates on the image, correlated to the locations of the holes in the pepper-pot plate can be obtained from the center of intensity of each light spot. Since all spots of the pepper-pot holes are arranged in the nodes of a regular rectangle grid it is sufficient to apply the implemented searching algorithm only for a whole row or column. The results are stored as reference information for future calculations in the project database.

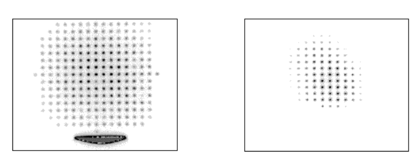

Figure 2: Light spots from the calibration with the laser beam (left) and real beam data, obtained with the CCD – camera.

[1] INR-Kiev, work done at GSI
[2] ITEP-Moscow, work done at GSI

3.2 A practical, fully implemented algorithm for determination of emittances

The set of light spots on the viewing screen, having different brightness levels, shapes and sizes represents the intensity distribution in the 4-dimensional phase space. Obviously, if the emittances of the two transverse phase planes can be considered to be independent of each other the same information about the intensity distribution in the 2-dimensional phase planes should be contained within each row considering the horizontal phase plane, respectively within each column (vertical phase plane). Therefore, a simplified algorithm for emittance calculations based on the conventional slit-detector measurement ideology has been implemented and will be explained considering the measured spot pattern of Fig. 3. Due to the finite emittance of the ion beam no regular grid can be fitted to this light spot pattern. An interactive graphic tool has been implemented to give a skilled operator the possibility to generate a nonlinear grid as shown for example in Fig. 4.

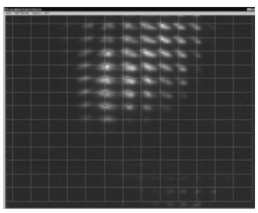

Figure 3: Spots of a Ni-beam on the viewing screen behind the pepper-pot.

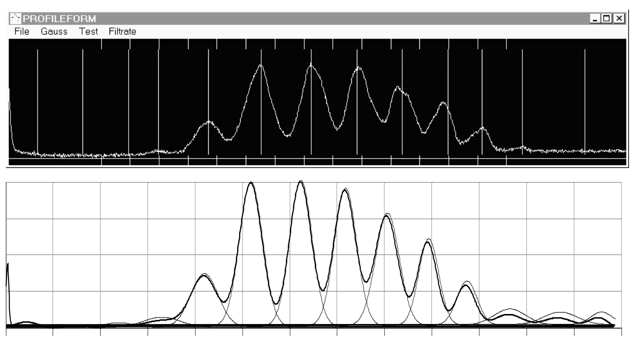

Figure 4: Non-linear grid manually adjusted in the PROFILE window(top) fitted curve (bottom).

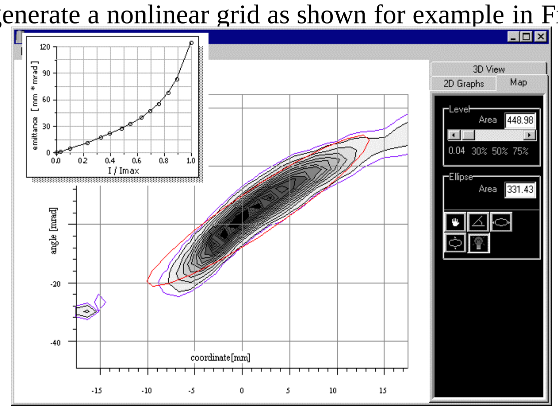

Figure 5: Horizontal emittance contour map window and emittance-current dependence (top left corner).

Here the ticks on top of the figure represent the observed light spot position from the calibration procedure. The long lines have been adjusted manually by an operator. To improve the separation of the peaks a fit procedure assuming Gaussian shapes of the peaks can be applied to the data as also shown in Fig. 4. As a result we get the divergences along each row or column of the pepper-pot holes. Referring to the conventional slit-detector system this corresponds to the profile measurements behind the slit. To prepare the data for further processing a cubic 2D spline fit is applied to interpolate data between lines. For calculation of the relevant emittance parameters and to provide graphics output in kind of maps like Figure 5, trees of contours corresponding to different intensity levels are created. Additionally, the program gives possibility to display and to print 3D surfaces of processed data sets.

3.3 Description of a second, pure mathematical algorithm

For exploitation of the experimental results the recorded images are treated digitally by a numerical data analysis program. The main procedures of the image

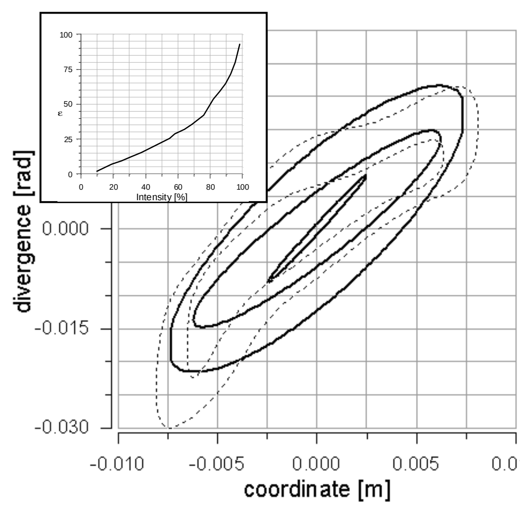

Figure 6: The lines of equal intensity and their best fitted ellipses built by the new algorithm (see text).

processing algorithms can be characterised as follows:

- In a first step a smoothing process along all pixels in each line of the image is performed. It has been decided to use the least squares method with Legendre polynomials as a basis. The discrete function I=I(x) is approximated in the interval $[x_0,x_n]$ by polynomials:

$$I(x) = \sum_{k=0}^{m} c_k \cdot L_k(x),$$

with $m \leq n$. Figure 7 demonstrates the effect of smoothing. Experience has shown that it is sufficient to apply the smoothing procedure only along the horizontal pixel-lines. After the smoothing

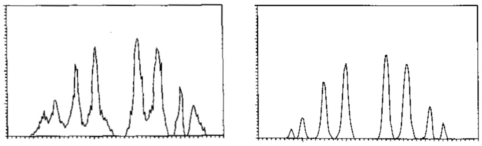

Figure 7: Measured data along one pixel line(left) and after smoothing(right)

procedure has been carried out the information about the intensity distribution *I(i,j)* is available. Here *i,j* are the numbers of a pixel (*i=1…1280, j=1…1024)*.

- Next is a procedure to detect and distinguish each spot. The algorithm starts at the position of the centre hole defined by the laser calibration. Two cases have to be considered: in the simple case the spot is placed around a hole and therefore the position of the spot is known. In the second case the spot is placed in some distance from the hole which means the intensity at the hole is zero. In this case a spot searching routine will be applied looking in a spiral motion pixel by pixel around the hole position. Assuming no overlap due to very large emittances, all detected spots can be definitively assigned to a hole. Figure 8 gives an example of one detected spot.

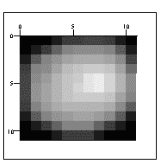

Figure 8: Example of a detected spot

- In the third step the vertical and horizontal size of each spot is determined. The routine starts at the detected spot, looking for the borders in the 4 coordinate directions (x, -x, y, -y) characterising the spot sizes in 4 directions: left, right, up and down.
- For further processing the two projections (vertical and horizontal) of one spot are needed. Determining the maximum values along all vertical lines the horizontal projected peak will be found. Applying the same procedure along all horizontal lines the vertical projected peak can be found.
- Next step is an approximation of the projected spot curves by Gaussian functions. Since in general the projections will not be of symmetrical shape, the left and right sides of the curves are described separately by two Gaussian functions. As a result, each spot is described by 4 Gaussian functions (2 for each direction) determined by σ_r, σ_l, σ_u, σ_d, the maximum intensity I_o, and Δx, Δy to describe the location in relation to the corresponding hole position. Figure 9 shows two projected peaks from experimental data and the approximation by the 4 Gaussian functions.

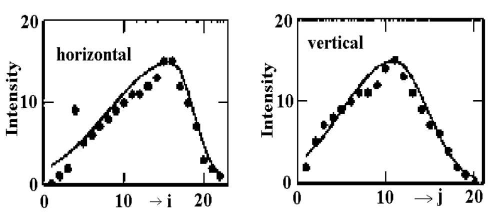

Figure 9: Projected peaks and corresponding Gaussian approximation.

Using the Gaussian approximations it is now possible to determine the divergences for different fractions of the maximum intensity. From the formula

$$I(x) = I_0 \cdot \exp(-\frac{(x-x_0)^2}{2\sigma^2})$$

the linear deviation is determined by

$$\Delta x = \sigma \cdot \sqrt{2 \cdot \ln \frac{I_0}{I(x)}}.$$

First, the set of data has to be normalised to the maximum intensity. Then, as an example, the divergence XR' is given by

$$XR' = \frac{(dx + \Delta xr) \cdot h}{L}$$

with dx = x_o-$x_{hole,}$, where x_o is the position of the maximum intensity within a spot and x_{hole} is the coordinate of the corresponding hole. The value of h is determined by h=Δh/Np, where Δh is the spacing between two holes and Np is the number of pixels between two holes. In terms of the fractions PR [$0 \le PR \le 1$] and the normalised intensity IN_m, Δxr is given by

$$\Delta xr = \sigma r \cdot \sqrt{2 \cdot \ln\left(\frac{IN_m}{PR}\right)}.$$

- In the next step 5 matrixes are formed. Four matrixes XR', XL',YU',YD' describing the divergence in the directions left, right, up, down and one matrix representing the total spot intensities. To determine now the 2-dimensional emittance in the horizontal phase plane the averages for each vertical column are calculated. Since the coordinate in x-direction is given by the index i of each column the phase plot is determined.
- For the determination of Twiss parameters a graphical method as well as the statistical evaluation can be applied.

The results of the calculation shown in Fig. 6 agree with the results obtained earlier (see Fig. 5).

REFERENCES

[1] Domke, M. et al., DIPAC 1997, LNF-INFN Frascati, (1997), p. 141-143.

A FAST PROTECTION SYSTEM FOR NARROW-GAP INSERTION DEVICE VESSELS

M J Dufau, R J Smith, CCLRC Daresbury Laboratory, Warrington, UK.

Abstract

Presented in this paper are details of an electronic, beam position based interlock system, which has been designed to protect narrow - gap insertion device vessels from the thermal damage that would result from mis steered beam. Details of system design and operational experience are presented, and the paper concludes with an outline proposal for a system enhancement, that would offer diagnostic information immediately prior to an excessive beam displacement trip.

1 INTRODUCTION

In 1998 a major programme of upgrade work was completed on the Synchrotron Radiation Source (SRS), Daresbury Laboratory UK. The upgrade involved the installation of two insertion devices, multipole wigglers, with the intention of enhancing the versatility of the SRS as a synchrotron light source.

When an analysis in to the effect of beam impinging the walls or flanges of either of the associated narrow-gap vessels, as a result of mis-steer, was conducted, a probability of permanent thermal damage, occurring within several seconds of time was indicated. Water-cooling as an engineering solution could be applied to the upstream flanges, but the walls of the vessels would still be extremely vulnerable. Thus the requirement for a protection system to prevent potential thermal destruction of either vessel was founded.

Two systems have been built to the design that subsequently evolved, and have since January of this year provided vessel protection with unfaltering reliability.

2 SYSTEM DESCRIPTION

Protection of a vessel is accomplished by tripping off the Radio Frequency (RF) source when conditions that are potentially thermally damaging to a vessel prevail. The primary interlock signals to achieve this are generated by excessive vertical beam displacement through a vessel, or excessive rise in temperature of the walls of a vessel. Vertical beam displacement signals are provided by Electron Beam Position Monitors (EBPMs) installed within a vessel (two off, upstream and downstream). An array of thermocouples supervised by a Programmable Logic Controller (PLC) provides the excessive temperature signal.

Since all combinations of stored beam and injection energy are deemed to be a safe operating area, an Energy Sensitive Bypass renders beam displacement interlocks inactive during injection. This facilitates steering through the narrow gap of a vessel at injection, by permitting a wider tolerance on beam displacement.

The organisation of primary interlocks is illustrated in Figure 1.

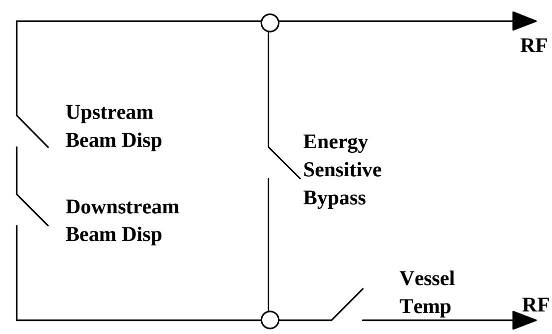

Figure 1: Organisation of primary interlocks

Because confidence in the reliability of primary interlocks is paramount, secondary interlock signals are required to become active, when the integrity of electronic hardware or support signals is suspect. These secondary interlock signals monitor the performance of the electronics for the EBPMs, Total Current Monitor (TCM), power supplies, PLC and also a Direct Current Transformer (DCCT) which provides an energy level proportional signal from the dipole magnet current.

The organisation of all system interlocks both primary and secondary is illustrated in Figure 2, which also includes a keyswitch-controlled bypass of the beam displacement interlocks.

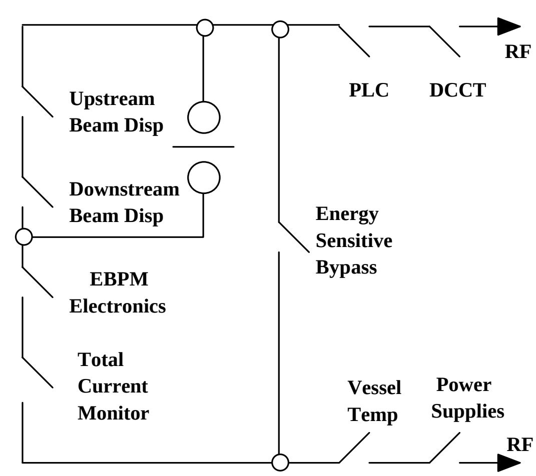

Figure 2: Organisation of primary and secondary interlocks

This bypass permits a wider tolerance on beam displacement at energies greater than injection energy, and is included for possible accelerator physics application.

3 INTERLOCK DESCRIPTIONS

The hardware output of individual interlocks, whether primary or secondary, is a pair of normally open, volt-free relay contacts. These are concatenated in the manner of Figure 2 to provide a galvanic loop output to the RF system. On failure of an interlock, the appropriate pair of contacts will open and trip off the RF source and consequently the beam. Because contact pairs are of ‘normally open’ configuration the scheme is fail safe. An auxiliary pair of relay contacts is presented to the SRS control and monitoring system for display purposes.

In compliance with the interface standard for the SRS control and monitoring system, a failed interlock is latched, and cannot be reset until the condition that initiated the failure has been remedied.

3.1 Primary Interlocks

Commercial EBPM signal processing electronics (Bergoz), are employed for upstream and downstream beam displacement measurements, to generate corresponding interlocks by comparison with adjustable, pre-set, bipolar thresholds. By comparison with additional thresholds of lesser magnitude (nominally 1.0 mm equivalent), advanced beam displacement warning signals are also generated; these warning signals are OR functioned to drive an audible sounder.

The third primary interlock is generated if any single thermocouple from of an array of 32 devices, that are distributed and mounted about the walls of each vessel, indicates a local temperature in excess of a pre-set threshold. Individual threshold levels are embedded in the software of the supervisory PLC.

3.2 Secondary Interlocks

Failure of a secondary interlock signal occurs if the integrity of electronic hardware or support signals becomes suspect. Hardware performance is monitored by constant detection of the presence of appropriate confidence signals; confidence of support signals is achieved by comparison of signal level relative to a pre-set reference value. Power supply tolerances are set at +/- 10% of required value.

Each of the two installed systems in the SRS is equipped with a dipole current measuring DCCT to provide signals that are proportional to energy level. Confidence monitoring for these is achieved by additional cross coupling of signals between the systems. For more than two systems this would not be practicable; a self-contained monitoring scheme would have to be sought.

4 PRACTICAL CONSIDERATIONS

4.1 Noise Immunity

By design, the output of a vessel protection system when active, will trip off the RF source and destroy the beam. Consequently, the effect of noise and electrical interference can be catastrophic, as was demonstrated in the early design stages of the system under discussion.

To eliminate noise problems standard techniques have been applied during system construction, but to guarantee noise rejection, a form of filtering has been included across the input of all interlock sources. For valid recognition of an interlock source signal the signal must be present for a specific duration, 100 milliseconds for primary interlocks, 1.0 second for secondary interlocks. These times define the response of the system to an interlock failure.

The excessive vessel wall temperature interlock from the PLC system, and the interlock reset signal from the SRS Control System, both generated externally to the system crate, switch 24 volt lines in an effort to reduce noise.

4.2 Status Display

Full instantaneous display of the status of all interlocks is available via a colour display monitor at a control console in the SRS Main Control Room. Through a control console, interlock resets are also effected.

Early operational experience with this form of interlock status display, demonstrated that consideration needed to be given to the order and manner that failed interlocks are displayed, if a lucid interpretation of events were to be achieved. This is because at beam loss due to a valid interlock failure, a number of other interlocks fail due to their reliance on the presence of beam to maintain safe status. Thus without care, interlock status display would not separate cause from effect.

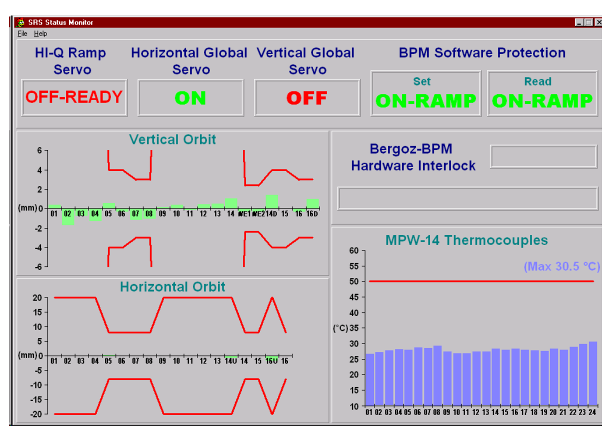

Figure 3: Status display

Trapping’ and displaying the first interlock to fail, i.e.

the valid interlock, surmounted the problem.
Consequential failed interlocks whose status is initially suppressed may subsequently be displayed by the application of a system reset. A page of displayed interlock status is shown as Figure 3. Also installed in the SRS Main Control Room is a hardware display panel for each system, on which is mounted digital panel meters, displaying upstream and downstream beam displacement in direct millimetres. The audible alarm sounder detailed in Section 3.1, light emitting diode indications of the status of the Energy Sensitive Bypass and global interlock status are also mounted on the panel.

This auxiliary display panel is shown as Figure 4.

Figure 4: Auxiliary display panel

4.3 General Details

With the exception of the PLC based vessel wall temperature monitoring system, all electronic hardware is housed in a 3U-high eurocrate, which has been kept compact without loss of versatility by judicial allocation of functions between modules.

Figure 5: Hardware arrangement

As shown in Figure 5 signal monitoring and threshold adjustments are accessible on module front panels; all system input and output cables including EBPM button signals, enter through the crate rear panel via appropriate connectors. Spare module slots in the crate are sealed with blank front panels to maintain Electromagnetic Compatibility. The front panel apertures visible in Figure 5 are to permit forced air cooling of the EBPM processing cards, a requirement found to be necessary to achieve the desired performance stability of the said cards.

5 SYSTEM ENHANCEMENT PROPOSAL

Figure 6 shows a schematic illustrating a proposal for an enhancement that offers beam position diagnostic information, immediately prior to tripping the RF.

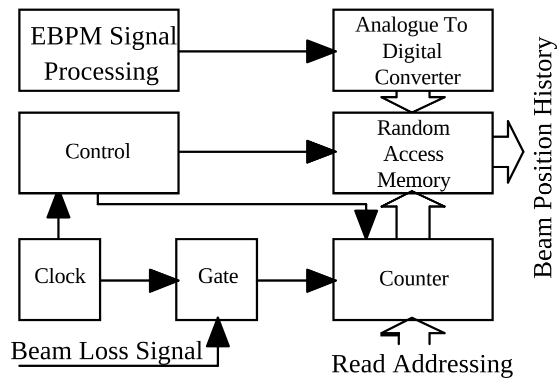

Figure 6: Beam loss data recording system for IDs

Samples of the digitised beam position signal are stored in Random Access Memory (RAM) locations during write mode. A cyclic counter whose serial input is fed from a clock source provides the addressing for the locations. On beam loss the address counter is 'frozen' when the clock is inhibited, capturing in digital form the recent history of beam position. Addressing the locations via the parallel input of the counter can access the stored samples when the RAM is set to the read mode. Accessed samples could be read digitally or converted to analogue form.

5 CONCLUSIONS

This paper has detailed a design for a fast, high performance system, for the protection of narrow-gap insertion device vessels. The system is versatile, and suitable for application to most vessels that are equipped with upstream and downstream vertical EBPMs.

REFERENCES

[1] D. M. Dykes et al., "The SRS Multipole Wiggler Vacuum Vessel Protection System", Proceedings, 6th EPAC, Stockholm, (1998).

The Closed-Orbit Measurement System for the CERN Antiproton Decelerator

M. Le Gras, L. Søby, D. J. Williams
CERN, Geneva, Switzerland

Abstract

The closed-orbit measurement system for the new Antiproton Decelerator (AD) employs 59 electrostatic pick-ups (PU). The intensity range from 2×10^{10} down to 10^7 particles poses challenging demands on the dynamic range and noise of the head amplifier. A low noise-amplifier has been developed, having an equivalent input noise of $0.6\,\mathrm{nV}/\sqrt{\mathrm{Hz}}$, allowing beam positions to be measured to ± 0.5 mm with 5×10^6 particles. Two different gains take care of the large dynamic range. After amplification and multiplexing, the PU signals are fed to a network analyser, where each measurement point corresponds to one PU. The network analyser is phase locked to the RF of the AD, thus acting as a "tracking filter" instrument. An orbit measurement takes from 0.2 to 12 s depending on the IF-bandwidth of the network analyser, selected according to the beam intensity, and the precision required. At the end of the network analyser sweep the data are read via a GPIB interface and treated by a real-time task running in a VME based Power PC.

1 INTRODUCTION

The AD is a new machine, replacing the previous low-energy antiproton facility, which consisted of AC, AA and LEAR. In the AD, antiprotons of 3.5 GeV/c are injected and decelerated down to 100 MeV/c, to be ejected to the experimental area in the centre of the machine. During deceleration, on intermediate plateaus, stochastic cooling and electron cooling is performed. On each intermediate energy level the orbit must be measured, and if necessary, corrected.

2 BEAM AND SIGNAL PARAMETERS

The PUs in the AD are made of metal sheets, accurately cut and mounted in metal tubes fitted inside the vacuum chamber. One annular electrode provides the intensity signal (Σ). The difference signal (Δ) is derived from 2 semi-sinusoidal electrodes. The Δ/Σ–ratio together with the PU sensitivity gives an intensity independent beam position. The signal levels on the electrostatic PU electrodes are calculated using Eq. 1 below:

$$\hat{V} = \frac{Ne}{C}\frac{l}{S}\frac{\pi}{2}B_{\mathrm{f}} \quad [\mathrm{V}] \qquad (1)$$

Where N is the number of particles, C the electrode capacitance, e the elementary charge, l the electrical length of the PUs, S the AD circumference, $\pi B_{\mathrm{f}} / 2$ the ratio of peak to average line density. $B_{\mathrm{f}} = 1$ yields a signal level of 4.2 µVp per electrode at $1\mathrm{x}10^7$ particles and a differential PU sensitivity of 0.1µVp / mm. In a 20 MHz system with an equivalent amplifier input noise of $2\,\mathrm{nV}/\sqrt{\mathrm{Hz}}$, the signal-to-noise (S/N) ratio is approximately 0.01 for 1 mm of beam position, or in other words a resolution of ~100 mm !. It is clear that a reduction of bandwidth and input noise is necessary. On the other hand, one wants to observe the bunches of high intensity beams of 10^{10} particles on an oscilloscope, which demands a large bandwidth. In the AD the revolution frequency varies from 1.6 to 0.17 MHz and the minimum bunch length is in the order of 100 ns. For good bunch observation a system bandwidth of 10 kHz-20 MHz is thus necessary.

3 THE HEAD AMPLIFIER

It was therefore decided to build a head amplifier of the following specification:

	Intensity range: $1x10^7 - 5x10^8 \overline{P}$	**Intensity range:** $5x10^8 - 10^{10} P$
Input imp.	5 MΩ // 49 pF	5 MΩ // 18 pF
Gain	47 dB	20 dB
Bandwidth	10 kHz-20 MHz	10 kHz-50 MHz
Input noise	$0.6\,\mathrm{nV}/\sqrt{\mathrm{Hz}}$	$6\,\mathrm{nV}/\sqrt{\mathrm{Hz}}$
CMRR	>66 dB	>66 dB
Max. Output	1.5 Vp in 50 Ω	1.5 Vp in 50 Ω

Table 1: Head amplifier specification

To achieve the very low noise performance required of the head amplifier in the high gain mode, a technique using paralleled Junction Field Effect Transistors (JFETs) [1] was used. A simplified diagram of an input stage is shown in Fig. 1.

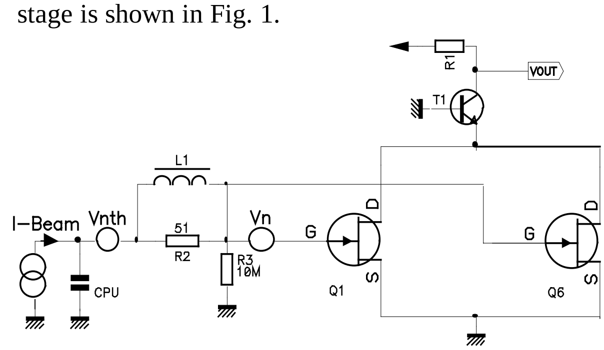

Figure 1: Simplified diagram of head amplifier

The total equivalent input noise is dominated by the voltage noise of the JFETs and the thermal voltage noise of *R2* // ω*L1*. The voltage noise of the JFETs [2] is given by:

$$V_n = \sqrt{8kT \ / \ N3gm} \quad [\mathrm{V} / \sqrt{\mathrm{Hz}}] \qquad (2)$$

where g_m is the transconductance [A/V], *N* the number of JFETs in parallel, *k* [J/°K] Boltzman's constant and *T* [°K] the absolute temperature. The thermal voltage noise of the input filter is given by:

$$V_{nth} = \sqrt{4kT \left| R_2 \ // \ \omega L_1 \right|} \quad [\mathrm{V} / \sqrt{\mathrm{Hz}}] \qquad (3)$$

In the case of a capacitive source, the current noises of the JFETs and *R3* can, in our frequency range, be considered as bypassed by the PU capacitance, and are therefore ignored. The total equivalent input noise is solely determined by the voltage noises and becomes;

$$V_{n,in} = \sqrt{V_n^{\ 2} + V_{nth}^{\ \ 2}} \quad [\mathrm{V}/ \sqrt{\mathrm{Hz}}] \qquad (5)$$

It is possible to select the value of L_1, such that V_n mainly determines the input noise, in the frequency rang of interest. Since V_n decreases with $\sqrt{N}$ and the signal decreases linearly with *N*, due to the increase in input capacitance, there exists a value for *N* for which the S/N ratio is optimum. A plot of the theoretical S/N ratio for *N* paralleled JFETs is shown in Fig. 2 below. In practice, due to dissipation and amplifier oscillations, this number could not exceed *N*=6. As seen on this plot, it is possible to gain another 17% in S/N-ratio by having a total of 16 JFETs in parallel, but for a differential input stage this would add 3W dissipation and require extra cooling. A differential amplifier with 2 x 6 JFETs in parallel has been developed, with an equivalent differential input noise of $0.6\,\mathrm{nV}/\sqrt{\mathrm{Hz}}$.

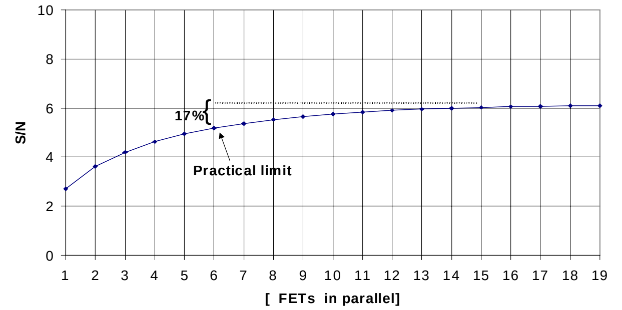

Figure 2: S/N-ratio with 10^7 particles, 1 mm, 1 kHz BW

4 THE TRACKING FILTER

Even though a very low noise amplifier is used, with the full bandwidth the signal to noise ratio is still <<1. In such a system it is very difficult to resolve the PU-signals using averaging. It was therefore decided to pass the PU signals trough narrow bandwidth filters i.e. 1 kHz, in order to reduce the noise level. The minimum S/N ratio in 1 kHz bandwidth is then ~ 5.

Using a commercial network analyser to measure the Δ/Σ –ratio, bandwidth is restricted by the different IF-filters. It also gives the possibility to phase lock on to an external reference signal, and in this way, beam positions are measured at a wide range of bunch frequencies. In our case the network analyser locks onto the RF of the AD.

5 THE SYSTEM

A block diagram of the orbit measurement system is shown in Fig. 3. The 59 PU-signals are amplified using the low-noise amplifiers located very close (0.7 m) to the PUs. Transmission to the control room (~100 m) is

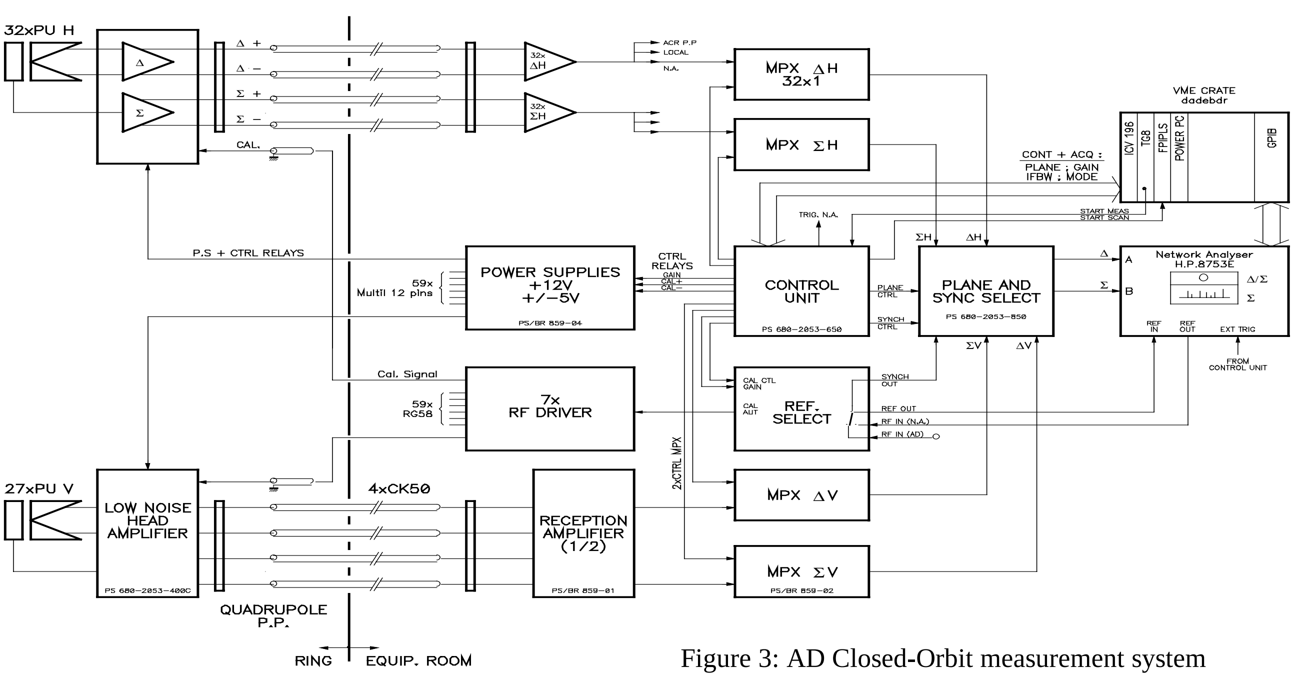

Figure 3: AD Closed-Orbit measurement system

differential, and after the reception amplifiers the signals are fed to the network analyser via multiplexers (MPX).
When the Control Unit receives an external trigger, it starts the sweep of the network analyser at the same time as the MPXs. It was foreseen to trigger the network analyser on a point-by-point basis, but unfortunately this was not possible in the external reference mode. Instead the trigger starts a complete sweep (101 points) on the network analyser and at the same time the Control Unit increments the MPXs with exactly the same Δt as between the points on the network analyser. Each point on the network analyser corresponds to 1 PU.
The Plane and "Sync" Select unit selects the plane in which to measure. It also supplies a synchronous signal, which is switched to the network analyser after the scan of the MPXs has finished. This gives the possibility to verify that both the network analyser and MPXs are advancing at the same speed. When the software reads the data, the amplitude of the synchronous pulse is also checked.
It is possible to calibrate the electronics. In this mode the network analyser source sends a 1 MHz, CW signal via the RF-drivers to the input of each amplifier. The Δ/Σ-ratio from the amplifiers is then measured and stored for position calculations.
The Control Unit gives the possibility to choose between 4 different IF-bandwidths, which should be set accordingly on the network analyser, i.e. 1 kHz, 300 Hz, 100 Hz, and 10 Hz. In this way optimisation with respect to intensity, precision and duration, is obtained. With an IF-bandwidth of 300 Hz a complete orbit measurement takes approximately 600 ms.
Network analyser and Control Unit are controlled via a VME based Power PC C-program, which every 1.2 s sends the required control parameters, and whenever a measurement has taken place, reads the data from the network analyser. The data read from the network analyser consists of the normalised data (Δ/Σ) and the Σ-data. The latter is used to verify the intensity range and to check the validity of the signals. After data treatment with the previously stored calibration data and the PU data, the beam positions are calculated and stored in memory for orbit displays.

6 RESULTS

In total 59 low noise amplifiers, having a differential input noise of $0.6\,\mathrm{nV}/\sqrt{\mathrm{Hz}}$, were installed in AD-ring close to the PUs. The orbit measurement system was tested during the running in of the AD in October-December 1998. Orbits were measured in the intensity range $2\mathrm{x}10^{10}$ to $5\mathrm{x}10^{6}$ particles. From $2\mathrm{x}10^{10}$ to $5\mathrm{x}10^{7}$, the measurement does not change with intensity as shown on Fig. 4. Below this intensity, at certain PUs close to the accelerating cavity, the measurements deviate from the high intensity values. It was found that RF-signals from the cavity leak into the head amplifiers and interfere with the PU-signals. Shielding and grounding around the low-noise head amplifiers close to the cavity have to be improved. This should make it possible to measure orbits with down to $5\mathrm{x}10^{6}$ particles without significant errors.

7 ACKNOWLEDGEMENTS

The authors would like to thank R. Boudot for his invaluable help during the installation of the system.

REFERENCES

[1] R. B. Hallgreen, "Paralleled transconductance ultra low-noise preamplifier", Rev. Sci. instrum.59(9), September 1988.
[2] Y. Netzer, "The Design of Low-Noise Amplifiers", Proc. of the IEEE, Vol. 69, 728 (1981)

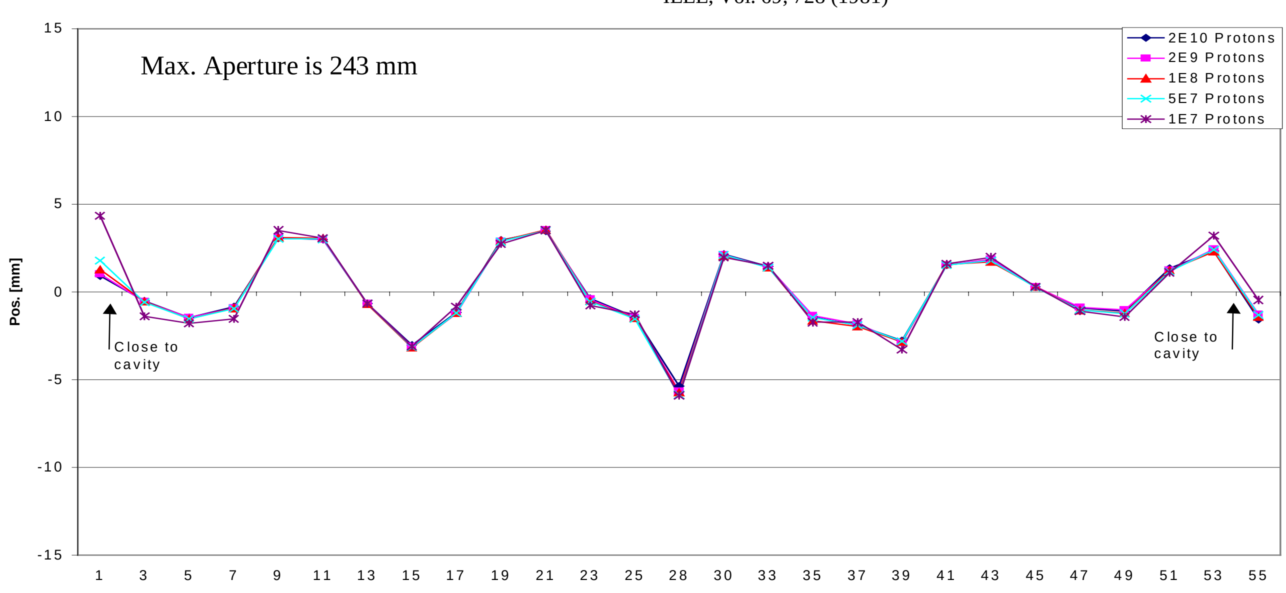

Figure 4: Vertical orbits measured at different intensities

EMITTANCE AND DISPERSION MEASUREMENTS AT TTF

M. Castellano, A. Cianchi, V. A. Verzilov, INFN-LNF, CP 13, 00044 Frascati, Italy
L.Catani, G.Orlandi INFN- Roma 2, Italy

Abstract

It is well known that beam dispersion , along with the Twiss parameters and emittance, contributes to the beam spot size. So that, in general, anomalous dispersion is an undesirable event and must be minimized by careful tuning the machine. If not, when the spot size is used to infer beam emittances, as it is the case of the "quadrupole scan" method, basically employed at TTF, the unknown dispersion can lead to overestimated values for the emittance. This paper presents the first attempt to determine the dispersion function at several points of the TTF Linac and to separate its contribution to the local emittance measurement, performed by means of the OTR imaging technique.

1 INTRODUCTION

Since the beginning of this year, TESLA Test Facility (TTF) is operated with Injector II equipped with a laser driven rf gun. Injector II is designed to generate electron beams with an emittance of 20 mm mrad (normalized) at a bunch charge of 8 nC , an option needed for a TESLA Linear Collider, and with an emittance of 2 mm mrad at 1 nC in a FEL mode [1]. In both cases it is important to preserve emittances as small as possible up to the end of the linac. For this purpose the beam emittance is monitored at several points along the accelerator.

The results of the TTF commissioning with Injector I have shown that, while at the injector level the measured values for the emittance were in agreement with designed specifications, in the high energy region of the linac a certain emittance growth was observed. Measurements were performed by means of the "quadrupole scan" method in which the rms beam size is measured as a function of the strength of one or several quadruples situated upstream a beam profile monitor. Since in this method the beam size is used to infer beam emittances, there are suspicions that an unknown dispersion could contribute to the beam spot size, thus leading to overestimated values for the emittance.

In practice, the beam dispersion arises due to misalignment of beam line elements or off-axis beam transporting. Once generated at some place, it will propagate through the machine. In general, an anomalous dispersion is an undesirable event, since it can significantly increase the beam size at places where that is expected to be particularly small: at interaction points of colliders or undulator sections of FELs. Careful tuning the machine is sometimes needed to minimize the beam dispersion.

This paper presents the first attempt to determine the dispersion function of the TTF Linac. Measurements were performed by means of the OTR imaging technique widely employed at TTF [2]. Two different kind of dispersion measurements were done at two positions of the linac.

2 DISPERSION AND EMITTANCE MEASUREMENT BY MULTIPLE "QUADRUPOLE SCAN" .

At the position between first and second acceleration modules, after the so-called "bunch compressor II", we attempted to determine simultaneously the beam emittance and both the spatial and angular dispersions by means of a multiple scan. A schematic diagram of a layout is shown

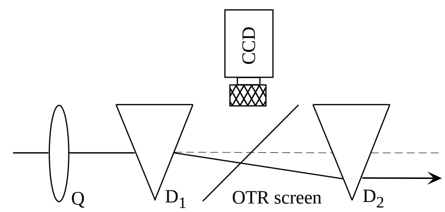

Figure 1: Schematic layout for multiple scan dispersion and emittance measurements.

in Fig. 1. A quadrupole Q followed by a bending dipole D_1 allowed to change the beam spot on a OTR screen, images of which were registered by a CCD camera. A second dipole D_2 behind the screen was employed to drive the beam through the second acceleration module and, thereby, prevent quenches in superconducting cavities due to the beam dumping inside the cryomodule.

As known, in the presence of the dispersion the first-order squared beam size on the screen is given by

$$x^2_{rms} = \sigma_{11}(s) + \left(\eta(s)\frac{\Delta p}{p}\right)^2 , \qquad (1)$$

where $\sigma_{ij}(s)$ stands for elements of the σ- matrix defined at the position s (OTR screen), $\eta(s)$ is the dispersion function at this position and $\Delta p/p$ is the momentum spread. In the linear optics, an evolution of the σ- matrix from point to point of the beam line is controlled by the transfer matrix. In particular, the transformation of the element σ_{11} from the entrance face of the quadrupole Q (position 0) to the position s is described as follows

$$\sigma_{11}(s) = m^2_{11}\sigma_{11}(0)+2m_{11}m_{12}\sigma_{12}(0)+m^2_{12}\sigma_{22}(0), \qquad (2)$$

where m_{ij} denotes elements of the 3×3 transfer matrix. In the same manner, the dispersion function on the screen is determined by its value and derivative at the entrance of the quadrupole

$$\eta(s) = m_{11}\eta(0) + m_{12}\eta'(0) + m_{13} . \qquad (3)$$

The element m_{13} of the transfer matrix is the lattice dispersion produced by the dipole D_1 that adds on to the beam dispersion when the beam passes through the dipole. Substituting Eqs. (2) and (3) into Eq. (1), we get

$$x^2_{rms} = m^2_{11}a_1 + 2m_{11}m_{12}a_2 + m^2_{12}a_3 + 2m_{12}m_{13}a_4 + 2m_{12}m_{13}a_5 + m^2_{13}a_6 \,. \qquad (4)$$

In [3], Eqs. (1)-(3) were exploited to simultaneously obtain the emittance, beam dispersions and other beam parameters, by measuring the rms beam size at different focusing fields, followed by solving a corresponding set of nonlinear equations. Meanwhile, Eq. (4) reveals that by appropriate combinations of the initial beam parameters to be found, the problem becomes linear with respect to new parameters a_i:

$$\begin{aligned} a_1 &= \sigma_{11}(0) + \eta(0)^2 r^2 \,, \\ a_2 &= \sigma_{12}(0) + \eta(0)\eta'(0) r^2 \,, \\ a_3 &= \sigma_{22}(0) + \eta'(0)^2 r^2 \,, \\ a_4 &= \eta(0) r^2 \,, \\ a_5 &= \eta'(0) r^2 \,, \\ a_6 &= r^2 \,, \\ r &= \Delta p/p \,. \end{aligned} \qquad (5)$$

In this case a least-squares fitting algorithm may be easily applied if one makes the beam size scan by varying the strength of the quadrupole. However, one should bear in mind that if m_{13} is equal to zero, it is impossible to separately obtain from the fit elements of the σ- matrix and dispersions. If m_{13} is kept constant, in principle, all the parameters may be resolved, but the method does not seem quite reliable due to possible inaccuracies in measurements. The best fashion is to measure several scans when m_{13} is changed from scan to scan (by varying the dipole field). Then a_i and, hence, beam parameters are found by applying a single fit to all scans. As minimum, two scans are necessary. Once the σ-matrix is estimated, the beam emittance is found according to the formula

$$\varepsilon = \sqrt{\sigma_{11}(0)\sigma_{22}(0) - \sigma^2_{12}(0)} \qquad (6)$$

Results of the practical realization of the described method are shown in Fig. 2, where two scans of the squared rms beam size for two different dipole current of $1.1A$ and $-5.0A$ are given. Measurements were performed for the horizontal plane only. The effect of the dipole field change was detected as a quite measurable shift of the scan curve. However, when applying the least-squares fit to the both curves we found that it was impossible to estimate correctly a momentum spread from the data. We identified this failure with a smallness at used dipole currents of the last term in Eq. (4) compared to others. In fact, in the linear model an exceedingly small value of m^2_{13} provokes an unacceptably large value for a_6 that is the squared momentum spread.

Due to the fact that there was no tool available at the position to measure this parameter it was taken as a variable in the fit.

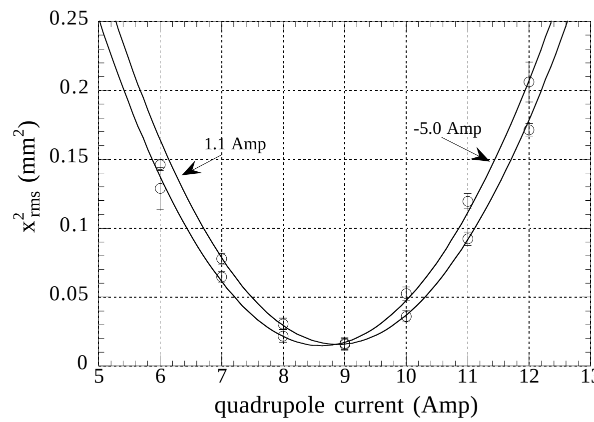

Figure 2: Two quadrupole scans of the squared rms beam size for two different values of the dipole current together with the least-squares fit to the data.

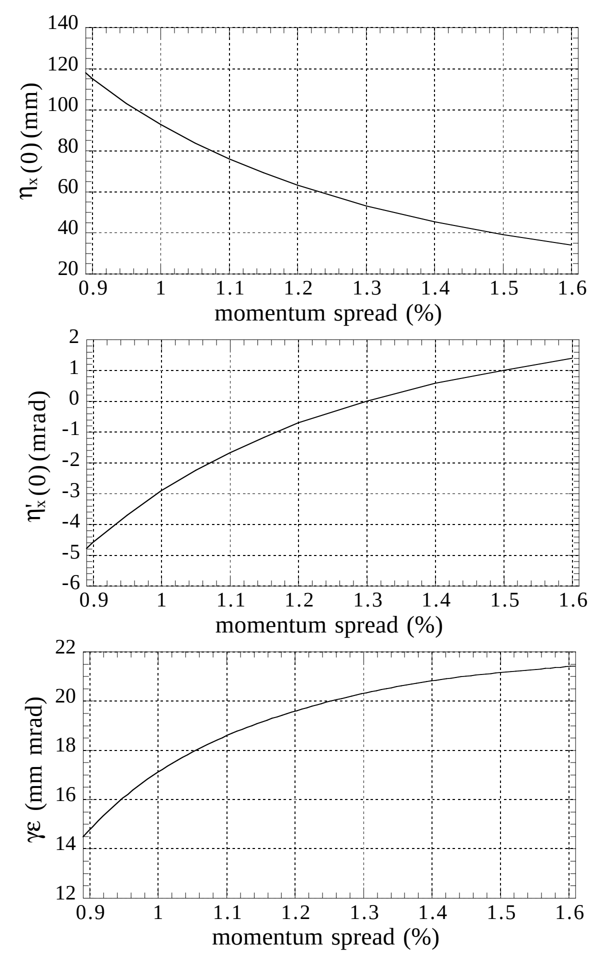

Figure 3: The spatial dispersion, angular dispersion and normalized emittance in the horizontal plane versus the momentum spread.

Fig. 3 plots the fit estimations for the spatial and angular dispersion together with the normalized emittance versus the momentum spread that is varied around its ”default” value of 1%. Emittance estimations are quite consistent with a value of about 20 mm mrad that was measured at the injector level by a multislit mask method for the 8 nC bunch charge. From this comparison we conclude that the momentum spread was likely larger then 1.25%, that is, in turn, in agreement with the measurement of the total beam energy variation along the macropulse found to be of the order of 5% [4]. Finally, the following limits for the dispersions can be given:$\eta_x(0) < 60$mm; $\eta'_x(0) < 2$mrad.

3 DISPERSION MEASUREMENT BY BEAM ENERGY VARIATIONS

This standard technique is based on the definition of the spatial dispersion

$$\eta = \frac{\Delta x}{\Delta E/E} \quad (7)$$

and consists in the measurement of the transverse beam displacement Δx when stepping the beam energy in a small range ΔE about its nominal value E.

The measurement was carried out in the experimental area. An energy variation of $\pm 1.54\%$ was effected by adjusting the rf system. Transverse beam positions were obtained as centers of gravity of beam spot profiles registered by the OTR beam profile monitor. To make it possible to derive both the dispersion function and its derivative, measurements were repeated for three different values of the quadrupole strength of a doublet situated 1.4 m upstream the OTR screen. For every rf and quadrupole strength settings, 40 beam images were recorded to provide a better statistics. Beam positions were obtained by averaging over all images, and beam displacements by averaging over different beam energies. Nevertheless, it turned out to be impossible to get data for the vertical plane, because the beam size in this plane was unacceptably large to reliably detect the small beam displacement.

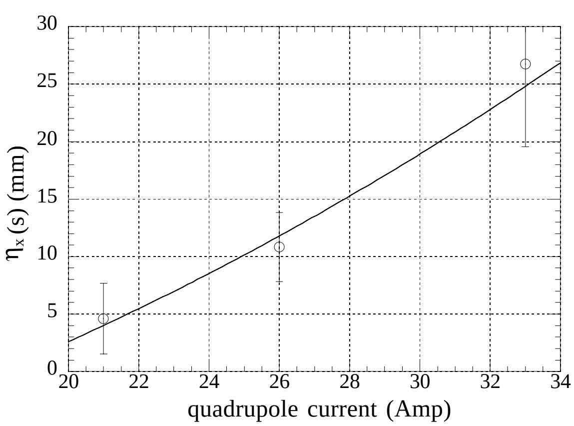

Figure 4: Spatial dispersion in the horizontal plane versus the quadrupole current and least-squares fit to the data.

Fig. 4 shows the horizontal spatial dispersion at the position of the screen as a function of the quadrupole current. To infer both the spatial and angular dispersions a fit must be applied to the $\eta(s)$ measurements. By making use of Eq. (3) with $m_{13} = 0$, these quantities can be found at the entrance of the doublet. A least-squares fit to the data shown in Fig. 4 gives following estimations for the dispersions:$\eta_x(0) = 12.7$mm; $\eta'_x(0) = 0.9$mrad.

4 CONCLUSIONS

The first attempt to determine the beam dispersion and to study its effect on the beam emittance was undertaken at TTF. Two different measurements were performed at two positions of the linac.

By the multiple quadrupole scan method we found upper limits for the dispersion and emittance at the position of the bunch compressor II based on an assumption about the momentum spread. In the experimental area we performed the dispersion measurement by the beam energy variation.

5 REFERENCES

[1] S.Schreiber, *The rf-gun based injector for the TESLA Test Facility Linac*, Proc. of 1998 EPAC.

[2] M.Castellano et al., Proc. of 1997 DIPAC, 195.

[3] Sung Oh Cho et al., Nucl.Instr. and Meth., A407 (1998) 359.

[4] M.Castellano et al.,*Time resolved energy measurement of the TESLA test facility beam through the analysis of optical transition radiation angular distribution* , Proc. of 1999 PAC.

DIPOLE MODES STUDY BY MEANS OF HOM COUPLERS AT SBTF

N. Baboi*, M. Dohlus, A. Jöstingmeier, N. Holtkamp, M. Wendt, M. Nagl,
J. Boster and H. Hartwig, DESY, Notkestr. 85, 22603 Hamburg, Germany

Abstract

High order modes (HOM) are generated by the interaction of a bunched beam with an accelerator environment. They may act destructively on following particle bunches, leading to an increase of the transverse oscillation amplitude and finally to the deterioration of the emittance. Dipole modes have been studied at the S-Band Test Facility at DESY. One accelerating structure, specially designed for this test linac, is equipped with waveguide pick-ups for measuring the HOMs. For one part of the experiments, a modulation of the transverse offset of the bunches at the structure entrance has been induced using a fast broadband kicker and the effect was measured with a precise stripline BPM. No high impedance modes were clearly found in the structure, which has been detuned and damped by both the tapered geometry of the structure and an absorbing stainless steel coating applied on the iris tips.

1 THE S-BAND TEST FACILITY

The very high luminosity, 10^{33} cm^{-2}s^{-1}, required for future linear colliders presume high charge, small cross section bunches. The main problem is that these bunches strongly interact with the accelerator environment, leading to the excitation of electromagnetic fields, the so-called high order modes (HOM). Off-axis bunches excite transverse HOMs, generating the transverse wake field:

$$\boldsymbol{W}'_{\perp}(s) = \sum_l 2\boldsymbol{k}'_{\perp\, l} \sin(\omega_l \frac{s}{c}) \exp(-\frac{\omega_l}{2Q_l}\frac{s}{c}), \qquad (1)$$

where $s > 0$ is the distance behind the bunch and ω_l, $\boldsymbol{k}'_{\perp\, l}$ and Q_l are the angular frequency, the transverse loss factor per unit length and the quality factor of mode l.

This wake field acts on the following bunches entering the structure, which leads to the deterioration of the beam properties, mainly to an increase in the emittance and a large energy spread. The modes with a low Q may be damped before the next bunches arrive, so that the main contribution to the wake fields will be given only by the modes with a high $\boldsymbol{k}'_{\perp}$ and a high Q.

The S-Band Test Facility (SBTF) was built at DESY in the framework of a study of a 500 GeV linear collider based on the S-Band technology [1]. Based on the experience in this frequency range (e.g. SLC), an accelerating structure was specially designed for SBTF, paying attention to reducing the HOMs quality factors. The main purpose of the here described experiments is to find most dangerous HOMs that are excited by using the beam.

* Home address: NILPRP, Bucharest

Layout The electron beam is accelerated to a maximum of about 100 MeV by the injector section and a first accelerating structure [2]. The two next accelerating structures, specially designed for this test facility, could give the beam 300 MeV maximum. The first and the second structures are fed through a power splitter by the same klystron [3], while a second klystron feeds a third one.

In Fig. 1 the second accelerating structure, is represented together with a stripline BPM ([4]) which allowed the monitoring of single bunches, distanced by a minimum of 8 ns. A kicker and a steering magnet are placed between the first and the SBTF structures. The current monitors and some elements that were not used during the experiments are not shown. The very fast counter travelling wave kicker [5] can

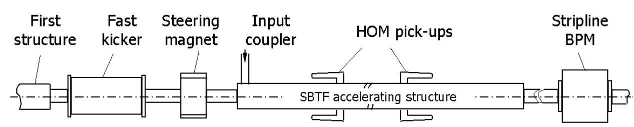

Figure 1: Experimental setup of the kicker experiment

impart on bunches with 35 MeV energy a maximum kick of 400 μrad, which, in case no HOMs act on the bunches, would be seen at the location of the BPM as an offset of 2.4 mm (the autofocusing was taken into account).

The SBTF accelerating structure and HOMs The 6 m long accelerating structure is a constant gradient one, working in the $2\pi/3$ mode at a frequency of 3 GHz. The iris radii are tapered along the 180 cells. In order to avoid phase and amplitude dependent transverse kicks, the input coupler is symmetric and has a power splitter on top.

Special attention has been given to the HOM attenuation. It has been found in simulations that the main contribution to the transverse wake field is given by the modes in the first, third and sixth dipole passbands. While the level of $\boldsymbol{k}'_{\perp\, l}$ in the first passband is of the order of $7.5 \cdot 10^{12}$ V/Cm^2, in the sixth passband a few modes with loss parameters up to $6.8 \cdot 10^{13}$ V/Cm^2 have been found [6].

The frequency detuning induced by the iris tapering leads to the decoherence of the long range wake field. Due to the recoherence effects of the HOMs, damping of the dipole modes is also necessary. On the other hand, modes in the first passband are trapped inside the structure, which makes the use of a few HOM dampers along the structure not efficient. Instead, damping is achieved by covering the iris tips of the cells with a thin stainless steel layer [7, 1]. For the SBTF structures, only the iris tips of cells 1 to 20 and 111 to 121 were covered with such a layer. The calculations made for the first dipole band for a SBTF structure indicate that about half of the modes were damped to Qs less than 5000, while the rest are distributed between 5000 and about 14000, which is the Q level for a pure copper structure. Further damping of the HOMs is provided in the last cells by a colinear load that replaces the output coupler.

The HOM Couplers The first SBTF structure is provided with two HOM couplers with four orthogonal waveguides (cutoff frequency 4 GHz) at one cell for measuring the position of the structure relative to the beam [8] (see Fig. 2). Two opposing waveguides are used for one polarization plane. Azimuthal wall slots are used for coupling.

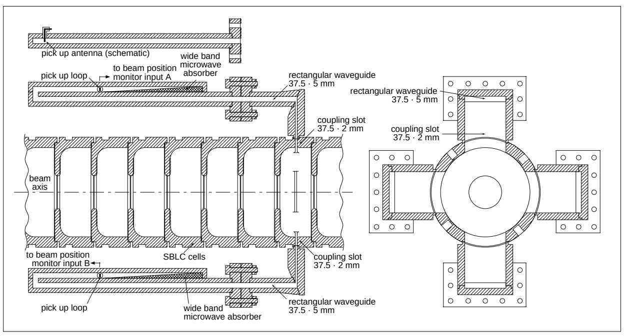

Figure 2: Cross-section of the accelerator structure with a HOM coupler

2 EXPERIMENTAL SETUP

Single-bunch experiments A bunch is shot off-axis through the SBTF accelerating structures exciting wake fields. The signal from the eight HOM coupler waveguides is viewed on both a spectrum analyzer and on an oscilloscope. In order to better reject the strong fundamental mode and other monopole modes, the two horizontal waveguides, as well as the vertical ones, of the first coupler were combined through a magic-T hybrid combiner.

When sweeping the bunch transversely in the structure, the power of a dipole mode will vary as the square of the bunch offset. A minima will be attained when the beam is in the middle of the structure. This can be used to steer the beam in the middle of the structure, or, inversely, to align the structure with respect to the beam axis [1]. Due to the very localized coupling of the modes to the beam, it is even possible to detect the local offset of the structure as a function of the mode frequency.

Multi-bunch experiments When a bunch train is sent off-axis through the structure, some modes add coherently, while others are attenuated. The modes that satisfy the relationship $\omega_l = m\,\omega_b$, where ω_b is the bunch angular frequency and m is an integer, will be strongest excited.

Kicker experiment The aim is to excite only one dipole mode at a time. By means of a fast kicker, a sine modulation is imparted on the transverse offset of the bunches coming out of the first structure. The offsets dx_i of individual bunches at the entrance of the second accelerating section will be then:

$$dx_i = dx_0 \sin(i\omega_K t_b + \varphi), \text{ with } i = 0 \div n-1, \quad (2)$$

where dx_0 is the maximum offset at the entrance of the structure, ω_K is the kicker frequency, t_b is the time interval between the bunches and φ the phase of the first bunch in the train with respect to the kicker signal.

In the accelerating structure a bunch will be deflected by the transverse wake fields excited by all the previous bunches. The kick of bunch i, dx'_i, is given by:

$$dx'_i = \frac{eq_b}{E} \sum_{j=0}^{i-1} W_\perp((i-j)t_b c)\, dx_0 \sin(j\omega_K t_b + \varphi), \quad (3)$$

where E and q_b are the bunch energy and charge. It was assumed that the change in offset of bunch j is much smaller than dx_j and that the energy gain in the structure is much smaller than the initial energy.

A long bunch train will reach a steady state configuration after the damping length of the highest impedance dipole mode. A resonance will occur when $\omega_K = |m\omega_b - \omega_l|$, where ω_b is the bunch frequency and m an integer [9]. The amplitude of this resonance depends on $\boldsymbol{k}'_{\perp\, l}$.

3 RESULTS

Single-bunch experiments The spectra of the HOM fields excited by a 1.4 nC bunch have been measured and special attention has been given to the first dipole band. The frequency range seen from the first waveguides is about 4.16 ÷ 4.3 GHz, while from the second ones is 4.28 ÷ 4.45 GHz. Interesting to remark is that the fundamental mode could not be seen even before the installation of the power combiners. Two unexpected modes have been seen, one from each coupler, at 4.125 and 4.135 GHz, respectively. They are well separated from the first dipole band and have a much lower Q. Their dipole character has been deduced. These additional modes come from the couplers geometry and are localized around these.

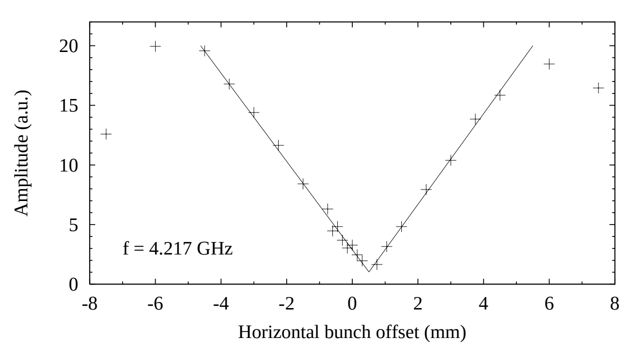

Figure 3: The amplitude of the mode at 4.217 GHz from the horizontal waveguides as a function of the bunch offset

For more modes the signal amplitude was measured as a function of the beam offset. The curve obtained for a mode at 4.217 GHz is shown in Fig. 3. The dipole character can be clearly seen in the linearity of the two sides of the curve. At both sides the signal amplitude decreases due to bunch loss at the irises. The field minima is not 0 because of the misalignment of the structure or a tilt of the beam, meaning that this mode is always excited in some cells. A comparison of the minimum power positions and the geometrical straightness could not be done due to the missing data regarding cell alignment.

Multi-bunch experiments The bunch train was limited to 20 bunches $\times$ 24 ns due to the at the date performances of the klystron. The energy at the entrance of the structure was 65 MeV. For the kicker experiment, the pulse length was prolonged from 0.6 μs to 1 μs (flat top), so that 40 bunches $\times$ 24 ns could be accelerated. In Fig. 4 the spectra from the coupled first horizontal waveguides for 20 bunches $\times$ 24 ns is shown. It can be seen that the modes around 4.125 (the mode induced by the waveguides), 4.167, 4.208 and 4.25 GHz (= $m\omega_b/2\pi$) have higher amplitude than the other ones. Due to the limited number of bunches more modes around these frequencies are amplified.

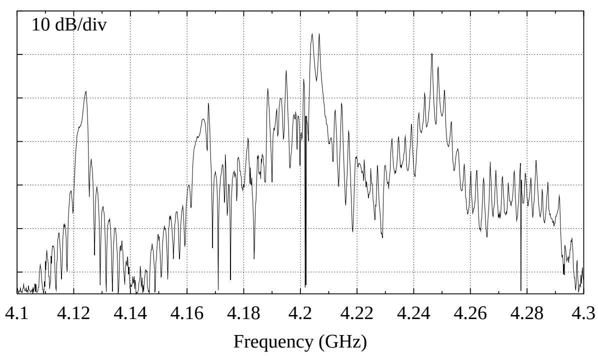

Figure 4: Spectrum from the coupled first horizontal waveguides with 20 bunches $\times$ 24 ns

For the *kicker experiment* a train of 40 bunches with 35 MeV was used. The modulation frequency was varied from 0 to 21 MHz in steps of 0.2 MHz. The difference and the sum signals from the horizontal pick-ups of the stripline BPM were plotted on an oscilloscope. A FFT was performed from the difference signal on the oscilloscope.

In Fig. 5 such an FFT for $\omega_k/2\pi = 14$ MHz is shown. The central signal is given by the bunch frequency. At each side, two strong signals at 2.5 MHz could be seen already before any signal was applied on the kicker. This was associated with a modulation seen on the current signal at the exit of the first accelerating section and is thought to come from the non-uniform signal of the klystron.

The signal from the kicker could always be seen and, for $\omega_k/2\pi$ less than about 9 MHz, it was altered by the 2.5 MHz signal. The amplitude of the signal from the kicker varied only slightly with ω_k, so that we could not say with certitude if a high impedance HOM was excited or if this variation is due to the harmonics from the number of bunches (1 MHz). During the kicker frequency sweep, we looked in parallel at the spectra between 4.1 and 4.3 GHz from the first HOM couplers and for many frequencies at the first and sixth passbands as well. No mode was seen to be amplified in these frequency ranges.

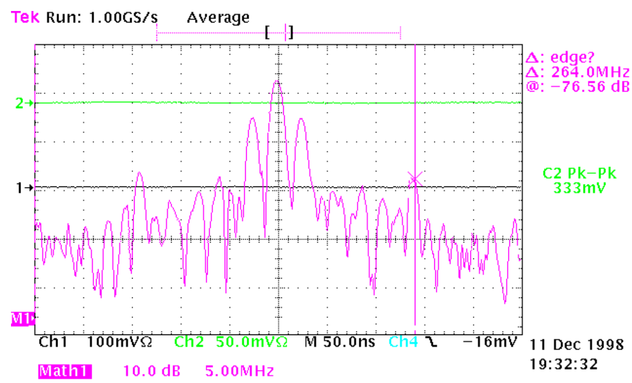

Figure 5: FFT of the BPM difference signal for a kicker modulation of 14 MHz

4 CONCLUSIONS

By using the beam, HOMs have been excited and viewed by means of HOM waveguide couplers. Some passbands could be distinguishes. The dipole character of the modes in the first passband was deduced. Based on the local coupling of the modes to the beam, the local offset of the structure was deduced. The amplification of the modes whose frequencies are at multiples of the bunch frequency has been observed when using a bunch train. In the kicker experiment, no resonant amplification of the beam offset due to HOMs could be observed.

Acknowledgment We want to thank P. Schmüser, R. Brinkmann, H. Weise for the fruitful discussions. Special thanks to the MIN group and to the Russian collaborators from MEPhI, whose name list is too long to be mentioned here, but whose work made possible these experiments.

5 REFERENCES

[1] R. Brinkmann, G. Materlik, J. Rossbach and A. Wagner (eds.), DESY Report: DESY 1997-048, Vol. II, 1997

[2] M. Schmitz, Proc. 1996 Int. Linac Conf., Geneva, Switzerland, 1996; M. Schmitz for the SBLC study group, Proc. IEEE, Vancouver, 1997

[3] S. Choroba, J. Hameister and M. Kuhn, 19th Int. Linac Conf., Chicago, 1998; DESY Report: DESY-M-98-11F, 1998

[4] W. Radloff and M. Wendt, IEEE PAC 1995, Dallas, pp. 2616, 1995; DESY Report: DESY-M-95-08AG, 1995

[5] B.I. Grishanov et al., DESY Report: TESLA 96-11, 1996

[6] A. Jöstingmeier, M. Dohlus, C. Rieckmann and A.S. Omar, Proc. IEEE Particle Accelerator Conf., Vancouver, 1997

[7] M. Dohlus et al., DESY Report: DESY 96-169, 1996

[8] A. Jöstingmeier, Proc. IEEE MTT-S Symp, Boulder, 1997

[9] S. Fartoukh, DESY Report: TESLA 98-07, 1997

Aspects of Bunch Shape Measurements for Slow, Intense Ion Beams

P Forck, F Heymach, U. Meyer, P Moritz, P Strehl
Gesellschaft fur Schwerionenforschung GSI, Planck Strasse 1, 64291 Darmstadt, Germany.

Abstract

For the characterisation of the ion beam delivered by the new High Current LINAC at GSI, the time structure of bunches and the knowledge concerning their intensity distribution in longitudinal phase space is of great importance. At least 100ps time resolution and the capability of measuring long tails in the distribution were design parameters. Taking advantage of Rutherford-scattering to reduce the count rate, a direct time of flight measurement technique using diamond detectors can be applied. First results are reported. Plans for determine the energy of individual ions by detecting secondary electrons emitted from a thin C foil using 1m drift are discussed.

1 DESIGN OF BUNCH SHAPE MEASURING DEVICES

Knowledge of the distribution of ions within a bunch and longitudinal emittance is needed for the matching between different LINAC acceleration components as well as for the comparison to calculations, in particular in the case where space charge effects play a role. For the new high current heavy ion LINAC developed at the GSI, which consist of a 36 MHz RFQ (energy 120 keV/u) and two IH-structures (final energy 1.4 MeV/u) [1] space charge effects have to be considered. The commissioning just started in spring 1999 and will be continued until the end of ‘99 and a maximum pulse current of 15 emA for heavy ions like U^{4+}, corresponding to 10^9 ions per bunch is expected. Having a typical phase spread of ±15° corresponding to 2ns in time, a resolution of at least 100ps is needed to visualise mismatch or space charge effects. Due to the low velocities, capacitive pick-ups cannot be used.

During the commissioning a movable test bench is installed behind each section [2, 3]. To measure the time structure and the longitudinal emittance of the bunches a new designed device is mounted there, which is based on a time-of-flight method using diamond particle detectors [5], where the arrival time of the ions is measured relative to the acceleration rf, see Fig. 1. The excellent time resolution of a diamond detector is used, but one has to make sure, that less than 1 ion per bunch hits the detector. For this purpose Rutherford-scattering by a thin gold foil is used as an attenuator. The technical outline and preliminary results are discussed.

In addition a second method is under development, which is suitable for the bunch time structure measurement within one macro pulse. This is an adaption of the well known method by Ostroumov et al. [6], but instead using secondary electrons from an intersecting wire, the electrons of the residual gas atoms will be used. The time information carried by the electrons is converted to spatial differences by an rf-deflector and detected with a spatial resoluting MCP. The reader is referred to [3] for further details.

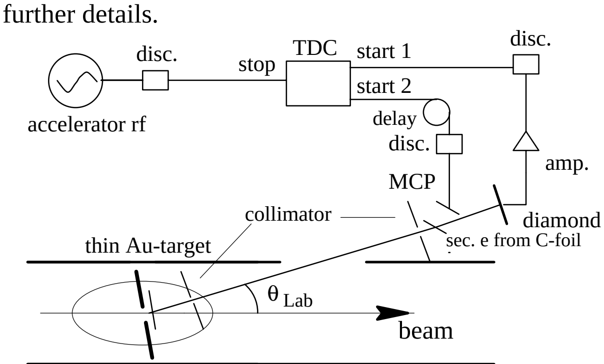

Figure 1: Schematic sketch of the designed TOF method with particle detectors far the bunch shape measurement (see Sec. 2) and phase space distribution (see Sec. 5).

2 RUTHERFORD-SCATTERING CONSIDERATIONS

The precise timing signal from particle detectors is used since several decades for the determination of the bunch structure and the energy spread of slow ion beams. But the direct bombardment of the detector can only be used for very low ion currents to prevent multiple ion hits within one bunch. We like to study space charge effects and therefore the count rate on the detector is reduced by Rutherfordscattering, see Fig. 1. A 120 μg/cm^2 (equals to a thickness of ≈60 nm) gold foil is used as the target. We choose a laboratory angle Θ_{Lab} = 7.5° together with a collimator having ∅ 0.5 mm holes and 16 cm distance on pneumatic feed-throughs. The attenuation of this system is shown in Fig. 2 as a function of the laboratory angle for the RFQ output energy for different ions. The chosen angle prevents from multiple hits for moderate ion currents, while for the highest possible ion currents the count rate can be varied by de-focusing the ion beam. For these considerations, the centre-of-mass energy as well as the broadening of the centre-of-mass solid angle due to the target recoil has been taken into account [4], which depend on the scattering angle, the projectile energy and the ratio between the projectile and target masses. As shown in the figure, the attenuation for the gold target varies only by a factor of 2 for the interesting projectiles for a fixed specific energy. The attenuation scale with the inverse specific energy squared.

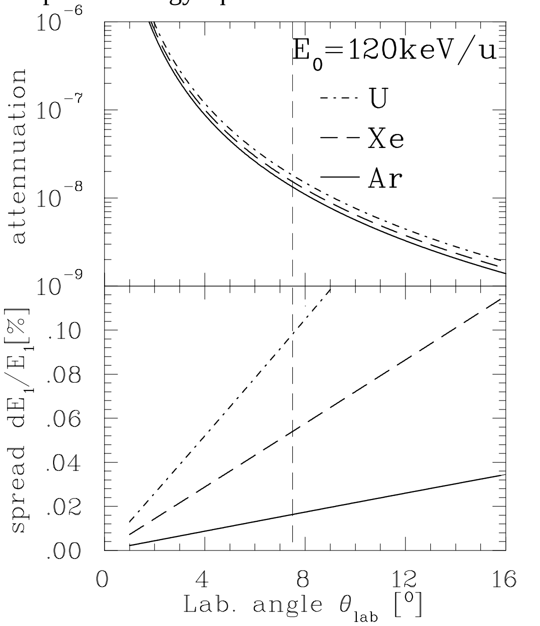

Figure 2: The fraction of scattered ions (top) within the chosen solid angle $\Delta\Omega_{lab}$ = 2.5 - 10-4) for an ion beam diameter of 10 mm and the energy spread of the projectile dEi /Ei (bottom) by Rutherford scattering for a 120µg/cm^2 gold target as a function of the scattering angle θ_{lab}.

A finite solid angle is equivalent to an energy spread dE_1 /E_1 of the projectile, shown in Fig. 2, due to different energy releases to the target atoms, also shown in Fig. 2. The effect depends strongly on the projectile/target mass ratio and a heavy nuclei target is preferred here. For the chosen gold target, the energy spread for light ions is much lower than the needed resolving requirements of the beam energy spread of ΔW/W = 0.1%. But for heavier ions, like U, the resolution is limited. The relative energy spread dE_l/E_l by the target is independent of the projectile energy.

One might think of an other limiting factor, that is the multiple scattering inside the gold target, but according to an estimation in Ref. [4] the probability of multiple scattering is below 1.5 % for the 120 keV/u U projectiles and decreases for lower masses and higher energies; in the case of 120 keV/u it is about 0.75 °%.

Beside the projectile, the target nuclei can also leave the interaction zone due to the energy release by the collision. But the fraction of recoils inside the chosen solid angle around θ_{lab} = 7.5° is below 3x10^{-4} of the scattered projectiles. Therefore it is to low to spoil the resolution.

One drawback of this method is the sensitivity of the gold foil: One has to be very carefull not to heat the foil to the melting point. For our case we have to make sure by beam defocusing, that the beam intensity is below a factor of 1000 compared to the expected maximum. In addition the mechanical stability of the ∅5 mm self-supporting foil is low.

3 DETECTORS AND ELECTRONICS

The scattered ions are detected by diamond detectors; 3 detectors are mounted on feed-throughs downstream at spacing of about 20 cm, 61 cm and 102 cm, respectively. These fast detectors are used in our laboratory since several years for high energy ion detection [5], but so far not for ions, having a range much lower than the detector thickness.

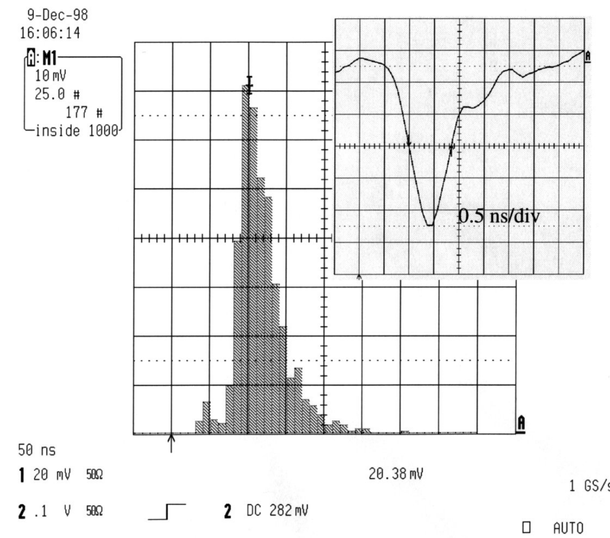

Figure 3: Pulse-height distribution of a diamond detector with 300 keV/u C^{4+} and one typical pulse as an inlet.

Beside the very low radiation damage, we gain mainly from the very fast signals, having a rise time below 1 ns, as shown in Fig. 3. This is important for the high timing requirements. A high voltage biased amplifier with more than 2 GHz bandwidth was developed at GSI [5]. To suppress the 36 MHz pick-up from the acceleration frequency careful shielding and a Notch-filter is needed. The conversion to logical pulses is done by a double threshold discriminator developed at GSI [7]. Via two thresholds the onset of the pulse is extrapolated. With careful adjustment, a timing error of less than 30 ps is expected with this equipment.

The logical pulses serve as a start of a VME time-to digital converter (CAEN V488), having a resolution (least significant bit) of 25 ps. It is stopped by the signal from the 36 MHz rf master oscillator, which drives the power amplifiers for the acceleration rf. A standard leading edge discriminator is used to get logical pulses, a division to 12 MHz is used for fitting to the TDC range. The converted data are stored in a FIFO for reading after the end of the macro-pulse, so a digitisation rate of 250 kHz is reached. In addition the counts can be stored in a FIFO based scaler (SIS 3801) for making off-line cuts with respect to the time within the macro-pulse. The data are send from the VME to a VMS workstation for storage and analysis.

4 FIRST RESULTS

First test measurements have been done recently at the RFQ test bench with 120 keV/u Ar^+ ions with non-optimized beam setting.

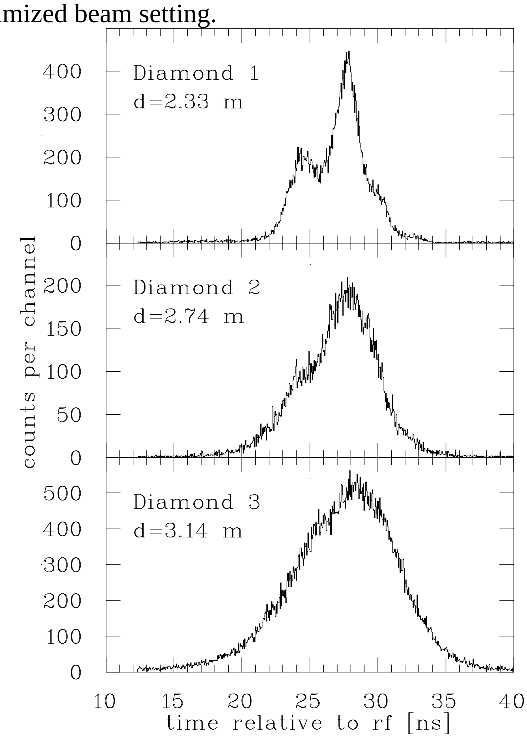

Figure 4: Bunch shape signal from a 120 keV/u Ar^+ beam observed on three diamond detectors with the given distance form the RFQ output, recorded with a time resolution of 48 ps per bin.

The bunch shape is plotted in Fig. 4, showing the functionality and the resolving power of the new device. With the three detectors the dispersion of the bunches can be visualised. The distance from the RFQ output to the gold target is 2.12 m and to the three detectors 2.33 m (Diamond 1), 2.74 m (Diamond 2) and 3.14 m (Diamond 3), respectively. Like expected from numerical simulations [1] the bunch shape is non-Gaussian. The width of the central peak measured with the closest diamond is about 2.2 ns and has pronounced side peaks. These side peaks are smeared out by the beam energy width $\Delta W/W$ after the drift of 1 m, as expected from calculations. The measurements have been done with a 100 times lower beam current as the design current, where the longitudinal emittance is larger. The low current was used to avoid destruction of the gold foil. A measurement with the shown statistics needs several minutes, corresponding to some 10^3 macro-pulses having 1 ms length. The time is limited by the 5 µs conversion time of the TDC. During the ion bombardment a drop of the efficiency (more precisely of the pulse-height) of the diamond was detected with unknown reason.

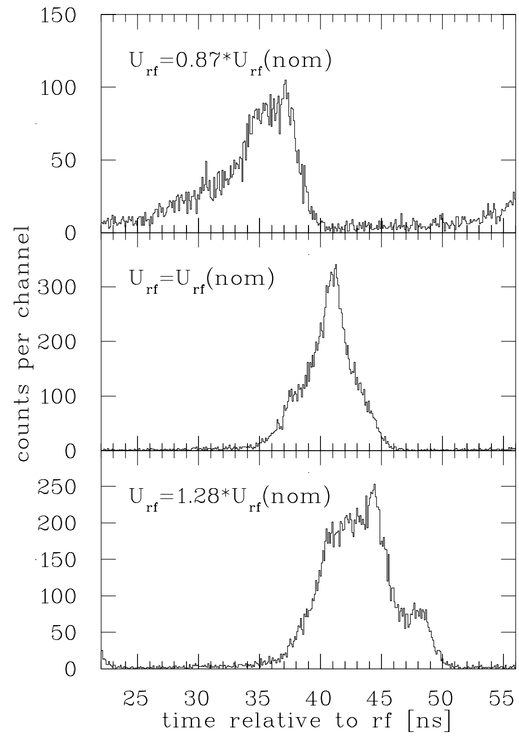

Figure 5: Bunch shape signal from a 120 keV/u Ar^+ beam with different amplitudes of the RFQ rf field.

In Fig. 5 the effect on the bunch shape for different amplitudes of the RFQ tank is shown. The amplitude is varied by ±10% of the nominal value, where the acceleration to the nominal energy is still possible; a different setting as compared to the previous figure is used. Besides a shift of the bunches center-of-mass a strong influence on the structure is visible using the first diamond detector. As expected no significant change on the mounted capacitive pick-up is visible due to the very low velocities, showing the high capability of the applied time-of-flight method.

The data shown are from first tests and are quite encouraging. More careful investigations have to be done, in particular concerning the limits of the resolution, given by the energy spread at the target and the discriminators setting. More measurements, in particular with higher currents, and comparison to theoretical calculations are needed.

5 MEASUREMENT OF PHASE SPACE DISTRIBUTION

With the setup not only the projection to the time axis of the bunches seems to be measurable, but also the energy distribution by determination of the time-of-flight. As an upgrade a second foil made of 5 µg/cm^2 (equals to ≈25 nm) is inserted between the scattering target and the diamond detector. Several secondary electrons are emitted by each ion from this surface [8]. The electrons are accelerated by a electric field of ≈1 kV/cm to a MCP (Hamamatsu F4655-10) 2 cm apart, equipped with a 50Ω anode giving pulses with ≈1 ns width. For the time difference of the arrival here and at the diamond detectors 2 or 3 the time-of-flight and therefore the relative energy of an individual particle is calculated and the full phase space distribution could be plotted from a series of measurements. Again the resolution is limited by the scattering process: Here the total energy straggling is important, which amounts e.g. 0.1% in the case of Ar ions. The timing of the electronics is quite critical as a first test has shown.

Acknowledgment

The support and discussion by D. Wilms during the measurements are gratefully acknowledged.

6 REFERENCES

[1] U. Ratzinger, Proc. XVllllntern. Lin. Acc. Conf., Geneva, Switzerland, p. 288 (1996), W Barth et al., Proc. XIX Intern, Lin. Acc. Conf., Chicago, USA, (1998).
[2j P. Forck, P Stiehl, this proceedings.
[3] P. Forck, A. Peters, P. Stiehl, Proceeding of 6th EPAC. Stockholm, Sweden, p. 1500 (1998).
[4] see e.g. J.R.Tesmer, M. Natstasi Handbook of Modem Ion Beam Material Analysis, Material Research Society, Pittsburgh (1995).
[S] P. Moritz et al., Proceeding of 3th DIRAC, Frascati, Italy, p. 153 (1997), E. Berdermann et al., Proc. XJDWllnt. Winter Meeting ofNucl. Phys., Bormio (1998).
[6] YV Bylinsky et al., Proc. 4th European Part. Acc. Conf., London, p 1702 (1994) and references therein.
[7j C. Neyer, 3rd Workshop on Electronics for LHC Experiments, London, CERN/LHCC/97-60 (1997).
[8] P. Koschar et al., Phys. Rev A 40, 3632 (1989)

EXPERIENCE WITH STRIPLINE BEAM POSITION MONITORS ON THE TESLA TEST FACILITY LINAC

P. Castro, DESY, Hamburg, Germany
P. Patteri, F. Tazzioli, INFN, Frascati, Italy

Abstract

Measurement and correction of beam position are very important for the optimization of beam characteristics and alignment in the Tesla Test Facility (TTF) linac. We describe and present measurements with beam of the performance of the stripline beam position monitors (BPMs) in operation and in order to determine the beam response.

1 INTRODUCTION

Beam position measurement and correction are essential in the TTF linac for collider applications and for the VUV FEL experiment [1]. Beam orbit correction algorithms use the knowledge of the machine lattice in the form of response matrix (element R_{12} in Transport [2] notation) in order to find a combination of corrector strengths which reduces the rms beam position offsets at the BPMs. These correction procedures involve several BPMs and corrector magnets, and require precise measurements of beam position and a good knowledge of the transport matrix.

A series of experiments has therefore been performed to determine the linearity region and range of the BPM response and its offset with respect to the magnetic centres of adjacent quadrupoles. Measurements of the response matrix are compared to the one calculated from known quadrupole gradients and measured beam energy. Results on BPM gains fitted to the measurements will be presented. Correlated beam position jitters, which affect trajectory and emittance measurements, have been measured. Here we will present only a choice of characteristic measurements. For a more exhaustive treatment see [3].

Several measurements have been performed both on TTF phase one and phase two layouts. Phase one had an injector with low charge per bunch (40 pC), high bunch repetition rate (216 MHz) and only one accelerating module (beam energy up to 120 MeV). Phase two has an injector with high bunch charge (1-8 nC), low rep. rate (1 MHz) and two accelerating modules (energy up to 250 MeV

In Fig. 4 is shown a sketch of the lattice layout of the TTF phase one in the high energy area after the accelerating module, with the location of the stripline BPMs. The focusing is provided by quadrupole doublets. There are also other types of BPMs on the TTF linac, both outside and inside the cryostats, which contain the accelerating modules. These additional BPMs are based on cavities and have a higher resolution than the stripline BPMs. Here we will limit our discussion to the stripline monitors, which were specified for a resolution of 0.1mm, considered sufficient for beam alignment in the low frequency TTF accelerating modules, having a large bore.

2 STRIPLINE BPMS

We will summarize briefly the characteristics of the stripline BPMs, which have been extensively described elsewhere [4, 5]. The stripline BPMs are 17 cm long and have a 3 cm bore radius. The readout electronics are based on the AM/PM circuit, which gives directly a normalized output proportional to beam displacement and independent of current. The response is linear within ±5mm and then deviates from linearity and saturates at about 1 cm. An output curve measured by scanning with a correcting magnet without any magnetic lenses between it and the BPM, is shown in Fig. 1.

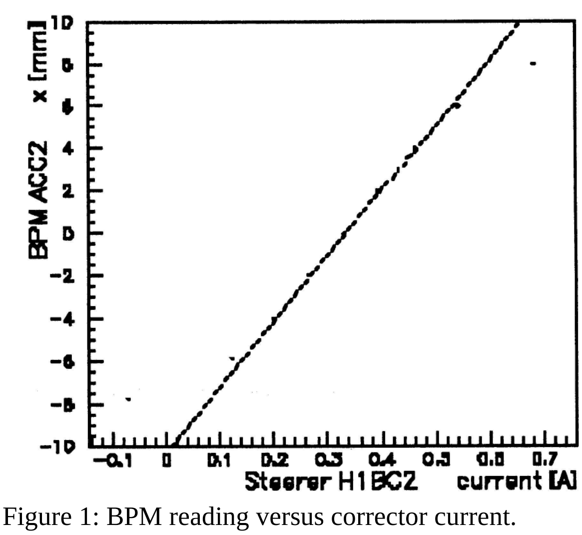

Figure 1: BPM reading versus corrector current.

The front end electronics had to be redesigned for the phase two, where the period between bunches is larger. The new design provides for single bunch response [6]. A typical output pulse is shown in Fig. 2. The acquisition system tracks the waveform until the middle of the flat top and then holds the corresponding value.

The electronics offset is set to zero using the beam induced signals. The voltage from one vertical (horizontal) electrode is split into equal branches and applied to the horizontal (vertical) ones. The overall output voltage is then set to zero by acting on a phase shifter in series with one of the inputs to the phase comparator of the AM/PM circuit.

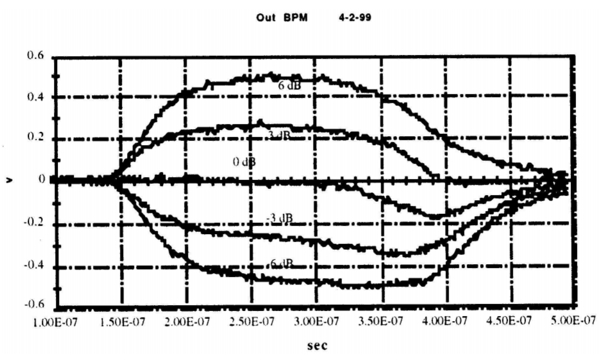

Figure 2: Typical output pulses from the fast BPM readout electronics for various beam positions, simulated by unbalancing the input signals.

The electronics for the phase one, having a slow response averaged over about 100μs, has shown low noise and good stability. The jitter was comparable with the resolution, 0.025 mm as determined by the least significant bit. Drifts in BPM gains over several days were less than 10%. The new fast electronics have a larger bandwidth and therefore a higher jitter, about 0.1mm.

3 Q-POLE MAGNETIC CENTER MEASUREMENT

A beam passing at a distance v from the center of a quadrupole with strength k receives a deflection α = kLy where L is the length of the quadrupole. A change of the quadrupole strength Δk leads to a change of deflection $\Delta\alpha$= (Δk)Ly , which is proportional to the beam offset at the quadrupole. The beam deflection at the quadrupole changes the beam trajectory at the downstream BPMs. Observing the position shift at the downstream BPM as a function of the position at the upstream BPM close to the quadrupole, one obtains a measurement of the position of the quadrupole magnetic centre with respect to the BPM magnetic centre. The horizontal and vertical corrector dipoles ahead of the upstream BPM are used to steer the beam at approximately the 0, ±2 mm, ±4 mm readings of the upstream BPM. In Fig. 3 are plotted the position measurements at the downstream BPM versus the beam positions measured at the BPM close to the quadrupole, for three values of the quadrupole current. The best fit of the dashed line (I=6 A) and the dotted line (I=10 A) coincide at Y = 0.13 mm.

Systematic errors on the determination of the quadrupole magnetic centre are due to the angle of the beam trajectory at the upstream BPM. For a BPM to Q-pole distance of 1 m and an angle of 0.1mrad the error is 0.1 mm.

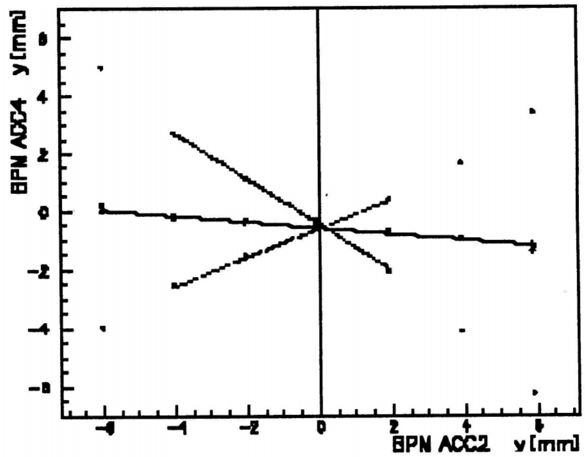

Figure 3: Measured beam position at BPM ACC4 versus measured beam position at the quadrupole doublet ACC2 set to 8 A (full line), 6 A (dashed line) and 10 A (dotted line).

4 RESPONSE MATRIX MEASUREMENTS

The shift of the beam transverse position at a given BPM due to a corrector field located upstream is given by the R_{12} element of the transport matrix. The so-called "response matrix", which is used for correcting beam trajectories, contains the R_{12} elements of the transport matrices between correctors and BPMs. In order to obtain detailed information on BPM gains, corrector magnets and quadrupole gradients, we compare the measured response matrix with the model response matrix.

The beam position shift Δx_{mn} measured with BPM m due to a change in the corrector magnet deflection n is given by.

$$\Delta x_{mn} = g_m \theta_n R_{12,mn}$$

where g_m is the gain of the BPM m. These parameters g_m and θ_n are varied to minimize the x^2 deviation between the model and measured response matrices

$$X^2 = \sum_{n,m} \frac{(R_{12,mn}(k_i).\theta_n g_m - \Delta x_{mn})^2}{\sigma_m^2}$$

where σ_m is the measured beam position error of BPM m averaged over 20 pulses . The fit parameters in R_{12} are the strengths k_i of both quadrupoles in the doublets. The beam energy is measured with a spectrometer magnet with a typical error of 3%.

The fit parameters g_m and θ_n are inversely correlated, therefore, depending on the initial values given to the fit parameters, a different set of results is obtained. We scale the gains $g_{m,}$ so that their mean value is equal to unity.

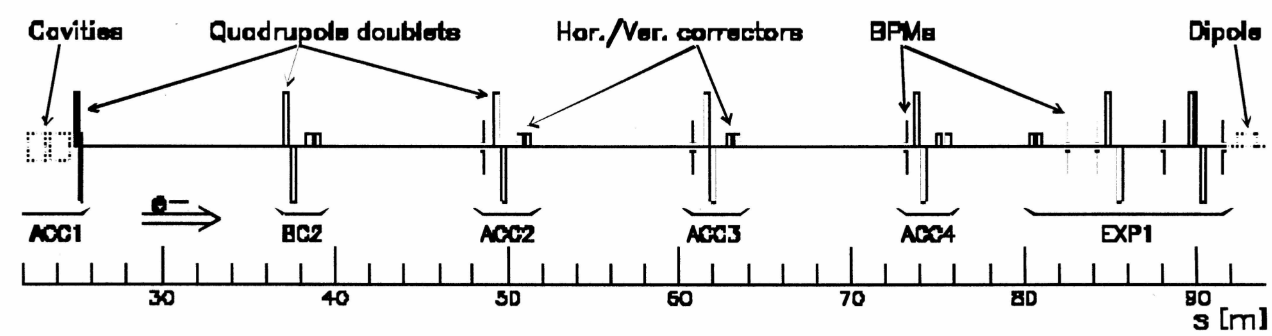

Figure 4: Magnetic layout of beam transport channel after the first accelerating section.

After scaling also the corrector strengths, the mean values of the θ_n obtained are only a few per cent higher than the expected value. This indicates that the calibration of the BPMs is on the average very good. However, the rms variation of θ_n is about 7%, which is larger than the magnetic field error expected (<1%). A reason for that can be hysteresis effects on corrector magnets. Results of BPM gains are shown in Table 1.

Table 1: Results of horizontal BPM gains from the analysis of three response matrix measurements

BPM	σ_x [mm]	Horz. Gain I	II	III
ACC2	0.030	1.08	1.09	1.08
ACC3	0.060	0.89	0.89	0.89
ACC4	0.070	0.98	0.98	0.96
1EXP1	0.020	1.05	1.04	1.05
2EXP1	0.025	1.00	1.00	1.02
3EXP1	0.035	1.88	1.95	1.84
4EXP1	0.025	1.21	1.15	1.15

5 CONCLUSION

Stripline BPMs are used in the TTF beamline with a resolution better than 0.05 mm. Their linearity, gain and stability has been studied. The BPMs provide a linear response in the range of about ±5 mm. The relative gain error is within ±10%. The measurement of the magnetic centre offset of a quadrupole with respect to the nearby BPM resulted in about 0.1 mm. The stability of the BPM readings is good, allowing to detect beam position jitter due to other sources in the beam line.

6 ACKNOWLEDGMENTS

We wish to thank L. Cacciotti of the TESLA group of LNF for his invaluable work on both the versions of the BPM electronics. We are grateful to R. Lorenz for many helpful discussions and help during all phases of BPM test and operation.

7 REFERENCES

[1] A VUV Free Electron Laser at the TESLA Test Facility at DESY- Conceptual Design Report, TESLA-FEL note 95-03
[2] D. Carey -The optics of charged particle beams- Harwood Academic Publishers.
[3] P. Castro -Beam position measurements in the TTF linac- TESLA note 98-29.
[4] R. Lorenz -Measurement of beam position in the Tesla Test Facility linac- 1996 Linac Conference, 527.
[5] M. Castellano et al. -TTF Stripline Readout system- EPAC 1996, 1633.
[6] L. Cacciotti, P. Patteri, F. Tazzioli -The new front end module of the TTF Stripline BPMs- TESLA note 98-18.

High Current Precision Long Pulse Electron Beam Position Monitor

Scott D. Nelson[1], Yu Ju (Judy) Chen, Thomas Fessenden, Clifford Holmes,
Lawrence Livermore National Laboratory. Livermore, California, USA

Abstract

Precision high current long pulse electron beam position monitoring has typically experienced problems with high Q sensors, sensors damped to the point of lack of precision, or sensors that interact substantially with any beam halo thus obscuring the desired signal. As part of the effort to develop a multi-axis electron beam transport system using transverse electromagnetic stripline kicker technology [1,2], it is necessary to precisely determine the position and extent of long high energy beams for accurate beam position control (6 - 40 MeV, 1 - 4 kA, 2 microsecond beam pulse, sub millimeter beam position accuracy.) The kicker positioning system utilizes shot-to-shot adjustments for reduction of relatively slow (< 20 MHz) motion of the beam centroid. The electron beams passing through the diagnostic systems have the potential for large halo effects that tend to corrupt position measurements.

1 INTRODUCTION

The constraints dictated by these beam diagnostic requirements indicate a system that has the advantage of only measuring high energy beams (such that sensitivity to intensity can be small). On the other hand, positional accuracy needs to be sub millimeter in order to define the outer bounds of the beam for determination of the correct transport parameters. As a result, a low Q structure allows for a faster response time and different parts of the beam will not effect the measurement of the beam position during later times. The completed diagnostic system involves a high accuracy beam position detection system, a data acquisition system, a computer controlled feedback system (to control the stripline kicker pulser waveforms) and the kicker pulsers themselves.

The precision beam position monitors are utilized as part of the kicker beam deflection system [3] which requires precise beam control to successfully position the beam through the subsequent output divergent septum beampipe. Accuracies of 0.5 mm are desirable for use with the kicker system and accuracies of 0.1 mm are needed for the proposed target system [3].

2 BASELINE BUG TESTING

As part of the development effort, the existing beam position monitors (a.k.a. BPM's or beam bugs) were tested to evaluate their long pulse performance. Since evolution

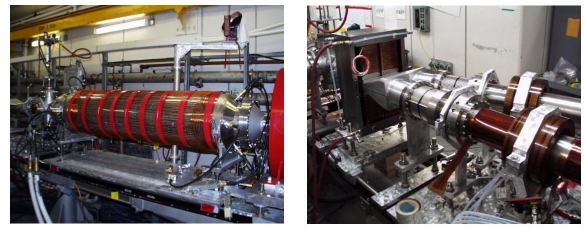

Figure 1. The quad stripline kicker (left) in the Experimental Test Accelerator (ETA-II) beamline as part of the verification experiments [3]. Downstream of the kicker, the deflected beam passes through the septum magnet (right) and into the divergent beam lines.

of the existing BPM's has been an on-going process for many years, they were used as part of the baseline experiments to determine the feasibility of using this type of design for long pulse efforts. Other designs used in beam position measurements were examined but these designs have compatibility problems with long pulse beams, with beams with high degrees of halo, or suffer from charge build up problems over the course of the beam pulse.

To simulate the long pulse beam, a pulser capable of several microseconds and kilovolts was used to drive the test stand. The stand consists of a tapered coaxial section

Figure 2. The beam position monitor test stand (left) used for measuring the accuracy and response of the various BPM's. The stand was driven by a variety of pulsers including a fast rise time pulser and a long pulse Velonex^{TM} pulser with capabilities above one kilovolt and beyond six microseconds (left).

on each end of the test stand. This provides an impedance match to 50Ω and exhibited excellent spectral uniformity agreeing to within 0.15 dB. These sections drive the straight section of beampipe which is offset to allow for displacing the current conductor with respect to the BPM. Displacements of up to one centimeter were examined. Displacements significantly beyond one centimeter cause

[1]Email: nelson18@llnl.gov

higher order modes to be established due to the beam pipe discontinuity at the displacement points. Note that the center conductor is fixed with respect to the tapered coaxial sections and so displacement of the BPM causes the center conductor to get closer to one side of the BPM thus simulating the displaced beam. One drawback of the Velonex™ pulser is its characteristic requiring a total output waveform integrating to zero. Thus, for the unipolar pulse there is a long baseline tail on the data. In this case, the decay rate for this tail has a time constant of 94 µs (its peak voltage is only 3% of the main pulse) but data beyond the main pulse should be ignored.

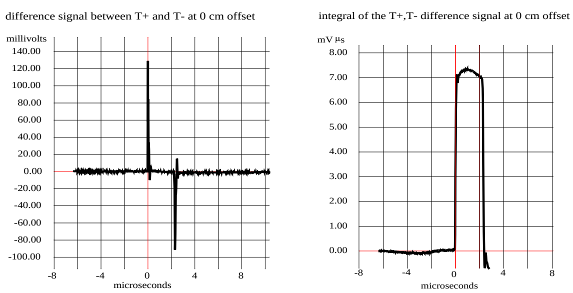

Figure 3. The waveform on the ***left*** *shows the difference signal between two opposite output ports on the BPM when the current carrying conductor is on-axis. This allows the performance of each channel to be calibrated before displacing the current carrying conductor; thus allowing for greater precision. The waveform on the* ***right*** *shows the integral. In this case, it corresponds to the positional error of this BPM and can be unfolded from the final data. [The hash in the waveforms on the left in figures 3 and 4 is a graphing artifact and is not representative of the noise in the signal. The noise is 2 mV. ed.]*

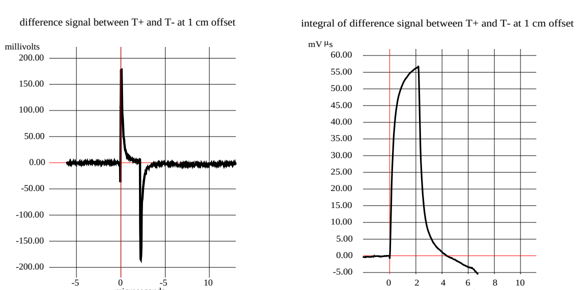

*Figure 4. Two channels on opposite sides of the BPM are acquired with a displacement of one centimeter . The difference is then computed (****left****) and the position is found by integrating (****right****). Notice that the vertical scale in Figure 4 is significantly different than that of Figure 3.*

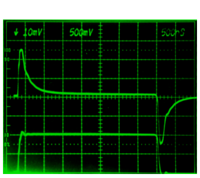

Figure 5. The region between the leading and trailing edge is magnified here exposing the baseline offset between the leading and trailing edges of the pulse.

Figure 5 shows a close up view of the differential signal with a one centimeter offset of the current conductor. Observe the baseline shift in the waveform which is caused by preferential coupling to the port closer to the current conductor. Acquiring each channel from the beam position monitor separately allows for greater control of the unfolding of the data. In the cases shown in Figures 3 and 4, the total waveforms are represented by 15,000 points with 30 points defining the rise time of the pulse.

3 BPM DESIGN AND TEST

3.1 Drawbacks of Existing BPM's

The existing test stand generates a maximum of twenty amps and so the saturation of the ferrite material is not an issue. But at an operating point of 1 - 4 kiloamps for 2 µs, a beam pulse would saturate the existing ferrite material simply due to the limited number of volt-seconds in the existing material. Likewise, the existing mechanical fabrication process for the BPM's involves several hand assembly steps as evident in the difference between on-axis signals shown in Figure 3. Although precise for a hand assembled component (appx. 1% position error due to assembly), greater precision between ports is desired in order to achieve the necessary beam position precision and to avoid extensive calibration unfolding after every data set.

As part of the effort, several other BPM concepts [4,5,6,7,8] were also considered. Although the test results for the existing beam position monitors in ETA-II looked encouraging, performance parameters for the long pulse beam test would saturate the ferrite material in the existing BPM's. Likewise, initial experimental evidence [9] indicates that thin films can survive direct exposure to 2 µs beams for profile measurements.

3.2 Unfolding BPM Position Data

To determine the position of the beam from the waveforms generated by the BPM's, it is necessary to take into account the calibration of each port of the BPM (both time and amplitude correction) and to remove differences between the port responses. The early time coupling effect comes from [9] with voltage V produced at a port

$$V(\theta, \rho, t = 0) = I_b K \frac{1 - \rho^2}{1 - 2\rho\cos\theta + \rho^2}$$

with the beam at relative displacement $\rho = r/r_a$ from the centerline (r_a = beampipe radius) and at an angle θ with respect to the port in question (0^o is directed toward the port). K is a calibration constant related to the resistance of the foil and may be determined using the on axis case, $\rho = 0$. The curves in figure 6 illustrate the variations for t=0; but expressions are available for general expressions in t.

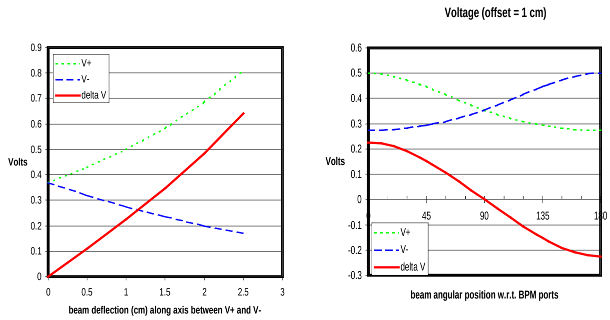

Figure 6. The various parameters of the received voltage are related to the position of the beam centroid in the beampipe. Note that the underlying equation assumes that the beam radius is small with respect to its displacement.

3.3 Design Parameters for Long Pulse BPM's

As a consequence, the design parameters for the long pulse high precision beam position monitors were determined to allow for a 2 µs beam pulse [10] at 2 kA. Since the skin depth for materials such as nichrome and stainless steel is 6 µm at 70 MHz, the thickness of the existing material can be expanded. 1 mil stainless steel foil, having a surface resistivity of 0.036Ω/square, yields a bulk resistance, R, of 3.4 mΩ across the portion of the foil exposed to the flux in the BPM

$$R = \frac{1}{\sigma_s \delta_s}\left(\frac{V_m \sigma_n \delta_n}{V_p / Z_0}\right)$$

where σ_s, σ_n are the conductivities for stainless and nichrome respectively, δ_s, δ_n are the skin depths (in this case the material thicknesses dominate so $\delta_s=\tau_s$, $\delta_n=\tau_n$), V_m, V_p were the voltages during the coefficient determination (0.37V and 1 kV respectively). V_p was fed into the Z_0 = 50Ω transmission line that drives the test stand.

4 CONCLUSIONS

The precision required as part of the operation of the kicker and target systems dictates a high precision beam position monitor with an accuracy between 0.5 and 0.1 mm. In the case of the kicker system, these BPMs must also be able to withstand a 2 µs long 2kA beam pulse. Initial results with the existing BPMs indicate that operation with a two microsecond beam at two kiloamps will be possible provided that:

1. Data is acquired from each BPM port separately. This allows the calibrations for each port to be unfolded from the data.

2. Measurements of the radiation effects on cables [11] indicate that several volts can be induced onto typical RF cables at high X-ray levels. However, for most applications there should be sufficient shielding around the various incidental X-ray sources.

3. Partition the vertical scale of the signal using multiple data acquisition systems. This may be necessary until reater dynamic range (more than 8 bits) is available from ommonly available high speed acquisition systems. The ade-off is signal-to-noise errors caused by the partitiong.

4. Time resolution from commonly available high speed cquisition systems is more than adequate for these appliations. It is important to get sufficient resolution on the ading edge of the pulse such that the rise time of the inteal is preserved. Self triggering on the received waveorm reduces jitter in the measurement.

5. Signal cables should be of sufficient quality to preserve the leading edge of the pulse. More importantly, they should be matched and low in dispersion in order to avoid problems during the difference calculations.

6. Although the range of currents over which the BPM must operate is large, the necessary precision at each current level can be different. Thus the low current levels used in the calibration process do not have to be single-shot acquisitions. The benefits of laser welded foils, made possible by the move to 1 mil stainless, are expected to alleviate some of the existing error in the BPMs caused by hand welding the 0.2 mil nichrome foils

5 ACKNOWLEDGMENTS

Thanks go to Jim Dunlap for his efforts and assistance efforts in performing the beam bug measurements. This work was performed under the auspices of the U.S. Department of Energy by the Lawrence Livermore National Laboratory under contract No. W-7405-Eng-48.

6 REFERENCES

[1] M. Burns, "DARHT Accelerators Update and Plans for Initial Operation," 1999 Particle Accelerator Conference (PAC99), New York, New York, USA, March 29 - April 2, 1999.

[2] Y. J. (Judy) Chen, "Precision fast kickers for kiloampere electron beams," 1999 Particle Accelerator Conference (PAC99), New York, New York, USA, March 29 - April 2, 1999.

[3] S. Sampayan, et. al., "Experimental investigation of beam optics issues at the bremsstrahlung converters for radiographic applications," 19th International Linear Accelerator (LINAC98) Conference, Chicago, IL, August 23-28, 1998, LLNL UCRL -JC-130417

[4] A. Hofmann, "Beam Diagnostics and Applications," Beam Instrumentation Workshop '98, SLAC, Stanford University, California, U.S.A., included as part of the American Institute of Physics Conference Proceeding 451.

[5] R. Lorenz, "Cavity Beam Position Monitors," Beam Instrumentation Workshop '98, SLAC, Stanford University, California, U.S.A., included as part of the American Institute of Physics Conference Proceeding 451.

[6] R. Jung, "Image Sensor Technology for Beam Instrumentation," Beam Instrumentation Workshop '98, SLAC, Stanford University, California, U.S.A., included as part of the American Institute of Physics Conference Proceeding 451.

[7] B. Fellenz and J. Crisp, "An Improved Resistive Wall Monitor," Beam Instrumentation Workshop '98, SLAC, Stanford University, California, U.S.A., included as part of the American Institute of Physics Conference Proceeding 451.

[8] K. W. Struve, "Electrical Measurement Techniques for Pulsed High Current Electron Beams," Measurement of Electrical Quantities in Pulse Power Systems-II, National Bureau of Standards, Gaithersburg, Maryland, March 5-7, 1986, LLNL UCRL-93261

[9] B. Carlsten, Los Alamos National Laboratory, THOR 2 microsecond facility used for DARHT component verification. Private communication.

[10] T. J. Fessenden, "Beam Bugs - Asymptotic Response," Lawrence Livermore National Laboratory, Beam Research Memo 88-8, February 2, 1988.

[11] M. Brubaker, "Optical Based Beam Position Monitor," Los Alamos National Laboratory, Private communication.

Status of the DELTA Synchrotron Light-Monitoring-System

U. Berges, K. Wille
University of Dortmund, Institute for Accelerator Physics and
Synchrotron Radiation, 44221 Dortmund, Germany

Abstract

A synchrotron radiation source like DELTA needs an optical monitoring system to measure the beam size at different points of the ring with high resolution and accuracy.

The measurements with the present synchrotron light monitors show that beam sizes larger than 250 μm can be measured. The measured emittance is of the order of the theoretical values of the optics and goes down to 8 nm rad. The magnification of the system can simply be increased by adding another lens to measure smaller emittances and beamsizes down to 100 μm. In this case you still have an optical image of the beam availiable, but sometimes the position of the camera has to be adapted due to the great magnification of the optical system. The image processing system which is based on a VME Framegrabber makes a two dimensional gaussian fit to the images from different synchrotron light-monitors.

First tests with monochromatic components of the synchrotron radiation (500 nm and 550 nm) and with short time cameras (shutter time down to 1/10000 s) have been performed. A two-dimensional PSD has been installed to measure slow beam motion. To measure small beam sizes, especially in the vertical plane, diffraction elements will be used.

This paper gives an overview over the present installation and the results.

1 INTRODUCTION

The **D**ormund **El**ectron **T**est **A**ccelerator facility DELTA consists of a 35 - 100 MeV LINAC, a 35 - 1500 MeV ramped storage ring called **Bo**oster **Do**rtmund (BoDo) and the electron storage ring called Delta (300 - 1500 MeV).

Both transverse beam sizes of the Booster and the electron storage ring Delta are measured by optical monitoring using synchrotron radiation from bending magnets and commercial CCD-cameras. Therefore, we installed several optical synchrotron radiation monitors at different points of the two rings (see figure 1). By using nearly dispersion free points of the storage ring, we are able to measure the transverse horizontal emittance down to 8 nm rad. Because of the not optimal orbit due to not optimal alignment of the magnets at the moment the beam size and emittance seems to be larger than the theoretical values.

In addition to the imaging system a photodiode is sometimes used at the synchrotron light monitor 1 to measure beam current. The results are in good agreement with the data of a BERGOZ PCT current monitor at Delta.

We also use a two-dimensional PSD at the synchrotron light monitors 2 (Delta) and 4 (BoDo) to measure slow beam motion.

2 DESIGN OF THE SYNCHROTRON LIGHT MONITORING SYSTEM

Two types of synchrotron radiation monitors both using the visible components of the synchrotron radiation are installed in the ring. One synchrotron light monitor of Delta reflects the optical part of the synchrotron radiation outside the shielding, so that parts of the optical system are accessable during runtime of the machine. The other synchrotron light monitors are completely inside the shielding.

2.1 *Synchrotron light monitor inside shielding*

This type of synchrotron light monitor is installed at the booster [1] and at the storage ring. Only the optical magnification of the systems is different because of the higher emittance of the booster and the corresponding beamsize. The synchrotron radiation coming from a bending magnet hits a copper mirror inside the vacuum. The optical part is reflected $90°$ in the vertical plane, the X-rays are absorbed. The mirror made of OFHC-Copper is mounted on a watercooled mirror holder and has optical quality for the visible region of the synchrotron radiation. Up to now no surface damage due to radiation or heat loading could be observed (315 mA average beam current @1.3 GeV and 170 mA @1.5GeV). After passing a vacuum quartz window the intensity of the synchrotron light can be varied by several neutral density filters (up to optical density 12.8 at the moment). The source point of the synchrotron radiation is focused on the CCD-camera. We achieve a magnification of 1.43 (Delta) respectively 0.14 (BoDo). Due to the magnification the alignment of the CCD-camera is critical. A computer driven mirror is installed so that the image of the beam on the CCD-Chip can be moved in both transverse directions as there is no access to the optical components during runtime of the machine because of the radiation protection. The longitudinal position of the camera is important to choose the correct focus point. It is adjustable during runtime of the machine. Because of the big depth of focus of the optical systems it is less critical.

The sensitivity of this synchrotron light monitor at Delta is high enough to detect the first turn. At BoDo this synchrotron light monitor works reliable at energies higher

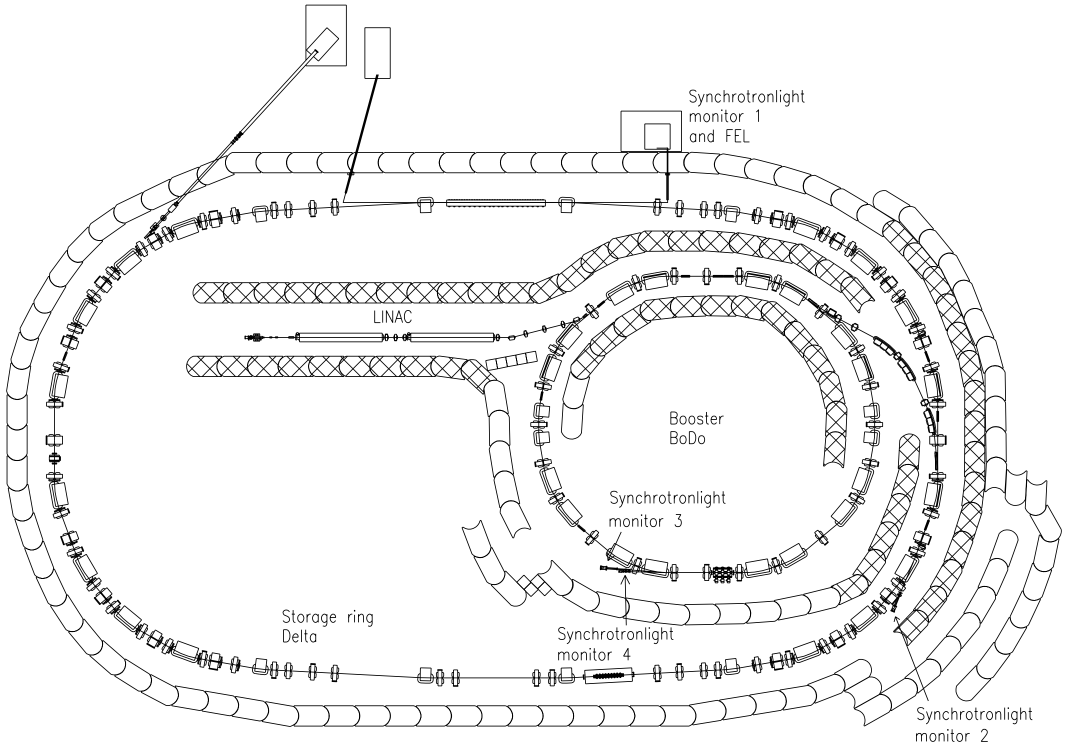

Figure 1: Positions of the Synchrotron Light Monitors at Delta

than 100 MeV. For lower energies the sensitivity is not high enough.

The advantage of these synchrotron light monitors is that the image is permanent available to the operator. Due to radiation protection beamshutters must be closed during injection time so that the image of the synchrotron light monitor outside shielding is then not available.

A two-dimesional PSD is installed at the same outlet chamber (synchrotron light monitor 4) with a magnification of 0.5 (achieved by a two lens telescope) to detect slow motion of the beam. All components are in the plane of the booster and show no radiation damage up to now. Only the vacuum quartz window becomes partly dark after 5 years of operation.

2.2 Synchrotron light monitor outside shielding

This synchrotron light monitor is installed at the end of one of the long straight sections of the storage ring. By varying the longitudinal position of the first lens it is possible to use also the spontaneous undulator radiation for diagnostic instead of the synchrotron radiaotion from bending magnets. It's design is shown in figure 2. The synchrotron radiation coming from a bending magnet hits a mirror inside the vacuum. The optical part is reflected 90° in the horizontal plane. The X-rays pass the mirror. This mirror is also used to reflect the spontaneous undulator radiation for the FEL-experiment FELICITA I. After passing a vacuum glass window the visible light crosses the shielding and is again refelected 90° in the horizontal plane. The source point of the synchrotron radiation is focused with a magnification of 0.13 by a lens (f = 1000 mm). The intensity of the synchrotron light can be varied by several neutral density filters (up to optical density 12.8) and by crossed linear polarizing filters. The synchrotron radiation is splitted. One part hits either a photodiode to measure the beam current or a 2-dimensional photosensitive detector (PSD) to measure the beam current and slow movements (below 10 kHz) of the beam simultaneously. The other part of the synchrotron radiation is focused by a second lens on a CCD-camera so that we achieve a magnification of 0.39. As this source point is nearly dispersion free the beam dimensions are less smaller than those expected at the synchrotron light monitor inside the shielding of Delta. So the magnification

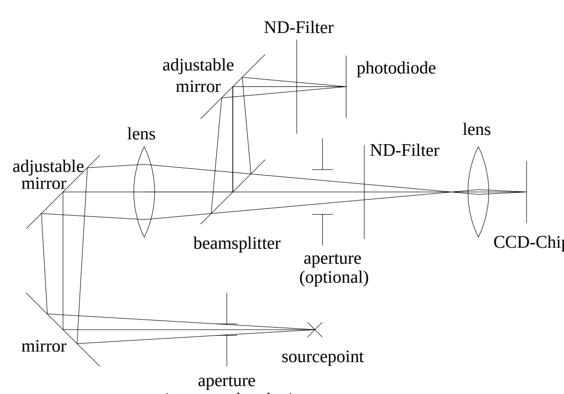

Figure 2: Schematic diagram of the DELTA synchron light monitor outside the shielding

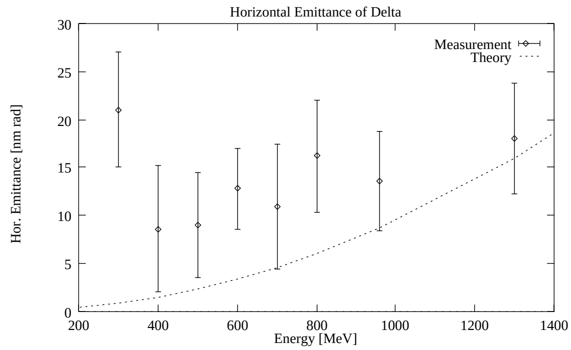

Figure 3: Horizontal Emittance of Delta versus Energy

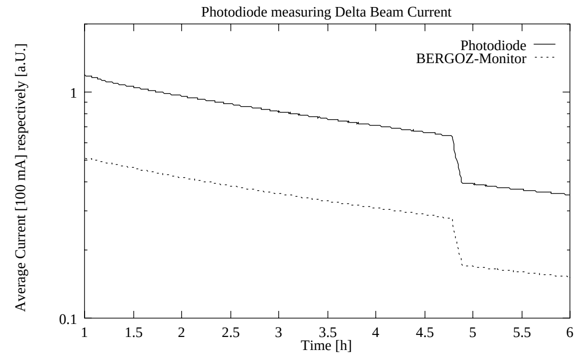

Figure 4: Average beam current of Delta measured by a photodiode and BERGOZ PCT

of the synchrotron light monitor outside the shielding is increased by a third lens to resolve the low vertical beamsizes if necessary. The alignment is done by adjustable mirrors outside the shielding. This synchrotron light monitor can even detect a few microamps of stored beam.

2.3 Image processing system

The video signal of the synchrotron light monitors can permanently be displayed on TV screens in the control room. An image processing based on the VME Framegrabber ELTEC IC40 is also done. It digitizes the images from the different synchrotron radiation monitors [2]. The software enables also a calibration of the optical magnification. It generates a gaussian fit to a chosen part of the image. This fit is made iteratively until the result is stable. The software calculates also the centre of the image and enables subtraction of a constant background or another image. The digitized image is stored on a harddisk of the HP Workstations.

3 RESULTS OF THE MEASUREMENTS

3.1 Delta

Beam size and emittance measurements have been done as a function of energy (see figure 3) with the actual optics. The magnification of the system has been checked by bumps with steering coils and by measuring the movement of the center of the beam due to changes of the RF frequency.

First investigations concerning beam widening because of increasing energy spread due turbulent bunch lenghening have successfully been performed [4].

The influence of monochromatic filters in the optical path of the synchrotron radiation was not measurable.

Also beam current measurements using a photodiode have successfully been performed (see figure 4).

First measurents with the PSD show significant beam motions up to 600 Hz. This is in good agreement with the measurements done by a short time CCD-camera with variable shutter times down to 1/10000 s.

3.2 BoDo

Beam size and emittance measurements have been done as a function of energy and time within a diploma thesis [3].

4 FUTURE IMPROVEMENTS

- The sensitivity of the BoDo synchrotron light monitor has to be inceased.
- The lifetime measurement using a photodiode or a PSD has to be installed permanently inside the shielding. The necessary hardware is being built.
- The image processing system has to be improved. Usage of the software has to be made more comfortable.
- The lower limit of the measured vertical beam size at Delta has to be determined. To improve the measurable vertical beam size special diffraction elements and monochromatic components of the synchrotron radiation can be used.

5 CONCLUSION

The present synchrotron light monitoring system at DELTA allows to measure beam sizes larger than 100 μm and emittance larger than 8 nm rad. The sensitivity is high enough to detect first turn. After improving the system a minimal beamsize of 50 μm and an emittance of 1 nm rad should be measurable.

6 REFERENCES

[1] U. Berges: ‘Lage- und Profilauswertung des Elektronenstrahls am Booster BoDo über Synchrotronstrahlung’, Diploma Thesis, University of Dortmund, Germany 1995

[2] M. Preuß: ‘Integration der Strahldiagnose mittels Synchrotronlicht in das Kontrollsystem von DELTA’, Diploma Thesis, University of Dortmund, Germany 1997

[3] C. Di Maio: ‘Messung der Emittanz am Booster Dortmund über Synchrotronstrahlung’,Diploma Thesis, University of Dortmund, Germany 1996

[4] K. Dunkel, private comunication, DELTA, University of Dortmund, Germany 1996

ROLE OF PRE-WAVE ZONE EFFECTS IN TR-BASED BEAM DIAGNOSTICS

V.A.Verzilov, INFN-LNF, CP 13, 00044 Frascati, Italy

Abstract

Transition radiation (TR) is nowadays intensively exploited by a number of techniques to characterize different beam parameters. These methods are based, sometimes implicitly, on standard formulae, and used often without paying due attention to their applicability. In particular, standard expressions are only first-order asymptotic, i.e., strictly speaking, valid at infinity. In this paper TR is examined in a spatial domain where conventional results are no more exact and variations in radiation properties are observed. Under certain conditions, for example, at long wavelengths or very high energies the effect is so considerable that should be taken into account in accurate beam measurements.

1 INTRODUCTION

Transition radiation is nowadays intensively exploited by a number of techniques to characterize different beam parameters. These methods are based, sometimes implicitly, on the standard theory of TR, whereas, often it is not fully applicable under conditions of measurements. Therefore, refinements of the theory become essential for both the design of experiments and interpretation of results.

There is a class of phenomena appearing because the electromagnetic field of a relativistic particle has quite macroscopic dimensions. In fact, while the particle itself can certainly be considered a point, its electromagnetic field occupies a finite space, outer border of which scales in the transverse (to the particle trajectory) plane roughly as $\lambda\gamma$, where λ is the radiation wavelength and γ is the relativistic factor. Since, eventually, the source of TR is the particle field interacting with the interface between two media, its size is that of the field. Strong variations in radiation properties are expected when $\lambda\gamma$ exceeds the dimension of a screen used to produce the radiation. Another relevant effect is that, the transverse extension of the TR source appears to be responsible for that the radiation needs to propagate over a substantial distance before acquiring all the well-known properties. Both effects may occur at the same time interfering with each other. In this paper an outline of the second problem is given along with the results of calculations related to applications in beam diagnostics.

2 THEORETICAL BACKGROUND

It is widely accepted that forward TR is formed over the so-called *formation length*, whereas, backward TR can be collected very close to the source. Meanwhile, as shown bellow, it is not always the case. Even backward TR evolves over a distance of the same order as the formation length of forward TR. This fact has to be taken into account in beam diagnostics, since backward TR is typically used in measurements and a space available for the experimental instrumentation is often limited by practical reasons.

Only in the *wave zone* the standard formulae can be used. The wave zone is treated in this paper as a spatial domain where the radiation field at any arbitrary point can be considered a plane wave. In other words, in the wave zone the source is seen as a quasi-point one. Therefore, the "border" of the wave zone is determined by the dimension of the source.

To make clear physical arguments we consider an extended coherent source of a radiation. Let O and S be

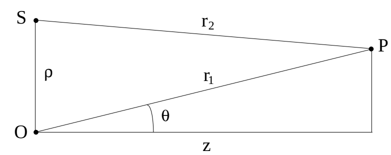

Figure 1: Waves emitted by two different points O and S of the source reach an arbitrary point P with a phase difference $\Delta\varphi = k(r_2 - r_1)$, where k is the wave vector.

two points on the source surface separated by a distance ρ (Fig. 1). Generally, waves emitted by these points at the same phase will arrive at an arbitrary observation point P with a phase difference $\Delta\varphi$. For all the source points between O and S to contribute at P fully constructively, the phase difference must be $|\Delta\varphi| \ll \pi$. Assuming the observation point to be far from the source, so that $z \gg \rho$, the above condition becomes

$$\left|\frac{\rho^2}{z} - 2\rho\theta\right| \ll \lambda \,. \qquad (1)$$

Thus, for the given distance z only a source region of the size ρ satisfying Eq. (1) forms mainly the field at P. On the other hand, to obtain a constructive interference from all the points of the source, the radiation must be collected far enough. It should be noted that in our definition, with ρ being the size of the source, Eq. (1) specifies the border of the wave zone. The obvious conclusion is the larger the dimension of the source the farther the wave zone from it.

For TR the size of the source is of the order of $\lambda\gamma$ and the characteristic angle of emission is $\theta \sim 1/\gamma$. This gives for the wave zone

$$z \gg \lambda\gamma^2 \,. \qquad (2)$$

Now we will touch upon the mathematical aspect of the problem. Let's consider backward TR emerging when a normally incident particle with a charge q and a velocity $v \to c$ hits a perfectly conducting infinite screen. In this case only transverse components of the field are essential and the spatial-spectral distribution of TR, that is the radiation power per unit of the frequency and per unit of the transversal area, valid at any distance (except, perhaps, very short ones), can be written in the form [1]:

$$\frac{\mathrm{d}^2W}{\mathrm{d}\omega\mathrm{d}\mathbf{u}} = \frac{q^2}{\pi^2c}|\Phi(u,w,\gamma)|^2\,, \qquad (3)$$

where dimensionless variables $u = k\rho$ and $w = kz$ are used and

$$\Phi(u,w,\gamma) = \int_0^\infty \frac{t^2\mathrm{d}t}{t^2+\gamma^{-2}}J_1(ut)\mathrm{e}^{\mathrm{i}w\sqrt{1-t^2}}\,. \qquad (4)$$

At large distances $w \gg 1$ the integral in Eq. (4) can be approximated by the contribution from the vicinity of a single point where the derivative of the phase in the exponential vanishes. The size of the domain around this so-called "stationary" point t_s, giving the main contribution to the integral, is of the order of $1/\sqrt{w}$. When this quantity is much smaller then the range $0 \le t \le 1/\gamma$, within which the fractional part undergoes a maximum variation, the latter may be approximated by its value at t_s. Then Eq. (3), in turn, approximates the classical formula for TR. Therefore, for the standard theory to hold true a condition $1/\sqrt{w} \ll 1/\gamma$, that is fully equivalent to Eq. (2), must be fulfilled. It is worthwhile to note that, even in the wave zone, the standard expression is asymptotic, i.e. strictly speaking, valid at infinity.

At shorter distances, i.e. in the pre-wave zone, the solution of Eq. (3) differs from the standard one. The reason is that, for $w \le \gamma^2$, the poles $t = \pm\mathrm{i}/\gamma$ of the fractional factor turn out to interfere with the contribution from the stationary point. Therefore, a proper account of these singularities should be taken in the complex plane. However, a detailed analysis of the problem goes beyond the scope of this paper. Instead, in the following, we give the results of numerical calculations based on Eq. (4), aiming to demonstrate the role of pre-wave zone effects in beam diagnostics.

3 EFFECT ON THE TR ANGULAR DISTRIBUTION AND RELATED BEAM DIAGNOSTICS

The angular distribution of TR can be used to obtain an information about the beam energy and beam angular divergence [2, 3]. This technique seems to be attractive, since, it does not require dispersive sections and can be performed at any position along an accelerator. Characterizing capabilities of the method, we note that in [3], when measuring the variation of the beam energy along the macropulse at TTF, a relative accuracy of the order of 1.5 % was achieved though conditions were not optimized for the measurements.

The beam energy measurements are based, essentially, on such a property of TR as the position between the central depth and the peak that is $1/\gamma$ according to the standard theory. Meanwhile, if measurements are performed in the pre-wave zone, this is no longer true.

To obtain an angular distribution from the spatial one, in Eqs. (3) a new variable $x = u/w\gamma$ is introduced. In relativistic regime $x \approx \theta\gamma$. An advantage of use of this variable is that all the results given below are independent of the beam energy.

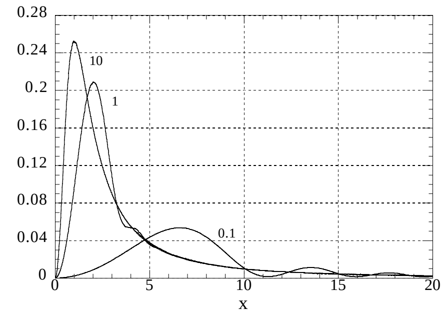

Figure 2: TR angular distribution $\frac{\pi^2c}{q^2}\frac{\mathrm{d}^2W}{\mathrm{d}\omega\mathrm{d}\mathbf{x}}$. Numbers by the curves are distances w from the screen in units of γ^2

Fig. 2 shows TR angular distributions at different distances from the emitting screen. While at $w = 10\gamma^2$ the angular distribution is quite consistent with the classical form, at $w \le \gamma^2$ the difference is significant. The distribution changes its form and becomes wider. Fig. 3 shows

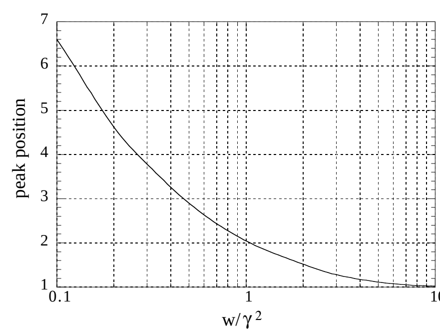

Figure 3: Peak position versus the parameter w/γ^2.

the the angular peak position x_{peak} with respect to the center $x = 0$ as a function of the distance from the source. As seen, the distance between the peak and the center increases very rapidly with decreasing w in the region $w \le \gamma^2$.

Thus, in the pre-wave zone the TR angular distribution differs from the classical one and can affect beam energy measurements. Since such kind of measurements are normally performed for visible light, the effect should be measurable from $\gamma \sim 1000$ and higher.

4 EFFECT ON TR SPECTRA IN BUNCH LENGTH MEASUREMENTS

Recently, a capability of methods based on coherent transition radiation (CTR) to measure the length of ultra-short bunches has been demonstrated. In this technique [4] the bunch longitudinal dimension can be extracted from the measured CTR spectrum if that of incoherent TR is precisely known. In the case of the classical flat incoherent spectrum, the spectrum of CTR is directly proportional to the bunch form-factor.

It has been also recognized that there are practical factors as the detector bandwidth, diffraction, etc., that cause losts in the low-frequency part of spectra thus leading to a considerable uncertainty in the bunch length determination. The corresponding analysis for effects of diffraction and the size of the emitting screen on bunch length measurements was given [5].

As shown below, spectra of TR, collected in the prewave zone, are distorted at low frequencies and, thereby, become a limiting factor in bunch length diagnostics. Fig. 4 presents spectra of TR calculated for ”detectors” of different apertures located at 1 meter from the screen for a wavelength range typical in bunch length measurements. Spectra are normalized to corresponding classical flat spectra. All the spectra exhibit a reduction in the intensity for long wavelengths. The effect is weaker for larger detector apertures and becomes clearly marked for higher beam energies. The energy dependence of the spectra is due to the

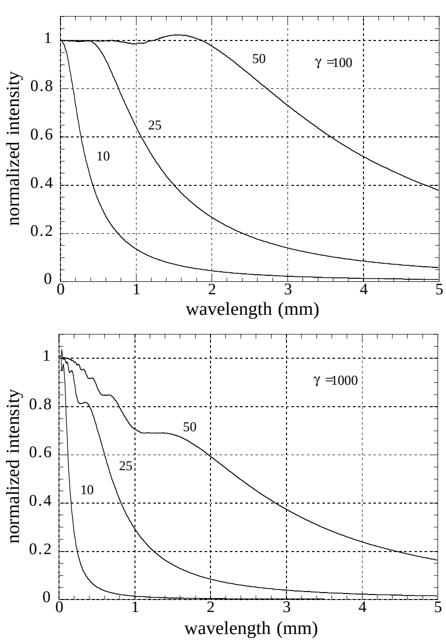

Figure 4: Spectra of TR at a distance of 1 m from the screen integrated over the ”detector” apertures given in millimeters next to the curves.

fact that the border of the wave zone moves very rapidly (quadratically) away from the screen with increasing the beam energy. At the same time, the dependence on the aperture shows that low frequencies are not fully lost; a redistribution of the frequency contents, as a result of interference, rather takes place, namely, the central part of the angular (or spatial) distribution is depleted with low frequencies. For the sufficiently large aperture all frequency components may be, in principle, collected.

In Fig. 5 spectra are given for the detector aperture of 25 mm, as it is placed at different distances from the screen. The distortion of the spectra becomes stronger with increasing either the energy or the distance. The unexpected,

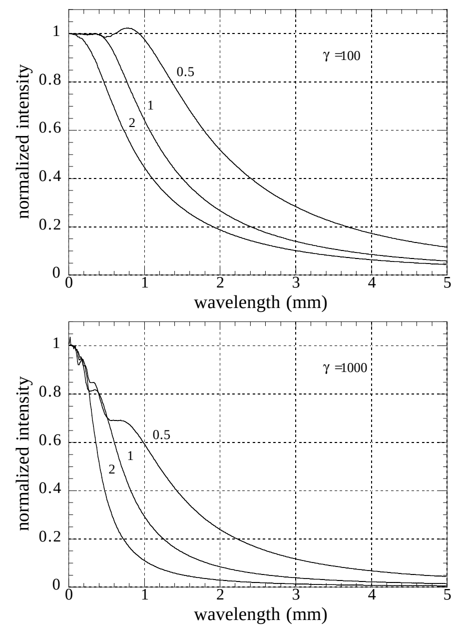

Figure 5: Spectra of TR at different distances (given in meters next to the curves) integrated over the ”detector” aperture of 25 mm.

for the first view, effect of the distance is a simple consequence of a variation in the detector angular acceptance. If the radiation is collected in a fixed cone the situation changes to the opposite one, namely, the distortion of the spectra becomes smaller with the distance increase.

5 CONCLUSIONS

Backward TR evolves over the distance comparable with the formation length of forward TR and acquires all the well-known properties only in the wave zone. In the prewave zone TR characteristics are quite different from the classical ones. This fact must be taken into account in TR-based beam diagnostics.

6 REFERENCES

[1] V.L.Ginzburg and V.N.Tsytovich, *Transition radiation and transition scattering* (Adam Higler, Bristol, 1990).

[2] D.Giove et al.,*Optical Transition radiation measurements on the elettra linac*, Proc. of 1997 PAC.

[3] M.Castellano et al.,*Time resolved energy measurement of the TESLA test facility beam through the analysis of optical transition radiation angular distribution* , Proc. of 1999 PAC.

[4] W.Barry, AIP Conference Proceedings 320 (1997) 173.

[5] M.Castellano et al., Preprint LNF-99/005(P).

A METHOD FOR MEASUREMENT OF TRANSVERSE IMPEDANCE DISTRIBUTION ALONG STORAGE RING

V. Kiselev, V. Smaluk, BINP, Novosibirsk, Russia

Abstract

A new method for measurement of transverse couple impedance distribution along storage ring is described. The method is based on measuring of a closed orbit deviation caused by local impedance. Transverse impedance acts on the beam as a defocusing quadrupole, strength of which depends on the beam current. If a local bump of closed orbit has been created at the impedance location, then the orbit deviation occurs while varying the beam current. The local impedance can be evaluated using the orbit deviation measured. Measurement technique is described, the method accuracy is evaluated. The method described was successfully used for measurement of the impedance distribution along the VEPP-4M storage ring.

1 INTRODUCTION

The impedance approach is widely used to describe interaction of bunch particles with induced wake fields. In this case, vacuum chamber is considered as set of sections with frequency dependent impedance.

Knowledge of impedance allows qualitative estimates and predictions of the beam stability, and evaluation of the instability thresholds and increments. Calculation of impedance for complex vacuum chamber is quite a cumbersome problem, which should be solved at the initial stage of accelerator design. Since the accelerator was already built, measurement of the impedance and its distribution along the ring makes possible an explanation of various collective effects observed.

There are precise methods to measure some integral characteristics of the impedance.

So, by measuring energy loss factor and current dependence of bunch length one can evaluate integral values for both resistive and reactive components of longitudinal impedance. The resistive component of transverse impedance can be found from measurements of decrement of fast damping of coherent betatron oscillations. The reactive component of transverse impedance can be found by measuring current dependence of coherent betatron frequency shift [1,2].

Methods for measurement of local impedance using beam orbit measurement system are developed and successfully used in CERN [1]. So, distribution along the ring of the resistive component of longitudinal impedance one can obtain by calculation of the difference of two radial orbits measured with different current values. Measurement of betatron phase advance on pickups gives distribution of the reactive component of impedance. These methods yield impressive results if the total effects measured are rather big and much greater than pickup coordinate resolution and accuracy of betatron phase measurement. There are 300 µm of the orbit deviation and 30º of the phase advance for LEP. Terminal number of sections having impedance simplifies matters. For LEP, as for the most of modern accelerators, major part of total impedance is determined by high order modes (HOM) of RF cavities, placed in one or two straight sections.

Our attempts to use these methods at the VEPP-4M had failed, firstly because of the effect predicted is an order less than at LEP, secondly because the impedance structure differs essentially from the LEP one.

The main contribution into the total impedance of the VEPP-4M [2] is made by about 50 places of violation of vacuum chamber homogeneity like sharp change of cross section or ceramic insert, and 16 vertical electrostatic separators and 3 radial ones. All of them are mainly placed in the technical and experimental straight sections and in the half-ring inserts, and results in TMC-instability of vertical motion. The radial aperture is more than twice larger than the vertical one, and collective effects are 5 times weaker.

To solve the problem a new method for impedance measurement was developed.

2 BASIS OF THE METHOD

A possibility to measure impedance of an individual section is based on the following assumptions.

By comparing the expression for coherent shift of betatron frequency [2]:

$$\Delta Q = -\frac{1}{8\pi} \cdot \frac{I_a \cdot \langle Z_\perp \beta \rangle}{E/e}$$

with the formula for small detuning of betatron frequency by an additional defocusing force:

$$\Delta Q = -\frac{1}{4\pi} \cdot \frac{\Delta Gl}{H\rho} \cdot \beta$$

one can conclude that the product of an amplitude value of bunch current I_a by the transverse impedance $Z_\perp$ is the defocusing lens strength ΔGl. Current dependence of this strength indicates a possibility of its switching on/off. If at the lens location we induce the local distortion of closed orbit (bump) and then compare two orbits measured with the lens switched on (large current) and switched off (small current), we obtain the orbit deviation in the form of a wave propagating from the lens location.

Amplitude of the wave:

$$\Delta y(s) = \frac{\Delta I_a \cdot Z_\perp}{4 \cdot (E/e) \cdot \sin \pi Q} \cdot \sqrt{\beta \cdot \beta(s)} \cdot y$$

where ΔI_a is the amplitude current difference, β is the beta function at the bump location, gives information about the transverse impedance value $Z_\perp$ of the section where the bump y is located.

Note, that a limitation of the bump length exists. It is desirable that betatron phase advance $\Delta\psi$ for the bump length will not exceed π. Otherwise if there are two sections with equal values of impedance at the bump and phase advance between the sections is $\Delta\psi = \pi$, then the wave amplitude outside the bump will be $\Delta y(s) = 0$, and all the orbit deviation will be at the section of bump. Because of small number of pickups at this section the measurement accuracy will be poor.

Let's estimate a value of the effect. If the whole impedance of a ring would be located in one place, the wave amplitude could easy be found from the expression for coherent tune shift value ($\sin \pi Q \cong 1$):

$$\Delta y_{\max} \cong 2\pi \Delta Q \cdot y$$

For the VEPP-4M, if $\Delta Q = 0.03$ and $y = 5$ mm, then $\Delta y = 1$ mm. Thus, the effect is notable enough even considering the fact that the impedance is distributed among the 50 places.

In reality, typical value of coherent tune shift is $\Delta Q \cong 0.8\nu_s$, where $\nu_s \cong 0.02$ is synchrotron frequency of the VEPP-4M. Therefore, to increase the effect, all the measurements have been performed with a feedback [3] switched on, the tune shift was $\Delta Q = 0.035$.

Frequency dependence of the impedance was not measured in these experiments, all the measurements have been done with the bunch length fixed, $\sigma_s \cong 8$ cm.

The question now arises of correct interpretation of the results measured by the method. Some results of theoretical study and numerical simulation can be used here.

For rotationally symmetric structure [4] like RF cavity, electromagnetic field can be expanded in the series of azimuthal harmonics, proportional to $\cos m\varphi$ and $\sin m\varphi$. The transverse impedance is proportional to:

$$Z_\perp \sim r_0^m \cdot r_1^{m-1}$$

The strongest impedance is determined by the dipole field harmonic ($m = 1$), and is proportional to the transverse position r_0 of the leading particle, but independent of the position r_1 of the test one.

For particles near the axis, higher harmonics can usually be neglected.

Thus, for measurement of impedance of axial symmetric structure, if the bump value is specified by 1/3 of the aperture, when the beam current is under threshold ($r_0 = r_1$), the orbit wave amplitude is determined only by dipole component of transverse impedance.

For rotationally non-symmetric structure but symmetric about coordinate plane, such as elliptic or rectangular vacuum chamber, separator plates, etc, the crossing terms in the field expansion arise, and notable part of transverse impedance is determined by quadrupole harmonic [5]. While the dipole harmonic always defocus the beam, the influence of the quadrupole harmonic is defocusing in one direction, but it is focusing in the orthogonal one. By this is meant that conclusion about impedance value can not be reached from single measurement in one direction, there is a need to measure dependence $Z_x = F(x, y)$.

For structure lacking any symmetry like pin SR collector, scraper, etc, conclusion about impedance can be made only if the field topography is measured detailed enough.

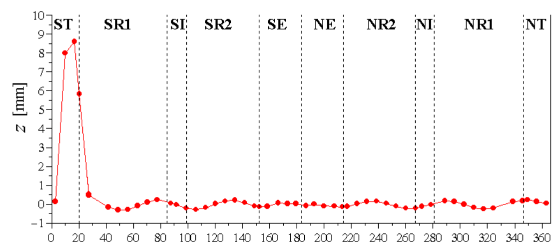

Figure 1: Vertical orbit bump.

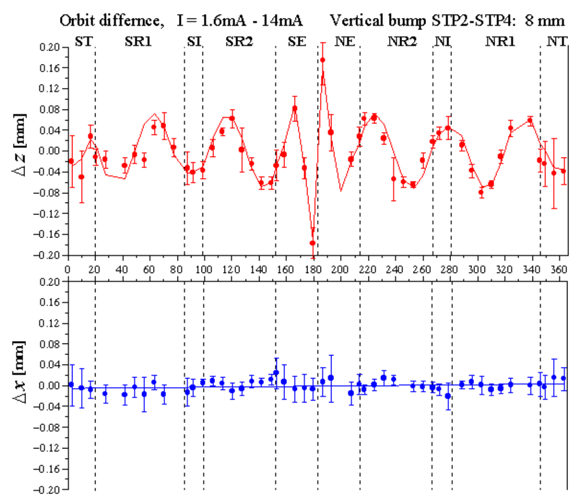

Figure 2: Orbit deviation: measurement and simulation.

3 MEASUREMENT TECHNIQUE

The impedance measurement procedure for some section of a ring consisted in the following. Prior to measurements the vertical and radial orbits were corrected to zero so that r.m.s. deviation would not exceed 0.5 mm. The orbit is measured and memorized at two current values: the maximum (15÷20 mA) and the minimum (of the order 1 mA). Then, the local vertical orbit distortion was produced on the measuring section (Fig.1) and orbit measurement were performed at two different current values close to those given above.

A difference of two vertical orbits measured with and without a bump at the ST section is shown in Fig.1. There are pickup data versus the VEPP-4M azimuth. The VEPP-4M is a mirror-symmetrical racetrack storage ring with the 366 m circumference. The ring consists of: the technical straight section NT-ST; the half-rings SR, NR with the inserts SI, NI; and the experimental straight section SE-NE with mini-beta insert in the centre. The azimuth zero is in the centre of the technical straight section NT-ST.

The bump shown in Fig.1 is in the section included 3 vertical electrostatic separators, 3 of 5 RF cavities, and 5 sections with the vacuum chamber inhomogeneity.

The difference of the four orbits measured as described above enables us to eliminate errors caused by non-linear characteristics of pickups and their current dependencies. This orbit difference is pure effect determined by an integral value of beta-weighted transverse impedance of the section of bump location.

Fig. 2 shows such the differences of vertical and radial orbit measured by pickups when the 8.5 mm vertical bump (Fig.1) was induced. There are error bars in Fig.2, which sizes correspond to measured values of pickup resolution [6]. R.m.s measurement error is about 20 µm. The results of numerical simulation are also shown in Fig.2 (solid line). This provides possibility to determine the beta-weighted impedance value $<Z_\perp\beta_z>$ on the bump length. In this case it is $<Z_\perp\beta_z>\cong 2.1$ MΩ.

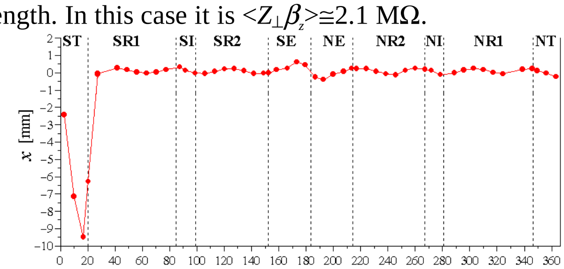

Figure 3: Radial orbit bump.

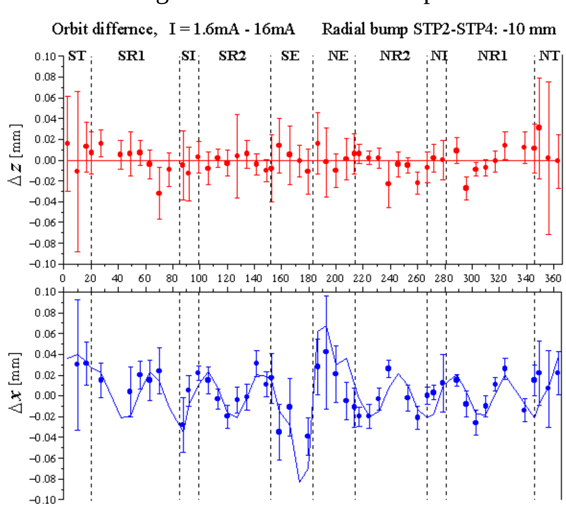

Figure 4: Orbit deviation: measurement and simulation.

To evaluate the contribution of HOM of RF cavities into the impedance value, a radial bump (Fig.3) was induced and the orbit differences were measured (Fig.4).

Unlike Fig.2 the vertical orbit deviation do not give a significant information, but the radial one is a wave, amplitude of which corresponds to the impedance value of HOM of the 3 RF cavities: $<Z_\perp\beta_z>\cong 0.7$ MΩ.

If a radial bump was induced in other places of the ring, there was not a considerable effect, unlike a vertical bump.

4 EXPERIMENTAL RESULTS

Since the orbit bump has a finite length, it is convenient to introduce the notion of specific beta-weighted impedance per unit length: $\Delta<Z_\perp\beta_z>/\Delta s$. Figure 3 shows the $\Delta<Z_\perp\beta_z>/\Delta s$ distribution along the VEPP-4M storage ring measured by the method described above.

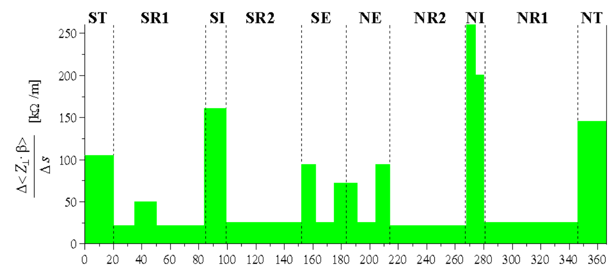

Figure 5: Distribution of the VEPP-4M impedance.

As is expected, the main contribution into the total impedance of the VEPP-4M is made by the vacuum chamber inhomogeneities in inserts (SI, NI) technical section (NT-ST) and experimental section (SE-NE). The half-rings are rather smooth except for the section on azimuth s = 40 m where the local limitation of vertical aperture is observed.

5 CONCLUSION

The method described is rather universal, it provides beam-based measurements of two-dimensional topology of wake field which acts on a bunch at the orbit bump location. The data measured can be used to obtain a harmonic set of local transverse impedance. Frequency dependence of the impedance can also be measured if bunch length is varied.

REFERENCES

[1] A.Hoffmann, “Impedance Measurement, Computation and their Interpretation”, Proc. of EPAC’96.

[2] V.Kiselev, V.Smaluk, “Experimental Study of Impedances and Instabilities at the VEPP-4M Storage Ring”, Proc. of EPAC’98.

[3] G.Karpov, V.Kiselev, V.Smaluk, N.Zinevich, “The Fast Head-Tail Instability Suppression in Multibunch Mode at VEPP-4M”, These proceedings.

[4] T.Weilland, “Comment on Wake Field Computation in the Time Domain”, NIM, 216(1983).

[5] S.Heifets, A.Wagner, B.Zotter, “Generalized Impedances and Wake in Asymmetric Structures”, SLAC/AP110, Jan 1998.

[6] A.Kalinin, V.Smaluk, “Data Processing for Turn-by-turn Beam Position Monitor”, Proc. of HEACC’98.

Appendices

List of Authors

Bold papercodes indicate primary authors

Institutes List

BESSY
Berliner Speicherring-Gesellschaft für Synchrotronstrahlung mbH, Berlin, Germany
- Bakker, R.
- Georgen, R.
- Kuske, P.
- Kuszynski, J.

BINP
Budker Institute of Nuclear Physics, Novosibirsk, Russia
- Kalinin, A.
- Karpov, G.
- Kiselev, V.
- Smaluk, V.
- Zinvich, N.

CERN
Geneva, Switzerland
- Boccard, C.
- Bogey, T.
- Bosser, J.
- Bovet, C.
- Burns, A.J.
- Burtin, G.
- Camas, J.
- Colchester, R.J.
- Ferioli, G.
- Fischer, C.
- Gras, J.J.
- Hiller, H.
- Jackson, S.
- Jensen, L.
- Jones, O.R.
- Jones, R.
- Jung, R.
- Koopman, J.
- Koziol, H.
- LeGras, M.
- Manarin, A.
- Papis, J.P.
- Pignard, G.
- Rawnsley, W.
- Rossa, E.
- Rybaltchenko, K.
- Schmickler, H.
- Sillanoli, M.
- Surback, C.
- Søby, L.
- Vismara, G.
- Vouillot, J.M.
- Williams, D.J.
- de Vries, J.

CLRC
Daresbury Laboratory, Warrington, UK
- Dufau, M.J.
- Hill, S.F.
- Marks, N.
- Owen, H.L.
- Smith, R.J.
- Smith, S.L.

DELTA
Institute for Accelerator Physics and Synchrotron Radiation, University of Dortmund, Germany
- Berges, U.
- Jankowiak, A.
- Weis, T.
- Wille, K.

DESY
Deutsches Elektronen Synchrotron, Hamburg, Germany
- Baboi, N.
- Boster, J.
- Castro, P.
- Dohlus, M.
- Geitz, M.
- Hartwig, H.
- Holtkamp, N.
- Jöstingmeier, A.
- Nagl, M.
- Patteri, P.
- Tazzioli, F.
- Wendt, M.
- Willeke, F.

ELETTRA
Sincrotrone Trieste, Trieste, Italy
- Ferianis, M.

ESRF
The European Synchrotron Radiation Facility, Grenoble, France
- Joly, B.
- Naylor, G.A.
- Plouviez, E.
- Scheidt, K.
- Weinrich, U.

FNAL
Fermi National Accelerator Laboratory, Batavia, IL, USA
- Tassotto, G.
- Zagel, J.

FSU Jena
Institut für Festkörperphysik, Friedrich Schiller Universität, Jena, Germany
- Neubert, R.
- Vodel, W.

GSI
Gesellschaft für Schwerionenforschung, Darmstadt, Germany

- Dolinska, M.
- Domke, M.
- Eickhoff, H.
- Forck, P.
- Heymach, F.
- Hoffmann, T.
- Liakin, D.
- Meyer, U.
- Moritz, P.
- Peters, A.
- Reeg, H.
- Strehl, P.

IAP
Institut für angewandte Physik der Johann Wolfgang Goethe Universität
- Dölling, R.

IHEP
Institute for High Energy Physics, Protvino, Russia
- Limberg, T.
- Solodovnik, F.
- Wittenburg, K.

IKP
Forschungszentrum Jülich GmbH, Jülich, Germany
- Dietrich, J.
- Keil, J.
- Mohos, I.

INFN-LNF
Laboratori Nazionali di Frascati dell'INFN, Frascati, Italy
- Castellano, M.
- Cianchi, A.
- Sannibale, F.
- Verzilov, V.A.

INFN-LNL
Laboratori Nazionali di Legnaro, Legnaro, Italy
- Milardi, C.
- Serio, M.
- Stella, A.

LANL
Los Alamos National Laboratory, Los Alamos, NM, USA
- Smith, M.T.
- Tomei, T.L.
- Wilmarth, J.E.

LLNL
Lawrence Livermore National Laboratory, Livermore, CA, USA
- Chen, Y.J.
- Fessenden, T.
- Holmes, C.
- Nelson, S.D.

MSI
Manne Siegbahn Laboratory Of Physics, Stockholm, Sweden
- Källberg, A.
- Simonsson, A.

PSI
Paul Scherrer Institut, Villigen, Switzerland
- Dehler, M.
- Jaggi, A.
- Pollet, P.
- Schilcher, T.
- Schlott, V.
- Uršič, R.
- deMonte, R.

RAL
Rutherford Appleton Laboratory
- Adams, D.J.
- Tilley, K.
- Warsop, C.M.

TRIUMF
Vancouver, Canada
- Boudsko, A.

Participants List

— A —

Finn **Abildskov**
University of Aarhus
fa@ifa.au.dk
Denmark

— B —

Nicoleta-Ionela **Baboi**
DESY
nicoleta@mail.desy.de
Germany

Ulf **Berges**
DELTA
Berges@delta.uni-dortmund.de
Germany

Torsten **Bergmark**
The Svedberg Lab.
torsten.bergmark@tsl.uu.se
Sweden

F **Boccard**
CERN
f.boccard@cern.ch
Switzerland

Claude **Bovet**
CERN
claude.bovet@cern.ch
Switzerland

Alan James **Burns**
CERN
alan.james.burns@cern.ch
Switzerland

— C —

Rainer **Cee**
Max-Planck-Institut für Kernphysik
r.cee@mpi-hd.mpg.de
Germany

Yu Ju **Chen**
LLNL
chen29@llnl.gov
USA

Andy **Chesworth**
Daresbury Laboratory
a.chesworth@dl.ac.uk
United Kingdom

Giovanni **Ciavola**
INFN-LNS
ciavola@lns.infn.it
Italy

Jim **Clarke**
Daresbury Laboratory
j.a.clarke@dl.ac.uk
United Kingdom

Daniel **Cocq**
CERN
daniel.cocq@cern.ch
Switzerland

— D —

Tommaso Eric **d'Amico**
CERN
Tommaso.DAmico@cern.ch
Switzerland

Jürgen **Dietrich**
Forschungszentrum Jülich GmbH
j.dietrich@fz-juelich.de
Germany

Rudolf **Dölling**
Paul Scherrer Institut
doelling@psi.ch
Switzerland

Michael **Dufau**
Daresbury Laboratory
m.j.dufau@dl.ac.uk
United Kingdom

Mike **Dykes**
Daresbury Laboratory
d.m.dykes@dl.ac.uk
United Kingdom

— E —

Hartmut **Eickhoff**
GSI
H.Eickhoff@gsi.de
Germany

— F —

Mario **Ferianis**
SINCROTRONE TRIESTE
ferianis@elettra.trieste.it
Italy

Gianfranco **Ferioli**
CERN
gianfranco.ferioli@cern.ch
Switzerland

Claude **Fischer**
CERN
claude.fischer@cern.ch
Switzerland

Peter **Forck**
GSI
p.forck@gsi.de
Germany

— G —

Terence **Garvey**
Laboratoire de l'Accelerateur Lineaire
garvey@lal.in2p3.fr
France

Marc Alexander **Geitz**
DESY
geitz@sun52a.desy.de
Germany

Jose Luis **Gonzalez**
CERN
jose.luis.gonzalez@cern.ch
Switzerland

Jean-Jacques **Gras**
CERN
jean.jacques.gras@cern.ch
Switzerland

Stephen Andrew **Griffiths**
Daresbury Laboratory
s.a.griffiths@dl.ac.uk
United Kingdom

— H —

Mark **Heron**
Daresbury Laboratory
m.t.heron@dl.ac.uk
United Kingdom

Cheryl **Hodgkinson**
Daresbury Laboratory
c.l.hodgkinson@dl.ac.uk
United Kingdom

Tobias **Hoffmann**
GSI
t.hoffmann@gsi.de
Germany

David **Holder**
Daresbury Laboratory
d.j.holder@dl.ac.uk
United Kingdom

Colin **Horrabin**
Daresbury Laboratory
c.w.horrabin@dl.ac.uk
United Kingdom

— J —

Heinz **Jakob**
CERN
heinz.jakob@cern.ch
Switzerland

Andreas **Jankowiak**
DELTA
jankowiak@delta.uni-dortmund.de
Germany

Lars **Jensen**
CERN
lars.jensen@cern.ch
Switzerland

Benoit **Joly**
ESRF
bjoly@esrf.fr
France

Roland **Jung**
CERN
roland.jung@cern.ch
Switzerland

— K —

Anders **Källberg**
Manne Siegbahn Lab.
kallberg@msi.se
Sweden

Tony **Kershaw**
CLRC Rutherford Appleton Laboratory
A.H.Kershaw@rl.ac.uk
United Kingdom

Jean Marc **Koch**
ESRF
jmkoch@esrf.fr
France

Heribert **Koziol**
CERN
heribert.koziol@cern.ch
Switzerland

Peter **Kuske**
BESSY
kuske@lenin.acc.bessy.de
Germany

Jens **Kuszynski**
BESSY
kuszynski@bii.bessy.de
Germany

— M —

Angelo **Manarin**
CERN
angelo.manarin@cern.ch
Switzerland

Fabio **Marcellini**
INFN Frascati
marcel@lnf.infn.it
Italy

Neil **Marks**
Daresbury Laboratory
n.marks@dl.ac.uk
United Kingdom

Ole **Marqversen**
CERN
ole.marqversen@cern.ch
Switzerland

Brian **Martlew**
Daresbury Laboratory
b.g.martlew@dl.ac.uk
United Kingdom

Giovanni **Mazzitelli**
INFN-LNF
mazzitelli@lnf.infn.it
Italy

Peter **McIntosh**
Daresbury Laboratory
p.a.mcintosh@dl.ac.uk
United Kingdom

Karl Hubert **Mess**
DESY
mess@desy.de
Germany

Istvan **Mohos**
Forschungszentrum Jülich IKP
i.mohos@fz-juelich.de
Germany

Peter **Moritz**
GSI
p.moritz@gsi.de
Germany

Andrew James **Moss**
Daresbury Laboratory
a.j.moss@dl.ac.uk
United Kingdom

G **Mrotzek**
Daresbury Laboratory
g.mrotzek@dl.ac.uk
United Kingdom

— N —

Graham **Naylor**
ESRF
naylor@esrf.fr
France

Scott **Nelson**
LLNL
nelson18@llnl.gov
USA

David **Norman**
Daresbury Laboratory
d.norman@dl.ac.uk
United Kingdom

— O —

Adrian **Oates**
Daresbury Laboratory
a.oates@dl.ac.uk
United Kingdom

Patrick **Odier**
CERN
patrick.odier@cern.ch
Switzerland

Hywel **Owen**
Daresbury Laboratory
h.owen@dl.ac.uk
United Kingdom

— P —

Jean-Pierre **Papis**
CERN
jean-pierre.papis@cern.ch
Switzerland

Andreas **Peters**
GSI
A.Peters@gsi.de
Germany

Eric **Plouviez**
ESRF
plouviez@esrf.fr
France

Patrick **Pollet**
Paul Scherrer Institut
patrick.pollet@psi.ch
Switzerland

Mike **Poole**
Daresbury Laboratory
m.w.poole@dl.ac.uk
United Kingdom

— Q —

Paul **Quinn**
Daresbury Laboratory
p.d.quinn@dl.ac.uk
United Kingdom

— R —

Ernst Ulrich **Raich**
CERN
ulrich.raich@cern.ch
Switzerland

Pantaleo **Raimondi**
CERN
pantaleo.raimondi@cern.ch
Switzerland

Hansjörg **Reeg**
GSI
h.reeg@gsi.de
Germany

VM **Rybin**
Moscow State Eng Physics Institute
rybin@aie.mephi.ru
Russia

— S —

Fernando **Sannibale**
INFN-LNF
sannibale@Inf.infn.it
Italy

Bertus Kees **Scheidt**
ESRF
scheidt@esrf.fr
France

Volker **Schlott**
Paul Scherrer Institut
volker.schlott@psi.ch
Switzerland

Hermann **Schmickler**
CERN
hermann.schmickler@cern.ch
Switzerland

Mario **Serio**
LNF-INFN
mario.serio@lnf.infn.it
Italy

Ansgar **Simonsson**
Manne Siegbahn Lab.
simonsson@msi.se
Sweden

Victor **Smaluk**
Budker Institute of Nuclear Physics
smaluk@inp.nsk.su
Russia

Rob. **Smith**
Daresbury Laboratory
r.j.smith@dl.ac.uk
United Kingdom

Susan **Smith**
Daresbury Laboratory
s.l.smith@dl.ac.uk
United Kingdom

Richard JE **Smith**
Daresbury Laboratory
r.j.e.smith@dl.ac.uk
United Kingdom

Lars **Søby**
CERN
lars.soby@cern.ch
Switzerland

Alessandro **Stecchi**
INFN-LNF
stecchi@lnf.infn.it
Italy

Angelo **Stella**
INFN Frascati
stella@lnf.infn.it
Italy

Peter **Strehl**
GSI
P.Strehl@gsi.de
Germany

Victor **Suller**
Daresbury Laboratory
v.p.suller@dl.ac.uk
United Kingdom

— T —

Gianni **Tassotto**
FNAL
tassotto@fnal.gov
USA

Franco **Tazzioli**
INFN
tazzioli@lnf.infn.it
Italy

Kevin **Tilley**
CLRC Rutherford Appleton Laboratory
k.tilley@rl.ac.uk
United Kingdom

Lidia **Tosi**
Sincrotrone Trieste
tosi@elettra.trieste.it
Italy

— V —

Viktor **Verzilov**
INFN-LNF
verzilov@lnf.infn.it
Italy

Giuseppe **Vismara**
CERN
giuseppe.vismara@cern.ch
Switzerland

Wolfgang **Vodel**
Friedrich Schiller University Jena
p7vowo@rz.uni-jena.de
Germany

Jörg **Voigtländer**
Forschungszentrum Rossendorf
j.voigtlaender@fz-rossendorf.de
Germany

— W —

Arden **Warner**
FNAL
warner@fnal.gov
USA

Christopher **Warsop**
CLRC Rutherford Appleton Laboratory
c.m.warsop@rl.ac.uk
United Kingdom

Manfred **Wendt**
DESY
wendt@ux-bello.desy.de
Germany

James E **Wilmarth**
LANL
wilmarth@lanl.gov
USA

Kay **Wittenburg**
DESY
Kay@pktr.desy.de
Germany

Andy **Wolski**
Daresbury Laboratory
a.wolski@dl.ac.uk
United Kingdom

Di **Wright**
CLRC Rutherford Appleton Laboratory
D.M.Wright@rl.ac.uk
United Kingdom

— Z —

James **Zagel**
FNAL
zagel@fnal.gov
USA

Production Notes

The DIPAC1999 proceedings volume and web site for JACoW were produced using the same scripts as DIPAC2001 and DIPAC2003.

The work on DIPAC 1999 for JACoW (Joint Accelerator Conferences on Web) was started in November 2004. It based on a proceedings volume in PDF which was available online from http://srs.dl.ac.uk/dipac/index.html (Nov. 2004). The proceedings volume was split into single paper contributions which were named as found in the workshop's timetable (IT for Invited Talks, CT for Contributed Talks, PS for Posters Sunday, and PT for Posters Tuesday). Each of these pdf files was then processed to conform to the JACoW standard paper size (see http://www.jacow.org/jacow/templates/templates.htm). The abstracts which are displayed on the web pages are the abstracts found in papers.

The scripts developed for JACoW conferences (see http://accelconf.web.cern.ch/accelconf/jacow/TM_2003_Trieste/slides/wrapper.pdf) depend on metadata in XML files. For the DIPAC1999 there were no such metadata readily available, so Brigitte Azzara, Andreas Peters, and Volker RW Schaa reconstructed the file by hand. The generated XML file consisted of 1355 lines of meta data describing each paper contribution. A PERL script was developed to read this XML file and transform it to <html>, \pdfTEX, and command files, providing all necessary means to generate the proceedings web site and conference proceedings.

A script run produced 226 pages for the proceedings web site (http://bel.gsi.de/dipac1999/). These pages consist of lists for *Sessions*, *Authors*, *Keywords*, and *Institutes* with all available cross links. All these pages are coded in UNICODE (UTF8), making math formulas and symbols in abstracts possible (no formulas in this conferences, but see for example abstract PT09, and PS07 for symbols), as well as showing the correct writing of names like **Uršič**. For alphabetic sorting of author names a rule based method is used honouring accented letters, umlauts, etc.

The script generated 53 pdfTEX wrappers for each single raw pdf-file, and one for the proceedings file. *Raw* pdf-files are papers conforming to the JACoW editor's guideline without page numbers, running title, and session names. A separate script generates for each pdf-file up to five keywords from the JACoW keyword list (five top most used keywords in the pdf-file). A pdfTEX wrapper transforms the raw pdf-file into one that has all hidden fields (*Title*, *Subject*, *Author*, *Keywords*) filled, in addition to page numbering, session names, and conference details.

No manual intervention of the script-generated pdfTEX file was necessary to achieve the printed output at hand. Embedding of division sheets between sessions, preface material, lists of authors, institutes, participants, papers, and affiliation details were configurable by means of a configuration file. The proceedings pdf-file, which can be downloaded from the proceedings web site (http://bel.gsi.de/dipac1999/papers/proceedings.pdf), features a completely cross-linked document with links from table of contents, list of authors, and institutes to papers.

The final version of the proceedings was made using pdfTEX (version 1.20a) with macro packages *pdfpages* (version v0.3e) and *fancyhdr* (version v2.1). Thumbnails for the pdf files have been generated using *thumbpdf* (version 3.7.1). All software is available from the TEXCollection 2004 (http://www.dante.de/software/cdrom/texcollection/ and http://www.tug.org/texlive/texcollection.html).

The script is supported by the SPMS (Scientific Program Management System) and will be available from the JACoW site.

December 2004
Volker RW Schaa